

Swansea University
Prifysgol Abertawe

Understanding Scale Growth on Carbon Steel Tubes During High Temperature Processing

Megan Elizabeth Kendall

Swansea University



Submitted to Swansea University in fulfilment of the requirements for the Degree of Doctor of Engineering

June 2025

Copyright: the author, Megan Elizabeth Kendall, 2025

Abstract

Conveyance tube manufacturing is a high temperature process which promotes rapid surface oxidation. During heat treatment, an oxide mill scale layer grows on tube surfaces. Inconsistent spalling of this layer from the outer tube surface contributes to yield loss, surface degradation, and tool wear. Experimental and theoretical studies of curved surface oxidation struggle to accurately recreate industrial processes. The computational thermochemistry software, Thermo-Calc©, was used to investigate external oxidation kinetics during conveyance tube manufacturing. A model was developed using the Stefan problem, tailored thermochemical databases, and a numerical solution to the diffusion equation. Particular attention was paid to geometric effects. There was strong agreement between oxide mass gain predictions by the model and equivalent thermogravimetric experiments. However, poor agreement between oxide thickness gain predictions by the model and industrial samples revealed scope for further work addressing transient heating, porosity, and thermomechanical manufacturing operations. Continuous oxide thickness data derived from the Thermo-Calc© model were used to evaluate thermal, growth, and manufacturing-related oxide stress. An Advanced Oxide Scale Failure Diagram (AOSFD), relating critical strain to instantaneous oxide thickness, was developed using these stress data. The AOSFD was used to demonstrate the impact of the transition to induction heating technology on oxide failure, namely improved electromagnetic control and changes to temperature control margins. Overall, this project demonstrates the use of computational techniques to predict geometry-specific oxide kinetics, and how the resulting data can be used to predict the mechanical state of the oxide. The continuous data presented are ideal for the development of an AOSFD which can predict how a given thickness of oxide will fail, if at all, depending on its strain state. The AOSFD is simple to use and therefore offers a practical tool for making informed decisions during conveyance tube manufacturing.

Declarations and Statements

This work has not previously been accepted in substance for any degree and is not being concurrently submitted in candidature for any degree.

Signed.....  .....

Date..... 23/06/2025.....

This thesis is the result of my own investigations, except where otherwise stated. Other sources are acknowledged by footnotes giving explicit references. A bibliography is appended.

Signed.....  .....

Date.....23/06/2025.....

I hereby give consent for my thesis, if accepted, to be available for electronic sharing

Signed.....  .....

Date..... 23/06/2025.....

The University's ethical procedures have been followed and, where appropriate, that ethical approval has been granted.

Signed.....  .....

Date..... 23/06/2025.....

Contents

Abstract i

Declarations and Statements ii

Acknowledgements vii

List of Figures ix

List of Tables xxiv

Publications xxvii

Nomenclature xxviii

Chapter 1 Project Context, Background, and Literature Review 1

1.1 Project Aim and Objectives 3

1.2 The Conveyance Tube Manufacturing Process 4

1.2.1 Materials Selection 4

1.2.2 Cold Forming 5

1.2.3 High-Frequency Induction Welding 5

1.2.4 Heat Treatment 9

1.2.5 Stretch Reduction 10

1.2.6 Descaling 13

1.3 External Oxidation of Iron 15

1.3.1 Scale Kinetics and Morphology 15

1.4 Mechanical Analysis of Oxide Scale during TMP 21

1.4.1 Adhered Scale Behaviour 32

1.4.2 Delaminated Scale Behaviour 34

1.5 Reactive Scale Management 41

1.5.1 Oxidation-Resistant Coatings 41

1.6 Proactive Scale Management 45

1.6.1 Manufacturing Parameter Control 45

1.6.1.1 Atmospheric Composition and Combustion Theory 45

1.6.1.2 Steel Grade and Composition 58

1.6.1.3 Geometry 68

1.6.2 Oxide Scale Failure Diagrams 76

1.6.2.1 Oxide Failure Diagram Considerations for Conveyance Tube Manufacturing 80

1.6.3 Study of Oxidation via Computational Techniques 91

1.6.4 Study of Oxidation via Experimental Techniques 96

1.7 Theoretical Foundations for the Computational Study of Oxidation 102

1.7.1 Diffusion Theory 102
1.7.2 Wüstite Thermodynamic Model 108
1.8 Conclusions following Literature Review 116
1.9 Thesis Structure 118
1.10 Research Flowchart 119
Chapter 2 Methodology 120
2.1 Experimental Techniques 120
2.1.1 Metallographic Preparation 120
2.1.2 Optical Emission Spectroscopy 126
2.1.3 Simultaneous Thermal Analysis 128
2.1.3.1 Thermogravimetric Analysis 129
2.1.4 Atmospheric Furnace Normalisation Replication 132
2.1.5 Electron Microscopy 134
2.1.6 Nanoindentation 137
2.1.7 X-ray Diffraction 139
2.1.8 White Light Interferometry 147
2.2 Computational Techniques 147
2.2.1 Numerical Integration 147
2.2.1.1 Crank-Nicolson Scheme 147
2.2.1.2 Composite Simpson's Rule 149
2.2.2 CALPHAD and Gibbs Free Energy Minimisation 150
2.2.3 Moving Phase Boundary Methodology 151
2.2.4 Molecular Dynamics 154
Chapter 3 Development of a Computational Model of Oxidation Kinetics Using Thermo-Calc© 157
3.1 Sample Characterisation 158
3.1.1 Materials 158
3.2 Model Definition and Development 165
3.2.1 User-defined Thermodynamic and Kinetic Databases 168
3.2.1.1 Thermodynamic Database 169
3.2.1.2 Kinetic Database 173
3.2.2 Computational Domain Definition 176
3.2.3 Microstructural Defect Pre-Processing 184
3.3 Initial Thermo-Calc© Model Results 197
3.3.1 Model Validation 199

3.4 Conclusions from Chapter 3 216
Chapter 4 Investigation of Effect of Curvature on Oxidation Using Thermo-Calc© 217
4.1 Oxidation for Cylindrical Geometry 218
4.1.1 Parametric Study 221
4.1.2 Volume Changes with a Moving Phase Boundary 228
4.1.3 Radial Dependency Study 232
4.1.4 Grain Boundary Effects 236
4.2 Validation 237
4.2.1 Microstructural Imaging 237
4.2.2 Thermogravimetry 246
4.3 Conclusions from Chapter 4 273
Chapter 5 Mechanical Modelling of Oxide Scale Stability 275
5.1 Application to Analytical Models 276
5.1.1 Thermal Stress in the Oxide 276
5.1.2 Growth Stress in the Oxide 291
5.1.3 Oxide Plastic Power Law via Nanoindentation 303
5.1.4 Manufacturing-Induced Stress Evaluation and Overall Experimental Validation using X-ray Diffraction 311
5.2 Mapping Stress in the Oxide 321
5.3 Conclusions from Chapter 5 321
Chapter 6 Development of an Advanced Oxide Scale Failure Diagram 323
6.1 Oxide Scale Failure Diagram Development 324
6.2 Application of the Advanced Oxide Scale Failure Diagram 330
6.2.1 Case Study: Tube Oxidation and the Transition to Induction Heating Technology 330
6.2.2 The Effect of Normalisation Temperature Control During Induction Heating 333
6.3 Conclusions From Chapter 6 343
Chapter 7 Conclusions 344
Chapter 8 Research Impact 347
8.1 Qualitative Impact Analysis 347
8.1.1 Materials and Waste Management 347
8.1.2 Manufacturing Technology and Plant Life 348
8.1.3 Industry 4.0 and Digital Steelmaking 349
8.1.4 Technology and Infrastructure Design for Decarbonisation 350
8.1.5 Product Perception 351

8.2 Quantitative Impact Analysis 351
Chapter 9 Future Work 353
9.1 Multi-Phase Oxide Boundary Modelling 353
9.2 Silicon and Its Interaction with Oxidation 353
9.3 Artificial Intelligence and Data-driven Technology Implications 355
9.4 Quantifying Thermofluid Phenomena during Thermogravimetric Analysis 357
Chapter 10 Appendices 358
Chapter 11 References 370

Acknowledgements

Dr Liz Sackett - am fraint i fod dan oruchwyliaeth rhywun sy'n rym natur pur. Mae dy agwedd bositif, ragweithiol, a phenderfynol wedi fy nghynnal dros bob eiliad o'r bennod unigryw hon. A pha le y baswn i heb dy arbenigedd ar draweffaith a pharatoi metalograffig?

Dr Michael Auinger - am bopeth. Nid yw geiriau'n ddigon i mi fynegi pa mor ddiolchgar ydw i am y rhan anferth dy fod wedi cyfrannu i'm prosiect. Rwyt ti wedi dod â'r heulwen i'm profiad efo dy drafodaeth academaidd frwdfrydig, cefnogaeth dechnegol ac emosiynol, a phersonoliaeth hyfryd. Diolch o galon.

Dr Mark Coleman - am rannu dy holl ddoethineb microsgopau efo fi. Nid ydw i'n credu y baswn i wedi dod o hyd i'm hyder yn y labordy heb yr holl ddysgu gennyt.

Dr Hollie Cockings - am fod yn gefn cadarn i mi trwy'r cyfnod tywyllaf. Ni faswn i wedi dod o hyd i'm nerth i barhau heb dy gymorth di. Diolch am gredu ynof.

Dr Chris Owen - am ddangos brwdfrydedd di-feth dros y prosiect wrth iddo esblygu a'm cefnogi efo dy holl wybodaeth ddiwydiannol.

M2A - am yr holl gyfleoedd gwerthfawr i archwilio a thyfu a'm cyfoedion bendigedig, **Ffyon Moody**, **Meg McNamee**, **Liam Haglington**, a **Sadaf Ali**, sydd wedi bod yn gefn parhaus i mi.

Coleg Cymraeg Cenedlaethol - am yr holl hyfforddiant a chyfleoedd yn fy mamiaith, a'm ffrindiau hyfryd, **Maisie Edwards**, **Alpha Evans**, ac **Emily Evans**, yng Nghangen Abertawe.

Evelyn Davis - am y cannoedd o alwadau fideo a'th gyfeillgarwch cariadus trwy'r da a drwg.

Ranmini Philomin - am fod y peth gorau i ddigwydd i mi yn fy mlwyddyn gyntaf yn Abertawe, er gwaethaf Covid a'n tŷ'n syrthio i deilchion. Diolch am helpu ac annog fi i gofleidio yn fy mhanda mewnol coch!

Ifan Llywelyn - am fod y ffrind mwyaf amyneddgar a charedig. Diolch am aros wrth fy ochr ar hyd y llwybr hwn.

Huw Kendall - am ddangos i mi sut i weld ochr ysgafnach bywyd. Mae dy agwedd positif ac anturus ar fywyd yn ysbrydoliaeth gyson i mi.

Nain (**Marie Walker**) - am yr holl erthyglau papur newyddion a cheisio ar bob cyfrif i ddeall pob agwedd o'm hymchwil! Diolch am roi i mi'r cariad diddiwedd a'r gwreiddiau Cymraeg sydd wedi fy siapio.

Mam a Dad (**Ann** a **Nigel Kendall**) - Mae eich cariad a gwerthoedd yn sylfaen ac angor i bopeth fy mod yn gwneud. Diolch o galon am eich ffydd ddi-feth ynof, eich anogaeth gadarn, a'r holl ffyrdd eich bod wedi fy nghadw ar y trywydd iawn mewn bywyd.

This research was funded by COATED M2A from the European Social Fund via the Welsh Government (c80816), the Engineering and Physical Sciences Research Council (Grant Ref: EP/S02252X/1), and Tata Steel UK Ltd.

Er cof am fy anwyliaid diweddar sydd yn parhau i fod efo mi mewn ysbryd - fy nhaid annwyl, ***Maurice Robert Walker****, a hefyd fy modryb ac ewythr cariadus,* ***Enis*** *a* ***James Acton****.*

Y tri ohonynt a'm bendithiodd efo eu cariad a ffydd mewn bywyd a thu hwnt, a chyflwynaf y gwaith hwn iddynt.

♥ Yn hafan gobaith hyd y wawr ♥

List of Figures

[¤ - figure created by author]

Figure 1.1: Schematic sequence of the conveyance tube manufacturing process ¤. 4
Figure 1.2: Fe-C binary system phase diagram generated, using Thermo-Calc© 2025a [33], for the region associated with the mass percent contribution of carbon stipulated by BS EN 10217-2 (<0.16%wt C for P235GH and <0.20%wt C for P265GH) [4] for conveyance tube steel grades ¤. 5
Figure 1.3: (a) Schematic diagram of high-frequency induction welding set up [40] (adapted from source) (b) Photograph of operational high-frequency induction weld set-up at TSUK Tubes site in Corby ¤. 7
Figure 1.4: Fe-C system phase diagram annotated to demonstrate effect of welding and heat treatment [32] (adapted from source). 7
Figure 1.5: Macrograph of the bulk (A), heat-affected (B), and weld (C) regions of high-frequency induction welded low carbon strip steel used in tube manufacturing [35]. 8
Figure 1.6: The isothermal transformation (TTT) and continuous cooling transformation (CCT) curves for the typical low carbon, low alloy steel grade used to manufacture conveyance tubes. The diagrams were generated in JMatPro® by Philip Addae as part of their MSc project work at Swansea University. The presentation of the diagrams has been adapted by the author of this thesis. 10
Figure 1.7: Radyne induction furnaces for tube normalisation [62]. 11
Figure 1.8: Chart correlating the power requirement (in kHz), based on the product of line speed, wall thickness, and HAZ width, to the voltage requirement for sufficient induction heating-based normalisation [41]. 12
Figure 1.9: Schematic showing how a multi-pass stretch reduction of a conveyance proceeds (adapted from source [63]). 13
Figure 1.10: Schematic of hydraulic (left) and mechanical (right) descaling techniques on a curved surface ¤. 14
Figure 1.11: (a) Annotated graph of scale thickness against time showing linear, mixed, and parabolic kinetic behaviour at different stages of oxidation, and (b) a schematic showing Wagner's parabolic oxidation model ¤. 16
Figure 1.12: Idealised, scaled representation of the multi-phase oxide layer evolved during normalisation ¤. 18
Figure 1.13: Scanning electron microscope image of approximately 150μm of oxide scale formed on low carbon steel at 975°C for 800s [77]. 19
Figure 1.14: Optical light microscope image of approximately 20μm of oxide scale formed on low carbon steel at 1000°C for 2.5s [71]. 20
Figure 1.15: Scanning electron microscope image of approximately 80μm of oxide scale formed on low carbon steel at 900°C for 12s. The cooling rate used was 5°C.min^{-1} [59]. 20
Figure 1.16: The development of stress and failure modes in oxide layers formed on curved surfaces [84]. 23
Figure 1.17: Comparison of dimensionless oxide thickness profile for Pilling-Bedworth ratios (PBRs) of (a) 1.0 and (b) 1.766 [85]. 26

Figure 1.18: Separation stress-temperature plot highlighting the transition from Mode I to II failure at a given temperature influenced by steel chemistry [77]..... 27
Figure 1.19: Backscattered electron microscope image of approximately 40μm of an oxide scale cross-section formed at 830°C for 300s, showing evidence of through-thickness transverse cracking [122]. 36
Figure 1.20: Backscattered electron microscope image of approximately 200μm of an oxide scale cross-section formed at 1150°C for 100s, showing evidence of through-thickness transverse cracking and the beginning of interfacial delamination initiating at the crack base and propagating along the steel-scale interface [122]. 36
Figure 1.21: Backscattered electron microscope image of approximately 100μm of an oxide scale cross-section formed at 1150°C for 100s, showing evidence of delamination within the oxide at a phase boundary [122]..... 37
Figure 1.22: SEM-EDS mapping of carbon (C), silicon (Si), and iron (Fe) contributions for a cross-section of carbon steel specimens coated using a silicon carbide (SiC)-based anti-oxidation coating and heated to 1000°C [136]. 44
Figure 1.23: Photograph of tube entering the gas-barrel normalisation furnace at TSUK Tubes site ¤..... 49
Figure 1.24: Graph of superstoichiometric combustion (air-fuel ratio) [147]..... 51
Figure 1.25: Scanning electron microscope image of 'Si16' silicon steel oxidised at 1200°C for 1 min in 15% humid layer (left) with an enlarged image of fayalite (right) [169]. 65
Figure 1.26: Scanning electron microscope image of approximately 40μm of oxide scale formed on ductile iron pipes [173]..... 66
Figure 1.27: An energy dispersive spectroscopy (EDS) line scan performed by Grant to characterise oxide scale phase on scale grown in atmospheric replication experiments on P195GH ('E41') [9]. 67
Figure 1.28: Raman spectra of central inner oxide layer from UE41 steel. Savitzky–Golay smoothing was applied of the second order polynomial [9]..... 68
Figure 1.29: XRD powder scan (2$\boldsymbol{\theta}$) of the Outer and Intermediate Oxide layer of UE41 steel and Reitweld refinement conducted to determine crystal structure present within the oxide layers [9]. 68
Figure 1.30: Schematic of an Advanced Oxide Scale Failure Diagram (AOSFD) developed by Schütze et al. [186]..... 76
Figure 1.31: Electron Back Scatter Diffraction (EBSD) phase diagram of the surface (A), intermediate (B), and interface (C) layers of oxide scale formed on low-alloy, high-strength steel [216]. 100
Figure 1.32: FCC wüstite crystal sub-lattice structure (left) annotated with octahedral and tetrahedral hole geometries (right) ¤. 110
Figure 1.33: A flowchart outlining the input and output of experimental, computational, theoretical, and literature-derived data at each stage of the project, including key equations for each stage of research ¤. 119
Figure 2.1: Metallographic mounting orientations for planar samples which are mounted in a 32mm diameter cylinder of thermosetting resin (Bakelite) for metallographic preparation and imaging ¤..... 121

Figure 2.2: Delaminated oxide fragments at the inner wall surface of a 15 nominal bore (n. b.) normalised tube sample ¤. 122
Figure 2.3: Air gap (highlighted in red) between the inner wall surface of a 20 nominal bore (n.b.) tube sample and its Bakelite thermosetting mounting resin ¤. 122
Figure 2.4: Intact oxide adhered to the steel and Bakelite at the outer surface of (a) 15 nominal bore (n. b.) and (b) 20 n.b. tube samples ¤. 123
Figure 2.5: Annotated photograph of oxidised 15 nominal bore (n.b.) conveyance tube mounted in a thin layer of polyester cold-set resin ¤. 126
Figure 2.6: GD-OES apparatus set-up (adapted from source) [264]. 127
Figure 2.7: Photograph of (a) NETZSCH STA 449 F3 Jupiter® simultaneous thermal analyser, (b) dimensioned 3mmx3mmx3mm coupons pre-heating, (c) E24 (top) and E41 (bottom) disintegrated coupons in their alumina crucibles post-heating ¤, and (d) enlarged image of crucibles mounted in the automatic sample changer which has a capacity of 20 coupons. Original images (a), (b), and (d) by J Grant [9]. 129
Figure 2.8: Carbolite Gero Ltd High Temperature TGA Tube furnace used to perform furnace replication experiments and obtain continuous thermogravimetric data ¤. 131
Figure 2.9: Technical drawing (taken from model TF1 16/100/450 furnace manual) of vertically mounted Carbolite Gero Ltd High Temperature TGA Tube furnace (model TF1 16/100/450) [272] (adapted from source). 131
Figure 2.10: Photographs of the novel atmospheric furnace box developed for a Nabertherm N 41/H furnace, to achieve a desired gas flow rate and stoichiometry to replicate normalisation experiments. The furnace box is show in its open (A), closed (B), and fully inserted with inlets and exhausts (C) position. Images taken by J Grant [9]. 132
Figure 2.11: Photograph (A) and schematic diagram (B) of the bespoke vortex mixing system designed in the work of Grant during their development of an atmospheric furnace. Images taken by J Grant [9]. 133
Figure 2.12: Typical set-up for a scanning electron microscope [275]. 134
Figure 2.13: Mounting of an X-ray spectrometer on to a typical electron column comprising a thermionic electron gun and electromagnetic lens system [278]. 136
Figure 2.14: Vickers indentation geometry specified in BS EN ISO 6507-1 [282]. 138
Figure 2.15: Diffraction of X-rays by a crystal lattice [286]. 140
Figure 2.16: Principal axes aligned with tube to obtain plane stress with $\sigma_3 = 0$ in the axial direction [286] (adapted from source). 141
Figure 2.17: The reflection used during the $\cos\alpha$ method [287]. 142
Figure 2.18: Conventional experimental set-up of a laboratory-based diffractometer [288]. 143
Figure 2.19: Schematic showing fully bonded steel-oxide interface with a layer, h_1, of oxide and a layer, $2h_1$, of steel both with their own respective mechanical properties ¤. 145
Figure 2.20: Schematic of the Crank-Nicolson (CN) scheme. Discretisation of the space-time ($x - t$) domain, to numerically determine the value of function, f, at nodes i and j, is achieved using finite difference expressions ¤. 148
Figure 2.21: Graphical representation of Simpson's rule ¤. 149

Figure 2.22: Graphical representation of composite Simpson's rule ¤. 150
Figure 2.23: Schematic showing the process of Gibbs Free Energy Minimisation in the context of Thermo-Calc© [301]. 151
Figure 2.24: Schematic showing the metal-oxide-gas system used to predict oxidation kinetics from diffusion theory ¤. 153
Figure 2.25: Schematic of the time and length scales of mechanical modelling techniques [309]. 154
Figure 2.26: Graphical representation of the Lennard-Jones potential, $U_{LJ}=U_{interatomic}$, showing how interatomic repulsion and attraction exist on either side of the minimum energy potential 'well' at a separation, $R = d_{atom}$, of 1.12 times the equilibrium separation, $\sigma = \sigma_{bond}$, (adapted from source) [311]. 155
Figure 3.1: Region of the overall research flowchart (see Figure 1.33) which is under discussion in this chapter. 157
Figure 3.2: Schematics of (a) tube product and (b) as-received nose crop samples of E41 grade steel, annotated with dimensions, carbon content, and mechanical properties (yield strength, σ_Y, ultimate tensile strength, σ_{UTS}, and ductility, ε) ¤. 159
Figure 3.3: Schematics of (a) tube product and (b) as-received nose crop samples of E24 grade steel, annotated with dimensions, carbon content, and mechanical properties (yield strength, σ_Y, ultimate tensile strength, σ_{UTS}, and ductility, ε)) ¤. 160
Figure 3.4: As-received nose crop samples of (a) E24, and (b) E41 ¤. 160
Figure 3.5: Relative uncertainty as a function of % mass content according to Weiss data [316]. 161
Figure 3.6: Phase diagram, generated using Thermo-Calc©, up to 0.5 mass percent carbon (0.5 wt% C) in E24 (P265GH). The major (by mass percent) alloying elements silicon (0.1800 wt% Si), manganese (0.9970 wt% Mn), phosphorous (0.0169 wt% P), sulphur (0.0056 wt% S), chromium (0.0310 wt% Cr) contributions were included based on the Optical Emission Spectroscopy results shown in Table 3.2. The carbon content measured was 0.1030 wt% C ¤. 165
Figure 3.7: Phase diagram, generated using Thermo-Calc©, up to 0.5 mass percent carbon (0.5 wt% C) in E41 (P235GH). The major (by mass percent) alloying elements silicon (0.0230 wt% Si), manganese (0.4560 wt% Mn), phosphorous (0.0110 wt% P), sulphur (0.0090 wt% S), chromium (0.0190 wt% Cr) contributions were included based on the Optical Emission Spectroscopy results shown in Table 3.2. The carbon content measured was 0.0940 wt% C ¤. 165
Figure 3.8: Equilibrium phase diagram of Fe-O system with the temperature thresholds for normalisation, T_{norm}, and stretch reduction, $T_{stretch}$, marked at 950°C and 800°C respectively ¤. 167
Figure 3.9: Fe diffusion coefficient for O diffusion in α, γ, and δ phases against reciprocal of temperature [100]. 175
Figure 3.10: Comparative plot of model convergence study quantitative central processing unit (CPU) data (left) associated with a given timestep for the initial oxide thickness, $\delta_{oxide,max\ predicted}$, (right) predicted by the model for planar samples soaked at 1000°C for 3 mins ¤ 178

Figure 3.11: Comparative plot of model convergence study quantitative central processing unit (CPU) data (left) associated with a given timestep for the initial oxide thickness, $\delta_{oxide,max\ predicted}$, (right) predicted by the model, with a new user-defined database, for planar samples soaked at 1000°C for 5 mins ¤. 181
Figure 3.12: Diagram depicting opposite direction, equal magnitude migration of boundaries during scale growth ¤. 182
Figure 3.13: Schematic of metal-gas phase boundary (pre-oxidation) with two boundary conditions applied in line with Hallstrom et al.'s study [234] ¤..... 183
Figure 3.14: Schematic of bulk and grain boundary regions described according to their low and high diffusivity respectively [364]. 185
Figure 3.15: Graphical description of Harrison's kinetic classification of diffusion regimes A, B, and C [364] (adapted from source). Arrows show changes in temperature, $\boldsymbol{T}$, and time, $\boldsymbol{t}$. 187
Figure 3.16: Comparison of oxide thickness gain, δ_{ox}, over time, $\boldsymbol{t}$, predicted without microstructural considerations (red) and using a kinetic database accounting for grain boundary diffusion of Fe within the substrate (blue) ¤. 189
Figure 3.17: Plot of the effect of grain size, $\boldsymbol{d}$, on effective diffusion, D_{eff}, (normalised against bulk diffusion, D_{bulk}) (left) and grain boundary volume fraction, $\boldsymbol{gk}$ (right) ¤. 191
Figure 3.18: Comparison of oxide thickness gain, δ_{ox}, with time, $\boldsymbol{t}$, predicted without microstructural considerations (red) and using a kinetic database accounting for grain boundary diffusion of Fe cations within the substrate and scale (wüstite phase) (blue) ¤..... 192
Figure 3.19: Comparison of oxide thickness gain, δ_{ox}, with time, $\boldsymbol{t}$, predicted using a kinetic database accounting for divalent (blue) and trivalent (red) cation vacancies, i.e. porosity ¤. 193
Figure 3.20: FEGSEM image of oxide formed on E41 heated to 1000°C during conveyance tube manufacturing at TSUK Tubes ¤. 195
Figure 3.21: FEGSEM image of oxide formed on E41 heated to 1000°C during conveyance tube manufacturing at TSUK Tubes ¤. 195
Figure 3.22: Comparison of oxide thickness gain, δ_{ox}, with time, $\boldsymbol{t}$, predicted using a kinetic database accounting for labyrinth effects, using a labyrinth factor, $f_{labyrinth}$,of 3 ¤. 197
Figure 3.23: Model oxide thickness, δ_{ox}, prediction, annotated with the calculated parabolic rate coefficient, $k_{p,thickness}$, for a 3mm thickness planar Fe surface soaked at 1000°C for a time, $\boldsymbol{t}$, of 5 minutes ¤. 198
Figure 3.24: SEM image of oxide, of average thickness 225±9µm, formed on 30x30mm E41 planar sample after replicating Grant's 'STCA1-STCA3' cycle - heating to 950°C for 30 mins in a 10% O_2-90% N_2 atmosphere ¤. 199
Figure 3.25: Thermal cycle ($\boldsymbol{T-t}$) used during STA validation experiments ¤. 200
Figure 3.26: Kinetic profiles for E24 (dotted line) and E41 (dashed line) samples used in STA investigation (1000°C, 5 minutes) in the form of overlayed oxide mass gain, $\Delta m_{ox,}$- time, $\boldsymbol{t}$, (based on mass-to-thickness conversion in Equation 3.35) and temperature, $\boldsymbol{T}$, -time plots ¤..... 201

Figure 3.27: Schematic showing assumed pre-, x_1, and post-oxidation, x_2, dimensions of post-oxidation samples in (a) isometric and (b) end views ¤. These dimensions are used to calculate the oxide thickness gain, δ_{ox} ¤. 202
Figure 3.28: Comparison of 1D geometry domain in Thermo-Calc© model (right) and the cubic simultaneous thermal analysis (STA) samples (left) ¤. 203
Figure 3.29: Diagram showing hypothetical extension of computational domain into the third dimension (right) for validation comparison with the real 3D simultaneous thermal analysis (STA) sample (left) ¤. 203
Figure 3.30: Comparative plot of mass gain, Δm_{ox}, following heating to 1000°C for a time, t, of 300s for Thermo-Calc© Fe model (red) vs. STA testing for E24 (green) and E41 (blue) tube grades, annotated with parabolic rate constant, k_p ¤. 206
Figure 3.31: Demonstration, on a plot of oxide mass gain, Δm_{ox}, against time, t, of how the isothermal heating region may exclude some of the parabolic heating region and lead to an inaccurate assessment of parabolic rate constant ¤. 210
Figure 3.32: Pearson correlation coefficient, r, result for E24 simultaneous thermal analysis (STA) data plot of oxide mass gain, Δm_{ox}, against time, t, ¤. 211
Figure 3.33: Pearson correlation coefficient, r, result for E41 simultaneous thermal analysis (STA) data plot of oxide mass gain, Δm_{ox}, against time, t, ¤. 212
Figure 3.34: Demonstration of lack of insight into linear and parabolic trends provided by both the Pearson correlation coefficient, r, and its square, r^2, for E24 simultaneous thermal analysis (STA) data plot of oxide mass gain, Δm_{ox}, against time, t, ¤. 212
Figure 3.35: Demonstration of lack of insight into linear and parabolic trends provided by both the Pearson correlation coefficient, r, and its square, r^2, for E41 simultaneous thermal analysis (STA) data plot of oxide mass gain, Δm_{ox}, against time, t, ¤. 213
Figure 3.36: Local gradient, m_{local}, plot for each datapoint of E41 simultaneous thermal analysis (STA) data ¤. 214
Figure 3.37: Local gradient, m_{local}, plot for each datapoint of smoothed E41 simultaneous thermal analysis (STA) data ¤. 215
Figure 3.38: Local gradient, m_{local}, plot for each datapoint of smoothed E41 simultaneous thermal analysis (STA) data compared to the original STA oxide mass gain, Δm_{ox}, against time, t, data ¤. 215
Figure 4.1: Region of the overall research flowchart (see Figure 1.33) which is under discussion in this chapter. 217
Figure 4.2: Geometry used for initial hollow cylindrical geometry set-up test [NOT TO SCALE] ¤. 218
Figure 4.3: Comparison of lower austenite interface position of zero, i.e. the origin, for planar case (left) and 35mm for the cylindrical (tube) case (right) during a three minute normalisation simulation in Thermo-Calc© ¤. 219
Figure 4.4: Plot of Thermo-Calc© model predicted oxide thickness, δ_{oxide}, against time, t, using a flat plate geometry (blue) and hollow cylinder geometry (red) at 950°C for three minutes ¤. 219
Figure 4.5: Plot of the absolute difference between predicted oxide thicknesses, δ_{oxide}, at corresponding datapoints for planar and cylindrical geometries, $|\delta_{oxide,planar} - \delta_{oxide,cylinder}|$, under identical thermochemical conditions. This figure

demonstrates the strength of the positive linear relationship (with a linear correlation coefficient, $R2$, of 0.999) between the difference, $|\delta_{oxide,planar} - \delta_{oxide,cylinder}|$, and the number of spatial datapoints solved¤.....221
Figure 4.6: Timestep profiles for planar and cylindrical geometries used in 950°C, 3min normalisation simulation ¤.....221
Figure 4.7: Dimensioned cross-sections of the three smallest products (15 n.b., 20 n.b., and 25 n.b.) supplied as part of the Install® Plus range. Dimensions are defined according to a set outer diameter and wall thickness. Wall thicknesses of the sample are 'heavyweight' ¤.....222
Figure 4.8: Bar charts highlighting the difference in Thermo-Calc© model predictions of thickness gain, δ_{ox}, mass gain per unit surface area, Δm_{ox}, and parabolic (thickness-based, $k_{p,thickness}$, and mass-based, $k_{p,mass}$) rate constant across the three sample geometries provided by TSUK Tubes, including a dimensional manufacturing tolerance of ±10% and using heavy weight wall thickness values ¤.....224
Figure 4.9: Graph showing the effect of wall thickness, r_{wall}, on Thermo-Calc© model predictions of thickness gain, δ_{ox}, mass gain per unit surface area, Δm_{ox}, and parabolic (thickness-based, $k_{p,thickness}$, and mass-based, $k_{p,mass}$) rate constant on a 21.3mm (15 n.b.) outer diameter, OD, tube ¤.....224
Figure 4.10: Graph showing the effect of wall thickness, r_{wall}, on Thermo-Calc© model predictions of thickness gain, δ_{ox}, mass gain per unit surface area, Δm_{ox}, and parabolic (thickness-based, $k_{p,thickness}$, and mass-based, $k_{p,mass}$) rate constant on a 26.9mm (20 n.b.) outer diameter, OD, tube ¤.....225
Figure 4.11 Graph showing the effect of wall thickness, r_{wall}, on Thermo-Calc© model predictions of thickness gain, δ_{ox}, mass gain per unit surface area, Δm_{ox}, and parabolic (thickness-based, $k_{p,thickness}$, and mass-based, $k_{p,mass}$) rate constant on a 33.7mm (25 n.b.) outer diameter, OD, tube ¤.....225
Figure 4.12: Graph showing effect of outer diameter, OD, (in the ±10% manufacturing tolerance range associated with 15 n.b., 20 n.b., and 25 n.b. tubes) on Thermo-Calc© model predictions of thickness gain, δ_{ox}, mass gain per unit surface area, Δm_{ox}, and parabolic (thickness-based, $k_{p,thickness}$, and mass-based, $k_{p,mass}$) rate constant. A medium weight wall thickness, r_{wall}, of 3.2mm was used ¤. 226
Figure 4.13: Graph showing effect of outer diameter, OD, (in the ±10% manufacturing tolerance range associated with 15 n.b., 20 n.b., and 25 n.b. tubes) on Thermo-Calc© model predictions of thickness gain, δ_{ox}, mass gain per unit surface area, Δm_{ox}, and parabolic (thickness-based, $k_{p,thickness}$, and mass-based, $k_{p,mass}$) rate constant. A heavy weight wall thickness, r_{wall}, of 4.0mm was used ¤. 226
Figure 4.14: Diagram showing changes in cylinder outer radius before (left) and after (right) surface oxidation (adapted from source) [89] ¤. 229
Figure 4.15: Graph showing the linear relationship between computer processing unit (computation time), CPU, and the number of datapoints, $N_{datapoints}$, required for the Thermo-Calc© model of oxidation kinetics for a cylindrical geometry ¤..231
Figure 4.16: Plots of volume gain, ΔV_{ox}, against tube inner radius, IR, (left) and its reciprocal (right) ¤. 233
Figure 4.17: Plots of mass-based, surface area normalised parabolic rate coefficient, $k_{p,mass}$, against tube inner radius, IR, (left) and its reciprocal (right) ¤. 234

Figure 4.18: Plot of model-predicted oxide thickness gain, δ_{ox}, for inner radii, ***IR***, in the range 0.5-1000mm, with an enlarged view of the dimension range associated with Tata's Install® Plus 235 products (heavyweight wall thickness) ¤. 235
Figure 4.19: Plot of predicted mass-based, surface area-normalised parabolic rate coefficient, $k_{p,mass}$, for inner radii, ***IR***, in the range 0.5-1000mm, with an enlarged view of the dimension range associated with Tata's Install® Plus 235 products (heavyweight wall thickness) ¤. 235
Figure 4.20: Plots demonstrating the effect of inner radius, ***IR***, changes on oxide thickness, δ_{ox}, predictions by the model with a hollow cylindrical geometry ¤. 237
Figure 4.21: Plots demonstrating the effect of inner radius, ***IR***, changes on mass-based, surface area-normalised parabolic rate coefficient, $k_{p,mass}$, predictions by the model with a hollow cylindrical geometry ¤. 237
Figure 4.22: As-received samples of Install® Plus tubes in the as-welded (left) and post-normalisation (right) condition ¤. 238
Figure 4.23: Machined sample ready for use in the thermogravimetric furnace, labelled with inner, ***ID***, and outer diameter, ***OD***, dimension definitions ¤. 238
Figure 4.24: Optical light microscopy images of the microstructure of 15 nominal bore (n.b.) tube samples in the bulk (top) and HAZ (bottom) at the pre- (left) and post-normalisation (right) stages ¤. 239
Figure 4.25: Schematic of three approximately equidistant locations used to take mean measurements of oxide thickness, δ_{ox}, for a 15 nominal bore (n.b.) tube having undergone normalisation at 1000°C for three mins ¤. 240
Figure 4.26: Secondary electron emission imaging of outer edge of 15 nominal bore (n.b.) tube pre-normalisation and post-weld ¤. 241
Figure 4.27: Stress diagram for beam in pure bending [82] (adapted from source). 242
Figure 4.28: Secondary electron emission imaging for outer edge of 15 nominal bore (n.b.) tube sample post-normalisation ¤. 243
Figure 4.29: Evidence of oxide raft slip in a 15 nominal bore (n.b.) sample normalised at 1000°C for 3 mins ¤. 243
Figure 4.30: Evidence of oxide raft slip in a 15 nominal bore (n.b.) sample normalised at 1000°C for 3 mins ¤. 244
Figure 4.31: Secondary electron emission image of spalled oxide at the inner edge of a 15 nominal bore (n.b.) tube sample post-normalisation ¤. 245
Figure 4.32: Annotated separation stress-temperature plot highlighting the transition from Mode I to II failure at a given temperature influenced by steel chemistry [77] (adapted from source). 245
Figure 4.33: Technical drawing (taken from model TF1 16/100/450 furnace manual) showing the incorporation of a mass balance into vertically mounted Carbolite Gero Ltd High Temperature TGA Tube furnace (model TF1 16/100/450) (adapted from source). 246
Figure 4.34: 20 nominal bore (n.b.) sample and nichrome wire during pre-testing mass assessment ¤. 247
Figure 4.35: Absolute difference between the thermocouple and furnace temperature data, $|T_{thermocouple} - T_{furnace}|$, with the isothermal soak region enlarged ¤. 248
Figure 4.36: Technical drawing (taken from model TF1 16/100/450 furnace manual) showing the incorporation of a mass balance and thermocouple into vertically mounted

Carbolite Gero Ltd High Temperature TGA Tube furnace (model TF1 16/100/450) (adapted from source [272]). 248
Figure 4.37: Plot of sample mass, $\boldsymbol{m}$, (left) and temperature, $\boldsymbol{T}$, (right) against time, $\boldsymbol{t}$, for a tube normalisation heat treatment replica thermal cycle on a 15 nominal bore (n.b.) tube sample ¤. 249
Figure 4.38: Schematic of the streamline profile induced during vortex induced vibration (VIV), within the furnace work tube, associated with laminar ($\boldsymbol{Re} \ll 200{,}000$), viscous ($0.1 < \boldsymbol{St} < 1$) thermally-induced gas flow around the sample blunt body. 251
Figure 4.39: Frequency spectrum, $\boldsymbol{f}$, for the isothermal period of a 1000°C normalisation heat treatment cycle on a 15 nominal bore (n.b.) steel conveyance tube ¤. 253
Figure 4.40: Ceramic furnace tube dummy sample (38mm outer diameter, $\boldsymbol{OD}$, 3mm wall thickness, $\mathbf{r_{wall}}$, and 25mm length, $\boldsymbol{L}$) suspended from the refractory shield using nichrome wire. Cut-out sections in the refractory shield allow the thermocouple to be positioned within the shield radius once the assembly is in the furnace work tube ¤. 254
Figure 4.41: Mass and temperature profiles for a representative normalisation cycle using a refractory (Al_2O_3) 'dummy' sample. Annotated to include evaluation of signal-to-noise ratio (SNR) and coefficient of variance (CV) in the isothermal (left) and non-isothermal (right) data regions. The higher SNR and lower CV in the non-isothermal data region indicates higher quality data with less noise ¤. 254
Figure 4.42: Comparison of ceramic sample (a) before and (b) after normalisation treatment. The nichrome suspension wire shows evidence of oxidation and deformation under the cyclic loading of the sample pendulum motion ¤. 256
Figure 4.43: (a) Pre-test setup of 15 n.b. sample with annotations (b) indicating the potential for double pendulum motion due to difference resonant frequencies of the sample leading to different displacements, $\boldsymbol{x}_{\mathbf{sample}}$, and wire, $\boldsymbol{x}_{\mathbf{wire}}$ ¤. 256
Figure 4.44: Frequency spectrum, $\boldsymbol{f}$, for the isothermal period of during a 1000°C normalisation heat treatment cycle on an alumina tube ¤. 257
Figure 4.45: Combined sample mass, $\boldsymbol{m}$, -temperature, $\boldsymbol{T}$, plots for the steel (15 nominal bore) (blue) and ceramic (green) samples following a representative normalisation thermal cycle ¤. 258
Figure 4.46: Combined sample mass, $\boldsymbol{m}$, -temperature, $\boldsymbol{T}$, plot for oxide mass gain on 15 nominal bore (n.b.) sample ¤. 258
Figure 4.47: Sample mass, $\boldsymbol{m}$, -temperature, $\boldsymbol{T}$, plot for oxide mass gain on 15 nominal bore (n.b.) sample with enlarged regions exhibiting damped free vibration during heating and cooling due to heating and cooling, and forced vibration during the isothermal period due to vortex induced vibration (VIV). 259
Figure 4.48: Oxide mass gain, $\boldsymbol{\Delta m_{ox}}$, observed during model simulation and thermogravimetric dwell data for a 15 nominal bore (n.b.) tube during a normalisation heat treatment cycle at 1000°C for a time, $\boldsymbol{t}$, of 5 mins ¤. 260
Figure 4.49: Instantaneous mass-based parabolic rate coefficient, $\boldsymbol{\Delta m_{ox}}$, plotted against time, $\boldsymbol{t}$, for the isothermal period of thermogravimetric ('Experimental') testing (left) and model (right) data, which lasts approximately 15 minutes ¤. 261
Figure 4.50: Oxide mass gain, $\boldsymbol{\Delta m_{ox}}$, observed during model simulation and thermogravimetric (TGA) dwell data for a 15 nominal bore (n.b.) tube during a

normalisation heat treatment cycle at 1000°C for a time, t, of 5 mins. The TGA dwell data has gone through Fourier transform operations to suppress resonance caused by vortex induced vibration ¤. 262
Figure 4.51: Instantaneous mass-based parabolic rate coefficient, $k_{p,mass}$, plotted against time, t, for the isothermal period of thermogravimetric ('Experimental') testing (left) and model (right) data, which lasts approximately 15 minutes. The experimental data has gone through Fourier transform operations to suppress resonance caused by vortex induced vibration ¤. 262
Figure 4.52: Schematic of three locations used to take mean measurements of oxide thickness for a 15 nominal bore (n.b.) tube having undergone normalisation at 1000°C for 15 mins in a thermogravimetric furnace ¤. 263
Figure 4.53: Optical microscopy inspection of oxide formed on outer edge of 15 nominal bore (n.b.) conveyance tube sample oxidised in a thermogravimetric furnace at 1000°C for 15 mins. The left image highlights the phase regions whilst the right image highlights particular features related to oxide morphology and spalling risk ¤. 264
Figure 4.54: Light microscopy images of the outer edge of a 15 n.b. sample heated for 3 hrs in the TGA furnace, revealing (a) a thick, porous oxide of 401.0±4.3μm with ¤ (b) clear phases (wüstite, magnetite, haematite) in the ratio observed ¤ in (c) literature example with thickness 124±32μm [60]. Equivalent industrial samples viewed via FEGSEM reveal a (d) much thinner, compact, homogeneous oxide of 15.8±0.7μm ¤. In this case, the wüstite, magnetite, and haematite phases (present at $T > 833$K) are denoted as 3, 1, and 2, respectively to match Wilkstrom et al. [60]. 265
Figure 4.55: Annotated field emission gun electron micrograph, obtained via the backscatter electron detector (BED), from location E showing evidence of porosity, phase boundaries in the oxide, and interfacial roughness at some phase boundaries ¤. 267
Figure 4.56: Annotated field emission gun electron micrograph, obtained via the backscatter electron detector (BED), from location B showing evidence of through-thickness cracking and interfacial failure ¤. 270
Figure 4.57: Annotated field emission gun electron micrograph, obtained via the backscatter electron detector (BED), from location C showing evidence of interfacial failure-initiated through-thickness cracking in the absence of sufficient cold-set resin coverage. The thinner compact layer of homogeneous oxide remains intact and adhered ¤. 271
Figure 5.1: Region of the overall research flowchart (see Figure 1.33) which is under discussion in this chapter. 276
Figure 5.2: Plot of stress, σ, -strain, ε, data obtained from molecular dynamics (MD) simulation of tensile test of wüstite across a temperature range of $200 \leq T \leq 1500$K. The physically invalid range found at strain greater than 0.1, is excluded from data analyses and denoted by thinner lines and a shaded region ¤. 278
Figure 5.3: Plot of filtered stress, σ, -strain, ε, data (window size = 15) obtained from molecular dynamics (MD) simulation of tensile test of wüstite across a temperature range of $200 \leq T \leq 1500$K ¤. 279

Figure 5.4: Plot of elastic modulus, $\boldsymbol{E}$, as a function of temperature, $\boldsymbol{T}$, based on molecular dynamics (MD) simulation results for $600 \leq \boldsymbol{T} \leq 1400$K (with no filter, and using a range of filter windows from 5-20) and extrapolated data from the literature [419]. Outside of the literature data range of $973 \leq \boldsymbol{T} \leq 1273$K (grey shading) the experimental data has been extrapolated using linear regression ¤. 280
Figure 5.5: Plot of elastic modulus, $\boldsymbol{E}$, as a function of temperature, $\boldsymbol{T}$, based on molecular dynamics (MD) simulation results for $600 \leq \boldsymbol{T} \leq 1400$K, extrapolated data from the literature [419] and predictions based on Anderson's analytical derivation of Wachtman's equation [431]. Outside of the literature data range of $973 \leq \boldsymbol{T} \leq 1273$K (grey shading) the experimental data has been extrapolated using linear regression ¤. 282
Figure 5.6: Schematic demonstrating the evolution of tensile and compressive stress, $\boldsymbol{\sigma}$, over time, $\boldsymbol{t}$, in the oxide depending on the temperature, $\boldsymbol{T}$, at which cooling begins and therefore the relative values of coefficient of linear thermal expansion, $\boldsymbol{\alpha}$, which influence the rate of thermal contraction of the steel ('m') and oxide ('ox'). A 1D viewpoint is used as the arc length of the tube considered, $\boldsymbol{Ltube}$, is small compared to the radius of curvature of the tube ¤. 284
Figure 5.7: Plot of elastic modulus, $\boldsymbol{E}$, as a function of temperature, $\boldsymbol{T}$, for the oxide scale (blue) and steel substrate (red) ¤. 285
Figure 5.8: Plot of linear thermal expansion coefficient, $\boldsymbol{\alpha}$, as a function of temperature, $\boldsymbol{T}$, for wüstite ¤. 285
Figure 5.9: Plot of linear thermal expansion coefficient, $\boldsymbol{\alpha}$, as a discontinuous function of temperature, $\boldsymbol{T}$, due to a phase change, for the steel substrate (left), with enlarged views (right) of each temperature region demonstrating the linear function in that region ¤..... 286
Figure 5.10: Convergence study for composite Simpson rule-based numerical integration, used to derive oxide thermal stress, $\boldsymbol{\sigma_{ox,T}}$, with a convergence condition of a less than 1% change in integral between successive iterations ¤. 288
Figure 5.11: Stress developed in the oxide, $\boldsymbol{\sigma_{ox,T}}$, due to thermal expansion coefficient mismatch between the steel substrate and oxide layer during cooling including error bars calculated using the Composite Simpson error condition. The error of negligible value at <<1% of the magnitude of stress predicted at that value (15.4GPa) and when plotted as error bars is therefore in invisible compared to the scale of the thermal stress data. Stress is plotted against the instantaneous oxide thickness, $\boldsymbol{\delta_{ox}}$, computationally predicted based on kinetic and diffusion theory. Expressions for linear coefficient of thermal expansion as a function of temperature were derived from lattice parameter data based on molar volume data. ¤. 289
Figure 5.12: Stress developed in the oxide, $\boldsymbol{\sigma_{ox,T}}$, due to thermal expansion coefficient mismatch between the steel substrate and oxide layer plotted (left) against instantaneous oxide thickness, $\boldsymbol{\delta_{ox}}$, on a logarithmic scale alongside the error, $\boldsymbol{\sigma_{ox,T}}$, associated with its calculation (right) via the composite Simpson rule ¤. 290
Figure 5.13: Plot of full integral-based ('representative') analysis (red) of thermal stress, $\boldsymbol{\sigma_{ox,T}}$, in the oxide, compared to the 'basic' equivalent (blue), against oxide thickness, $\boldsymbol{\sigma_{ox,T}}$. The representative analysis accounts for internal constraint by adhesion to metal substrate, temperature-dependency of elastic modulus and linear

coefficient of thermal expansion, and the thermal expansion discrepancy between the metal and oxide. The basic analysis assumed that mechanical properties of the metal and oxide are independent of temperature and does not account for the effect of the difference in coefficient of thermal expansion between the oxide and the metal to which it is adhered ¤. 291
Figure 5.14: 'Stretch drawing' of a cylindrical oxide layer (continuous outwards expansion of a constant thickness oxide under biaxial tension) ¤. 293
Figure 5.15: Mohr's circle of normal, $\boldsymbol{\sigma}$, and shear, $\boldsymbol{\tau}$, describing the biaxial tension state observed during oxide growth analogously to a stretch drawing procedure ¤. 294
Figure 5.16: Plots of principal stress, σ_1, against oxide thickness, δ_{ox}, (left) and time (right) as oxidation proceeds ¤. 294
Figure 5.17: Oxide through-thickness stress, σ_1, distribution under strain-hardening pure bending where $\boldsymbol{M}$ is the applied bending moment and $\boldsymbol{y}$ is the distance from the neutral axis ($\boldsymbol{y} = \boldsymbol{0.5t}$ at the outer edges) [82]. 295
Figure 5.18: Dimensional theory for derivation of expression of geometric effect growth stress in oxide scale ¤. 297
Figure 5.19: Plot of Fe mole fraction across the global computation domain, for a 15 nominal bore (n.b.) tube, revealing details about the instantaneous position of the metal-scale interface during oxidation (based on a moving phase boundary theory) ¤. 299
Figure 5.20: Plot of Fe mole fraction across the global computation domain, for a 20 nominal bore (n.b.) tube, revealing details about the instantaneous position of the metal-scale interface during oxidation (based on a moving phase boundary theory) ¤. 299
Figure 5.21: Plot of hoop (blue) and radial (red) stress, σ, as a function of time, $\boldsymbol{t}$ ¤. 301
Figure 5.22: Plot of hoop (blue) and radial (red) stress, σ, as a function of model-predicted oxide thickness, δ_{ox} ¤. 301
Figure 5.23: Optical light microscope image taken in-situ pre-nanoindentation on a 15 n.b. tube sample to corroborate typical oxide thickness values of ~20μm ¤. 304
Figure 5.24: Schematic showing the descriptive geometry of a blunted Berkovich indenter and the relevant contact mechanics theory necessary to analyse the force, **P**, present in a convex-planar surface elastic contact scenario ¤. 305
Figure 5.25: Plot of measured load, $\boldsymbol{P}$, against indenter displacement, $\boldsymbol{hind}$, based on measured (red) and analytically predicted (blue) values (at location 1) ¤. 307
Figure 5.26: Load, **P**, -displacement, $\mathbf{h_c}$, plot (full loading-unloading cycle) for location 3 showing the presence of surface roughness-related anomalies in force data at higher displacements during loading ¤. 308
Figure 5.27: Logarithmic plot of true stress, σ_{true}, against true strain, ε_{true}, for location 1 of a 15 nominal bore (n.b.) tube sample ¤. 309
Figure 5.28: Plot of engineering stress, $\boldsymbol{\sigma}$, against engineering strain, $\boldsymbol{\varepsilon}$, for each location using the raw nanoindentation data and their respective power law prediction for three locations along a 25mm length of 15 nominal bore (n.b.) tube sample ¤. 310
Figure 5.29: Plots of effective stress, σ_{eff}, at the outer edge of tube wall using dimensions specified for heavyweight range of Install® 235 range. The transition from a

thin-walled elastic-plastic to strain hardening model is observed at an inner radius, ***IR***, of approximately 15mm ¤. 310
Figure 5.30: Plots of effective stress, σ_{eff}, at outer edge of tube wall using inner radii dimensions in the range 0.5-1000mm. The transition from a thin-walled elastic-plastic to strain hardening model is observed at an inner radius, ***IR***, of approximately 15mm whilst further transition to a thick-walled, strain hardening model is observed at 200mm ¤. 311
Figure 5.31: Photographs of the four tube samples used during their mark-up stage (Image taken by Chris Truman, University of Bristol). 312
Figure 5.32: A photograph of the residual hoop stresses measured at 180° for T1 (Image taken by Chris Truman, University of Bristol). 313
Figure 5.33: The diffraction Debye-Scherrer (D-S) ring (left) and peak at a diffraction angle at 156.396° (right) for the residual hoop stresses measured at (0°,71mm) on T1. (Image generated by Chris Truman, University of Bristol). 314
Figure 5.34: Hoop and axial stress, $\boldsymbol{\sigma}$, state of full length (Tube 1 and Tube 2) and 25mm 15 nominal bore (n.b.) sectioned (Tube 3 and Tube 4) carbon steel conveyance tube samples before (Tube 1 and Tube 3) and after (Tube 2 and Tube 4) normalisation at weld (θ = 0°) and parent metal locations (θ = 90°, 180°, 270°) ¤. 315
Figure 5.35: Hoop and axial stress, σ, state of full length (Tube 1 and Tube 2) and 25mm 15 n.b. sectioned (Tube 3 and Tube 4) for oxide scale found on carbon steel conveyance tube samples before (Tube 1 and Tube 3) and after (Tube 2 and Tube 4) normalisation at weld (θ = 0°) and parent metal locations (θ = 90°, 180°, 270°) ¤. 316
Figure 5.36: Compass plot of hoop (left) and axial (right) stress states in the steel substrate at various positions around the tube circumference, including the weld seam (0°) ¤. 317
Figure 5.37: Compass plot of hoop (left) and axial (right) stress, σ, states in the oxide scale at various positions around the tube circumference, including the weld seam (θ = 0°) ¤. 317
Figure 6.1: Region of the overall research flowchart (see Figure 1.33) which is under discussion in this chapter. 324
Figure 6.2: Advanced Oxide Scale Failure Diagram (critical failure strain, $\boldsymbol{\varepsilon critical}$, against failure mode-based, $\boldsymbol{\phi}$, operation parameter, $\omega_{0,\Phi}$) for a 15 nominal bore (n.b.) conveyance tube after normalisation using the full range of oxide thicknesses predicted, heated for 22 hours at 1000°C, by the Thermo-Calc© model developed in Chapter 3 and Chapter 4 ¤. 325
Figure 6.3: Measurement of typical radius of decohesion, R_{dec}, at three different circumferential locations on a 15 nominal bore (n.b.) post-normalised tube ¤. 327
Figure 6.4: Plot of critical failure strain, $\varepsilon_{critical}$, against failure mode-based, $\boldsymbol{\phi}$, operation parameter, $\omega_{0,\Phi}$) for a 15 nominal bore (n.b.) conveyance tube after normalisation up to the oxide thickness gain associated with normalisation heat treatment (99.7µm after 4 mins) predicted, at 1000°C, by the Thermo-Calc© model developed in Chapter 3 and Chapter 4 ¤. 329

Figure 6.5: Plot of critical failure strain, $\varepsilon_{critical}$, against oxide thickness, δ_{ox}, for a 15 nominal bore (n.b.) conveyance tube after normalisation up to the oxide thickness gain associated with normalisation heat treatment (99.7μm after 4 mins) predicted, at 1000°C, by the Thermo-Calc© model developed in Chapter 3 and Chapter 4 ¤. 330

Figure 6.6: Advanced Oxide Scale Failure Diagram (Plot of critical failure strain, $\varepsilon_{critical}$, against oxide thickness, δ_{ox},) for a 15 nominal bore (n.b.) conveyance tube normalised at 1000°C (T_{norm}) for 3 mins, forming 99.7μm of oxide. For identical thermal conditions, 'A' represents the resultant strain for 99.7μm of gas-barrel furnace-grown oxide, while 'B' represents the resultant strain for 99.7μm of induction-grown oxide. For accessibility, each failure mode boundary is denoted by both colour and symbols indicating their start and end datapoint ¤. 332

Figure 6.7: Plot of oxide thickness, δ_{ox}, against normalisation temperature, T_{norm}, for a 15 nominal bore (n.b.) conveyance tube normalised at 1000°C for 3 mins ¤. 335

Figure 6.8: Plot of mass-based parabolic rate coefficient, $k_{p,mass}$, against normalisation temperature, T_{norm}, for a 15 nominal bore (n.b.) conveyance tube normalised at 1000°C for 3 mins ¤. 335

Figure 6.9: Plot of thickness-based parabolic rate coefficient, $k_{p,thickness}$, against normalisation temperature, T_{norm}, for a 15 nominal bore (n.b.) conveyance tube normalised at 1000°C for 3 mins ¤. 336

Figure 6.10: Plot of thermal strain, $\varepsilon_{thermal}$, against normalisation temperature, T_{norm}, for a 15 nominal bore (n.b.) conveyance tube normalised at 1000°C for 3 mins ¤. 337

Figure 6.11: Plot of growth strain, ε_{ox}, against normalisation temperature, T_{norm}, for a 15 nominal bore (n.b.) conveyance tube normalised at 1000°C for 3 mins ¤. 338

Figure 6.12: Plot of resultant strain, ε_{total}, against normalisation temperature, T_{norm}, for a 15 nominal bore (n.b.) conveyance tube normalised at 1000°C for 3 mins under induction (red) and gas-barrel (blue) heating ¤. 339

Figure 6.13: Advanced Oxide Scale Failure Diagram (Plot of critical failure strain, $\varepsilon_{critical}$, against oxide thickness, δ_{ox},) for a 15 nominal bore (n.b.) conveyance tube normalised at 1000°C (T_{norm}) for 3 mins, forming 99.7μm of oxide. For identical thermal conditions, 'A' represents the results strain for 99.7μm of gas-barrel furnace-grown oxide, while 'B' represents the resultant strain for 99.7μm of induction-grown oxide. For accessibility, each failure mode boundary is denoted by both colour and symbols indicating their start and end datapoint ¤. 340

Figure 6.14: Advanced Oxide Scale Failure Diagram (Plot of critical failure strain, $\varepsilon_{critical}$, against oxide thickness, δ_{ox},) for a 15 nominal bore (n.b.) conveyance tube normalised at 1100°C (T_{norm}) for 3 mins, forming 149μm of oxide. For identical thermal conditions, 'A' represents the results strain for 149μm of gas-barrel furnace-grown oxide, while 'B' represents the resultant strain for 149μm of induction-grown oxide ¤. 340

Figure 6.15: Advanced Oxide Scale Failure Diagram (Plot of critical failure strain, $\varepsilon_{critical}$, against oxide thickness, δ_{ox},) for a 15 nominal bore (n.b.) conveyance tube normalised at 1200°C (T_{norm}) for 3 mins, forming 198μm of oxide. For identical thermal conditions, 'A' represents the results strain for 198μm of gas-barrel

furnace-grown oxide, while 'B' represents the resultant strain for 198μm of induction-grown oxide ¤. 341
Figure 6.16: Advanced Oxide Scale Failure Diagram (Plot of critical failure strain, $\varepsilon_{critical}$, against oxide thickness, δ_{ox},) for a 15 nominal bore (n.b.) conveyance tube normalised at 1300°C (T_{norm}) for 3 mins, forming 267μm of oxide. For identical thermal conditions, 'A' represents the results strain for 267μm of gas-barrel furnace-grown oxide, while 'B' represents the resultant strain for 267μm of induction-grown oxide ¤. 341
Figure 6.17: Advanced Oxide Scale Failure Diagram (Plot of critical failure strain, $\varepsilon_{critical}$, against oxide thickness, δ_{ox},) for a 15 nominal bore (n.b.) conveyance tube normalised at 1400°C (T_{norm}) for 3 mins, forming 333μm of oxide. For identical thermal conditions, 'A' represents the results strain for 333μm of gas-barrel furnace-grown oxide, while 'B' represents the resultant strain for 333μm of induction-grown oxide ¤. 342
Figure 10.1: Calculations of average grain size using mean line intercept technique for 15 nominal bore (n.b.) samples (a) pre-normalisation at the outer edge, (b) post-normalisation at the outer edge, (c) post-normalisation at the inner edge, and (d) post-normalisation at the outer edge ¤. 359
Figure 10.2: Average oxide thickness (14.9±1.3μm) measured for a 15 nominal bore (n.b.) conveyance tube ¤. 359
Figure 10.3: Mean oxide thickness (16.6±0.3μm) measured for a 15 nominal bore (n.b.) conveyance tube ¤. 360
Figure 10.4: Average oxide thickness (15.8±0.7μm) measured for a 15 nominal bore (n.b.) conveyance tube ¤. 361
Figure 10.5: Average oxide thickness (382.6±63.5μm) measured for a 15 nominal bore (n.b.) conveyance tube ¤. 362
Figure 10.6: Average oxide thickness (401.0±4.3μm) measured for a 15 nominal bore (n.b.) conveyance tube. Location B was not included in calculations of average oxide thickness and standard deviation as it represents the phenomenon of oxide phase interfacial failure ¤. 363
Figure 10.7: Schematic of dimension changes during expansion of a solid ¤. 366

List of Tables

Table 1.1: Alloy element composition limits specified by BS EN 10217-2 (Welded steel tubes for pressure purposes - Technical delivery conditions [Part 2: Electric welded non-alloy and alloy steel tubes with specified elevated temperature properties]) [4] for steel grades P235GH and P265GH. 59

Table 2.1: Summary of the grinding, polishing, and etching parameters used to metallographically prepare samples. 125

Table 3.1: Alloy element composition limits specified by BS EN 10217-2 (Welded steel tubes for pressure purposes - Technical delivery conditions [Part 2: Electric welded non-alloy and alloy steel tubes with specified elevated temperature properties]) [4] for steel grades P235GH ('E41') and P265GH ('E24'), compared to cast analysis (CA) results performed on-site at TSUK Tubes [314, 315]. '×' indicates no limit data given in BS EN 10217-2. Several elements have been redacted ('[redacted]') to protect the exact steel composition identity of TSUK Tubes' product. 159

Table 3.2: Sample composition data, obtained via optical emission spectroscopy (OES), for the two steel grades used for conveyance tubes, P265GH ('E24') and P235GH ('E41'). Uncertainty in the OES data was calculated using Weiss' data and Nelis and Payling's calibration curve [316]. The OES data was compared to cast analysis (CA) data from TSUK Tubes. Several elements have been redacted ('[redacted]') to protect the exact steel composition identity of Tata's product. 163

Table 3.3: Table showing the pre-exponential factors, D_0, activation energy, $\boldsymbol{Q}$, and resultant diffusion coefficient, $\boldsymbol{D}$, at 1273K, as predicted by different literature sources, for oxygen, O, and iron, Fe, in austenite, α-Fe, ferrite, β-Fe, wüstite, FeO, and magnetite, Fe_3O_4. 180

Table 3.4: Harrison kinetic regime classification quantitative analysis results for austenitic FCC steel. Kinetic regime is assessed quantitatively using parameters α and β, for a given time, t, and temperature, T, which are derived as function the diffusivity, D, grain size, d, segregation factor, s, and grain boundary width, δ. 188

Table 3.5: Comparison of oxide thickness, δ_{ox}, and thickness-based parabolic rate coefficient, k_p, for model and literature results for a sample soaked for 5 mins at 1000°C.. 207

Table 4.1: Combinations of outer diameter, $\boldsymbol{OD}$, and wall thickness, r_{wall}, dimensions. Wall thickness can vary ±10% from the prescribed wall thickness in the medium (^{m}) and heavy (^{h}) weight cases. The dimension combinations of the 15(*), 20(**), and 25(***) nominal bore (n.b.) products, specified in Tata's technical specifications [2], are highlighted. 223

Table 4.2: Mean oxide thickness, δ_{ox}, measured on the outer edge of three 15 nominal bore (n.b.) conveyance tube samples normalised in industry (Tata Steel UK Ltd). The average oxide thickness in industry, $\delta_{ox,ind}$, is therefore 15.8±0.7μm. 241

Table 5.1: Mechanical properties, (elastic modulus, $\boldsymbol{E}$, Poisson ratio, $\boldsymbol{\upsilon}$, coefficient of thermal expansion, $\boldsymbol{\alpha}$) of the steel substrate and wüstite phase oxide scale evolved at ambient (298K) and tube normalisation (1273K) temperatures, $\boldsymbol{T}$ (assuming isobarothermal conditions)..... 277

Table 5.2: Mean, $\boldsymbol{\mu}$, and standard deviation, $\boldsymbol{\sigma}$, of difference between simulated and experimental values of elastic modulus, $\boldsymbol{Esim,i}$, at temperature, $\boldsymbol{T}$, in different data ranges. 280
Table 5.3: Molecular weights, M_r, and densities, $\boldsymbol{\rho}$, of metal and oxide used to calculate growth strains. 296
Table 5.4: Description of the methodologies used to calculate principal strains, $\boldsymbol{\varepsilon}$, and stresses, $\boldsymbol{\sigma}$, for different mechanical conditions. 303
Table 5.5: Plastic power law parameters (strength coefficient, $\boldsymbol{K}$, and strain hardening coefficient, $\boldsymbol{n}$) determined via nanoindentation at three locations along a 25mm length of 15 nominal bore (n.b.) tube sample. 309
Table 5.6: Hoop stress, σ_h, evolved in the oxide due to different stress sources during conveyance tube manufacturing. 321
Table 6.1: Definition of parameters used to construct an Advanced Oxide Scale Failure Diagram (AOSFD) for wüstite on a curved surface. Fields marked with an asterisk (*) are geometrically dependent and require revision if the tube sample is changed. 326
Table 6.2: Arc length of spalled oxide, L_{spall}, measured on the outer edge of three 15 nominal bore (n.b.) conveyance tube samples normalised in industry (Tata Steel UK Ltd). The radius of decohesion, L_{spall}, is therefore 21.8±0.6μm. The ratio between the mean oxide thickness, δ_{ox}, are also presented to show the overall arc length of the oxide captured in the electron micrograph frame, L_{frame}, and the angle subtended, $\boldsymbol{\theta}$, by the total thickness of oxide captured in each frame. 327
Table 6.3: Comparison of gas-barrel ('gas') and ('ind') and induction heating methods for normalisation in terms of their effect on stress, $\boldsymbol{\sigma}$, and strain, $\boldsymbol{\varepsilon}$, components evolved from oxidation- (thermal and growth) and manufacturing- (forming and drawing) related sources. 331
Table 6.4: Comparison of strain, $\boldsymbol{\varepsilon}$, evolved in a ~100μm oxide scale formed using normalisation with gas-barrel ('gas') vs. induction ('ind') heating, to critical strain ('crit') for each potential failure mode. 333
Table 6.5: Time, t_{fail}, and number of datapoints, $N_{datapoint}$, at which the Thermo-Calc© oxide kinetic model failed for each temperature, T_{norm}, due to complete consumption of the steel substrate. The maximum soak time for each temperature before complete consumption of the substrate, $t_{soak,max}$, is also shown. 334
Table 8.1: Quantitative analysis of different aspects of impact within this project based on impact time horizon, social scale, spatial scale, and domain/s. A score was assigned to each level of each category, from 1-3. In the case of domain, a score of 1 was given to each domain, with the exception of intermediary domains which received a score of 0.5. The maximum scores were used to determine relative impact reach, $\boldsymbol{R}$, and the number of impact domains were used to determine relative significance, $\boldsymbol{S}$. 352
Table 10.1: Oxide thickness measurements for a 15 nominal bore (n.b.) conveyance tube. Three measurements were taken at three points at each location ('A', 'B', and 'C'). A mean oxide thickness, δ_{ox}, and its standard deviation are calculated. ... 360
Table 10.2: Oxide thickness measurements for a 15 nominal bore (n.b.) conveyance tube. Three measurements were taken at three points at each location ('A', 'B', and 'C'). A mean oxide thickness, δ_{ox}, and its standard deviation are calculated. ... 360

Table 10.3: Oxide thickness measurements for a 15 nominal bore (n.b.) conveyance tube. Three measurements were taken at three points at each location ('A', 'B', and 'C'). A mean oxide thickness, δ_{ox}, and its standard deviation are calculated. ... 361

Table 10.4: Oxide thickness measurements for a 15 nominal bore (n.b.) conveyance tube. Three measurements, taken at three points at each location ('A', 'B', and 'C') and comprising two interfacially separated parts ('a' and 'b'). A mean oxide thickness, δ_{ox}, and its standard deviation are calculated. 362

Table 10.5: Oxide thickness measurements for a 15 nominal bore (n.b.) conveyance tube. Three measurements, taken at three points at each location ('A', 'B', and 'C'). A mean oxide thickness, δ_{ox}, and its standard deviation are calculated..... 363

Publications

The following publications were the result of the work in this project:

- M. Kendall, M. Coleman, H. Cockings, E. Sackett, C. Owen, and M. Auinger, "Computational Thermochemistry for Modelling Oxidation During the Conveyance Tube Manufacturing Process," *Metals*, vol. 14, no. 12, December 2024. [Online]. Available: https://doi.org/10.3390/met14121402
  [Impact Factor = 2.6, Q1 for Metals and Alloys]

- M. Kendall, M. Auinger, C. L. J. Robinson, C. Owen, and E. Sackett, "In Situ Thermogravimetric Analysis of Curved Surfaces During High-Temperature Oxidation," *Materials,* vol. 18, no. 11, May 2025. [Online]. Available: https://doi.org/10.3390/ma18112463.
  [Impact Factor = 3.1, Q1 for Metallurgy and Metallurgical Engineering]

Nomenclature

Symbol	Variable	Unit
$A_{contact}$	Projected area of the elastic contact	m^2
A_{e3}	Annealing temperature	K
A_i, B_i, C_i, D_i	Layer-specific constants	-
A_{ind}	Indenter area function	m^2
$A_{n=1...N}$	Amplitude	m
A_r	Avogadro's constant	mol^{-1}
B_G	Gruneisen constant	Pa
C_f	Load frame compliance	$m.N^{-1}$
C_{unload}	Unloading stiffness	Pa
D_{ind}	Indenter diameter	m
$D_{k,0}$	Pre-exponential factor of diffusion coefficient	$m^2.s^{-1}$
D_k	Diffusion coefficient	$m^2.s^{-1}$
E'	Modified elastic modulus	Pa
E_r	Reduced modulus	Pa
E_0	Elastic modulus at absolute zero	Pa
F_c	Cutting force	N
F_s	Shear force	N
F_t	Thrust force	N
I_{coil}	Applied current	A
J_k	Species flux	$m^2.s$
K_{Ic}	Mode I fracture toughness	$MPa.m^{0.5}$
$K_{S/O}$	Stoichiometric ratio of scale mass per unit mass of oxygen in the oxide scale	-
$K_{combined}$	Parameter based on the combined mechanical properties of the substrate and oxide	-
K_{ic}	Mode i stress intensity factor	$MPa.m^{0.5}$
L_{frame}	Arc length of oxide in frame	m
L_{probe}	Probe length	m
L_{spall}	Arc length of spalled oxide	m
L_{tube}	Tube length	m
$M_{k,0}$	Pre-exponential factor of mobility	$m^2.s^{-1}$
M_k	Mobility	$m^2.s^{-1}$
M_r	Molar mass	g
M_r	Molecular weight	$g.mol^{-1}$
N_{atom}	Number of atoms	-
N_{body}	Number of bodies	-
N_{coil}	Number of coil turns	-
$N_{datapoint}$	Number of datapoints	-
N_s	Normal-to-shear force	N
N_{sine}	Number of discrete sine function components	-
P_{ij}	Total system pressure	Pa
P_{ind}	Indentation load	N
P_{max}	Peak load	N

R_{dec}	Initial radius of the zone of decohesion	m
R_{dec}	Radius of decohesion	m
R_{ind}	Indenter radius	m
R_{sample}	Tube inner radius	m
R_{tube}	Tube radius of curvature	m
R_u	Universal gas constant	$J.mol^{-1}.K^{-1}$
R_u	Universal gas constant	$J.mol^{-1}.K^{-1}$
R_Ω	Resistance	Ω
$S_{empirical}$	Experimentally measured stiffness	$N.m^{-1}$
T_c	Curie temperature	K
T_{norm}	Normalisation temperature	°C
$T_{stretch}$	Stretch reduction temperature	°C
T_0	Debye temperature	K
$U_{interatomic}$	Interatomic potential	J
V_A	Thermal expansivity	$m^3.K^{-1}$
V_{bulk}	Bulk metal contribution	-
V_{coil}	Electromotive force induced	V
V_{gain}	Oxide volume gain	m^3
V_m^k	Molar volume of species k	$m^3.mol^{-1}$
V_{ox}	Oxide volume gain	m^3
V_{oxide}	Oxide volume gain	m^3
V_s	Volume per mole of volume carrying species	$m^3.mol^{-1}$
W_r	Molecular weight	$g.mol^{-1}$
a_c	Crack dimension	m
a_{intr}	Intrusion size	m
c_i^t	Concentration at a given node, i, and time, t	$mol.m^{-3}$
c_k	Species concentration	$mol.m^{-3}$
c_p	Specific heat capacity	$J.kg^{-1}.K^{-1}$
d'	Interplanar spacing	m
d_{atom}	Interatomic separation	Å
$d_{contact}$	Contact diameter	m
d_{tip}	Blunted tip diameter	m
d_0	Unstrained interplanar spacing	m
f^*	Geometrical parameter	-
$f_{correlation}$	Correlation factor	-
f_i	Arbitrary function used to define moving point average equation	-
f_k	Volume fraction	$m^3.mol^{-1}$
$f_{labyrinth}$	Labyrinth factor	-
g_k	Grain boundary volume fraction	-
h^*	Dimensionless oxide thickness	-
h_c	Contact depth	m
h_{ind}	Indenter displacement	m
k^*	Rate of reaction dimensionless parameter	-
k_B	Boltzmann constant	$J.K^{-1}$

$k_{p/l,0}$	Parabolic rate coefficient pre-exponential factor (parabolic, p, or linear, l)	$g^2.cm^{-4}.s^{-1}$ (mass-based) $cm^2.s^{-1}$ (thickness-based)
$k_{p/l}$	Rate coefficient (parabolic, p, or linear, l)	$g^2.cm^{-4}.s^{-1}$ (mass-based) $cm^2.s^{-1}$ (thickness-based)
k_y	Hall-Petch constant	$Pa.m^{0.5}$
n_{AOSFD}	Scale Failure Diagram level	-
n_k	Number of tracers	-
n_m	Number of metal atoms	-
n_{work}	Strain hardening exponent	-
r_{atom}	Atomic radius	Å
$r_{indenter}$	Indenter radius	m
r_{rough}	Surface roughness amplitude	m
r_{wall}	Tube wall thickness	m
t^*	Dimensionless time	-
t_{Fe}	Cation transport number	-
u_k	Element contribution	-
$u_{x,y}$	x-wise deformation	m
$u_{y,x}$	y-wise deformation	m
x_d	Mole fraction of intrinsic defects	-
x_{sample}	Sample displacement	m
x_1	Pre-oxidation sample dimension	m
x_2	Post-oxidation sample dimension	m
z_i	Valency for migrating ions	-
$\Delta_f g_d$	Molar Gibbs energy of formation of intrinsic defects d	$J.\ mol^{-1}$
$\alpha_{interfacial}$	Interfacial metal contribution	-
α_k	Diffusing cation valency	-
$\alpha_{surface}$	Fraction of oxide formed at the outer surface of the scale	-
β_{Bohr}	Bohr magneton number	-
γ_r	Oxide roughness	m
γ_0	Scale-metal interface fracture energy	$J.m^{-2}$
δ_{ox}	Oxide thickness	m
$\bar{\varepsilon}$	Effective strain	-
ε_{ox}^h	Oxide hoop strain	-
ε_{ox}^r	Radial hoop strain	-
ε_t	True strain	-
ε_z	Principal strain	-
ζ_{bend}	Bend ratio	-
θ_{arc}	Angle subtended by arc length	°
λ_g	Growth parameter	-
λ_{rough}	Surface roughness period	m
μ_k	Chemical potential	$J.mol^{-1}$
μ_s	Coefficient of static friction	-
ρ_{bend}	Radius of curvature of bending	m
ρ_{ox}	Scale density	$kg.m^{-3}$
$\bar{\sigma}$	Effective stress	Pa
σ_S	Saturation stress	Pa

σ_Y	Yield strength	Pa
σ_{FeO}	Electrical conductivity	$S.m^{-1}$
σ_Y	Yield strength	Pa
σ_{bond}	Minimum stable bond length	Å
σ_h	Hoop stress	Pa
$\sigma_{ox,T}$	Thermal stress	Pa
$\sigma_{ox,g}$	Growth stress	Pa
σ_{ox}	Oxide scale stress state	Pa
σ_r	Radial stress	Pa
σ_t	True stress	Pa
σ_ϕ	Stress acting along an inclined direction	Pa
τ_{xy}	Shear stress on the $x-y$ plane	Pa
$\omega_{o,\phi}$	Operation history parameter, $\omega_{o,\phi}$, specific to failure mode ϕ	-
ω_0	Natural frequency	Hz
ϕ_i	Phase angle	rad
Δm_{ox}	Oxide mass gain	g
A	Surface area	m^2
B	Temperature-dependent constant	Pa
C	Atomic number contrast	-
D	Base diameter	m
E	Elastic modulus	Pa
F	Force	N
G	Gibbs energy	$J.\ mol^{-1}$
H	Hardness	$kg.mm^{-2}$
H	Enthalpy	$J.K^{-1}$
K	Power law hardening coefficient	-
L	Gibbs energy interaction parameter	$J.\ mol^{-1}$
M	Scale displacement vector	-
N	Normal force	N
OD	Tube outer diameter	m
P	Pressure	Pa
Q	Activation energy	$J.mol^{-1}$
Q	Net heat change of the system	J
R	Impact reach	-
Re	Reynolds number	-
S	Dimensionless stored energy function	-
S	Entropy	$J.K^{-1}$
S	Relative impact significance	-
St	Strouhal number	-
T	Temperature	K
U	Internal energy of the system	J
V	Volume	m^3
W	Work done by the system	J
X	Frequency spectrum	Hz
Z	Atomic number	-
a	Acceleration	$m.s^{-2}$

a	Lattice parameter	Å
c	Defect size	m
d	Grain size	m
f	Frequency	Hz
g	Gravitational constant	$m.s^{-2}$
h	Numerical interval	-
k	System stiffness	$N.m^{-1}$
m	Mass	kg
n	Strain hardening exponent	-
p	Porosity volume fraction	-
q	Integer power	W
r	Radial coordinate	m
r	Pearson correlation coefficient	-
s	Segregation factor	-
t	Time	s
u	Moving phase boundary velocity	$m.s^{-1}$
v	Velocity	$m.s^{-1}$
v	Poisson's ratio	-
x	Stoichiometric parameter	-
y	Distance within the sheet axis from the neutral axis	m
z	Axial coordinate	m
Δv_r	Molar relaxation volume	$m^3.mol^{-1}$
Φ	Magnetic field	T
Ω	Crystal molar volume	$m^3.mol^{-1}$
Δt	Computational timestep	s
Δx	Computational node width	m
α	Coefficient of thermal expansion	K^{-1}
α	Harrison kinetic theory penetration parameter	-
α	Stress ratio	-
α	Rake angle	°
β	Leclaire parameter	-
β	Volumetric thermal expansion coefficient	K^{-1}
β	Strain ratio	-
δ	Grain boundary width	m
ε	Strain	-
ζ	Damping ratio	-
η	Backscatter coefficient	-
θ	Azimuthal coordinate	°
λ	X-ray wavelength	m
μ	Mean	-
ξ	Composite Simpson rule error bound	-
ρ	Density	$kg.m^{-3}$
σ	Stress	Pa
σ	Standard deviation	-
τ	Shear stress	Pa
υ	Poisson ratio	-

φ	Pilling-Bedworth ratio	-
χ	Rotates in the plane normal to that of the Bragg angle	rad
ψ	Angle of rotation of the sample	rad
ω	Frequency	Hz
ϕ	Azimuthal coordinate	°
ϕ	Shear angle	°
2θ	Bragg angle	°
2φ	Berkovich indenter half-induced angle	°

Abbreviation	Meaning
ABOP	Analytical Bond Order Potential
AC	Alternating Current
AES	Auger Electron Spectroscopy
AFA	Alumina-Forming Austenitic
AFR	Air-fuel ratio
AIM	Advanced Imaging of Materials
AOSFD	Advanced Oxide Scale Failure Diagram
BC	Boundary Condition
BCC	Body-Centred Cubic
BED	Backscatter Electron Detector
BFPA	British Fluid Power Association
BMCR	Boiler Maximum Continuous Rating
BSE	Backscatter Secondary Electron
CA	Cast Analysis
CALPHAD	Computational Coupling of Phase Diagrams and Thermochemistry
CCD	Charged Couple Device
CCT	Continuous Cooling Transformation
CEF	Compound Energy Formalism
CFD	Computational Fluid Dynamics
CN	Crank-Nicolson
CPU	Central Processing Unit
CSID	Corrosion Stress Interaction Diagram
CV	Coefficient of Variance
DFT	Discrete Fourier Transform
DSC	Differential Scanning Calorimetry
D-S	Debye-Scherrer
DTA	Differential Thermal Analysis
d.p.	Decimal Place
EBSD	Electron Backscatter Diffraction
EDS	Energy Dispersive Spectroscopy
EDM	Electrical Discharge Machining
EMF	Electromotive Force
FCC	Face-Centred Cubic
FDM	Finite Difference Method
FEA	Finite Element Analysis
FEGSEM	Field Emission Gun Scanning Electron Microscope
FFT	Fast Fourier Transform

FVM	Finite Volume Method
GPS	Generalised Plane Strain
GUI	Graphical User Interface
HAZ	Heat Affected Zone
HFI	High-Frequency Induction
HP	High Pressure
HVAC	Heating, Ventilation, and Air Conditioning
ID	Inner Diameter
IL	Inner Layer
IR	Inner Radius
LEFM	Linear elastic Fracture Mechanics
LHS	Left-Hand Side
MBE	Model-Based Engineering
MCA	Multi-channel Analyser
MD	Molecular Dynamics
ML	Machine Learning
n.b.	Nominal bore
NPL	National Physical Laboratory
OD	Outer Diameter
ODE	Ordinary Differential Equation
OEM	Original Equipment Manufacturer
OES	Optical Emission Spectroscopy
OL	Outer Layer
OPD	Optical Path Difference
OPS	Oxide Polishing Suspension
OR	Outer Radius
OSFD	Oxide Scale Failure Diagram
PAG	Prior Austenite Grain
PBR	Pilling Bedworth Ratio
PDE	Partial Differential Equation
PIP	Profilometry-based Indentation Plastometry
PMRC	Pilot Manufacturing Research Centre
POI	Position of Interface
RANS	Reynolds Averaged Navier Stokes
RHF	Reheat Furnace
RHS	Right-Hand Side
RMS	Root Mean Square
S6	Stordy 6” Mill
SaMI	Steel and Metals Institute
SCH	Schedule (in the context of pipe dimensioning)
SEM	Scanning Electron Microscopy
SER	Stable Element Reference
SIMS	Secondary Ion Mass Spectrometry
SNR	Signal-to-Noise Ratio
SPS	Simple Plane Strain
SR2	Stretch Reduction Mill 2
STA	Simultaneous Thermal Analysis
s.f.	Significant Figures
TDLAS	Technologies Laser Diagnostic System
TGA	Thermogravimetric Analysis

TMP	Thermomechanical Processing
TTT	Temperature-time-transformation
UDF	User-defined Function
UV	Ultraviolet
VFE	Vacancy Formation Energy
VGM	Variable Grid Method
VIV	Vortex Induced Vibration
WDS	Wavelength Dispersive Spectrometry
XPS	X-ray Photoelectron Spectroscopy
XRD	X-ray Diffraction

Chapter 1 Project Context, Background, and Literature Review

In the UK, the production of 'Cast iron & steel tubes & pipes' has doubled since 1997 [1]. Carbon steel conveyance tubes are key engineering components used in fluid transport applications such as Heating, Ventilation, and Air Conditioning (HVAC), refrigeration, and petrochemical transport. Clearly, the dimensional range of conveyance tubes is as vast as their applications and outer diameter can vary from a few centimetres for domestic central heating water supply to several metres for oil and gas delivery. The latter example may often be referred to as pipeline or pipe, which raises the question of which nomenclature is most appropriate for the smaller conveyance products (with a maximum outer diameter and wall thickness of 165.1mm and 5.4mm respectively) manufactured at Tata Steel UK Tubes' (TSUK Tubes) Corby site [2].

The British Fluid Power Association (BFPA) stipulate that the critical difference between a tube and pipe is their dimensional definitions [3]. Tube size is defined by the nominal outside diameter and wall thickness, with the latter being directly related to working pressure. In contrast, pipe size is defined by its nominal inside diameter (often referred to as the 'nominal bore') and wall thickness (usually referred to as 'schedule' or SCH). There may therefore be a difference in outer diameter and schedule for pipes with the same nominal bore due to manufacturing operations such as threading, and as such pipe schedule is not directly related to its working pressure. The British Standard BS EN 10217-2 '*Welded steel tubes for pressure purposes. Technical delivery conditions. Electric welded non-alloy and alloy steel tubes with specified elevated temperature properties'* [4], which TSUK Tubes' conveyance tubes adhere to, makes exclusive use of the term 'tube' and defines products accordingly, based on their outside diameter and wall thickness. Whilst geometry has a part to play in conveyance tube integrity, the steel grade composition is also limited by the same standard to ensure a minimum yield strength.

Heat treatment is critical across the spectrum of steel processing operations [5], including 'downstream product' manufacturing of conveyance tubes, to achieve this minimum yield strength. The microstructural homogeneity which heat treatments can yield is essential for achieving the consistent mechanical properties necessary for high integrity tube service [6]. However, the iron oxide ('scale') formed on the external tube surface at high temperatures is an undesirable by-product. The yield loss associated with oxidation of steel can be as high as 3% [7]. The TSUK Tubes storage warehouse has a capacity of 20,000 tonnes [8], hence up to

600 tonnes of additional feedstock is required to fill the warehouse due to oxidation yield losses. The cost incurred for this additional hot rolled coil steel is almost £400,000 [9, 10]. Adhesion of the scale is often inconsistent for heat-treated conveyance tubes due to their geometry, substrate condition, and the temperature used for heat treatment (~950°C). Any spalled scale demands additional processing resources as uncontained scale can lead to plant contamination and damage, whilst any intact scale is liable to be rolled in to the steel and increase the likelihood of product rejection by customers where poor surface quality calls the product integrity into question [11, 12]. For example, corrosion cracking is exacerbated by geometric correction operations which induce residual stress, such as stretching operations to achieve the correct product dimensions, and corrosion media such as oxide scale, making heat treated conveyance tubes prone to this damage mode [13]. Krzyzanowski et al. identified product surface quality as one of two main domains where detailed knowledge of oxide scale is important (the other being thermo-tribological effects) [14]. Furthermore, oxide scale acts as a thermal insulator which affects component thermal and hardness profiles during tube manufacturing and service [15, 16]. 90% of failures by overheating are accounted for by superheater, reheater, and wall tubes, with the most severe failures seen in tubes with high levels of steam-side oxide scale accumulation [17]. World steel production increased seven-fold in the period from 1950-2020 and is projected to grow by a further 1.5 times to meet ever-increasing demand by 2050 [18]. As such, the steel industry is considered vital for the global economy. Furthermore, emerging technologies which support statutory decarbonisation [19], such as hydrogen energy, will continue to depend on reliable conveyance infrastructure [20, 21]. However, high temperature oxidation continues to present technical, economic, and environmental challenges. The efficiency of the augmented design infrastructure, energy economy, and manufacture of steel products, and specifically conveyance tubes, can only be maximised when oxide scale is understood and controlled in terms of its kinetics and adhesion. For example, the continued operation of power and chemical plants which have been in operation for decades, depends on an accurate remaining life assessment which incorporates the effect of scale [17].

Scale control has already been shown to reduce material loss [7], improve product surface quality [22-24], improve heat transfer efficiency [15, 25], and reduce energy consumption [15, 25, 26]. The augmentation of computational power in the 21st century lends itself to faster throughput of manufacturing innovation for increasingly complex scenarios,

compared with a purely experimental or analytical approach [27-29]. The core aim of this project is to explore the potential for a computational approach for modelling high temperature oxidation, particularly on curved surfaces, and evaluate the potential for the results of such modelling to inform manufacturing decisions and preventative maintenance regimes which promote well-understood and controlled oxide kinetics and adhesion. A system which is optimised to control oxide will be one step closer to achieving the most efficiently manufactured and highest integrity products possible.

1.1 Project Aim and Objectives

Aim

To explore the potential for the use of computational modelling to investigate the effect of conveyance tube manufacturing parameters on oxide scale kinetic and mechanical behaviour.

Objectives

1. To use computational thermodynamics to predict oxide thickness gain and model external oxide scale kinetic and mechanical response under conveyance tube manufacturing conditions.
2. To validate the oxide scale computational model output data and the data derived on its basis using quantitative experimental techniques assessing kinetic and mechanical response.
3. To investigate the effect of curved surfaces, and specifically tube geometry, on oxide scale behaviour under representative thermomechanical manufacturing conditions.
4. To use kinetic and mechanical response data to develop and implement an Advanced Oxide Scale Failure Diagram to identify the critical strain failure mechanism/s associated with different conveyance tube manufacturing parameters and operation history.

1.2 The Conveyance Tube Manufacturing Process

TSUK Tubes' low carbon steel thick-walled conveyance tubes are employed in wide-ranging building and industrial services applications, e.g. air conditioning, heating (, i.e. HVAC systems), petrochemical transport, where high pressures, e.g. refrigeration, and temperatures, e.g. steam system, are possible. The manufacturing process must be designed to achieve the material and mechanical properties necessary for these service conditions. Steel is ubiquitous in modern society and the sector is crowded. Therefore, plants must optimise their processes to maximise product quality, capacity, and process flexibility but minimise cost. The main manufacturing operations used during the manufacturing process are shown in the schematic in Figure 1.1. Tata's Install® range of hot-finished conveyance tubes are manufactured with bespoke dimensions defined by the customer comprising outer diameters in the range 21.3 to 165.1mm and wall thickness from 6.3mm to 15.1mm [2].

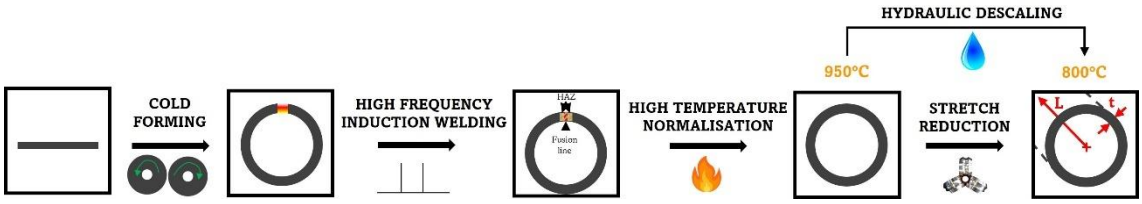


Figure 1.1: Schematic sequence of the conveyance tube manufacturing process ¤.

1.2.1 Materials Selection

Low carbon (max. 0.2wt% carbon [30]), low-alloy steel is delivered to the TSUK Tubes site at Corby as a coil formed from a continuous cast billet. The typical phase of the received material is ferrite and pearlite. Beyond the solvus, the hypoeutectoid, uniform dual-phase alloy comprises ferrite ('α') and alternating layers ('lamellae') of BCC-structured ferrite ('A') and cementite ('B'), i.e. pearlite ('A'B') (see Figure 1.2). Figure 1.2 highlights how the core methodology used in Thermo-Calc© (Gibbs Free Energy Minimisation – see Section 2.2.2), and its preference for thermal stability, affects the output phase diagram. At low carbon concentrations (<0.02 wt%), graphite (crystalline carbon [31]) is formed below a critical temperature in the range 400-750°C depending on the given carbon concentration, with higher carbon concentrations associated with a higher critical temperature. In contrast, conventional Fe-C phase diagrams typically predict the formation of cementite (Fe_3C) in the same temperature-concentration region, and the critical temperature associated with this phase transformation is conventionally defined as A_1 [32]. Graphite is a more thermally stable carbide than cementite [31], and its therefore favoured as the predicted carbide phase

formed below A_1 when using a Gibbs Free Energy Minimisation technique such as within computational thermodynamics software [33].

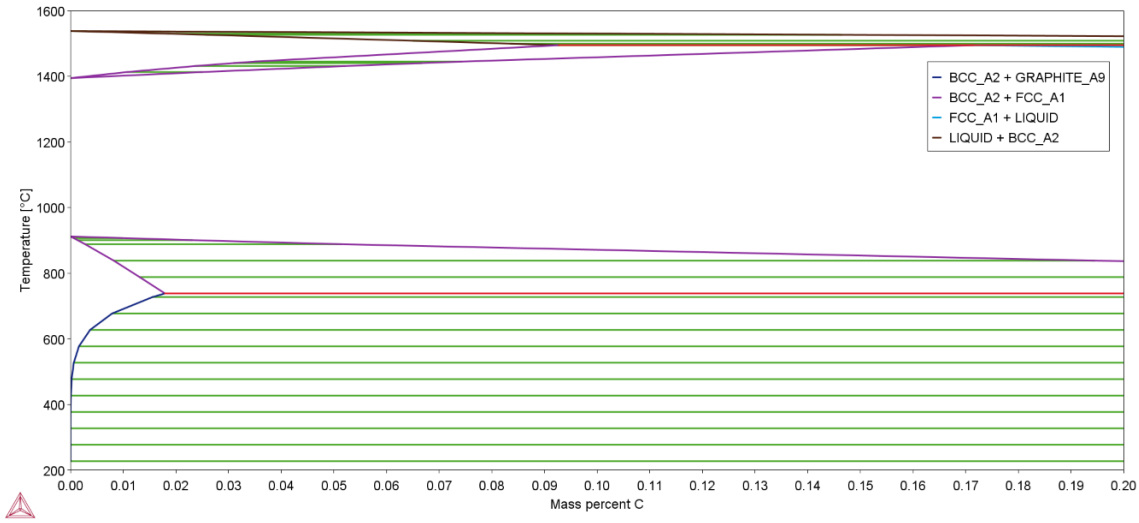


Figure 1.2: Fe-C binary system phase diagram generated, using Thermo-Calc© 2025a [33], for the region associated with the mass percent contribution of carbon stipulated by BS EN 10217-2 (<0.16%wt C for P235GH and <0.20%wt C for P265GH) [4] for conveyance tube steel grades ¤.

1.2.2 Cold Forming

The steel sheet then passes through an accumulator series and is cold worked (associated with improved surface finish and machinability [34]) by forming rolls into the required hollow, cylindrical geometry (see Figure 1.3a). At this stage, the sheet still has a fine, homogenous microstructure, ensuring technical standard-defined good mechanical properties.

1.2.3 High-Frequency Induction Welding

High-frequency induction (HFI) welding is a solid-state, filler-free, resistive upset welding technique, favoured for its excellent geometrical properties (specifically cylindricity and consistent wall thickness) at a faster and cheaper rate than the forged seamless alternative [2]. Seamless tubes are specifically forged via the rotary pierced process [35] where the billet is forced around a moulding plug. Although thicker walled tubes are possible via a seamless approach, the pressures encountered by typical conveyance tube applications do not demand this [2].

HFI welding exploits the principle of induction heating – a non-contact, flame-free heating technique. A solenoid coil, with a given number of coil turns,

$\boldsymbol{N_{coil}}$, is supplied with alternating current (AC), inducing its own magnetic field, $\boldsymbol{\Phi}$, which is continuously changing in magnitude and direction over time, $\boldsymbol{t}$, in phase with the applied

current, $\boldsymbol{I_{coil}}$ [36]. When an electrical conductor, such as the formed steel pre-weld tube, is placed inside the coil, electromagnetic induction initiates localised electrical ('eddy') currents in the steel, in accordance with Faraday's (see Equation 1.1), where $\boldsymbol{V_{coil}}$ is the electromotive force induced, and Ohm's Laws (Equation 1.2), where $\boldsymbol{R_{\Omega}}$ is resistance [36]. The steel's own high electrical resistivity [37] causes Joule heating. Eddy currents heat from the part surface, i.e. the part region closest to the induction coil, to a depth defined by the AC frequency.

$$\boldsymbol{V_{coil} = -N_{coil}\frac{d\Phi}{dt}}$$

Equation 1.1

$$\boldsymbol{V_{coil} = I_{coil}R_{\Omega}}$$

Equation 1.2

Complete heating to the full depth of the part relies on subsequent thermal conduction and thus incurs an appropriate soak time defined by the steel's conductivity [37]. Although Joule heating is the dominant heating mechanism, the magnetic nature of steel [37] also generates a small amount of heat via hysteresis losses as there is material resistance to the continuous magnetic field direction change as the material's dipoles respond by continuous realignment. Current is the most influential variable during induction heating, although heating rate and depth can also be adjusted by changes to the coil turn number and spacing, and part-coil coupling distance [38].

Overall, a key feature of induction heating is that the part becomes its own heating element wherein the highest temperature is generated, controlled, and confined to the region in direct proximity to the coil. Thus, induction heating is a fast and accurate localised heating technique. HFI welding is highly localised, with the solenoid coil being applied only around the join region, which will achieve some restraint of heating of the bulk metal.

Formation of the weld via material melting and interdiffusion occurs upon joint face contact by two-side pressure squeeze rolls. The weld bead is removed to avoid corrosion-related service life implications associated with internal stress raisers, crevice generation, and turbulent transition trigger [39].

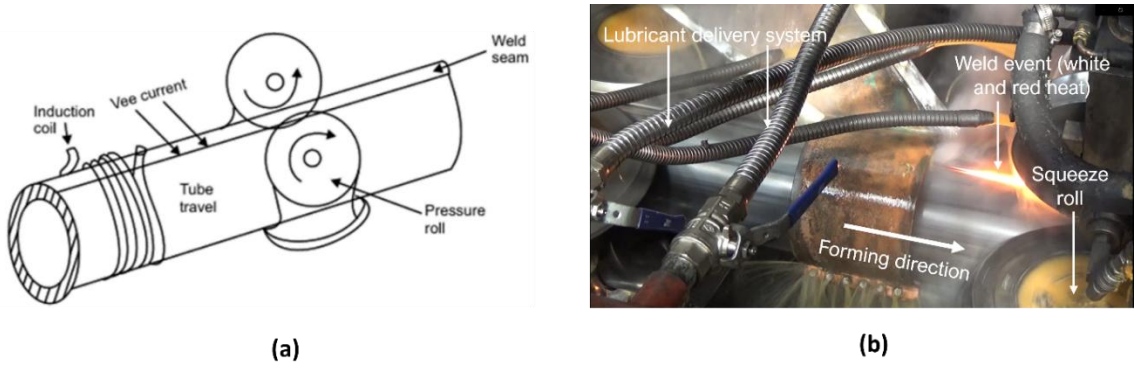


Figure 1.3: (a) Schematic diagram of high-frequency induction welding set up [40] (*adapted from source*) (b) Photograph of operational high-frequency induction weld set-up at TSUK Tubes site in Corby ¤.

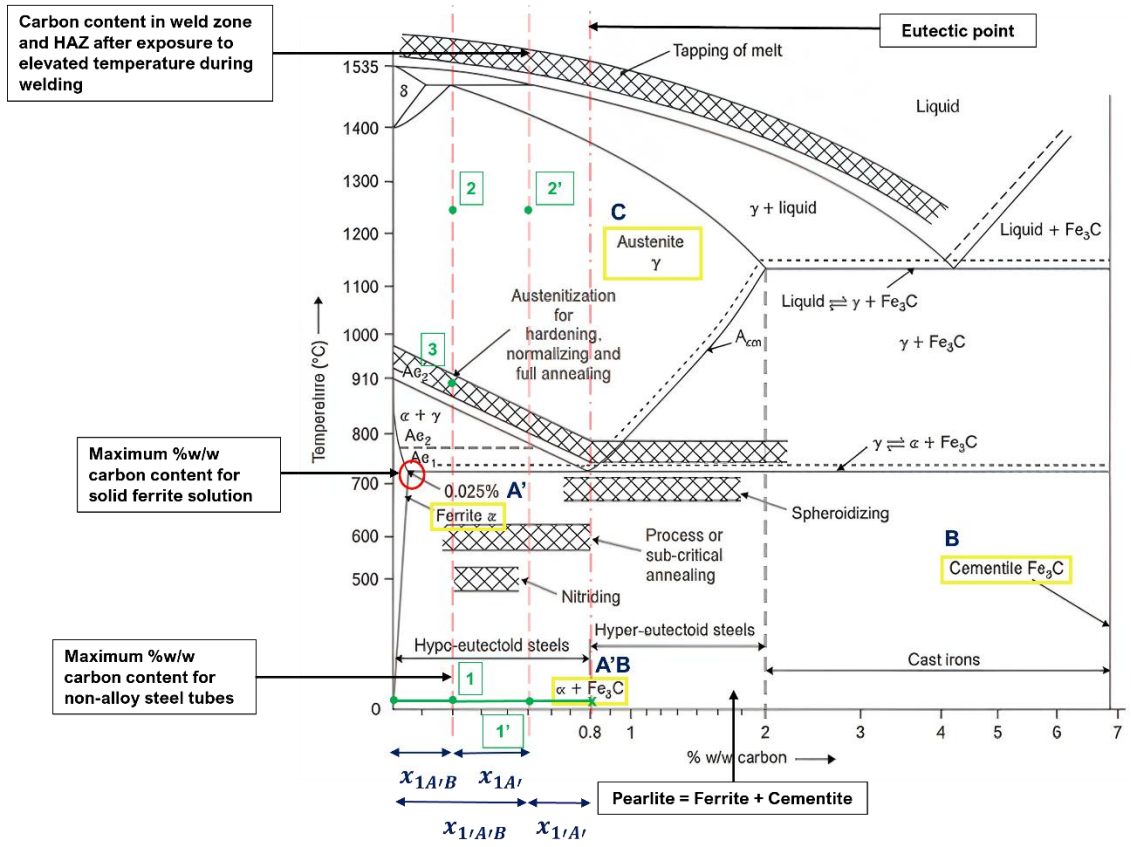


Figure 1.4: Fe-C system phase diagram annotated to demonstrate effect of welding and heat treatment [32] (*adapted from source*).

Inconsistent material and mechanical properties are found in the weld fusion line and heat-affected zone (HAZ). High temperatures, and subsequent generation of a temperature gradient across the bulk component material, generate microstructural inconsistency (see Figure 1.5) and an undesirable mechanical property deterioration (reduced strength, ductility, toughness, and pressure integrity). This deterioration is associated with the increased likelihood of corrosion and splitting, particularly at the bulk-to-HAZ zone boundary where the microstructural inhomogeneity is most prevalent [40]. Although, the

HAZ can be reduced in size by using a higher AC frequency during welding [41]. The Hall-Petch equation (see Equation 1.3) [42] highlights the optimal grain refinement condition where the influence of dislocation locking, i.e. pinning, via constant, $\boldsymbol{k_y}$, and grain size, $\boldsymbol{d}$, on material strength, $\boldsymbol{\sigma_y}$, is shown compared to its baseline strength, $\boldsymbol{\sigma_0}$, disregarding any microstructural changes. Therefore, the rapid cooling of the post-weld period promotes higher localised strength where smaller grains are formed.

$$\boldsymbol{\sigma_y = \sigma_0 + \frac{k_y}{\sqrt{d}}}$$

Equation 1.3

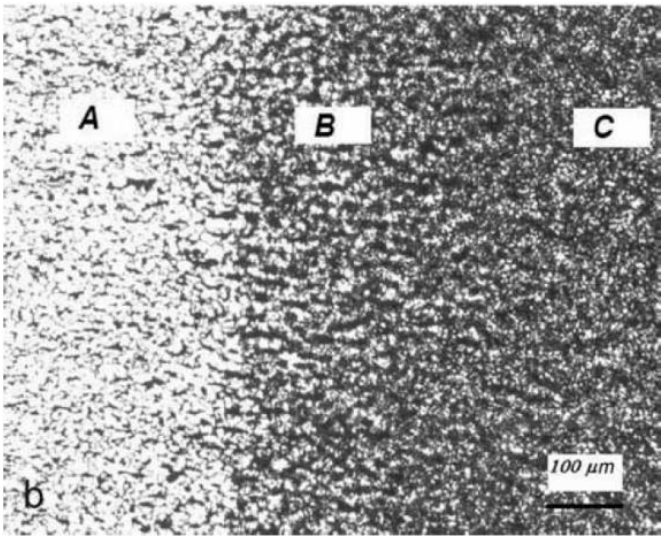


Figure 1.5: Macrograph of the bulk (A), heat-affected (B), and weld (C) regions of high-frequency induction welded low carbon strip steel used in tube manufacturing [35].

This inconsistency is attributed to increased solid-state carbon solubility (and its associated increased bulk grain and precipitate coarsening rate) in the weld zone due to higher temperatures (>1000°C [35, 43] – close to the material melting point [44]), and a phase transition from pearlite to austenite ('C') (from state 1 to state 2 in Figure 1.4). As well as solid solubility and temperature, diffusivity influences this kinetic phenomenon [10]. However, precipitate-related effects due to welding are assumed negligible due to the short length of time spent welding [45]. Due to increased carbon solubility in the austenitic region, interdiffusive effects allow carbon pick-up in the weld region, resulting in a higher carbon solution content nearer the weld (up to 0.5wt% [46]) (from 2 to 2' in Figure 1.4). Ultimately, the temperature gradient evolves a microstructural gradient, with the most significant austenitic grain coarsening being found in the regions exposed to the highest temperature (greater than the homogenising temperature). Hence, as the weld region cools

rapidly, a different phase of steel will form. Crucially, cooling is fast enough to minimise the time available for carbon atoms to move through the metallic crystal lattice and form larger carbides [10]. Therefore, the low carbon content and intermediate cooling rate will evolve increased pearlite levels in the HAZ compared to the bulk alloy [47] (shown by the application of the Lever Rule in Figure 1.4 where length $\boldsymbol{x_{1'A'B}} > \boldsymbol{x_{1A'B}}$). Although higher yield strength is attributed to this change [6], it is of negligible consequence when restricted to such a comparatively small region.

1.2.4 Heat Treatment

The HAZ and residual stresses found in the tubes after cold forming increase risk and cost for both Tata and its customers across all stages of fabrication, installation, and service life, wherein tearing, corrosion, and premature failure are likely [48]. To correct this microstructural inconsistency and coarseness, restore bulk mechanical properties, and improve corrosion resistance, the tubes are heated to a temperature of over 900°C in a walking beam furnace, which restores the bulk to the desirable austenitic phase, before cooling in air (full-pipe, high temperature normalisation). The normalisation temperature is set at the full annealing temperature, $\boldsymbol{A_{e3}}$, plus 100°C [49]. The entire tube is heated to the austenitic region, i.e. state 3, thus experiencing carbon pick-up across the entire component, and on cooling the entire tube reaches the higher pearlite content at 2'. The HAZ is eliminated, and the uneven distribution of internal residual stresses caused by thermal deformation is relieved via recovery, recrystallisation, and grain growth in the austenitic phase [50]. Hence, hot-finished tubes have several advantages over their cold-forged equivalents, including improved toughness, ductility, and pressure integrity, giving them an overall higher factor of safety [2]. Normalisation soak time is ultimately dependent on exact product requirements, however, industrial conventions such as '1hr per inch thickness' [51] and generalised heat treatment soak time tables [52] indicate that normalisation will occur in the minutes-hours range. For example, if the '1hr per inch' rule is applied to the range of wall thickness prescribed in BS EN 10217-2 [4], a soak time range of 4-36min can be expected for the 1.4-16mm wall range (0.06-0.6in) [2]. The prescribed soak time also dictates the speed of the walking beam as the tube is continuously moving. Cooling rate also influences microstructure [53, 54] and, for low carbon steels, slower cooling rates allow for greater carbon diffusion and pearlite growth. However, bainite will form if the temperature is not high enough to allow sufficient diffusion (see Section 1.7.1) [55]. Figure 1.6 shows the isothermal transformation (TTT) and continuous cooling transformation (CCT) diagrams, for

a typical tube grade prior austenite grain (PAG) [56] size of <10µm (see Section 4.2.1), which indicate that the lower carbon diffusion associated with faster cooling and lower temperatures promotes the formation of harder, lower strength bainite [48, 57, 58]. A smaller PAG can also lead to premature phase transformation at higher temperatures, as smaller grains provide a greater surface area of grain boundaries which act as sites for bainite nucleation [55]. Hence, the furnace-based cooling associated with normalisation favours slower cooling rates which promote the growth of the fine, pearlitic microstructure necessary to achieve the minimum tensile strength and ductility (see Section 1.2.3) for the tube products [2], as defined in BS EN 10217-2 [4].

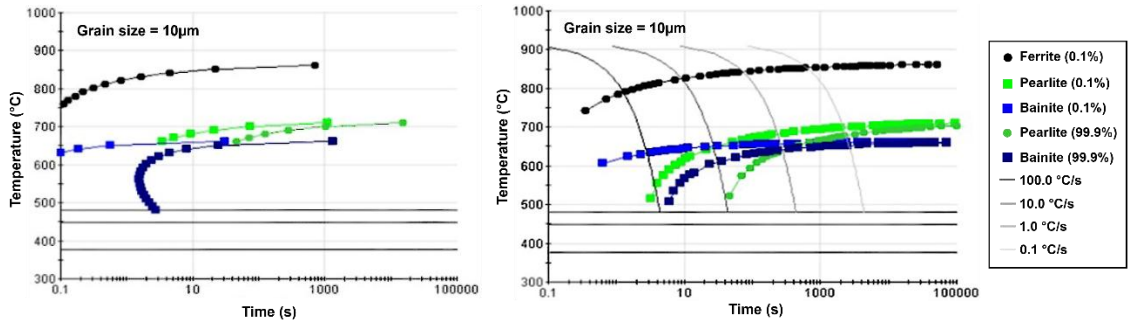


Figure 1.6: The isothermal transformation (TTT) and continuous cooling transformation (CCT) curves for the typical low carbon, low alloy steel grade used to manufacture conveyance tubes. The diagrams were generated in JMatPro® by Philip Addae as part of their MSc project work at Swansea University. The presentation of the diagrams has been adapted by the author of this thesis.

Oxide Scale Challenges

TSUK Tubes uses an air-fuel combustion reheat furnace wherein the tubes are heated via radiation from the furnace walls and roof and via convective action of the hot combustion products (CO_2, H_2O, and O_2 [59]). A multi-phase layer of dark-coloured, brittle iron oxide ('scale') is evolved during normalisation due to substrate reaction with the evolved oxygenated gaseous environment, i.e. the reheating furnace is fuel-fired so oxygen-bearing species, as well as free oxygen, are evolved and oxidise the steel surface [60]. In the tube manufacturing process at Corby, scale growth is constrained by shorter heat treatment periods (15-20 minutes – 2-3hrs at hot mill in Port Talbot) but experimental evidence suggests that a thickness of several hundred microns is still evolved [9]. More details regarding oxidation theory are provided in Section 1.3.

1.2.5 Stretch Reduction

The final step in tube manufacturing involves thermomechanical processing (TMP). The range of tube wall thicknesses offered by TSUK Tubes (Install®, Inline™, Inflow™, etc) (in

accordance with those prescribed in BS EN 10217-2 [61] is achieved by a multi-pass (3-5% reduction per stand, with the greatest reduction occurring in the first few stands, for example, in Reskovic et al.'s study of internal stress and tearing of stretch reduced tubes, 57% of diametric reduction occurred during the first four of 12 passes [35]) stretch reduction, using stencil matrices formed from rolling stands, wherein final tube wall thickness is dependent on the maximum allowable deformation and stress constraints of the steel at the processing temperature. This will define both the per-pass and total wall reduction. The processing temperature is defined by achieving a balance between strain hardening and softening to minimise deformation-induced point and line defects (which are also defined by chemical composition, initial microstructure and deformation condition, deformation rate), and maintaining the material in the austenitic region. Furthermore, to prevent wall tearing, especially in the weld region, diametric and wall thickness reduction must be optimised via application of a constant coefficient of plastic extension at each pass [35]. TSUK Tubes use the combined efforts of a 100m gas barrel system to perform a 2-3 minute normalisation at 700-750°C in an air-fuel mixture, followed by 30s 'top-up' period at 850-1040°C for 30s in an induction furnace (the proposed temperature range being wide due to the need to consult nominal bore and other product specification values to determine a specific value) as shown in Figure 1.7.



Figure 1.7: Radyne induction furnaces for tube normalisation [62].

As previously discussed, AC frequency is critical for achieving the amount of heat required for induction normalisation [41] and defined by how the wall thickness of the tube being normalised equates to the reference depth of the steel above its Curie temperature, e.g. 10kHz for wall thicknesses up to 5mm [41]. However, this kind of calculation is usually

streamlined by the use of charts (see Figure 1.8) which provide a factor by which the product of production line speed, HAZ width, and wall thickness, i.e. material flow rate, should be multiplied to obtain the necessary power rating (in kW) for a certain degree of heating. However, these charts rely on assumptions about treatment temperature and the inductor to tube air gap width.

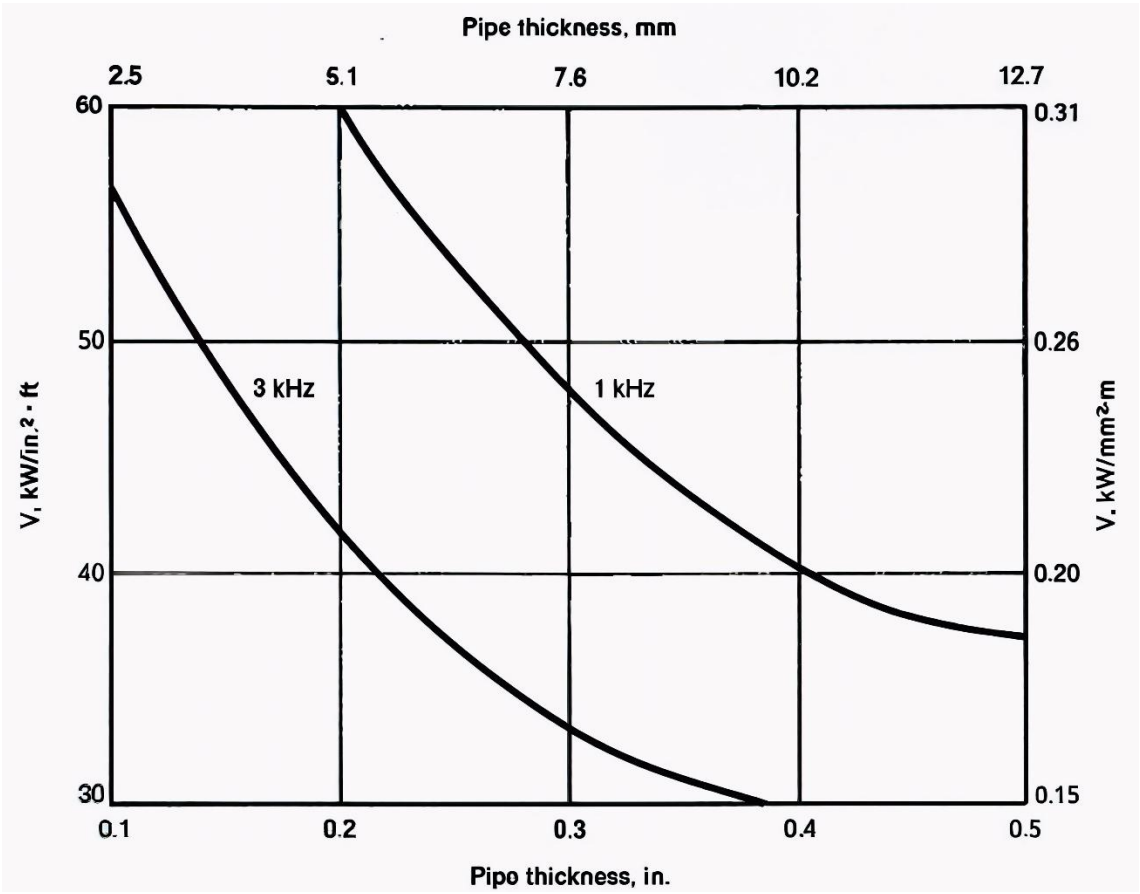


Figure 1.8: Chart correlating the power requirement (in kHz), based on the product of line speed, wall thickness, and HAZ width, to the voltage requirement for sufficient induction heating-based normalisation [41].

Ideally, scale would be perfectly adhered to the tube inner surface and provide corrosion protection and consistent surface quality. However, during the induction furnace-based stretch reduction (see Figure 1.9) which follows normalisation to obtain bespoke dimensions, mechanical stresses and strains cause the scale to spall (interfacial debonding between the steel substrate and oxide scale), leading to surface wear and substrate exposure. This has environmental and economic consequences for yield loss (up to 3% due to scaling alone [7]), aesthetic implications for this 'premium' marketed product due to either compaction of scale to the substrate surface ("rolled-in effect") and/or inadequate adherence of value-added coatings, e.g. anti-corrosion paint [2], and in-service surface performance problems.

The normalisation treatment is also considered a heat transfer-improving pre-treatment for the stretch reduction, which prevents an unequal reaction of the base and weld regions to deformation stress and interpass softening by regulating and reducing internal stresses in the weld region. Hence, the choice of normalisation temperature is an important balance between sufficiently high to achieve full normalisation and softening, but not so high that softness reaches a level where plant conveyance tooling deforms the tube geometry. However, it should be noted that stretch reduction is a complex thermomechanical forming process in itself and it is challenging to obtain enough empirical data to analyse it [63].

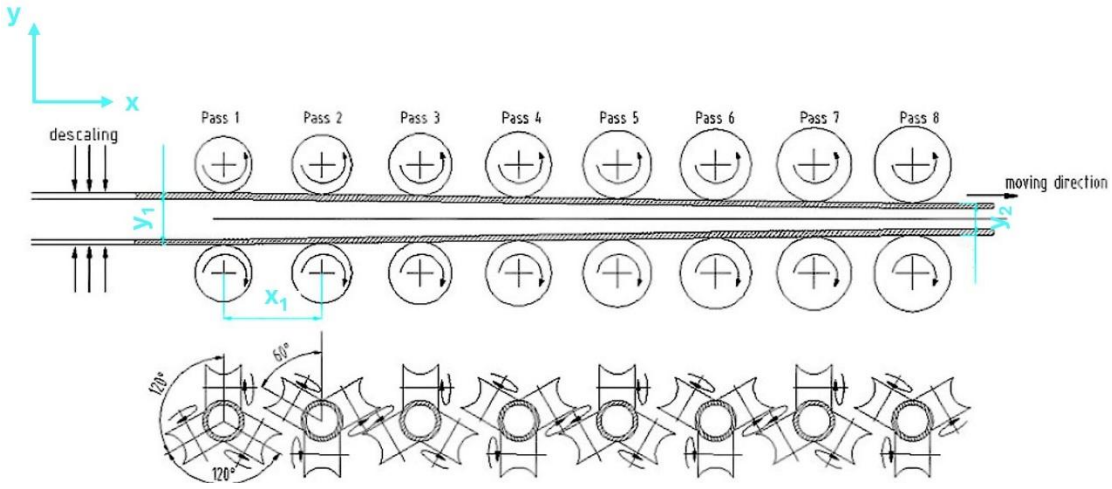


Figure 1.9: Schematic showing how a multi-pass stretch reduction of a conveyance proceeds (*adapted from source* [63]).

1.2.6 Descaling

Finally, descaling can be performed either hydraulically (via a high-pressure water jet) or mechanically (via shot peening) (see Figure 1.10). This is a continuous process necessary to counteract the rapid rescaling which occurs within seconds at high temperatures [22]. Most of the scaling does occur during normalisation, but there will also be a thin layer of scale arising from the high temperatures of slab coiling and tube welding.

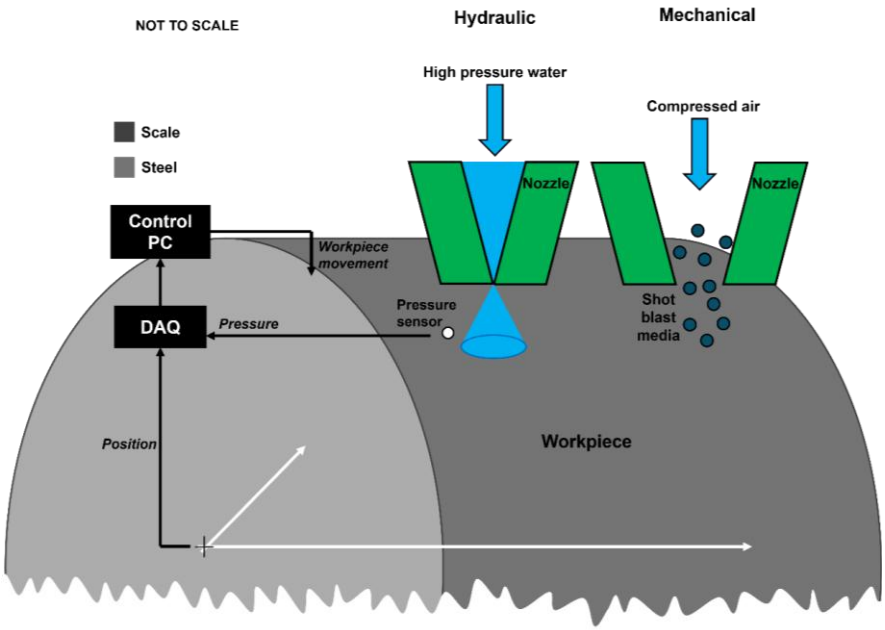


Figure 1.10: Schematic of hydraulic (*left*) and mechanical (*right*) descaling techniques on a curved surface ¤.

Hydraulic and mechanical (shotblast) descaling methods are used post-normalisation and post-stretch reduction respectively. Scale delamination occurs when the sum of impact, thermal, and oxidation stresses exceeds a critical failure value. These phenomena are discussed in greater detail in Section 1.4. Typically, hydraulic descaling is used for its combined benefits of reduced 'rolled-in effect' (scale compaction) [11] and partial cooling to the ideal stretch reduction temperature of ~800°C. In particular, thermal stresses arise from the difference in the effect of temperature change caused by discrepancy in thermal expansion coefficient between not only the scale and substrate [64, 65] but also between the individual phases of scale formed under certain thermal conditions [66]. Furthermore, Abuluwefa et al. [67] remarked that spalling can be accelerated by geometry, dimensions, and service environments which intensify stress fields, e.g. corners, mechanical vibrations, thermal stress, and surface defects. This is particularly important for the tube geometry considered in this project where forming procedures inherently introduce internal and external stresses. Hence, understanding of the scale morphology and kinetics, how it is adhered, and its likelihood of spalling both prior to and during descaling can help inform models of scale formation and descaling as well as optimise processes such as tube production.

Commercial Challenges due to Scale

Tata aims to reflect the high quality of its 'premium' product by offering a technical specification package, steel grade traceability, and support over the entire tube service life

[2]. Unfortunately, customer opinion of the product is undermined by the aesthetic disadvantages of rolled-in and/or spalled scale, despite the mechanical advantages of a hot-finished over a cold-formed tube (see Section 1.2.4). Furthermore, Tata itself is negatively impacted by the yield loss associated with scale [7]. Hence, Tata wishes to reduce external scale (without losing the anti-corrosion advantages of scale on the internal tube scale [68]) to an aesthetically, technically, and economically acceptable level.

1.3 External Oxidation of Iron

External oxidation of iron isotopes, a chemical reaction, within steel is accelerated by the energy intensive high temperatures and oxidising atmosphere found within reheat furnaces (at any stage of steel manufacturing). Reheat furnace treatments vary depending on the product. Within this project, the two main areas of product are the hot-rolled strip products produced in Tata's hot mill in Port Talbot and the tube production line in Corby. Maximum temperatures in the reheat furnaces can reach 1300°C [69] and 1000°C for each site respectively, with Corby using a lower temperature to account for the need for a minimum level of hardness during tube geometry forming. The mill scale formed has a multi-phase structure comprising iron (II) and iron (III) oxide species. The specific composition will depend on the stability of each phase, but in this project, reheating consistently proceeds at temperatures greater than 570°C where wüstite ($Fe_{1-x}O$) is stable and a stoichiometric ratio of $0.88 \leq 1-\boldsymbol{x} \leq 0.95$ is achieved [69].

1.3.1 Scale Kinetics and Morphology

Low carbon steel oxidation kinetics is defined by either a linear or parabolic rate law (dependent on instantaneous oxidation time and temperature considered [70]) as shown in Figure 1.11.

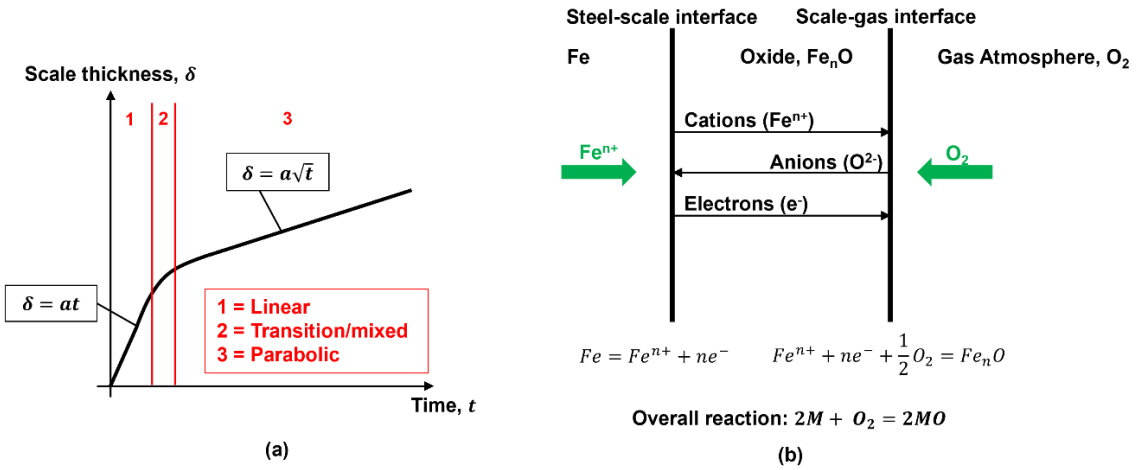


Figure 1.11: (a) Annotated graph of scale thickness against time showing linear, mixed, and parabolic kinetic behaviour at different stages of oxidation, and (b) a schematic showing Wagner's parabolic oxidation model ¤.

As most steel reheat treatments are high temperature (>250°C) processes, including tube normalisation, a logarithmic rate law description is not appropriate [28, 71, 72]. Initially, external oxidation of steel is governed by phase boundary processes at the steel-scale (SSI) and scale-gas (SGI) interfaces. For the SGI, the rate of mass transport of oxygen-containing gas to the surface for adsorption, splitting to free oxygen, chemisorption, lattice incorporation, nucleation, and growth [73], is the most critical interface phenomenon and governs the linear rate law, i.e. it is assumed that there is minimal ion diffusion through the scale. In the linear case, oxygen flux, $\boldsymbol{J_O}$, is not dependent on scale thickness, $\boldsymbol{\delta_{ox}}$, and can be kinetically assessed using mass gain, $\boldsymbol{\Delta m_o}$, per unit time, $\boldsymbol{t}$, for a given sample area, $\boldsymbol{A}$, eventually evolved Equation 1.5 where scale thickness and time are related via a rate coefficient, $\boldsymbol{k_x}$.

$$\boldsymbol{J_{O^=}} = \frac{\boldsymbol{\rho_{ox}}\, \boldsymbol{d\delta_{ox}}}{\boldsymbol{K_{S/O}}\, \boldsymbol{dt}} = \frac{\boldsymbol{\Delta m_o}}{\boldsymbol{A\Delta t}}$$

Equation 1.4

$$\boldsymbol{\delta_{ox}} = \boldsymbol{k_x t}$$

Equation 1.5

Once the iron (Fe) cations control the oxidation rate, scale thickness will become more influential, even though the same mass gain assessment can be used. Introduction of an expression involving cation spatial concentration gradient ($\frac{\Delta \boldsymbol{C_{Fe(2+/3+)}}}{\boldsymbol{\delta_{ox}}}$, i.e. the change in Fe cation concentration, $\Delta \boldsymbol{C_{Fe(2+/3+)}}$, over the scale thickness, $\boldsymbol{\delta_{ox}}$) and diffusivity, $\boldsymbol{D_{Fe(2+/3+)}}$, can be used alongside a double integration to obtain a parabolic (Fick's law-style) oxidation rate relation based on the scale density, $\boldsymbol{\rho_{ox}}$, time, $\boldsymbol{t}$, and the stoichiometric ratio of scale

mass per unit mass of oxygen in the oxide scale, $K_{S/O}$ (see Equation 1.7). The quotient term in Equation 1.7 can be expressed as the parabolic rate coefficient, k_p.

$$J_{O^=} = \frac{\rho_{ox}\, dx_{scale}}{K_{S/O}\, dt} = \frac{\Delta m_o}{A\Delta t} = D_{Fe(2+/3+)} \frac{\Delta C_{Fe(2+/3+)}}{\delta_{ox}}$$

Equation 1.6

$$\delta_{ox}{}^2 = \frac{2D_{Fe(2+/3+)} K_{S/O} \Delta C_{Fe(2+/3+)}}{\rho_{ox}} t = k_p t$$

Equation 1.7

In any case, the rate coefficient, k_x, follows an exponential Arrhenius-type profile dependent on a pre-exponential constant, $k_{x,0}$, activation energy of oxidation, Q, absolute temperature, T, and universal gas constant, R_{gas}. Hence, oxide gain is also a function of temperature.

$$k_x = k_{x,0} e^{-\frac{Q}{R_{gas}T}}$$

Equation 1.8

To maintain equilibrium and high metal activity as oxidation proceeds, there must be oxygen (anion) and iron (cation) diffusion and ion flux levels must be maintained as the flux path lengthens due to scale thickening. Surface reaction rate, i.e. SGI activity, must fall to satisfy this constraint via a reduction in iron ion diffusion, making it the rate-controlling step. This kinetic change triggers a transition from a linear to parabolic rate law profile. Hence, kinetics is controlled by the dynamic balance of oxygen adsorption and iron ion diffusion during scale thickening. Such changes in the adsorption-diffusion balance lead to the multi-phase characteristics of the scale [70].

Many studies apply a purely parabolic oxidation model [59]. However, Schluckner et al. [28] argued that this neglects the influence of different combustion environments, referring to Wilkstrom et al.'s study [60] of the effect of atmospheric oxygen variation on oxidation kinetics. Both Wilkstrom et al. and Abuluwefa et al. [67] demonstrated how lower oxygen concentrations could prolong the adsorption-dependent linear rate law stage to a non-negligible length due to slower mass transport, and Wilkstrom et al. also proposed the existence of a significant linear-to-parabolic transition region (see Figure 1.11). Tata's tubes experience high temperatures for an extended period and sufficient exposure to oxygen so a parabolic rate law can be assumed. Wagner's descriptive and predictive model for parabolic oxidation uses ionic and electronic charge transfer and balance during simultaneous metal

oxidation and free oxygen reduction to characterise alloy element distribution [70]. However, their model assumes a scale with a perfect microstructure and adhesion, i.e. they ignore the possibility of defects, e.g. cracks, porosity etc, whose propagation could be accelerated by the high temperatures and mechanical work of tube stretch reduction. This is particularly important as high temperatures, such as those used in tube normalisation, are associated with greater development of defects during cooling [22]. Such propagation has been shown to interrupt oxidation diffusion mechanisms [74] and its effect on kinetics and morphology must therefore be considered. Specifically, delaminated scale allows steel to be exposed to the combustion environment and rapid rescaling initiates on the same surface [69].

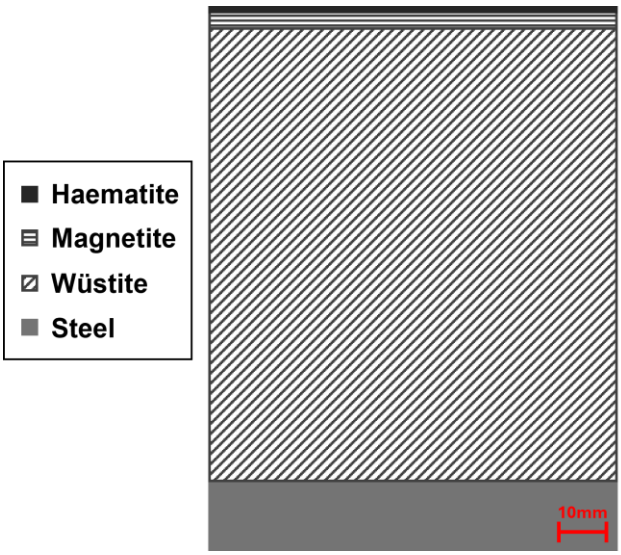


Figure 1.12: Idealised, scaled representation of the multi-phase oxide layer evolved during normalisation ¤.

Changes in diffusion mechanisms are also important when considering the multi-phase scale layer formed (see Figure 1.12) at high temperatures ($\boldsymbol{T}$ > 600°C [28]), comprising wüstite (FeO), magnetite (Fe_3O_4), and haematite (Fe_2O_3) in a respective 95:4:1 ratio [70, 75] (although the ratio displays minor variation in the literature due to experimental uncertainty [15, 71, 74]). Each phase's independent chemical, physical, mechanical, and tribological properties [22, 66] are governed by the level of exposure to both oxygen and iron ions, e.g. wüstite is the dominant phase, within which iron diffusion is fastest [75], with the lowest oxygen and highest iron content respectively, owing to proximity to the steel surface [75]. Metal and oxygen content also affects crystallographic characteristics, with wüstite, magnetite, and haematite displaying cubic, inverse spinel, and rhombohedral structures respectively [22]. Iordanova et al. [72], amongst others [76, 77], argue that the strong influence of ion diffusion phenomena on oxidation further supports the assumption

of a parabolic rate law for high-temperature investigations. The relative thicknesses of the three phases also reflect this assumption of bulk diffusion-controlled (, i.e. parabolic) oxidation and local thermodynamic equilibrium at phase interfaces as wüstite has a much greater iron diffusion coefficient, i.e. the activation energy of iron diffusion through wüstite is lower than magnetite and haematite [59]. It should be noted that cooling rate within the study of oxidation is critical to obtain an accurate representation of oxides formed at high temperatures. Cooling rate must exceed a threshold value (2°C/min) to evolve non-equilibrium conditions sufficient to prevent wüstite decomposition below the eutectoid temperature of 570°C [22]. Figure 1.13, Figure 1.14, and Figure 1.15 show the typical multi-phase scale formed on low carbon steel heated to normalisation range temperatures (900-1000°C) for normalisation range soak times (up to 5 mins) [59, 71, 77].

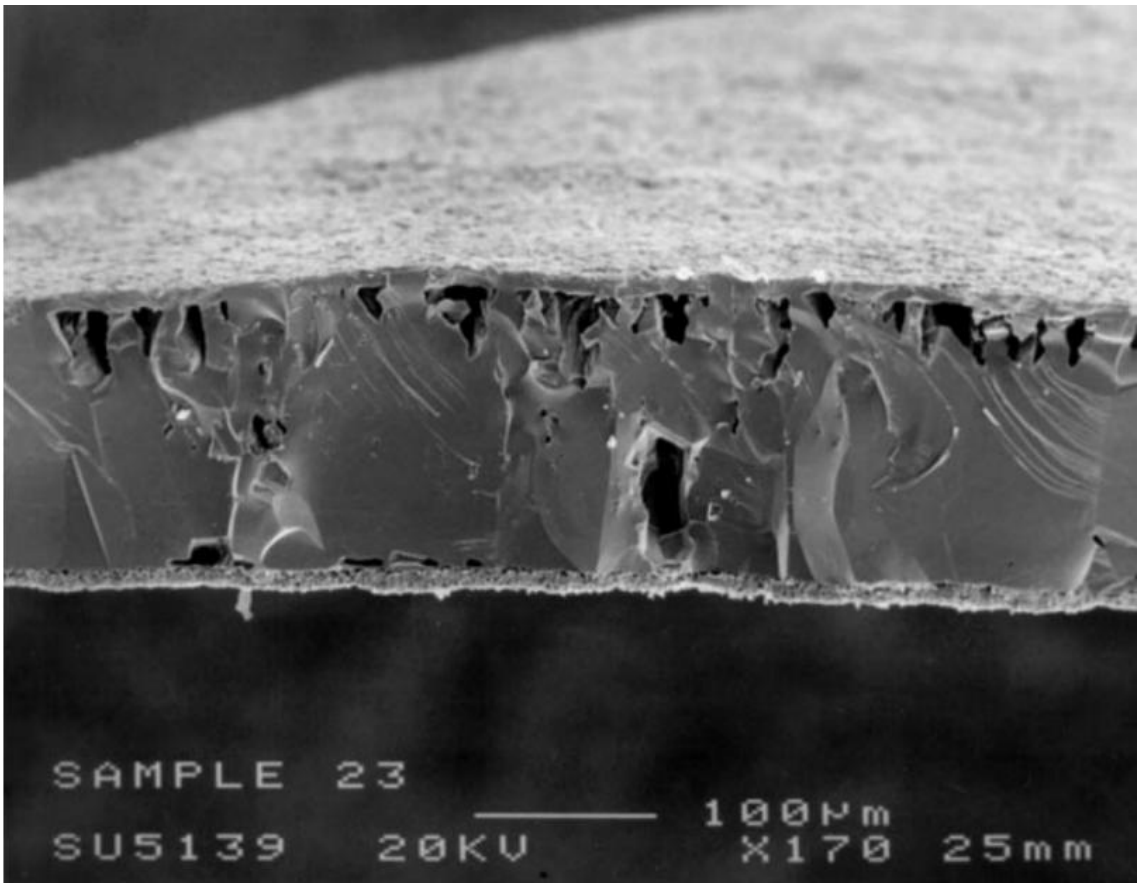


Figure 1.13: Scanning electron microscope image of approximately 150µm of oxide scale formed on low carbon steel at 975°C for 800s [77].

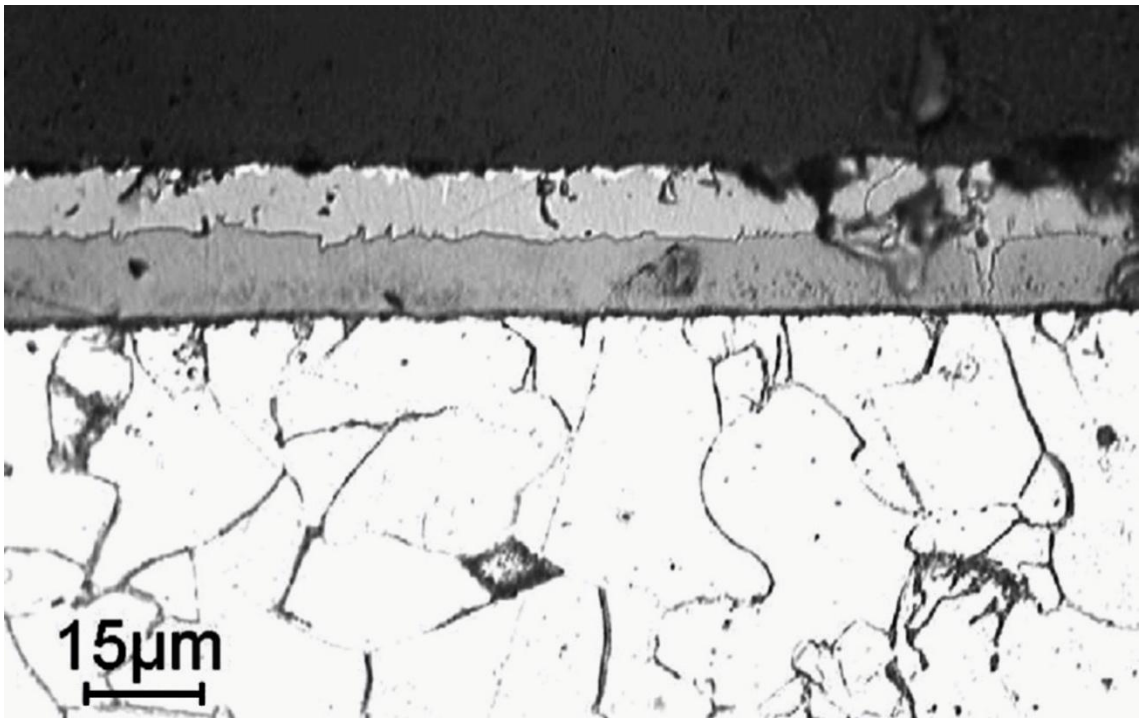


Figure 1.14: Optical light microscope image of approximately 20µm of oxide scale formed on low carbon steel at 1000°C for 2.5s [71].

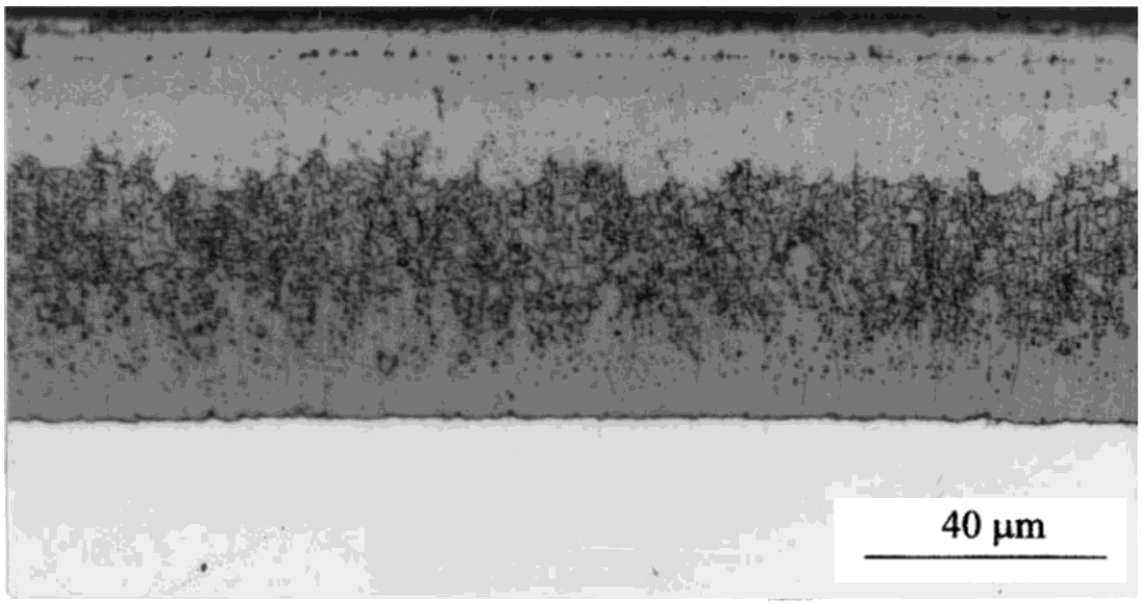


Figure 1.15: Scanning electron microscope image of approximately 80µm of oxide scale formed on low carbon steel at 900°C for 12s. The cooling rate used was 5°C.min^{-1} [59].

1.4 Mechanical Analysis of Oxide Scale during TMP

Stretch reduction, i.e. high-temperature deformation, and the high mechanical strain and stress it inherently introduces creates ideal conditions for oxide spalling, which is already promoted by internal growth and thermal stresses evolved during oxidation and post-normalisation cooling respectively. As well as undesirable surface condition, spalling leads to a loss of passive corrosion protection from the inner tube surface [64]. The protective effect of the inner surface oxide not only depends on chemical constraints, namely high thermodynamic stability, slow self-diffusion of oxide forming elements, low oxide vapour pressure, and impermeability to aggressive environmental elements and compounds, but also the oxide's stress state with respect to its adhesion to the substrate, thermal and mechanical compatibility with the substrate, and erosion resistance [78, 79]. Protective healing can also blunt and close existing partial thickness cracks become thereby reducing failure probability. However, if a protective oxide fails, the minimum content of the necessary alloying element for oxide formation must be present in the exposed metal substrate to achieve protective healing at the failure site. Hence, for regions of the inner surface which do not meet this criterion due to significant subsurface zone depletion, minimising oxide failure is still pertinent. This therefore confines debate, as to whether the ideal scale should be perfectly adhered or highly descalable, to only the outer tube surface. Since inner tube wall surface condition is less of a concern and corrosion prevention is important in fluid conveyance applications [80], scale investigations are confined to the outer tube wall surface. However, it should be noted that proposals for a thick (several millimetres [59]) but highly descalable oxide are undesirable during tube manufacture, not least due to the associated material yield loss, but also due to the poorer surface quality, increased asset contamination, and slower line speed resulting from increased descaled volume (C. Owen, personal communication, November 28, 2023). This will ultimately simplify any future scale-up of a novel oxidation-resistant coating application technique. Although stretch reduction and/or tube geometry have been investigated, hot strip rolling, i.e. steel sheet coiling, has been far more widely studied in terms of oxide kinetics [81]. However, the difference between the respective TMP techniques, i.e. rolling vs. stretch reduction, must be considered. Coiling is a non-isothermal operation wherein slower cooling occurs (rather than isothermal heating during stretch reduction) which can lead to a different scale composition [64]. During industrial-scale steel strip rolling, strip width is much larger than strip thickness so width deformation is assumed negligible and pure

bending is expected [23]. Bending imparts both normal and shear stress without a change in thickness of the material, i.e. plane strain conditions [82], whereas tube stretch reduction involves a more complex stress-strain profile depending on the required change in tube bore and wall thickness [83]. However, in both cases, there is interaction, i.e. surface contact, with conveyance tooling, e.g. work rolls. Conveyance tooling is harder than the hot steel so is assumed a rigid body [23].

Unlike oxide kinetics, oxide mechanics has received greater attention for curved surfaces. Evans argues that epitaxial constraint-induced stress generated normal to the oxide-metal interface on a planar surface will be negligible if strain mismatching is accommodated by intrinsic dislocations [84]. However, curved surface oxidation is an example of constrained growth where the continuity conditions at the oxide-metal interface during growth evolve a tensile resultant force normal to this interface (for both convex and concave surfaces) (see Figure 1.16). Furthermore, for convex surfaces, such as the external surface of a conveyance tube, compressive, in-plane normal stresses are induced in the oxide layer, resulting in its compressive shear failure, tensile fracture, and buckling depending on the strength of the oxide-metal interface [84].

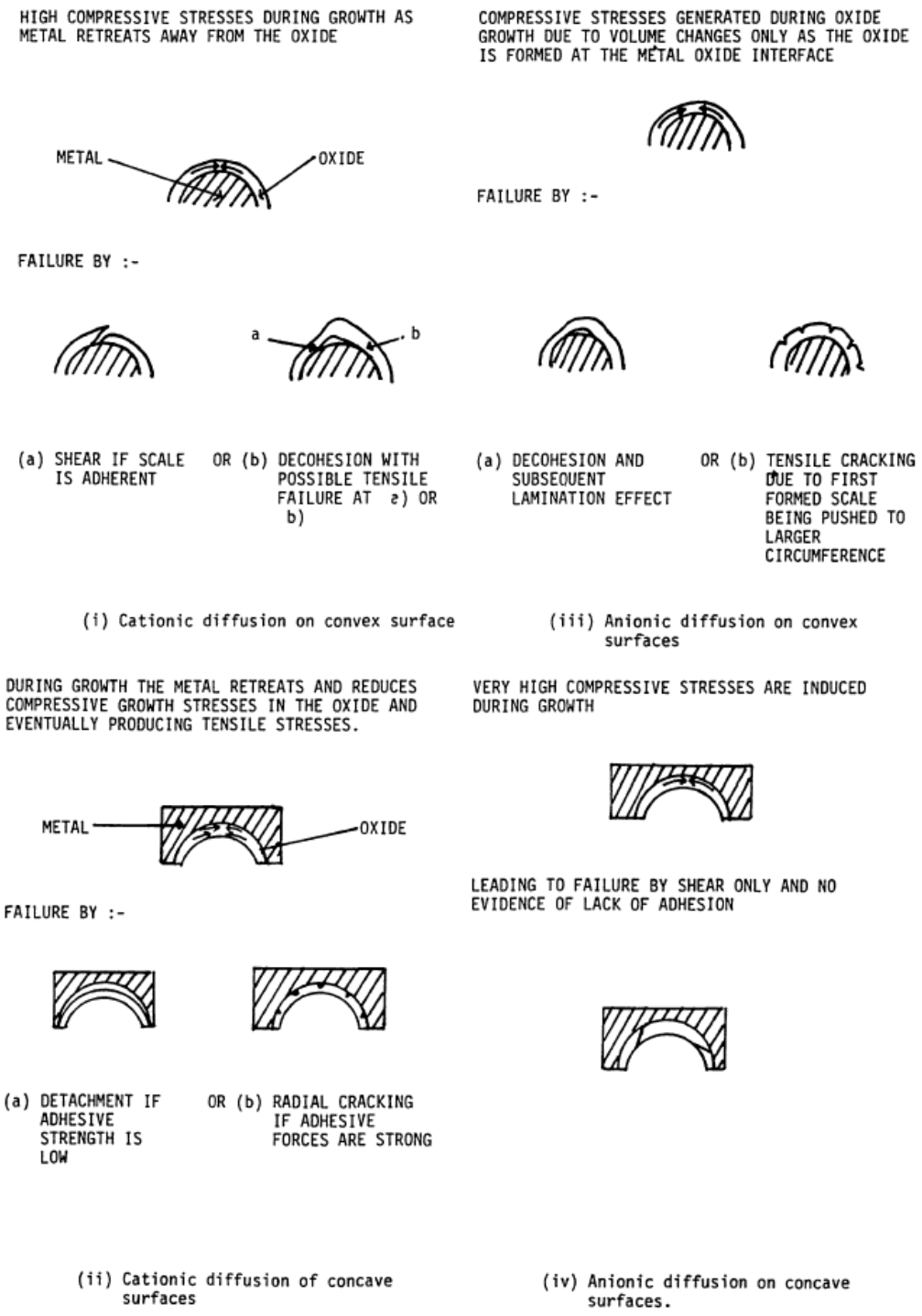


Figure 1.16: The development of stress and failure modes in oxide layers formed on curved surfaces [84].

Krzyzanowski et al. argue that although an oxide scale model should ideally be included in finite element macro models, the low thickness of the oxide scale relative to its steel substrate can cause numerical difficulty during coupling, e.g. large time increments yielding a nonpositive stiffness matrix [79]. Entchev et al. conducted a numerical study of non-planar oxidation geometries on titanium (Ti) [85]. They argue that existing models of oxidation of metals fail to consider the effect of volumetric expansion, which is commonly associated with this class of materials, and works which do account for this phenomenon are

exclusively experimental. A model is required which also accounts for volumetric expansion. As with the conventional model of diffusive oxidation, Entchev et al. propose that the moving steel-scale and scale-gas interface phase boundaries exist due to the consumption of the metal substrate and expansion of the oxide respectively, where oxygen diffusion is the driving factor, which was also discussed by Evans [84]. Several assumptions are also made during model derivation, namely, instantaneous oxidation reaction at the steel-scale interface, rigid body motion of the metal substrate, constant scale concentration, thermodynamic equilibrium at the scale-gas interface, an initially oxygen free metal substrate, an isothermal system (due to rapid energy dissipation as oxidation is an exothermic reaction), and constant physical parameters.

Only 1D versions (planar, cylindrical surface, cylindrical hole, spherical surface, i.e. 'shapes of engineering significance' [86]) of Entchev's proposed model [85] can be solved without considering additional momentum balance equations. Although analytical solutions to the planar oxidation model (obtained from a different author discussing planar oxidation of silicon) are available via dimensionless variables and a growth parameter, $\boldsymbol{\lambda_g}$, used to express oxide thickness as a function of time (see Equation 1.9), solutions to oxidation problems in cylindrical coordinates discussed can only be obtained numerically.

$$\boldsymbol{\delta_{ox} = \lambda_g \sqrt{4t\mathcal{D}_{(O_2,TiO_2)}}}$$

Equation 1.9

For investigation of oxidation of a cylinder surface and oxidation of a cylindrical hole, the former and latter applying to the external and internal tube surfaces respectively, Entchev et al. used a Finite Difference Method (FDM) formerly used to solve 2D oxidation problems without volumetric expansion. An unconditionally stable scheme can be developed using backward-time discretisation [87] and forward space schemes [88]. A convergence study showed time and spatial steps of 100 and 0.5ms respectively were necessary to achieve convergence after 2-3 iterations in approximately 120s. The input parameters (density, molecular weight, concentrations and diffusivity coefficient) were obtained from the literature for an oxidation temperature of 700°C. Crucially, it is accounting for the difference in molar densities of the metal substrate and its scale which results in oxide expansion and therefore accounts for volumetric expansion. For validity's sake, the scheme was also applied to the 1D planar case. The method successfully converged to the analytical solution described in Equation 1.9. Figure 1.17, comparing the dimensionless oxide

thickness, h^*, against dimensionless time, t^*, profile, demonstrates how accounting for volumetric expansion can affect oxidation. Figure 1.17a shows how when volumetric expansion is not accounted for oxide thickness increases faster than the planar case in the cylinder surface case but slower in the cylindrical hole case. This is attributed to the fact that as the substrate is consumed by oxidation, the radius of the outer and inner surfaces decreases and increases respectively [89]. This is where a limitation of the model gets highlighted. It was discussed in Section 1.7.1 that the 1D approach to diffusion modelling does not reflect the multi-axial nature of oxidation. Uniaxial oxidation is only assumed if residual stress is absent, i.e. in this case the substrate and scale would need to have near-equal CTEs (or alternatively the scale viscosity would need to inhibit instantaneous viscous relaxation). Only under these conditions can a single normal component of strain be assumed. However, the formation of scale at the surface in the case of tube oxidation means lateral oxidation strain components must exist to account for the CTE mismatch and residual stresses. The dilatational model is therefore more appropriate [89]. The Pilling-Bedworth ratio (PBR), φ, is proposed method for quantifying the effect of dimensional changes associated with oxidation. The PBR represents the ratio of oxide to metal volume as a measure of stress arising from volume dilatation during conversion of a metal to its oxide, which can be measured via deformation analysis, i.e. dimensional changes [90-92]. Such dimensional changes are typically attributed to metal-to-oxide transformation, phase and/or microstructural transformations within layers, or new oxide formation in the existing oxide (also known as intrinsic growth stress). However, for volumetric expansion accounted for by a PBR of 1.766 (see Figure 1.17b), oxidation in both cylindrical cases is faster than the planar case. Furthermore, there is a change in profile for the later stages of cylindrical hole oxidation. Whilst the characteristics of cylindrical surface are unchanged, cylindrical hole oxidation is accelerated by the dominance of the oxide expansion when the hole radius due to oxidation after a given time is significantly smaller than the initial radius. Both cylindrical cases take longer to reach full oxidation when volumetric expansion is accounted for. However, for the case of external conveyance tube oxidation, the outcome is unchanged. Furthermore, oxidation was assessed for a much longer period (up to 72hr) in this study than in TSUK Tubes normalisation and there is negligible discrepancy between all 1D geometries in the early stages of oxidation.

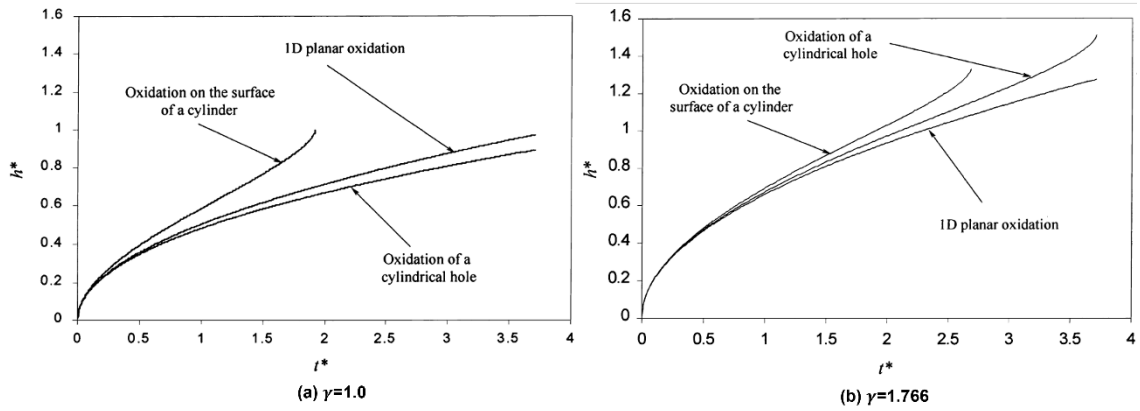


Figure 1.17: Comparison of dimensionless oxide thickness profile for Pilling-Bedworth ratios (PBRs) of (a) 1.0 and (b) 1.766 [85].

Cylindrical cases results were also validated using experimental data from the Materials and Structures Laboratory at Texas A&M University [85]. For three experimental test samples with different initial diameters, results showed that the model underestimates and overestimates oxide thickness for the surface and hole cases respectively.

Imbrie and Lagoudas [93] hypothesise that for the oxidation of a solid cylinder surface, short oxidation times yield a compact, well-adhered scale, similar to that observed on a 1D planar sample, i.e. curvature has no effect. However, longer oxidation times (>18hr) generated deviation of the cylindrical geometry from the flat plate. The compact layer thins as its boundary at the SSI moves towards the SGI and a porous, layered oxide structure is left in its wake. As new oxide layers form, preceding layers continuously expand and thus so do individual pores. This demonstrates the importance of the consideration of volumetric expansion in order to account for the evolved pore size distribution, with largest pores near the SGI. Interestingly, unlike flat plate specimens, failure is most often observed as radial cracks with the circumferential cracks associated with SSI failure more likely attributed to cooling. The details concerning failure are summarised in Krzyzanowski and Beynon's study of oxide failure during tensile loading for two different grades of mild steel [94]. Figure 1.18 highlights how a transition temperature exists where the separation stress for the oxide scale overtakes its oxide-metal interface counterpart, i.e. oxide cohesion is greater than oxide-metal adhesion and failure mode transitions from Mode I to II accordingly. Mode I failure described by Krzyzanowski and Beynon albeit for planar surfaces [77], is associated with a higher adhesive strength between the substrate and scale than the cohesive strength of the oxide itself. This is in contrast with flat plate specimens where failure is more often observed as Mode II, i.e. longitudinal cracks due to SGI failure and the higher cohesive

strength than adhesive strength. Oxide failure modes are discussed in greater detail in Section 1.4.

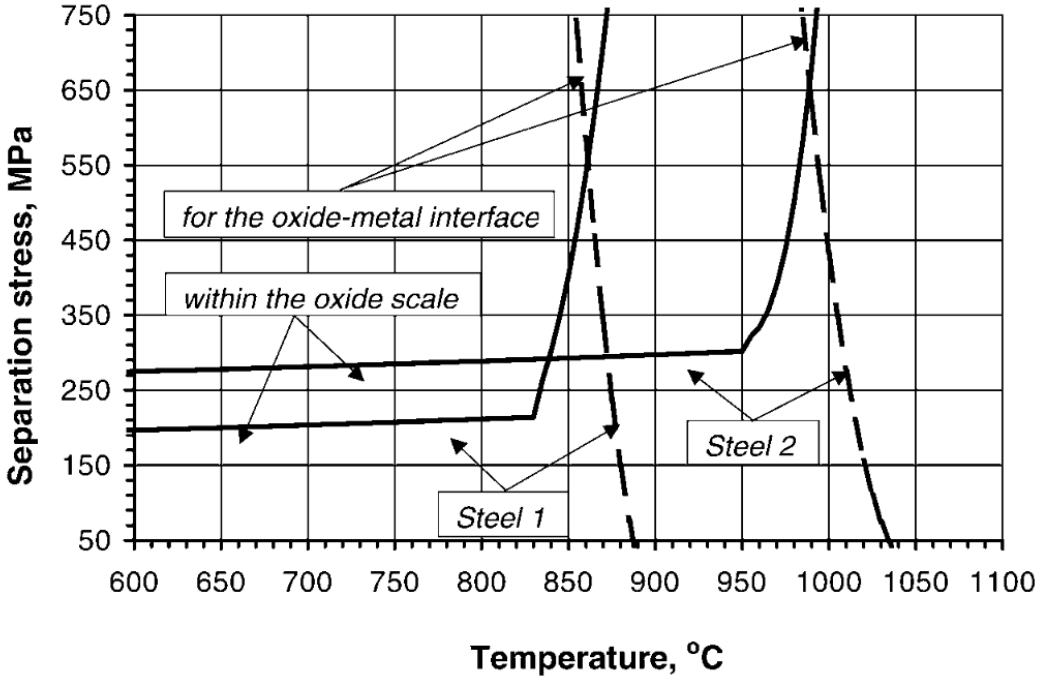


Figure 1.18: Separation stress-temperature plot highlighting the transition from Mode I to II failure at a given temperature influenced by steel chemistry [77].

However, oxidation of a cylindrical hollow (which is comparable only when assuming plane strain, i.e. no axial stress applied) showed no such similarities to flat plate specimens, even with the same test conditions. There was no evidence of scale detachment at any time and the scale surface was smoother than the other samples. Crucially, the stress state found in the inner surface of the hole, i.e. the tube, inhibits void initiation and expansion. Lateral growth strain arises in the oxide but expansion is constrained by the metal, leading to compressive stress in the oxide scale [89, 95]. The compressive stress in the oxide scale induces higher tensile hoop stresses in the metal substrate so that the compressive stresses in the metal, which evolve due to oxygen dissolution into its crystal lattice, are offset and overall stress is reduced, thus reducing the likelihood of exceeding the critical fracture value. The 'pre-stress' state evolved by the oxide is beneficial and a common technique to improve tube strength via compound cylinder systems [96].

As such, porosity phenomena can contribute significantly to an explanation of why Entchev et al.'s model over- and underestimates oxide thickness for the solid cylinder and cylindrical surfaces respectively. In particular, they highlighted how porosity becomes less uniform and pores become larger as the oxide thickens and preceding oxide layers expand Due to the

presence of oxygen in the diffusion couple (substrate and scale undergoing heat treatment), it can be assumed that the Kirkendall porosity effect is significant [97]. Substitutional diffusion of oxygen via vacancy diffusion, which is entropically favourable due to the high disorder associated with an imperfect vacancy-containing crystal, dominates due to the high localised distortion demands associated with the correlated movement of direct place exchange migration. Only a vacancy mechanism can allow differing fluxes, i.e. differing diffusivities in the couple's constituent materials, which exists to oppose the resulting flow of atoms from the higher diffusion coefficient material into the lower (according to Fick's 1st Law) via an equal and opposite direction pore-forming flow of vacancies. Porosity can become problematic when pores expand to restore the equilibrium concentration of vacancies which optimises configurational entropy and defect formation enthalpy [85, 98]. However, it must be noted that Yamaguchi and Someno [99] identified that oxygen diffusion in wüstite is a function of oxygen potential so the dominant diffusion mechanism must be via interstitial cations. This cannot be explicitly reflected in Entchev et al. [85] but can be reflected in a modified diffusion coefficient [100].

Aside from the mechanical state of the substrate itself [101], clearly simultaneous high-temperature oxidation and manufacturing processes will generate stresses in the oxide due to thermal deformation, mechanical loading, and most importantly in this context, growth stress due to oxidation itself. This situation lends itself to visualisation by a corrosion stress interaction diagram (CSID) which comprises each stage of oxide material life. The five stages of this diagram comprise oxide mechanical failure, healing by continuing reaction, protective potential plateau, surface crack initiation and/or material consumption and crack propagation and/or accelerated material consumption (end-of-life). Overall, the steps described highlight how the cycle failure and repletion of oxide scale will eventually be exhausted as the substrate subsurface zone becomes depleted below critical oxidation levels. Further corrosion can then induce surface crack growth and material consumption to an extent that the load-bearing cross-section is decreased. Corrosion can also assist crack propagation and accelerate material consumption which ultimately leads to component failure. Hence, oxidation is as much a problem mechanically as it is kinetically and once an oxide has reached stage III without a sufficient material design reservoir, the component is no longer suitable for safe operation. Schütze highlighted that the range of stress situations and proposed models have not been collated before their review paper addressing stress affects during high temperature corrosion [102].

For a low oxygen solubility scenario as is found in austenitic steels in conveyance tube manufacturing [103], the oxide will develop a compressive growth stresses as it increases in volume compared to the substrate, i.e. PBR > 1 [104]. This is true provided that the oxide grows at the interface so that stress cannot be relaxed by movement of the free surface [104]. It has already been highlighted that such stress, when it exceeds the critical value for buckling, plays an important role in oxide spalling phenomena which plague tube manufacturing (although it should be noted that oxides with a yield stress lower than their buckling stress are more likely to fail via relief by plastic flow) [105-107]. Although in situations where oxide formation on the outermost surface of the free layer favours stress relaxation by accommodating volumetric changes normal to the free surface, even in this case the presence of macroscopic and/or microscopic curvature will induce stress. Rhines and Wolf proposed a mechanism for growth stress generation during oxidation dominated by bulk cation diffusion on a planar nickel surface, where anion diffusion rate matched the bulk diffusion rate so that oxide forms along existing grain boundaries perpendicular to the metal-scale interface, i.e. within the existing oxide [108]. They argue that only with perpendicular orientation of oxide grain boundary growth can lateral strain be generated, requiring concurrent inward oxygen and outward metal diffusion, and a lack of rigid body displacement to accommodate any strain. It should be noted that changes to grain boundaries due to oxidation parallel to the metal-oxide interface are not considered due to the ability to relax related stress by movement of the free surface. Only oxide formed on grain boundaries normal to the metal-oxide interface is considered.

However, Speight and Harris highlighted that vacancy-ion interchange was not accounted for and thus the potential for anion diffusion along existing oxide grain boundaries was replaced by oxide growth in cracks or pores in the existing oxide [109]. Evans therefore proposed a model for growth stress generation in planar metal samples with grain boundary-wise anion diffusion in the existing oxide. They proposed that the oxide intrusion at the metal-oxide interface will lead to localised volume changes which cannot be relaxed by the moving phase boundary (in the absence of thermal relaxation) [105]. However, Clarke noted that for high temperature treatments, such as normalisation, the substrate can usually accommodate relaxation by plastic flow [110].

Solving for growth stress in the oxide is achieved by finding a closed elastic solution for the stress field and including a boundary condition which equates free surface traction to zero [107]. Obtaining a closed form solution usually results in assuming a uniform stress field and

applying a stress at the free surface equivalent to the mean stress field calculated for that position. The mean stress field can be taken from Head's expression for a dislocation near a planar two phase interface [111]. Ultimately, the mean stress, in terms of linear elasticity, comprises the superposition of the dislocation array stress field and stress field applied to satisfy the zero traction free surface boundary condition. Within discussions of mean compressive stress in the oxide, it should be noted that mean normal stress perpendicular to the interface is relaxed by free surface motion as previously discussed and has a value of zero, and mean shear stress due to dislocation is an odd function of $\boldsymbol{y}$ $\left(-\boldsymbol{f}(\boldsymbol{x}) = \boldsymbol{f}(-\boldsymbol{x})\right)$ [112] also making it zero.

Assuming an oxide layer of thickness, $\boldsymbol{\delta_{ox}}$, infinite dimensions in the $\boldsymbol{x}$ and $\boldsymbol{y}$, and compressive state associated with a Pilling-Bedworth ratio (PBR), $\boldsymbol{\varphi}$, greater than unity, the average compressive stress in the oxide, $\boldsymbol{\bar{\sigma}_{ox}}$, can be expressed as a function of thickness, elastic modulus, $\boldsymbol{E}$, grain size, $\boldsymbol{d}$, and intrusion size, $\boldsymbol{a_{intr}}$, via an integration of stress components derived for the metal substrate (see Equation 1.10).

$$\boldsymbol{\bar{\sigma}_{ox}} = -\frac{\boldsymbol{4a_{intr}E\varphi^{\frac{1}{3}}}}{\boldsymbol{d\pi\delta_{oxide}}}\left[\boldsymbol{d} - \boldsymbol{a}\tan^{-1}\left(\frac{\boldsymbol{d}}{\boldsymbol{a_{intr}}}\right)\right]$$

Equation 1.10

The size of the oxide grains and intrusions are therefore influential for a given oxide thickness and material parameters. A key conclusion by Evans [84] was that although compressive growth stress increases with oxide grain size, when intrusion size is controlled, it eventually becomes insensitive due to the decrease in extent of the stress field in the y-direction with increasing oxide grain size, which leads to cancellation of adjacent stress fields. However, increasing intrusion size dramatically increases compressive stress, with a six-fold increase in intrusion size leading to an equivalent increase in compressive stress. Hence, shrewd selection of the intrusion size is critical for accurate stress prediction. Evans argues that an improved strategy to educated estimation would be to predict the growth kinetics of the parameter, which are in turn phenomenologically coupled to stress [84]. Previous work has shown that anion transport rate is reduced under high compressive stress when the anion vacancy transport rate is less than that of the ion itself [113]. It is therefore suggested that this will lead to an upper limit of attainable oxide intrusion size.

However, Srolovitz and Ramanarayanan [107] highlighted that the mean oxide compressive stress is not a function of oxide thickness when thickness exceeds half that of the grain size.

However, they also suggest that oxide thickness will have an upper limit once any change in strain energy associated with volumetric increase is equal to the change in chemical free energy due to the same phenomenon. It is at this point that new oxide formation will change to a relief-promoting mode such as at the metal-oxide interface, prone to voids due to cation outward diffusion and therefore delamination, or existing oxide free surface growth. Hence, Evans' model [84], which accounts for the former mode, is appropriate. However, Srolovitz and Ramanarayanan [107] report a discrepancy between their own and Evans' results, arguing that the latter incorrectly modelled the dislocation dynamics. Furthermore, for curved surfaces, even with an unconstrained free surface, the introduction of new oxide between the metal and existing oxide, leads to stresses and strains at the surface radii as the metal retreats, as it is consumed by oxidation, and loses contact with the existing oxide. In other words, any surface curvature (where the minimum ratio between the grain size and surface curvature is 1:20 [114]) will inhibit the oxide from following volume changes in the oxidising substrate, leading to elastic and creep deformation [106]. Furthermore, the previously only lateral (hoop) stress found in planar examples is extended to a 2D state to include perpendicular (radial) compressive stress, which Clarke highlights is at a maximum at the metal-scale interface [114]. Lateral strain is also higher in the cylindrical than planar case due to the presence of edge dislocations necessary to accommodate surface curvature during oxidation. However, Stott and Atkinson argue that creep and plastic deformation phenomena are often neglected in quantitative models [115]. Finally, Schütze felt it important to comment on the effect of intrinsic growth stresses on perceptibly damage-free oxide scale after high temperature treatment [102]. Atkinson previously observed that oxygen transport rate through a growing scale can exceed values typically seen during solid-state diffusion [116]. They argued that intrinsic growth stresses lead to localised opening of grain boundaries via microcracking which can promote oxidation by allowing gas cavity migration and transport of non-oxygen species to the substrate. Within this mathematical model, many estimates must be made for the instantaneous oxide state in the absence of kinetic data, namely the Pilling-Bedworth ratio, oxide intrusion lateral dimension, and oxide thickness.

Geometric stresses are most commonly predicted using Manning's analysis of the effect of geometry on oxide scale integrity, which can be used to predict strain in the oxide [106]. They emphasise that the source of the metal supplied for oxidation is of great importance suggesting that a fraction,

$\boldsymbol{V_{bulk}}$, will come from the metal bulk via vacancy dispersion, and the remainder will come from the metal surface immediately below the oxide. Similarly, a fraction, $\boldsymbol{\alpha_{surface}}$, of the oxide forms at the outer surface of the scale, and the remainder at the metal-scale interface. In the planar case, the oxidation front displacement rate needed to maintain scale integrity and contact to the metal will not result in stress as the front proceeds unimpeded (assuming uniform oxidation across the surface and homogeneity between the oxide and metal). However, Steiner et al. highlighted the need to consider the degree of surface vs. interface oxidation when selecting appropriate values of $\boldsymbol{V_{bulk}}$ and $\boldsymbol{\alpha_{surface}}$ [117]. For example, the idealised case of $\boldsymbol{\alpha_{surface} = 1}$ (total surface oxidation) cannot be applied, although surface oxidation is being modelled, as previous discussions have already emphasised the effects of simultaneous cation and anion transport during oxidation of iron. The scale displacement rate can be related to metal loss, $\boldsymbol{\frac{d\delta}{dt}}$, via the scale displacement vector, $\boldsymbol{M}$, in Equation 1.11 [106]. Equation 1.11 also relies on the PBR, $\boldsymbol{\varphi}$, which is a function of the molecular weights, $\boldsymbol{W_r}$, and densities, $\boldsymbol{\rho}$, of the metal oxide (to obtain a ratio of oxide and metal volume contributions) and can be expressed using Equation 1.12.

$$\boldsymbol{M = \varphi\left(1 - \alpha_{surface}\right) - \left(1 - V_{bulk}\right)}$$

Equation 1.11

$$\boldsymbol{\varphi = \frac{V_{oxide}}{V_{metal}} = \frac{W_{r,oxide}\rho_{metal}}{W_{r,metal}\rho_{oxide}}}$$

Equation 1.12

1.4.1 Adhered Scale Behaviour

While oxide scale is adhered to the steel substrate, its effect on surface roughness will subsequently alter metal forming operations, i.e. plastic material flow, such as stretch reduction, which rely on metal-tool contact. Furthermore, oxidation introduces two additional interfaces for consideration: the steel and scale interface (SSI) and the scale and tool interface (STI). Additional added-value protective and/or aesthetic coatings, e.g. galvanic, polymer [2], are often applied to conveyance tubes which introduces a further interface between the scale and coating (SCI). When considering hot strip rolling, Jiang et al. argued that its effect on surface roughness and metal forming demands a deeper understanding of the deformation, tribological, and heat transfer characteristics, of low carbon steel oxide scale [23]. They identified temperature, reduction, and rolling speed as

key factors affecting plastic material flow. Jiang et al. [23] developed a FEA model of the surface asperity profiles of both the steel and scale before rolling to assess the effect of friction, rolling speed, and temperature on surface roughness post-rolling. As with other studies [15, 73], a pure wüstite layer was assumed given its significant contribution to the classical three-phase layer model [90]. As such, it was hypothesised that complete scale failure under the shear friction imposed by scale-roll contact (modelled by a modified Coulomb law) would proceed via a raft sliding mode [118] due to the absence of the weakest planes associated with the three-phase layer and scale-steel interfacial weakness at high temperatures. However, Jiang et al. [23] remark that temperature variation was only based on external thermal cycles and did not consider internal heating due to plastic deformation. Overall, it was stated that flow stress defines the onset and rate of asperity buckling which characterises final surface condition.

During their experimentally validated investigations, Jiang et al. [23] identified temperature and reduction as control parameters, due to their effect on the proportional constant of the flow stress equation. The hot strip rolling interface coefficient of (static) friction was defined as being in the range of $0.1 \leq \boldsymbol{\mu_s} \leq 0.5$ for both the SSI and STI. Both the steel and scale showed increased roughness as $\boldsymbol{\mu_s}$ increased at the STI. Although, it was highlighted that very thin (<1μm) scale may lead to deformation of the SSI when stress is applied to STI [23]. However, with sufficiently thick scale to avoid this phenomenon, surface roughness increase at the STI was twice that of the SSI. Given that surface asperity interaction for two solids leads to one interfacing with another under pressure and their sliding with respect to each other [119], lower friction will reduce the rolling pressure demand and thus reduce damage by asperity clashing, i.e. lower interfacial pressure reduces asperity deformation-related damage. No such trends were observed by Jiang et al. when $\boldsymbol{\mu}$ varied at the SSI [23]. Although rolling speed was not deemed to influence surface roughness, even at diameters much larger than the validatory experimental data used, temperature was shown to increase scale surface roughness, as predicted by the flow stress equation presented. This was attributed to the temperature dependence of scale mechanical properties, with higher temperatures yielding a greater degree of plastic deformation and thus greater surface roughness. For rolling speeds in the range 0.12-0.72ms^{-1}, up to 25% more roughness was observed at $\boldsymbol{T}$ = 1025°C rather than 800°C.

1.4.2 Delaminated Scale Behaviour

However, oxide formed in air at high temperatures is susceptible poor scale adhesion to the steel [59, 75]. In response to the slow preparation, poor adhesion, and high porosity of air-based pre-oxidation treatments on metals, Wang et al. compared the kinetics, morphology, and adhesion of external scale formed on an Ni-16Fe-4Mo alloy both in air ('air oxidation'), and electrochemically ('electrochemical oxidation') [24]. Although both methods yielded parabolic growth of a conductive and passivating oxide scale on their metallic anode (although this process was faster for electrochemical oxidation), initial investigation using SEM revealed a compact, homogeneous and uniform scale with no spalling or cracking when grown electrochemically ('electrochemical scale'). In contrast, the scale grown in air exhibited ridge-shaped bulges, severe spalling and surface roughness. Through-thickness transverse cracks in the scale, and voids and cracks propagating parallel to the SSI were also observed in the air-based scale ('air scale'). The transverse cracks in particular inhibit complete surface passivation and promote continuous intergranular oxidation. Hence, although contextually in this project a thinner scale from the air scale is favourable, its advantages are undermined by this lack of oxidation resistance and poor oxide condition.
During air oxidation, kinetic and mechanical phenomena combine to promote poor scale adhesion. The faster diffusion rate of outward direction (from SSI to SGI) iron cations than inward direction diffusion of oxygen anions leads to metallic vacancy injection at the SSI (and also evolves an unfavourable electric field in the SGI to SSI direction). The circular voids, which form and coalesce under the Kirkendall effect due to the undesirable overall net ionic flux [97], are also deformed to ellipsoids [24]. This is due to the compressive stress state associated with the combination of growth [120] and thermal [64] stresses associated with oxidation and high temperature cycling respectively. Stress concentration is found at the poles the major axis of these delamination-inducing voids.
These phenomena are not observed during electrochemical oxidation, primarily due to anodic polarisation of the metal substrate. The flow of charged particles between the substrate, oxide, and solution, i.e. current across the electrode-electrolyte interface, observed during oxidation is sufficient to cause a positive potential shift which anodically polarises the substrate [121]. This, and the arising favourable electric field direction from SSI to SGI, accelerates corrosion and reduces metal vacancy injection by increasing the rate of oxygen diffusion. This promotes a reduction in defects both within the scale (cracks) and at the SSI (cracks and voids) leading to increased scale compactness and adhesion. However,

the introduction of external stress (and associated variation due to geometry effects), as found during tube stretch reduction, is not considered in Wang et al.'s work [24].

As previously discussed, scale deformation, fracture, delamination, and spalling, is partially caused by the mechanical loading evolved during stretch reduction. However, once the metal substrate is exposed by scale spalling, the thermomechanical scenario is altered again as tool-metal contact leads to increased friction and heat transfer [81, 122]. Krzyzanowski and Beynon [122] argue that neither previous computational nor analytical models could simultaneously analyse heat transfer and deformation at the tool-workpiece interface during tensile loading of secondary scale (via hot roll contact), accounting for scale effects. They propose that a lack of scale high-temperature ductility data, amongst other thermomechanical parameters, has led to oversimplifications via previously discussed prevalent assumptions of perfectly compact and adhered scale. However, they argued that considerations of scale failure under loading meant that metal extrusion into widening scale cracks and tool-substrate contact period information could be accurately obtained, in this case via experimental data and imaging. It was hypothesised, before the high-temperature tensile test was performed, that the highest strain rates are observed near or at the surface (10-15 times the nominal value) and are therefore the most probable scale fracture sites.

Experimental results in Krzyzanowski and Beynon's [122] investigation firstly revealed two failure modes either side of a critical temperature, as were alluded to in Section 1.4.1. SEM imaging revealed shear through-scale cracking (mode I), i.e. evidence of brittle failure in the form of rectangular spalled areas (see Figure 1.19), at temperatures below 600°C. Above this value, failure transitioned to mode II with unfractured scale raft slipping along the SSI (or along the oxide phase boundaries in the case of a multi-phase scale), i.e. evidence of ductile caused by deformation stress exceeding that for viscous flow without fracture (see Figure 1.20). The strength of the SSI relative to the oxide's own strength defines the transition between failure modes: mode I demands an SSI which is stronger than the oxide, whilst mode II demands the opposite [77].

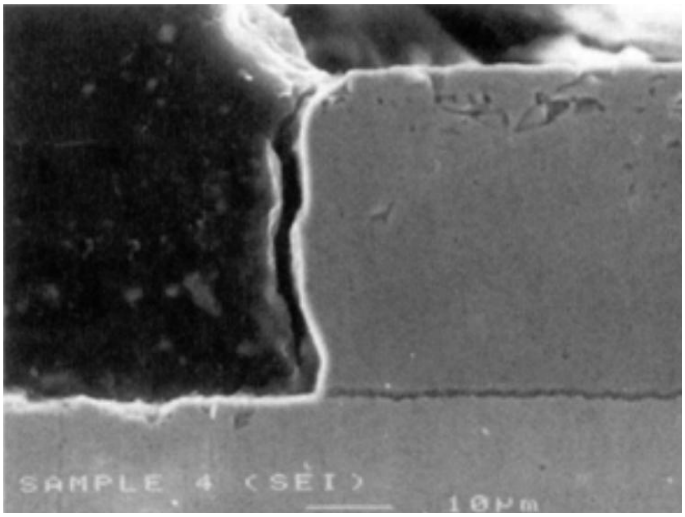


Figure 1.19: Backscattered electron microscope image of approximately 40μm of an oxide scale cross-section formed at 830°C for 300s, showing evidence of through-thickness transverse cracking [122].

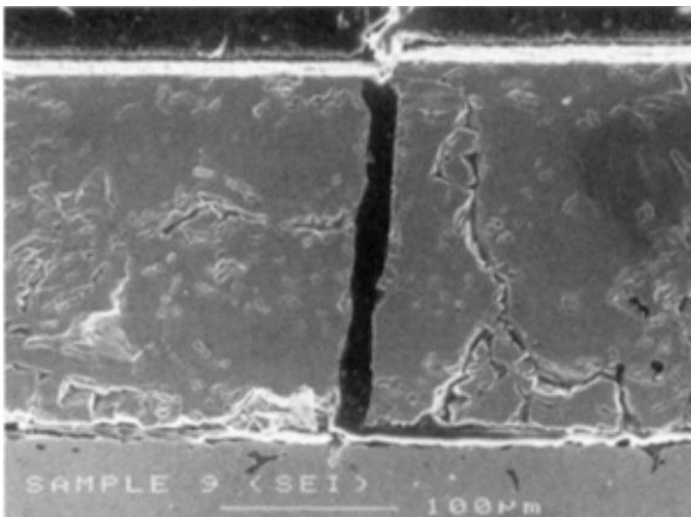


Figure 1.20: Backscattered electron microscope image of approximately 200μm of an oxide scale cross-section formed at 1150°C for 100s, showing evidence of through-thickness transverse cracking and the beginning of interfacial delamination initiating at the crack base and propagating along the steel-scale interface [122].

Given the strong influence of porosity level on scale failure mode, Krzyzanowski and Beynon [122] reasoned that the individual phase layers within the scale, and the potential for their interfaces to be mode II failure sites (see Figure 1.21), should be considered separately. Differences in porosity and crystal morphology were observed and attributed to inward oxygen transport and metal cation diffusion dependency respectively [120], with the inner layer containing a large number of uniformly distributed pores whilst the outer layer was notable for its larger, less equiaxed crystals. The inner-outer layer interface was proposed as a potential delamination site [122].

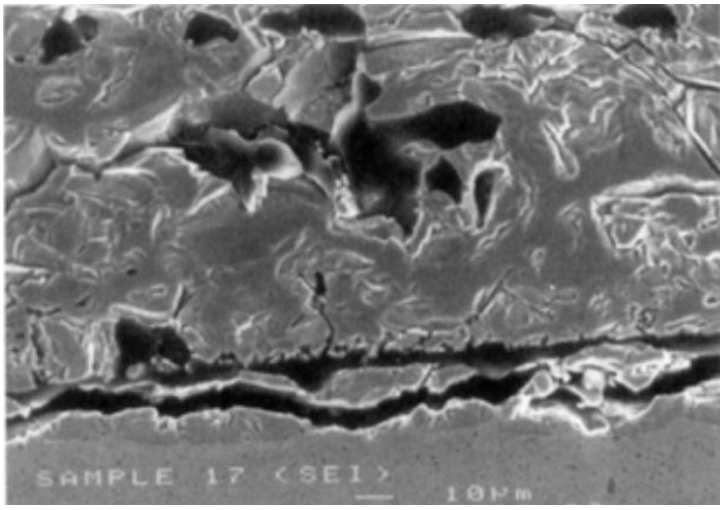


Figure 1.21: Backscattered electron microscope image of approximately 100µm of an oxide scale cross-section formed at 1150°C for 100s, showing evidence of delamination within the oxide at a phase boundary [122].

This sort of failure was observed in non-homogeneous scales formed above 1150°C, with evidence of a much more porous (up to 1mm void) and thicker spalled outer layer. The inner layer was minimally porous and well-adhered even after large strain application at this temperature. It was at lower temperatures (<850-900°C) that mode I failure was observed in all scale thicknesses and morphologies. Thus, initially brittle mode I scale failure is defined by Linear elastic Fracture Mechanics (LEFM), assuming small defects, and brittle phenomena. As temperature increases, ductile mode II failure is observed and defined by stress distribution and interfacial cohesion strength, before differences at a phase level led to mode II-style failure at the inner-outer scale layer interface beyond 1150°C. In their assessment of steel grade composition effects, Krzyzanowski and Beynon [122] provide further evidence for these effects, and for the need for further work focusing on quantitative relationships between failure mode transition and the deeper understanding of slipping mechanism at the delamination zone (SSI or otherwise) as a physical basis for micro-modelling [77]. The effect of strain was highlighted by the fact that higher temperature, thicker, and higher strain rate scales delaminated more than their lower temperature, thinner counterparts, even if they were less homogenous. This demonstrated that ultimately, temperature, strain, and strain rate were the most influential parameters when defining how scale cracking, slipping, and adherence.

Lee et al. [64] comment that, although spalling is attributed to the fracture of the SSI, the process is accelerated by microstructural damage and the related influence of several factors including deformation dimensions, e.g. bending curvature (or wall thickness change in this project), volume fraction, residual stress, defect dimensions, e.g. porosity diameter, crack length, scale thickness, and interfacial roughness. They focused on the effect of interfacial

roughness and assumed a perfect microstructure for simplification. Kalasin et al. [123] looked specifically at the adhesion behaviour and surface quality of the thinner and less pure scales evolved on Electric Arc Furnace-heated (EAF) low carbon rolled steel samples and, crucially, did not assumed a defect-free scale microstructure. Mechanical adhesion testing revealed transverse cracking followed by complete localised spalling, with thicker slabs showing a lower spalling ratio and, although they proved that scale thickness was independent of slab thickness, this was not the case for adhesion phenomena. Lee et al. argued that interfacial roughness was a critical factor as it had previously been reported that normal interfacial stress due to bending, which defines interfacial fracture, and residual stress due to the thermal expansion coefficient differential are amplified by roughness features acting as key fracture sites. Furthermore, Zambrano et al. [22] demonstrated the strong dependence of roughness on temperature when investigating low carbon steel oxidation up to 1200°C, demonstrating how oxidation kinetics influenced scale thickness and its related effect on oxidation-promoting metal ion diffusion. However, they did not discuss the effect of these changes on spalling behaviour.

Lee et al. [64] developed an FEA model, following a detailed approach to determine the temperature-dependent thermo-mechanical properties of the steel and scale. The consideration of material properties as a function of temperature will be crucial in this project. Krzyzanowski and Beynon also highlighted, in their own computational hot rolling model [77], that temperature-dependent functions are the only way to acquire accurate information about transient axisymmetric metal-scale flow, viscous sliding, and failure in tension. Crucially, their approach couples the macro-model of the external mechanical loading with the micro-model of scale failure to reveal how the former influences the latter. However, they also emphasised the importance of the consideration of the thermal behaviour of the SSI, citing the 10-15 times lower thermal conductivity of scale compared to steel as a source of SSI weakening at high temperatures leading to fracture and slipping phenomena defined by interfacial cohesive and adhesive strengths and stress distribution. This detailed study could form the basis of a tube geometry-specific model of SSI behaviour under stretch loading, which could be extended to include an SCI (see Section 1.4.1).

Lee et al. [64] also showed the positive correlation between roughness and traction, and higher rates of interfacial failure at peaks and inflections. They comment that shear interfacial stress has previously been ignored but demonstrated its relevance by showing how inflections within high-frequency roughness were dominated by the shear stress

component. Additionally, Lee et al. [64] showed that the inclusion of thermal residual stress in the model was pertinent to the magnification of the existing stress field, leading to increased premature interfacial failure. Whilst it was recognised that little can be done to alter thermal behaviour, it was recommended that a controlled reduction rate could minimise interfacial roughness. These conclusions were corroborated by Noh et al.'s FEA study [65], again highlighting influence of interfacial roughness and non-negligible effect of shear interfacial stress on spalling behaviour, especially at surface inflections. Krzyzanowski and Beynon [77] also agreed that a critical shear stress value, and its transmission from the substrate to adherent scale, was responsible for transition scale sliding from a viscous to frictional mode. Again, this demonstrates the complexity of the mechanical situation of the SSI and how the introduction of a coating on a tube geometry could add complexity (see Section 1.4.1). Also, although it was agreed that roughness-free interfaces were also stress-free, this is an unrealistic scenario in practice where constant interaction with mill conveyance equipment will inevitably incur roughness.

Furthermore, both Lee et al. [64] and Noh et al. [65] found that thicker scales experienced lower normal interfacial stress due to a reduction in longitudinal stress attributed to increased proximity to the zero-strain neutral axis of bending. However, inspection of industrial data by Lee et al. [64] revealed the opposite phenomenon, i.e. increased spalling for thicker scales. Whilst this could be a stress-related phenomenon, it was attributed to the assumption of defect-free scale [124]. This highlights the need for experimental validation during computational model development to assess the validity of assumptions and their effect on accuracy. A scale failure map demonstrated how an increased scale thickness can trigger wedging failure solely due to internal growth and thermal stresses, therefore thicker scales are associated with a weaker interface (due to higher internal stresses) and more pre-bending fracture. Thus, oxide descalability must account not only for the external loads which evolve during TMP, but also the scale's own natural tendency to spall due to the thermal and growth stresses which depend on manufacturing parameters.

Matsuno et al. [120] specifically explored the impact of growth (oxidation) stress on descalability during a high-temperature hydraulic descaling operation. They exposed their rimmed steel samples to a number of conditions including isothermal and non-isothermal conditions and thermal shock via both argon (Ar) gas spraying and hydraulic (water jet) descaling. However, during descaling, water pressures only reached 15% of those used in industry, and for a much shorter seconds-long period. More attention could be paid to the

effect of fully scaling-up to industrial scale, and its effect on scale behaviour, utilising the scope available via a computational approach. However, they were still able to show how blister formation, which precedes spalling, occurs in a defined temperature-time envelope which can be expanded, thus increasing the likelihood of spalling, by application of mechanical (high-pressure water) or thermal (cold shock) stress. However, it was highlighted that blistering (when not caused by gas-based processes such as decarburisation) still occurred prior to the introduction of thermal stresses, i.e. oxidation stress must ultimately control blistering. Matsuno et al. suggested that oxidation stress puts adhered scale into a state of compression which generates the blister and subsequent plastic deformation of the detached scale drives blister growth. Whilst the former is easy to prove given the high plasticity of wüstite at high temperatures [15], spalling is more complex. Early hypotheses suggested oxidation stress-induced wüstite plastic slip generates clefts between slipped scales and the steel, leading a loss of SSI contact and blister-initiating pores. However, scale-steel adhesion is also clearly important and shown to be dependent on temperature and scale thickness. In particular, Hulley and Rolls' [125] conclusion of cohesive strength being three times higher than adhesive strength supports Krzyzanowski and Beynon [77] comments regarding the temperature-critical transition of scale failure mode from cracking to spalling where interfacial weakening means scale cohesive strength is dominant.

Ultimately, Matsuno et al. also proposed that oxidation stress is the dominant cause of adhesive failure within the combined effect of stress and adhesion vs. cohesion strength dominance, since temperature will accelerate oxidation and cause greater compressive volume dilatation [120]. The effect of such mechanisms, as well as the potential for internal stress relief via plastic deformation during stretch reduction, should be considered within this project with respect to the specific thermomechanics of the TMP used.

Scale surface condition has also been shown to be affected by furnace atmosphere conditions, with lower stack oxygen concentration and oxygen enrichment levels evolving a more highly adhered scale (especially at longer furnace exposure times) [69]. Matsuno et al. [120] observed higher levels of porosity were observed in the inner third of the scale layer closest to the steel-scale interface when higher levels of oxygen enrichment were applied. However, steel grade was demonstrated to have the most influence on adhesion behaviour and surface condition with carbon content affecting intactness and alloy elements such as nickel and copper causing surface enrichment-related effects.

1.5 Reactive Scale Management

Scale can be managed via a proactive or reactive approach. Reactive scale management, which aims to eliminate the problem after detection by identifying its root causes and amplifiers after repeated incidence [126], can take the form of oxidation-resistant coatings (oxidation-resistant coatings may also be referred to by some authors as anti-oxidation coatings). Grant demonstrated how passive and active oxidation-resistant coatings are a cost-effective reactive scale management approach [9].

1.5.1 Oxidation-Resistant Coatings

Although changes to the furnace atmosphere and parameters have potential to control oxidation and oxide behaviour [16, 28, 67, 127, 128], the benefits of furnace atmosphere control may be offset by high costs. Protective coatings are a cheaper but effective alternative [129, 130].

Grant tackled the conveyance tube scale growth problem by designing two novel anti-scale coatings which were assessed via oxide thickness, surface condition, and bulk mechanical property measurements [9]. 'SOPAC 20' is a water-based inorganic coating comprising sodium polyphosphate, polyacrylic acid crosslinker, and a 20-30μm recycled glass additive. It has advantages of low cost, spray-coat compatibility, and easy synthesis. This passive barrier coating was shown to reduce oxidation by 82% but initial energy dispersive spectroscopy (EDS) analysis highlighted the precipitation of phosphate into the oxide layer, with potential for formation of a composite.

The second, active coating was based on a reinforced mullite ($2Al_2O_3{\cdot}2SiO_2$) system but only demonstrated an impressive oxidation reduction of 87% under maximum adhesion and with the addition of a porosity-blocking zirconia (ZrO_2) reinforcement to prevent oxygen precipitation. However, for both coatings developed, scale-up to application at an industrial scale within the existing manufacturing infrastructure was challenging. Torkar et al. [131] successfully demonstrated the protective capabilities of ceramic (deemed suitable due to high melting points and high-temperature chemical stability) silica- and alumina-based coatings to decrease iron loss via scaling by up to 60%, dependent on time, temperature, substrate composition, and furnace atmosphere. However, the authors did not explore the effect of these factors on coating protective behavioural variation, e.g. optimal coating performance in the range 1000-1200°C was followed by the coating becoming ineffective beyond the upper limit. Furthermore, there was no exploration of the overall mechanism

which enables substrate isolation from the oxidising atmosphere.

Yu et al. [27] sought to expand on the success of similar ceramic-based coatings designs [132] which achieved a 98% reduction in scale mass gain. Oxidation kinetics was constrained to the initial linear rate law for the entire heating period, demonstrating how the coating inhibited iron ion diffusion. However, success was confined to stainless steels and heavily dependent on their characteristically high chromium (Cr) content. Optimal iron ion diffusion-inhibiting passive barrier protection by a chromium III oxide (Cr_2O_3) layer only exists whilst Cr supply is sufficient, and chromite and scale spalling will occur once bulk Cr levels are depleted enough to allow iron ion diffusion. The protection provided by the chromite (Cr_2FeO_4) intermetallic layer following iron ion diffusion offers less protection and is likely to spall and expose the substrate. Liu et al. [132] propose that by designing a coating to slow oxygen diffusion to a rate slower than that of the growth stress-induced chromium oxide layer spalling and self-healing cycle, thus maintaining the protective passive layer, iron ion diffusion is inherently inhibited. However, Yu et al. highlight that the low chromium levels in low carbon steels mean that oxidation prevention via passive iron ion diffusion is not a reliable technique [27]. They propose that anti-oxidation coating design must prevent both iron and oxygen diffusion via an interface layer and argue that scale microstructural condition and its effect on diffusion was more important than manufacturing parameters for anti-oxidation coating design. This is another reason not to assume a microstructurally perfect scale in this project (see Section 1.4.2).

Yu et al. suggested that, based on the effects of crystal field stability and sub-lattice location, intermetallic crystal lattices with minimal octahedrally-located Fe^{2+} ions will exhibit the best oxidation inhibition [27]. They argued that hercynite ($FeAl_2O_4$) was a viable option and furthermore that advances in computational power would enable a more detailed study of ion diffusion behaviour via molecular dynamics. For experimental validation purposes, Yu et al.'s hercynite coating was prepared from a water-based slurry of alumina-synthesised mullite, sodium silicate binder, sodium polyacrylate dispersant. Both Yu et al. [27] and Liu et al. [132] argued that their coating solutions, which were prepared at a small-scale for experimental validation purposes, were low cost and easy to apply to a range of different steel grades. However, this was not demonstrated at an industrial scale. The technical and economic performance of the novel anti-oxidation coatings developed during Grant's work [9], at a small-scale similar to that in [27, 132], should be assessed at a larger scale.

Yu et al.'s results [27] confirmed their hypothesis that Fe^{2+} vacancy formation energy (VFE)

variations across different sub-lattice sites within different compounds dictate surface oxidisability. This was shown by the fact that the computational model developed evolved activation energy values 106% and 83% higher than that of magnetite for chromite and hercynite respectively. Although hercynite therefore has a lower Fe^{2+} diffusion inability than chromite, it still has excellent anti-oxidation capability alongside its ability to be sourced from a wider range of materials, especially considering that chromite cannot form naturally on low carbon steel, making hercynite both effective and practical as an anti-oxidation coating. Experimentally derived lower linear and parabolic rate law constants (50% and 21% of bare samples for linear and parabolic hercynite-coated samples) and an earlier parabolic transition for coated compared to bare samples indicated not only a lower oxidation rate but also the dominance of ion diffusion as the rate-controlling phenomenon. XRD and EDS were used to confirm hercynite as the active compound achieving anti-oxidation properties, as well as the presence of a gap between the coating and substrate which indicated sufficient coating-substrate CTE differential to maintain descalability whilst preserving surface condition. However, they did not investigate coated surface condition against the bare samples, or any changes in natural spalling tendencies due to the coating.

Silicon strongly influences carbon steel oxidation behaviour via formation of diffusion-inhibiting mixed metal oxides [60, 77, 133, 134]. Silicon carbide (SiC) as an anti-oxidation coating was explored [135] and found to have favourable properties which are relevant for tube applications including good abrasivity (for post-machining of threads etc) and corrosion resistance, thermal shock stability (good for hydraulic descaling [120]), strength at elevated temperatures, and high thermal conductivity (to achieve the necessary temperatures on the substrate for full normalisation). Fu et al. [136] proposed that SiC is suitable for low carbon steels and prepared a coating comprising SiC, silicate, and chromite as the major components. Crucially, they considered coating application and used ball milling to constrain particle size during spraying. This will also be important when considering scale up of any coating application to the conveyance tube manufacturing line. However, the use of mass loss as a measure of scale level does inherently assume perfect descaling efficiency, and the development of coating-related intermetallics at the SSI and their effect on scale adhesion alongside that of the intended intermetallic is ignored, i.e. there is an assumption that all the post-descaling surface is steel.

The anti-oxidation effect of the high-Si coating was promising at 77% and 85% for 1 and

2hr soak periods respectively, and in all cases anti-oxidation effect was at least 64%. The potential of the effect of manufacturing parameters was again highlighted as higher temperatures and longer soak times were associated with higher levels of sintering, i.e. a denser coating, which better isolated the substrate from the atmospheric oxygen and prevented iron ion diffusion. However, anti-oxidation effect was found to be limited by unidentified phases formed beyond critical temperatures. In addition to the classical three-phase scale layer, high levels of carbon, silicon, and iron, were detected at the scale-coating interface (SCI) by SEM-EDS analysis (see Figure 1.22). This was deemed evidence for the anti-oxidation diffusion-inhibitive barrier created by the reaction of silicon and iron to form an intermetallic compound. Intermetallic levels increased with higher temperatures, i.e. faster reaction rates, and longer soak times, but there was an upper limit to this temperature trend owing to sufficient energy supplied to decrease and increase silicon and iron contributions respectively in the intermetallic, which explained the evidence of increased iron ion diffusion, i.e. reduced anti-oxidation performance. Fu et al. [136] also observed a second anti-oxidation mechanism at work, as blisters formed by generation of a carbon-containing gas atmosphere, derived from SiC, were shown to isolate the substrate from the atmosphere and further prevent iron ion diffusion via SSI contact loss.

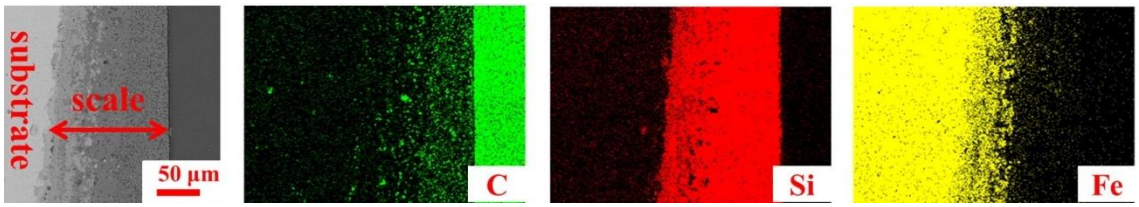


Figure 1.22: SEM-EDS mapping of carbon (C), silicon (Si), and iron (Fe) contributions for a cross-section of carbon steel specimens coated using a silicon carbide (SiC)-based anti-oxidation coating and heated to 1000°C [136].

Yu et al. [137] also explored how an existing high performance, low cost ceramic aluminium-Al coating design could be improved to streamline coating application. They argued that the commonly used sodium silicate (Na_2SiO_3) binder [27, 131, 136], in its alkaline state, could exothermically react with aluminium and increasing coating viscosity, thus reducing spray coating efficiency. Their aluminium-silicon-modified aluminium powder ('ASMA') system therefore used SiO_2 to encapsulate and stabilise the Al particles. Compared to both standard aluminium-silicon (AS) and bare samples, the ASMA-coated samples exhibited the best anti-oxidation effect with a 52% and 98% reduction in parabolic rate constant respectively, and with protection over a wider temperature range. Due to sinter density variations and the improved surface isolation associated with minimised

density, the ASMA system was optimised in a slightly higher temperature range than in this project. Enhanced sintering was attributed to the presence of additional compounds, especially cristobalite and mullite, formed during an exothermic reaction absent from the original AS system. These were shown to lower diffusion activation energy and octahedral occupation of Fe^{2+} in magnetite, thus reducing iron ion diffusion and stabilising intermetallic layers.

Both porosity level and intermetallic stability are key mechanisms for anti-oxidation coating design success. However, coating synthesis and anti-oxidation mechanism often have a system-specific design [9, 27, 129, 130, 132, 135-137]. In the case of steel tube normalisation, there must be coating compatibility with the substrate for adequate pre-normalisation adhesion and high-temperature stability during normalisation. Furthermore, consistent post-normalisation delamination, of both the coating and scale, is required to maintain the external tube surface quality which the coating was brought in to protect. Hence, coating solutions (and reactive approaches in general) are often only successful in the short-term [126], until changes to the system, e.g. substrate composition, normalisation thermal cycle, demand a response in the form of a coating re-design to optimise it for the new system.

1.6 Proactive Scale Management

Proactive management is a more time-consuming approach which relies on researching options with unknown outcomes, with the aim of solving future problems before they arise. However, the benefits of proactive management are broader in application and last longer than reactive management [126], as they can contribute to forecasting, i.e. predicting how (potentially expensive and time-consuming) manufacturing approach changes could influence problems, such as scale, prior to implementation, e.g. how transition to induction furnace normalisation and its different heat transfer characteristics will affect scale behaviour [81]. Proactive management techniques are also easier to transfer to an industrial scale [126].

1.6.1 Manufacturing Parameter Control

1.6.1.1 Atmospheric Composition and Combustion Theory

Currently, normalisation is performed in a conventional natural gas furnace, with the gaseous alkane requiring no fuel preparation, ensuring good air-fuel mixing, and promoting a rapid combustion reaction. However, gaseous fuels are expensive and require a gas network pipeline connection. The burner in the furnace has two purposes: to mix the air

and fuel and to stabilise the flame. Burner flames are either partially or fully pre-mixed, but always turbulent, ensuring safety, reliability, and efficiency. The burner must also specifically be designed to minimise emissions of carbon monoxide (CO) and nitrogen oxides (NO_x). In the tube normalisation scenario, temperature is a key parameter, but high efficiency is also generally associated with minimised excess air and/or oxygen levels. This can be achieved by operating as close to the stoichiometric air-fuel mixture as possible. Under (ideal) equilibrium conditions, alkane combustion should proceed as shown in Equation 1.13 [138].

$$\boldsymbol{C_nH_{2n+2} + a\,O_2 \rightarrow b\,H_2O + c\,CO_2}$$

Equation 1.13

However, non-equilibrium conditions are common and incomplete combustion may arise, leading to the reaction described by Equation 1.14.

$$\boldsymbol{C_nH_{2n+2} + a\,O_2 \rightarrow b\,H_2O + c\,CO_2 + d\,CO}$$

Equation 1.14

Furnace atmosphere composition can vary significantly and Schluckner et al. [28] remarked on the importance of considering furnace atmosphere and the effect of individual atmospheric component species. Abuluwefa et al. conducted a two-part study [67, 139] investigating the effect of binary, ternary, and quaternary gas atmospheres on scale kinetics, morphology, and phase composition. In part I, conclusions were derived from laboratory-based oxidation experiments for binary systems, where linear behaviour was observed and flux and adsorption rate-controlled fluidic mass transport theory was used, i.e. a linear rate law was assumed initially [128]. Hence, calculated linear reaction rate constants were assumed to be proportional to the number of oxygen gas molecules on the substrate surface which is itself dependent on the number of gaseous molecular collisions being proportional to the square root of temperature. Kinetic dependency on these parameters explains the positive correlation between atmospheric free oxygen content and oxidation rate. However, the persistence of the linear rate law throughout the oxidation period, rather than transition to a parabolic law, was evidence of further idealised assumptions made within analytical oxidation models, namely isothermal conditions (but oxidation continues during heating and cooling, i.e. outside the soaking period) and ductile scale (based on the assumed dominance of plastically deformable wüstite [15]). The detail loss incurred by these assumptions was highlighted by the results of Wilkstrom et al.'s more complex simultaneous

study of the effect of temperature, time, and gas and substrate composition on scaling degree [60] which found some deviation from the anticipated linear-parabolic behaviour during non-isothermal oxidation. Schluckner et al.'s study [28] also refers to the effect of scale embrittlement on the ensuing dominance of phase boundary (linear) rather than diffusion (parabolic) processes.

Although, like laboratory-controlled experiments, computational models must involve some idealisation, their increased temporal and economic efficiency means a greater degree of complexity can be obtained with a faster rate of refinement [140-142]. Auinger et al. [143] comment that, besides knowledge of failure origins associated with it, reliable prediction of the tendency of a material to form high-temperature corrosion products is a challenging task without exposure tests of several thousand hours. Wilkstrom et al.'s comparative study of laboratory vs. industrial furnace-produced data [60] is an example of scope for a computational approach within this project. Although they observed similar oxide morphology and phase composition phenomena for both data sets, the industrially evolved scale was 15-24% (up to 0.5mm) thicker than laboratory samples. This was partially attributed to 20 additional minutes given for oxidation, with time being a more restricted resource in the laboratory, as well as the use of instantaneous argon quenching. Furthermore, with ternary and quaternary atmospheres [67] and for a full-scale industrial furnace with a quaternary atmosphere at normalisation range temperatures [139], Abuluwefa et al. observed the anticipated linear to parabolic rate law profile, and the 'mixed' regime suggested by Wilkstrom et al. [60]. This was mainly achieved by efforts to more accurately model the reheat furnace environment, for example by the introduction of a soaking time term from previous work [144] and consideration of non-isothermal effects. Abuluwefa et al. [139] also argue that the use of a linear rate model is justified by evidence of its dominance even in the mixed regime and that halving the percentage free oxygen concentration (and hence molecules available for mass transport per unit volume) at low levels led to a 35% decrease in oxidation rate, showing strong dependency. However, it is possible that the oxidation period was not long enough to reach full parabolic transition, or the use of isothermal linear rate constants for the entire experiment skewed data fitting towards the linear rate law. Zambrano et al.'s study [22] also highlighted the limitations of a purely laboratory-based approach, attributing discrepancy between their laboratory and industrial sample phase composition profiles to both temperature variation and furnace atmospheric composition differences. Information about the realistic industrial situation is

arguably more desirable for TSUK Tubes and a computational model could provide this. Furthermore, thickness differences in Wilkstrom et al.'s study [60] were also attributed to other more complex and stochastic phenomena such as furnace turbulence and through-scale, oxygen diffusion-promoting cracks, which were exacerbated by the higher surface area of the industrial samples upon which the linear adsorption mechanism depends (as opposed to thickness dependency for the parabolic diffusion mechanism). The latter phenomenon also inhibits parabolic rate ion diffusion via porosity. It is noted that such porosity, amongst other defects, are also potential delamination initiation sites [60], hence reinforcing the questionability of assuming perfect scale adherence [124]. This is also a case against the assumption of pure wüstite as if phase composition significantly deviates from the conventional ratio [70], the influence of the more brittle magnetite and haematite phases becomes important [15].

When considering gas atmosphere alongside the issue of spalling effects, several studies have highlighted that the two are intrinsically linked [66, 128]. For example, both Basabe et al. [66] and Sheasby et al. [128] demonstrated the correlation between higher levels of water vapour and increased adhesion due to increased scale plasticity and creep which could ultimately reduce the number of parabolic oxidation-inhibiting scale-steel gaps evolved. Hence why despite the effect of manufacturing parameters, such as atmospheric composition, once scale integrity is compromised, its own effects will control oxide behaviour, especially kinetics. Thus Sheasby et al. [128] concluded that any effects on oxide by parameters such as porosity, atmosphere composition, and steel grade, will be on the oxidation rate rather than oxide thickness.

Grant characterised the oxide in furnace replication experiments based on the air-fuel combustion atmosphere at Corby [9]. However, attention was mainly paid to other reheat parameters, namely temperature and soak time. Variations in the furnace atmosphere could provide valuable insight into optimisations that could be performed to minimise scale growth during reheat. Intense heating in an enclosed structure, i.e. furnace, is the best way to optimise combustion efficiency, fuel consumption, and process control. However, exploiting these advantages (over open-air combustion) requires the critical rate determining step(s) to be identified.

Gas-Barrel Furnace Theory



Figure 1.23: Photograph of tube entering the gas-barrel normalisation furnace at TSUK Tubes site ¤.

Conventional furnaces burn fuel and air (oxygen) to release thermal energy as heat, some of which is transferred to the charge. As discussed in Section 1.2, tube normalisation is performed in gas-barrel furnace which generates heat in this way (see Figure 1.23) using natural gas or potentially manufactured gases from the blast furnace and coke oven where possible. Crucially, due to the highly variable properties of gas fuels [145], changes to the gas fuel may halt combustion or introduce hazards, e.g. denser gases may not disperse sufficiently during a leak and accumulate to explosive levels. However, a significant proportion of the heat generated is lost via the flue gas, charging doors, external surfaces, and waste products, i.e. delaminated scale. Fuel-based furnace efficiencies are therefore often quite low [146]. Alongside efficiency, furnace designers want to obtain a satisfactory product from the furnace, use minimum fuel and/or energy, minimise capital costs, manning levels during operation, and maintenance costs, and maximise lifetime and safety. Improved efficiency objectives are generally driven by economic factors, namely capital cost, depreciation, interest, fuel and electricity costs, maintenance, and environmental levies.
A continuous reheat furnace is used at the Tata hot mill to maximise opportunities for energy recovery and minimise heat loss during shutdown periods, but normalisation at TSUK Tubes demands a batch process so that soaking temperatures can be maintained for an extended period to ensure full microstructural homogenisation and internal stress relief (see Section 1.2.4). Heating regions are characterised as pre-heat, heat, and soak zones and transition between the zones is achieved by water-cooled walking beams. During pre-heating, heating rate (rates often being more important than temperatures) is maintained at a level low enough to prevent overheating and minimise reflective scale formation which will reduce radiant heat transfer [25]. Flue gas load recuperation can be performed in this

zone which can prolong the life of the recuperator inlet metal by reducing the flue gas temperature and improve overall furnace efficiency. The heat zone is where most heat transfer occurs, whilst the soak zone allows the temperature across the tube to equalise. Although combustion comprises many intermediate, unstable free radical-generating mechanisms, the overall exothermic, reversible reaction can be summarised as a Simply Chemically Reacting System (SCRS) of complete or incomplete combustion of carbon (where a hydrocarbon fuel is used) (see Equation 1.15 and Equation 1.16 [147]).

$$C + O_2 \rightarrow CO_2$$

Equation 1.15

$$2C + O_2 \rightarrow 2CO$$

Equation 1.16

The gas fuel is typically introduced as a particulate suspension which follows the classical model of two-stage particulate combustion. Volatiles create an initial shell around the fuel particle allowing it to burn as a shrinking sphere until consumed. Char burning then commences at the particle surface. Combustion physics is equally important as this enables chemical reaction by bringing the oxygen in to contact with the fuel. The combustion rate-defining steps are mixing, ignition, chemical reaction, and product dispersion. Mixing typically takes seconds (compared to milliseconds for the other steps) and is therefore the rate-determining step [147]. Hence, combustion is controlled by the rate and completeness of fuel-air mixing. Furthermore, insufficient fuel-air mixing also leads to unburnt carbon monoxide in the flue gases, wasting potential fuel energy. Achieving satisfactory fuel-air mixing, and therefore efficient combustion, demands an adequate air supply (often minimally super-stoichiometric as diffusional mixing is not perfectly homogeneous but too much excess air will reduce thermal efficiency and increase pollutant production – see Figure 1.24) and effective burner design. Air has the greatest influence on mixing as its mass requirement is typically 10 times that of the fuel, therefore giving it greater momentum [147]. Air can be supplied to the fuel at the primary (during fuel pre-mixing and conveyance to the furnace combustion chamber) and secondary (through designated channels and ducts to the furnace combustion chamber) stages. Introducing primary air can help control mixing rate and flame stability, but secondary air is important for optimising stability, emissions, and thermal release by using a multi-nozzle configuration to optimise mixing via jet entrainment. In addition to the air and fuel, reducing atmospheres can be introduced in

scenarios such as tube manufacturing to minimise scale formation. Such an atmosphere can be generated via intentional sub-stoichiometric combustion to generate carbon monoxide, or via supply of special atmospheres such as hydrogen. However, there are additional risks associated with these techniques including increased atmospheric toxicity and explosion risk respectively.

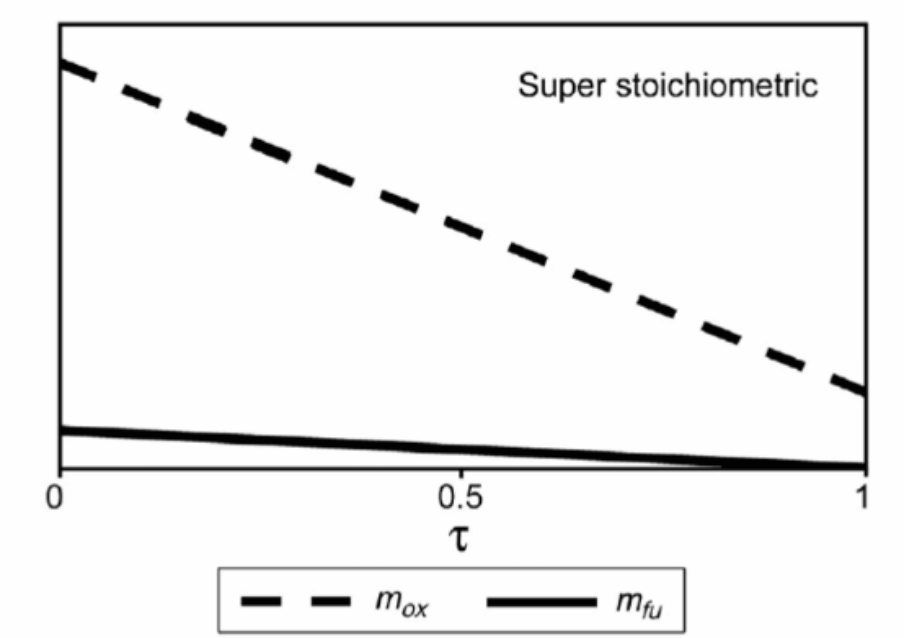


Figure 1.24: Graph of superstoichiometric combustion (air-fuel ratio) [147].

The industrialised world is evolving fast with a paradoxical demand for higher product quality at a lower cost [148]. However, in the energy-intensive steel industry not only are the reheat furnaces expensive energy consumers but also sources of material yield and product quality loss due to scale growth. A key development is the suggestion that scale growth should be accounted for in reheat furnace models, as it was hypothesised that the difference in thermophysical properties between the steel and scale, e.g. conductive heat transfer coefficient, affects heat transfer phenomena and hence heat treatment efficiency. Torres et al. [15] studied through-scale thermal conduction using an implicit finite difference regime assuming a parabolic rate law. A valuable outcome of the study was the observation that similar results were obtained for a three-phase scale layer model compared to a wüstite-only equivalent and a three-phase model was thus deemed over-complicated for scale kinetics investigations. However, only the three-phase model can provide temperature distribution and layer integrity, which should not be disregarded, especially when considering adhesion.

Torres et al.'s study and the expansion of computational resources prompted revision of

previous modelling approaches which ignored scale growth. Jang et al. [73] used a coupled radiative and transient conduction 2D model to compare the temperature and scale thickness profiles of high carbon steel modelled with and without high-temperature, parabolic scale growth. The model including scale exhibited better agreement with experimental data provided by technical research and development literature, with lower slab surface and scale surface temperatures obtained for the model with scale. Lower slab surface temperatures were attributed, as suspected, to the low thermal conductivity of the scale which decelerates heat transfer to the slab. However, lower scale surface temperatures were attributed to the higher specific heat capacity of the scale. This demonstrates the importance of considering scale in any assessments of the tube manufacturing process, i.e. not only high-temperature normalisation but also thermomechanical processing (TMP) such as stretch reduction. The dominance of wüstite in the classical three-phase scale layer [15] is a sound justification for not modelling all three phases, which would complicate the model and incur computational and economic costs. However, it should be noted that this can only be assumed to be the case for heating models as a multi-phase scale composition may be more influential during delamination [28, 122, 136].

Different reheating technologies have been considered to tackle environmental and economic issues associated with traditional fossil-fuel based combustion furnaces. Schluckner et al. [28] explored both oxygen-enriched air-fuel (OAF) and oxy-fuel combustion (OC) processes designed to improve combustion efficiency via a reduction in flue gas losses and increase in maximum flame temperature via changes in partial pressures of oxidising species, e.g. CO_2, H_2O, N_2 etc. Like Jang et al. [73], they argued that previous studies were restricted on flow-chemistry interaction, temperature distribution, and scale formation details by the limitations of computational power accessibility. With the continued growth of computational power availability, Schluckner et al. proposed that there were now sufficient resources within workplace computers to fully consider the specifics of scale formation and how the atmosphere evolved (and the local concentration of individual atmospheric components) alters its kinetics and mechanisms, e.g. ion diffusion (see Section 1.3.1). Again, assuming pure wüstite, at a sufficient oxidation time and temperature T>600°C, oxidation rate law was modelled as purely parabolic. This agreed with Poirier et al.'s experimental study of the effect of oxygen-enriched combustion using a two-chamber natural gas combustion furnace [69]. They found that samples heated to 1100°C for up to 4hrs exhibited increasingly parabolic oxidation processes shown by a reduction in the

magnitude of the line of best fit y-intercept value as stack oxygen concentration increased, even without any oxygen enrichment (which was found to have a negligible effect anyway). This showed the importance of controlling the furnace atmosphere, via stack oxygen concentration, if scale kinetics is to be controlled.

Schluckner et al.'s CFD model [28] was able to predict local and temporal-based species and temperature distributions in good agreement (±5%) with experimental data. The observed deviation was attributed to the physical idealisation associated with the use of an Arrhenius-based rate law to determine rate law constants, from which experimentally determined real-world values will inevitably deviate, and the introduction of measurements inaccuracies. The behaviour of the model when the scale is modelled as three-phase may deviate further due to the empirical behaviour of the phases which can often not be idealised. Ultimately, the most accurate and useful understanding of tube oxidation will come from balancing the strengths and limitations of experimental, analytical, and computational approaches.

Schluckner et al.'s results [28] showed that local species concentration is as influential as temperature on scale thickness. Unsurprisingly, higher levels of oxygen, where local species concentration was generally defined by the turbulent flow profile of the furnace, were associated with thicker scale and an earlier transition to the post-parabolic linear rate law region. However, a less immediate observation was the correlation between higher levels of water vapour, which accompanies higher oxygen levels as a by-product of an increased combustion rate [149] (see Equation 1.3 and Equation 1.4), and accelerated scale formation, accompanied by an earlier transition to the parabolic rate region. This aligns with Sheasby et al.'s hypothesis [128] that water vapour promotes prolonged SSI adhesion, and supports Basabe et al.'s statement [66] that water vapour local concentration is the second most influential atmospheric species for oxidation after oxygen. This highlights a dilemma of the more fuel efficient and faster heating technologies discussed in Schluckner et al.'s study (with OAF consuming 22% less fuel) [28]. Whilst both oxy-fuel and oxygen-enriched furnaces produced less scale (9% and 47% respectively), the higher levels of water vapour evolved by more efficient combustion could simultaneously promote scale growth. Furthermore, stricter safety regulations will be incurred by the increased upper flammability limit associated with increased oxidisability within the furnace atmosphere. Hence, application of combustion technologies discussed by Schluckner et al. [28] at TSUK Tubes is confined to pre-heating stages which do not reach oxidising temperatures ($\boldsymbol{T}$ < 750°C [28]) so that the faster heating properties can be exploited without creating a high-

temperature scale-favouring atmosphere. Landfahrer et al. [16] numerically modelled a full-scale reheating furnace for investigation of the effect of scale on heat transfer in low carbon steel tubes via extension of Schluckner et al.'s study [28]. The key advantage of their model was the coupling of two independent simulations (stationary combustion and single-tube transient heating) in place of a more computationally demanding fully transient, chemical kinetics analysis. Landfahrer et al. [16] also argue that their extension of the computational domain better reflects the species distribution in the combustion atmosphere. During experimental validation via mass change measurements, the acceptable model deviation was attributed to rescaling during tube furnace exit. Confidence in the model was reinforced by comparison to Schluckner et al.'s original model [28] and an analytical parabolic rate law, both of which ignored scale insulating effect. Given that all three models and experimental data exhibited identical scale temperatures, and deviation came when considering steel temperatures, the scale thickness underestimation associated with Schluckner et al.'s [28] and the analytical model was attributed to disregarding the scale insulating effect. Landfahrer et al. [16] were also able to support Schluckner et al.'s conclusions [28] of the dominance of the effect of thermal behaviour over species concentration-influencing gas flow dynamics on scale kinetics.

Although Landfahrer et al.'s study [16] provided a more computationally accurate and efficient description of scale insulating effect, all studies neglected to address Torres et al.'s [15] original adhesion-related assumptions of perfect scale-substrate contact and absence of microstructural defects. Another key assumption in Torres et al.'s study was plastic behaviour of the steel and scale above 560°C. This is acceptable assumption based on the dominance of plastic wüstite and magnetite but Abuluwefa et al. [139] argue that magnetite is brittle and prone to spalling, and that variations in furnace atmosphere which affect phase composition could also alter heat transfer. A brittle magnetite model was used to apply worst case scenario strains and hence the steepest thermal gradients. Overall, differences in approach often stem from a difference in investigative focus, e.g. Abuluwefa et al. [139] consider only the effects of furnace atmosphere on scale whereas Torres et al. [15] consider heat transfer and its interaction with specific phase composition at a given temperature (scale, steel, and environmental). Therefore, microstructural integrity and material deformability are key considerations during adhesion considerations within this project. Regardless, controlled atmosphere furnaces are expensive so induction furnaces, which can achieve accelerated heating at a lower cost and higher efficiency [150], are the favoured

potential development at TSUK Tubes. However, work has not been performed on the effect of changing from gas-barrel to induction heating (specifically that of accelerated heating and atmospheric differences), with the exception of Krzyzanowski and Beynon [77] who simulated induction heating by stipulating a time and space function fixed temperature boundary condition at the SSI. Also, transfer to induction-based normalisation aligns with Tata's commercial decarbonisation priorities and could form some basis to Capital Expenditure applications for such a technology change at TSUK Tubes (once the Technology Readiness Level (TRL) sufficient for induction heating of industrial-scale tube surface load is reached [151]). Given the large energy consumption of gas-barrel furnaces, induction technology can only be justified if the electrical energy demand can be satisfied by a carbon-neutral resource [151]. In addition to sponsor company priorities, the introduction of novel heating techniques, such as induction, aligns with a broader international effort to decarbonise the steel industry [152]. The vast range of advanced steel grades now available, with complex and highly specified alloy compositions, does not complement the net zero-promoting Circular Economy strategy, for Wales [153], the UK [154], and beyond [155], based on zero waste and high manufacturing control levels [156]. It is argued that a diverse range of microstructural and mechanical properties within a smaller range of steel grades could be achieved by taking a 'Late Stage Product Definition and Integration' approach [152]. TMP will need to be more closely monitored and controlled to achieve this, via techniques such as online material monitoring [157] and fossil-free heat treatment furnaces, e.g. induction, Near Infrared (NIR) [150], as well as a deeper understanding of the selected TMP itself, i.e. normalisation in this project.

As alluded to in Section 1.2, stretch reduction is already performed using a Radyne induction furnace (see Figure 1.7). However, TSUK Tubes have been using induction furnaces for heat treatment at all stages of the manufacturing process for their smallest (15, 20, and 25 nominal bore) tubes since 2023 [158]. The physical principles for heating in an induction furnace are identical to that described in Section 1.2. However, when considering post-weld normalisation, there are specific parameters which must be considered. As highlighted by Unver et al. [150], there a several advantages to induction technology as a proven technology in metal production. These include reasonable maintenance costs, compact installation, localised heating capacity, potential for automation, product purity via vacuum or inert atmosphere-based working, and, on average, higher heating efficiency (dependent on material) [150, 159, 160]. The ability to precisely regulate heating conditions,

via control of electrical (, e.g. current frequency), thermal (, e.g. cooling conditions), and geometric (, e.g. coil geometry) input parameters, is a key advantage of induction technology in scale management efforts (provided electrical load capacity demands can be met) [161].

Zhao et al. explored the effect of variable pipe wall thickness on the heating efficiency of induction heating used for heat treatment of pipes for thermomechanical applications [160]. They emphasise that soak times using induction heating are susceptible to extension by the need to achieve a uniform heat distribution throughout the pipe section under the action of the induction coil. This could undermine the time-saving qualities of induction heating highlighted by Unver et al. [150]. Zhao et al. also argue that non-uniform heating could also lead to loss of heating efficiency and workshop capacity, increase in energy consumption and ultimately delay progress in automated production in large-scale manufacturing processes [160]. Although they focus on the microstructural consequences for the steel, changes to soak time have already been shown to affect oxide kinetics and adhesion, as well as the effect of adhered oxide scale on thermal emissivity and absorption discussed earlier in this chapter. They highlight that the complex interaction of electromagnetic and heat transfer phenomena during induction heating results in a strong influence of the induction coil by: shape (the oval coil as the best for achieving uniform magnetic flux distribution), current (adjustments to both density and frequency), air gap (a narrower air gap will promote faster temperature rise), and component feed rate (a faster feed will improve temperature uniformity across the component). They also highlight the challenge of a narrow processing window in controlling temperature distribution, which also applies for Tata's conveyance tube manufacturing process, which totals only ~15 mins. Zhao et al. [160] sought to determine the optimal combination of coil structure, current magnitude, i.e. power, and soak time to achieve their target temperature range of 890-900°C in steel tubes with a wall thickness (and therefore air gap when using an equal cross-section coil) variation of 30mm. In contrast to conveyance tubes, the pipes investigated by Zhao et al. had a deliberate angular motion at a constant velocity to aid uniform heating. Two key assumptions were made which would be invalidated by the presence of oxide scale when compared to conveyance tube manufacturing. Firstly, fluctuations in workpiece density were neglected. Secondly, constant workpiece emissivity was assumed. Neither of these assumptions are true when a layer of oxide scale is present on the workpiece [15, 25, 66, 73], and the impact of the oxide scale on the physics of induction heating will be exacerbated by

the inconsistent oxide thickness along the tube surface reported by TSUK Tubes (see Section 1.2). However, since coil geometry is designed to match a specific product specification, it is possible that the effect of oxide scale could be incorporated into future coil design and electromagnetic parameters, for components such as steel tubes. This would be financially viable on a sufficiently large scale of manufacturing like conveyance tubes.

Overall, Zhao et al. [160] used a finite element approach to demonstrate that increasing the current from 3000A to 5500A can increase heating efficiency and in turn reduce heating time by a factor of four, using an equal or variable cross-section coil. However, they remarked on the limitations of benefits beyond the Curie temperature (780°C) [162] where an inavoidable loss in magnetic permeability reduces the heating rate. However, increasing current has a negative impact on heating quality, with large difference in temperature exhibited by the inner and outer walls on the pipe - up to 12.5% and 14.2% using 5500A on a variable and equal cross-section coil respectively. In the variable cross-section coil, this difference resulted in a 50°C overshoot in the temperature of the higher wall thickness part, whilst the thinner wall thickness part simultaneously failed to reach the target temperature range. Although conveyance tubes do not have a variable wall thickness once the manufacturing process is complete, the effect of coil cross-section geometry shown by Zhao et al. is still relevant when considering the stretch reduction process used to alter wall thickness, as well as the wide range of tube dimensions, manufactured, i.e. resulting air gaps. As previously discussed, only a single coil can be designed and installed, but its heating quality will be susceptible to fluctuation in the case of agile manufacturing of conveyance tubes. Dynamic power control is a potential solution and Drobenko et al. argue that models for ferromagnetic materials undergoing high temperature induction heating should account for the temperature dependence of material properties (particularly electrical conductivity) and elastic-plastic deformation, and non-linear dependencies of magnetic properties [161]. They numerically predicted the temperature and electromagnetic field parameters, and subsequent temperature-dependent magnetisation, polarisation, and deformation of a long cylindrical, thermo-sensitive ferromagnetic solid under high temperature inductive heating. One use of Drobenko et al.'s approach [161] was to ensure a predefined residual stress level by minimisation heat treatment duration. Residual stresses were partially controlled by electric current frequency (the other control function being related to cooling conditions) varied in the range 0.05-8kHz. This is an example of dynamic power control, a technique also employed by Zhao et al. to manage overheating of thinner wall thickness sections of

their variable cross-section pipe [160]. Their numerical results revealed that a low carbon steel tube, with dimensions in the range of Tata's conveyance tube (inner radius, $\boldsymbol{IR}$ = 100mm, wall thickness, $\boldsymbol{r_{wall}}$ = 10mm), will be uniformly heated when the current frequency is less than 500Hz and subsequently experience compressive residual stress at the external surface. However, it should also be noted that, for a constant current, heating rate slows when the temperature exceeds the Curie temperature and the tube material loses its ferromagnetic properties. This effect is minimised when the maximum current frequency in the range is used (8kHz). This relates to Di Luozzo et al.'s work on numerical modelling of induction on carbon steel tubes during joining [163]. They highlighted the importance of the relationship between magnetism and penetration depth, stating that during induction heating 86% of heat generated is concentrated at the outer layer of the workpiece. However, for a carbon steel tube of similar dimensions to a Tata 15 nominal bore (n.b.) conveyance tube, penetration depth can increase from only 6% of the total tube wall thickness, with a higher temperature at the outer surface, to approximately the entire wall thickness once the Curie temperature is exceeded and the material transitions from a ferromagnetic to paramagnetic state. In the latter case, the more uniform heat distribution combined with high levels of radiation heat loss at the outer surface can result in a higher temperature at the inner surface [15].

Overall, electric current frequency has a non-linear relationship with the time taken to reach the target temperature (970°C) [161]. For example, Drobenko et al. demonstrated that increasing the frequency from 0.3kHz to 0.8kHz decreases the time taken to heat the tube surface region to target temperature from 15.5s to only 1s. Hence, an appropriate selection of electric current frequency will aid in minimising the heating period within the allowable residual stress limits. Their study demonstrated that, for a maximum allowable residual stress of 100MPa, the maximum allowable electric current frequency is 530Hz. Assuming that the tubes in Drobenko et al.'s study are scale-free and not subjecting to any external mechanical stresses from manufacturing, the maximum allowable residual stress stipulated can be set equivalent to the thermally induced stress component during conventional gas-barrel heating.

1.6.1.2 Steel Grade and Composition

In addition to thermomechanical processing (TMP) parameters, steel alloy element composition will influence final product microstructure [164]. Although carbon is clearly the most important alloy element, with its heavy influence on strength and ductility, there

is an extensive list of additional alloy elements available. The E41 and E24 grades used by TSUK Tubes are classified as non-alloy (alloying element contributions below critical values defined in steel grade classification standard BS 10020 [165]), low carbon (<0.3wt% carbon [166]), high-strength (strength is the defined minimum critical parameter as opposed to a mild steel where formability is the chosen parameter, although formability requirements can still be set for any grade [166]). However, as can be the case, "high strength" steels may be so in name only where strength requirements are met, but the grade performs better in terms of ductility. This is true of the Tubes grades which exhibit the excellent ductility necessary for forming and reduction (see Section 1.2) alongside moderate strength. Table 1.1 outlines the alloy elements (and their respective mass contribution) found in the E41 and E24 grades.

Table 1.1: Alloy element composition limits specified by BS EN 10217-2 (Welded steel tubes for pressure purposes - Technical delivery conditions [Part 2: Electric welded non-alloy and alloy steel tubes with specified elevated temperature properties]) [4] for steel grades P235GH and P265GH.

PxxxGH	≤ wt %										
	C	Si	Mn	P	S	Cr	Ni	Al	Cu	Nb	Ti
235	0.16	0.35	1.20	0.025	0.020	0.30	0.30	0.020	0.30	0.010	0.03
265	0.20	0.40	1.40	0.025	0.020	0.30	≤0.30	0.020	0.30	0.010	≤0.03

Alloy Effects

Alloy elements influence microstructure and steel material and mechanical properties primarily through their effect on the Fe-C equilibrium phase diagram (see Figure 1.2). Austenitic stabilisers, e.g. Ni, Mn, Co, N, Cu, open the gamma field region by increasing the $\gamma + \delta$ transformation temperature and depressing the $\gamma + \alpha$ transformation temperature, to create an open or expanded gamma field. Ferritic stabilisers, e.g. Al, P, Nb, restrict the gamma field region by suppressing the $\gamma + \delta$ transformation temperature and increasing the $\gamma + \alpha$ transformation temperature, to create a closed or contracted gamma field. There are also carbide formers, e.g. Ti, V, Mo, Cr, which interfere more directly with the microstructure, contracting the gamma field by reducing the required carbon content [167]. Elements can be distributed within the alloy in several possible ways, namely as an intermetallic, an inclusion, a carbide compound, in a free state, or in a homogeneous solution in iron.

The changes to microstructure brought about by alloy elements carry several tangible benefits for tubes:

- Many alloy elements (Cr, Co, Mn, Ni, N, Si, Ti) offer increased strength [167], particularly at high temperatures, which increases certainty that tubes will satisfy their minimum yield strength requirement as defined by BS EN 10217-2 [4] and at the higher temperatures found in some tube applications, e.g. steam conveyance, boilers.
- Nitrogen can increase hardness [167] which will reduce damage levels on the tube during manufacturing and service.
- Machinability is a key property which can be enhanced by additions of B, Mn, S, and N [167] to improve groove- and thread-adding operations which may be required for customers to join and assemble tubes in service.
- Wear resistance is of particular importance for conveyance applications where the inner tube surface is under constant dynamic force from transported fluids. Additions of Cr and Mn can improve wear resistance [167].
- The internal tube surface is also susceptible to wet corrosion but, alongside the anti-corrosion effects of the scale layer itself, Cr, Cu, Ni, and Ti can improve corrosion resistance [167].
- Niobium is a particularly important alloy element in the tubes application as it is required by TSUK Tubes in their low interstitial content, high temperature heat treatment application as it suppresses the austenitic transformation temperature and therefore improves hardenability [164]. In non-alloy, low carbon steels, Nb can also have a positive effect on the HAZ by expanding the non-recrystallisation temperature range (although weld thermal energy input is equally important in the HAZ (see Section 1.2). Finally, precipitations of carbide and nitride compounds of Nb can increase hardness which reduces damage levels of the tube during manufacture and service [164].

Chen et al. [168] argued that insufficient attention had been paid to low and ultra-low carbon steels when considering the effect of steel composition on oxide kinetics and morphology. Furthermore, Iordonova et al. [72] highlighted that substrate material is a primary independent variable affecting oxidation rate and West et al. [5] remarked on the effect of steel composition on oxide grain structure.

Poirier et al. demonstrated that carbon content could be linked to scale intactness due to increased levels of CO_2 escape from the SSI at higher carbon levels [69]. They concluded, in their study of furnace atmosphere effects on scale kinetics and adhesion, that steel grade was

by far more influential than any oxygen content changes. They commented on how several elements can lead to increased adhesion, namely Cu, Cr, and Mo, and referred specifically to how higher levels of Ni in their samples were associated with greater surface enrichment and adhesion-enhancing metal-scale entanglement. This may have further implications for the increased use of scrap steel as the steel industry transitions to greater use of electric arc technology [156]. Chen et al.'s study took two grades of low carbon Al-killed steel ('1' and '2') (suitable for high strength applications, e.g. HDG), one ultra-low carbon interstitial free (IF) steel ('3') (suitable for high formability applications, e.g. deep drawing of automotive body), and one Si-killed steel ('4'), which underwent hot rolling, and investigated, firstly, their differing microstructures. Steel 4 was cold-rolled and not annealed but this difference in processing route was not considered. The key differences between the steel grades were their microstructure, e.g. Steel 1 exhibited partially recrystallised ferrite grains with fine spherical carbide streaks while Steel 3 had larger grains with no streaks, and scale growth linear to parabolic law transition temperature. However, the authors were varied in the depth of their explanation of the effect of alloy chemistry on these differences. For example, steels 1 and 2 had similar compositions and processing conditions, and exhibited a uniform, well-adhered, thick, blister-free classical three-phase scale layer, in disagreement with a previous study which observed irregular, less adherent scales with atypically thicker magnetite and haematite layers. This was attributed to marginally higher silicon and aluminium levels, but with no further explanation owing to a lack of detailed work on the topic and a need for further study. However, when considering the significant levels of blistering of the slow-growing, thin, non-adherent, and irregular scale on steel 3, in contrast to author expectations of similar behaviour to steels 1 and 2 due to ultra-low carbon levels, the effect of titanium was considered in detail. It was proposed that titanium oxide forms more uniformly at lower temperatures and provides a barrier for iron ion diffusion across the interface leading to thinner layers of magnetite and haematite. Titanium oxide is then lost with longer oxidation periods and higher temperatures, therefore uniform scale growth resumes, causing blistering.

In agreement with other studies [60, 77, 133, 134], silicon was the most influential element, leading to higher than average magnetite and haematite levels on steel 4. Krzyzanowski et al. [77] comment that silicon can alter steel-scale interactions by the formation of silicon-based mixed oxide fayalite (Fe_2SiO_4) which interferes with adhesion behaviour via changes to interfacial separation stress. Wilkstrom et al. [60] agree that silicon is often the most

influential element when alloy content is low overall and the observed effect of other elements, e.g. copper, manganese, is mild [28]. They [60] describe how at high reheat temperatures, the low thermal gradient evolved between the slab and atmosphere means a fast exothermic fayalite reaction initiates and the development of significant latent heat and poor heat transfer conditions melts the fayalite and Fe-O systems, causing enhanced diffusion which generates further heat. The dense protective outer magnetite layer cannot form during this rapid mechanism, i.e. iron ion diffusion is inhibited, so molten mass is lost. Hence, to avoid slab damage, the thermal cycle must be controlled to ensure magnetite formation precedes that of fayalite. Within this project, the influence of thermal profile and steel grade on oxidation should be considered not only for samples of the two steel grades used at TSUK Tubes ('E41' for 195GH and 235GH [4] and 'E24' for 265GH [4]), but for coated samples where complex intermetallic interactions are anticipated based on the introduction of additional chemical compounds, and their comparative effect on adhesion should be assessed.

Krzyzanowski et al. [77] comment, when comparing oxidation of different steel grades, that scale morphology is unaffected by composition, and that porosity levels of each phase and their failure mode are the key areas for consideration of effect of composition. They take porosity as a relative indicator of adhesive strength (also investigated by Poirier et al. [69]) where increased porosity (both distribution- and size-wise) is more evenly distributed and smaller in steel 2 at lower temperatures than steel 1. This leads to the conclusion of a difference in the temperature-dependent mechanical properties of the different steel grade oxides. Variations in porosity were also detected at a phase-based level and therefore reinforce the importance of the consideration of scale at the phase level when investigating adhesion. In the absence of any other parametric variation, the difference in porous behaviour of the two steel grades had to be attributed to composition but this could not be attributed to a single alloy element without further investigation. In addition to porosity, and its related effects on adhesion, Krzyzanowski et al. [77] also observed that, alongside steel grade, temperature affects scale failure mode, of which two were identified for low carbon steel oxides (as outlined in Section 1.4). The first mode occurred at low temperatures and high strains due to tension-induced, parallel-to-interface cracks, i.e. the interface is stronger than the scale, whilst the second occurred at high temperatures and uniaxial tensile loads due to scale slipping along the interface, i.e. interface is weaker than the scale. The two failure modes present as through-thickness cracks and spalling respectively. Hence,

ultimately it was shown how temperature and substrate composition define the point at which interfacial separation stress dominates over the initially dominant scale separation stress and failure occurs by spalling rather than cracking. This demonstrates how the mechanical properties of the scale are not as relevant to adhesion at higher temperatures, i.e. stronger scale does not mean better adhesion, the effect of steel grade on the SSI is paramount. Krzyzanowski et al. cited quantification of interfacial separation stress as a key area for further work, where silicon content is clearly important.

Additional Investigations into Silicon and Adhesion

As discussed above, silicon, along with manganese and aluminium, is added to enhance mechanical properties including elasticity limit, strain strength, ductility, and formability. Silicon (Si) is an element liable to segregate towards the scale-metal interface at high temperatures. A mixed oxide will be formed. Note that in the case of manganese (Mn), the same segregation phenomenon will result in solid solutions in the scale. Si in steel forms an interfacial (steel-scale) silica ($\boldsymbol{SiO_2}$) passivating layer initially, and there may be some internal oxidation in steels with >0.3 wt.% Si. Although steel-scale adhesion is lower on Si steels than on pure iron, the silica and/or fayalite ($\boldsymbol{Fe_2SiO_4}$) to substrate adhesion is stronger and introduces descaling challenges [169]. As previously mentioned, the exothermic reaction between iron oxide, specifically wüstite ($\boldsymbol{Fe_{1-x}O}$) in the liquid form in this case, with silicate ($\boldsymbol{SiO_2}$), i.e. oxidised silicon from the alloy composition [170], leads to the formation of $\boldsymbol{Fe_xO_y/SiO_2}$ compounds (see Equation 1.17). Fayalite (ferrous orthosilicate), $\boldsymbol{Fe_2O \cdot (SiO_4)}$, is the iron-silicate system product with the greatest effect on steel surface quality. Notably, the rhombic crystal of fayalite has a lower melting point than its individual constituent parts 1205°C compared to 1377°C and 1723°C for wüstite and silicate respectively [171]. If molten, fayalite has a low wetting angle and can easily penetrate inter-granular capillary spaces (within the existing oxide and steel) and furthermore, when in the molten state, can dissolve any existing silica and extend the capillary spaces. Once solidified, this action enhances scale adhesion by forming a 'mechanical key' [172] which restricts uniform descaling. This can be true during both mechanical, e.g. shot peening or chemical descaling, e.g. pickling [169]. However, although this phenomenon is apparent and adhesion-promoting in steels containing <0.5 wt.% Si, the

capillary action of fayalite must be accompanied by the eutectic system found only above 1177°C [169-171] where the binary system $\boldsymbol{FeO - Fe_2O \cdot SiO_4}$ melts.

$$\boldsymbol{2FeO + SiO_2 \rightarrow 2FeO \cdot (SiO_2)}$$

Equation 1.17

However, the temperature of tube normalisation does not reach this value (see Section 1.2). For the low silicon content found in Tata Tube steel grades, silica formed at the SSI is anticipated to react with wüstite and form the spinel fayalite product. Furthermore, at the given normalisation temperature (<1173°C), scale is anticipated to consist of an outer wüstite layer and inner wüstite-fayalite 'conglomerate layer' interspersed with discontinuous fayalite bands [172]. Mouayd et al. [169] noted that their thermogravimetric analysis (TGA) of three different silicon contents (0.02wt.%Si, 1.6wt.%Si, 3.2wt.%Si – with the first being the most representative of tube composition) confirmed the transition from passivation to accelerated oxidation at high temperatures (>1100°C). Although their oxidation times (up to 15 mins) were consistent with values found during tube manufacturing, it was highlighted that, along with the random distribution of Si on the steel surface, shorter oxidation times made kinetic values appear random.

Si is an important element as its reaction with oxygen, favoured over iron hence passivation, affects both oxidation kinetics and adhesion. The initial passivating layer inhibits Fe^{2+} diffusion to the substrate surface and a thin, silica-rich scale is evolved. Passivation stops at temperatures >1200°C. Changes to morphology were observed for an increased silicon content (1.6 wt.%Si) with a clear wüstite-fayalite eutectic layer (provided oxidation temperature was less than the eutectic melting point of 1180°C). Beyond the eutectic melting temperature, a continuous fayalite layer is visible with some wüstite grains contained within the layer. If oxidation is long enough to develop a thickened fayalite layer which directly causes failure of the steel-scale interface due to solidification volume shrinkage and thermomechanical stress (see Figure 1.25). The highest silicon content (3.2 wt.%Si) sample produced the longest passivation period which evolved a discontinuous scale of islands surrounded by a very thin passivating layer. Externally, the islands are curved wüstite and internally a curved matrix of wüstite containing fayalite grains. Island formation is attributed to local passivating layer rupture followed by enhanced iron diffusion through defects and/or grain boundaries. It should be noted that oxidation is not stopped by silica, only slowed, due to the low diffusion coefficient of iron in silicon oxide.

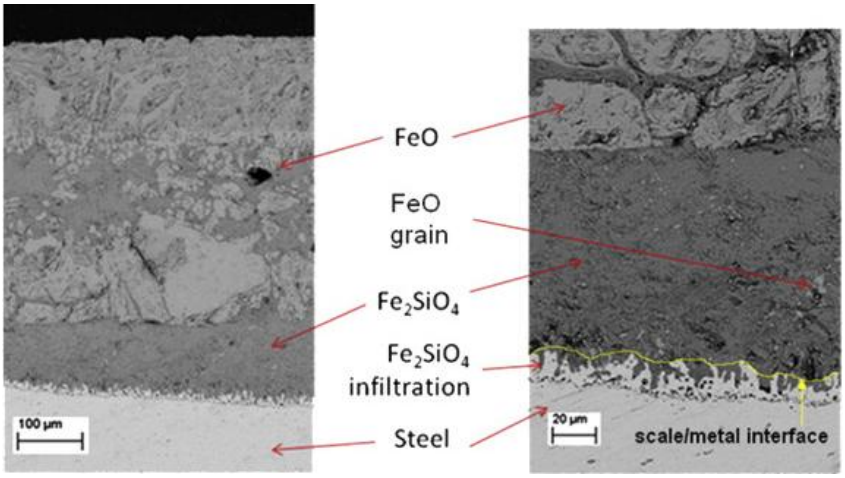


Figure 1.25: Scanning electron microscope image of 'Si16' silicon steel oxidised at 1200°C for 1 min in 15% humid layer (*left*) with an enlarged image of fayalite (*right*) [169].

Although this phenomenon is enhanced by increased temperature, this trend is limited to temperatures below the eutectic temperature (1173°C) beyond which the molten wüstite-fayalite system promotes higher diffusivity (diffusion coefficients) of iron and oxygen ions to the SGI, than in the solid silicon oxide system. 0.02wt.%Si showed less evidence of these phenomena in Mouayd et al.'s study, so it remains to be seen whether they are more apparent in tube grade steels which are expected to have higher contents, but not as high as other sample grades used in the study discussed here [169].

The most relevant study relating to silicon in the context of tube manufacturing was performed by Wassilkowska and Dabrowski during their investigation of ductile iron pipeline used in water transport infrastructure [173]. These cast components are subjected to annealing to obtain the ferritic matrix necessary for sufficient ductility to allow the minimum 10% elongation necessary for a diametric range of 80-2000mm (with a minimum wall thickness of 3mm). It has already been noted that although annealing and normalising temperatures occupy the same range (920-960°C for annealing), the cooling rates diverge owing to furnace-based and air-based cooling respectively [37]. Annealing and normalising soak times are also significantly different with hours- versus minutes-long cycle durations respectively. Two pipe geometries, A (DN 150_e4.5 - nominal diameter 150mm, wall thickness 4.5mm) and B (DN 100_e6.2 – nominal diameter 100mm, wall thickness 6.2mm) were studied. The same composition was used in both samples (3.3-3.8 wt% C, 1.5-2.5 wt% Si). The total oxide scale layer thickness for pipe A was measured at 40µm and its composition was shown to be transversely inhomogeneous. A 2µm layer of iron-rich oxide with silicon dispersions (9 Si-49 O-42 Fe wt%) was observed closest to the substrate, followed by another 2µm layer comprising silicon oxide with a low iron contribution (16.0

Si-50.8O-33.2Fe wt%). Longitudinal cracking was observed between the substrate and initial iron-rich oxide layer due to weak matrix-scale adhesion, although this was likely induced by metallographic preparation techniques (see Figure 1.26). The main scale constituent comprising the remainder of the scale layer was essentially 'silicon free' (1.4 Si-41.6 O-57 Fe wt %) and separated from the lower structure by a 'pronounced' interface boundary. Pipe B evolved a much thicker scale over approximately 100µm comprising two distinct sub-layers denoted by significant differences in surface roughness, porosity and composition contrast (observed using backscatter electron imaging). Cracking was observed between the sub-layers, owing to differences in phase plasticity and hardness. The thinner (30µm), rougher, darker inner sub-layer exhibited a homogeneous microstructure of fine silicon dispersions and iron oxide (5.2 Si-36.3 O-58.5 Fe wt%), with visible micro-porosity. Much larger porosity is observed in the thicker, coarser ferric top layer (1.8 Si-34.0 O-64.2 Fe wt%). The application of this observation was highlighted as the potential to improve corrosion resistance by mechanically removing the top oxide layer to expose the silicon-rich layer.

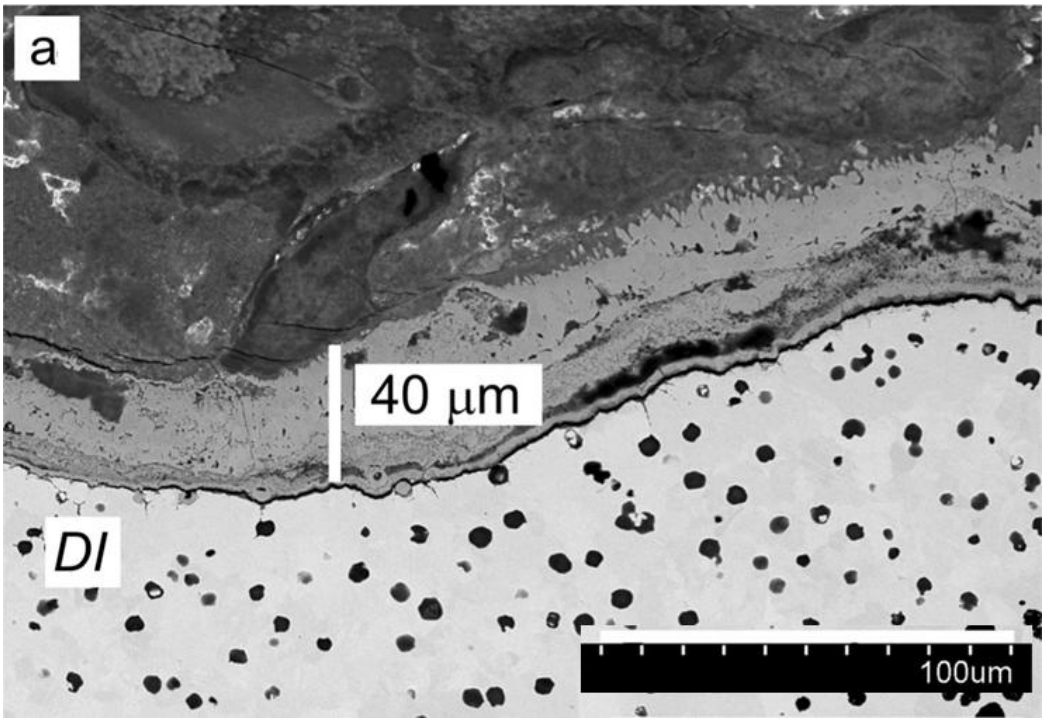


Figure 1.26: Scanning electron microscope image of approximately 40µm of oxide scale formed on ductile iron pipes [173].

Wassilkowska and Dabrowski [173] did not discuss the pipe geometry variables potentially responsible for the observed scale morphology variations. It appears that a thinner wall and larger nominal diameter (Pipe A) generates a thinner oxide scale layer with a steep silicon

concentration gradient (a 6-fold change in Si concentration was observed across a 40μm thick region). However, a thicker wall and smaller nominal diameter (Pipe B) evolved a thicker scale (2.5 times greater than Pipe A) with a silicon concentration gradient only half as steep as Pipe A.

However, a further key element of Grant's work was the comprehensive characterisation of conveyance tube manufacturing steel grades, identifying wüstite as the dominant stable oxide phase using energy dispersive spectroscopy (EDS) (see Figure 1.27), Raman spectroscopy (see Figure 1.28), and high resolution X-ray diffraction (XRD) (see Figure 1.29) [9]. Analysis was performed on oxide samples retrieved from industry and grown in atmospheric replication experiments to establish a detailed knowledge of phase morphology to aid oxidation-resistant coating design. In contrast to the studies described previously [169, 170, 173], Grant did not observed evidence of silicon precipitation into the oxide scale from both industry and laboratory samples, concluding an absence of fayalite and associated silicon compounds in the oxide [9]. However, as previously discussed, experimental studies often cannot take a holistic approach towards a scale-generating manufacturing process. In the case of conveyance tubes, and similar non-planar products (see Section 1.7.1), there is significant thermomechanical processing which will affect oxide kinetics and adhesion [23, 64, 106, 118], but cannot be captured within an in-situ oxidation test.

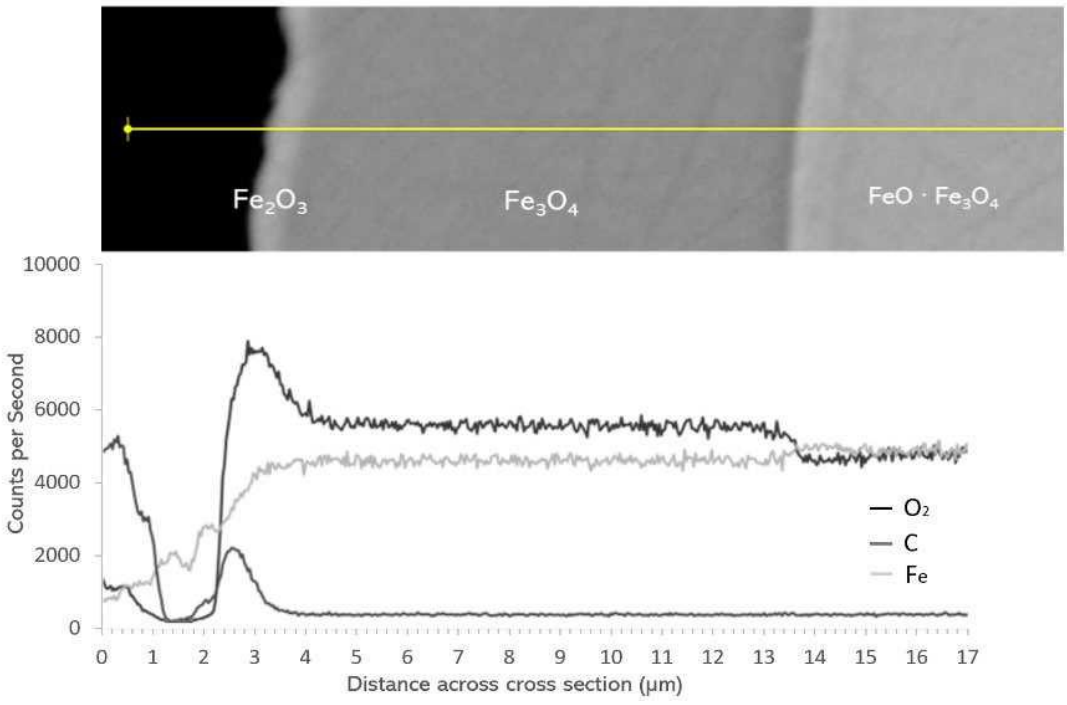


Figure 1.27: An energy dispersive spectroscopy (EDS) line scan performed by Grant to characterise oxide scale phase on scale grown in atmospheric replication experiments on P195GH ('E41') [9].

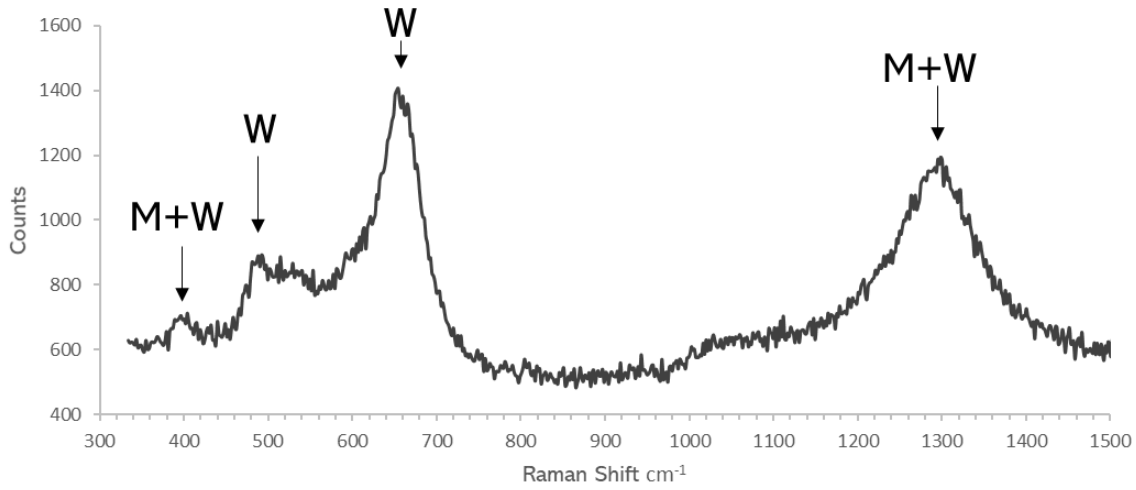


Figure 1.28: Raman spectra of central inner oxide layer from UE41 steel. Savitzky–Golay smoothing was applied of the second order polynomial [9].

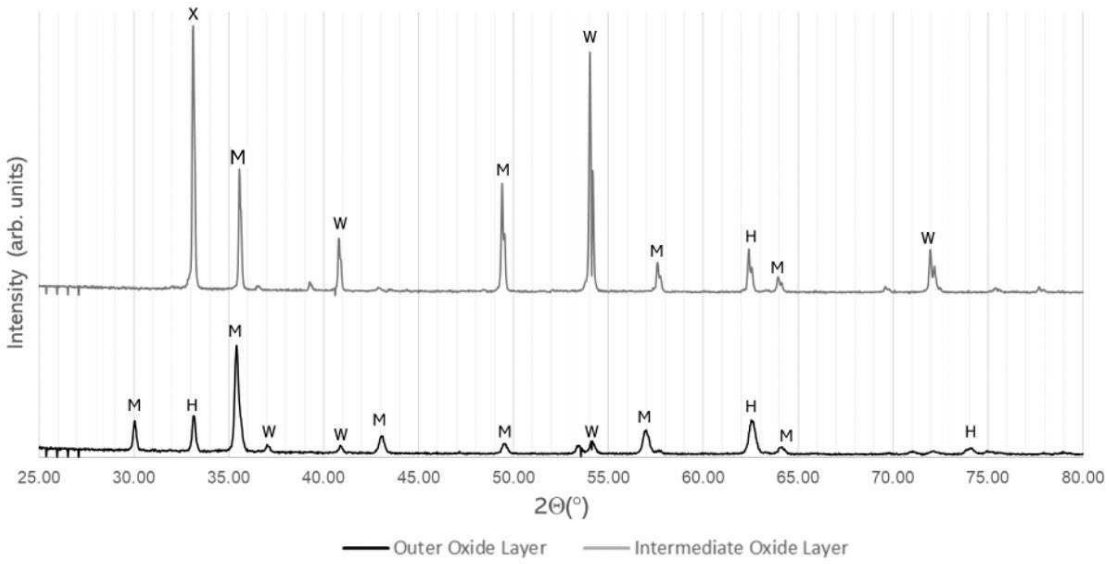


Figure 1.29: XRD powder scan (2$\boldsymbol{\theta}$) of the Outer and Intermediate Oxide layer of UE41 steel and Reitweld refinement conducted to determine crystal structure present within the oxide layers [9].

1.6.1.3 Geometry

Numerous authors have taken a proactive scale management approach and investigated the effect of manufacturing parameters on scale kinetics, morphology, tribological, and mechanical behaviour. Namely, these parameters were atmospheric composition, furnace type and heat transfer behaviour, and substrate tribology but the review thus far highlights how the literature refers almost exclusively to steel and slab manufacture when considering oxide scale, with little attention paid to the effect of any variation in geometry on oxide characteristics, e.g. tube geometry. However, scale growth on tubes presents specific challenges. Despite an apparent lack of the study of the effect of external scale, there is a considerable body of work investigating various aspects of external scale on the inner tube

surface arising from steam-accelerated high-temperature oxidation of steel (usually stainless) superheater tubes [174]. Boiler systems, and specifically the superheat region, experience some of the most extreme engineering service conditions, namely high temperatures (up to 1000°C) and pressures (up to 30MPa [175-177]). In their study predicting oxide scale growth in superheater and reheater tubes, Purbolaksono et al. [178] commented on findings that almost 90% of failures from long-term overheating arose in superheater, reheater and wall tubes. Several phenomena contribute to this figure. Firstly, and as is most relevant in the relation to this project, the external gas flow from the coal-fired furnace used to reach supercritical temperatures introduces coolant flow-reducing ash deposits, which expose the tubes to excessive external heat flux, and a temperature-reducing thin gas film on the external surface. However, as ash deposition is more problematic in coal-fired furnaces [179], external scale phenomena are neglected in favour of ash deposit studies in the case of boiler system superheater tubes. Furthermore, although external scale is neglected in their own and other works [180], Purbolaksono et al. clearly state that scales on both the internal and external surfaces can insulate against heat transfer from the tube wall to the steam. This is due to their low thermal conductivity, as well as decreased heat flux via conduction across the tube wall, resulting in reduced cooling and increased tube metal temperatures, which results in a 'runaway reaction' as increased scale growth promotes higher temperatures which in turn accelerate scale growth [178].

Jiang et al. included a descaling layer of tube material, due to its effect on heat transfer, in the form of a specific heat transfer coefficient in the unified heat transfer equation which formed the partial basis for their Finite Element (FE) model of carbon steel tube multi-pass stretch reduction (albeit in seamless tubes) [63]. They argue that previous FE models had achieved convergence based on unrealistic assumptions, including assuming a negligible effect of hydraulic descaling on heat exchange. However, it should be noted that they continued to assume complete success of the descaling process, therefore neglecting the effect of any remaining adhered scale on heat transfer. They demonstrated that variation in transverse material flow around the tube circumference depends on the proximity to the position of the roll groove shape angle and leads to transverse wall thickness variation. At the 30° position of the roll groove shape angle, the steel temperature is higher due to greater conversion of plastic flow into heat, leading to lower material strength. It is suggested that inclusion of an adhered scale layer would predict a higher tube wall temperature and further affect the variation of wall thickness (depending on burner position relative to the

tube circumferential surface). Hence, scale could have an additional effect on product quality compliance.

Tubes with higher than predicted wall temperatures are liable to creep fracture, with 10% of power plant breakdowns caused by scale-related creep ruptures [181]. In a worst-case scenario, increase of the tube wall temperature to the same level as the flue gases (>900°C) can allow tubes to boil dry and reach the inlet, i.e. maximum, flue gas temperature [181]. Creep damage can also be exacerbated when scales are thick enough to reduce the available load-bearing cross-section. Ennis and Quadakkers [177] commented that for a 5mm wall thickness tube, which is almost within Tata's conveyance tube wall thickness range (see Section 1.2), a 1mm thick scale, i.e. 1mm wall thickness loss, will be significant enough to increase component stresses. Furthermore, depletion of strengthening alloy elements which are selectively oxidised could enhance this deterioration in response to component stress. This is particularly true in the conveyance tube case where silicon is added to increase mechanical strength but ultimately selectively oxidised to form the fayalite mixed oxide layer discussed previously. Finally, Ennis and Quadakkers [177] concluded that scale spalling, again an inevitable outcome in conveyance tube manufacturing where TMP exacerbates stresses arising from scale-metal thermal conductivity mismatch (see Section 1.4), could enhance overheating by blocking regions which are crucial for appropriate heat transfer. Huang et al. [175] also remarked that cracks in the scale pre-spalling could provide tunnels for steam (or oxygen in the project case) to attack the underlying metal substrate which would be overheated and less resistant to oxidation due to the presence of scale. Purbolaksono et al. [178] argue that an accurate scale prediction, internally in their study but arguably true for external cases, could aid in remaining life predictions.

Silveira et al. [180] investigated external oxide scale microstructure, morphology, composition, and adhesion, and their effect on high pressure (HP) steel reformer tube magnetic properties. They proposed that oxidation is one of the factors associated with lifespan-decreasing premature damage to tube external surfaces. Vertical installation of the reformer tubes generated a spatial temperature function along the tube length therefore samples were taken at various locations (1.9m, 2.7m, and 3.5m from the roof) from a tube in operation for 90,000hrs. Circumferential dimensions of the investigated tubes were not provided so a direct comparison to conveyance tubes cannot be made. Investigation of the oxide phase microstructure and morphology using backscattered secondary electron (BSE) SEM images revealed the typical structure associated with the alloy under investigation.

Compared to the tube grades studied within this project, the alloy displayed very high levels of niobium and titanium modification and even the lower level alloy elements which contribute the most to the tube grades (silicon and manganese) were present at levels approximately 1000 times greater in Silveira et al.'s alloy compared to conveyance tube grades.

The oxide sub-surface 'transformed' (chromium carbide depleted) region, observed between the substrate bulk and oxide layer, was followed by a silicon-rich layer. Silicon has already been shown to be influential during oxidation with its formation of an intermetallic SSI layer and can be attributed to its high affinity to oxygen which allows oxide formation in low oxygen partial activity regions. The next layer, comprising chromium (III) oxide (Cr_2O_3) and $MnCr_2O_4$, was attributed to the high levels of manganese in the alloy and its rapid diffusion through Cr_2O_3. Image processing software also revealed a general increase in oxide and transformed region thickness at increased temperatures, in agreement with strip and slab-based studies. However, the oxide thickness did not increase at the same rate as its transformed region counterpart. This was attributed to the partial spalling of the outermost Fe and Ni-rich layer of magnetite (Fe_3O_4) and $NiFe_2O_4$ formed at the highest oxygen partial pressures and the residual thermal stresses and high porosity which compromises adhesion to the neighbouring oxide layer.

Landfahrer et al. [16] conducted a computational study of steel tubes in the reheating furnace. The primary objective of the investigation was to assess the impact of oxide scale insulating effect on tube temperature profile in the reheating furnace. Specifically, it was identified that unlike an empirical mass loss study, numerical and analytical studies could distinguish between individual tube surfaces, wherein there are greater differences for a tube compared to a strip or slab due to differences in surface area, fluid dynamics phenomena, and heat transfer processes. A key element of this study was establishing a suitable thermofluid model of the reheat furnace interacting with the tube, which comprised a combustion and flow element. The former determined the temperature, velocity, and species distribution derived from a stationary furnace simulation based on a spatially resolved heat flux profile and single-tube transient simulation to obtain a motion and heating description respectively. The latter determined turbulence derived from the RANS equations with realisable $\boldsymbol{k-\varepsilon}$ BCs and a steady laminar flamelet model.

In both cases, the tube geometry was highly influential in determining the set-up of the model as well as the details of the output data. For example, a User-defined Function (UDF)

was required to account for variation in local thermal conductivity for a spatially constant layer thickness, which would of course be different for tubes. Furthermore, the use of Schluckner et al.'s model [28] acknowledges the dependence of the steel surface condition on the species concentration and surface temperature (both spatially dependent variables) over tube or direction of movement. Landfahrer et al. [16] showed the effect of geometry as underpredictions of scale thickness were attributed to the mitigation the scale insulating effect by the high surface area to volume ratio of tubes, i.e. faster rate of scale formation. Similarly, the minor (1.5%) difference in scale thickness between the inner and outer tube surfaces was attributed to the difference in temperature between the two surfaces.

The thermodynamics of the reheat system, and its interaction with the geometry, was again proved to be important in Sun and Yan's numerical study of thermal profile and oxide thickness on T91 superheater steel tube surfaces [182]. They commented that superheater tubes, similarly to conveyance tubes, are exposed to high temperature gas on the outer surface and high pressure on the inner surface (although the latter is less the case for conveyance tubes [61]) and that although superheater steel oxide growth had been given attention in the literature, studies were again confined to planar samples. Although a different grade of steel was used, oxide scale was acknowledged to be influenced by the same factors, namely alloy composition, microstructure and surface condition, temperature, pressure, and manufacturing parameters. While oxide scale was acknowledged as a separate issue described as a 'major contributor' to tube rupture, the key objective of Sun et al.'s study [182] was to investigate the inextricable link between heat transfer and oxide thickness so that the most appropriate steel grade could be selected for the tube material to avoid overheating via a comprehensive knowledge of tube wall temperature along the steam flow path. Furthermore, it was remarked that a numerical approach to achieving this output was more achievable than empirical studies wherein wall temperature measurements for long operation periods were hindered by high temperature damage to the equipment. The study itself therefore comprised an analytical prediction of tube wall temperature, using local energy and mass balance, and an iterative derivation of oxide scale growth using the parabolic oxidation, Arrhenius equation, and basic heat transfer theories. Although oxide scale growth was recognised as influential on heat transfer, it was only considered on the inner surface of the superheater tubes, with only ash deposits from natural gas combustion considered on the external surface where scale is considered in this project.

In simulating temperature profile, the specific tube geometry must be considered when

applying assumptions, namely that the tube is uniformly heated in the circumferential direction and a single circumferential section of a calibrated tube segment will have a constant oxide scale thickness. It is also assumed that the calculated temperature of a segment will be its mean temperature. This is in addition to the non-geometry related assumptions of a long period of heating ('Boiler operates under the BMCR load for a long time') and constant thermophysical properties of the metal, oxide scale, and ash deposits. Division of the tube into segments defined by their position and radially independent heat flux allows thickness of oxide scale to be calculated using Equation 1.7 and a cubic polynomial for ferritic-martensitic steel T91 fitted by the same authors [176]. Numerical iteration was used to reduce the disparity between the thermal deviation-based steam temperature prediction, when taken as the oxide scale growth temperature, $\boldsymbol{T_{gr}}$, and internal oxide scale surface temperature, $\boldsymbol{T_{w1}}$, calculated using the calibrated tube heat transfer equation, to less than 0.1, i.e. $\left|\boldsymbol{T_{w1}} - \boldsymbol{T_{gr}} < 0.1\right|$. The superheater tubes compared well in terms of dimensions (outer radius of 38.1mm and wall thickness of 5-5.9mm) and conditions for the outer surface (average flue gas temperature of 859°C) with the conveyance tubes considered in this project. Fluid dynamic phenomena also had to be considered in assessing heat transfer, another aspect heavily influenced by geometry [183]. Sun and Yan's results [182] were in agreement with empirical values measured on three as-received superheater power plant tubes, and higher temperatures and longer service times were associated with thicker oxide scale following a parabolic growth profile. A significant observation was that although the inner and outer wall and ash deposit surfaces on the flue gas side showed an increase in temperature with service time, steam-side equivalents were constant or exhibited a slight decrease. This shows the strong influence of the scale on heat transfer, far more than ash deposits. However, this highlights that scale growth anticipated from flue gas reaction was not also considered for its effects on heat transfer. Furthermore, since oxide scale thickness was shown to be unsurprisingly dependent on temperature and service time, and steam temperature increased along the steam flow path, scale thickness at segmental positions increased accordingly. For example, at a position of higher convection coefficient and higher flue gas temperature, there was a sharp increase in scale thickness. This can ultimately lead to tube overheating due to a lack of heat transfer. Dependence of thermodynamic phenomena on geometry was also highlighted when considering the outer wall temperature, whose value was dependent on spatially resolved thermal conductivity, material thickness and tube wall inside and outside diameter ratio, as well as non-geometric

factors (medium temperature and steam side heat transfer coefficient) and increased in the direction of steam flow. Fluctuations in metal wall temperature were influenced more by thermodynamic heat flux phenomena, namely higher heat transfer coefficient and heat flux with flue gas cross flow than parallel flow, than steam temperature. Uncertainty analysis revealed an expanded tube wall temperature uncertainty of ±7-10°C which resulted in a relative oxide scale thickness uncertainty of 10%. However, ultimately it was concluded that optimal oxide scale growth predictions using this method depended on an accurate description of the gas temperature field along the heating surface.

Since superheater and reheater tubes operate at a continually increasing temperature, scale thickness predictions must be a function of time and temperature. Purbolaksono et al. [178] computationally modelled a 100mm length section of the steam, tube, and flue regions of a seamless ferritic low-alloy steel. Aside from its seamless manufacturing route (conveyance tubes being welded), the outer diameter (approximately 50mm) and low alloy chemical composition all fell within a comparable range for the conveyance tubes studied in this project. Wall thickness (approximately 5mm) fell just outside the Tata's conveyance tube range. The external flue gas environmental temperature, modelled using a forced convection cross flow heat transfer over the initially bare tubes, was also comparable at 900°C (see Section 1.2) although a pure magnetite scale was assumed on the tube steam side.

Purbolaksono et al.'s study [178] used the Larsen-Miller parameter reported by other authors for steam-side scale on ferritic 1-3% chromium steel to predict scale thickness. As with Silveira et al.'s study [180], thermal profile and scale thickness were calculated based on an iterative approach centred around numerical and analytical predictions of steam temperature and scale thickness respectively. It was noted that although thick scale growth on iron conventionally follows a parabolic rate law, as discussed in Section 1.3, extremes of steam and flue gas temperature could trigger an exponential (logarithmic) rate law. This study affirmed the relevance of geometry, particularly given its finite element approach to heat transfer modelling.

Purbolaksono et al.'s results [178] from the initially scale-free tube models revealed several influential factors. Most importantly, geometry was shown to affect growth rate. Whilst thinner walled tubes exhibited less scale formation and therefore less severe metal temperature increase, they were more susceptible to dramatic changes in operational hoop stress [184]. However, thicker tubes may exhibit more severe microstructural changes, due to selective oxidation, which promotes material degradation on top of the higher metal

temperatures associated with increased scale thickness. Steam mass flow rate was shown to affect scale thickness, with a lower rate associated with impaired flow and more opportunity for scale growth. Although internal flow is not relevant for conveyance tube manufacturing specifically, the scale spalling phenomenon referred to by Ennis and Quadakkers [177] could enhance this effect due to the effect of induced roughness on external gas flow dynamics. Changes to the steam temperature itself also showed how higher temperature metals showed reduced oxidation resistance. Finally, the convection coefficient between the tube outer surface and flue gas environment was shown to affect scale thickness, which was often influenced by the tube furnace location. For example, the higher convection coefficient and flue gas temperature associated with tubes directly facing the furnace section yielded thicker scales. Results were in good agreement with as-received tube samples. Hence, overall, a reduction in scale growth could be achieved by higher steam mass flow rates, lower steam and flue gas temperature and lower tube inner diameter and wall thickness. Improved scale growth prediction can only be achieved with accurate assessments of these and heat transfer parameters.

Huang et al. [175] argued that without the implementation of alloys with higher oxidation resistance at the plant design stage, all other solutions to oxide scale failure, within the operation and maintenance routines, also depend on comprehensive analysis of the stress field. Furthermore, Trojan and Taler [185] remarked that high alloy costs mean application-specific selection of steel grades, namely to avoid superheater overheating in this case, still depends on knowledge of tube wall temperature over its entire length. Although Trojan and Taler argued that the considerable contribution of steam superheater damage to boiler failure instances warrant the high cost of monitoring or modelling, as previously stated by Sun et al. [176], field measurements using on-line monitoring are difficult in high temperature settings, and Huang et al. [175] agree that numerical simulation of oxide scale stress field, using theoretical analysis and "…reasonable simplification…" is an "…efficient and effective method…". However, tube reheat parameters do not satisfy the steady state oxide scale stress fields which have been comprehensively developed. Rapid temperature changes in the steam or flue gas, which is particularly true in conveyance tube manufacturing where reheat processes can be as short as two minutes during stretch reduction and only as long as 15 minutes during normalisation, demand an unsteady thermal profile to represent significantly variable temperature distribution. Typically, thermal profiles during reheating follow an initial transient profile followed by a longer

period of steady state behaviour [186]. Huang et al. remark that unsteady thermal processes are less well studied. Additionally, they highlighted that it had been shown widely applied planar models do not yield as accurate results as a multi-layered hollow cylinder model when studying tubes [187].

1.6.2 Oxide Scale Failure Diagrams

Schütze identified the need not only to assess the critical strain for different oxide scale failure mechanisms (covered by Oxide Scale Failure Diagrams (OSFDs) [186]), but also the considerable impact of physical defects (pores, cavities, and microcracks) [186]. They summarised much of this failure information in an Advanced Oxide Scale Failure Diagram (AOSFD) relating failure mechanism susceptibility based on strain, $\boldsymbol{\varepsilon}$, defect size, $\boldsymbol{c}$, and an 'operation' parameter, $\boldsymbol{\omega_{o,\phi}}$, where $\boldsymbol{\phi}$ reflects the specific failure mode described (see Figure 1.30).

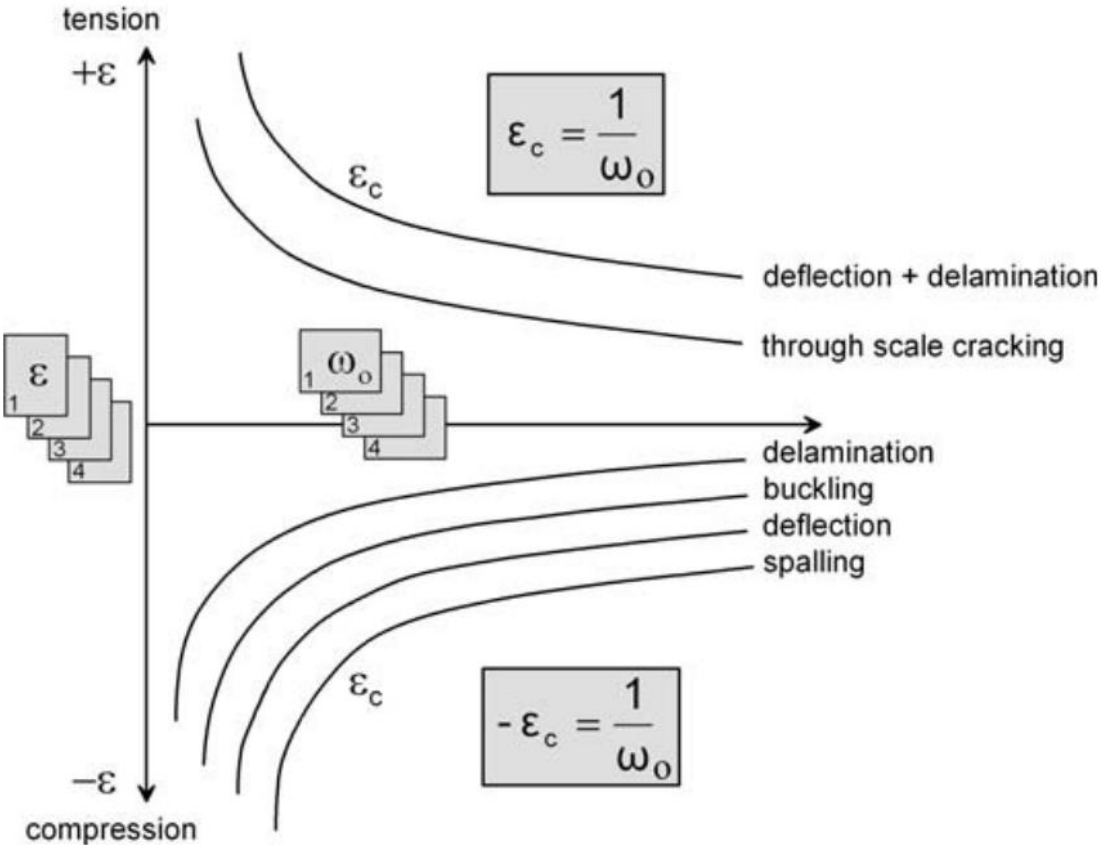


Figure 1.30: Schematic of an Advanced Oxide Scale Failure Diagram (AOSFD) developed by Schütze et al. [186].

Fracture Mechanics Theory of Oxide Failure

Schütze highlighted that the mechanical properties of an oxide scale refer to all its parameters which characterise its cohesion, adhesion, and deformation [188]. However, at

high temperature especially, failure analysis of oxide cannot be limited to conventional elastic (elastic and shear modulus, Poisson ratio) and plastic/creep (ductile-brittle transition temperature, stress-strain and stress-strain rate relationships) properties. Analysis should ideally include oxidation-related properties which characterise pseudoplasticity associated with simultaneous brittle microcracking and continuous healing via oxidation. Hancock et al. also highlighted the need to consider fracture mechanics phenomena within their works on oxide stability and failure [189, 190]. To perform this analysis, oxidation-related properties comprise the distribution and orientation of physical defects (at the metal-scale interface or within the scale), interface geometry, and scale fracture toughness [188]. The change in temperature across the normalise-cool cycle ($\boldsymbol{\Delta T_{norm} - \Delta T_{cool}}$) is too large to neglect temperature effects on elastic modulus. Hence, the theory presented below is appropriate for a 'Level 3' AOSFD which can incorporate the high impact parameters of conveyance tube manufacturing into a comprehensive operation parameter.

Compressive Failure

Krzyzanowski and Beynon proposed two modes for oxide spalling (see Section 1.4.2) [77, 188]. In any case, there is a critical strain energy achieved at a certain extent of scale deformation which is sufficient for separation along the scale-metal interface, i.e. critical spalling strain $\boldsymbol{\varepsilon_c^s}$ [188]. This critical value is a function of the scale thickness, $\boldsymbol{\delta_{ox}}$, and the scale-metal interface fracture energy, $\boldsymbol{\gamma_o}$. However, since metallographic preparation challenges make it challenging to eliminate surface roughness, interfacial fracture energy must be modified to account for the height,

$\boldsymbol{r_{rough}}$, and length,

$\boldsymbol{\lambda_{rough}}$, of the oxide roughness, $\boldsymbol{\gamma_r}$ (see Equation 1.18 and Equation 1.19 – note that $\boldsymbol{E_{ox}}$ should be given in GPa for the latter equation). Both modes proceed as tube cooling occurs and provided the strain is entirely thermal, a critical temperature drop, $\boldsymbol{\Delta T_c}$, can be calculated based on the difference between the metal and scale coefficients of thermal expansion, $\boldsymbol{\Delta\alpha}$ (see Equation 1.20).

$$\frac{\mathbf{1}}{\boldsymbol{\varepsilon_c^s}} = \boldsymbol{\omega_{o,s}} = \left(\frac{\boldsymbol{\delta_{ox}} \cdot \boldsymbol{E_{ox}} \cdot (\mathbf{1} - \boldsymbol{\nu})}{\mathbf{2}\boldsymbol{\gamma_r}}\right)^{\mathbf{1/2}}$$

Equation 1.18

$$\gamma_r = \gamma_0\left(1 + \frac{0.1E_{ox}}{2\gamma_0}\frac{r_{rough}}{\lambda_{rough}}\right)$$

Equation 1.19

$$\Delta T_c = \frac{\varepsilon_c^s}{\Delta\alpha}$$

Equation 1.20

However, since in the case of mode II failure, buckling is anticipated to precede through-thickness cracking, i.e. spalling, a conservative criterion, ε_c^b, for mode II based on buckling can be introduced by introducing the initial radius of the zone of decohesion, R_{dec} (see Equation 1.21). Initiation of through-thickness crack deflection, ε_c^{cd} from the interface towards the scale surface can follow buckling and precede spalling.

$$\frac{1}{\varepsilon_c^{b/cd}} = \omega_{o,b} = \omega_{o,cd} = \frac{1-\nu^2}{k_{\omega_o}} \cdot \left(\frac{R_{dec}}{\delta_{ox}}\right)^2$$

$$(k_{\omega_{o,b}} = 1.22\ for\ buckling, k_{\omega_{o,cd}} = 3.75\ for\ crack\ deflection)$$

Equation 1.21

There is an alternative criterion based on the assumption that plastic oxide yield strength, σ_Y, is 10% of its elastic modulus ($\sigma_y \approx 0.1E_{ox}$). Assuming that brittleness is a dimensionally dependent concept [188], there will be a critical scale thickness, δ_{ox_c}, below which the oxide failure is ductile (see Equation 1.22). This critical scale thickness can be used in Equation 1.18 to find a critical strain below which scale deformation will be ductile.

$$\delta_{ox_c} = \frac{2.8\gamma_r E_{ox}}{{\sigma_Y}^2}$$

Equation 1.22

Interfacial cracking is another precursor to spalling when there is stress (compressive or tensile) acting on an interfacial defect-containing system in the direction parallel to the scale-metal interface and at the interfacial location with peak roughness amplitude. Equation 1.23 uses a local tensile stress intensity factor, K_{Ic}, based on the half-length of the critical defect, c, and geometrical parameter, f^*, and highlights how a thinner scale with greater surface roughness and smaller defects can tolerate greater compressive strain before failure.

$$\frac{1}{\varepsilon_c^{if}} = \omega_{o,if} = \frac{f \cdot (\pi c)^{1/2}}{K_{Ic}} \cdot \frac{2E}{(1 + r/\delta_{ox}) \cdot (1+\nu)}$$

Equation 1.23

Finally for compressive scenarios, the case of shear stress (see Equation 1.24) is relevant if it is necessary to take an actual stress situation into account at the failure initiation site, i.e. spalling as a result of stress components evolved from a physical defect being in a shear stress situation like at an oxide grain boundary or dislocation movement plane and also that the defect is large enough to reduce the shear failure criterion to a value that preceded interfacial failure [186]. Although ultimately dependent on shear orientation, a good approximation is $\boldsymbol{\sigma = \tau\sqrt{3}}$ [186]. Crucially, the most conservative criterion can be obtained using shear deformation fracture toughness, $\boldsymbol{K_{IIc}}$ or $\boldsymbol{K_{IIIc}}$, if available, otherwise the $\boldsymbol{K_{Ic}}$ value gives the least conservative criterion.

$$\frac{\mathbf{1}}{\boldsymbol{\varepsilon_c^{sh}}} = \boldsymbol{\omega_{o,sh}} = \frac{\mathbf{2}\boldsymbol{K_{Ic}}}{\boldsymbol{f E_{ox}\sqrt{\pi c}}}$$

Equation 1.24

Tensile Failure

Tensile failure analysis is simpler by comparison and based on conventional fracture mechanics (see Equation 1.25) [102]. Oxide fracture toughness calculated either based on crack geometry (see Equation 1.26) or oxide surface fracture energy (see Equation 1.27).

$$\frac{\mathbf{1}}{\boldsymbol{\varepsilon_c^{t}}} = \boldsymbol{\omega_{o,t}} = \frac{\boldsymbol{f \cdot E(\pi \cdot c)^{1/2}}}{\boldsymbol{K_{Ic}}}$$

Equation 1.25

$$\boldsymbol{K_I = \sigma_{if}\sqrt{\pi c} f}$$

Equation 1.26

$$\boldsymbol{K_{Ic} = \sqrt{2\gamma_0 E_{ox}}}$$

Equation 1.27

It should be noted that individual failure modes may combine under certain loading conditions [12]. For example, under tension transverse cracks may develop (initiated at the metal-oxide interface) and build up to such a density that interfacial cracks develop at the corners of the transverse cracks and lead to oxide raft delamination. Hence, some failure modes, such as interfacial cracking, can exist in both tensile and compressive stress states. If there is a significant number of defects with the potential to interact mechanically, a composite defect size, $\boldsymbol{\bar{c}}$, may be required, often leading to an overprediction of individual defect size [188].

1.6.2.1 Oxide Failure Diagram Considerations for Conveyance Tube Manufacturing

Porosity can also be included in the form of the porosity volume fraction, $\boldsymbol{p}$, typically 25% in experimentally investigated scales [128], which is highly relevant when considering the comments by Schütze that it is invalid to assume that scale thickness alone is the significant parameter [186] (see Equation 1.28). This highlights why the AOSFD abscissa should use the scale property parameter, $\boldsymbol{\omega_{o,\phi}}$, as opposed to scale thickness, $\boldsymbol{\delta_{ox}}$.

$$\boldsymbol{E} = \boldsymbol{E}(\mathbf{1} - \boldsymbol{p})$$

Equation 1.28

Mechanical Analyses of Oxide Scale on Curved Surfaces

Huang et al.'s model [175] was developed based on T92 steel superheater tubes which had an outer diameter and wall thickness well within the lower range of Tata's conveyance tubes. The steam-side oxide scale was anticipated to comprise an inner Fe-Cr spinel and outer magnetite layer of equal thickness. It remains to be seen whether the assumption of a duplex or triplex morphology changes the stress field description. For simplification, the scale was assumed to be a single uniform thickness layer, although this was the first cited case of using physical properties based on the mean of the component phases, rather than use of a single dominant phase. Although the assumption of equal contribution by two phases observed allowed this approach, application of the same approach to the vastly differing contributions of the three phases observed on conveyance tube grades would not be valid. Crucially, the scale and substrate are both assumed to be isotropic and elastic, with oxide scale growth stresses being neglected. Neglect of growth stress seems to conflict with delamination studies performed on external oxide scale (discussed in Section 1.4). It is likely that, due to the high temperatures associated with superheater tube operation, oxidation stress would be relieved by creep of both the tube metal substrate and its steam-side scale, with creep being a prevalent phenomenon as shown in the failure cause rates previously discussed. Dong et al. [191] showed that a pure elastic oxidation stress approach to predicting substrate and scale deformation resulted in considerable stress overestimates which would initiate scale failure. Scale failure is prevented when creep relaxation effects are considered in analytical model, leading to an improved agreement with experimental data [191]. Work investigating critical stress and adhesion in this model must consider whether this assumption can be made for conveyance tube manufacturing.

To obtain a comprehensive stress field description, namely thermal stress under the

circumstances if growth stress is neglected and mechanical stress is not deemed present, a heat transfer model was developed. Thermal stress was asserted to arise when the temperature distribution of the substrate and scale deviated from the steady initial conditions associated with the newly installed tube, presuming a long period of operation without significant condition variation. The Finite Volume Method (FVM) was used to obtain the transient temperature field from the one-dimensional heat conduction governing equation. It should be noted that steam-side heat transfer was attributed only to convection, whilst gas-side transfer comprised simultaneous convection and radiation, which is pertinent to conveyance tube studies in this project. Furthermore, it was highlighted that the integral thermofluid properties, namely dynamic viscosity, thermal conductivity, and specific heat of the flue gas, are all influenced by coal content (although this is not relevant for the conveyance tube natural gas furnace), gas temperature, and excess air coefficient. The gas temperature was calculated based on the intermediate point temperature of the superheater inlet and the outlet of its preceding component. The value came to 981°C, slightly higher than typical conveyance tube normalisation and stretch reduction values (see Section 1.2). However, as with Purbolaksono et al.'s study [178], iterative operations were needed to account for the effect of transient thermal processes, and the insulating effect of scale, on changes to the metal temperature and its gas-side heat transfer coefficient (convection and radiation again). Analytical expressions for radial displacement and stress components were defined in order to predict failure against critical values. The equation for critical failure strain, defined by Schütze et al. [186], highlighted the dependence on oxide scale fracture toughness, applied strain, and physical defect size.

Firstly, results showed complete inconsistency in the temperature response at each node, although the trend was observed that temperature variation nearer the oxide-steam interface was more severe. It was also highlighted that analytical theory shows how free thermal strains are dependent on temperature field variation, which therefore ultimately leads to variation in oxide scale sublayer thermal strains. In particular, hoop stress was shown to be further influenced by time and radial position, with much higher hoop stresses in regions closer to the oxide-steam interface making them liable to rapidly propagating cracks, i.e. inner scale surface more likely to spall.

Significant variation in the hoop stress profiles at different radial nodes showed that steady stress analysis would be unsafe as the final steady stress was 8.9MPa lower than the peak value for the first radial node. However, by accounting for transience in thermal profiling, it

was shown that duration of steam temperature could be adjusted to mitigate against oxide failure via steam temperature control systems. Specifically, lower peak values of hoop stress were observed in tubes subjected to longer durations in steam temperature. For example, an increase in exposure duration of 120s led to a 6.3MPa decrease in peak hoop stress. The validatory AOSFD supported this conclusion, but for larger durations, the effect of relative increase was less noticeable. However, this is still a cheaper and less involved option than increasing variation duration. Furthermore, larger durations lead to a reduction between that peak and final steady hoop values, thus favouring the simpler steady state approach to temperature field analysis. Finally, it was shown that hoop stress increases with oxide scale thickness, with thicker scale also have lower critical failure stresses. Since tubes with long operating times or higher temperatures (the latter being more relevant for conveyance tubes) exhibit thicker scales, they should be inspected more carefully. Perhaps this should also be true for the as yet neglected external oxide scales. However, investigation of the relationship between scale thickness and hoop stress at specific radial nodes did reveal that thicker oxide scales are only more liable to crack initiation and propagation at locations near the inner scale surface. Near the scale-substrate interface, the opposite is true, i.e. lower stresses are observed for thicker scales.

Trojan and Taler [185] focused their study on how scale and ash deposits affect the details of superheater thermal simulation, specifically in terms of the heat transfer complexity they introduce on the already complicated tubular cross-flow heat exchange scenario. However, again, external scaling was neglected. Their study highlights a key difference between superheater and conveyance tube reheat scenarios and they comment that ash deposition and fouling is prevalent in coal-fired furnaces, whereas the conveyance tubes discussed in this work are heated in either natural gas-fired or induction furnaces. However, superheater tubes are still the region of highest temperature within their system. Trojan and Taler remark on one of the key challenges of superheater modelling, despite computational power developments, namely the inability to simultaneously simulate flue gas- and steam-side thermofluid phenomena. The boiler combustion chamber and convection section must be combined via 3D fire side modelling and 1D tube side model for water and/or steam (depending on specifics). Arguably, external scaling of tube reheating should therefore be easier as it only depends on flue gas behaviour both internally and externally.

Partial differential equations (PDEs) were used to describe the spatial and temporal profiles of steam, tube wall, and flue gas temperature. Tube metal, steam-side scale, and ash deposit

were all assumed to have temperature-dependent physical properties. Again, the FVM was used to solve the system of equations for both fluids (steam and gas). FVM heat balance equations for the steam, tube wall, and flue gas were then developed and solved using the over-relaxation method [192]. It should be noted that, when considering thermofluid response, attention was paid to the arrangement of tubes, e.g. in-line, in the superheater and its effect on heat transfer coefficients, and was developed to be flexible to parallel, cross, or mixed flow arrangements. This was deemed crucial in reducing the demand on alloy selection by minimising the maximum tube metal temperature.

With reference to the surface deposits, which are assumed to cover the entire internal and external surfaces, external surface ash deposits are anticipated to reduce tube wall temperature whilst the converse is true for steam-side inner surface scale (assumed to be a single phase layer for simplification which is a common procedure described within this review). This leads to the worst-case scenario mechanism of reduced convective and radiative heat transfer from the flue gas to tube metal due to the insulating effect of the ash deposits (a phenomenon already discussed for external scale on conveyance tubes in Section 1.6.1) and reduced conductive heat transfer from the tube metal to steam-side scale, due to low thermal conductivity of both the deposit and scale. This leads to the same oxidation-promoting 'runaway' heating reaction previously described in Section 1.6.1.3, as tube wall temperature rises and negatively impacts stress rupture life.

Results showed that Trojan and Taler's numerical method for superheater thermofluid operation could be used to investigate gas-side ash deposition, steam-side scale, and non-uniform flue gas radial temperature distribution over a range of operating conditions, including temperatures close to those found during conveyance tube reheating.

Comparisons of computed and measured steam temperature rise over the whole superheater allowed ash deposit thermal resistance to be calculated. It was shown that ash-fouled superheater tubes, made from Russian steel grade 20, exhibited a reduction in heat flux absorption by the steam which manifested as a steam outlet temperature decrease of 70K. The steam temperature increase over the tube length was only half that observed in clean tubes. Overall, tubes in areas of high flue gas temperature showed the largest temperature increase regardless of surface condition. The small (a few degrees Kelvin) temperature drop observed over the tube wall thickness was also attributed to the deposit layer insulation (due to its low thermal conductivity), which itself had a significant temperature increase.

Furthermore, delaminated ash deposit build can interfere with and reduce flue gas flow rate,

and subsequently steam temperature. Steam-side scale was also shown to affect steam temperature, with scale-fouled tubes displaying a 25K lower steam outlet temperature and 57K increase in tube wall temperature, which translated to a 16% decrease in superheater output. Overall, steam temperature was shown to change along the steam flow path, in agreement with other studies discussed in this chapter, with an overall increase of approximately 30K in a 1213K upstream flue gas. Excessively heated tubes were shown to experience decreased steam mass flow rate which allowed a greater temperature increase (approximately 5K). For example, a 153K increase in flue gas temperature led to a 4% reduction in steam mass flow rate. This made a case for increasing steam mass flow rate for safety reasons, to ensure sufficient tube cooling to prevent creep and stress rupture. It was concluded that both steam-side scaling and ash deposition led to steam outlet temperature reduction and tube wall temperature rise, although steam-side scale phenomena were deemed to dominate the latter.

Although, as discussed, scale kinetics, morphology, and composition, are affected by time, temperature, thermal cycling and pressure, adhesion response is determined by scale failure-inducing damage parameter accrual [186]. However, most high-temperature studies assume a flat specimen of steel upon which oxide can grow unrestrained. Sabau and Wright [193] highlighted that flat plate studies also assume a semi-infinite steel thickness and uniform temperature in the steel and oxide (other superheater-specific steam temperature and pressure assumptions are also made but are less relevant when considering conveyance tubes). Sabau and Wright aimed to develop existing methodologies to account for oxide growth-induced stress and inelastic effects, e.g. creep, by investigating the stainless steel grade T22. To allow this development at a reasonable rate, the typically multi-phase scale was assumed to be defect-free with a uniform thickness, composition, and phase. Scale properties, namely coefficient of thermal expansion, were derived from the mean of the real oxide constituent phases (50% contribution from each). Due to the existence of a thermal cycle used within boiler systems, comprising a full and partial load, a modification of the conventional parabolic oxidation law was applied. Crucially, the external tube environment was assumed to be deposit-free thus neglecting the possibility of oxide growth and delamination, and its effect on heat transfer. In this project, clearly the key aim is to emphasise the effect of any scale growth on tube thermomechanical response, especially scale kinetics and adhesion. However, in Sabau and Wright's study the film coefficient for heat transfer from the flue gas to tube surface was based on a clean tube surface.

Temperature reached the conveyance tube normalisation only at full load of 1200°C although this was applied at higher pressure (2bar) and for longer (14hrs) than for conveyance tubes. The tube studied had similar dimensions to Tata's conveyance tubes with an outer diameter of 38-64mm and wall thickness of 5mm. Sabau and Wright comment that the common assumption of internal steam temperature being equal to the critical oxide growth temperature, $\boldsymbol{T_{gr}}$, could not be applied in their study due to the existence of a thermal boundary layer between the oxide and steam leading to the oxide surface temperature exceeding that of the steam. For simplicity, the oxide was assumed to grow only at the scale-steam interface where oxidation temperature was the oxide surface temperature. As with previous studies discussed in this section [175, 176, 178, 182], an iterative approach to temperature and oxide thickness prediction was required to obtain an acceptable error of 0.1°C. The effect of the heat transfer boundary condition was demonstrated as scale thickness for the same period with the boundary condition included was double that of the study without.

The stress-strain state in the oxide was recognised as being heavily dependent on thermal deformation arising from the variable temperature profile associated with boiler conditions. Free thermal strain was identified as a function of the temperature-dependent coefficient of thermal expansion. However, where an isothermal temperature distribution is commonly used, this was replaced with a spatially dependent temperature profile. Temperature variation-based hoop strain and stress values revealed that the oxide is in tension during cooling from full to partial boiler load. However, stress and strain variations within the oxide were ten times greater for the partial than full load. Furthermore, it was found that an increased oxide thickness led to an increase in maximum stress and strain values but a decrease in their minimum and average values. The former was attributed to the increased temperature difference between the reference (non-uniform temperature distribution at high load) and partial load state at the SSI (where the highest temperature is found), whilst the latter was attributed to the temperature increase associated with thicker oxide scales and the shape of the thermal expansion variation.

When expanding the approach out to a tube (hollow cylindrical) geometry, plasticity, viscoelastic creep (, i.e. relaxation), and transient effects were neglected. elastic modulus and Poisson's ratio were assumed constant within the temperature range explored and axial force was assumed to be zero. It was remarked that when CTE is constant, analytical solutions for cylindrical geometry are available in the literature. Both Simple Plane Strain

(SPS) ($\boldsymbol{\varepsilon_\theta} = 0$) and Generalised Plane Strain (GPS) ($\boldsymbol{\varepsilon_\theta} \neq 0$) cases were considered.

To assess the validity of the tube geometry analytical theory and assumptions, a test calculation was performed on a compound hollow cylinder comprising two component tubes representing the 5mm thick tube metal and 200μm thick internal surface oxide scale with equal elastic moduli and Poisson's ratios but differing CTEs (this is comparable with set-ups used for low carbon steel and for outcomes in conveyance tube manufacturing). The tubes were cooled from the full load (590°C) to partial load (460°C) conditions whilst neglecting pressure effects. However, heating was not investigated which would be necessary for conveyance tube manufacturing applications. It was highlighted that the negative cylindrical hoop strain is equivalent to the total thermal strain experienced, whilst the flat plate positive hoop strain only comprises stress-generating hoop strain components. Therefore, only the stress-generating hoop strain components should be reported during comparison involving cylindrical geometry. Finally, it was emphasised that steam pressure on the internal tube surface was able to evolve strain during load transition in addition to thermal deformation via CTE mismatch. Although pressure effects are not expected in conveyance tube manufacturing, it is still valuable to note that although both temperature and pressure effects led to a net increase in hoop strain, at full load only pressure effects act and these are conversely associated with decreased hoop strain when steam pressure decreases (whilst thermal deformation unsurprisingly leads to increased hoop strain). This explains the ten times greater stress and strain variations in the partial load oxide layer compared to its full load equivalent. The minimal influence of oxide scale thickness on hoop strain was attributed to the neglect of viscoelastic creep.

Overall, although accounting for geometry is often confined to assuming an infinitely long flat plate, Sabau and Wright [193] conclude that specific cylindrical geometry analytical solutions provided sufficiently different results to justify their application as a better option. It has already been discussed in previous sections how scale spalling can accelerate oxidation as fresh substrate surfaces are systematically exposed. However, Steiner [194] remarks that numerical modelling of stress and strain arising in oxide scales incurs high computational and economic effort whilst not always allowing deep insight into the effect of basic physical parameters which analytical models provide. In commencing their analytical study of oxide spalling, Steiner [194] first commented on the importance of elastic modulus (with a notably low difference between its value for alloy substrates and their oxide) and Poisson's ratio (taken as the same value for the substrate and oxide phases to simplify the analytical

algebra) during stress calculations. However, these mechanical data are scarce in the literature. The combined stress effects of oxidation, temperature change, radial thermal gradient, and internal and external gas pressures were discussed.

Growth stress, arising from volumetric increase associated with oxygen uptake, depends on whether scale is internal or external, and isotropic or radial. For austenitic steels, such as are seen during conveyance tube normalisation, the dominance of Cr^{3+} migration favours the development of external oxide, i.e. oxygen ions are diffusing as well as iron and chromium (III) for ferritic martensitic steels so they experience both external and internal oxidation [195]. Furthermore, assuming radial (anisotropic) oxide growth and absence of axial strain, growth stresses are a purely geometric, mono-axial effect only observed on curved surfaces (where planar surfaces have an infinite radius of curvature which drives quotient-based strain equations to 0) [106]. This supports Sabau and Wright's conclusions on the significant impact of geometry on spalling [193]. Anisotropic radial volume increase on a curved surface will therefore be accompanied by hoop strain which increases linearly from zero at the SSI to a maximum at the SGI (except for the condition PBR = 1). Compressive hoop stress in the steel substrate is countered by tensile hoop stress in the scale. If isotropic volume change, a more realistic scenario, were to be accounted for this would improve mechanical scale stability by generating a purely compressive stress state once superposed on to the anisotropic contribution. However, the appropriate bending test data for the isotropic contribution is not available so the basic assumption continues to be applied in Steiner's work. Although lower temperatures than those experienced in conveyance tube studies were investigated (500-600°C), it was still relevantly shown that growth stresses are most important in high temperature zones due to the rapid increase in oxidation with temperature, i.e. a higher oxidation rate was associated with a faster increase in tensile hoop stress. The effect of creep was investigated by generating analytical predictions with creep both accounted for and not accounted for.

It was highlighted that the tensile stresses observed at the outer surface of the scale should be connected to its fracture when they exceed critical fracture values. Thus, higher rates of fracture should be seen on alloys with higher oxidation rates. In terms of flaw size, it is anticipated that this is connected to scale thickness, as is critical scale failure strain, and its size is time-dependent if there is void and/or pore growth during vacancy migration, i.e. critical fracture stress will decrease with time as oxidation proceeds. Ultimately, stress calculations discussed by Steiner are only valid in the linear elastic (pre-cracking) case as

fracture leads to desirable stress relaxation and subsequently initiation of a new stress cycle [196]. As scale growth continues post-cracking, the cracked scale is displaced ahead of its intact part (outside for austenitic alloys, inside and outside for ferritic-martensitic alloys). As was also previously discussed, stress can also arise from temperature change. Steiner [194] assumes a bi-axial stress state during isotropic thermal expansion where tube spatial temperature profile is homogeneous. Significant difference exists between the substrate and scale thermal expansion coefficient (the scale value is always significantly lower but this is particularly true for austenitic alloys where the difference is twice that of ferritic-martensitic alloys [194]). Overall, this leads to tensile and compressive stress in the substrate and scale respectively. Naturally, this phenomenon is present in both planar and curved geometries. The absence of data for oxide thermal expansivity in 2002 led Steiner to take values from that of chromium (III) oxide (Cr_2O_3). They suggested that values may be higher than that of Cr_2O_3, thus leading to lower hoop stress. Although there are two known scale spalling mechanisms (wedging and buckling [23, 94] as discussed under different terms in Section 1.4), large defects (relative to the scale thickness) were not anticipated by Steiner [194], or indeed in Tata's conveyance tubes, so wedging is the anticipated failure mechanism. Biaxial stress can also arise from thermal gradients established within each individual material. Steiner also derived analytical expressions for this phenomenon, although a lack of thermal conductivity data even for Cr_2O_3 meant data had to be taken from ZrO_2 instead. Finally, although internal and external pressure were recognised as stress-generating, this was less relevant for conveyance tubes which experience only ambient pressure during manufacture. However, during service, some elevated internal pressures may arise which could be explored. Nevertheless, the scope of this project is constrained to the spalling during tube manufacture.

Manning analytically investigated the effect of curvature, specifically on tube surfaces, on scale adherence, highlighting that scale failure not only causes spalling, but also initiates transition between kinetic regimes (parabolic, linear, logarithmic etc [28, 70-72]) [106]. Curved geometry effects can contribute to both resulting strain applied on the oxide layer due to curved surface oxidation and changes to scale resistance to external strain application. In contrast to uniform oxidation on a flat surface where the scale is normally unrestrained and able to accommodate volume expansion, curved geometry is often responsible for stresses in addition to those generated by epitaxial restraint (although the latter was too complex and specific to consider in Manning's work).

To calculate oxide strain on a curved surface, Manning assessed the rate of displacement of the formed scale bulk from an arbitrary reference point in the substrate. This assumed that scale integrity and substrate contact can only be maintained via displacement of the scale relative to the metal. On a flat surface, since this displacement is unimpeded, no stress is generated. However, on both macro- and microscopic scales, curvature of the oxidising surface can inhibit volume changes therefore elasticity and creep are necessary to maintain scale adherence and integrity once stress generation reaches a maximum value, i.e. total strain energy increases as the curved surface oxide thickens to the limit of the scales integrity. As shown in Equation 1.11 and Equation 1.12, a scale displacement vector, $\boldsymbol{M}$, describe scale displacement rate and determine a limiting strain criterion can be used to predict curved surface scale oxide scale integrity limits. Ultimately, hoop strain is applied to the oxide scale via a radial stress acting across the interface. The analysis of particular interest by Manning was work on oxidation of iron wire at 550°C. This was particularly relevant considering the observed growth of a multi-layer (duplex) scale which is more reflective of the triplex scale anticipated for the grade and manufacturing conditions of conveyance tubes. However, Manning only aimed to identify curvature limits before mechanical failure for a single layered scale's ability to follow metal retreat during oxidation. This analysis was performed using a dimensionless stored energy function, $\boldsymbol{S}$, for which scale integrity loss accompanies at values greater than unity. Manning hypothesises that, alongside the potential for metal-oxide interfacial fracture at $\boldsymbol{S}$ values greater than unity, an alternative outcome could be changes in oxidation mechanism. Duplex layer growth, with a strain displacement vector of approximately 0, would lead to a reduction in stored strain energy, i.e. promoting adhesion, whereas vacancy dispersion, which causes $\boldsymbol{M}$ and $\boldsymbol{V}$ to tend to 0 and 1 respectively, could allow the scale structure to be stabilised without fracture.

Manning also assessed the effect of curvature on scale adhesion (strain limit) criteria which they considered to have previously been neglected. Stress analysis of flat, concave, and convex geometries via the Mohr's circle method allowed for visualisation of the effect of curvature on maximum shear stress compared to planar values. Results showed that a convex surface would increase maximum shear stress (to a value within the failure envelope) whilst a concave surface led to a decrease in maximum shear stress. Thus, it was concluded that, compared to planar geometries, concave and convex surfaces should have increased and reduced resistance to interfacial fracture respectively, with fracture occurring

at an angle to the interface. However, these conclusions only apply when thetube radius, $\boldsymbol{R}$, is not significantly larger than the oxide thickness, $\boldsymbol{\delta_{ox}}$, otherwise planar geometry failure criteria can be used. Based on existing studies of equivalent conveyance tube steel grades, it is anticipated that scale thickness should be deemed negligible compared to the tube inner radius (although clearly its effect on manufacturing even at low thicknesses is non-negligible) and therefore if only geometry and scale for the static tube are considered, flat plate geometry techniques can be used. However, the effect of the stretch reduction external mechanical stress must also be considered, and how this differs between a planar and curved geometry. Furthermore, it was argued by Manning that radial tensile stress due to interfacial curvature could encourage radial stress-enhancing vacancy condensation and progressive loss of scale adhesion. However, again this effect was deemed small when $\boldsymbol{\delta} \ll \boldsymbol{R}$. Finally, Manning commented on the influence of the strain displacement factor. For $\boldsymbol{M} = 0$ (or a high oxide growth rate), it was concluded that stress relief would have to come from periodic lamination or spalling. Furthermore, oxidation-induced deformation, such as oxide jacking associated with breakaway corrosion processes at $\boldsymbol{M} > 0$, was concluded to be influence by $\boldsymbol{M}$. Ultimately, $\boldsymbol{M}$ is of significance in instances where mechanical effects affect or arise from oxidation.

Oh's work [197] sought to build on the likes of Manning [106], Steiner [117], and Entchev et al. [85]. However, a key aspect of their work was their desire to eliminate assumptions of instantaneous reaction at the metal-oxide interface, and the absence of oxygen dissolution into the metal substrate [197]. Instead, they based their perturbation analysis on four assumptions: frame of reference results in stationary metal, first order oxidation at SSI with respect to oxygen, no spatiotemporal dependence of oxide molar density, and an initially oxygen free metal. They also highlighted that the initial oxide velocity cannot be zero if there is a significant density difference between the metal and oxide.

Given that both the boundaries (metal-scale and scale-gas) move during oxidation, and the physical tube region boundary is inherently non-rectangular, requiring a variable grid approach [198], Oh [197] applied a Landau coordinate domain transformation to transfer the moving boundaries on to fixed domains (the 'boundary immobilisation method'). A Variable Grid Method (VGM) allows the broad-spectrum uncertainty, associated with data collection approach, multiple dataset aggregation, and accumulation of data products during analysis to name a few, to be accommodated within the communication of spatial patterns, i.e. geometry, via variable grid cell size [199]. Lagoudas and Ding discussed domain

transformations in greater detail in their work [200], where in particular they commented that previous attempts to solve boundary value problems only considered transformations for boundary position as a spatial function. This was addressed by Oh [197] who applied a second Landau transformation to account for spatiotemporal boundary position variation. Oh's results evolved a valid dependence of their rate of reaction dimensionless parameter, $\boldsymbol{k}^*$, on oxidation thickness, with rate of reaction-controlled oxidation ($\boldsymbol{k}^* = \mathbf{1}$) having a linear, time-independent profile which transitions to a fully parabolic diffusion-controlled regime as $\boldsymbol{k}^*$ reaches very high values ($\boldsymbol{k}^* \to \infty$). Their data were in good agreement with the numerical and experimental results discussed previously in this chapter, but crucially Oh argues that, unlike these authors, they have considered reaction rate, volume expansion, and oxygen dissolution. Manning [106] remarks on a limitation of their own approach, namely that they had assumed entirely brittle oxide fracture and that this was not justified when considering fatigue effects. However, they stated that they hoped that their work would contribute to more complex studies on the effect of surface geometry and mechanical deformation on high temperature oxidation phenomena.

1.6.3 Study of Oxidation via Computational Techniques

Ultimately, oxidation is already a complex phenomenon dependent on several parameters but is complexified further when a multi-stage manufacturing process such as conveyance tube production is introduced and more so with the introduction of a value-added coating. Hence, a comprehensive and accurate understanding of tube oxidation could be derived from a computational model. Numerically derived models, and the importance of understanding parametric effects via predictive modelling to improve manufacturing design and control, are not constrained to simplified cases by the solvability of their defining equation as for analytical equivalents. However, Cleeman et al. reflect that spatiotemporal discretised physics-based computational models have limited ability to make real-time predictions, i.e. operate on trends rather than instantaneous predictions, and machine learning would need to be employed to achieve real-time predictions [201].

It has now been established that it is important for manufacturing efficiency's sake that the mechanism and extent of high-temperature oxidation of low carbon steel is characterised as a function of alloy composition, temperature, time, growth kinetics, geometry and service environment, i.e. a multivariate parametric interaction problem. Pillai et al. [29] agreed this was the case in their review of models for oxidation-based high-temperature degradation. However, in a system where several parameters influence system behaviour, an

experimental approach to characterisation can quickly escalate to demand significant resources [202]. As previously discussed, computational process modelling, when optimally designed, can identify routes to minimise costs, improve product quality, and increase output, based on an accurate and fast assessment of scale spalling. There are several manufacturing benefits including faster and cheaper product and process innovations, reduced downtime and maintenance, reduced material usage, and, overall, more robust processes. The generation and processing of increasingly large data sets, arising from modelling and continuous monitoring, to improve manufacturing efficiency is a significant element of Industry 4.0 [203]. Original Equipment Manufacturers (OEMs), such as Boeing, have made strides into how the traditional V-cycle model for system design can be enhanced by incorporating Model-Based Engineering (MBE) to create a 'Diamond Model' [204]. Computational models can also reveal details about material compatibility and degradation, which is of particular relevance when considering the interaction of proposed anti-scale coating designs with the steel and scale. The validity and completeness of any such models will depend on knowledge of the material properties and behaviour of the steel, scale, and coatings. Steel has been extensively characterised as a ubiquitous engineering material [10], however, as previously discussed, the material properties of the scale phases are certainly contentiously variable, whilst the inherent novelty of oxidation-resistant coating designs from Grant's work for conveyance tube grades demand individual characterisation [9]. Where there is a particular interest from this project in the adhesion behaviour of scale, the development of coating-related intermetallic or composite materials at the SSI, or elsewhere, due to high temperatures, is an important area for investigation. Introduction of the organic-based coatings complexifies the system (see Section 1.5.1). For example, in a 12-component system 66 binary systems could arise even before considering ternary or quaternary possibilities [205], which could be experimentally characterised using advanced imaging, but computational materials engineering software could provide a faster and more accurate insight.

Discussion of tube geometry oxidation studies in Section 1.6.1.3 highlighted that typical oxide thickness predictions come from input of temperature-time profiles based on analytical or computational predictions of thermofluid phenomena. However, this method still requires considerable involvement via definition of any equations and models, and translation of their results into a suitable rate constant parameter functions such as in Sun et al.'s work [176]. In light of the challenges of alloy design as a similarly multi-physics (phase

equilibria, diffusion kinetics, and defects) process affected by changes to chemical composition and processing conditions across different length scales, Kwon et al. present a materials design loop for high temperature alloys [206]. They argue that physics-based models can only offer insight into length and time scale-specific rather than suggest commercially viable new alloy chemistries or processing conditions. However, the alternative approach of training surrogate machine learning models with chemical composition, processing, and testing data for a similar existing alloy, does not have the scientific foundation in physics and chemistry to prevent false results, i.e. they are a 'black box'. The data-driven approach, which computationally incorporates scientific features using computational approaches, is successful in preventing false results.

CALPHAD (Calculation of Phase Diagrams), i.e. computational coupling of phase diagrams and thermochemistry, is one such approach and can be used to investigate the thermodynamics and material properties of an oxidising system via phase equilibria outputs [207]. As a minimum, it must be possible to describe the enthalpy, entropy, and Gibbs' free energy of a solution (generally described using the sub-lattice modelling-based Compound Energy Formalism (CEF) for solid oxide systems [208, 209]) as a function of temperature and composition in order to perform accurate and versatile thermodynamic calculation [210]. Consequently, as with any computational model, descriptive accuracy, i.e. complexity, must be balanced with mathematical feasibility based on the Central Processing Unit (CPU) resources available so that model solve time is not excessive. However, ever-increasing computational power availability is accompanied by options for increasingly complex feasible models [29]. Poerschke [211] presented a top-level modelling pipeline, which lends itself to adaption for the key areas of this project, comprising the initial oxide and service environment, coating architecture, oxide accumulation, oxide-coating interaction, and coating performance. Ultimately, as discussed by Poerschke, there is likely to be a reaction between any solid oxide system and an introduced coating, and it is pertinent to ask questions such as: What would make the two systems more likely to react, e.g. temperature, time composition? If there is a reaction, what would be the products? Compared to the scale and/or coating separately, how much more or less likely are the products to spall or adhere? Poerschke argues that understanding and prediction of spalling-based surface degradation relies on the answers to these questions, i.e. understanding of the "interplay" between substrate, scale, and coating, and the answers rely on the thermodynamic information provided by computational materials engineering modelling when systems become complex.

Finally, one aspect which appears to be absent from the literature, is the consideration of how, if at all, any improvement in scale control translates to a quantifiable improvement in tube performance in terms of its lifetime and hence marketability, which is paramount in a commercial industrial context such as at TSUK Tubes. Pillai et al. [29] appear to be the only authors to devote attention to the consideration of lifetime, although their study is concerned with chromium- and aluminium-based oxides. They present metal loss, spalling rate, and coating compatibility and degradation as suitable lifetime assessment parameters. They argue that an assessment of scale kinetics, morphology, and coating interaction are all relevant in evaluating these parameters and argue that computational techniques are suitable to achieve this. Within this project, if both experimental and computational techniques can be used to characterise such parameters within the interest of understanding adhesion and coating behaviour, there will be a potential additional benefit of the ability to quantify tube lifetime improvement achieved by the coatings, and this has not been considered for Fe systems. Pillai et al. do highlight the limitations of computational thermodynamic databases, namely difficulties in defining realistic boundary conditions (BCs), accounting for interfacial behaviour, e.g. displacement, and the lack of multi-component data, e.g. diffusion data is only available for major matrix phases (FCC, BCC etc). However, as the Fe-C system in the low carbon region is occupied by major matrix phases with only a small number of major elements (more than 6 can be challenging), and the relevant databases for modelling Fe oxides are regularly maintained and updated, a computational approach should still provide valuable information. However, it should be noted that computational methods based on scientific features have a limited search space and are therefore restricted to application in lower order systems and Kwon et al. argue that only data-driven, physics-coupled methods can expand the search space whilst adequately capturing underlying physics and chemistry [206]. They derive synthetic microstructural features (stable phase volume fraction and individual alloy element solubility in this case), using CALPHAD to assess the degree of supersaturation of key phases, and used the results to augment a raw experimental dataset for 17 elements. The machine learning (ML) model was then trained based on this set and correlation analysis was used to identify the most impactful features (on creep resistance of alumina-forming austenitic (AFA) stainless steels). As with all computational techniques, the study's ability to rapidly explore a higher dimensional space is limited by the number of computational thermodynamic calculations that can feasibly be performed. For example, decreasing the domain grid space (individual

alloy element contribution) by a factor of 10wt% leads to a 10^6 increase in the number of hypothetical AFA alloys. Crucially, their correlation analysis revealed the relationships between different phase volume fractions and creep resistance, in agreement with experimental results and prior knowledge albeit a few discrepancies attributed to the neglected effect of precipitation kinetics of the secondary phase and the influence of niobium content on prevention and promotion of grain boundary sliding. They also concluded that their approach is adaptable to different material property optimisations for multi-component alloys.

Software Options

CALPHAD-based software options available at Swansea University include Thermo-Calc©, FactSage™, and JMatPro®, which were reviewed with a view to their use in oxide stability modelling. A key aspect of this investigation was an awareness that the steel-scale phase interface (initially the steel-gas interface before any scale is formed), and its diffusive phenomena, holds the critical role in kinetic oxidation behaviour as this is where external oxidation reactions occur.

Thermo-Calc©

Thermo-Calc© has an extensive material thermodynamic database. This is important for all stages of the oxide phase stability and kinetic modelling approach (discussed in Section 1.7) but particularly the generation of an equilibrium phase diagram to determine the molar fraction contribution of different steel and scale phases under different thermal cycles. However, not all oxide phase mobility data are available within Thermo-Calc© and therefore simulations which demand this, such as in this project, require the user to work with the more time-consuming console mode to introduce user-defined thermodynamic and mobility databases. However, valuable technical support is available via the maintenance license and using a command line-based approach makes the methodology more repeatable, where more user control is available.

FactSage™

FactSage™ ultimately had the least scope for oxide kinetic modelling as the existing FToxid database does not contain any mobility data at all. Also, there is no option for manual use-defined database input.

JMatPro®

JMatPro® is specifically designed for multi-component alloys used in industrial settings and deployed to assess their material and mechanical properties as a function of a defined heat treatment. This may be a useful function for later work within the project looking at scale adhesion behaviour (see Section 1.4). General Steel is one of the core databases available within the existing Swansea University license. However, in terms of direct diffusion analysis, there was only a Graphical User Interface (GUI) option confined to discrete analysis modules, so the lack of phase data, e.g. when attempting a simple heat treatment calculation in the designated module, the simulation failed due to the relevant phases not being detected.

1.6.4 Study of Oxidation via Experimental Techniques

Experimental validation of curved surface oxidation is challenging, particularly due to limitations of equipment used in in-situ oxidation investigations. Thermogravimetric (TGA) furnaces, which provide continuous mass gain data, are often limited in their sample size capacity so only very small tubes can be used, or tubes have to be sectioned which causes machining-induced residual stress [17, 18]. Furthermore, there are issues with TGA measurements as they give the total oxidation on a sample and neglect the effect of the gas flow on the extent of oxidation in each part of the sample geometry, as shown in the work by Mori et al. [212]. Therefore, any experimental value derived from TGA curves is an average over the entire geometry which does not address the differences between the surface on which the flow is incident and the surface facing away from the flow. This is a strength of modelling in its ability to distinguish between the two and the reason for focusing on the modelling studies and then subsequently correlated these with the total oxidation thickness measured after heat exposure (the latter being subject to errors due to spalling of poorly adherent oxides). Furnaces with a larger sample size capacity do not usually have TGA equipment so rely on pre- and post-heat treatment high resolution mass balance measurements of the sample. High temperature oxides are known to be brittle as seen in observation by the authors and as reported by the literature [5, 19-21]. This brittle nature makes scale spalling inevitable so that material is lost between transferring the sample from the furnace to a mass balance, in addition to losses during sample cooling before it is removed from the furnace due to thermal mismatch between the metal and oxide.

More generally, Krzyzanowski et al. commented that data collected in controlled laboratory experiments are often "…far removed…" from high-temperature industrial processing conditions, making it difficult to define basic oxide scale properties [14]. Realistic laboratory testing can encounter problems with measurement access and many tests are often required to construct a full description of industrial operations comprising each element of system behaviour. However, all computational modelling relies on idealised assumptions to obtain a sufficiently accurate output within economic and time constraints and will inevitably require experimental validation to confirm the credibility of its predictions both for and beyond the original context and response [213]. Furthermore, Kryzazanowski et al. argue that optimal quantitative characterisation of oxide scale behaviour depends on a combined methodology of experiments, e.g. microscopy for surface layer structure, and physically-based modelling, to offer the most detailed insight into and better predictions of manufacturing events [75].

Advanced imaging techniques can characterise scale morphology, composition, and kinetics using scanning electron microscopy (SEM), X-ray diffraction (XRD), and thermogravimetry (TGA). Sun et al.'s [71] XRD study of low carbon steel oxide scale, alongside the unsurprising observation of thicker scales with higher temperatures and longer soak times, revealed more nuanced details about individual phase components. For example, although the overall trend is a positive correlation between scale thickness, soak temperature, and soak time, the magnetite phase thinned with increased soak temperature and time. Similarly, Iordanova et al.'s study [72] demonstrated how extreme thinness of the haematite layer rendered it only detectable by a grazing incidence method. Furthermore, XRD data has provided evidence that the phases are not always confined to their own distinct layer and may evolve within other layers due to temperature-induced phase transitions [5, 123]. XRD analysis could validate conclusions drawn from CALPHAD-based computational oxidation analysis of scale phase composition and coating interactions under the different manufacturing conditions described. Morphological characterisation can be performed by an SEM-EDS analysis [60]. However, Singh Raman et al. [214] reasoned that SEM and XRD are ultimately restricted to thick scales (>10μm), whilst alternatives X-ray photoelectron and Auger spectroscopy are restricted to very thin scales of less than 1μm. However, they agree that phase composition analyses are essential for any thickness if the oxidation reaction mechanism, material lifetime, and dry corrosion degree are to be fully understood, especially with respect to manufacturing parameter variation. Hence, they present Laser

Raman spectroscopy, a structural characterisation technique based on bond strength and arrangement theory, to characterise oxide scale [215]. In agreement with authors using only XRD [5, 123], amongst other techniques [134], Singh Raman et al.'s results also detected magnetite within the wüstite layer due to cooling-induced proeutectoid decomposition, thermal expansion coefficient discrepancy, and the higher oxygen content in the environment during the ambient cooling of normalisation. Singh Raman et al. also argued that chemical characterisation was also necessary to evaluate surface quality, demonstrating how, for higher temperatures (T>570°C), scale is dominated by wüstite but can easily shift to less descalable forms, particularly haematite for slower cooling at lower temperatures. In particular, transformation of the wüstite into iron and magnetite eutectoid allows for very slow cooling rates [169]. For all cases, evidence of fragmentation was shown to correlate to poorer descalability. This has consequences for surface quality and restates the dilemma of whether the tube manufacturing process should aim for either a highly adhered scale which demands high surface quality or a highly descalable scale which could prematurely spallate during processing. It should be noted that, despite Raman spectroscopy's capability across a wide range of scale thicknesses, Zambrano et al. [22] highlighted how the near-identical Raman spectra of wüstite and magnetite can make them difficult to distinguish given that phases are rarely perfectly confined to distinct layers and often precipitate into each other (as was previously discussed for the eutectoid decomposition of magnetite in Section 1.3.1). They showed how XRD, alongside mechanical tests for micro-hardness and elastic moduli, could confirm phase identities. Ultimately, this highlights how experimental validation often depends on a combination of techniques, allowing for the constraints of the specific scenario under investigation.

Electron backscatter diffraction (EBSD) is another crystallographic characterisation technique which has been described as more powerful than traditional X-ray-based techniques in its ability to fully microstructurally and microtexturally characterise individual phases [134]. Birosca et al. [134] highlighted Higginson et al.'s work [133] which proposed a "…complex crystallographic texture relationship…" between the phase layers, substrate, and scale, which is important for characterising mechanical descaling. Higginson et al. demonstrated that this relationship was dependent on oxidation temperature and steel grade (specifically Ni and Si alloy content). EBSD is also a powerful technique for investigation of scale crystallographic orientation in response to cracking under different processing conditions. Wang et al. investigated grain boundary profiles and plastic strain-

induced local strain in low-alloy, high-strength steel samples via relative orientation differences of adjacent grains and local misorientation between adjacent pixels in a single grain respectively [216]. Hence, they were able to demonstrate increased fineness of magnetite grains in the joint seam layer which were therefore expected to store less strain energy, experience less plastic deformation [42], and evolve surface defects at a slower rate. This was supported by evidence of up to 50% lower local misorientation in the magnetite than other phases. There was also support for the influence of steel-scale mechanical property differences on the development of thermal and oxidation stresses which comprise scale integrity and affects its kinetics and morphology as crack propagation provides an undesirable route for stress relief via consumption of plastic work. Wang et al. also commented on the link between a 13% reduction in wüstite contribution to the scale, development of a magnetite 'joint seam layer' at the SSI, SSI gapping, and intergranular cracking [216] (see Figure 1.31). The joint seam layer was attributed to the cooling period where full austenitic decomposition temperature ($\boldsymbol{T}$=570°C) is approached and additional oxygen diffuses to the SSI via the defects formed due to thermally and oxidation-induced internal stresses (see Section 1.4). As cooling proceeds, internal stress is relieved by further defect propagation which promotes joint seam layer growth. The effect of individual phases will be important in considering not only scale adhesion behaviour in response to different manufacturing parameters but also the effect of their interaction with the novel oxidation-resistant coating solutions.

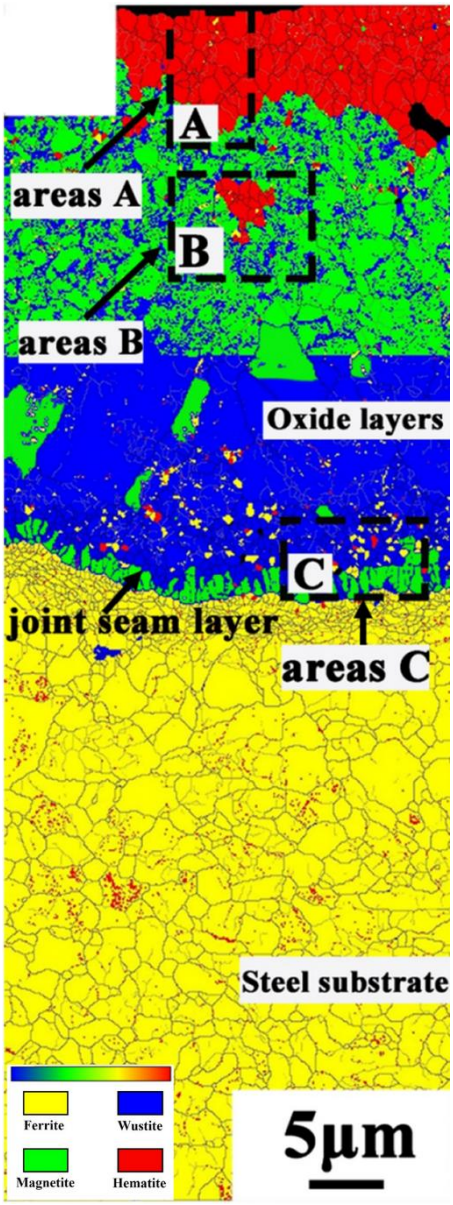


Figure 1.31: Electron Back Scatter Diffraction (EBSD) phase diagram of the surface (A), intermediate (B), and interface (C) layers of oxide scale formed on low-alloy, high-strength steel [216].

During thermomechanical processing techniques, such as the stretch reduction performed during conveyance tube manufacturing, the combined effect of strain heterogeneity and scale nucleation and growth on grain structure (both size and orientation) further promotes via the development of greater grain orientation variation at the SSI, and therefore local plasticity. The introduction of the properties of oxidation-resistant coatings could cause further variation, which must be characterised. However, again this study fails to consider the scale adhesion behaviour in response to the microstructurally and mechanically derived stresses associated with the specific thermomechanical processing (TMP) concerned. A computational approach could be beneficial in obtaining comparative information about how scale adhesion behaviour is altered by the introduction of the coating interface.

In addition to stress-strain characterisation using analytical theory, indentation systems can be used to experimental obtain stress-strain curves for systems where hardness is also of interest. Indentation techniques rely on the true stress-strain relationship (von Mises (equivalent plastic) stress as a function of equivalent plastic strain [217]). Unlike the Instrumented Indentation Technique (IIT) which relates load-displacement directly to stress-strain data, thus ignoring the complexities of the variable stress and strain fields during indentation, Profilometry-based Inverse FEM Indentation Plastometry (PIP) avoids load-displacement measurements. PIP employs iterative FEA simulation and the constitutive plasticity law [218], varying its parameters to the point of optimal agreement between the measured and modelled indentation result. PIP offers several advantages over nanoindentation and IIT, including no requirement for measurements during loading, no uncertainties associated with machine compliance, potential for in-plane anisotropy detection, and improved empirical sensitivity to the stress-strain profile [219]. Moreover, the reliability deficit in yield and ultimate tensile strength values associated with conventional hardness testing can only be mitigated if the focus is limited to only the ultimate tensile strength and a certain alloy, e.g. ferritic steel and/or thermo-mechanical treatment(although this is possible in the context of tube analysis where only two, very similar, low carbon steel grades are used in the single manufacturing process with the exception of induction and gas barrel heating for smaller and larger bore tubes respectively – see Section 1.2). Unfortunately, since the UTS is a nominal stress only with meaning in a uniaxial tensile testing context, no reliable information about yield onset or the true stress-strain curve can be obtained. Yield and true stress-strain data are however integral to inelastic component response prediction. Overall, PIP has the potential to fully capture the variable stress and strain fields during testing, directly from local regions [217]. Warwick et al. [220] conducted a study of how prior plastic deformation, as is found in Tata's tubes during normalisation and oxidation owing to the previous cold forming step described in Section 1.2, affects the stress-strain profile exhibited by metallic components. For example, higher plastic strain is found in the tubes' near-surface layers (due to mechanics theory described in the previous section) which promotes strain hardening to an extent which must be accounted for. It was anticipated that the effect of prior plastic deformation on subsequent component mechanical response is highly complex, owing to local changes in dislocation density, crystallographic texture, grain boundary structure, and precipitate and solute atom distribution. Warwick et al.'s study investigated flattened plain carbon steel

pipes in the range 5-9mm and 260-270mm of wall thickness and inner diameter respectively (a potential oil and gas pipeline application lying within the upper end of Install® 235 geometry and yield stress [2]) with their transverse place curvature having been reduced to zero. Springback was neglected during this study [82]. It should be noted that the wall thickness to diameter ratio is equivalent to the peak plastic hoop strain during flattening. P3' had the most similarity to the tubes under investigation in this project, with its high wall thickness to diameter ratio of (2.9% compared to a maximum of 3.5% observed in Install® 235 range [2]) and strain bursting phenomenon observed in low carbon, low alloy compositions owing to dislocation escape from carbon atmospheres and Luders band formation). P3 showed good consistency with its tensile plots, as did the other three pipe samples, generated a value of 300MPa and 500MPa for yield and tensile strengths respectively, thus showing PIP to be a reliable approach for stress-strain curve derivation. However, PIP is not suitable for the thin oxides observed on conveyance tubes owing to their suitability for microscale depth profiling of pure metals. Nanoindentation offers insightful data sets which can apply mN scale forces to nm range penetration depths. However, reliability of nanoindentation data in the context of stress-strain curve derivation is poor due to the size effects associated with very small indentation areas wherein an insufficient size of grain assembly is deformed in order to be representative of the bulk material deformation [219], i.e. nanoindentation does not allow for 'scale-independent' stress-strain profiles. To achieve scale-independent profiles, the indenter radius must be in the range 0.5-1mm and the load applied in the kN range [220]. Furthermore, since analytical theory has already shown that Tata's tubes are subject to work hardening [221], inferring the yield and/or ultimate tensile strength from a hardness value neglects the local and temporal variations in plastic strain during hardness testing [217]. For example, sites close to the indenter have already experienced large plastic strains at the point of yield onset at the edge of the plastic zone [217].

1.7 Theoretical Foundations for the Computational Study of Oxidation

1.7.1 Diffusion Theory

As discussed in Section 1.3.1, oxidation is a diffusion-controlled phenomenon – the process of migration of ions (in this case) from regions of high to low concentration [222]. It is therefore governed by the diffusion equation (see Equation 1.29) [200, 223]. The investigation of a cylindrical geometry transitions the diffusion equation from Cartesian

(x, y, z) to cylindrical coordinates (r, ϕ, z). Equation 1.30 gives the diffusion equation in cylindrical coordinates, as is appropriate for conveyance tube geometry, where c_k is the species, k, concentration as a function of time, t, and radial, r, azimuthal, ϕ, and axial position, z. The diffusion equation can be reduced to a function of only one cylindrical spatial coordinate, r, by considering 1D diffusion [200, 223].

$$\frac{\partial c_k}{\partial t} = D\frac{\partial^2 c_k}{\partial x^2}$$

Equation 1.29

$$\frac{\partial c_k}{\partial t} = \frac{1}{r}\frac{\partial}{\partial r}\left(r\frac{\partial c_k}{\partial r}\right) + \frac{1}{r^2}\frac{\partial^2 c_k}{\partial \theta^2} + \frac{\partial^2 c_k}{\partial z^2}$$

Equation 1.30

$$\frac{\partial c_k}{\partial t} = \frac{D}{r}\frac{\partial}{\partial r}\left(r\frac{\partial c_k}{\partial r}\right)$$

Equation 1.31

Diffusion can be quantified via diffusivity – the temperature-, composition gradient-, and pressure-dependent rate at which a particle migrates through a material. Thus, diffusivity, D_k, defines the speed at which transport equilibrium is reached. Solid-state diffusion is a multi-mechanism phenomenon. Lattice diffusion ('bulk' or 'volume') occurs when atoms or point defects, e.g. vacancies, interstitials, jump individually within the crystal. Lattice diffusion is much slower than line, planar, and surface diffusion mechanisms which arise from jumps along the surface, line defects, grain boundaries or dislocations. The latter are therefore termed 'high-diffusivity pathways'. Temperature and microstructure determine whether bulk or high-diffusivity pathway mechanisms dominate diffusion. When considering the vacancy mechanism driven process of scale-forming oxidation, it is highlighted that the sequence of jumps which comprise a vacancy's path through an atomic structure is not purely random and in fact influenced by the availability of vacancies to adjacent atoms, i.e. an atom with only one adjacent vacancy available is more likely to jump into that vacancy than any of the vacancy's surrounding atoms. This phenomenon decreases the diffusion coefficient and this decrease can by quantified via a labyrinth factor, $f_{labyrinth}$ (see Equation 1.32) [224].

$$D^* = fD_{random\ walk}$$

Equation 1.32

Without a driving force, the energy barrier to diffusion (specifically that required to allow an atom to jump to an empty lattice site) is defined by the free energy of migration, $\boldsymbol{G_m}$. Tagged atoms ('tracers'), such as dilute radioactive isotopes, can be introduced into a homogeneous material to monitor the rate diffusion via the mean square displacement of the tracer over time, derived from the Einstein formula for Brownian motion (see Equation 1.33 and Equation 1.34). The concentration gradient being the only diffusion driving force is a simplifying assumption however the true complexities of this are discussed later in Section 1.7. Equation 1.33 shows how the tracer diffusivity, $\boldsymbol{D_k}^*$, itself is defined by atomic mobility, $\boldsymbol{M_k}$ [222]. Unlike diffusivity, which is the constant of proportionality relating a species, $\boldsymbol{k}$, diffusion-induced molar flux and concentration gradient, mobility, although related to diffusivity via the universal gas constant, $\boldsymbol{R}$, and temperature, $\boldsymbol{T}$, (see Equation 1.34), is a charged particle property which expresses its ability to move through a medium under the action of an electric field [223].

$$\langle \boldsymbol{x_k}^2 \rangle = \boldsymbol{2D_k}^* \boldsymbol{t}$$

Equation 1.33

$$\boldsymbol{D_k}^* = \boldsymbol{RTM_k}$$

Equation 1.34

Both mobility (see Equation 1.35 and Equation 1.36) and diffusivity (see Equation 1.37) are functions of activation energy, $\boldsymbol{Q_k}$, universal gas constant, and temperature, and include a pre-exponential factor $\boldsymbol{M_{k,0}}$ and $\boldsymbol{D_{k,0}}$ respectively.

$$\boldsymbol{\Phi_k = -Q_k + RTln\ M_k^0}$$

Equation 1.35

$$\boldsymbol{M_k = \frac{1}{RT} e^{\left(\frac{\Phi_k}{RT}\right)}}$$

Equation 1.36

$$\boldsymbol{D_k = D_{k,0} e^{\left(-\frac{Q_k}{RT}\right)}}$$

Equation 1.37

Diffusion in interstitial alloys with small migrating interstitials, e.g. oxygen in iron, in dynamic equilibrium with each other is usually controlled by a continual vacancy migration mechanism since much less energy is required to produce a vacancy than interstitial [162]. Vacancy diffusion depends on the probability that a site is vacant as well as the probability that the atom migrating to the vacant site has sufficient energy to meet its activation value.

Diffusion is most heavily influenced by temperature, due to its effect on material components' ability to meet their activation energy threshold, and composition, hence why the most reliable diffusion investigations concern self-diffusion in pure metals [162]. Microstructural defects have also been shown to affect diffusion, with isolated point defects and vacancies restricting diffusion [225] except in the case of agglomerated defects and grain boundaries which can accelerate diffusion by providing lower resistance pathways for ionic movement [226]. However, the extent of this effect is restricted by the fact that grain boundary diffusion is far more significant than bulk diffusion, due to a lower activation energy [209, 227]. For example, quenched materials contain an excess vacancy concentration which promotes diffusion when vacancies combine [228].

The concentration of vacancies in a pure metal under constant pressure is temperature-dependent [228]. As previously discussed, vacancies, and their formation as an atom moves from the crystal surface to an empty interstitial host lattice site, are significant in diffusion phenomena. Accordingly, the excess entropy of vacancy formation is zero at 0K, and Gibbs energy of vacancy formation is described as a combination of vacancy formation enthalpy and vacancy formation heat capacity [229]. Within the context of CEF, a vacancy-containing crystal is treated as a solid solution between two 'end members' (the defect-free metal, $\boldsymbol{M}$, and its vacancy-only equivalent crystal). Hence, the Gibbs Energy function for a mixture is a combination of the Gibbs energy and equilibrium concentrations of the two end members, i.e. $\underline{\boldsymbol{G}}_{\boldsymbol{Va}}$, $\underline{\boldsymbol{G}}_{\boldsymbol{M}}$, $\boldsymbol{y}_{\boldsymbol{Va}}$, $\boldsymbol{y}_{\boldsymbol{M}}$ [230]. An interaction parameter, quantifying the metal-specific vacancy concentration, is also required to account for the fact that the vacancy compound energies are identical for a given crystal structure regardless of the host metal lattice. In metallic systems, the width of the charge accumulation or depletion layer at the surface during oxidation is extremely short, less than an atomic diameter, due to high electron mobility, so the effects of the electric field induced by ion movement are negligible [231].However, electron mobility in transition metal oxides is not always greater than ionic mobility [232], and a lower carrier density, results in a wider layer which generates an electric field sufficient to impact ionic mobility and vacancy concentration [233]. However, if there is sufficient electron mobility to compensate for any charge migration, the electric field induced will be also be negligible in an oxide system.

Obaied et al. [229] presented a thermochemical CEF-model for thermal vacancy formation based on physically realistic postulates, e.g. removes assignment of non-zero Gibbs energy to a (hypothetical) vacancy-only crystal, i.e. a hypothetical phase with its lattice entirely filled

with vacancies has its own Gibbs energy [230]. The reasons for non-zero values of Gibbs energy are attributed to the need to assign it a value to a (hypothetical) pure vacancy solution endmember and previous mathematical demonstrations (on solid solutions) of the generation of an artificial local Gibbs energy minimum for vacancy concentrations approaching 100% due to a configurational entropy contribution if the pure vacancy endmember is assigned a Gibbs energy of zero. The artificial minimum can only be removed if this endmember is destabilised by a positive Gibbs energy. Alternatively, a maximum vacancy concentration of 40% can be applied whilst the endmember value remains at zero. In pure metals, vacancy formation is due to configurational entropy and there is a positive vacancy formation enthalpy associated with bond breakage. Vacancies have a significant impact on mechanical and thermophysical properties and are most often described using Gibbs energy of vacancy formation, $\boldsymbol{G_{Va}}$, (see Equation 1.38), which represents the increase in Gibbs energy of the crystal when one mole of vacancies is created (assuming ideal dilution), and is related to the equilibrium vacancy concentration, $\boldsymbol{c_{Va}}^{\boldsymbol{eqm}}$ (the latter usually being obtained from calorimetric measurements) via temperature, $\boldsymbol{T}$, and Boltzmann constant, $\boldsymbol{k_B}$.

$$c_{Va}^{eqm} = exp\left(\frac{-\underline{G}_{Va}(T)}{k_B T}\right)$$

Equation 1.38

However, experimental measurements of vacancy concentration are complex and demand multiple techniques. It should be noted that Equation 1.38, derived via Gibbs energy minimisation, can only be applied to a system comprising one metal and vacancies. It would not be appropriate for a solid solution of metals or compounds, or phases with vacancy concentrations of ~20% on both the metal and oxygen sublattice.

As with all equilibrium vacancy concentrations, $\boldsymbol{y}$, Gibbs Free Energy minimisation is used (again assuming an isobarothermal system with a constant number of metal atoms, $\boldsymbol{n_m}$) and the vacancy Gibbs Energy function partial derivative is equated to the vacancy chemical potential, $\boldsymbol{\mu_{Va}}$ (see Equation 1.39).

$$\mu_{Va} = \left(\frac{\partial G}{\partial n_{Va}}\right)_{T,P,n_M} = \underline{G}_{Va} + RT\ln y_{Va} = 0 \;\therefore y_{Va} = \exp\left(-\frac{\underline{G}_{Va}}{RT}\right)$$

Equation 1.39

Overall, the above analytical details show how the variables of a successful computational diffusion depend heavily on accurate expressions for the mobility of all involved species (whilst the species molar fraction to substitutional element (oxygen) contribution, $\boldsymbol{u_k}$, and chemical potential derivative, $\frac{\partial \mu_k}{\partial u_k}$, are derived from the literature). Mobility must be assessed not only for bulk diffusion of iron and oxygen (though the latter is negligible compared to the former due to the higher concentration of cation vacancies, all vacancy-driven diffusion mechanisms within the system must be considered), but also the presence of grain boundary diffusion. Hallstrom et al. [234] argued that grain boundary diffusion is relevant in scales which have potential protective properties, e.g. the passive protective chromium (III) oxide layer developed on stainless steel. Steel oxide scale has similar protective properties [64] and overall mobility must be calculated via effective mobility, $\boldsymbol{M^{eff}}$, derived from a bulk, $\boldsymbol{M_b}$, and grain boundary, $\boldsymbol{M_{gb}}$, assuming type A kinetics [235], values of mobility and mobility as a linear variable (see Equation 1.40). $\boldsymbol{V_{gb}}$ is an estimate of the volume fraction of grain boundaries using the approximate grain boundary width, $\boldsymbol{\delta}$, and oxide grain size, $\boldsymbol{\phi}$ [234].

$$\boldsymbol{M^{eff} = V_{gb} M_{gb} + (1 - V_{gb}) M_b}$$

$$\left(\boldsymbol{V_{gb} = \frac{\delta}{\phi}}\right)$$

Equation 1.40

Application of Equation 1.40 relies on an assumption of a planar diffusion front (long diffusion period and small grains) to ensure diffusion field overlap around neighbouring grain boundaries. This can be reasonably assumed in compounds such as wüstite where the grains are small compared to the oxide scale thickness and therefore the metal-oxide interface is planar [234]. The final key assumption is that of an Arrhenius-type expression for $\boldsymbol{M_{gb}}$ which has an equivalent pre-exponential factor to that of bulk diffusion (see Equation 1.41), i.e. $\boldsymbol{M_{b,0} = M_{gb,0} = M}$, though the activation is halved for diffusion in line with the 'half-surface' assumption used to predict grain boundary diffusion during metal oxidation [234].

$$\boldsymbol{M_k = Ze^{-\frac{Q}{RT}}}$$

Equation 1.41

However, overall mobility data can be supplied by relevant bulk and grain boundary mobility databases within the DICTRA model in Thermo-Calc©. It is noted that alongside temperature, mobility is also influenced by oxygen partial pressure when considering oxide phases (unlike diffusion due to the strength of atomic binding) and the dopant effect of certain alloy elements [236].

1.7.2 Wüstite Thermodynamic Model

Hidayat et al. performed a comprehensive study of the iron-oxygen (Fe-O) system, wherein models for all three iron oxide scale phases found on E24 and E41 grade steels can be found [237]. They remarked that "…highly defective crystal lattices…" such as wüstite, specifically the prevalence of vacancies generated by divalent and trivalent interstitial iron cations, are the source of both outward cation and inward anion diffusion [238]. Vacancies allow ions to 'jump' and thus move through the crystal lattice unimpeded, provided enough energy is supplied [239]. Modelling of this process demands an understanding of the concept of sublattices, which are either tetrahedral or octahedral in the Fe-O system, and a wüstite lattice is the same as for a halite (NaCl) crystal where two FCC lattices, one for the cations and one for the anions, overlap and move against each other by a distance of half a unit cell (0.5, 0.5, 0.5) [240]. In general, within this system, both tetrahedral and octahedral sublattices can be occupied by both Fe^{2+} and Fe^{3+} cations, either individually or in combination with each other. Vacancies (Va) exist dependent on the balance of cations with a 2+ or 3+ vacancy, since with Fe^{3+} cations less irons atoms are needed to balance the O^{2-} ions and vacancies appear. However, diffusion can only occur within, rather than across, sublattices and thus a sublattice must be occupied by both cations (either valency) and vacancies to enable diffusion.

For stoichiometric mineral phases, any cation ordering variation has a negligible effect on the phase's physical (thermal, physical, and magnetic) properties [241]. However, in non-stoichiometric phases such as wüstite ($Fe_{1-x}O$ ($0.04 < \boldsymbol{x} < 0.12$), where $\boldsymbol{x}$ denotes the concentration of cation vacancies [241, 242]), variation in long- and short-range defect ordering significantly affects physical properties [241]. Equation 1.42 shows how $2\boldsymbol{x}$ trivalent cations must substitute for the divalent cations to maintain charge balance in the non-stoichiometric structure. As cations can occupy either octahedral sites or tetrahedral interstices, the fraction of octahedral vacancies depends on both the Fe^{3+} bulk composition and distribution. Equation 1.42 therefore also reflects mixed valency cations and variable

cation occupation of $\boldsymbol{x}$ octahedral and $\boldsymbol{t}$ tetrahedral sublattice sites (VI = octahedral, IV= tetrahedral).

$$\boldsymbol{VI}\left[\boldsymbol{Fe^{2+}}_{\boldsymbol{1-3x}}\boldsymbol{Fe^{3+}}_{\boldsymbol{2x-t}}\boldsymbol{Va}_{\boldsymbol{x+t}}\right]\boldsymbol{IVFe^{3+}}_{\boldsymbol{t}}\boldsymbol{O^{2-}}$$

Equation 1.42

However, it is noted by Hazen and Jeanloz [241] that the assumed ideal oxygen occupancy could be an oversimplification of the structural role of oxygen although it is anticipated that the uncertainty generated by these effects is negligible. It is also noted that cation self-diffusion and electrical conductivity, which are important parameters for mobility database development, also depend on the quantity and arrangement of defect clusters in wüstite. Oxygen uptake in wüstite is affected by time, temperature, and oxygen partial pressure, making it more difficult to predict. However, temperature is the most influential parameter due to the variation of tetrahedral vs. octahedral coordinated vacancies in iron. A smaller volume is associated with a higher number of octahedral vacancies, i.e. deviation from idealised FeO. Also, as temperature increases for a given composition, more tetrahedral iron forms, and the molar volume is reduced. On a similar theme, determination of thermal expansion coefficient for wüstite can be complicated by the rapid effect of temperature and pressure on defect cluster arrangement and exsolution extent, i.e. it is difficult to measure compression and expansion for a specific wüstite structural state.

Overall, wüstite has complex physical properties due to its non-stoichiometry (a common feature of transition metal oxides [242]) variable site distribution of iron, clustering of defects, long- and short-range ordering, and exsolution [241]. The level of non-stoichiometry in iron oxides is controlled by the concentration of cation (metal) vacancies evolved during the diffusion-controlled oxidation process and heavily influenced by temperature and oxygen partial pressure. Although ideal (stoichiometric) FeO's thermal expansivity can be predicted from average expansion coefficients of similar halite structured stoichiometric compounds with an intermediate cation size, e.g. NiO, MgO, CoO etc [241], observed values in non-stoichiometric wüstite were significantly lower owing to the non-stoichiometry of Fe^{3+} ions and high temperature oxidation. Notably, Hazen and Jeanloz [241] remarked that wüstite thermal expansion is not significantly affected by stoichiometry. Furthermore, deviation of stoichiometry in wüstite only becomes significant at temperatures lower than 800°C, i.e. below conveyance tube normalisation temperatures [242]. Assuming a close-packed FCC sub-lattice structure as found in halite phases (see

Figure 1.32), the unit cell parameter, $\boldsymbol{a}$, is calculated as a function of the atomic radius, $\boldsymbol{r}$, with divalent oxide anions and divalent iron cations occupying their ideal sites in the halite crystal lattice of the wüstite phase (see Equation 1.43) [28].

$$\boldsymbol{a = 2\sqrt{2}\, r}$$

Equation 1.43

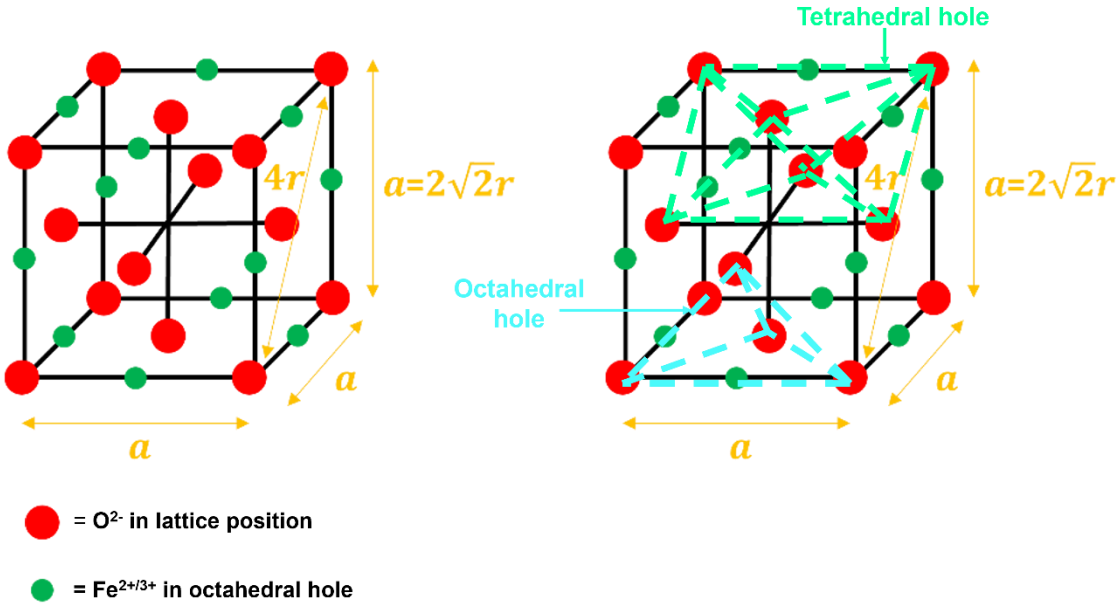


Figure 1.32: FCC wüstite crystal sub-lattice structure (*left*) annotated with octahedral and tetrahedral hole geometries (*right*) ¤.

Sub-lattice Response during High-Temperature Oxidation of Iron

Oxygen has a low solubility which can be enhanced by the presence of iron lattice vacancies which allow the oxygen concentration to reach a level equivalent to the vacancy concentration via strong oxygen-vacancy ($O - Va$) bonds [243]. Interstitial oxygen solute mobility is reduced by the presence of these strong $O - Va$ bonds. These phenomena are therefore absent in vacancy-free ferrite. Nevertheless, oxygen atoms occupy octahedral interstitial sites ideally and failing that will occupy tetrahedral interstitial sites and substitutional sites in that order of preference. In a vacancy-free ferrite lattice, octahedral oxygen atoms will migrate to other octahedral sites (passing through tetrahedral sites). However, where vacancies are present, an $O - Va$ pair can migrate together, although the energy barrier for $O - Va$ migration is approximately three times greater than that of single oxygen migration in a perfect lattice [243].

Hidayat et al. [237] argue that ultimately there is insufficient reliable quantitative data on sublattice site occupancy, defect composition, and defect clustering to develop a

comprehensive thermodynamic model of the halite-type wüstite structure (ideal stoichiometric or otherwise). Nevertheless, such a model is required to generate comprehensive analytical and computational models and they therefore accept the assumption made by Sundman et al. [244] that iron cations and vacancies can only mix on octahedral sublattice sites, i.e. iron cations present on tetrahedral sites are ignored. The resulting simplified sublattice formalism is given for wüstite below.

$$\left(\boldsymbol{Fe^{+2}}, \boldsymbol{Fe^{+3}}, \boldsymbol{Va}\right)_{\mathbf{1}}\left(\boldsymbol{O^{-2}}\right)_{\mathbf{1}}$$

Hallstrom et al. assert that diffusion of Fe can be modelled without consideration of its valency as crystal lattice electrons are significantly more mobile in wüstite than Fe cations at high temperatures (T > 600°C) [239]. The formula unit can therefore be simplified as below,

$$(\boldsymbol{Fe}, \boldsymbol{Va})_{\mathbf{1}}(\boldsymbol{O})_{\mathbf{1}}$$

which provides the necessary information to analytically define the system, specifically the flux, $\boldsymbol{J}$ (see Equation 1.44), and bulk chemical diffusion coefficient, $\boldsymbol{D}$ (see Equation 1.45), of both the iron and oxygen species via either species mobility, $\boldsymbol{M}$, or the tracer parameters (tracer diffusion coefficient, $\boldsymbol{D}^*$, and number of tracers, $\boldsymbol{n_k}$) which are intrinsically linked (see Equation 1.34), the former representing the thermally activated jump required for diffusion (dependent on the jump distance, species vibrational frequency, temperature, and activation energy barrier) and the latter existing due to diffusion without a species concentration gradient [239]. Mobility is the proportionality constant which relates diffusion to a concentration gradient, whilst mobility itself is dependent on a chemical potential gradient. Only a single term is required to define diffusion of both iron and oxygen ions in the wüstite system since only a single octahedral site type exists to allow for diffusion. Hence, Equation 1.44 and Equation 1.45 can be applied to either Fe or O, where $\boldsymbol{G}$ and $\boldsymbol{y}$ are the Gibbs energy and equilibrium concentrations of the two end members respectively, i.e. $\underline{\boldsymbol{G}}_{\boldsymbol{Va}}$, $\underline{\boldsymbol{G}}_{\boldsymbol{M}}$, $\boldsymbol{y}_{\boldsymbol{Va}}$, $\boldsymbol{y}_{\boldsymbol{M}}$.

$$\boldsymbol{J_k} = -\frac{\mathbf{1}}{\mathbf{2}}\left[\boldsymbol{y''_{Va}}\boldsymbol{y''_{k}}\boldsymbol{M''_{kVa}}\right]\frac{\mathbf{1}}{\boldsymbol{V_m}}\frac{\boldsymbol{\partial \mu_k}}{\boldsymbol{\partial z}} = -\frac{\boldsymbol{D_k}}{\boldsymbol{RT}}\frac{\boldsymbol{n_k}}{\boldsymbol{V_m}}\frac{\boldsymbol{\partial \mu_k}}{\boldsymbol{\partial n_k}}$$

Equation 1.44

$$\boldsymbol{D_k} = \frac{\mathbf{1}}{\mathbf{2}}\frac{\boldsymbol{RT}}{\boldsymbol{n_k}}\left[\boldsymbol{y''_{Va}}\boldsymbol{y''_{k}}\boldsymbol{M''_{FeVa}}\right] = \frac{\boldsymbol{D_{k^*}}}{\boldsymbol{RT}}\boldsymbol{n_{Fe}}\frac{\boldsymbol{\partial \mu_k}}{\boldsymbol{\partial n_k}}$$

Equation 1.45

Temperature Dependence of Wüstite Elastic Modulus

The non-stoichiometric nature of wüstite has been shown to have a significant effect on its elastic properties, although the bulk modulus has negligible sensitivity in the range $0.90 < 1 - \boldsymbol{x} < 0.98$ (stoichiometry being found at $\boldsymbol{x} = 0$) and is stable at ~150GPa [243]. Byggmastar et al. highlighted that smaller scale simulations of the behaviour of oxygen in iron are usually based on density functional theory (DFT) [243], which is a method to approximately solve the Schrodinger equation of a many ($\boldsymbol{N_{body}}$-) body system [245] (see Appendix 12). However, larger scale simulations which incorporate precipitation growth and/or long-range diffusion and clustering of point defects, require more computationally efficient methods, such as molecular dynamics (MD) or Monte Carlo (repeated random sampling) methods [246], and rely on interatomic potentials to describe individual atoms' interactions.

Molecular Dynamics (MD) simulations are a computational approach for investigating the atomistic level motion and interactions of molecular systems, and offer insight into atomic level structural and mechanical level properties, where Finite Element Models (FEM) are limited, e.g. short time scale simulations [246]. MD simulations had potential in mathematical models (precise analysis, large model library, multiscale modelling), potential functions (parameterisation and validation, complex system processing, extensibility and simplicity), chemical reactions and green processes (environmentally friendly, complex environment prediction, comprehensive understanding of reaction), and atomic/near-atomic manufacture (real-time control and monitoring). Arachchige et al. highlighted the potential for MD to offer insight into molecular mechanisms during iron-oxygen interactions for both dry and wet corrosion [68]. However, MD simulations are unable to tolerate scale effects and so struggle to accurately capture details across variable spatial and temporal scales and unified models ranging from atomic to macroscopic are challenging to integrate without incorporating major complexity and are confined to the nano scale as a result [246]. Furthermore, deriving precise potential functions which are valid across the description of a range of interactions and systems is challenging and restricts simulation data reliability. Byggmastar et al.'s approach centres around the analytical bond order potential (ABOP) formalism for the Fe-O elemental interactions, based on existing Fe-Fe and O-O interaction data. which, although originally derived for covalently bonded materials, is appropriate for metal-oxides [243].

Electrotransport Phenomena in Wüstite

Due to the charged nature of iron cations which diffuse towards the external surface, movement is defined by electric field effects rather than a chemical gradient. Wustite is a semiconducting oxide wherein conduction is nearly entirely facilitated by cation vacancy mobility and there is significant deviation from stoichiometry. Therefore, electrotransport phenomena of wüstite (transfer of material from one electrode to another by means of a direct current passing through the oxide [242]), must be considered when developing any diffusion-related databases. This is especially the case as electrotransport phenomena, and their dependence on oxygen partial pressure (specifically defect concentration equilibrium), are enhanced by increased temperature due to increased electrical conductivity [247]. Furthermore, although electrotransport phenomena happens throughout the crystal lattice volume, the effect is observed at the interface. This is important for this project where SSI adhesion is of interest. For a mobile cation within the lattice, with a soluble anode, i.e. migration of iron cations in the case of this model, a typical ionisation reaction would occur. However, this equation can be refined to maintain crystal lattice integrity by considering crystal sites (see Equation 1.46). Note the use of Kroger-Vink notation to describe the changes to atoms and/or defects [248].

$$\boldsymbol{M + V_M^{\times} \rightarrow M_M^{\times}}$$

Equation 1.46

Existing works identified by such as Burgmann [249], Catlow and Fender [250], and Cheetham et al. [251] have provided evidence for the presence of clusters in wüstite at high temperature. The clusters comprise vacancies ($\boldsymbol{Va}$) and trivalent iron cations ($\boldsymbol{Fe^{3+}}$) on octahedral and tetrahedral sites with overall charges between 0 and -2. The trivalent ions evolve from the need to preserve total crystal electroneutrality in the iron-deficient non-stoichiometric wüstite, leading to a $\boldsymbol{2xFe^{3+}: (1-3x)Fe^{2+}}$ ratio of cations [252]. Ultimately, Frenkel defects, an interstitial atom and vacancy pair [98], arise on interstitial tetrahedral sites as a result of ion vacancies formed during this electroneutrality restoring process [253].

In Cheetham et al.'s work the 4:1 ratio between cation vacancies and interstitial trivalent cations resulting from a large Coulomb energy term leading to a preference for occupation of tetrahedral sites with all nearest-neighbour cations vacant [252]. Clusters are generated by vacancy sharing at edges. Extended clusters, e.g. 6:2, 8:3, are more likely to display

corner-sharing. However, a high temperature structural study by Koch and Cohen [254] detected a limited level of short range ordering (in wüstite). Despite a lack of clarity surrounding whether some or all defects exist within a single cluster type (or are distributed over several types as well as free defects), which would assist in understanding whether diffusion through wüstite is supported by free defects, clusters, or both, Morin states that there is agreement in the literature regarding the overall mechanism [255]. For migration kinetics, a single elementary step exists with an increased activation energy at a higher molar fraction value. There are several experimental conclusions which support the concept that for the range of conditions which wüstite exists under, the migration kinetic mechanism is not significantly modified by stoichiometric deviation nor temperature change. Evidence for this claim from Greenwood and Howe [256] and Chen and Peterson [257] comprises:

- Activation energy remains constant even with stoichiometric deviation, i.e. activation energy remains constant with a constant level, $\boldsymbol{x}$, of deviation from stoichiometry and plot of iron tracer diffusion coefficient (logarithmic) against temperature reciprocal at a constant value of $\boldsymbol{x}$ yields a straight line.
- Activation energy is higher for a higher value of $\boldsymbol{x}$.
- For a moderate temperature range, the average cation jump frequency decreased with an increase in $\boldsymbol{x}$.

It can therefore be concluded from this evidence that oxide composition range has a greater influence on overall defect structure than temperature.

A correlation factor, $\boldsymbol{f_{correlation}}$, which describes the effect of previous jump direction on the subsequent diffusion jump, i.e. an atom is more likely to return to its original site than a new one due to the presence of a vacancy at the original site after atom and vacancy lattice position exchange, can be calculated using Equation 1.47 based on the wüstite electrical conductivity, $\boldsymbol{\sigma_{FeO}}$, cation transport number (derived from wüstite electrolysis experiments), $\boldsymbol{t_{Fe}}$, valency for migrating ions, $\boldsymbol{z_i}$, and, crucially, the iron tracer diffusion coefficient, $\boldsymbol{D_{Fe}}^*$ (which has been shown to remain quasi-constant or decrease with increasing deviation from stoichiometry) [255]. For FCC and BCC lattices the correlation factors are 0.8 and 0.78 respectively [162]. It should be noted that alloys exhibit lower self-diffusion energy than pure metals due to the preferential binding of vacancies to impurity atoms which accelerates solute atoms migration due to an enhanced vacancy concentration.

However, vacancy mobility through the lattice to vacancy sinks, i.e. their most stable positions, will be governed by their strength of binding to their impurity atoms.

$$f_{correlation} = 9.4 \times 10^{13} \left(\frac{D_{Fe}^{*}}{\sigma_{FeO} T} \right) \frac{z_i^2}{t_{Fe}}$$

Equation 1.47

Morin [255] laid out their methodology for the use of Equation 1.47 in electrotransport experiments. As wüstite samples are in thermodynamic equilibrium with their iron metal substrate, transport numbers were measured for the corresponding level of deviation from stoichiometry. Validity of wüstite electrical conductivity in the temperature investigated within Morin's study [255] was verified by an empirical Brouwer diagram ($\sigma_{FeO} - T$) plot [258]. However, due to a lack of direct data for tracer diffusion coefficient, extrapolation to a suitable $Fe - FeO$ molar fraction value at the respective deviation from Fe/FeO equilibrium stoichiometry was performed based on results by Chen and Peterson [257]. These values were shown to deviate from closest experimental results by a maximum of 10% and were therefore deemed sufficiently reliable.

1.8 Conclusions following Literature Review

Oxidation is a complex, multi-physics phenomenon. However, oxidation in the context of the conveyance tube manufacturing process at TSUK Tubes is further complexified by interacting manufacturing parameters, namely combustion atmosphere, furnace type, and substrate chemical composition, and the presence of a non-planar geometry. For example, it has been shown that finite elements methods may underpredict oxide scale thickness gain as the insulating effect of the oxide scale is mitigated by the high surface area to volume ratio of cylindrical geometries. As such, the true thermal profile of the tube is not reflected. Demand for agile manufacturing results in inevitable variation in these parameters in response to the range of tube specifications received from TSUK Tubes' customers. Furthermore, as the favoured reactive scale management approach, the introduction of oxidation-resistant coatings will further alter scale behaviour as the steel, scale, and coating interact with their environment and each other. However, whilst oxidation-resistant coatings offer a cheap and effective solution at laboratory scale, incorporation of industrial infrastructure to accommodate these coatings is technically and economically challenging. Some authors have explored how the increased computational resources available in the 21st century could be used to improve the depth and accuracy of knowledge surrounding scale kinetics, morphology, and adhesion. Physics-based modelling of the oxidation process has the potential to offer a faster, cheaper, more accurate, and more representative insight into oxidation kinetics and adhesion response to conveyance tube manufacturing parameters where analytical and experimental approaches are limited by oversimplification and/or practical equipment restrictions. Hence, understanding of the scale morphology and kinetics, how it is adhered, and its likelihood of spalling both prior to and during descaling can help inform models of scale formation and descaling as well as optimise processes. This is particularly true for the conveyance tube manufacturing process as the primary challenges to be addressed are uncontrolled scale growth and subsequent inconsistent spalling. There are several aspects of manufacturing variation which have significant scope for further work and are, most importantly, pertinent to the TSUK Tubes' manufacturing capabilities and priorities. Understanding scale kinetics and adhesion in the context of conveyance tube manufacturing presents several technical challenges which have received limited attention in the literature or been restricted to specific processes, e.g. steam-side oxidation of boiler tubes. The specific technical challenges associated with conveyance tube manufacturing which are yet to be addressed have been identified as the thermochemical properties of

wüstite (the dominant phase oxide scale observed on low carbon steel), the effect of curved geometry on oxide kinetics and mechanics, and the adaption of experimental validation techniques to investigation of curved surface samples of oxidation. Furthermore, greater attention must be paid to industrially transferrable conclusions about oxide scale formation via employment of tools such as Advanced Oxide Scale Failure Diagrams (AOSFDs). AOSFDs offer insight into the critical manufacturing conditions for different oxide scale failure modes but without the need for complex (and often unfeasible) coupling of models of different physical elements contributing to oxidation. AOSFDs also depend, in part, on continuous oxide thickness data, which computational techniques are better equipped to supply, and are also yet to be applied in a non-planar geometry and/or specific industrial process context, particularly in terms of thermomechanical processing of curved surfaces which has been shown to influence oxide scale kinetics and adhesion.

1.9 Thesis Structure

The methodology and principles for all the experimental and computational techniques used in this thesis are presented in Chapter 2. This thesis comprises four distinct work packages, arranged by chapter (Chapter 3 to Chapter 6), which address one or more of the research objectives outlined in Section 1.1. Chapter 3 details the development of a computational thermochemistry model, and associated thermodynamic databases, in Thermo-Calc© DICTRA to predict oxidation kinetics and oxide thickness gain. This work is supported by experimental validation. Chapter 4 outlines how the model developed in Chapter 3 is adapted for curved surfaces and documents the effect of changes to radial coordinate dimensions on oxidation kinetics, using the adapted model data which are experimentally validated. The adapted model data are then used in Chapter 5 to support a comprehensive mechanical stability analysis via a combination of analytical, computational, and analytical approaches which rely on knowledge of oxide thickness. The final work package is presented in Chapter 6 and documents the development of an Advanced Oxide Scale Failure Diagram, combining data from Chapter 3 to Chapter 5, to allow oxide failure mode to be forecast under different industrial process conditions. Figure 1.33 shows a flowchart of the research conducted, outlining the input and output of data and key equations derived from experimental, computational, and theoretical techniques, as well as data input from the literature. The core research comprises the following consecutive step pathway: Defining Equation, Intervening Variable, Moving Phase Boundary Solution, Oxide Thickness Gain Data, Stress (Thermal, Growth, And Manufacturing), Advanced Oxide Scale Failure Diagram (AOSFD), and Oxide Failure Mode/s Prediction. There are secondary pathways which comprise auxiliary work. For example, the vibration analysis and oxide mass-volume-thickness gain calculations used for model validation in Chapter 4 Section 4.2. Further examples include the use of molecular dynamics to assess oxide elastic modulus in Chapter 5 Section 5.1.1 and the use of nanoindentation to assess oxide plasticity during loading in Chapter 5 Section 5.1.3. At the start of Chapter 3-Chapter 6, the region of the flowchart associated with the work in the chapter is highlighted as part of the introductory information.

1.10 Research Flowchart

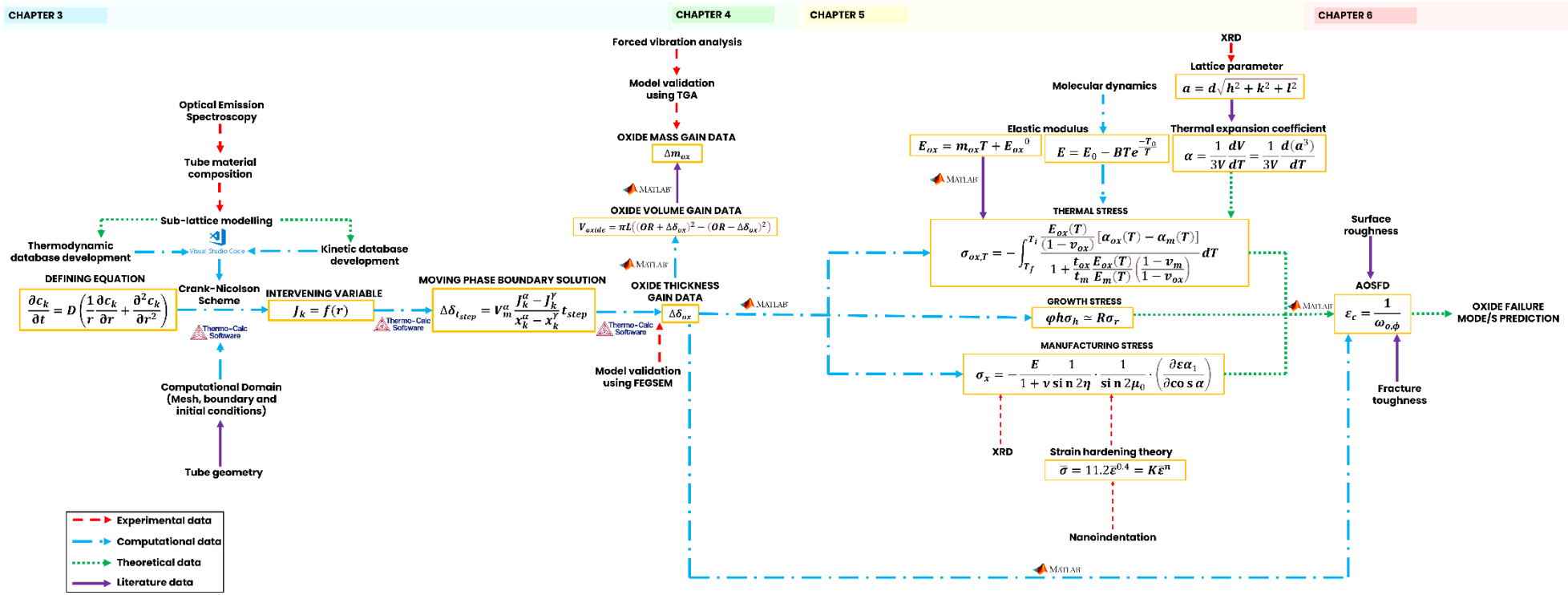


Figure 1.33: A flowchart outlining the input and output of experimental, computational, theoretical, and literature-derived data at each stage of the project, including key equations for each stage of research ¤.

Chapter 2 Methodology

The underlying theory for the major experimental and computational techniques used in this project are described in this chapter.

2.1 Experimental Techniques

2.1.1 Metallographic Preparation

A combination of trial and error in the laboratory, alongside technical recommendations from metallographic supplies companies [259] and previous studies in the literature [22, 260], were used to determine the best parameters to achieve a scratch-free surface on both oxide-free and oxidised 20x20x4mm samples, in anticipation of the empirical oxidation studies necessary for validation during computational model development. Standard metallographic preparation techniques and materials [259] were used:

- 80, 120, 400, 600, and 1200 grit grinding paper
- 9μm, 6μm, 3μm, and 1μm diamond polishing suspension
- 50nm colloidal silica oxide polishing suspension (OPS)
- Water-based 9μm, 6μm, 3μm,1μm and OPS polishing cloths [259]
- 20ml 5% Nital [22]
- Ethanol
- Water-based sodium sulphate detergent

Mounting

Planar samples were mounted transversely (see Figure 2.1) in electrically conductive thermosetting resin (Bakelite). It was anticipated that oxidised samples may experience embrittlement, delamination, and spalling due to thermal stresses evolved during resin thermosetting. However, due to the transverse mounting of the oxidised samples, it was expected that milling preparation could be extended to reach an un-delaminated layer of oxide.

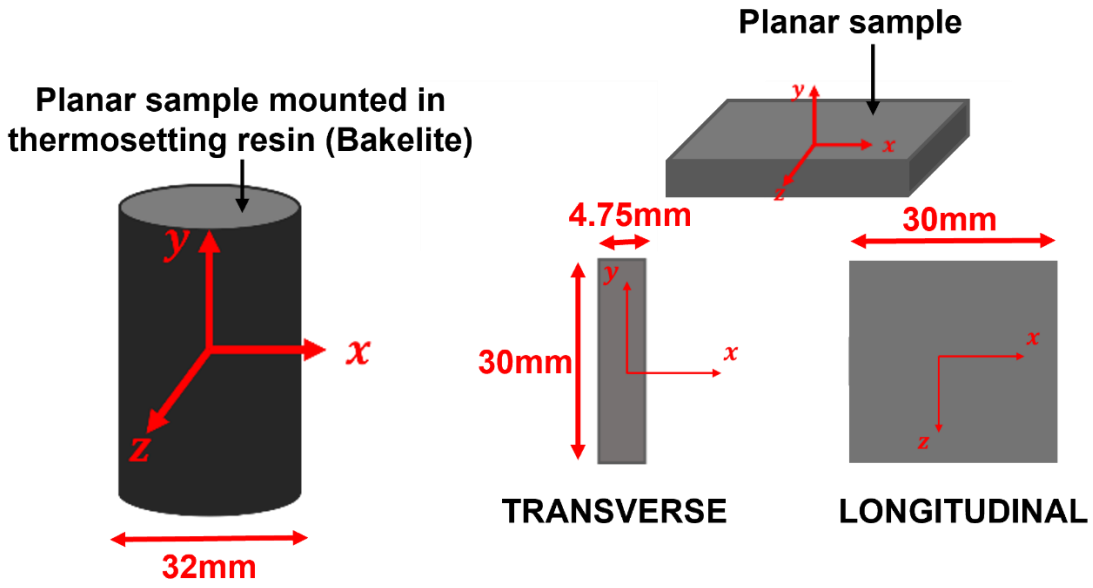


Figure 2.1: Metallographic mounting orientations for planar samples which are mounted in a 32mm diameter cylinder of thermosetting resin (Bakelite) for metallographic preparation and imaging ¤.

Mounting Challenges

Mounting of oxidised samples on the thermosetting resin revealed some problems with a large difference between the mount, steel, and oxide removal rate. The oxide was abraded at a faster rate, and this caused issues with undesirable steel-oxide delamination. This led to either the delaminated scale fragments becoming embedded in the Bakelite (see Figure 2.2) or the complete absence of scale at certain points around the inner scale circumference (see Figure 2.3). This was likely exacerbated by the high mounting temperature (up to 180°C) and pressure (250bar) used for the Bakelite. However, inconsistent scale delamination was far more of an issue for the inner surface of the tube since the Bakelite filling the tube bore was liable to pull oxide off the inner tube surface during thermal shrinkage post-mounting. In the outer surface case, the main focus of this project, the thermal shrinkage of the Bakelite encasing the outer tube surface will have compressed the oxide and encouraged it to remain adhered (see Figure 2.4).

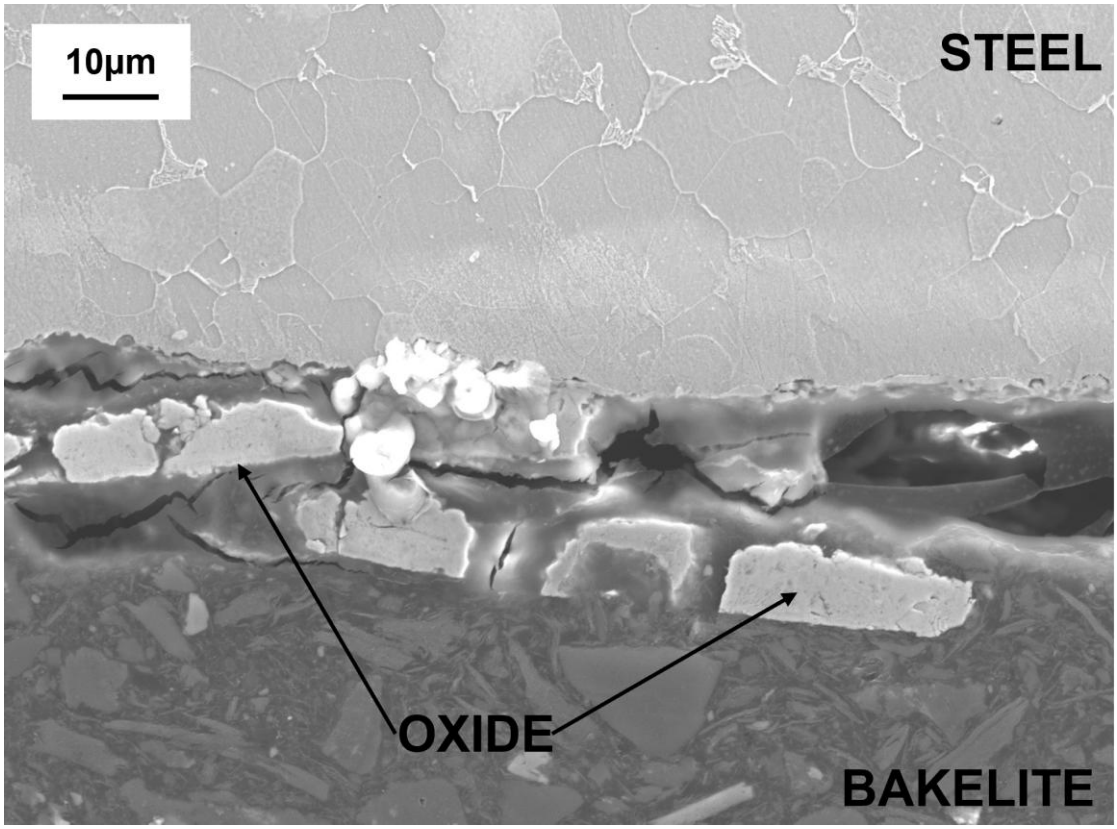


Figure 2.2: Delaminated oxide fragments at the inner wall surface of a 15 nominal bore (n. b.) normalised tube sample ¤.

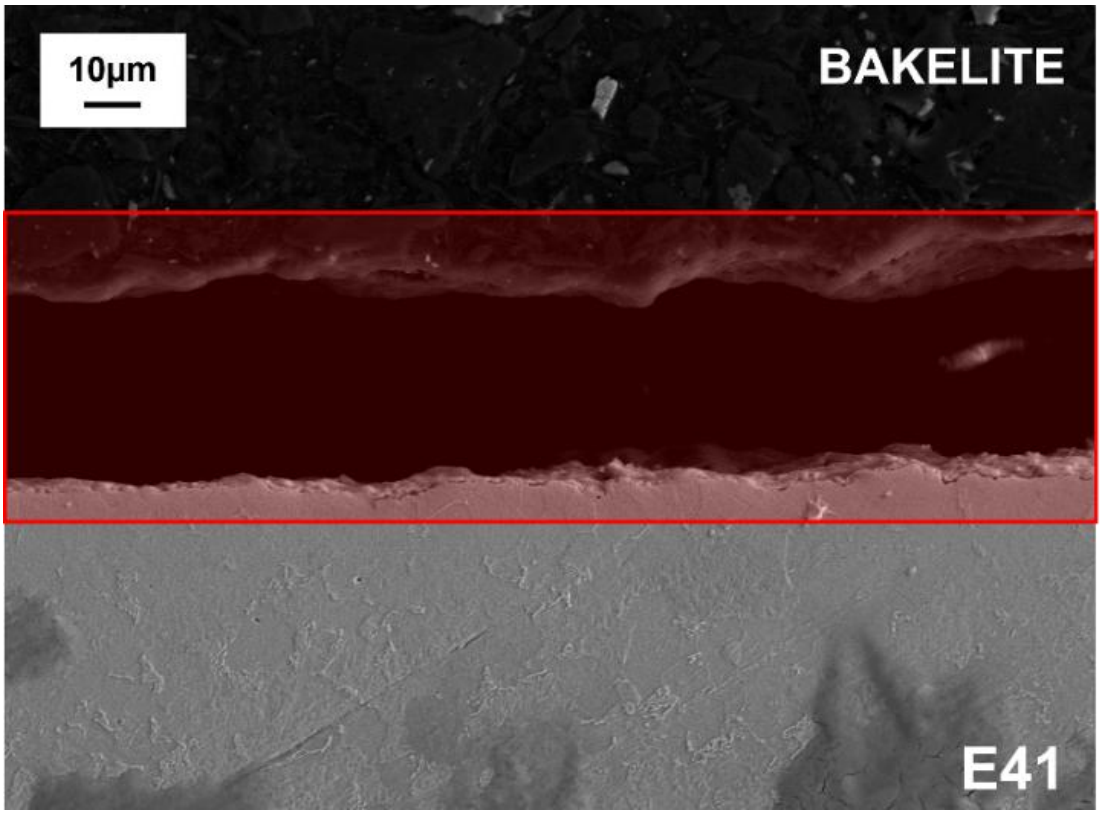
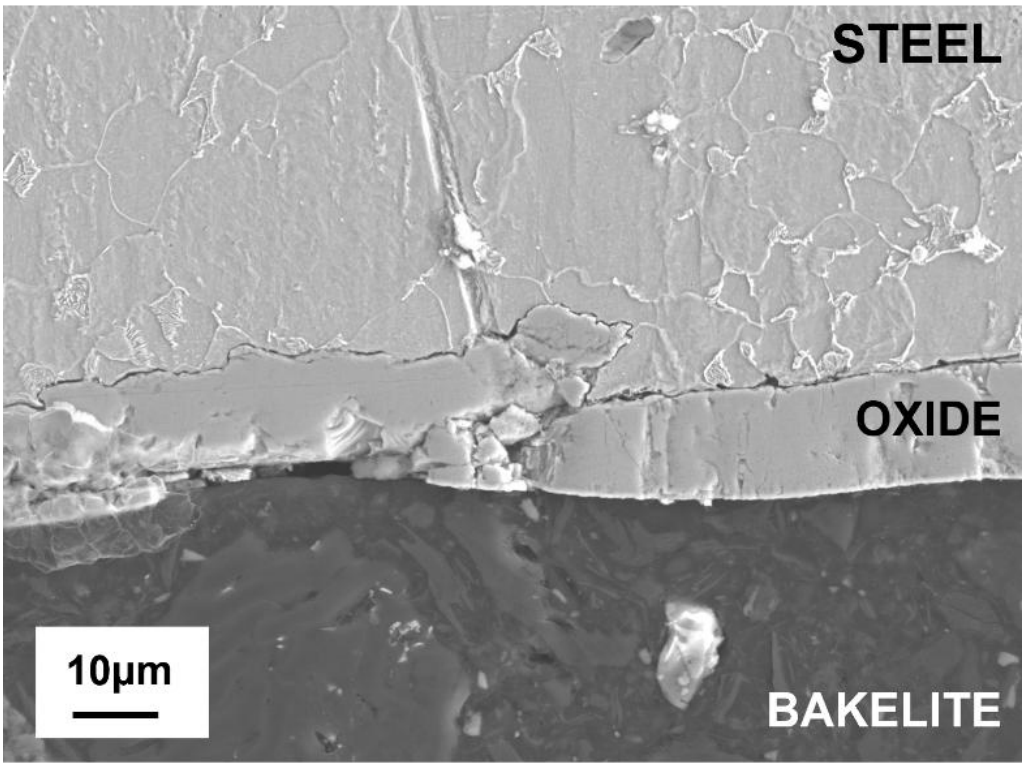
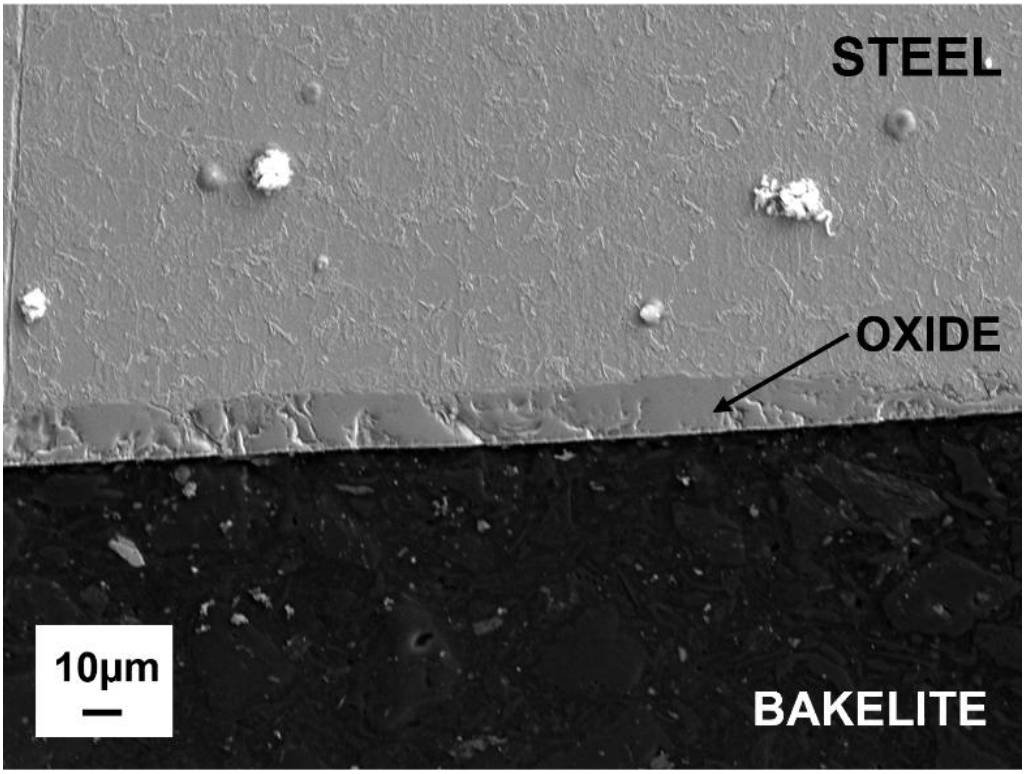


Figure 2.3: Air gap (*highlighted in red*) between the inner wall surface of a 20 nominal bore (n.b.) tube sample and its Bakelite thermosetting mounting resin ¤.



(a)



(b)

Figure 2.4: Intact oxide adhered to the steel and Bakelite at the outer surface of (a) 15 nominal bore (n. b.) and (b) 20 n.b. tube samples ¤.

Unmounted (pre-oxidation) samples were a challenge due to the low thickness (4-12mm) of the 20x20mm coupons used which made them difficult to hold.

Grinding

The optimum time for grinding to a planar surface with multi-directional, light scratches was found to be 5 minutes using water lubricated SiC grit paper at grades 80, 120, 400, 600, and 1200. For each subsequent grit paper, the sample was rotated by 90° to make it easier to see when the scratches from the previous grade grit paper were removed.

Polishing

Water-based polishing was performed for 3 minutes using 9μm, 6μm, 3μm, and 1μm diamond polishing suspensions. For oxidised samples, a further polishing stage was performed for 60s using a 50nm colloidal silica OPS using nitrile gloves.
Between every grinding and polishing stage, samples were washed with sodium sulphate detergent solution followed by ethanol to remove abrasive particles (from both the grinding paper and sample) which could promote damage during further milling. The samples were then also checked for major scratches under a light microscope. It was also found that it was important to wash the mounted samples with the sample surface aligned parallel to the solution flow to ensure run-off and prevent any moisture entering potential air gaps between the sample and Bakelite (as in Figure 2.3), resulting in additional corrosion products.

Etching

Where grain boundaries needed to be revealed, etching was performed for 15s using a 5% Nital (methanolic nitric acid) solution. However, etching can be an optional step if OPS is sufficient to reveal grain boundaries.
Overall, Table 2.1 provides a summary of the parameters necessary for mechanical sample preparation to a highly reflective, pre-etched finish with no deformation in the exposed bulk material surface layer. Prepared samples were stored in a desiccator cabinet to prevent exposure to wet corrosion-inducing oxygen and moisture.

Table 2.1: Summary of the grinding, polishing, and etching parameters used to metallographically prepare samples.

Operation	Grade/Composition	Time (s)	Rotational speed (rpm)
Grinding	80 grit	Until planar	300
Grinding	120 grit		
Grinding	400 grit		
Grinding	600 grit		
Grinding	1200 grit		
Polishing	9μm diamond suspension	180	150
Polishing	6μm diamond suspension		
Polishing	3μm diamond suspension		
Polishing	1μm diamond suspension		
Polishing	0.25μm colloidal silica OPS	60	150
Polishing	50nm colloidal silica OPS		
Etching	5% Nital solution	15	n/a

Between each stage of metallographic preparation, the sample was washed in hot water to remove excess abrasive particles and/or lubricant. It was ensured, via the microscope, that all scratches and defects in all directions had been milled away. Otherwise, grinding was continued at the same grade until an undeformed surface is revealed. Due to the curved geometry of the tube samples, and the propensity of the sample and Bakelite to undergo different levels of thermal expansion and contraction, there was potential for de-adhesion of the sample from the Bakelite and the gap created could be penetrated by the water-based lubricant. This could lead to wet corrosion of the sample and therefore the washing and drying stages were always performed with the sample surface parallel to the direction of water flow to minimise fluid ingress.

Mounting Oxidised Samples with Curved Geometries

Geometric effects in tube samples experience additional growth stress due to oxidation, as discussed in Section 1.4 [106]. Typically, the high levels of porosity and embrittlement in laboratory-grown iron oxide scales [22, 60] makes them especially susceptible to delamination during grinding and polishing. To improve oxide integrity for imaging, a thin layer of polyester resin for cold mounting was applied to all surfaces of the oxidised tube to seal the oxide in position before grinding (see Figure 2.5). Once the cold resin set, the

sample was mounted in Bakelite and prepared following all the steps above. To maximise the surfaces available for coating with Bakelite and optimise electrical conductivity for subsequent use in electron microscopy techniques, a pipette was used to remove any excess resin from the internal section of the tube.

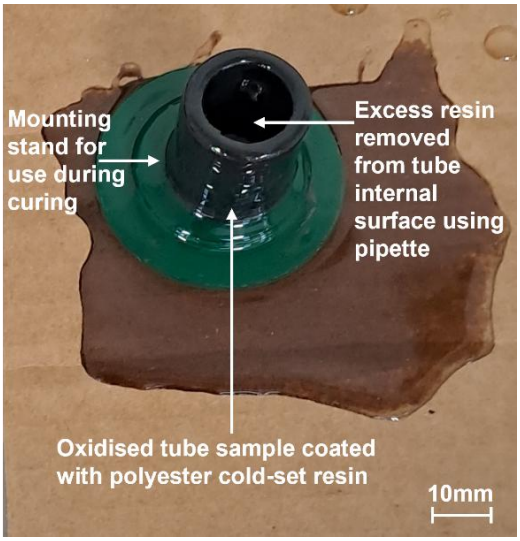


Figure 2.5: Annotated photograph of oxidised 15 nominal bore (n.b.) conveyance tube mounted in a thin layer of polyester cold-set resin ¤.

2.1.2 Optical Emission Spectroscopy

Optical Emission Spectrometry (OES) can be used to determine the bulk composition of liquid or solid-state plate or disc samples (where composition is independent of depth) of dimensions in the range 3-100mm [261]. It is favourable for application in steel industry applications due to its ability to quickly acquire online data in the harsh conditions of industrial furnaces using robust, low maintenance equipment and perform quick data post-processing [262].

A high voltage is applied across two electrodes (the sample being the anode) sufficient to generate an arc (thermionic- or field-emission initiated) or spark (only initiated by field emission) charged particles, e.g. electrons, anions, cations (dependent on OES type). The charged particles, produced from the cathode, strike the sample and force its constituent atoms to be ejected from the surface into the surrounding vacuous gas environment (this is known as sputtering) due to the intense heat generated by the impact of the charged particle stream. Sputtered atoms (analytes) are excited and ionised via inelastic collisions with electrons and other gaseous species in the plasma evolved from the sputtering process. During relaxation, excited analytes emit characteristic optical spectra (typically in the visible or ultraviolet (UV) ranges, i.e. 130-800nm [263]) which are sorted according to

wavelength by a dispersive diffraction grating (polychromator). Both qualitative (element identification) and quantitative (identified element concentration) analyses can be performed for almost all periodic elements once the analytes have been converted to electrical signals [264].

A Grimm type glow discharge (GD-OES) spectrometer (see Figure 2.6) is common due to its advantages over the traditional point-to-plane spark stand design, which are all attributed to the lower plasma density and ionisation and excitation temperatures associated with the use of a lower discharge current and subsequently less heat generation at the sample surface. Accelerating voltage is high (500-1200V) but average gas ion kinetic energy is low at <100eV [264]. For steel in particular, because of its compositional variation and the evolution of multi-phase steels [265], sophisticated compositional analysis techniques which can minimise analysis time, optimise detection limits and depth resolution, and maximise sensitivity, are necessary. GD-OES is most suitable in this case. GD-OES can also detect all elements above and including hydrogen on non-conductive materials. Compared to other techniques, namely Auger electron spectroscopy (AES), X-ray photoelectron spectroscopy (XPS), and secondary-ion mass spectrometry (SIMS), GD-OES has a good depth resolution without a high lateral resolution. Due to this, GD-OES is quicker for bulk material analysis, rather than the previously mentioned surface-sensitive techniques which would be more appropriate for oxidised surfaces.

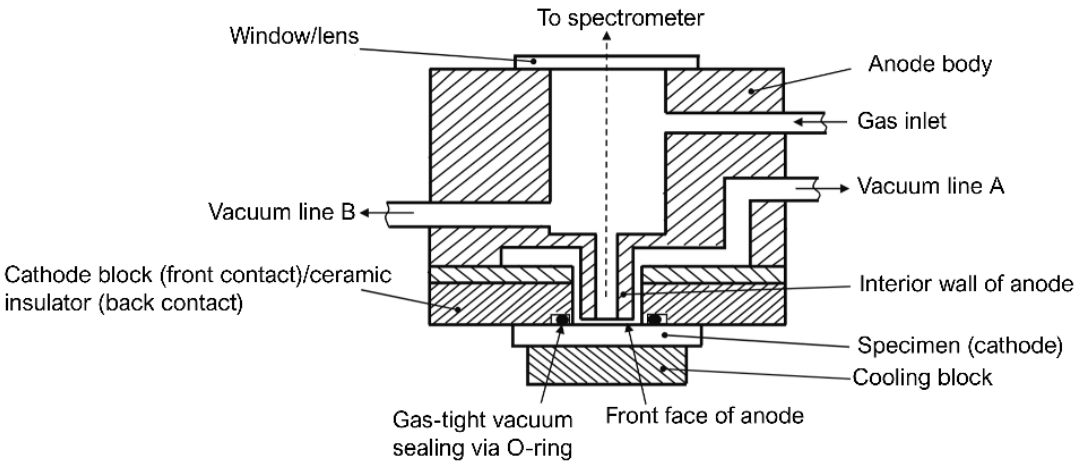


Figure 2.6: GD-OES apparatus set-up (*adapted from source*) [264].

2.1.3 Simultaneous Thermal Analysis

As individual thermal analysis techniques are unlikely to provide all necessary information about the tube oxidation system, complementary information from multiple sources is required. However, variations in the sample test environment are inevitable and therefore it cannot be assumed that complementary techniques will correlate precisely. Complex systems where multiple reactions are anticipated, e.g. different oxide phases evolved (see Section 1.3.1) and alternative reaction schemes are possible, e.g. anticipated reaction of alloy elements to form influential mixed oxides such as fayalite (see Section 1.6.1) and these are significantly influenced by sample size, form, and environment can display discrepancy even if the system is well understood and controlled. Hence, simultaneous measurement systems, known as simultaneous thermal analysis (STA), offer a synergistic effect via independently measured but precisely correlated data. Furthermore, simultaneous temperature measurement can also eliminate discrepancies in sample preparation and dissimilar ramp rates [9].

Thermogravimetric analysis (TGA), the measurement of mass change as a function of temperature or time at a constant temperature [266], and Differential Scanning Calorimetry (DSC), the measurement of energy adsorbed or released during heating, cooling or isothermal treatment [267], are complementary quantitative and qualitative techniques respectively suitable for all solid-gas reaction studies [268]. A key advantage of TGA-DSC STA is the ability to verify conclusions about material events represented by DSC sensor peaks using TGA data, e.g. phase transition. Conversely, DSC can assist in explaining anomalous or unexpected TGA curve features. For example, changes to rate of reaction, i.e. significant changes in TGA curve gradient, during solid-gas reactions, are usually connected to fluid phase generation. Further, the phenomenon of bubbles bursting within this fluid, observed as sharp troughs on the TGA curve, is usually confirmed by sharp endothermic spikes on the DSC trace.

Figure 2.7 shows the NETZSCH STA 449 F3 Jupiter® simultaneous thermal analyser, and the associated 3mmx3mmx3mm coupons of sample material, used in this project. Figure 2.7 shows the post-heat coupons, which disintegrate post-heating and are therefore difficult to use in any microstructural imaging, hence this is a solely quantitative technique.

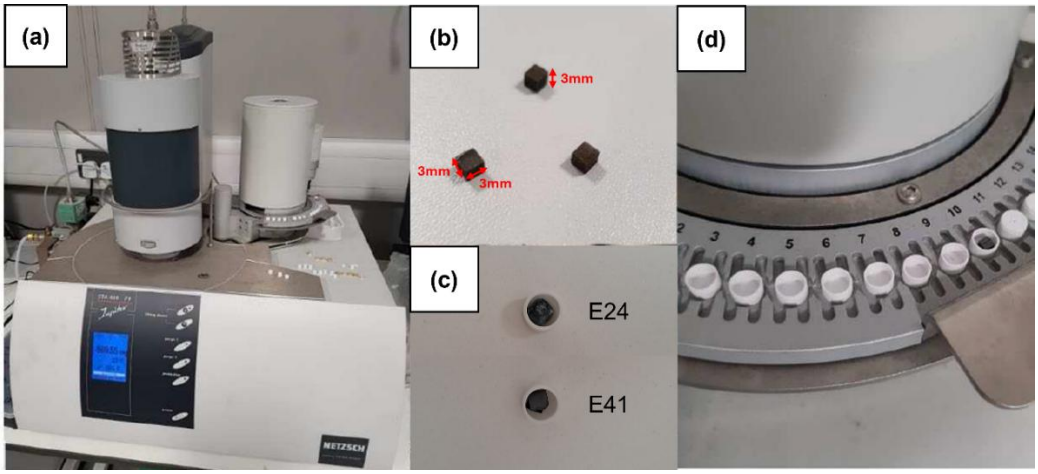


Figure 2.7: Photograph of (a) NETZSCH STA 449 F3 Jupiter® simultaneous thermal analyser, (b) dimensioned 3mmx3mmx3mm coupons pre-heating, (c) E24 (*top*) and E41 (*bottom*) disintegrated coupons in their alumina crucibles post-heating ¤, and (d) enlarged image of crucibles mounted in the automatic sample changer which has a capacity of 20 coupons. *Original images (a), (b), and (d) by J Grant [9].*

Differential Scanning Calorimetry

DSC depends on the measurement of temperature to investigate thermal changes in a sample compared to an inert reference. Unlike TGA, sample mass change is not a prerequisite for this technique. Furthermore, samples can be very small, as low as several mg. In DSC, the output signal is proportional to the thermal power difference between the sample and reference [269]. The instrument software has its own algorithm which converts the temperature difference measured by the thermocouples to difference power ($\frac{d\Delta q}{dt}$). Unlike its predecessor, Differential Thermal Analysis (DTA), DSC carries the advantage that when a signal is plotted against time, and the area enclosed in peaks corresponds to heat change, proportionality is independent of sample heat capacity. Although DSC used in combination with TGA is generally to qualitative ends, DSC can also perform quantitative measurements of heat capacity, enthalpy, purity, chemical kinetics, vapour pressure, and thermal conductivity.

2.1.3.1 Thermogravimetric Analysis

Thermogravimetric analysis (TGA) systems comprise mass balance, furnace, atmosphere control, crucible, thermocouple, temperature control and data collection equipment. The combination of the mass balance and furnace forms the thermobalance system which can vary in accuracy and precision [270]. The equipment used had a balance resolution of 0.1µm and balance drift of <5µg/hour [271]. The sampling rate of the thermocouple and mass balance was 0.2Hz. There is also a trade-off between selecting a sample size which is large enough (≥1g) to leave residue suitable for further chemical testing but small enough (can be

as low as 1mg) to maximise the potential for a steady and uniform temperature distribution in the sample. This also relies on selecting a furnace with a large enough isothermal zone. The thermocouples, which measure temperature via the fixed standard voltage across a two metal junction, rely on careful selection of highly refined pure elements or alloys, e.g. platinum vs. platinum alloyed with 13% rhodium offer high melting point and inertness [270], to produce reproducible, accurate results.

Thermogravimetric Analysis Furnace

Thermogravimetric data were also obtained from the in the Steels and Metals Institute (SaMI) simulation and integrity testing in extreme conditions (SINTEC) laboratory (see Figure 2.8). The technical drawing for this bespoke furnace is shown in Figure 2.9. This is a bespoke design vertically mounted tube furnace capable of uniform heating over a 300mm height up to 1400±5°C. During furnace operation, the mass balance (Mettler Toledo ICS425K-15LA) continuously weighs the entire work tube in addition to the sample itself, overall providing continuous mass gain data for the sample. A type 'R' (platinum-13% rhodium/platinum) thermocouple is attached to the heating chamber via a ceramic tube to obtain continuous temperature data. Tube samples had a single through-thickness hole in their wall to allow their suspension from the ceramic radiation shield arrangement using nichrome wire. The samples were weighed on a Fisher Scientific 0.0001g precision mass balance before testing, for calibration purposes.



Figure 2.8: Carbolite Gero Ltd High Temperature TGA Tube furnace used to perform furnace replication experiments and obtain continuous thermogravimetric data ¤.

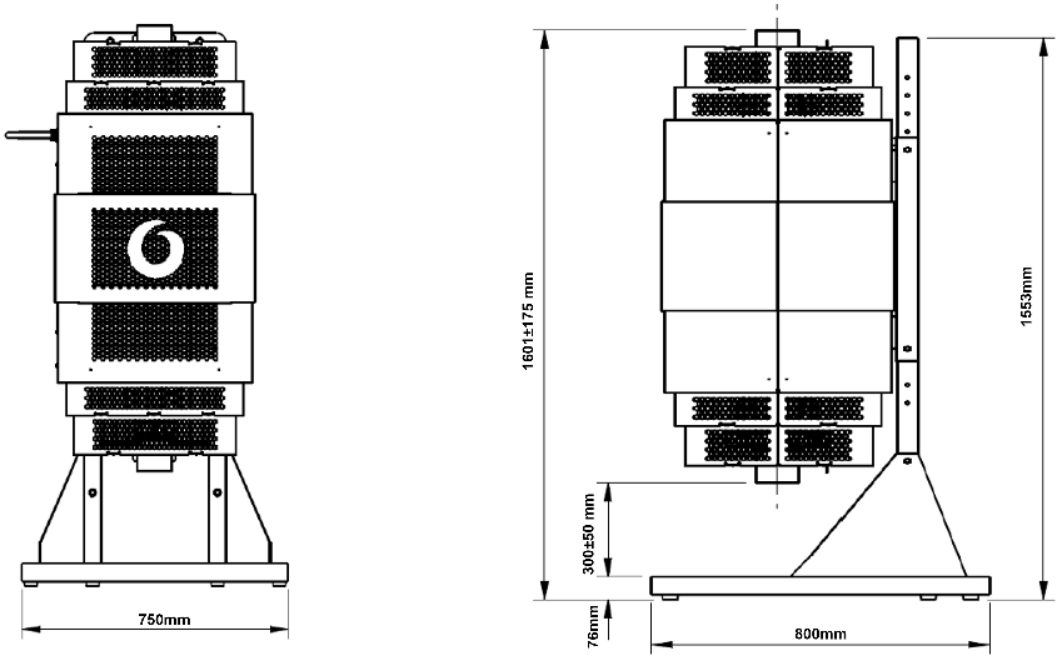


Figure 2.9: Technical drawing (taken from model TF1 16/100/450 furnace manual) of vertically mounted Carbolite Gero Ltd High Temperature TGA Tube furnace (model TF1 16/100/450) [272] (*adapted from source*).

Samples were subjected to a heating cycle representative of the conveyance tube normalisation treatment, i.e. 1000°C for 15 mins. The selected heating rate was set at 5K.min^{-1} (the maximum rate available within the furnace) although this was not directly relevant as investigations were only concerned with the isothermal region. The furnace

manual stipulates that the heating rate be constrained to $\frac{400}{Internal\ diameter\ (mm)}$, which for the 75mm internal diameter tube used gives a maximum heating/cooling rate of 5 °C.min^{-1} to minimise the risk of thermal shock [272]. Sample bore was limited by the work tube internal diameter of 90mm, especially as sample to tube contact should be limited to minimise surface contact and subsequent thermal conduction. Although an isothermal load was required to provide representative in-situ validation testing, the sample was inserted into a cold furnace to minimise the thermal stress on both the work tube and sample.

2.1.4 Atmospheric Furnace Normalisation Replication

Part of Grant's novel work was the development of an atmospheric furnace using existing hardware at Swansea University [9]. They used a Narbertherm N 41/H furnace to perform heat treatments within an atmospheric box supplied with a constant flow of the required gas stoichiometry using a novel gas mixing system comprising rotameter-controlled flow of carbon dioxide (CO_2), argon (Ar), nitrogen (N_2), and compressed air (see Figure 2.10). A pre-furnace stainless steel mixing chamber, with a 6 bar pressure release valve, was designed to vortex the gases used (see Figure 2.11). To ensure calibration of the gas leaving the mixing chamber, Grant also installed a Testo 300 LL flue gas analyser to examine in-situ oxygen (O_2) concentration which subsequently affects the required flow rate of CO_2 and N_2.

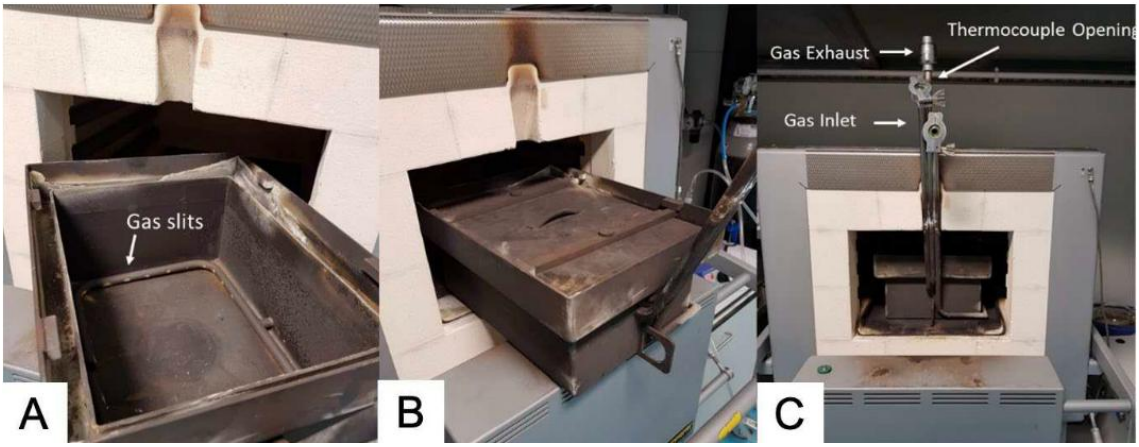


Figure 2.10: Photographs of the novel atmospheric furnace box developed for a Nabertherm N 41/H furnace, to achieve a desired gas flow rate and stoichiometry to replicate normalisation experiments. The furnace box is show in its open (A), closed (B), and fully inserted with inlets and exhausts (C) position. *Images taken by J Grant [9].*

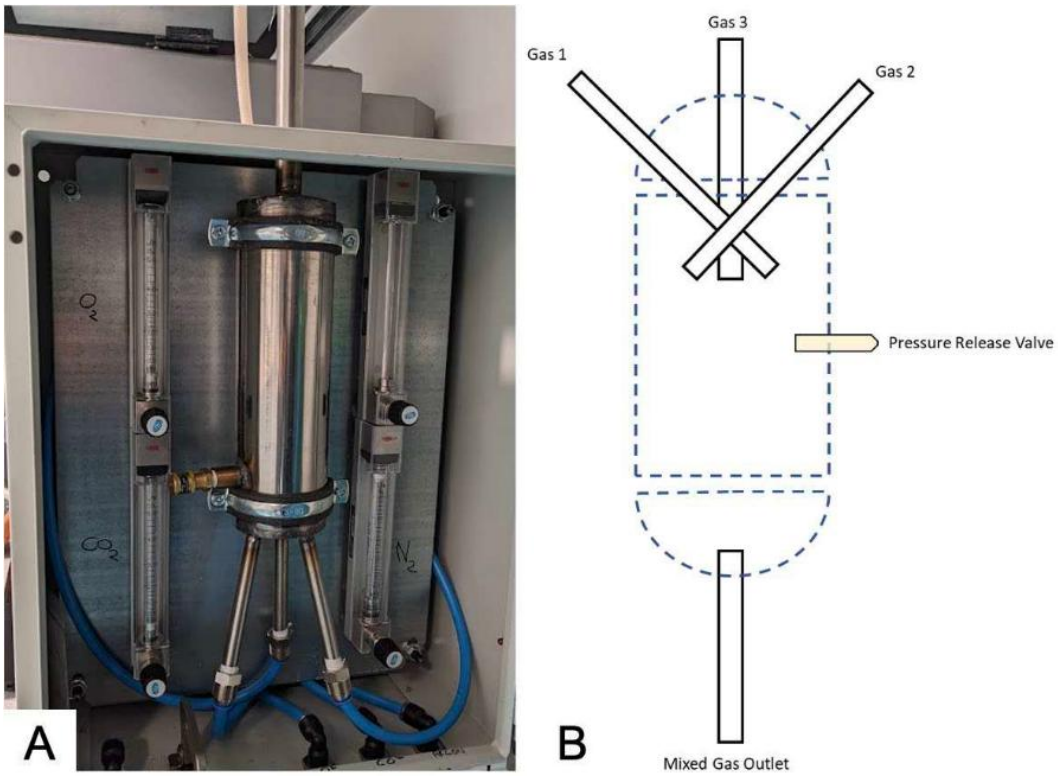


Figure 2.11: Photograph (A) and schematic diagram (B) of the bespoke vortex mixing system designed in the work of Grant during their development of an atmospheric furnace. *Images taken by J Grant [9].*

In this project, the atmospheric furnace equipment was used for an initial characterisation experiment. A gas flow rate of 12.5l.min^{-1} was set using the rotameters. During testing, the sample temperature was measured every second using RS Pro 1mm type K thermocouples, welded to a reference steel sample, and recorded using a Tenma 72-7715 thermometer.
A key advantage of Grant's atmospheric furnace was the ability to accurately replicate the normalisation stage of tube manufacturing by inserting samples after the furnace pre-heat and heating stages to achieve an isothermal treatment, and supplying Ar at a rate of 15l.min^{-1} to flush the furnace box after heat treatment. However, Grant's work focused on close thermal cycle replication, for their assessment of novel oxidation-resistant coating design, at the expense of accurate oxide gain quantification. Sample transfer between the furnace box and mass balance was susceptible to scale delamination. Furthermore, there was no capacity to continuously measure oxide gain, due to the bespoke gas stoichiometries and layout of the furnace infrastructure, which was a priority in this project's work on modelled oxide prediction and the value of continuous data for oxide integrity assessment, which is discussed in later chapters. Hence, the use of this furnace in this project was limited to initial characterisation.

2.1.5 Electron Microscopy

Electron microscopy uses electrons, as opposed to visible light, to image and characterise materials via the study of the surface, or near surface of bulk specimens [273, 274]. At a higher cost, electron microscopy offers higher resolution, magnification, depth of field, and versatility than its light equivalent. However, unlike light microscopy, the specimen has the potential to interact with the electrons physically, chemically, and/or thermally. All electron microscopes have an electron gun, condenser lens system, and signal detector as a minimum (see Figure 2.12).

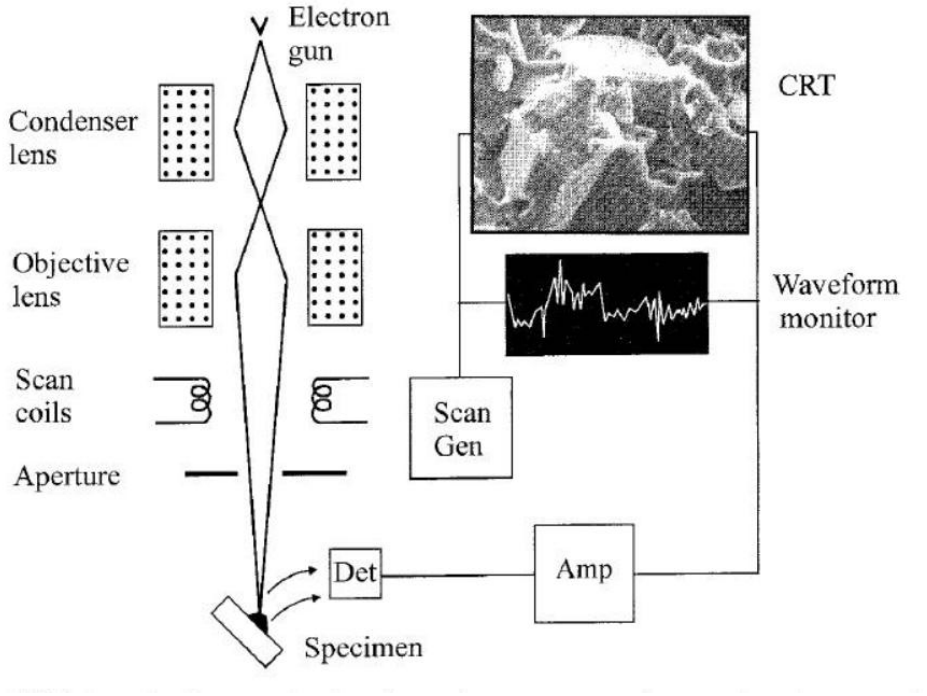


Figure 2.12: Typical set-up for a scanning electron microscope [275].

Localised outer electrons are the highest energy electrons with the lowest binding energies to the nucleus and are therefore readily removed from their atoms, i.e. with low energy input. For a higher brightness, a field emission gun is used where an extremely high strength electric field ($> 10^9$ V.m^{-1}) can force an electron to leave a metal surface without meeting the work function due to quantum tunnelling phenomena [276]. This is known as Field Emission Gun Scanning Electron Microscopy (FEGSEM). Hence, more electrons can be drawn from the tungsten and brightness can be increased by a factor of 1000 to 10^{13}A.m^{-2}.sr^{-1}. A key feature of field emission is that emitted electrons have well-defined energies with a spread of <0.5eV (unlike thermionic electrons which have an energy spread of 1-2eV). Hence, for both analytical and high resolution electron microscopy, field emission

sources provide the necessary high brightness and 'clean' monochromatic electron supply. Different types of radiation (see Figure 4.3) will have different interaction volumes, i.e. the degree to which they penetrate a sample, within the specimen but can only be detected if they escape the specimen. As secondary electrons have the smallest sampling volume, they give the best spatial resolution of all possible signals. FEGSEM systems usually have a spatial resolution approaching 1nm [277].

Backscatter detection can also provide information about surface composition, since the backscatter coefficient, $\boldsymbol{\eta}$, varies monotonically with atomic number, $\boldsymbol{Z}$. Equation 2.1 shows how backscatter coefficient is obtained using a rule of mixtures based on weight fraction.

$$\boldsymbol{\eta = -0.254 + 0.016Z - 1.86 \times 10^{-4} Z^2 + 8.3 \times 10^{-7} Z^3}$$

Equation 2.1

An atomic number contrast, $\boldsymbol{C}$, can be calculated and allows for distinction between phases, which will have different backscatter coefficients due to their different atomic numbers (see Equation 2.2).

$$\boldsymbol{C = \frac{\eta_1 - \eta_2}{\eta_1}}$$

Equation 2.2

In alloys, adjacent element or phase contrast may be small (1-5%), compared to topographic contrast which can approach 100% [277], so metallographic polishing to achieve a flat surface (unetched) is essential for effective backscatter contrast examination. For the Bakelite-mounted samples discussed in this project, optimal settings were found to be 12kV accelerating voltage and probe current of 8nA at a 10mm working distance.

Energy Dispersive Spectroscopy

As SEMs comprise an electron gun and electromagnetic lens system, i.e. an electron column (see Figure 2.13), can be equipped with an X-ray spectrometer which can reproduce the entire X-ray spectrum emitted from the sample surface to achieve materials microcharacterisation. The most common X-ray spectrometers are wavelength dispersive spectrometry (WDS) and energy dispersive spectroscopy (EDS). WDS is best suited to measuring peak intensity above background level for a single X-ray line with extreme accuracy, whilst EDS can detect and display most of the X-ray spectrum but with loss of

precision and resolution. Given that a broader knowledge of the overall composition of tube samples was required, EDS was selected as the analysis technique.

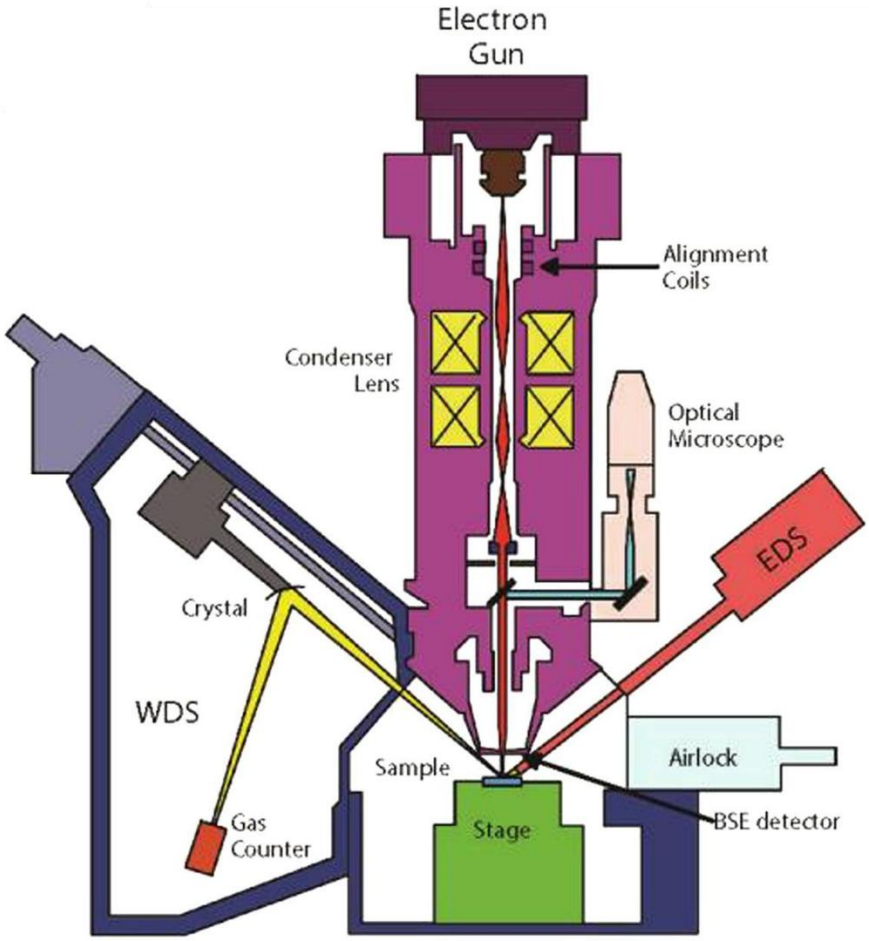


Figure 2.13: Mounting of an X-ray spectrometer on to a typical electron column comprising a thermionic electron gun and electromagnetic lens system [278].

EDS can detect all elements except hydrogen and helium in parallel with minimal preparation requirements The best results, i.e. maximum number of X-rays, are detected when the detector is at a close distance to the specimen (<20mm [279]). A histogram of energies, and subsequently compositional elements, is generated and stored by an appropriate analysis software. The analysis software used in this project is AztecFeature. EDS detectors are highly efficient and their collection angle is typically large at >0.5sr so quantitative and qualitative data can be acquired quickly (1-2 mins) at lower beam currents [279]. Finally, there are limitations on the detectability of trace elements using EDS, due to its low resolution (hence why peaks rather than bands are observed) and signal-to-noise ratio (SNR).

2.1.6 Nanoindentation

Nanoindentation is a standard experimental technique for assessing thin-film or small volume bulk mechanical properties (specifically hardness, $\boldsymbol{H}$, and elastic modulus, $\boldsymbol{E}$) [280]. As such, nanoindentation data can be used to evaluate strain-hardening components and fracture toughness, which are relevant properties in this project [281]. Quantification of mechanical properties comes from analysis of unloading data using the analytical model for deformation of an elastic half space by an elastic punch. This methodology relates the peak load contact area to the elastic modulus. A large portion of the theory associated with this technique is derived from classical elastic contact mechanics and the landmark works by Boussinesq, Hertz [119], and later Sneddon. Microhardness testing theory was used to derive Equation 2.3 based on the experimentally measured stiffness, $\boldsymbol{S_{empirical}}$, in the upper region of unloading of the load-displacement ($\boldsymbol{P_{ind} - h_c}$) graph. Equation 2.3 also shows how stiffness is a function of the reduced modulus, $\boldsymbol{E_r}$, which accounts for the elasticity of the indenter, and the projected area of the elastic contact, $\boldsymbol{A}$. Conveniently, Equation 2.3 is applicable for any indenter geometry which can be described as a body of revolution of a smooth function. Hardness, $\boldsymbol{H}$, can be calculated using the conventional relationship between peak load, $\boldsymbol{P_{ind,max}}$, and the contact area (see Equation 2.4).

$$\boldsymbol{S_{empirical} = \frac{dP}{dh} = \frac{2}{\sqrt{\pi}} E_r \sqrt{A}.}$$

Equation 2.3

$$\boldsymbol{H = \frac{P_{ind,max}}{A}}$$

Equation 2.4

Typically, nanoindentation utilises a Berkovich indenter, best described as a three-sided pyramid (conventionally manufactured from diamond). Its area-to-depth function is identical to that of a Vickers indenter shown in Figure 2.14 (as defined in BS EN ISO 6507-1 for Vicker's hardness testing methodology of metallic materials [282]). It should be noted that due to the fine scale of nanoindentation testing, the lack of atomic sharpness of the Berkovich indenter is significant and hence blunting must be accounted for [283]. However, the blunting effect simplifies the mechanical analysis since the tip profile can be approximated as spherical. It should be noted that a blunted tip will require a greater force to achieve the same displacement as its equivalent ideal conical indenter as there is a greater

surface area in contact with material to be deformed and pushed out of the way to allow the indenter to proceed.

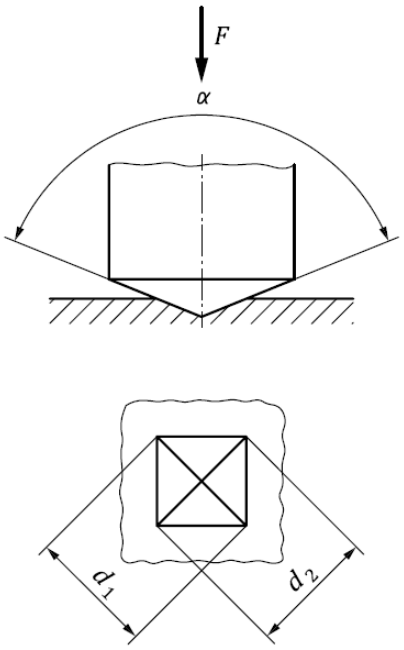


Figure 2.14: Vickers indentation geometry specified in BS EN ISO 6507-1 [282].

The success of the nanoindentation procedure also depends on knowledge of unloading stiffness, $\boldsymbol{C_{unload}}$, load frame compliance, $\boldsymbol{C_f}$ (see Equation 2.5), and the (diamond) indenter area function, $\boldsymbol{A_{ind}}$ (see Equation 2.6), the latter being most important due to their effect on the measured displacement, i.e. contact depth, $\boldsymbol{h_c}$, and material properties respectively. A typical indentation depth should be no more than 10% of the total thickness of the oxide to ensure that only the oxide is plastically deformed, since the deformation zone can extend several times further into the sample than the indentation depth itself [284].

$$\boldsymbol{C_{unload} = C_f + \frac{\sqrt{\pi}}{2E_r}\frac{1}{\sqrt{A}}}$$

Equation 2.5

$$\boldsymbol{A_{ind} = 24.5{h_c}^2}$$

Equation 2.6

The typical raw outputs of nanoindentation testing are load-displacement data. However, since the primary objective of nanoindentation testing in this context was to derive a plastic power law, stress and strain relations (both engineering, $[\boldsymbol{\sigma, \varepsilon}]$, and true, $[\boldsymbol{\sigma_t, \varepsilon_t}]$) are required to convert the data. Load, $\boldsymbol{P_{ind}}$, and contact area, $\boldsymbol{A_{contact}}$, can be obtained directly from the test results (see Equation 2.7), but the strain equation (see Equation 2.8) depends

on calculation of the contact diameter, $\boldsymbol{d_{contact}}$ (see Equation 2.9), and indenter diameter, $\boldsymbol{D_{ind}}$ (see Equation 2.10) based on the indenter radius, $\boldsymbol{R_{ind}}$, and displacement, $\boldsymbol{h_c}$ [285].

$$\boldsymbol{\sigma = \frac{P_{ind}}{A_{contact}}}$$

Equation 2.7

$$\boldsymbol{\varepsilon = \frac{d_{contact}}{D_{ind}}}$$

Equation 2.8

$$\boldsymbol{d_{contact} = \sqrt{\frac{4A_{contact}}{\pi}}}$$

Equation 2.9

$$\boldsymbol{D_{ind} = \frac{{R_{ind}}^2 - {h_c}^2}{{h_c}^2}}$$

Equation 2.10

In this project, nanoindentation data were collected using a Bruker Hysitron Ti 980 TriboIndenter. The peak load and contact depth were 143.8μN and 96.4nm respectively. The Triboscan software which accompanies the nanoindenter can also automatically calculate values of interest such as the contact area, contact stiffness, reduced modulus, and hardness (based on the mathematical relationships described above).

2.1.7 X-ray Diffraction

X-ray Diffraction (XRD) is a multi-faceted technique which capitalises on the three dimensional periodic arrangement of atoms in a crystalline material and its ability therein to induce diffraction (see Figure 2.15) [286]. Bragg's Law (see Equation 2.11) states that diffracted beams will interfere when their path difference, $\boldsymbol{2d'sin\theta}$, an integer multiple, $\boldsymbol{n}$, of the X-ray wavelength, $\boldsymbol{\lambda}$, such as in the case of atoms P and M or equally when there is no path difference at all such as in the case of atoms P and K. It should be noted that Equation 2.11 is only valid when analysis is performed on measurements taken normal to the atomic plane [286].

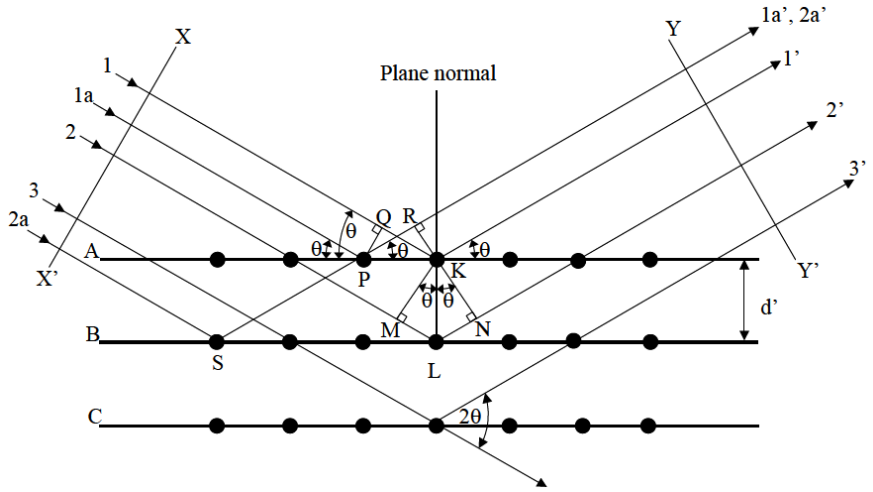


Figure 2.15: Diffraction of X-rays by a crystal lattice [286].

$$n\lambda = 2d'sin\theta$$

Equation 2.11

The different diffraction patterns obtained by variations in interplanar spacing, d', can be used to differentiate between different materials (if they are strain-free). If a material is subjected to strain, the elongations and contractions within the crystal lattice induce a change in interplanar spacing, causing a diffraction pattern shift. Precise measurement of this shift allows the strain to be quantified. If plane stress is assumed when taking a measurement of peak position, 2θ, within the surface (, i.e. $\sigma_3 = 0$), $n\lambda = 2d'sin\theta$, can be solved for interplanar spacing, d_n, using the known unstrained interplanar spacing, d_0, to obtain the (principal) strain, ε_z (see Equation 2.12). As such, the material's own interatomic planes can be used as internal strain gauges. In the case of conveyance tubes, in order for the plane stress criterion to be met ε_z must be the strain measured along the axial direction (see Figure 2.16). Tilting the specimen allows assessment of planes at any angle, ψ, (measured with respect to the axial direction), and strain to be calculated along that direction using Equation 2.13.

$$\varepsilon_z = \frac{d_n - d_0}{d_n}$$

Equation 2.12

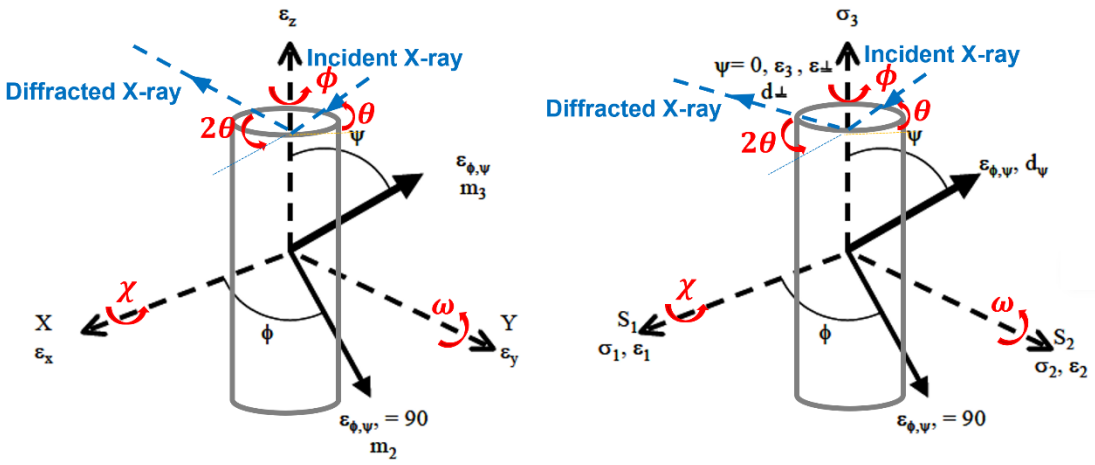


Figure 2.16: Principal axes aligned with tube to obtain plane stress with $\sigma_3 = 0$ in the axial direction [286] (*adapted from source*).

$$\varepsilon_{\psi} = \frac{d_{\phi\psi} - d_0}{d_n}$$

Equation 2.13

Ultimately, the single stress acting along an inclined direction, σ_{ϕ}, can be calculated using elasticity theory for an isotropic solid (see Equation 2.14). Equation 2.14 highlights how stress can be calculated in any direction based on two measurements - the first in the plane normal to the surface and the second in the plane containing the direction of the stress to be measured [286].

$$\sigma_{\phi} = \frac{E}{(1+\nu)\sin^2\psi}\left(\frac{d_{\psi} - d_n}{d_n}\right)$$

Equation 2.14

Finally, assuming zero stress at an interfacial separation of d_n and specimen tilt at $\sin^2\psi = 0$, the stress in a given direction can be expressed as a function of the gradient, m, of the $d - \sin^2\psi$ plot and the material's mechanical properties (see Equation 2.15). Alternatively, a series of equations can be used to predict residual stress and strain using the $\cos\alpha$ method based on a 2D detector capture of the entire Debye-Scherrer (D-S) ring and the azimuthal angle formed between the detector plane and location of the diffracted ray on the D-S ring (see Equation 2.16, Equation 2.17, and Equation 2.18), provided there is not high shear stress on the sample surface under investigation [287] (see Figure 2.17). A sample under residual stress will experience deformation of its D-S ring (either a translation of the ring centre under normal stress or a stretch operation under shear stress). The $\cos\alpha$ method carries the advantage of being able to measure residual strains with only one X-ray exposure so has a

shorter measurement time than the alternative $\boldsymbol{sin^2\psi}$ method, which requires a measurement of interplanar spacing in at least six directions for find its exact solution.

$$\sigma_\phi = \left(\frac{E}{1+\nu}\right) m$$

Equation 2.15

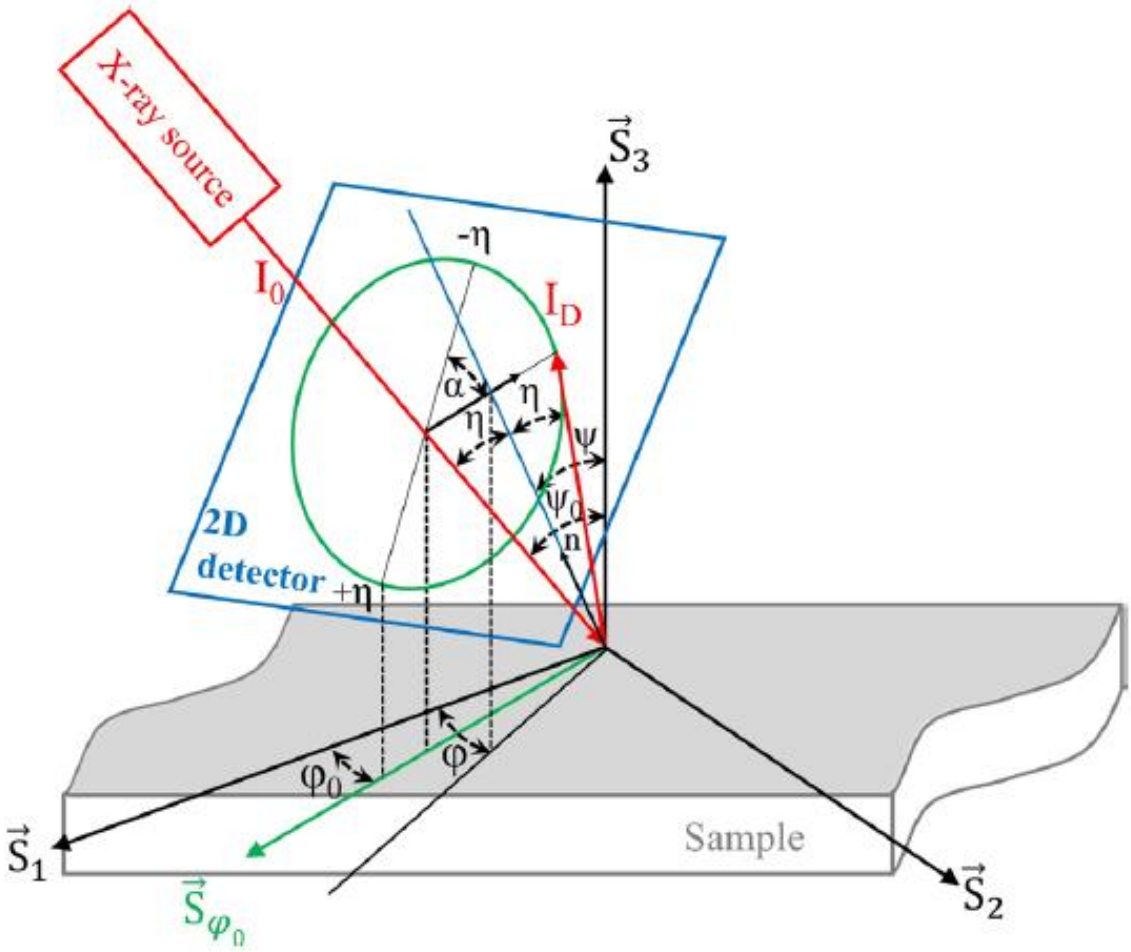


Figure 2.17: The reflection used during the ***cosα*** method [287].

$$\varepsilon = \frac{\Delta d}{d} = -\cot\theta\Delta\theta = (\theta_0 - \theta)\cot\theta_0$$

Equation 2.16

$$\varepsilon_{\alpha 1} = \frac{1}{2}\{(\varepsilon_\alpha - \varepsilon_\pi + \alpha) + (\varepsilon_{-\alpha} - \varepsilon_\pi - \alpha)\}$$

Equation 2.17

$$\sigma_x = -\frac{E}{1+\nu}\frac{1}{\sin 2\eta}\cdot\frac{1}{\sin 2\mu_0}\cdot\left(\frac{\partial\varepsilon\alpha_1}{\partial\cos\alpha}\right)$$

Equation 2.18

During measurement, the sample is usually rotated in the χ (chi) or ω (omega) direction.

Experimental Procedure

Figure 2.18 shows the components of a typical lab-based stress diffractometer comprising the monochromatic X-ray source, primary (components between the X-ray source and sample) and secondary (components between the sample and detector) optics.

The X-ray source is conventionally a typical X-ray tube employing the classic technique of accelerating a focused beam of electrons through a large potential difference to make a high energy collision with a metal anode (the anode selection and thus incident X-ray wavelength being critical for residual stress analysis). When selecting an appropriate anode, the sample fluorescence, diffraction angle, and choice of crystallographic plane must all be considered. Selecting a longer wavelength, such as chromium K-α for iron, ensures the radiation produced does not have enough energy to cause fluorescence. Furthermore, the wavelength selected should maximise the Bragg angle ($2\theta \geq 125°$) to ensure detectability of the strain for such small d-spacing changes (10^{-3} magnitude). The crystallographic plane is important due to the variability in deformation mechanism, i.e. interplanar comparisons are not valid. Hence, measurements made with different radiation wavelengths, i.e. penetration depths, are also not comparable.

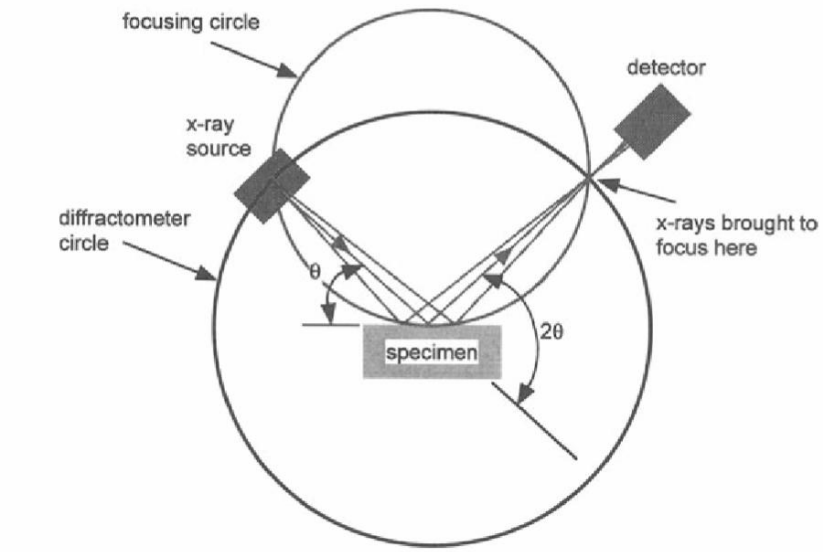


Figure 2.18: Conventional experimental set-up of a laboratory-based diffractometer [288].

Sample preparation was limited to light grinding (rough surface finishes can still be analysed) as X-rays can only penetrate a sample depth of 5-50μm [288] and mechanical preparation techniques can introduce additional surface residual stress. Similarly, any cutting methods should be selected carefully to avoid changing the residual stress state, e.g. Electro Discharge Machining (EDM). Conversely, any heat-related treatment could relax

residual stresses and invalidate results. Relaxation is also possible if measurements are taken too close to the sample edge so a minimum distance of 1mm was maintained between measurement locations and the sample edge, also allowing the sample surface to coincide with the diffraction circle centre of rotation. Finally, although the sample should ideally be flat, the tube samples were still able to be assessed provided the X-ray spot size was small enough in relation to the tube radius of curvature, $\boldsymbol{R_{tube}}$. To measure residual stress with ±10% accuracy, the spot size must be $\frac{\boldsymbol{R_{tube}}}{4}$ and $\frac{\boldsymbol{R_{tube}}}{2}$ for hoop and axial stress measurements respectively [288].

Sample positioning and measurement parameters are also important. Although the formation of the X-ray into a parallel beam reduces the diffractometer's sensitivity to errors, it does not eliminate errors altogether. The largest error source is the $\boldsymbol{d - sin^2 \psi}$ plot but introducing more tilt angles will improve accuracy. Further details of the standardised set-up during XRD-based residual stress analysis can be found in BS EN 15305 [289].

Interfacial shearing stress is induced by the difference in material properties of the steel substrate and external oxide layer (see Section 1.4), thus making deformation compatible for structural integrity. This must be accounted for during XRD data analysis. Existing theoretical descriptions of stress transfer through an interface exclude the tube steel-scale system by a combination of significant difference in stiffness ($\boldsymbol{E_{ox} \ll E_m}$), comparably negligible curvature at the interface scale compared to the overall component curvature, the lack of available data on frictional interfaces, and the non-negligible influence of stress variation across the oxide thickness [290]. Yin et al. therefore proposed an elastic, plane strain analytical model of stress transfer through a fully bonded interface of $\boldsymbol{i}$ layered materials with elastic modulus, $\boldsymbol{E_i}$, and Poisson ratio, $\boldsymbol{\upsilon_i}$ (see Figure 2.19) [290].

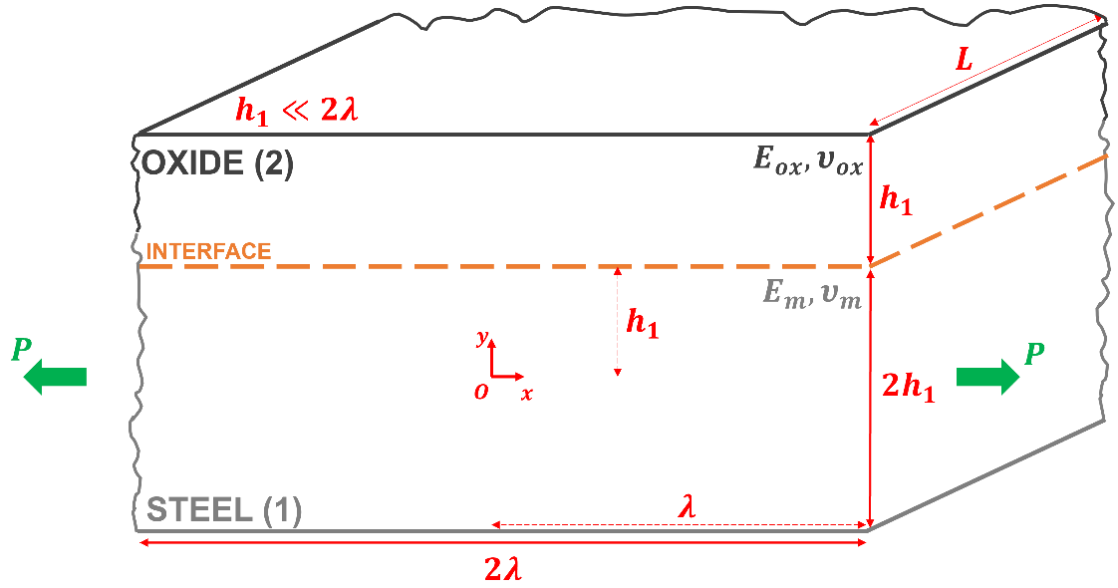


Figure 2.19: Schematic showing fully bonded steel-oxide interface with a layer, h_1, of oxide and a layer, $2h_1$, of steel both with their own respective mechanical properties ¤.

Figure 2.19 shows how, assuming that all points remain in the same plane post-deformation, the substrate is loaded in the x-direction and x-wise deformation, $u_{x,y}$, is therefore much greater than y-wise deformation, $u_{y,x}$, under the same load, P, making the y-wise deformation negligible ($u_{x,y} \gg u_{y,x} \ \therefore u_{y,x} \cong 0$). The plane assumption 2D constitutive laws are shown in Equation 2.19, Equation 2.20, and Equation 2.21, and the 2D equilibrium laws in Equation 2.22.

$$\sigma_{xx} = \frac{E_i}{(1+\nu_i)(1-2\nu_i)}\left[(1-\nu_i)u_{x,x} + \nu_i u_{y,y}\right]$$

Equation 2.19

$$\sigma_{yy} = \frac{E_i}{(1+\nu_i)(1-2\nu_i)}\left[\nu_i u_{x,x} + (1-\nu_i)u_{y,y}\right]$$

Equation 2.20

$$\tau_{xy} = \frac{E_i}{2(1+\nu_i)}u_{x,y}$$

Equation 2.21

$$\frac{\partial \sigma_{ij}}{\partial x_j} + F_i = 0$$

Equation 2.22

Solving for displacement is achieved by obtaining a decoupled partial differential equation (PDE) by assuming that there is no body force (per unit volume), $\boldsymbol{F_x = 0}$, at equilibrium (see Appendix 17). The PDE can be solved using the separation of variables technique to obtain the general solution in Equation 2.23 based on layer-specific constants, $\boldsymbol{A_i, B_i, C_i, D_i}$, and including an $\boldsymbol{\varepsilon_x{}^u}$ uniform strain term due to $\boldsymbol{P}$. The general solution can also be used to solve the $\boldsymbol{y}$-direction governing equation and obtain Equation 2.24 which contains boundary condition-determined functions $\boldsymbol{f_i(x)}$ and $\boldsymbol{g_i(x)}$.

$$\boldsymbol{u_x(x,y) = (A_i \sin d_i y + B_i \cos d_i y)(C_i \sinh cx + D_i \cosh cx) + \varepsilon_x^u x}$$

$$\boldsymbol{d_i = c\sqrt{\frac{2(1-v_i)}{1-2v_i}}}$$

Equation 2.23

$$\boldsymbol{u_y = -\frac{1}{2(1-v_i)} \int u_{x,x} dy + f_i(x) y + g_i(x)}$$

Equation 2.24

The steel-scale system is a two-layer system (steel substrate = layer 1, oxide 'coating' = layer 2). Yin and Prieto-Munoz identified layer 1's boundary conditions as no displacement in the $\boldsymbol{x}$-direction ($u_x|_{x=0} = 0$), and no y-wise shear stress on the $\boldsymbol{x}$-plane ($\boldsymbol{\tau_{xy}}\big|_{\boldsymbol{y=0}} = 0$) [290]. To obtain a fully closed elastic solution to the general solution proposed above for layer displacement, four further interfacial continuity boundary conditions must be defined. Namely, the displacements and stresses at the interface ($y = 0$) are equal: $\boldsymbol{u_x{}^1|_{y=0} = u_x{}^2|_{y=0}, \tau_{xy}{}^1|_{y=0} = \tau_{xy}{}^2|_{y=0}, u_y{}^1|_{y=0} = u_y{}^2|_{y=0}, \sigma_{yy}{}^1|_{y=0} = \sigma_{yy}{}^2|_{y=0}}$.

Assuming a defect-free oxide, the stress transfer from the significantly thicker substrate, $\boldsymbol{\sigma_{fo}}$, to the oxide, $\boldsymbol{\sigma_{so}}$, is given by Equation 2.25, where,

$\boldsymbol{K_{combined}}$, is a parameter based on the combined mechanical properties of the substrate and oxide [291, 292]. During scaling of any variable, the standard deviation will also be scaled by the same value [293] and this is therefore reflected in standard deviations associated with oxide stress.

$$\boldsymbol{\sigma_{fo} = K_{combined} \sigma_{so}, where\ K_{combined} = \frac{E_{ox}}{E_m} \frac{1 - v_{ox} v_m}{1 - v_{ox}{}^2}}$$

Equation 2.25

2.1.8 White Light Interferometry

White Light Interferometry (WLI) is a useful technique for non-contact roughness profiling of specular surfaces at risk of damage from a conventional roughness profile stylus. The technique depends on the ability to observe the interference patterns of interacting coherent (of equal frequency and constant phase difference) waves. The degree of coherence, i.e. fringe visibility, at corresponding pixels in the object images and reference planes, provides the necessary 3D image. Compared to monochromatic light-based interferometry, WLI can achieve 3D measurements of discontinuous surfaces with a large range and high precision to a resolution of 0.01nm and 0.1nm for height and width respectively with an RMS repeatability of 0.008nm [294]. Collimated light is scanned vertically (along the depth, $\boldsymbol{z}$, axis) at a given point, in steps corresponding to a change in optical path difference of less than a quarter of the shortest wavelength [295]. In this project, Grant's work using WLI to assess surface topography on tube-grade steels is used. Their work used a Veeco NPT9800 optical profiling system with a sampling resolution of 640x480 and sampling length of 3.65μm was used.

2.2 Computational Techniques

For all the computational work performed in this project an offline HP Z1 Tower G1i desktop PC workstation, within the Advanced Imaging of Materials (AIM) facility at Swansea University, was used. This computer is designed for applications such as computer-aided design, visualisation, 3D design and modelling, real-time rendering, and simulation, and has the CPU specification necessary (20 cores) to quickly execute a large number of instructions.

2.2.1 Numerical Integration

2.2.1.1 Crank-Nicolson Scheme

Fully implicit numerical schemes are used to solve linear systems of algebraic equations for all unknown nodes at a given timestep, such as the diffusion equation (see Equation 1.31) which is a partial differential equation (PDE). For a function $\boldsymbol{f} = \boldsymbol{f_{i,j}}$ in space-time ($\boldsymbol{x} - \boldsymbol{t}$) (see Figure 2.20) with the basic form $\boldsymbol{a}\frac{\boldsymbol{\partial^2 f}}{\boldsymbol{\partial x^2}} = \boldsymbol{b}\frac{\boldsymbol{\partial f}}{\boldsymbol{\partial t}}$ (where $\boldsymbol{a}$ and $\boldsymbol{b}$ are numerical coefficients) and known initial, $\boldsymbol{f(x, 0) = g(x)}$, and boundary conditions a numerical solution is possible. In Figure 2.20, each node in the $[\boldsymbol{i, j}]$ position represents the value of function $\boldsymbol{f_{i,j}}$ (see Figure 2.20). The Crank-Nicolson (CN) scheme [88] scheme uses a central difference

term [296] for the second space derivative (made implicit by the inclusion of the weighted average of the function at the jth and jth+1 position), $\frac{\partial^2 f}{\partial x^2}$, (see Equation 2.26 and Equation 2.27) and a forward difference term [296] for the time derivative, $\frac{\partial f}{\partial t}$ (see Equation 2.28). Each node in the $[i,j]$ position represents the value of function $f_{i,j}$ (see Figure 2.20).

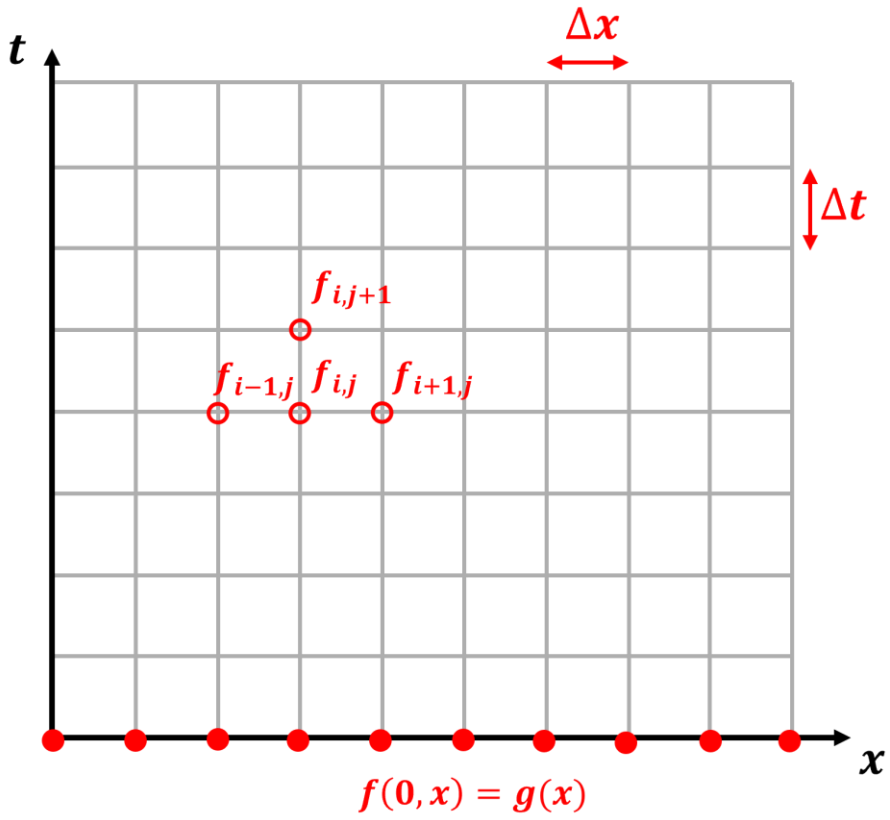


Figure 2.20: Schematic of the Crank-Nicolson (CN) scheme. Discretisation of the space-time ($x-t$) domain, to numerically determine the value of function, f, at nodes i and j, is achieved using finite difference expressions ¤.

$$\frac{\partial f}{\partial x} = \frac{f_{i+1,j} - f_{i-1,j} + f_{i+1,j+1} - f_{i-1,j+1}}{4(\Delta x)}$$

Equation 2.26

$$\frac{\partial^2 f}{\partial x^2} = \frac{f_{i+1,n} - 2f_{i,n} + f_{i-1,n} + f_{i+1,n+1} - 2f_{i,n+1} + f_{i-1,n+1}}{2(\Delta x)^2}$$

Equation 2.27

$$\frac{\partial f}{\partial t} = \frac{f_{i,j+1} - f_{i,j}}{\Delta t}$$

Equation 2.28

Once discretised, the system can be solved using Gaussian elimination [297].

2.2.1.2 Composite Simpson's Rule

Simpson's rule approximates a function, $\boldsymbol{f(x)}$, in a defined interval, $[\boldsymbol{a}, \boldsymbol{b}]$, by fitting a quadratic parabola (see Equation 2.29) through three known points at the beginning, $\boldsymbol{f(a)}$, mid-point, $\boldsymbol{f(m)}$, and end, $\boldsymbol{f(b)}$, of the interval (see Figure 2.21) [298].

$$\boldsymbol{f(x) = ax^2 + bx + c}$$

Equation 2.29

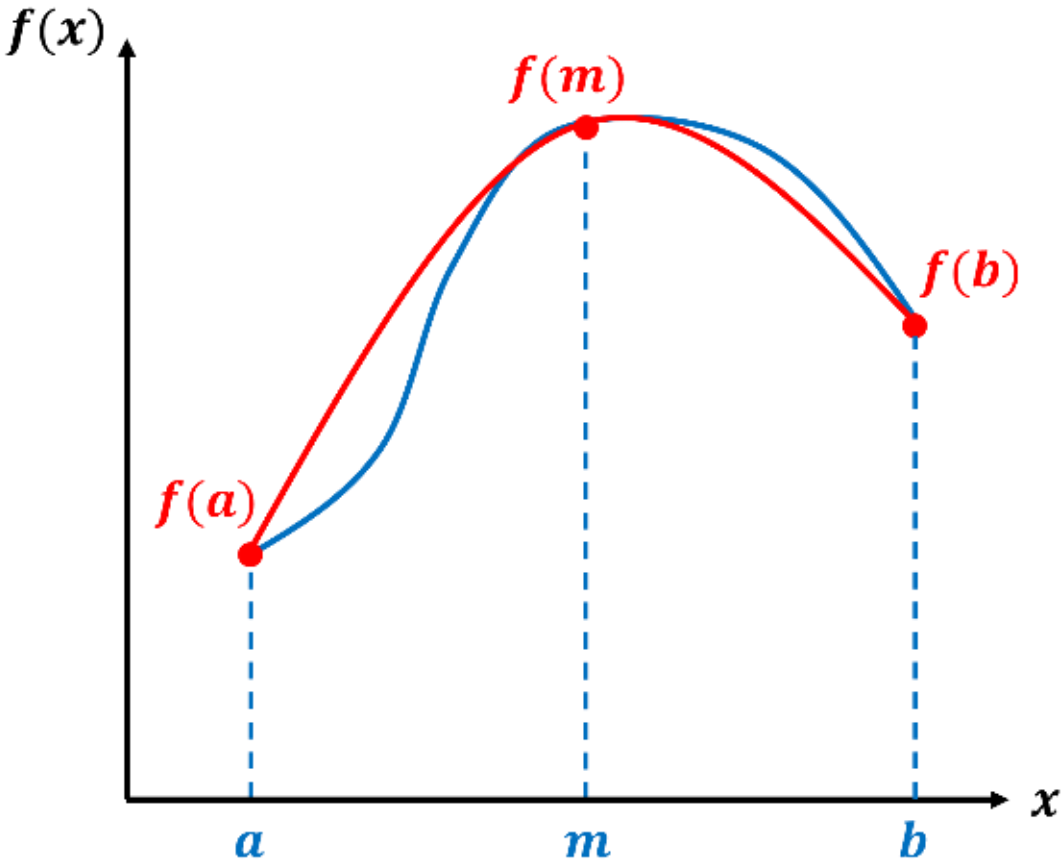


Figure 2.21: Graphical representation of Simpson's rule ¤.

The integral of the quadratic in Equation 2.29 is equivalent to the expression in Equation 2.30 and can hence be used to approximate the integral of a function, $\boldsymbol{f(x)}$.

$$\int_{a}^{b} \boldsymbol{f(x)\, dT} = \frac{\boldsymbol{b-a}}{\boldsymbol{6}} \cdot \boldsymbol{(f(a) + 4f(m) + f(b))}$$

Equation 2.30

The accuracy of the approximation can be made by applying the composite Simpson's rule and dividing the interval $[\boldsymbol{a}, \boldsymbol{b}]$ into a number, $\boldsymbol{N = 2n}$, of subintervals of width, $\boldsymbol{h}$ (see Figure 2.22). The sum of applying the Simpson's rule for each interval is given by Equation 2.31, i.e. the composite Simpson's rule (see Equation 2.31) [298].

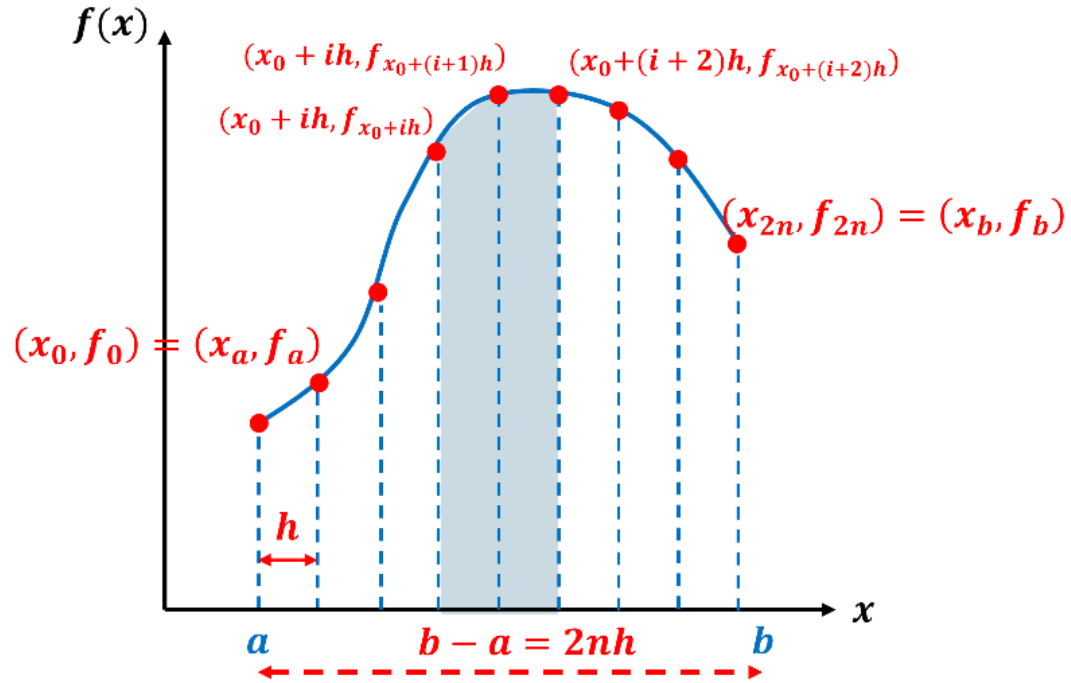


Figure 2.22: Graphical representation of composite Simpson's rule ¤.

$$\int_a^b f(x)\,dT = \frac{h}{3}(f_0 + 4f_1 + 2f_2 + 4f_3 + 2f_4 + \cdots + 4f_{n-1} + f_n)$$

$$where\ h = \frac{b-a}{2n}$$

Equation 2.31

The Composite Simpson rule error bound, ξ, is defined by the fourth derivative of the integrand function (see Equation 2.32) [298].

$$\xi \leq \frac{h^5}{2880N^4} f^4(x)$$

Equation 2.32

2.2.2 CALPHAD and Gibbs Free Energy Minimisation

The CALPHAD methodology can obtain a feasibility description for alloy system reactions and their most likely phase product (such as potential mixed oxides from oxidation-resistant coating interaction with the Fe-C system) via the Second Law of Thermodynamics and a Gibbs Free Energy minimisation [90, 205, 299]. The details of the Gibbs Free Energy Minimisation technique were first defined in the work of Gordon and McBride [300]. However, the technique is fundamentally based on the concept that a spontaneously reacting system will obey the Second Law of Thermodynamics (to increase overall universe entropy) and reach maximum total entropy (combining the system and surroundings) [300].

Movement in any direction in the composition space, i.e. to a different mole fraction value, $\boldsymbol{x}$, of a species, will violate the Second Law by causing an entropy decrease (for a given temperature, $\boldsymbol{T}$) [300]. In this state, the system has reached equilibrium and Gibbs energy reaches a minimum value. Equation 2.33 shows how enthalpy, $\boldsymbol{u}$, volume, $\boldsymbol{v}$, and entropy, $\boldsymbol{s}$, contribute to the Gibbs Free Energy Function, $\boldsymbol{g}$, (at a constant pressure and temperature) and thus how the functions provides a complete thermodynamic description of a system.

$$\boldsymbol{du + Pdv - Tds = dg \ \leq 0 \ (for\ an\ isobarothermal\ system)}$$

Equation 2.33

Such a system relies on a comprehensive thermodynamic database for all the elements concerned (obtained via experimental, analytical, empirical, and machine learning techniques) which undergoes assessment, model selection, optimisation, storage, and validation (see Figure 2.23).

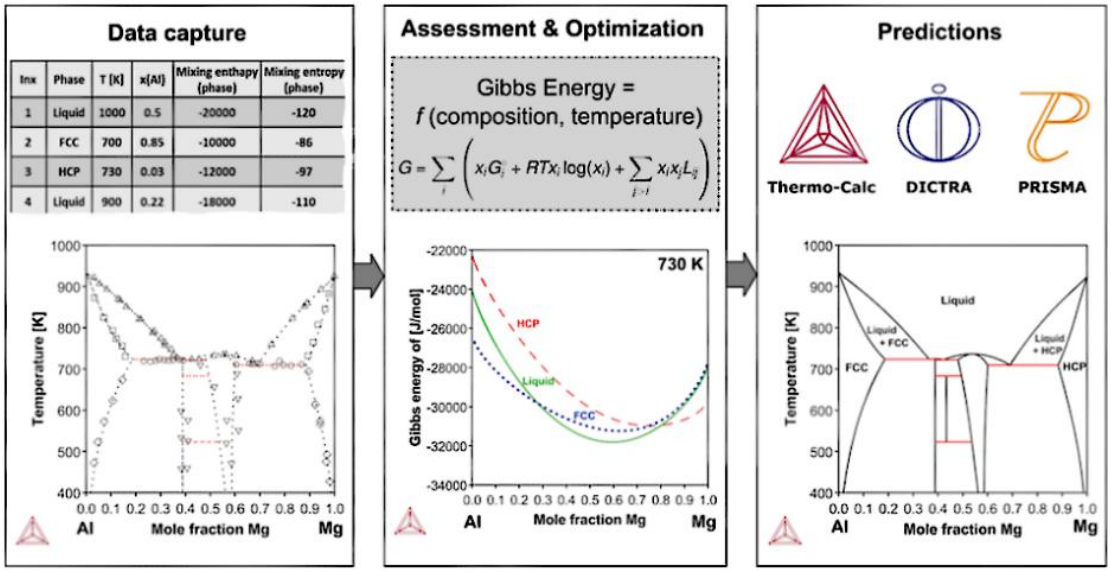


Figure 2.23: Schematic showing the process of Gibbs Free Energy Minimisation in the context of Thermo-Calc© [301].

2.2.3 Moving Phase Boundary Methodology

Hallstrom et al. presented a comprehensive demonstration of how oxidation kinetics (specifically oxide thickness growth rate) can be computationally predicted [234]. They used Thermo-Calc©'s Diffusion Module ('DICTRA') to numerically solve the 1D diffusion equation, i.e. for a planar geometry. Diffusion is relevant because when two phases have a different composition, transition between the two must be accompanied by diffusion of species in either one or both phases [302]. Xia et al. argue that the use of 1D system ignores the realistic 2D composition distribution of the material and restricts diffusion coefficient

calculations to fixed compositions or those that only vary compositionally in a single direction [303]. However, when only diffusion across a phase boundary is under investigation, the diffusion is inherently 1D and symmetry makes the 1D simulation more computationally effective to accurately represent the real-life situation in the modelling domain (see Equation 2.35).

$$\frac{\partial c_k}{\partial t} = div(-J_k)$$

Equation 2.34

$$\frac{\partial c_k}{\partial t} = \frac{\partial}{\partial x}(-J_k)\ (for\ a\ 1D\ geometry)$$

Equation 2.35

Since both species flux, $-J_k$, and temporal concentration gradient, $\frac{\partial c_k}{\partial t}$, are unknown variables, Equation 2.34 (mass conservation in the absence of chemical reactions) must be coupled to Equation 2.36 (Fick's 1st Law relating diffusive flux to concentration gradient), which relates flux and spatial concentration gradient, $\frac{\partial c_k}{\partial x}$, via a chemical diffusion coefficient, D.

$$J_k = -D\frac{\partial c_k}{\partial x}$$

Equation 2.36

$$\frac{\partial c_k}{\partial t} = D\frac{\partial^2 c_k}{\partial x^2}$$

Equation 2.37

These two coupled equations derive Fick's Second Law (see Equation 2.37). Computational solutions for the independent flux of metal cations and oxygen anions for the two phases (regions differentiated by substance state and characterised by separate parameter values [304]) defined in Figure 2.24 can be supplied to Equation 2.38, alongside volume and molar fractions which are experimentally (via advanced imaging techniques) and computationally defined (via phase diagram simulations (specifically for the left, i.e. metal, side of the phase boundary) when local equilibrium on either side of the phase boundary is assumed) respectively.

A moving phase boundary ('Stefan problem') formulation [305] for diffusion is used and the output of Equation 2.38 is a description of the migration rate of the boundary between two

phases, i.e. metal and oxide, when the flux of species $\boldsymbol{k}$ out of one phase and into another respectively is not balanced, i.e. $\boldsymbol{J_k^{\alpha} - J_k^{\gamma}} \neq 0$ [306]. The presence of the moving boundary renders this problem non-linear, combining PDEs and complicated interphase geometrical movement, and therefore difficult to find analytical solutions for without oversimplification. It should be noted that a sharp interface approach is applied where local equilibrium assumptions are concerned in this scenario, i.e. chemical potentials are continuous over a zero width interface which separates two different phases. The moving phase boundary approach is most suitable for isobarothermal binary systems where the interfacial compositions are fixed so the numerical efficiency of the approach can be maintained (larger systems require an iterative technique to obtain interfacial compositions) [307]. Thus, oxide thickness, $\Delta\boldsymbol{\delta_{t_{step}}}$, after a given time step, $\boldsymbol{t_{step}}$, can be predicted, and the cumulation of values from each time step shows the time-dependent kinetic trends (for a given temperature).

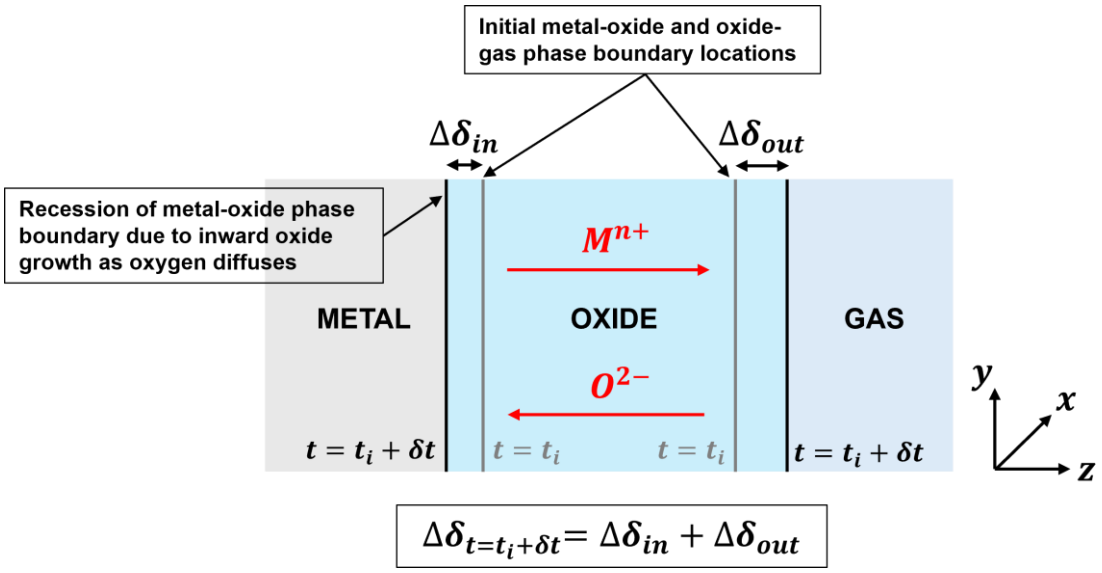


Figure 2.24: Schematic showing the metal-oxide-gas system used to predict oxidation kinetics from diffusion theory ¤.

$$\Delta\boldsymbol{\delta_{t_{step}}} = \boldsymbol{V_m^{\alpha}} \frac{\boldsymbol{J_k^{\alpha} - J_k^{\gamma}}}{\boldsymbol{x_k^{\alpha} - x_k^{\gamma}}} \boldsymbol{t_{step}}$$

Equation 2.38

For simplicity, molar volume, $\boldsymbol{V_m^k}$, is assumed to be constant and identical in both phases under investigation, i.e. $\boldsymbol{V_m^{k_{metal}}} = \boldsymbol{V_m^{k_{oxide}}}$ and $\frac{\partial V_m^k}{\partial t} = \frac{\partial V_m^k}{\partial x} = \mathbf{0}$. This is also true for thermal conductivity, $\boldsymbol{k}$, specific heat capacity, $\boldsymbol{c_p}$, and density. A key assumption is that of an infinitely thin transition region, the free boundary, between the two phases.

Further derivation theory, based on the relationship between species, volume, and molar fractions, concentration, chemical potential, and number of different species per anion site (see [239]), can be applied to Equation 2 to evolve an expression for the overall diffusion coefficient for each species (this is the widely accepted Ågren and Andersson formalism [308]).

2.2.4 Molecular Dynamics

Molecular Dynamics (MD) is used to model the mechanics of many individual atoms, with a known interaction potential, for nanometre and picosecond length and time scales respectively (see Figure 2.25).

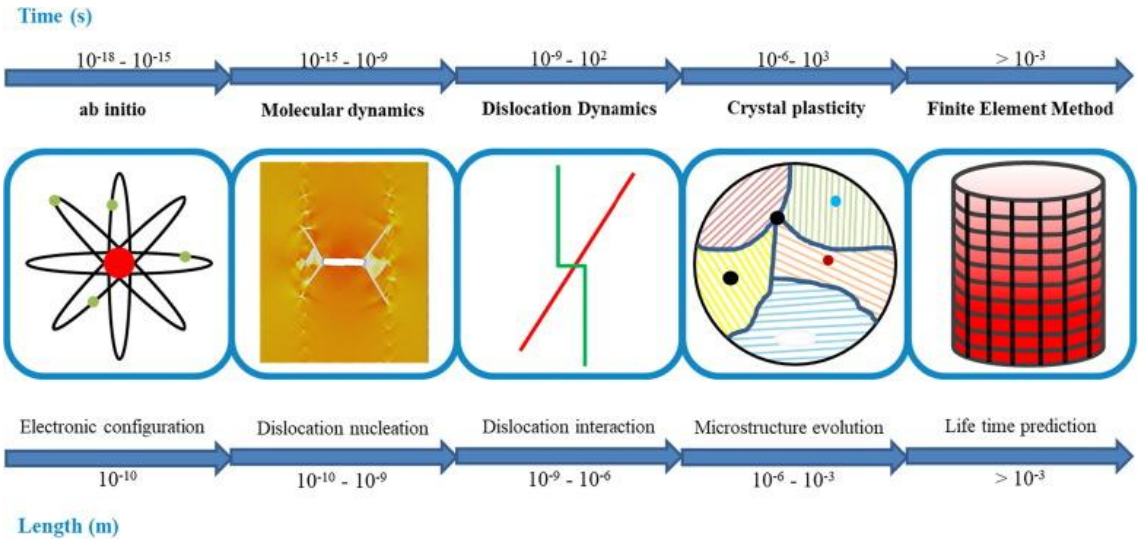


Figure 2.25: Schematic of the time and length scales of mechanical modelling techniques [309].

MD uses the initial position and velocity of the atoms to predict atom trajectory via an integration of Newton's Second Law of Motion (see Equation 2.39 where $\boldsymbol{F}$ is force, $\boldsymbol{m}$ is mass, and $\boldsymbol{a}$ is acceleration) to obtain expressions for position, $\boldsymbol{x}$, and velocity, $\boldsymbol{v}$, as a function of time, $\boldsymbol{t}$ (see Equation 2.40 and Equation 2.41) [309].

$$\boldsymbol{F = ma = m\frac{dv}{dt} = m\frac{d^2x}{dt^2}}$$

Equation 2.39

$$\boldsymbol{v(t) = \frac{x(t) - x(t - \Delta t)}{\Delta t}}$$

Equation 2.40

$$x(t + \Delta t) = 2x(t) - x(t - \Delta t) + a(t)\Delta t^2$$

Equation 2.41

An expression for the interaction of atoms, separated by distance d_{atom}, is given by the interatomic potential, $U_{interatomic}$, which represents a potential 'well' with a minimum stable bond length, σ_{bond}. Interatomic potential comprises an electron cloud (Pauli) repulsion and dipole-dipole (van der Waals) attraction term [310]. Typical potentials used in MD simulations are Lennard-Jones (see Figure 2.26) or Morse potentials [309].

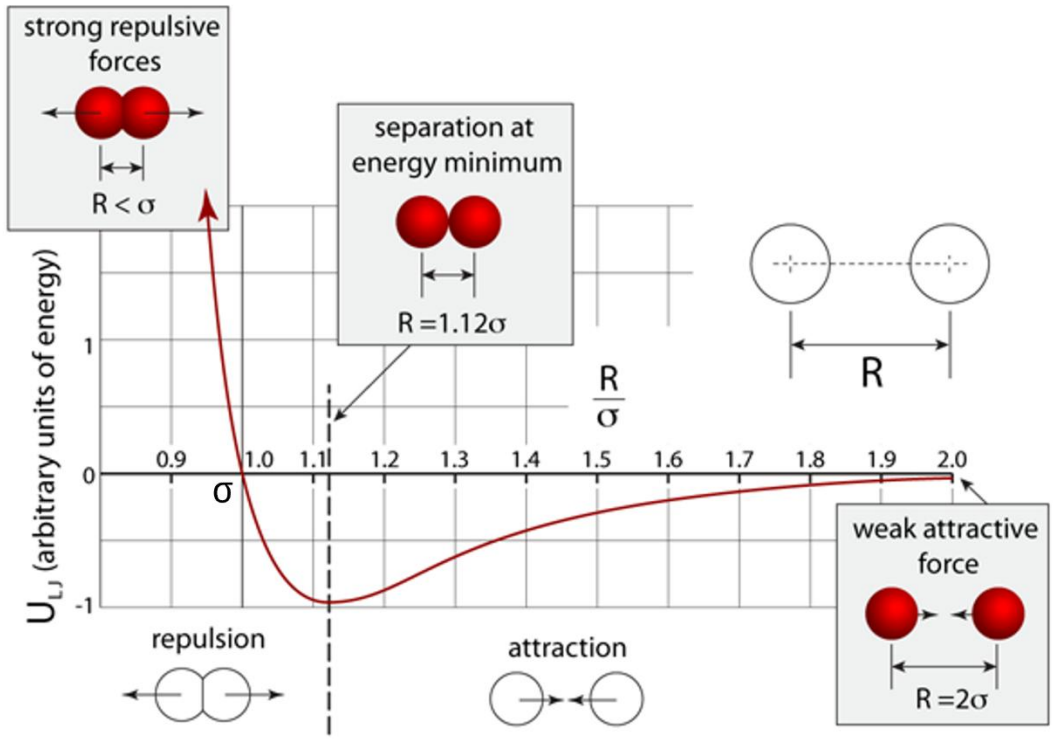


Figure 2.26: Graphical representation of the Lennard-Jones potential, U_{LJ}=$U_{interatomic}$, showing how interatomic repulsion and attraction exist on either side of the minimum energy potential 'well' at a separation, $R = d_{atom}$, of 1.12 times the equilibrium separation, $\sigma = \sigma_{bond}$, (*adapted from source*) [311].

However, Lennard-Jones and Morse potentials are not suitable for ionic bonds [312] and Tersoff potential is the first reported potential in the literature for ionic bonds [313]. In this work, a Tersoff-like atomic bond-order potential (ABOP) is used (see Equation 2.42) where the pair potential energy, $U_{interatomic}$, of two atoms i and j separated by distance, d_{atom}, is described as a function of the attractive, U_A, and repulsive, U_R, pair functions, interaction range cut-off function, $f(c)$, and bond order function, $\overline{b}_{ij}$ [243].

$$\boldsymbol{U_{interatomic} = \sum_{i} \sum_{j>i} U_{ij} = \sum_{i} \sum_{j>i} f_C(r_{ij}) \left[U_R \left(d_{atom_{ij}} \right) - \bar{b}_{ij} U_A(r_{ij}) \right]}$$

Equation 2.42

The force and interatomic potential are connected by Equation 2.43 and as the position and velocity in the system change, so therefore do both force and, in turn, potential.

$$\boldsymbol{F = -\nabla U_{interatomic}}$$

Equation 2.43

At the nanoscale, crystal lattices can allow dislocation motion and interaction, although nanocrack blunting and growth drives the deformation mechanism [309]. The stress response of the system is calculated using the total pressure of the system, $\boldsymbol{P_{ij}}$, based on Equation 2.44, where $\boldsymbol{N_{atom}}$ is the number of atoms, $\boldsymbol{T}$ is temperature, $\boldsymbol{V}$ is volume of the system, subscript $\boldsymbol{a}$ denotes atom, averaged over the number of atoms in the system.

$$\boldsymbol{P_{ij} = \frac{\sum_{a}^{N_{atom}} m_a v_{ai} v_{aj}}{V} + \frac{\sum_{a}^{N} d_{atom_{ai}} \cdot F_{aj}}{V}}$$

Equation 2.44

During uniaxial testing, the tensile test is replicated by freezing and pulling apart the layers of atoms at the top and bottom of the part [309]. The volume is allowed to contract along the axes perpendicular to elongation to ensure a uniaxial test and cell volume continuity. A periodic and non-periodic loading boundary condition is applied to the loading direction and non-loading directions respectively. The atoms move away from each other after each movement step of the frozen crystallographic layers. Initial strain will cause elastic stretching of bonds up to a critical interatomic distance where potential energy drops and there is onset of plastic deformation and, in extreme cases, failure. However, material yield and/or failure is often not observed due to an assumed perfect microstructure and high applied strain rates.

Chapter 3 Development of a Computational Model of Oxidation Kinetics Using Thermo-Calc©

In this chapter, a computational, thermochemical model for predicting oxide kinetics, using a Stefan moving phase boundary problem, is developed in Thermo-Calc® DICTRA diffusion module. Microsoft Visual Studio (VS) Code and Thermo-Calc©'s TDB Editor extension are used to encrypt User-defined thermodynamic and kinetic databases based on compilation of literature data. Microstructural defect theory is incorporated into the databases and used to improve the model representation of the conveyance tube manufacturing process. However, at this stage, a planar geometry is used to simplify the model development process.

With an optimised maximum timestep, the model resolves several hundred spatial data points in approximately two minutes, agreeing well with experimental validation via Simultaneous Thermal Analysis (STA). However, model inaccuracies associated with microstructure, alloy chemistry, stoichiometry, and propagated error during data conversion are identified and addressed to improve agreement between model and experimental values of oxide gain and parabolic rate coefficient. The region of the research flowchart (Figure 1.33) under discussion in this chapter is shown in Figure 3.1.

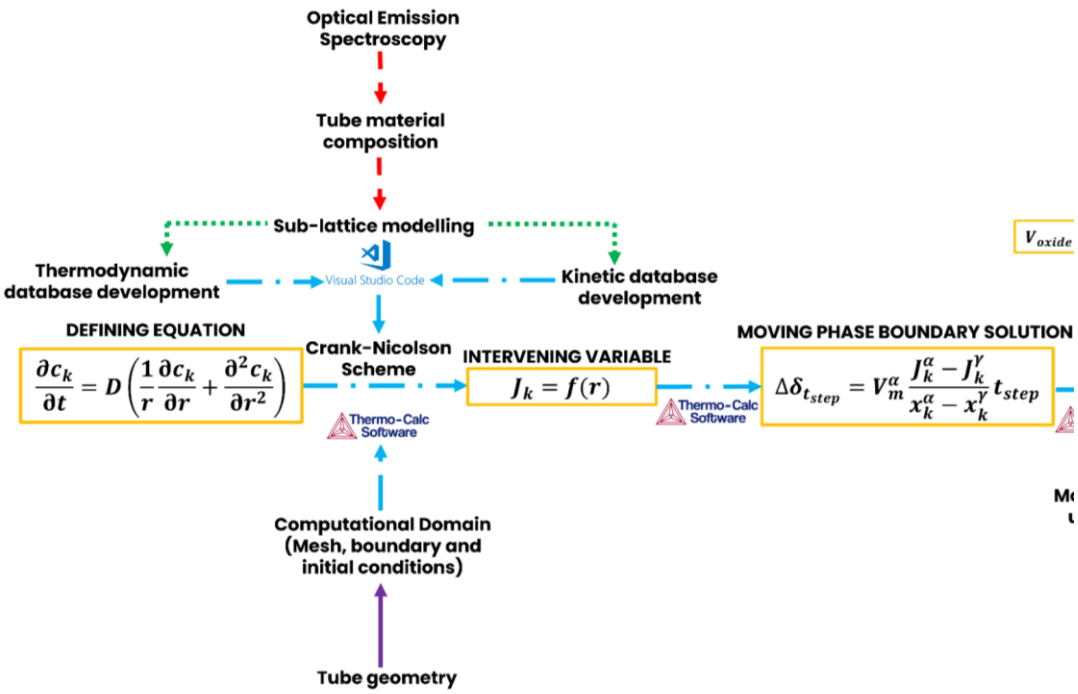


Figure 3.1: Region of the overall research flowchart (see Figure 1.33) which is under discussion in this chapter.

The work in this chapter also contributed to the following peer-reviewed publication:

- M. Kendall, M. Coleman, H. Cockings, E. Sackett, C. Owen, and M. Auinger, "Computational Thermochemistry for Modelling Oxidation During the Conveyance Tube Manufacturing Process," *Metals*, vol. 14, no. 12, December 2024. [Online]. Available: https://doi.org/10.3390/met14121402

3.1 Sample Characterisation

3.1.1 Materials

Test certification reports were provided for the nose crop samples from the TSUK Tubes (Tata) site at Corby [314, 315]. The reports contained the results of a tensile test (yield strength, tensile strength, elongation) performed by Tata to confirm the conformance of tube coil with the minimum yield strength defined in BS EN 10217-2 [4] for weldable steels P235GH and P265GH for high temperature and high pressure applications, which are referred to as 'E41' and 'E24' throughout for simplicity and in line with Tata internal nomenclature [138]. The numerical part of each grade denotes its minimum yield strength, 235MPa and 265MPa respectively, for a tube wall thickness of 16mm or less [30]. Cast composition data from cast analysis (CA) tests for both grades were also supplied within the same reports and are shown in Table 3.1.

Table 3.1: Alloy element composition limits specified by BS EN 10217-2 (Welded steel tubes for pressure purposes - Technical delivery conditions [Part 2: Electric welded non-alloy and alloy steel tubes with specified elevated temperature properties]) [4] for steel grades P235GH ('E41') and P265GH ('E24'), compared to cast analysis (CA) results performed on-site at TSUK Tubes [314, 315]. '×' indicates no limit data given in BS EN 10217-2. Several elements have been redacted ('[redacted]') to protect the exact steel composition identity of TSUK Tubes' product.

		Composition including permissible deviation stipulated by BS EN 10217-2 (%wt of element)							
Grade		**C**	**Si**	**Mn**	**P**	**S**	**Cr**	**Mo**	**Ni**
E41	*BS EN 10217-2*	≤0.16+0.02	≤0.35+0.05	≤1.20±0.10	≤0.025+0.005	≤0.020+0.005	≤0.30+0.05	≤0.08+0.03	≤0.30+0.05
	CA	0.10	0.01	0.45	0.012	0.01	[redacted]	[redacted]	[redacted]
E24	*BS EN 10217-2*	≤0.20	≤0.40	≤1.40	≤0.025	≤0.020	≤0.30	≤0.08	≤0.30
	CA	0.13	0.16	0.79	0.012	0.008	[redacted]	[redacted]	[redacted]
		Al	**B**	**Cu**	**N**	**Nb**	**Sn**	**Ti**	**V**
E41	*BS EN 10217-2*	≤0.020+0.005	×	≤0.03+0.05	×	≤0.010+0.005	×	≤0.03+0.01	≤0.02+0.01
	CA	[redacted]	[redacted]	[redacted]	[redacted]	[redacted]	[redacted]	[redacted]	[redacted]
E24	*BS EN 10217-2*	≤0.020	×	≤0.03	×	≤0.010	×	≤0.03	≤0.02
	CA	[redacted]	[redacted]	[redacted]	[redacted]	[redacted]	[redacted]	[redacted]	[redacted]

Figure 3.2 and Figure 3.3 shows the geometry and nominal strength and ductility values of the tube products manufactured from grades E41 and E24 respectively, as well as the dimensions of the nose crop samples in their as-received form. Figure 3.4 contains photographs of these samples.

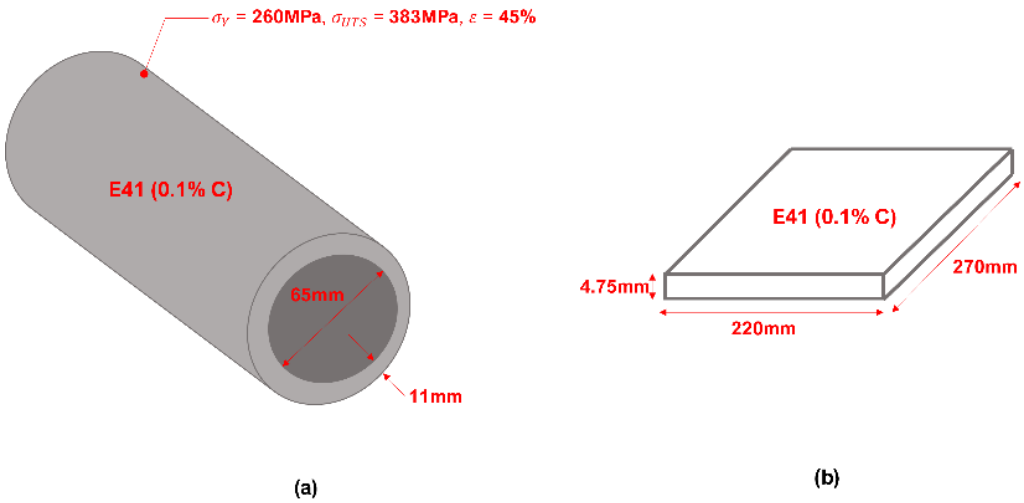


Figure 3.2: Schematics of (a) tube product and (b) as-received nose crop samples of E41 grade steel, annotated with dimensions, carbon content, and mechanical properties (yield strength, σ_Y, ultimate tensile strength, σ_{UTS}, and ductility, ε) ¤.

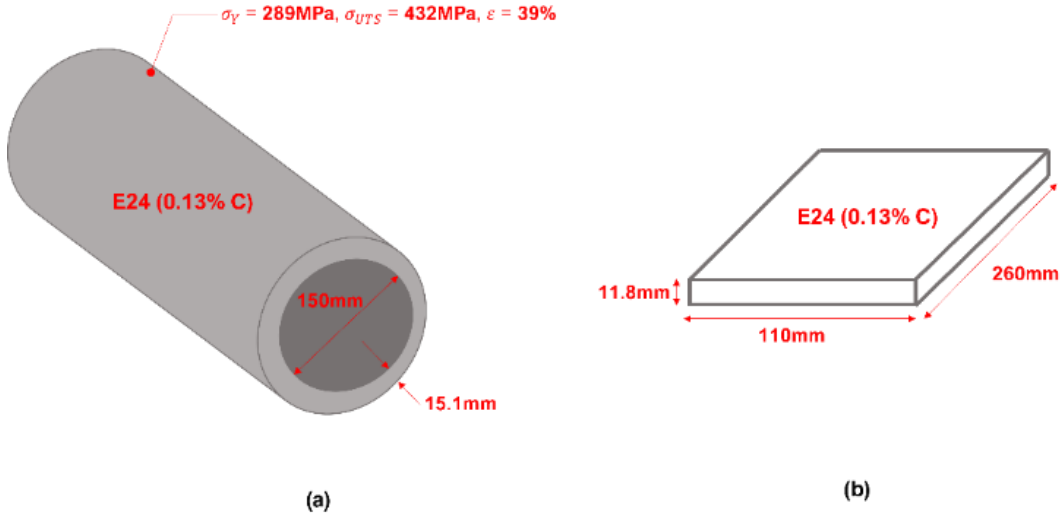


Figure 3.3: Schematics of (a) tube product and (b) as-received nose crop samples of E24 grade steel, annotated with dimensions, carbon content, and mechanical properties (yield strength, σ_Y, ultimate tensile strength, σ_{UTS}, and ductility, ε)) ¤.



Figure 3.4: As-received nose crop samples of (a) E24, and (b) E41 ¤.

Accurate modelling of the materials under investigation requires an accurate knowledge of their chemical composition. A 'spark test' was performed using an Optical Emission Spectrometer (see Section 2.1.2). For validation and comparison, the cast analysis (CA) data presented in Table 3.1 were compared with the mean of two OES tests performed on each of the two tube steel grades. Due to the presence of zero values in the boron and titanium contents for the E24 and E41 grades respectively, for E24 the mean OES value was used as the denominator during percentage difference calculations and the CA value for E41. During post-processing, the level to which the difference between OES and CA comparable data points was acceptable was assessed using relative uncertainty, $\boldsymbol{\varepsilon}$, for a given concentration, $\boldsymbol{c}$. Weiss [316] derived a power function for $\boldsymbol{\varepsilon(c)}$ (for alloy contribution) using a linear least squares fit of certified concentrations uncertainties and certified concentrations themselves (see Equation 3.1).

$$\boldsymbol{\varepsilon(c) = -0.401 \log c + 0.191}$$

Equation 3.1

This approach suited the heteroscedastic nature of random uncertainty [317] in GD-OES for multi-matrix applications where concentrations typically span several orders of magnitude. The units of $\boldsymbol{\varepsilon(c)}$ therefore make it easier to assess the statistical significance of the deviation of the OES and CA data. Nelis and Payling [318] produced a calibration curve from the resulting equation (see Figure 3.5). Error bars were added representing the acceptable relative uncertainty associated with the order of magnitude of the % mass content measured. Relative uncertainty between the OES and CA data was calculated using Equation 3.2.

$$Relative\ uncertainty\ (\%) = \frac{Measured\ value - Comparative\ value}{Comparative\ value} \times 100$$

Equation 3.2

In this case, the measured value comes from OES data, and the comparative value comes from CA data. The results of the comparative study are shown in Table 3.2.

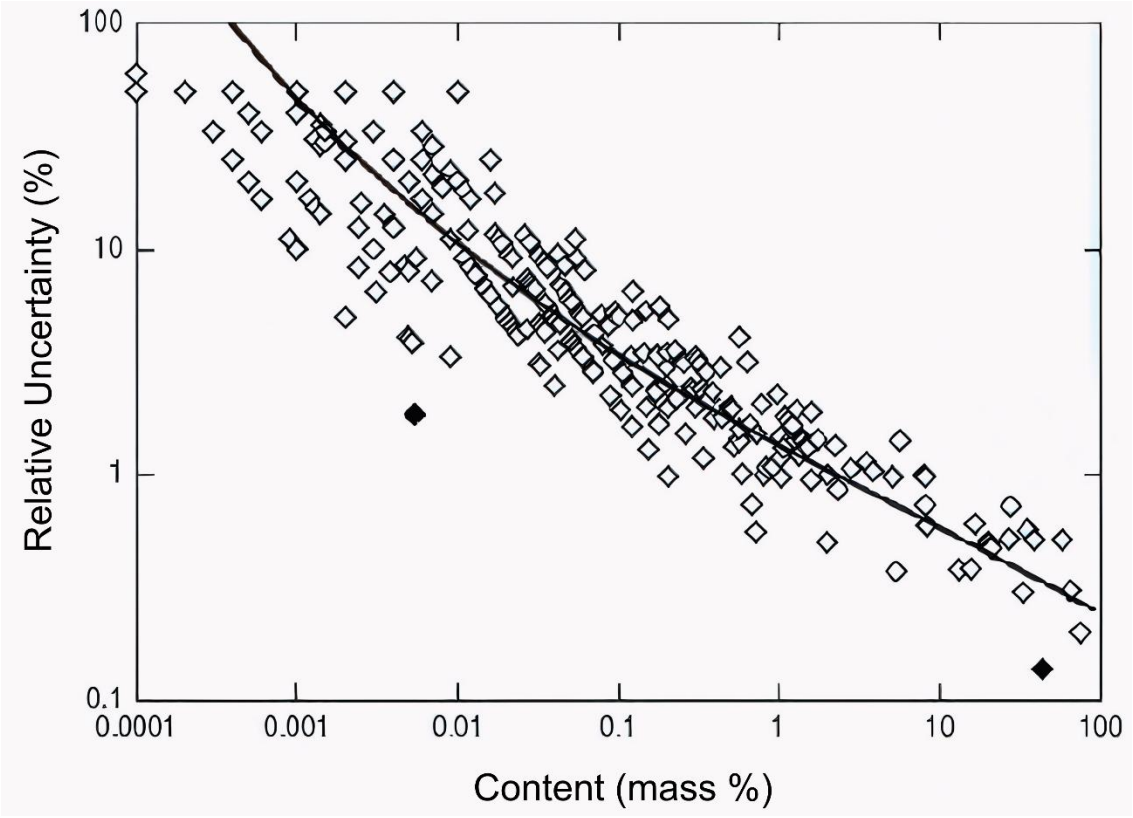


Figure 3.5: Relative uncertainty as a function of % mass content according to Weiss data [316].

E41

For the E41 grade, all alloy contributions fell within the ranges stipulated in BS EN 10217-2 for P195/235GH [4], i.e. the dataset passed its grade analysis test [319], but there was significant variation in percentage difference alloy contribution between the OES and CA values, ranging from 0 to 130%. Tin (Sn) was an outlier at 700% more tin detected by OES than CA. There was no consistency as to whether OES was an overestimate or underestimate where deviation from the CA values did not fall within the uncertainty range stipulated by the Weiss data (as described above). The problematic elements for E41 were silicon (Si), chromium (Cr), nickel (Ni), aluminium (Al), tin (Sn), copper (Cu), niobium (Nb), and vanadium (V). The greatest alloy contribution came from manganese (Mn), followed by aluminium (Al) and copper (Cu) (excluding carbon as the main steel-defining alloy element).

E24

Similarly, for the E24 grade, all alloy contributions fell within the ranges stipulated in BS EN 10217-2 [4] for P295GH, i.e. the dataset passed its grade analysis test [319], but there was significant variation in percentage difference alloy contribution between the OES and CA values, ranging from 0 to 105%. Niobium (Nb) was an outlier as 400% more was detected by OES than CA. There was no consistency as to whether OES was an overestimate or underestimate where deviation from the CA values did not fall within the uncertainty range stipulated by the Weiss function. The problematic elements were carbon (C), silicon (Si), manganese (Mn), phosphorous (P), chromium (Cr), nitrogen (N), niobium (Nb), tin (Sn), and titanium (Ti). The greatest alloy contribution came from manganese (Mn), followed by silicon (Si) and aluminium (Al) (excluding carbon as the main steel-defining alloy element). Thus, silicon plays a more significant role in E24 than E41 (ten times greater percentage contribution in E24 than E41). There was also twice as much manganese in E24 as in E41.

Table 3.2: Sample composition data, obtained via optical emission spectroscopy (OES), for the two steel grades used for conveyance tubes, P265GH ('E24') and P235GH ('E41'). Uncertainty in the OES data was calculated using Weiss' data and Nelis and Payling's calibration curve [316]. The OES data was compared to cast analysis (CA) data from TSUK Tubes. Several elements have been redacted ('[redacted]') to protect the exact steel composition identity of Tata's product.

Element	wt%					
	E24			E41		
	OES		CA	OES		CA
C	0.1030	±0.0052	0.1300	0.0940	±0.0094	0.1000
Si	0.1800	±0.0090	0.1600	0.0230	±0.0023	0.0100
Mn	0.9970	±0.0199	0.7900	0.4560	±0.0228	0.4500
P	0.0169	±0.0017	0.0120	0.0110	±0.0011	0.0120
S	0.0056	±0.0042	0.0080	0.0090	±0.0068	0.0100
Cr	[redacted]		[redacted]	[redacted]		[redacted]
Mo	[redacted]		[redacted]	[redacted]		[redacted]
Ni	[redacted]		[redacted]	[redacted]		[redacted]
Al	[redacted]		[redacted]	[redacted]		[redacted]
B	[redacted]		[redacted]	[redacted]		[redacted]
Cu	[redacted]		[redacted]	[redacted]		[redacted]
N	[redacted]		[redacted]	[redacted]		[redacted]
Nb	[redacted]		[redacted]	[redacted]		[redacted]
Sn	[redacted]		[redacted]	[redacted]		[redacted]
Ti	[redacted]		[redacted]	[redacted]		[redacted]
V	[redacted]		[redacted]	[redacted]		[redacted]

A potential explanation for the significant variation between GD-OES and CA data, outside the acceptable values defined by Weiss, could be the GD-OES technique itself. Pauna et al. [262] cite several reasons. Firstly, they remark that arc or spark movement can be erratic, leading to variation in sample test location which could have small fluctuations in alloy content and thus spectral intensity. However, this phenomenon is most prevalent for OES measurements performed on non-homogeneous samples and is nevertheless mitigated against by capturing data at multiple positions for a short period. However, instability in the plasma, which is already a complex environment with many potentially unknown simultaneous physical phenomena, can also arise from an unclear view of the light source for the spectrometer or too much atmospheric interaction during light propagation between

the source and spectrometer. Finally, reflection and interference phenomena can affect accuracy.

Review of the literature showed silicon to be an element of key interest during studies of oxide scale kinetics and adhesion (the main aspects of this project alongside the effect of geometry) [170, 172]. Furthermore, silicon is one of the key alloy elements which contribute to enhanced mechanical properties in steel grades [169]. However, the mechanical enhancement from silicon is limited situations where ferrite is the dominant phase, since silicon contributes to its stability but can also promotes the formation of softer martensite inclusions which deplete the bulk material hardness [56, 173]. Since it would be impossible to discuss every element in sufficient detail whilst prioritising the tubes aspect of this project, and as silicon makes one of the greatest contributions and highest difference in contribution between the two grades used by Tata, silicon effects will be a central area of consideration during adhesion investigations. Thermo-Calc© was used to generate a phase diagram of both alloys (see Figure 3.6 and Figure 3.7), including the most prevalent alloy elements (Si, Mn, P, S, Cr), to show how composition can vary with temperature. As discussed for Figure 1.2 (see Section 1.2.1), the Gibbs Free Energy Minimisation-based CALPHAD methodology in Thermo-Calc© favours the formation of the more thermally stable graphite carbide form in both phase diagrams. However, the addition of alloy certain elements, e.g. silicon, also promotes the formation of graphite due to their effect on carbon solubility [320]. Hence, graphite formation extends to a higher upper carbon concentration limit (> 0.4 wt% C) in the alloyed (see Figure 3.6 and Figure 3.7) compared to the pure iron-carbon binary system (see Figure 1.2).

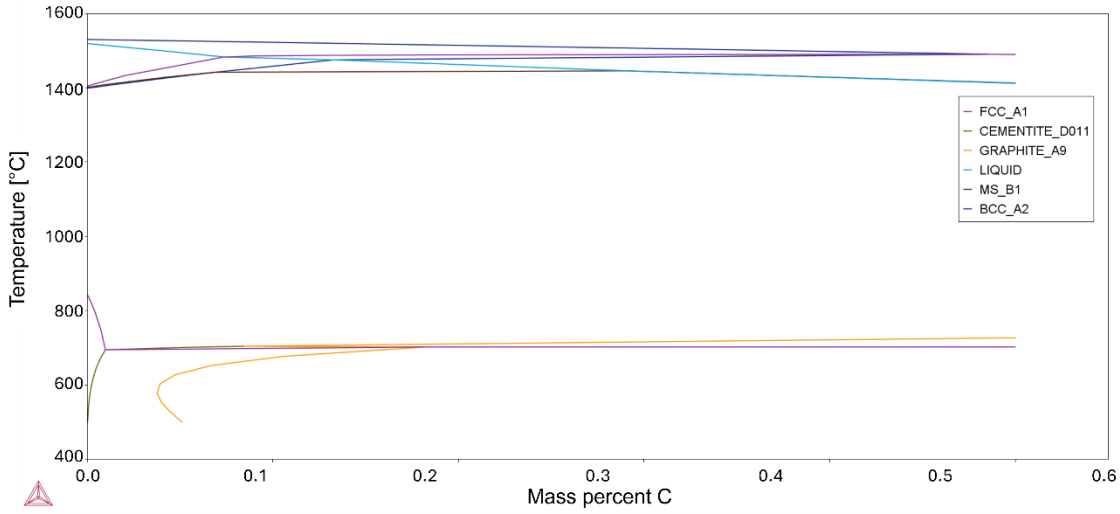


Figure 3.6: Phase diagram, generated using Thermo-Calc©, up to 0.5 mass percent carbon (0.5 wt% C) in E24 (P265GH). The major (by mass percent) alloying elements silicon (0.1800 wt% Si), manganese (0.9970 wt% Mn), phosphorous (0.0169 wt% P), sulphur (0.0056 wt% S), chromium (0.0310 wt% Cr) contributions were included based on the Optical Emission Spectroscopy results shown in Table 3.2. The carbon content measured was 0.1030 wt% C ¤.

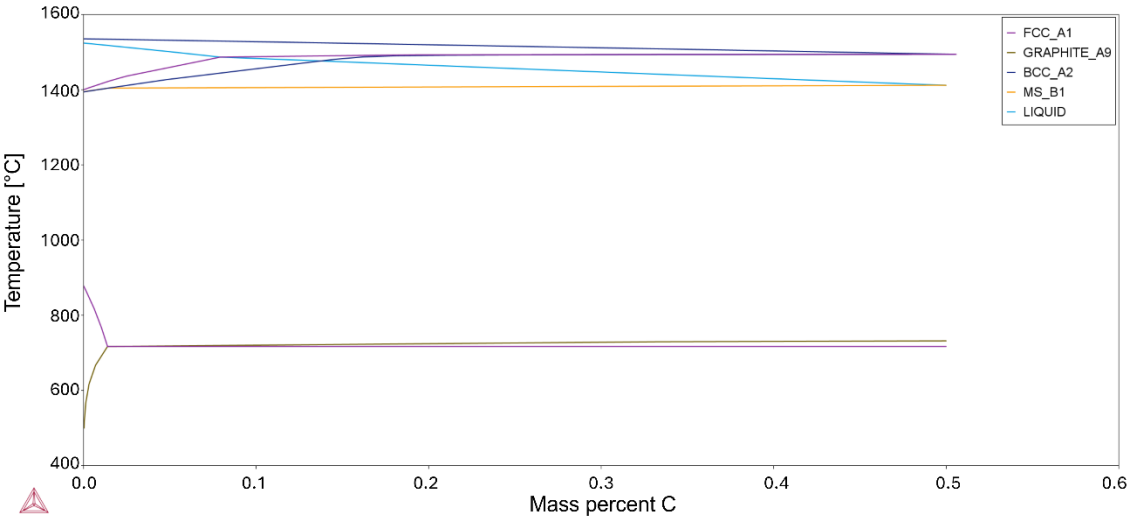


Figure 3.7: Phase diagram, generated using Thermo-Calc©, up to 0.5 mass percent carbon (0.5 wt% C) in E41 (P235GH). The major (by mass percent) alloying elements silicon (0.0230 wt% Si), manganese (0.4560 wt% Mn), phosphorous (0.0110 wt% P), sulphur (0.0090 wt% S), chromium (0.0190 wt% Cr) contributions were included based on the Optical Emission Spectroscopy results shown in Table 3.2. The carbon content measured was 0.0940 wt% C ¤.

3.2 Model Definition and Development

As has been extensively shown in the literature (see Section 1.3.1), the steel oxide scale formed during normalisation comprises three phases. As wüstite (FeO) is typically the dominant phase (95% contribution on average – see Section 1.3.1) in low carbon steel grades such as those used in conveyance tube manufacturing, this phase alone was initially modelled. Furthermore, Grant performed an extensive phase characterisation of the scale formed on P195GH, P235GH, and P265GH during conveyance tube manufacturing at TSUK

Tubes [2, 9]. Grant's work designing an oxidation-resistant coating for conveyance tubes (see Section 1.5.1) demanded a detailed knowledge of phase morphology and used EDS, Raman spectroscopy, and high resolution XRD to show that wüstite is the dominant, stable phase.

Whilst there is scope for the model to complexified to account for more phases, this simplification of the metal-oxide system is reasonable. For real-life applications, the simplification gives tangible results in a timely manner, without excessive computational demands, for a scenario which is challenging to accurately recreate experimentally. There are very limited data for oxide phase properties, all of which carry uncertainty and many of which have dependencies on several parameters, e.g. temperature, partial pressure. By incorporating more oxide phases, the overall confidence in the model would be reduced by the accumulation of all the assumptions of other data sources. It is recognised that the molar volume difference between the oxide phases could induce stress but the difference between the metal and an oxide is more significant and can reasonably be assumed that it will dominate the overall stress generated. For example, the coefficient of linear thermal expansion (CTE) for the metal is 1.4 times that of wüstite at normalisation temperatures, and at lower temperatures, i.e. after cooling, the CTE drops of only 0.4 times that of wüstite [10, 11]. Finally, a bulk diffusion coefficient is used in subsequent simulations as a representative and macroscopic diffusion value which accounts for many of the microscopic mechanisms of atom transport in a solid phase (discussed in Section 1.7).

System Definition

Thermodynamic data for the Fe-O binary system phase diagram calculation, necessary to determine phases present at a given temperature and their relevant mole and mass fractions, was obtained using the TCFE14 database ('Steels/Fe-Alloys'). Composition by mass was calculated from the chemical formula used within molar mass calculations [321] which yielded a composition of 77.8% Fe and 22.2% O. However, composition definition is not necessary within the initial system definition as diffusion theory inherently assumes that composition changes with distance. Furthermore, the region of FeO covers a certain range of iron and oxygen ratios instead of being a strictly stoichiometric compound, like Fe_3O_4 or Fe_2O_3, where the single phase regions are bounded by distinct, straight lines. Instead, initial compositions of oxygen and iron are supplied as left and right interface boundary conditions for each region respectively, i.e. austenite and wüstite, and are obtained from an Fe-O

equilibrium phase diagram generated in the Graphical Mode (see Figure 3.8), using mole fraction values at the Stretch Reduction Mill 2 (SR2) heat treatment temperature of 950°C.

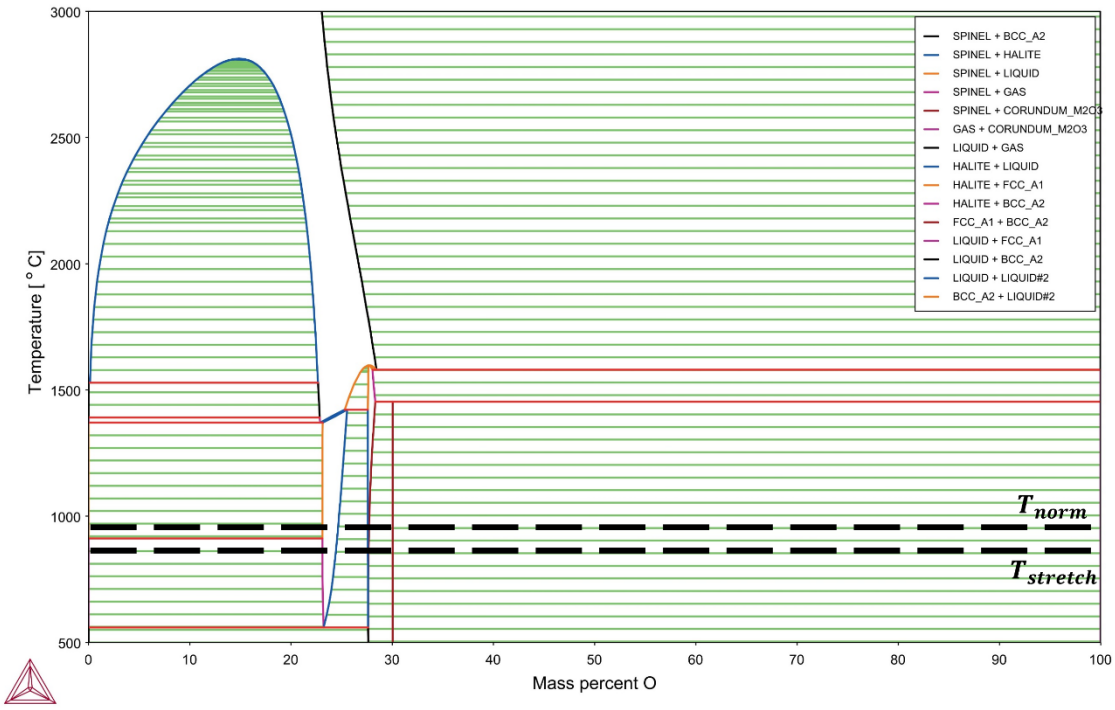


Figure 3.8: Equilibrium phase diagram of Fe-O system with the temperature thresholds for normalisation, T_{norm}, and stretch reduction, $T_{stretch}$, marked at 950°C and 800°C respectively ¤.

The SR2 Mill was selected for modelling in the first instance due to TSUK Tubes' contemporary transition from a partial gas barrel furnace heating approach to a fully induction based [158]. Pre-transition, tubes were heated to 750°C in the gas barrel furnace before completing full normalisation to 1000°C using induction heating. Only E41 is used in the SR2 mill. Composition can only vary along one spatial coordinate and only substitutional elements contribute to volume [307]. Thus, composition gradients for oxygen and iron in austenite and halite respectively were required from the phase diagram assessment. For the overall system of finite volume cells, composition gradients are only considered between cells rather than inside. The metal and scale regions are joined by a finite interfacial region comprising two cells (one from each region). Local equilibrium is assumed to hold between the two regions, with constant volume fractions of each phase. This is a critical assumption which allows the binary phase diagram tie line to be used to determine mole fraction values. If a ternary (or larger) system to be considered, a more complex approach to determining compositions at local equilibrium would be necessary [322].

3.2.1 User-defined Thermodynamic and Kinetic Databases

In the Graphical Mode System Definer, it was not possible to define the oxide region in the model as halite, which is the most accurate microstructural representation of the wüstite scale phase [244]. Inspection of the phase and phase composition inventory within the system definer revealed that mobility data, necessary to define diffusion, were not available in the Thermo-Calc© database for common oxide scale sub-lattices (halite, spinel, corundum etc), even in the newest thermodynamic, e.g. TCFE14 [323], and kinetic, MOBFE8 [324], databases. Consequently, oxide modelling using the Thermo-Calc© Graphical Mode was limited to internal oxidation [29] since mobility data was available in MOBFE8 for the diffusion of oxygen in common steel phases, e.g. austenite (FCC), ferrite (BCC). The available phases were BCC_A2, CEMENTITE, FCC_A1, FE4N_LP1, HCP_A3, and LIQUID. No mobility data were available for typical iron oxide phases, e.g. HALITE, SPINEL, CORUNDUM, therefore diffusion in these phases was automatically (and incorrectly) defined by the software as *NONE*. This issue was overcome by using Thermo-Calc©'s Console Mode to input a user-defined (smaller) mobility database (*FeOmob*) from example files supplied by Thermo-Calc©. The user-defined databases were encrypted in Microsoft Visual Studio (VS) Code using Thermo-Calc©'s TDB Editor extension [325]. In response to the lack of thermodynamic and mobility data available in Thermo-Calc© to assess the relevant Fe-O system oxide microstructures, thermodynamic and mobility databases had to be self-defined by the user in console mode. Although the *FeO* and *FeOmob* databases are available as part of the *exi3a* console mode example file in Thermo-Calc© [326], they only contain data for the spinel microstructure, whereas the halite sub-lattice is more appropriate to describe the wüstite phase (see Section 6.1). Thermodynamic and kinetic databases therefore had to be developed from analytical principles and literature data. The *exi3a FeO* and *FeOmob* databases were also used to support the development of the command lines of the user-defined database [326].

The same scientific methodology (system definition, initial and boundary conditions, post-processing etc) applies to the Console as to the Graphical mode, however the User must interact directly with the Command window to input command lines, which allows for greater flexibility with the software functionality, e.g. ability to switch the thermodynamic database to a user-defined one. These command lines can be saved as a *.TCM file.

Andersson et al. [308] developed a well-accepted formalism, aimed at combining thermodynamic and kinetic databases to maximise knowledge, for simple phases (non-

substitutional and/or substitutional-interstitial crystalline phases and disordered liquids) designed to capitalise on the power of the moving phase boundary approach [234] where knowledge of thermodynamic behaviour and volume diffusivities could translate to a deeper understanding of kinetics. The aim of Andersson et al.'s work [308] was to provide a formalism suitable for a model wherein all experimental diffusion information could be analysed. This formalism was used during the development of the user-defined database command lines.

3.2.1.1 Thermodynamic Database

Initial database set up relies on definition of constituent elements (Fe and O in this case along with vacancy and electron additions) in terms of their reference state (298.15K, 1bar) ('Stable Element Reference' - SER), and enthalpy and entropy of formation. Stoichiometric formulae are also needed for each species to include atomic and ionic states as well as compounds (haematite, magnetite, and wüstite). Gibbs Free Energy functions must be defined ready for minimisation which is an essential part of computational thermodynamics. The details of the Gibbs Free Energy Minimisation technique were discussed in Section 1.7. Minimisation of Gibbs Free Energy functions allows prediction of mole fractions in a system in equilibrium. These functions were taken from Sundman [244] and Kowalski and Spencer's [327] works describing the Fe-O system. Crucially, expressions for the wüstite phase, the dominant phase for an oxide scale, were added into the database and based on the function in Equation 3.3. For the expression of Gibbs free energy for wüstite (see Equation 3.3), a conservative upper temperature limit of 3000K was given as no such value was given in Sundman's paper.

$$\boldsymbol{G_{FeO} = -279318 + 252.848T\ -\ 46.12826Tln(T) - 0.0057402984T^2}$$

Equation 3.3

Experimental data is used to define these functions and in the case of molar volumes, $\boldsymbol{V_m^k}$, (defined at the reference state of 298.15K and 1atm) parameters of the linear coefficient of thermal expansion polynomial are empirically determined and the final expression is derived via a simple integration about $\boldsymbol{\Delta T}$ (see Equation 3.4 and Equation 3.5) [240, 328, 329]. This expression is known as the integrated thermal expansivity and is also defined as part of the thermodynamic database. Compared to the FeO database, austenite and wüstite were new entries into the database developed as part of this project, using the derivation

below. Lower temperature bound for expressions are usually taken as 298.15K, though upper bounds varied significantly in the region $3000K \leq \boldsymbol{T} \leq 6000K$.

$$\boldsymbol{V_m}^{\boldsymbol{non-magnetic}} = \boldsymbol{V_0^{non-magnetic}} \boldsymbol{e}^{\int_{T_0}^{T} 3\alpha\, dT} = \boldsymbol{V_0^{non-magnetic}} \boldsymbol{e}^{V_A} \ (\boldsymbol{T_0} = 298.15K)$$

Equation 3.4

$$\boldsymbol{3\alpha = a + bT + cT^2 + dT^3 + eT^{-2}} \ (298.15K \ < \boldsymbol{T} < \boldsymbol{T_m})$$

Equation 3.5

where $\boldsymbol{a, b, c, d}$ and $\boldsymbol{e}$ represent arbitrary, empirically defined constants which were reported by Lu et al. [328]. However, it should be noted that the expressions for each constant will be an approximation which neglects the temperature effect of thermal expansion. In reality, there is a temperature effect on thermal expansivity, $\boldsymbol{V_A}$, but the effect is small in the narrow temperature range investigated in this work.

For austenitic steel ($T_{m,low\ carbon\ steel} = 1537°C$ [10]),

$$a = 6.97895 \times 10^{-5} K^{-1};\ b = c = d = e = 0;\ V_0 = 6.72092 \times 10^{-6} m^3 mol^{-1}$$

$$\therefore \boldsymbol{V_A} = \int_{\boldsymbol{T_0}}^{\boldsymbol{T}} \boldsymbol{3\alpha}\ \boldsymbol{dT} = \int_{\boldsymbol{T_0}}^{\boldsymbol{T}} \boldsymbol{a}\ \boldsymbol{dT} = \boldsymbol{a}(\boldsymbol{T}\ -\ \boldsymbol{T_0})$$

$$V_A = VaT\ -\ V_0 a T_0 = 4.69050 \times 10^{-10} T\ -\ 1.39777 \times 10^{-7}$$

Numerical values are provided to the same degree of accuracy as the empirical data given in [328] used to derive the austenite thermal expansion. As with ferrite in the *exi3a* database, molar volume must be defined for both vacancies (Fe,Va) and oxygen (Fe,O). The presence of oxygen interstitial sites is essential for the solubility which influences oxidation-controlling electrotransport phenomena [330]. Default values of molar volume and integrated thermal expansivity were supplied, as performed in the *exi3a* database. Practice in *exi3a* and literature showed the use of BCC-Fe values as defaults ($\boldsymbol{V_0}$=7x10^{-6}m^3.mol^{-1} and $\boldsymbol{\alpha}$=1.5x10^{-5}K^{-1}) even when austenite is investigated [331, 332]. Note that $\boldsymbol{\alpha}$ is not a function of temperature during default value definition so integrated thermal expansivity, $\boldsymbol{V_A}$, is simply defined by Equation 3.6.

$$\boldsymbol{V_A = 3\alpha\Delta T}$$

Equation 3.6

For oxide phases the magnetic properties of iron must be considered. Its Curie temperature, when ferromagnetic (strong permanent magnetism caused by spontaneous electron spin alignment) to paramagnetic (weak temporary magnetism in the presence of an external

magnetic field) transition occurs, is 780°C [162]. Therefore, normalisation is accompanied by a shift to an overall paramagnetic state [333] and magnetism effects were therefore accounted for via amended phase descriptions of parameter definitions [325]. However, it should be noted that austenite is an antiferromagnetic phase and its shift to paramagnetism is defined by the Néel temperature which, although composition-dependent, is typically near room temperature [333, 334]. This required definition of antiferromagnetic factors and short-range order fraction of enthalpy. As the steel is austenitic at normalisation temperature, with an FCC sub-lattice structure, and antiferromagnetic state, values of -3.0 and 0.28 respectively were applied [326]. Composition-specific magnetism parameters of Curie temperature, $\boldsymbol{T_c}$, and Bohr magneton number, $\boldsymbol{\beta_{Bohr}}$ [335], are also required for the optimisation procedure which is used to calculate the contribution of magnetic ordering to Gibbs energy [326, 335]. Additionally, the Gibbs energy, $\boldsymbol{G}$, which is dependent on enthalpy, $\boldsymbol{H}$, temperature, $\boldsymbol{T}$, and entropy, $\boldsymbol{S}$, were defined (see Equation 3.7) [336]. For wüstite, the first two parameters were replaced by an interaction parameter, $\boldsymbol{L}$, associated with Gibbs energy of interaction.

$$\boldsymbol{G = H - TS}$$

Equation 3.7

Molar volumes and integrated thermal expansivities were also needed for the oxide phases. As with iron, only the reference molar volume is dependent on sub-lattice structure, unlike integrated thermal expansivity which is constant across different structures. However, application of the Gibbs energy pressure-dependency equation (see Equation 3.11 and Equation 3.13 [336]) demonstrates how coefficients of magnetite's Gibbs energy function can simply be applied to the reference molar volume for magnetite to derive its appropriate expression. The derivation depends on the first (see Equation 3.8) and second (see Equation 3.9) law of thermodynamics, where $\boldsymbol{U}$ is the internal energy of the system, $\boldsymbol{Q}$ is the net heat change of the system, and $\boldsymbol{W}$ is the work done by the system [337].

$$\boldsymbol{dU = dQ - dW}$$

Equation 3.8

$$\boldsymbol{dS = \frac{dQ}{T}}$$

Equation 3.9

As well as the expression for enthalpy,

$$\boldsymbol{H = U + PV}$$

Equation 3.10

For a reversible process ($\boldsymbol{dS = 0}$) in an isochoric system ($\boldsymbol{dV = 0}$) with only pressure-volume ($\boldsymbol{P - V}$) work, and where $\boldsymbol{W = PdV}$,

$$dG = dH - TdS - SdT$$

$$dG = dU + VdP + PdV - TdS - SdT$$

$$dG = TdS - PdV + VdP + PdV - TdS - SdT$$

$$\boldsymbol{dG = VdP - SdT}$$

Equation 3.11

Therefore, for a constant temperature ($\boldsymbol{dT = 0}$), Equation 3.12 shows $\Delta\boldsymbol{P}$ is constant but $\Delta\boldsymbol{G}$ changes (as with the coefficient in different sub-lattice structure Gibbs energy functions), $\boldsymbol{V}$ must change, i.e. $\Delta\boldsymbol{G}\ \alpha\ \boldsymbol{V}$. And for a constant reference temperature, $\boldsymbol{T_0}$,

$$\left(\frac{\boldsymbol{\partial G}}{\boldsymbol{\partial P}}\right)_{\boldsymbol{T}} = \boldsymbol{V}$$

Equation 3.12

And for a constant reference temperature, $\boldsymbol{T_0}$,

$$\frac{\boldsymbol{dG}}{\boldsymbol{dP}} = \boldsymbol{V} \therefore \Delta\boldsymbol{G} = \boldsymbol{V}\Delta\boldsymbol{P}\ (\Delta\boldsymbol{G} \propto \boldsymbol{V})$$

Equation 3.13

Assessment of molar volume fraction and integrated thermal expansivity demands knowledge of the physical behaviour of oxide phases, specifically for wüstite.
Unit cell volume was calculated from the cube of the unit cell parameter (see Figure 1.32 and Equation 1.43). For an oxygen anion radius of 1.35Å [29], the unit cell volume was $5.57\text{x}10^{-29}\text{m}^3$. Crystal structure theory also states that FCC unit cells contain four atoms [338]. Although wüstite is non-stoichiometric [241, 242], halite sublattice theory [339] was used to approximate that, if halitic compounds contain one of each constituent, i.e. X + Y → XY, one mole of a halitic compound would contain $\frac{\boldsymbol{A_r}}{\boldsymbol{4}}$ unit cells (where $\boldsymbol{A_r}$ is Avogadro's constant equalling $6.02\text{x}10^{23}\ \text{mol}^{-1}$[340]), totalling a molar volume of $8.38\text{x}10^{-6}\text{m}^3$ for wüstite. For fully stoichiometric wüstite, Hazen and Jeanloz reported a molar volume of 12.05-12.25cm^3 [241].

3.2.1.2 Kinetic Database

Elements, species, constituents and phases in the kinetic database were defined identically to those in the thermodynamic database, using the same data sources. Volume data took a standard value for all relevant volume-contributing substitutional phases (including oxygen gas) of $1x10^{-5}m^3mol^{-1}$ as defined in the Thermo-Calc© database management documentation [325]. Interstitial species ($\boldsymbol{O}$, $\boldsymbol{Fe^{2+}}$, $\boldsymbol{Fe^{3+}}$) were assigned as zero-volume species.

As well as the effects of temperature and concentration on diffusion, magnetic ordering was also considered. For steels, the model used in the mobility database must account for ferromagnetic to anti-ferromagnetic transformation that occurs at the Curie temperature which leads to a deviation of the linear relationship of the iron self-diffusion coefficient and temperature reciprocal, observed in several experiments in the literature [33]. Phase transformations are driven by free energy minimisation whose total value can have a significant magnetic contribution in steels (see Equation 3.14) [341].

$$\boldsymbol{G_{total}} = \boldsymbol{G_{bulk}} + +\boldsymbol{G_{magnetic}} + \boldsymbol{G_{interfacial}}$$

Equation 3.14

The high degree of magnetisation in ferromagnetic ferrite means there is a significant contribution from $\boldsymbol{G_{magnetic}}$ comprising external magnetic field (Zeeman) and demagnetising energies. This requires parameters reflecting the substitutional and interstitial (oxygen species) models of diffusion in the form of ALPHA = 0.3 and ALPHA = 0.6 respectively [325]. In anti-ferromagnetic austenite, the degree of magnetisation is low enough that the contribution of $\boldsymbol{G_{magnetic}}$ falls to 0 [341] and a general diffusion model can be used, i.e. the oxygen diffusion coefficient does not differ from the self-diffusion coefficient by more than an order of magnitude [342]. The key additional data for diffusion modelling enabled by this database were volume per mole of volume carrying species, $\boldsymbol{V_s}$, and the activation enthalpies and pre-exponential factors associated with the Arrhenius forms of diffusivity and mobility [222]. $\boldsymbol{V_s}$ value took a constant value of $1x10^{-5}m^3.mol^{-1}$ as defined by the authors of *FeOmob* in *exi3a*. Data was similarly available within this database for the disordered BCC_A2 (ferrite) and spinel (magnetite) phases. In the case of ferrite, mobility parameters for iron, comprising electrotransport-induced self-diffusion (the movement of atoms within a single phase driven by a thermal or concentration gradient [242]) and chemical diffusion (the mixing of atoms between two different phases driven by a concentration gradient, also known as interdiffusion [222]) were defined according to the temperature-dependent

exponent (see Equation 1.35). The temperature-dependent exponent contributes to the overall mobility equation (see Equation 1.36) used by Thermo-Calc© [343]. Magnetite's parameters were found in the complete Arrhenius form of mobility from [239]. Diffusion parameters for oxygen in iron were defined in the Arrhenius form of diffusivity, $\boldsymbol{D_k}$ (see Equation 1.37) [100, 344]. However, spinel had a more extensive description of mobility parameters within the database to account for the effect of multiple octahedral sub-lattice sites enabling more vacancy place changes to occur. Ferrite was the only phase to have a magnetic diffusion model applied, i.e. the whole diffusion matrix was calculated, due to the significant contribution of magnetic ordering in its ferromagnetic state [33, 222]. The model applied was the same as that applied within the thermodynamic database.

Diffusivity and mobility can be coupled via Equation 1.34 (allowing for suitable substitution of Equation 1.35) to demonstrate how the pre-exponential factor and activation energy are equal for diffusivity and mobility and diffusivity data from the literature can therefore be input as mobility parameters in the kinetic database.

If

$$M_k = \frac{1}{RT} e^{\frac{\phi_k}{RT}}$$

Where $\phi_k = -Q_k + RT \ln M_{k,0}$ and $D_k = RTM_k$.

$$\therefore\ D_k = e^{\frac{\phi_k}{RT}}$$

$$D_k = e^{-\frac{Q_k + RT ln M_{k,0}}{RT}} = M_{k,0} e^{-\frac{Q_k}{RT}}$$

$$\therefore\ D_k = D_{k,0} e^{-\frac{Q_k}{RT}}$$
$$\therefore D_{k,0} = M_{k,0}$$

$$\therefore M_k = \frac{1}{RT} e^{\frac{\phi_k}{RT}} = \frac{M_{k,0}}{RT} e^{-\frac{Q_k}{RT}} = \frac{D_{k,0}}{RT} e^{-\frac{Q_k}{RT}}$$

Data for the FCC_A1 (austenite) phase (iron and oxygen diffusivity as described for ferrite) came from [100, 103, 345] in a diffusivity form, as did that of halite in the widely accepted work of Kofstad [99, 346] whose results were corroborated by Chen and Peterson in their empirical study of the effect of deviation from stoichiometry on diffusion of iron in wüstite [257]. Austenite exists in an antiferromagnetic form [333] so magnetism was less influential for diffusion, since individual strong atomic magnetic moments are aligned to oppose each other and result in a weak overall magnetic field, and thus the entire diffusion matrix was

not required. Wüstite had less variations in sub-lattice octahedral configuration due to only having two sub-lattices and only octahedral lattices are suitable for diffusion.

There were discussions of validation of the kinetic (diffusivity and/or mobility) data given the significant spread of data collated by Mehrer and Bornstein [100] (see Figure 3.9) and the method of collection (often by extrapolation of alloy concentration variation back to 0wt%, e.g. [103]).

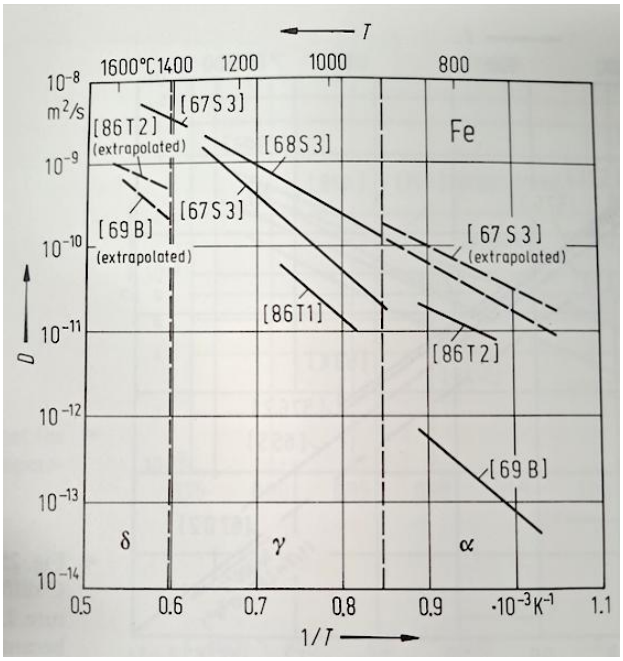


Figure 3.9: Fe diffusion coefficient for O diffusion in α, γ, and δ phases against reciprocal of temperature [100].

However, this spread is less significant at higher temperatures, i.e. reheat temperatures such as those used in tube manufacturing, as electrotransport phenomena become less influential [346]. Also, it was argued that it would be difficult to control a suitable experiment, e.g. elemental profiling, radioisotope tracing [347], to provide data that was as accurate than that already available in the literature. Overall, the sources used (Kofstad [346], Swisher and Turkdogan [348] and Takada et al. [344]) provide values widely accepted in the field and the latter two are fully collated in Landolt-Bornstein's series [100].

Initial application of the completed user-defined databases (referred to as the 'project-specific' thermodynamic and kinetic databases respectively from here on in) was unsuccessful due to a convergence error. Several changes, suggested by the Thermo-Calc© DICTRA documentation for database management and non-converging models, were tested to solve this issue. These included decreasing the boundary starting velocity, increasing the maximum allowable timestep, and increasing the CALFUN safety valve from the default value of 6 to the system component number value of 10. No improvement was seen. A

positive change was to introduce the use of automatic grid description. Although the scale layer was still geometric when automatically defined, interestingly the software applied a geometric grid to the austenite region as well. Although comparatively large, it is hypothesised that the mm-scale metal sample thickness renders it thin enough to spatial composition changes near the interface drastic enough to require a finer grid. Further inspection of the error highlighted that convergence was remaining elusive due to the defining function approaching a stationary point at the point of investigation. Investigation revealed that the wüstite mobility equation parameters, activation energy and pre-exponential factor (see Equation 1.36), had been transcribed from the literature in their original units (kcal.mol^{-1} and cm^2.s^{-1} respectively) rather than the appropriate SI units required for Thermo-Calc© (kJ.mol^{-1} and m^2.s^{-1} respectively). As the defining function contained a natural logarithm, and the lack of conversion of the data made the pre-exponential factor five orders of magnitude larger than the value in SI units, the resulting reciprocal derivative of the defining function meant that larger values of pre-exponential factor led to solutions tending to zero. Correction of the units produced a stable, convergent solution, however run time for a 180s simulation was slow at 169s when applying a maximum timestep of 1s.

3.2.2 Computational Domain Definition

The literature also showed why a parabolic rate law for oxidation kinetics can be assumed at high temperatures (see Section 1.3.1). An implicit Euler method was selected for the time discretisation where the unknown, concentrations are defined by coupled sets of equations. The Euler method is the simplest method for solving an initial value ODE where there is sufficient computational resources to devote to a minimised time step to obtain accuracy [349]. The simulation length, 180s, was defined by the mean of the heat treatment period range in the SR2 mill. The initial and minimum acceptable timesteps were both set at 0.1ms respectively. This was the value suggested in the *exi3a* example file provided in the Thermo-Calc© DICTRA console mode documentation [326]. The maximum acceptable timestep was evaluated according to the maximum acceptable timestep defined for a 1D parabolic equation using von Neumann (aka Fourier) stability analysis (see Equation 3.15) [350]. The typical self-diffusion coefficient of oxygen in wüstite, $\boldsymbol{D}$, was used from Kofstad's work [346]. Initial model set-up was performed based on the E24 grade, which had a thickness of 4.75mm. Thus, division of the austenitic region into its 10 linear nodes gave a node width,

$\boldsymbol{\Delta x}$, of 0.475mm. These input values resulted in a maximum timestep, $\boldsymbol{\Delta t}$, of 0.2ms based on the von Neumann stability criterion.

$$\boldsymbol{\Delta t \leq \frac{(\Delta x)^2}{2D}}$$

Equation 3.15

However, for the three minute simulation used in initial model development, a minimum of 900,000 iterations would be required (assuming an extreme scenario of the maximum timestep being used for all iterations). A test simulation using this condition did not converge within the 30 minute period allowed. This is longer CPU requirement, especially given the brevity of the normalisation treatment, but is still much quicker than performing heat treatment, metallographic preparation, and microscopic imaging of a real sample. This was also especially important given the much longer soak periods (up to 20 minutes) seen in the 6" Stordy (S6) mill . Furthermore, strip heat treatments, which may also be investigated using this model, are significantly longer (2-3 hours). Overall, use of this timestep condition was therefore deemed inefficient. Therefore, a convergence study was performed to assess the maximum timestep which provided the optimal balance of accuracy and computational efficiency, i.e. the shortest convergence time. The former and latter were quantified using the maximum predicted oxide thickness ($\boldsymbol{\delta_{oxide,max\ predicted}}$) and convergence period (CPU time) values respectively. CPU data are obtained from the .txt. document output of Thermo-Calc© model which states the total simulation time in seconds and the number of spatial datapoints resolved. The investigation began using the Console Mode default maximum timestep of 10% of the total simulation time (18s) and initially decreased the value in increments of 1% before dropping to 0.5%, 0.25%, 0.125%, and 0.0625% for finer analysis near the end of the study. Figure 3.10 is a comparative plot of the maximum oxide thickness predicted by the Thermo-Calc© model, $\boldsymbol{\delta_{oxide,max\ predicted}}$, and CPU time.

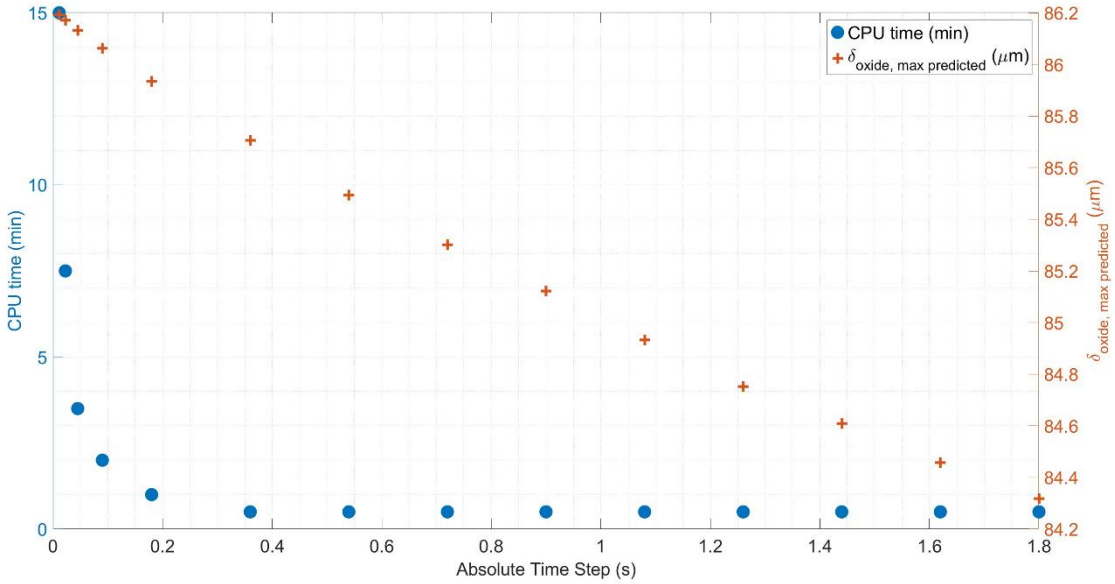


Figure 3.10: Comparative plot of model convergence study quantitative central processing unit (CPU) data (*left*) associated with a given timestep for the initial oxide thickness, $\boldsymbol{\delta_{oxide,max\ predicted}}$, (*right*) predicted by the model for planar samples soaked at 1000°C for 3 mins ¤.

Figure 3.10 shows how accuracy ($\boldsymbol{\delta_{oxide,max\ predicted}}$) can initially be linearly increased at a rate of 0.11µm for each decrease in timestep whilst maintaining a consistently low CPU time which was always less than 30s. However, decreasing timesteps below 0.2s led to a rapid increase in convergence time (doubling when timestep was decreased from 0.125s to 0.00625s), reaching a peak value of 15 minutes for the minimum timestep. The smallest timestep used before the rapid increase in convergence period began was 1.8s (1% of the total simulation time) and this was therefore deemed the optimal maximum timestep. After replacing the *exi3a* user-defined database [326] with the project-specific database, the simulation run time increased noticeably, more so than that just associated with an increase in the test time (from 180s reflecting the tube manufacturing conditions to 300s to reflect the longer STA tests for more established oxidation conditions). For the existing 1s maximum timestep, CPU demand increased from 77s with 204 datapoints to 259s with 324 datapoints. The 245% increase in convergence time seemed disproportionate to the 62% increase in model datapoints. This was attributed to the change in the multi-resolution grid approach, which was also partially the source of the more than five-fold increase in oxide thickness from ~85µm to 450µm. However, the increase in oxide thickness is mostly associated with the use of the User defined database which includes diffusion and mobility data for austenite and wüstite where previously the ferrite and spinel phase data from *exi3a* database had been used [326]. At 1000°C, where austenite and wüstite are the main steel and oxide phases respectively, the diffusion coefficient for oxygen in FCC iron predicted by the

expression is $1.99\times10^{-12}m^2.s^{-1}$, over 30 times greater than the diffusion coefficient for oxygen in BCC iron is $6.28\times10^{-11}m^2.s^{-1}$ so initially when mass transport dominates the oxidation mechanism, as described in Section 1.3, the oxygen can diffuse into the steel more quickly in the ferrite (see Table 3.3). Once the oxidation process is established and ionic transport assumes the role as dominant mechanism, diffusion through the oxide layer becomes more important. As Table 3.3 also shows, whilst there is only a single order difference in diffusion of iron through wüstite and magnetite, the biggest difference lies with the rate that oxygen diffuses through the oxide layer. Oxygen diffuses through wüstite over 500 times more quickly than magnetite, hence oxidation is faster and a thicker oxide is formed for a given period (see Equation 1.33). Transitions from a linear austenitic grid to an automated geometric grid and from a geometric halitic grid to a double geometric grid, although necessary to reflect the steep gradients of ion concentrations due to fluxing at both the steel-scale and scale-gas interfaces, introduced more unknowns needing to be solved, and thus greater computational demand. This also generates a matrix of unknown values for DICTRA to handle, requiring additional mathematical operations compared to the previous scalar quantity.

Table 3.3: Table showing the pre-exponential factors, D_0, activation energy, Q, and resultant diffusion coefficient, D, at 1273K, as predicted by different literature sources, for oxygen, O, and iron, Fe, in austenite, α-Fe, ferrite, β-Fe, wüstite, FeO, and magnetite, Fe_3O_4.

	D_0 ($m^2.s^{-1}$)	Q ($J.mol^{-1}$)	$D_{T=1273K}$ ($m^2.s^{-1}$)	Source
O in α-Fe	1.70E-05	1.69E+05	1.9867E-12	[348, 351]
O in ϐ-Fe	3.78E-07	9.21E+04	6.2841E-11	[344]
O in FeO	0.117	3.75E+05	4.7903E-17	[99]
O in Fe_3O_4	4.30E-11	2.11E+05	9.4461E-20	[352]
Fe in α-Fe	7.00E-05	2.86E+05	1.2862E-16	[353]
Fe in ϐ-Fe	4.60E-05	2.18E+05	5.2156E-14	[351]
Fe in FeO	8.60E-07	1.24E+05	6.8458E-12	[257]
Fe in Fe_3O_4 (movement in octahedral sublattice)	1.13E-06	110950	3.1647E-11	MOBFE8 [33]
Fe in Fe_3O_4 (movement in tetrahedral sublattice)	4.52E-06	122800	4.1318E-11	MOBFE8 [33]

A new convergence study was performed, working with larger time steps (see Figure 3.11) revealing how only increasing the maximum allowable timestep from 1s to 5s led to a 69% and 73% decrease in convergence time and datapoints for only a 1.1% change in maximum predicted oxide thickness. Beyond timesteps of 10s, there was a negligible change in CPU demand and a consistent <1% decrease in maximum predicted oxide thickness. A maximum allowable timestep of 10s (~3% of the total simulation test time) was therefore selected as the best balance of accuracy and CPU demands. Furthermore, higher maximum timestep values would represent a significant percentage of the simulation test time, thus making the mesh very coarse and decreasing computational accuracy. Additionally, using Equation 3.15 and the diffusion coefficient expression obtained from [99], in the optimal 10s timestep oxygen can be expected to diffuse 36.7μm, whereas the value for a 30s interval is almost twice that at 63.5μm. This also explains the steady decrease in oxide thickness as the time interval increases. Oxygen can diffuse further without a reaction in a longer interval and a thicker scale is formed before the slower process of oxygen diffusion through the oxide itself

is the dominant effect. However, it should be noted that this is not free diffusion [354] and there will also be effects associated with thermodynamic correction as an oxygen gradient develops as the oxide phase grows and stimulates diffusion of atoms in the bulk material towards the reaction interface [355].

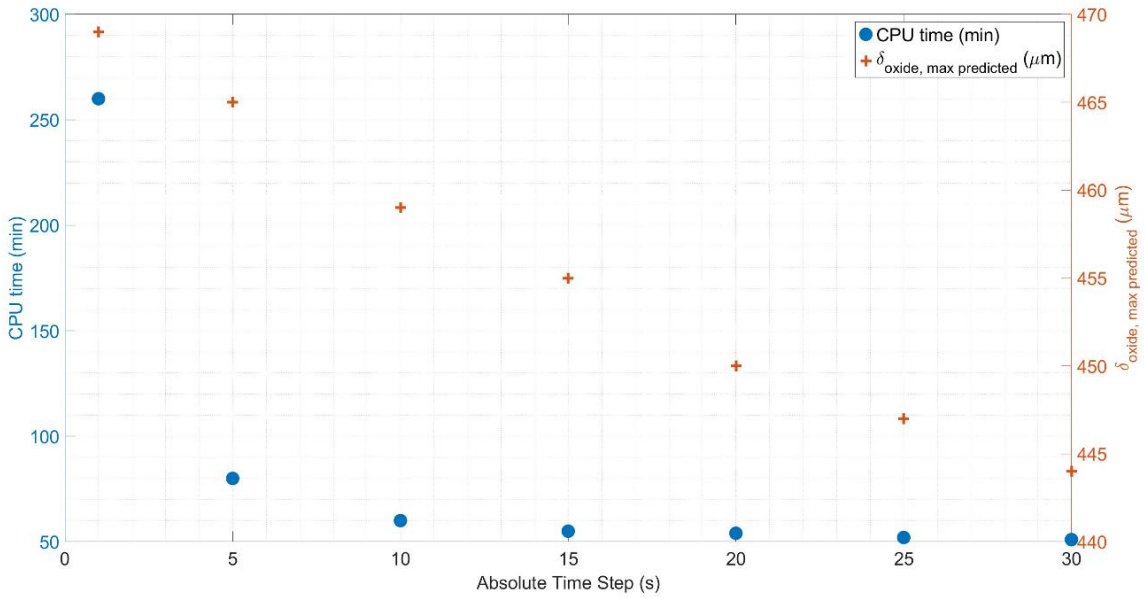


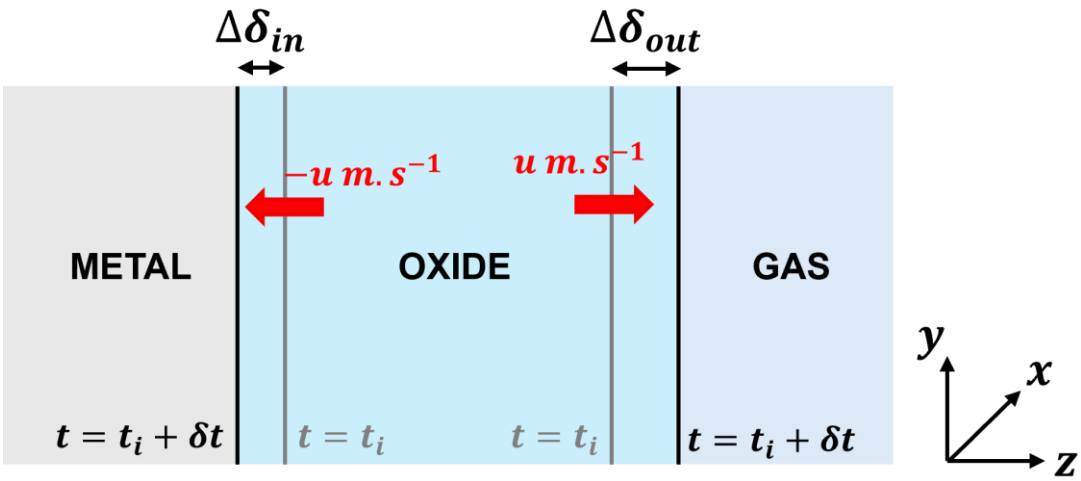
Figure 3.11: Comparative plot of model convergence study quantitative central processing unit (CPU) data (*left*) associated with a given timestep for the initial oxide thickness, $\delta_{oxide,max\ predicted}$, (*right*) predicted by the model, with a new user-defined database, for planar samples soaked at 1000°C for 5 mins ¤.

Initial and Boundary Conditions

Initial interface velocity was calculated based on Equation 3.16 (an adaption of the Moving Phase Boundary methodology described in Section 2.2.3) and a typical scale thickness of 100μm as found in the literature when considering conditions similar to that of conveyance tube manufacturing (see Section 1.2) at $5.56 \times 10^{-7} m.s^{-1}$. This positive value was used for the SGI interface as it migrated away from the initial metal surface, whilst the metal itself is oxidised leading to a migration of the SSI in the opposite direction at an equal speed, $\boldsymbol{u}$ (see Figure 3.12).

$$\boldsymbol{u} = \frac{\boldsymbol{\delta}}{\boldsymbol{t_{simulation}}}$$

Equation 3.16



$$\Delta\delta_{t=t_i+\delta t} = \Delta\delta_{in} + \Delta\delta_{out}$$

Figure 3.12: Diagram depicting opposite direction, equal magnitude migration of boundaries during scale growth ¤.

To solve the system boundary value PDE, i.e. Equation 1.29, the fully implicit Crank-Nicolson (CN) scheme was selected (see Section 2.2.1.1). Fully implicit systems are more numerically stable across a range of values of the mesh ratio parameter for discontinuous functions such as the discontinuity of oxygen concentration due to the presence of metal-scale interface [356]. Numerical integration, to determine concentration, c_i^t, (equivalent to the function, f_i^j, defined in Section 2.2.1) at a given node, i, and time, t, was achieved by applying the CN method (see Section 2.2.1) to Equation 1.29 (see Section 2.2.1) to obtain Equation 3.2 [88].

$$-rc_{i+1}^{t+1} + (1+2r)c_i^{t+1} - rc_{i-1}^{t+1} = rc_{i+1}^t + (1-2r)c_i^t + rc_{i-1}^t$$

where $r = \frac{D\Delta t}{2(\Delta x)^2} \leq \frac{1}{2}$

Equation 3.17

When computationally modelling any system, significant attention must be paid to the initial and boundary conditions applied to close this implicit system. Figure 3.13 shows how the system, containing two unknowns, is closed by assuming a 'closed' system on the metal side of the metal-gas interface, i.e. no diffusion of iron (Fe) in or out of that side of the system, and applying a fixed oxygen flux to the metal-gas interface, corresponding to the experimental atmosphere. This is valid since the whole thickness of the sample, and eventually tube wall thickness, is being modelled and the computational domain is therefore fully insulated [357]. The combination of these conditions allows the oxide layer to grow

outwards, i.e. external oxidation is assumed. To further reflect the assumption of wüstite as the oxide phase (due to its dominance in the classical three-phase layer), a low oxygen activity of $4.5 \times 10^{-4} m^2.s$, as suggested by the *exi3a* file authors [33], was applied by selecting the maximum value for oxygen permeability before accumulation to prevent phase transitions to magnetite and haematite, which are oxides with higher oxygen content. Oxygen activity is usually expressed as a partial pressure via Dalton's Law [358]. Standard reference conditions of 298K and 1bar were applied for the gaseous oxygen [359]. The oxygen concentration in the metal is presumed to remain constant for the duration of oxidation only when measured at a distance far enough from the SSI. Oxygen will dissolve in the metal close to the SSI up to a solubility limit. Crucially, Oh recognised that both boundaries (SGI and SSI) are moving [197].

Initial phase layer thicknesses must also be set. The metal thickness is obviously defined by the thickness of the sample under inspection. As discussed in Section 3.1, when considering the nose crop samples of the E41 and E24 grades used by TSUK Tubes, thicknesses of 4.75mm and 11.8mm were used respectively for a planar geometry. The value for initial oxide thickness must be minimal but non-zero. Examples within the Thermo-Calc© support package which use a moving phase boundary approach typically use a value of <0.1nm. Both regions are discretised as a finite number of nodes. The austenite region consists of 10 linearly spaced nodes, wherein composition is not expected to vary significantly. Conversely, the wüstite region consists of 50 geometrically spaced nodes, with a spacing factor of 1.05 (node-wise away from interface), to account for anticipated significant variation in composition in the oxide (as has been shown in the literature discussed in Section 1.3.1).

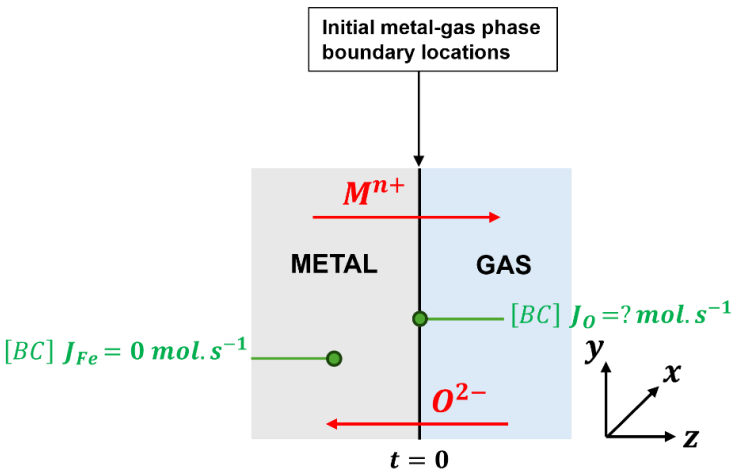


Figure 3.13: Schematic of metal-gas phase boundary (pre-oxidation) with two boundary conditions applied in line with Hallstrom et al.'s study [234] ¤.

Further Assumptions

During consideration of this binary system (Fe-O), there is an assumption, which may be less valid for steel with its intentional alloys, that foreign elements have been eliminated, i.e. not mistakenly incorporated into the binary system parameters so that their influence cannot be accurately assessed in future work.

Auinger et al. [227] also highlighted a key limitation of the DICTRA approach: although it avoids the need for a 2D approach by solving a 1D problem, in doing so it cannot represent oxidation of the complete microstructure, only provide local estimates of idealised geometrical cases, assuming radial symmetry, which may not agree with gas flow conditions.

3.2.3 Microstructural Defect Pre-Processing

Initial investigations, their methodologies and results alike, repeatedly highlighted the effect of assuming a perfectly compact oxide layer on model oxide thickness prediction accuracy. The internal surfaces generated by grain boundaries, interphase boundaries, and pores are highly disordered atomic structures which offer high diffusivity pathways [360]. For example, in De et al.'s work, diffusion in porous haematite showed a 200-fold increase compared to its perfectly compact equivalent [361]. There are also further non-idealised microstructural effects, namely labyrinth factor [29] and non-equilibrium trapping [362], which can affect diffusion. These were investigated in turn for their relative effect on the model output.

Grain Boundary Diffusion

Grain boundary diffusion is more prevalent at high temperatures as a high diffusivity pathway, especially during the oxidation of iron [360] (as was briefly discussed in Section 1.7). At higher temperatures, grain boundary diffusion is favoured compared to its surface equivalent since the activation energy of grain boundary diffusion in most metals is 0.4-0.6 times the bulk diffusion equivalent, making grain boundary diffusion up to six orders of magnitude faster [363, 364]. A simple mathematical analysis of Equation 1.37 demonstrates how the change in activation energy mentioned above, translates to a scaling factor equivalent to the root associated with the change. For example, where grain boundary diffusion activation energy is half its bulk equivalent, the grain boundary diffusion coefficient will be equivalent to the square root of the bulk equivalent (see Section 1.7.1). Hence, for values of bulk diffusion coefficient of below one, the most common scenario in diffusion analysis since $\boldsymbol{D_b} \ll 1$, the grain boundary coefficient diffusivity will be larger.

Pre-exponential factor variation is minimal so its effect is not considered. It should also be noted that there are limitations to the extent to which grain boundary and bulk diffusion coefficients can be compared as the overall transport rate along a grain boundary will also depend on its width [364].

According to Fisher's model [365] (see Figure 3.14), assuming that a grain boundary is isotropic, thin (atomic dimension level thickness, 0.5-1nm) and uniform, the grain boundary diffusion coefficient (also following an Arrhenius-type trend as seen in Equation 1.37), $\boldsymbol{D_{gb}}$, is much larger for a given species compared to its diffusivity in bulk grains (perpendicular to the grain boundaries), which are also isotropic but deemed to have low diffusivity.

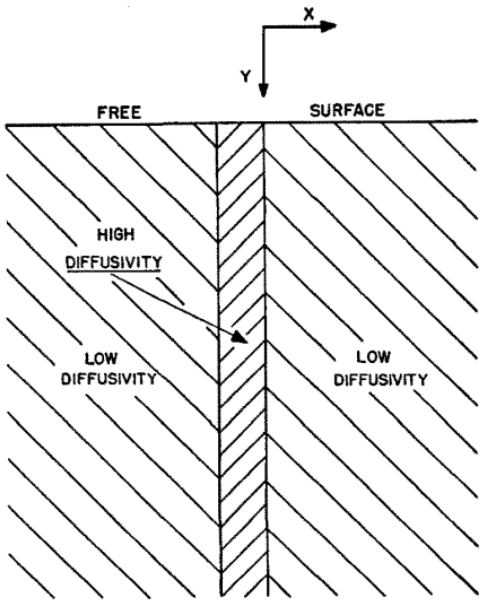


Figure 3.14: Schematic of bulk and grain boundary regions described according to their low and high diffusivity respectively [364].

The increased penetration depth, for a species diffusing from a surface normal to the grain boundary, into the grain boundary compared to bulk grains will also eventually lead to lateral leakage into adjacent bulk grains via volume diffusion. This process is described not only by Fick's Second Law (see Equation 3.18) but is also coupled to Equation 3.19 [364]. A key element of this mathematical analysis is the introduction of a segregation factor, $\boldsymbol{s}$, which modifies concentration continuity (see Equation 3.20 and Equation 3.21) when considering 'impurity', i.e. oxygen diffusion in a pure metal, or any alloy diffusion.

$$\frac{\partial c}{\partial t} = D\left(\frac{\partial^2 c}{\partial x^2} + \frac{\partial^2 c}{\partial y^2}\right),\ where\ |x| > \frac{\delta}{2}, c = c(x, y, t)$$

Equation 3.18

$$\frac{\partial c_b}{\partial t} = D_b \frac{\partial^2 c_b}{\partial y^2} + \frac{2D}{\delta}\left(\frac{\partial c}{\partial x}\right)_{x=\frac{\delta}{2}}, c_b = c_b(y,t)$$

Equation 3.19

$$Self - diffusion\ in\ a\ pure\ metal: \boldsymbol{c_b(y,t) = c(y,t)}$$

Equation 3.20

$$Impurity\ diffusion\ in\ a\ pure\ metal\ or\ diffusion\ in\ an\ alloy: \boldsymbol{c_b(y,t) = sc(y,t)}$$

Equation 3.21

Several parameters can be obtained during experiments [364] where average layered concentration is plotted against the penetration depth, i.e. a diffusion profile. The most important parameters are the $\boldsymbol{\alpha}$ parameter and the LeClaire parameter, $\boldsymbol{\beta}$ (see Equation 3.22 and Equation 3.23) which provide information about the degree of bulk and grain boundary penetration respectively. Note that both parameters are functions of segregation factor, $\boldsymbol{s}$, grain boundary width, $\boldsymbol{\delta}$, diffusivity, $\boldsymbol{D}$, and time, $\boldsymbol{t}$ (see Figure 3.15). A diffusion profile will also contain an initial near-surface region due to direct volume diffusion from the surface wherein the bulk diffusion coefficient can be measured [364].

$$\boldsymbol{\alpha = \frac{s\delta}{2(Dt)^{1/2}}}$$

Equation 3.22

$$\boldsymbol{\beta = \frac{s\delta D_{gb}}{2D(Dt)^{1/2}}}$$

Equation 3.23

The kinetic type is thus defined by the extent of this lateral leakage and can be classified using Harrison's classification of diffusion kinetics for a polycrystal depending on the domain of heat treatment temperature, $\boldsymbol{T}$, soak time, $\boldsymbol{t_{soak}}$, and grain size, $\boldsymbol{d}$ [366]. Type A kinetics is observed at high temperatures, long soak times and/or small grain sizes and the condition $\boldsymbol{(Dt)^{1/2} \gg d}$ is satisfied [364], i.e. the volume diffusion length is much greater than the grain size, as the volume diffusion fields around adjacent grain boundaries have significant overlap. Conversely, type B kinetics is associated with lower temperatures, shorter soak times and larger grain sizes, i.e. $\boldsymbol{s\delta \ll (Dt)^{1/2} \ll d}$ (noting that segregation factor and grain boundary width are now part of this condition). For reasonable soak times, type B kinetics comprises the widest and most convenient temperature range. Type B kinetics can also be characterised by $\boldsymbol{\alpha \ll 1}$ and $\boldsymbol{\beta \gg 1}$, i.e. deeper penetration into the grain boundaries than the bulk. Type C kinetics can be found at the lowest temperatures

and shortest soak times where bulk diffusion is 'frozen out' and lateral leakage is negligible. Type C is characterised by the condition $(\boldsymbol{Dt})^{\mathbf{1/2}} \ll \boldsymbol{s\delta}$ where $\boldsymbol{\alpha} \gg \mathbf{1}$, at a minimum of $\boldsymbol{\alpha} > \mathbf{10}$. A graphical description of the Harrison's kinetic regimes is shown in Figure 3.15. Calculations were performed to assess the kinetics regime classification. Literature values of 1nm and 1.1 were used for the grain boundary width, $\boldsymbol{\delta}$, and dimensionless segregation coefficient, $\boldsymbol{s}$, respectively [367, 368]. A ratio of 0.5 was assumed between grain boundary and bulk diffusion activation energies and applied accordingly to their diffusion equation [364].

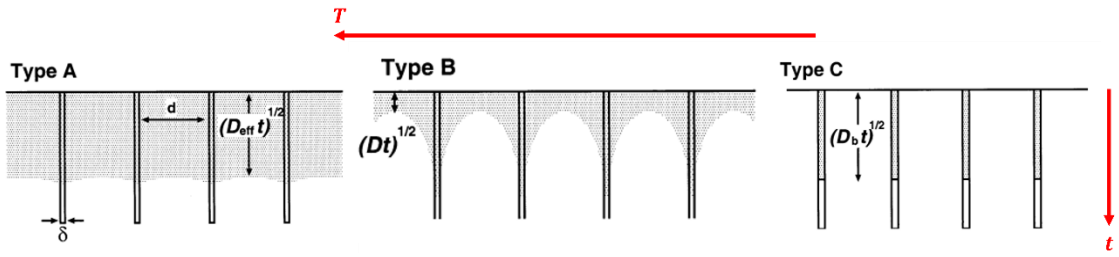


Figure 3.15: Graphical description of Harrison's kinetic classification of diffusion regimes A, B, and C [364] (*adapted from source*). Arrows show changes in temperature, $\boldsymbol{T}$, and time, $\boldsymbol{t}$.

For the average normalisation time of 3 minutes, the kinetic regime appeared to reside on the edge of type A and B kinetic regimes, with a volume diffusion length not much greater than the grain size calculated using mean line intercept of FEGSEM images (see Appendix 5) and the grain width and segregation product being significantly less than the volume diffusion length. The LeClaire parameter was also not much greater than one. Since type A kinetics is typically associated with high temperatures, small grain sizes, and long soak times, the first condition being met, and the second is a fixed value pre-normalisation (although this could be changed in a microstructural study beyond the scope of this work), soak time was deemed to be most influential in pushing the kinetic regime firmly into the A or B category. For a longer soak times, as are considered at other junctures during this project, of 12 and 24 hours, the dramatic increase and decrease in $\frac{(\boldsymbol{Dt})^{\mathbf{1/2}}}{\boldsymbol{d}}$ and $\boldsymbol{\beta}$ respectively clearly consigned the oxidation process to a type A regime with less influential grain boundary diffusion. This information is summarised in Table 3.4.

Hence, although the type A analytical theory was used for this project, the greater influence of grain boundary diffusion was considered alongside it due to the closeness of the B regime at the short normalisation times.

Table 3.4: Harrison kinetic regime classification quantitative analysis results for austenitic FCC steel. Kinetic regime is assessed quantitatively using parameters α and β, for a given time, t, and temperature, T, which are derived as function the diffusivity, D, grain size, d, segregation factor, s, and grain boundary width, δ.

Soak time (s) (T=1273K)	$\frac{(Dt)^{\frac{1}{2}}}{d}$	$\frac{(Dt)^{\frac{1}{2}}}{s\delta}$	α	β	Classification
180	10.5	5.44×10^{4}	9.19×10^{-6}	2.06	A/B
43200	157	8.43×10^{5}	5.93×10^{-7}	0.133	A
86400	222	1.19×10^{6}	4.19×10^{-7}	0.0940	A

In this work, a discontinuous solid state reaction occurs, resulting in chemical diffusion of species along a migrating reaction front, i.e. moving phase boundary (see Section 1.7.1). Thus, for type A kinetics, an effective diffusion coefficient, D_{eff}, can be calculated based on grain boundary volume fraction,
g_k (see Equation 3.24) [360]. Landolt-Bornstein's work compiles works where this calculation has already been performed, providing a modified diffusion coefficient accounting for grain boundary diffusion. This volume homogenisation was also referred to in mobility form in Section 1.7.1.

$$D_{eff} = g_k D_{gb} + (1 - g)D$$

Equation 3.24

For iron self-diffusion (austenitic FCC phase), the resulting pre-exponential factor and activation energy (see Equation 1.37) are $1.85\times10^{-6}m^2.s^{-1}$ and $251kJ.mol^{-1}$ respectively. Transition to these values, from the ideal diffusion coefficient, represented a 60% decrease and 15% increase in pre-exponential factor and activation respectively (which is in agreement with the value range stipulated by Mishin and Herzig [364]). Considering Equation 1.37, a noticeable decrease in diffusion coefficient would be expected for both these changes based on their mathematical relationship to diffusion coefficient ($y = mx$ and $x = e^{-z}$ respectively, where m represents the pre-exponential coefficient, and z the activation energy in these generic mathematical relations using arbitrary variables x, y, z). However, introduction of this diffusion coefficient into the kinetic database had no effect on the oxide thickness predicted by the model, compared to a simulation where grain boundary diffusion was not considered (see Figure 3.16). Since ion diffusion is predominantly through the oxide once a parabolic oxidation regime is established (see Section 1.3.1), this result

suggests that an observable change in oxidation behaviour is only observed when considering grain boundary diffusion in the oxide.

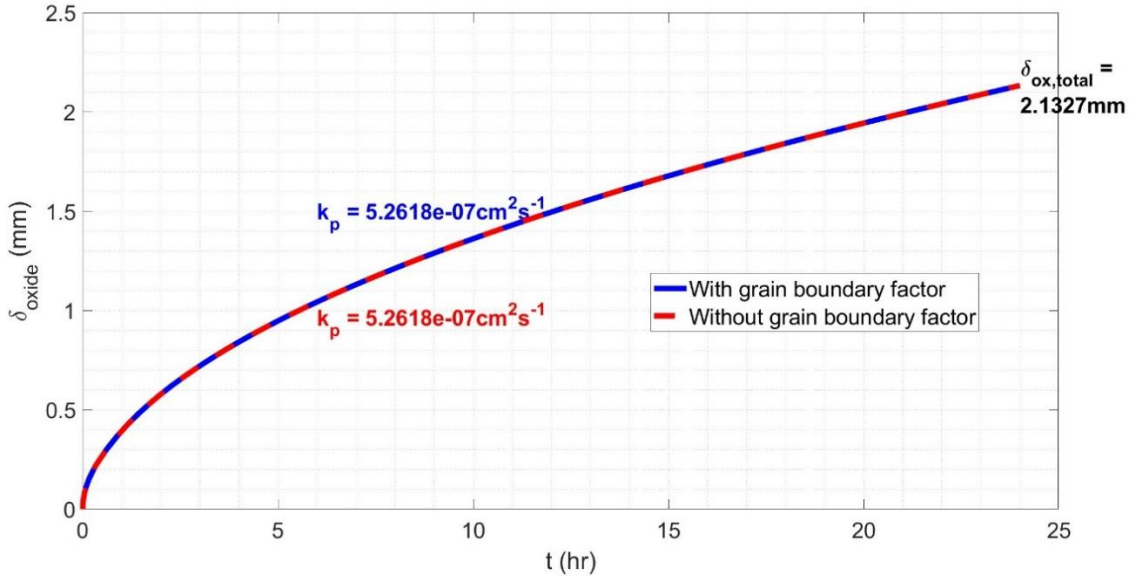


Figure 3.16: Comparison of oxide thickness gain, $\boldsymbol{\delta_{ox}}$, over time, $\boldsymbol{t}$, predicted without microstructural considerations (*red*) and using a kinetic database accounting for grain boundary diffusion of Fe within the substrate (*blue*) ¤.

This was confirmed in the work of Samal and Mitra [238], which states that scale growth proceeds via outward lattice diffusion of ions and electrons of the metal substrate, since the cation sublattices in wüstite have defects. However, in a classical three-phase oxide observed on iron, as previously described in Section 1.3.1, the oxygen content in the phase increases as the oxide-environment interface moves further from the substrate-oxide interface, outward cationic transport of iron along oxide grain boundaries as the dominant oxidation mechanism is overtaken by inward anionic transport. Transport of ions across the oxide layer, under the effect of chemical and electric potentials, ultimately controls the rate of oxidation. Fortunately, the oxides observed within this work are thick enough that Wagner's oxidation theory applies ($\boldsymbol{\delta_{ox}} < 2\mu m$). Within Samal and Mitra's work [238], attention is paid to their analysis of BCC iron with its medium grain size, but also their investigation of copper with fine grains due to its FCC lattice structure which is also observed in austenitic steel.

For samples oxidised for 10 hours in a dry air atmospheric electric furnace, high temperature oxidation rate was shown to decrease with decreasing grain size, for both pure iron and copper, although grain boundary diffusion was most prevalent during iron oxidation. However, this phenomenon has a limit up to a saturation point and the state wherein grain size is fine enough to limit surface area exposure for oxidation. The overall

mechanism responsible for this phenomenon was hypothesised as follows: an inward flux of vacancies arises due to metal diffusion along oxide grain boundaries, with the vacancies condensing at the substrate-scale interface to form cavities which lower local oxidation rate. The oxide can also dissociate at the grain boundary and open up to form a pore (this 'non-equilibrium trapping' is discussed in the following section). It was added that magnetite to haematite conversion could evolve enough stress to promote plastic inter-crystalline microcracking under differential contraction. Hence, grain boundary diffusion is further enhanced in the outer layers due to more diffusion paths associated with cracks. Eventually, the inner scale is no longer saturated with metal cations due to the metal to scale transfer being inhibited by vacancy pile-up. Hence, bidirectional diffusion of metal and oxygen no longer drives oxidation but rather the exclusive outward diffusion of metal cations. In conclusion, finer grains introduce more grain boundaries for metal cation diffusion, increasing the condensation of vacancies at the substrate-scale interface and inhibiting diffusion and thus oxidation whilst leading to an increased risk of oxide spalling in the industrial process. It should be noted that this phenomenon also negates the accelerating property of oxygen grain boundary diffusion along these high diffusivity short circuit pathways, since oxygen cannot access the metal cations.

With this additional information, diffusion data for iron in the wüstite itself was sourced from the work of Sasaki et al. [369] which stated that the ratio between the bulk, $\boldsymbol{D}$, and grain boundary, $\boldsymbol{D_{gb}}$, diffusion coefficients is at least 750 at high temperatures, i.e. $\frac{\boldsymbol{D_{gb}}}{\boldsymbol{D}} \geq 750$ ($\boldsymbol{T} = 1073K$). Equation 3.24 showed how an effective diffusion coefficient relies on the volume of homogenisation of the bulk and grain boundaries [370]. If grain boundary diffusion coefficient is considered a direct multiple, $\boldsymbol{k}$, of bulk diffusion coefficient where $\boldsymbol{k} = 750$ according to Sasaki, Equation 3.24 can be expressed as a function of $\boldsymbol{k}$ (see Equation 3.25).

$$\boldsymbol{D_{eff} = g_k k D_b + (1 - g) D}$$

Equation 3.25

Grain boundary volume fraction, $\boldsymbol{g_k}$, can be calculated using Equation 3.26 (assuming $\boldsymbol{d} \gg \boldsymbol{\delta}$) based on a mean line intercept for a 15 n.b. sample pre-normalisation to represent the initial conditions for oxidation (see Appendix 4) to identify an average grain size, $\boldsymbol{d}$, of 5.9μm and taking grain boundary thickness, $\boldsymbol{\delta}$, as 1nm as is conventional for most metals [367].

$$g_k = \frac{3\delta}{d}$$

Equation 3.26

However, it should be noted that average grain sizes were also calculated for 15 n.b. and 20 n.b. post-normalisation samples (also in Appendix 4) to reinforce the evidence for a smaller grain size enhancing diffusion by increase the grain boundary volume fraction (see Figure 3.17). Since the converse effect was reported by Samal and Mitra [238] due to vacancy pile-up associated with cation diffusion, this highlighted how without introducing porosity into the model, arguably not necessary given the evidence of homogeneity in the oxide and at its interface with the metal, the effect of grain boundaries on diffusion is dominated by their contribution of high diffusivity pathways which accelerate oxidation. Figure 3.18 shows the increase in oxidation rate and oxide thickness associated with the model when grain boundary diffusion is not (*left*) and is (*right*) accounted for in the kinetic database. However, as discussed in Section 1.7.1, the assumption of a planar diffusion front is a key element of this approach to modelling grain boundary diffusion.

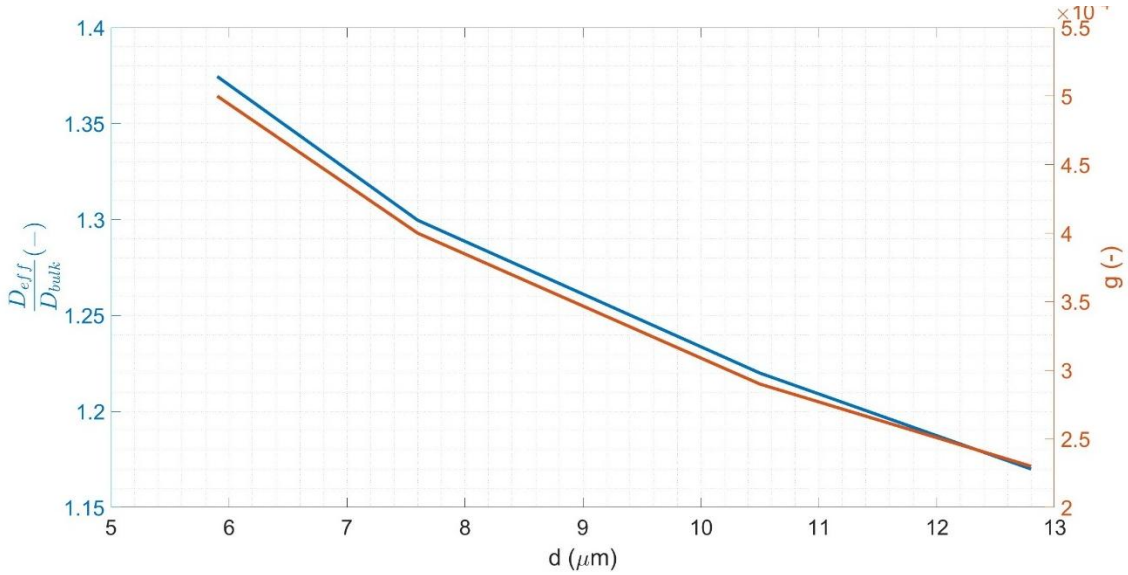


Figure 3.17: Plot of the effect of grain size, d, on effective diffusion, D_{eff}, (normalised against bulk diffusion, D_{bulk}) (*left*) and grain boundary volume fraction, g_k (*right*) ¤.

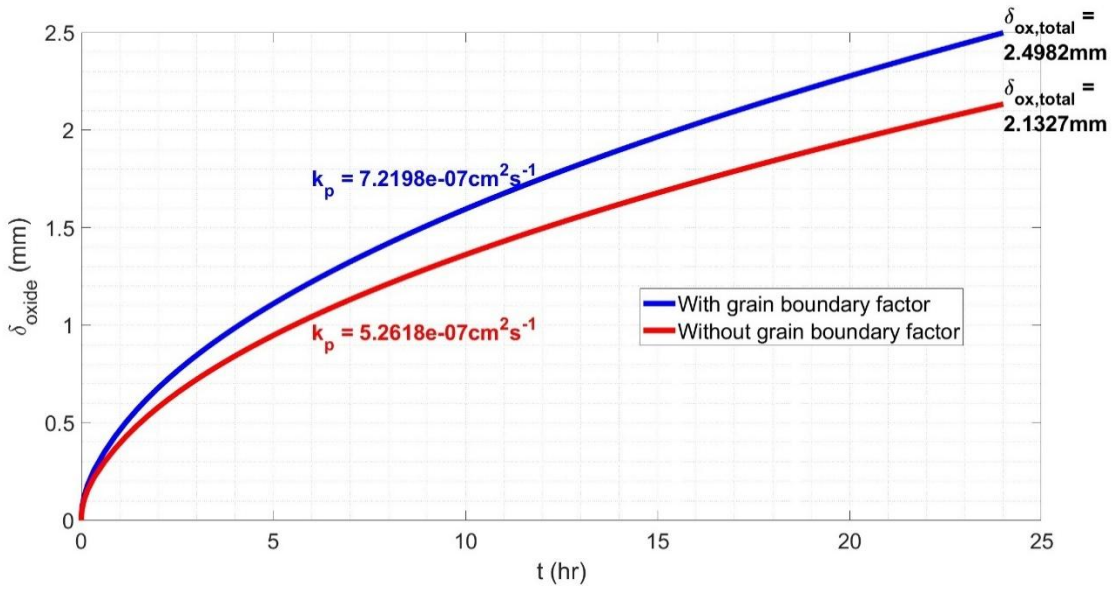


Figure 3.18: Comparison of oxide thickness gain, δ_{ox}, with time, t, predicted without microstructural considerations (*red*) and using a kinetic database accounting for grain boundary diffusion of Fe cations within the substrate and scale (wüstite phase) (*blue*) ¤.

Porous Medium Diffusion

For a binary oxide, $M_{1-x}O$, with non-stoichiometry, x, such as wüstite, $Fe_{1-x}O$, and a gas-solid diffusion couple state, a derivation using Darken's equation can be used to express the porosity-modified diffusion coefficient, i.e. vacancy diffusion coefficient, D_V, as a function of the cation chemical diffusion coefficient, driven by a chemical potential gradient, and the diffusing cation valency,

α_k (see Equation 3.27). However, in this case it is assumed that diffusivity of the metal cation is far greater than the gas anion, i.e. $D_{Fe} \gg D_O$ [223] .

$$D = (1 + \alpha_k) D_V$$

Equation 3.27

Oleksak et al. [371] discussed the importance of metal vacancy injection during high temperature oxidation of chromium alloys [234]. They showed that the generation and coalescence of vacancies, following outward chromium cation diffusion towards the metal-oxide interface to form the outer scale layer, promote a high concentration of vacancies at the metal-scale interface and therefore low density near-surface regions in the metal. The modified alloy surface then becomes oxidised the oxygen potential established at the metal-scale interface, ultimately forming the inner scale layer. Although not physically essential, oxygen ions may diffuse into the void regions. Given that it has been shown that vacancies are not predominantly annihilated, the diffusion coefficient must be modified to reflect this

microstructural change.

A more complex solution is required if the diffusion of the anion is non-negligible (discussed in Section 1.3.1) [372] where vacancy generation and annihilation ensure the electroneutrality condition is maintained [208, 209, 239, 244, 373], i.e. the Kirkendall effect [97] is coupled with local charge balance. Similarly to grain boundary diffusion effects, introduction of these values for the cation states in the kinetic database, had no effect on model output (see Figure 3.19), again reflecting the dominance of oxide properties, and the lack of relevant data.

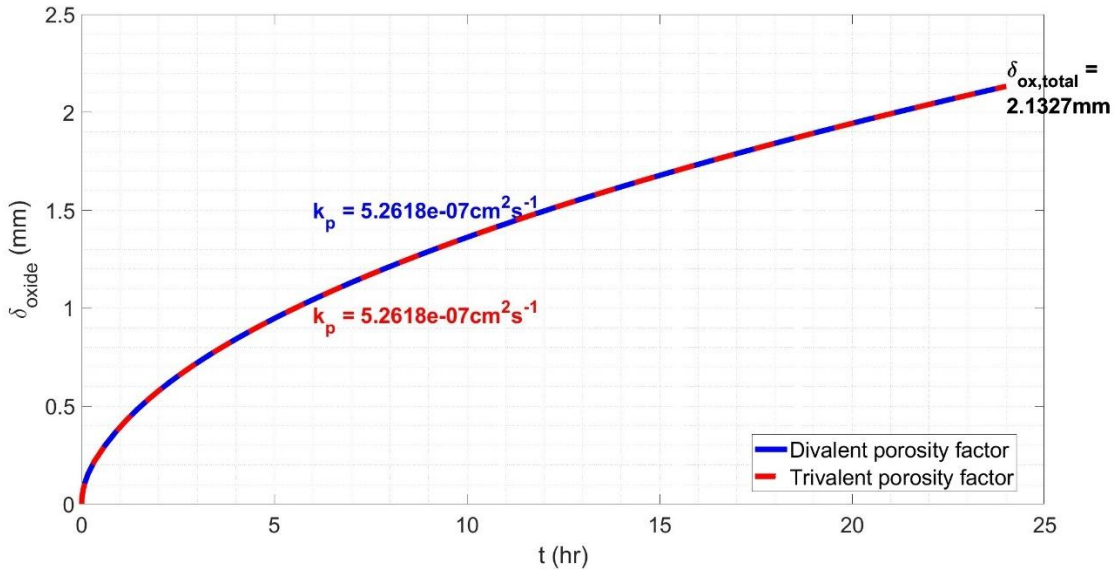


Figure 3.19: Comparison of oxide thickness gain, δ_{ox}, with time, t, predicted using a kinetic database accounting for divalent (*blue*) and trivalent (*red*) cation vacancies, i.e. porosity ¤.

Beyond the introduction of new high diffusivity pathways, pores, when large enough, can also promote non-equilibrium trapping [362]. During oxidation, large pores may allow oxygen ions to recombine to form their diatomic state, O_2 [200, 362]. For a system in equilibrium which obeys the Stefan-Boltzmann relation [337], i.e. a 'quasi-stationary' approximation, the number of oxygen in bubbles, i.e. trapping, and in solution (resolution) is assumed equal and allows for a single diffusion equation with an effective diffusion coefficient. However, for a rapid increase to a high temperature, such as is seen during normalisation, especially when using an induction heating method (see Section 1.2), this approximation becomes invalid and the two PDEs describing gas trapping and resolution cannot be simplified in the conventional form [109]. In the non-equilibrium case, both diffusion and trapping will affect gas concentration simultaneously, with diffusion only affecting the concentration of oxygen in solution, c, whilst trapping will affect oxygen both in solution and as bubbles, m. Concentration is a key variable during Fickian diffusion laws

(see Section 1.7.1). This most often occurs when the phase boundary velocity is much larger than solute (oxygen) diffusion velocity [374]. Such a system can only be solved numerically and evidence indicates that the diffusion constant is bounded by the bulk solute diffusion coefficients of the metal and oxide [374]. However, metal oxidation also satisfies a further property of non-equilibrium trapping, beyond the relative interface-diffusive velocity, as although not physically static, there is a net flux of vacancies across the steel-scale interface. Mandl et al. also found that high temperatures ($\boldsymbol{T}$ > 520°C) were associated with the onset of observable trapping in austenitic stainless steel with a steady surface supply of nitrogen (close to oxygen in atomic radius [375]), i.e. the onset of non-equilibrium trapping [376]. However, there is an argument that at a macroscopic scale, the size of related defects such as porosity is negligible, for example, whether pores are large enough to allow oxygen to recombine to its diatomic form to a significant extent. FEGSEM imaging of 15 n.b. and 20 n.b. samples post-normalisation (Figure 3.20 and Figure 3.21 respectively) revealed a good level of homogeneity in both samples at both the outer and inner edges as well as a single phase oxide which supported the use of wüstite as the oxide phase during model development. Previous research by Evans et al. [377] also suggested that oxidation inhibition by pores ultimately depends on their continuity, location and extent of elimination during plastic deformation. The latter is more extensive in tube manufacturing due to the extent of TMP (see Section 1.2.5) which may explain the homogeneous oxide nature.

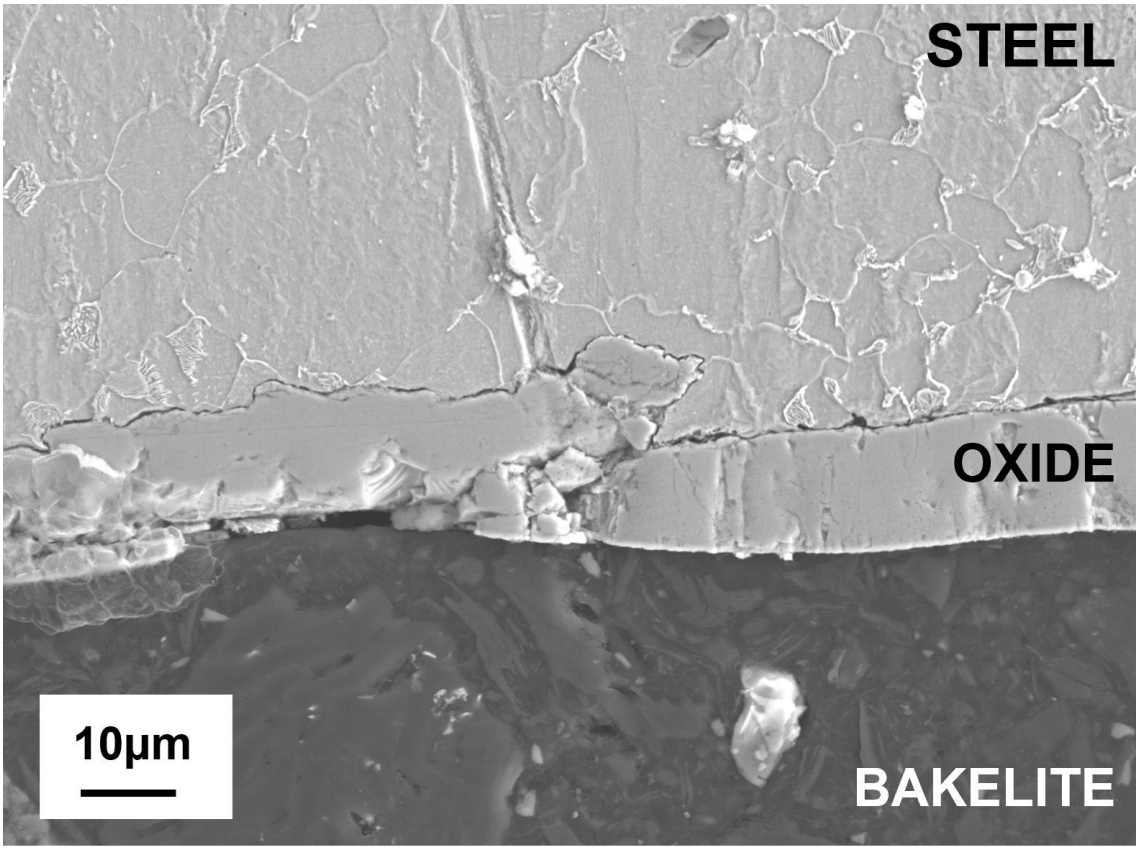


Figure 3.20: FEGSEM image of oxide formed on E41 heated to 1000°C during conveyance tube manufacturing at TSUK Tubes ¤.

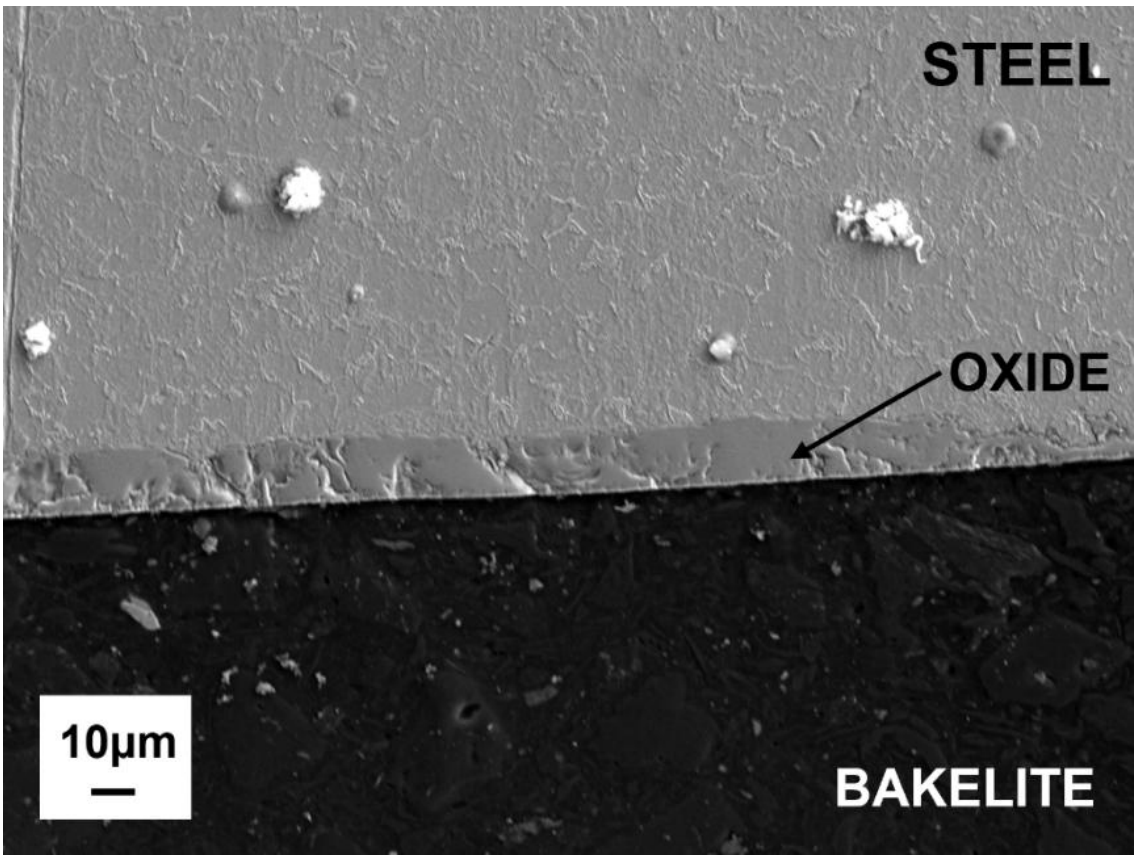


Figure 3.21: FEGSEM image of oxide formed on E41 heated to 1000°C during conveyance tube manufacturing at TSUK Tubes ¤.

Labyrinth Factors

The presence of carbides in the geometric structure as a dispersed phase can act as obstacles to diffusion, themselves with negligible diffusion, which increase the diffusion pathway and ultimately decrease diffusivity. An effective diffusion coefficient, $\boldsymbol{D_{eff}}$, can be calculated by multiplying the bulk diffusion coefficient by a labyrinth factor, $\boldsymbol{f_{labyrinth}}$, which raises the carbide volume fraction, $\boldsymbol{f_k}$, to an integer power, $\boldsymbol{q}$, (fitted retrospectively based on experimental data) (see Equation 3.28 and Equation 3.29) [378].

$$\boldsymbol{D_{eff} = \lambda D_0}$$

Equation 3.28

$$\boldsymbol{f_{labyrinth} = f_k^{\,q}}$$

Equation 3.29

For an austenitic steel, the most accurate simulations have been observed using a labyrinth factor of the order of 4 (beyond 500hrs exposure) or 5 (beyond 300hrs exposure) [379]. Given that normalisation is a far shorter process of only several minutes, a maximum labyrinth factor of 3 was used [379]. As labyrinth factors cannot be determined analytically, they must be adjusted to reflect experimental profiles. Fortunately, different labyrinth factors can be explored within the Thermo-Calc© console using the ENTER_LABYRINTH_FUNCTION command [326]. However, again, no difference was observed when the labyrinth factor was implemented (see Figure 3.22).

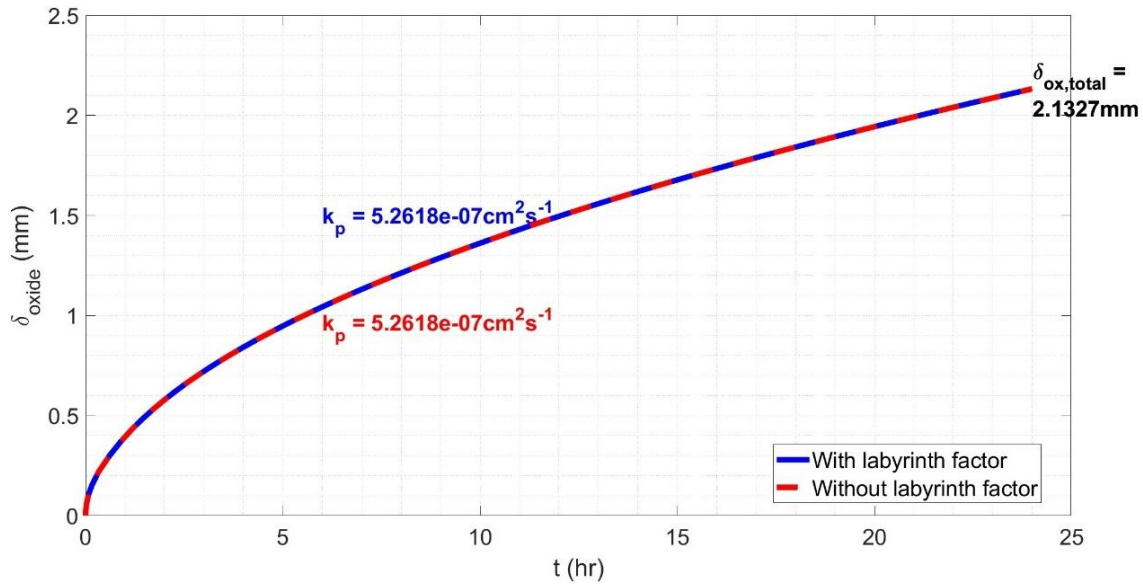


Figure 3.22: Comparison of oxide thickness gain, δ_{ox}, with time, t, predicted using a kinetic database accounting for labyrinth effects, using a labyrinth factor, $f_{labyrinth}$, of 3 ¤.

3.3 Initial Thermo-Calc© Model Results

Oxide thickness data (derived from wüstite upper and lower interface position data – see Equation 3.30) generated by the Thermo-Calc© model were automatically exported to an Excel file to allow it to be loaded into a MATLAB R2024b script and post-processed. Also, within the code, an initial check that the model results followed the anticipated oxidation kinetics theory (see Section 1.3.1) was introduced by checking that the maximum oxide thickness occurred at the maximum possible time, i.e. oxidation followed the anticipated parabolic profile. Although it was acknowledged that other oxidation profiles can also yield the same result, e.g. linear, this was only an arbitrary initial check. The results of this test were printed in the command window during the code run, allowing further investigation to be performed by the user if the data failed the test.

$$\delta_{ox} = POI(upper, wustite) - POI(lower, wustite)$$

Equation 3.30

The model oxide thickness prediction for a flat surface of 3mm thickness (with a unit surface area of $1m^2$) soaked at 1000°C for five minutes, is shown in Figure 3.23, which led to a predicted total oxide thickness of 124µm and a parabolic rate coefficient of $5.1x10^{-7}cm^{-2}.s^{-1}$. This was in reasonable agreement with flat surfaces assessed by Grant [9]. An average oxide thickness of 234.4±9.0µm was measured within the work although this was under idealised

furnace conditions, including atmospheric control. It could be argued that the scale formed is therefore representative of manufacturing conditions which are less well-controlled.

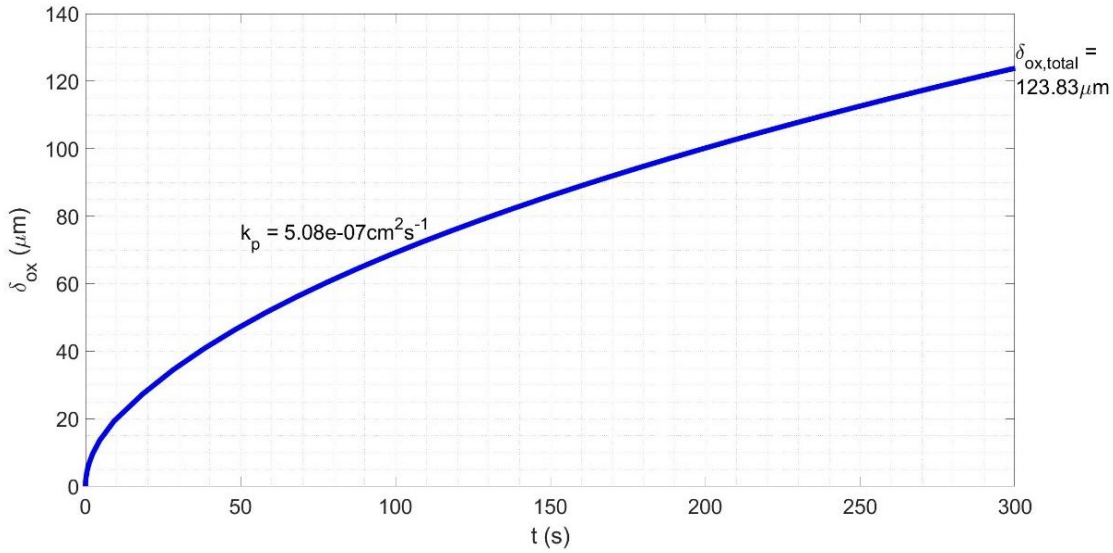


Figure 3.23: Model oxide thickness, δ_{ox}, prediction, annotated with the calculated parabolic rate coefficient, $k_{p,thickness}$, for a 3mm thickness planar Fe surface soaked at 1000°C for a time, t, of 5 minutes ¤.

To confirm the discrepancy, an identical 30x30mm sample of 1µm polished tube grade steel was heated using the same cycle as in the work of Grant [9]. SEM imaging of this sample revealed an oxide thickness of 227.6µm (see Figure 3.24). The high degree of scale intactness is also noted and highlights the lack of strain applied to the sample, which does not reflect the high mechanical strain observed during tube manufacturing. Finally, the model output provides continuous data the likes of which could not be provided using the furnace in the work of Grant [9] due to the lack of suitable TGA hardware and sample preparation limitations (mechanical grinding techniques and transfer between the furnace and mass balance and/or SEM made material loss inevitable given the brittle nature of the oxide) at Swansea University.

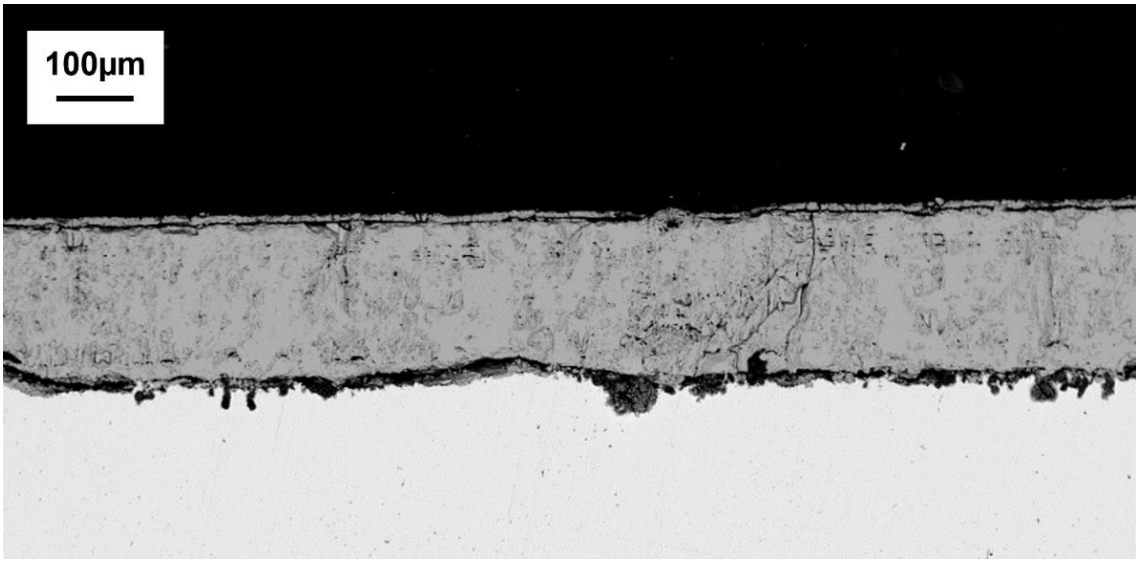


Figure 3.24: SEM image of oxide, of average thickness 225±9µm, formed on 30x30mm E41 planar sample after replicating Grant's 'STCA1-STCA3' cycle - heating to 950°C for 30 mins in a 10% O_2-90% N_2 atmosphere ¤.

3.3.1 Model Validation

STA Experimental Set-Up

Wire Electrical Discharge Machining (EDM) was used to generate 3x3x3mm cubic coupons of E24 and E41 tube grade steel to ensure comparable STA data. The heating action of the EDM approach introduced further oxidation to the machined coupon surfaces which were therefore cleaned using 4000 grit polishing paper and isopropyl alcohol. Each prepared coupon was placed in the centre of alumina crucible (which exhibit high thermal conductivity and inert behaviour towards oxygen at high temperatures [270]). Replica heat treatment in a 10% O_2-90% N_2 atmosphere was applied sequentially to each crucible. A ramp of $5K.s^{-1}$ was used for both the heating and active cooling periods [272], and the thermal cycle used is shown in Figure 3.25.

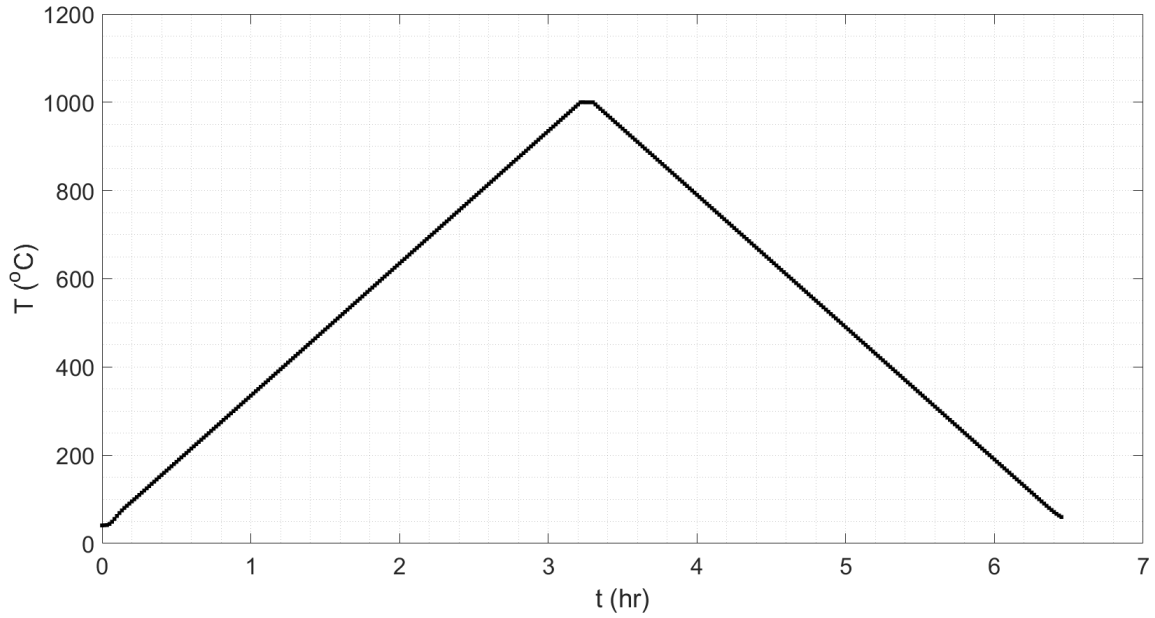


Figure 3.25: Thermal cycle ($\boldsymbol{T-t}$) used during STA validation experiments ¤.

Before running the thermal cycle, a 'blank' run was performed using an empty crucible to establish a buoyancy effect correction factor [270]. The high temperatures used during the experiment will evolve a significant change in gas density. Each coupon has a fixed volume, $\boldsymbol{V}$, which it displaces in gas equivalent when placed in the crucible. Archimedes' principle states that weight (related to mass via the gravitational force equation and Earth gravitational field constant, $\boldsymbol{g}$) of fluid displaced by a body is equal to the upward buoyant force, $\boldsymbol{F}$, exerted on that body [380]. Hence, since volume in the crucible is fixed, a decrease in density, $\boldsymbol{\rho}$, will lead to a decrease in buoyant force (see Equation 3.31) and sinking of the coupon. The lowering of the coupon under this effect can present as a mass gain not attributable to oxidation. The blank run allows this buoyancy-related mass gain to be quantified, and values can be corrected accordingly (either manually or automatically by software).

$$\boldsymbol{F = \rho V g}$$

Equation 3.31

STA Data Processing Approach

Mass gain data derived from the TGA output of the STA (see Figure 3.26) was converted to oxide thickness (to make direct comparisons with model output) using Equation 3.35, the derivation of which can be found in Appendix 2. The value of oxide (wüstite) density, $\boldsymbol{\rho_{oxide}}$, was calculated from its molar volume,
$\boldsymbol{V_m^{oxide}}$, defined in the thermodynamic database, and molar mass, $\boldsymbol{M_r}$ (see Equation 3.32).

The resulting value of 5914kg.m^{-3} agreed with taken as a mean of values found in the literature, 5941±826kg.m^{-3} [7, 16, 72, 73, 128, 381].

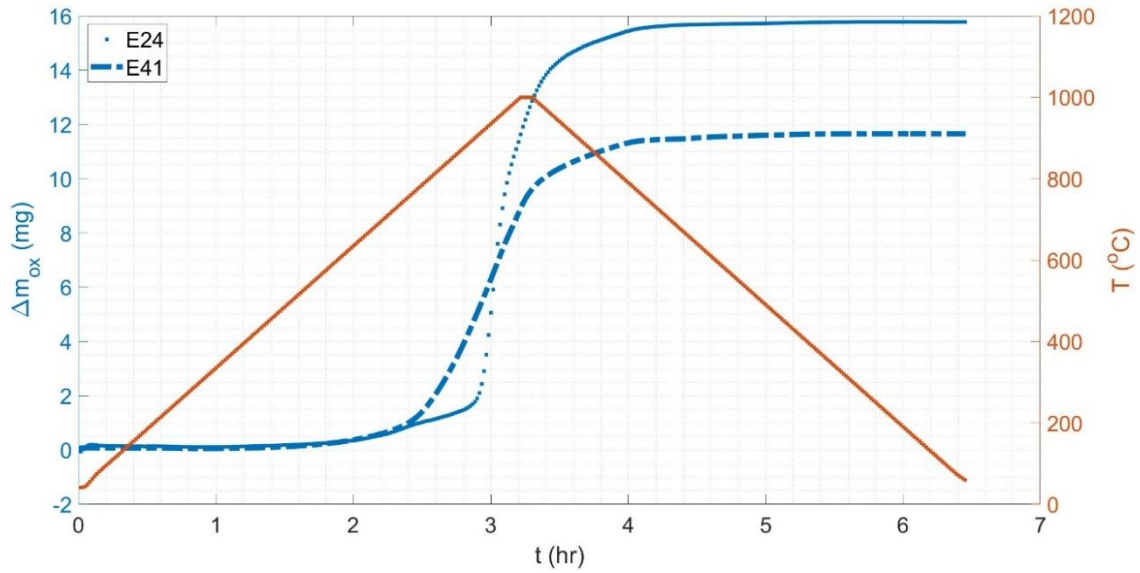


Figure 3.26: Kinetic profiles for E24 (*dotted line*) and E41 (*dashed line*) samples used in STA investigation (1000°C, 5 minutes) in the form of overlayed oxide mass gain, Δm_{ox}, - time, t, (based on mass-to-thickness conversion in Equation 3.35) and temperature, T, -time plots ¤.

$$\rho_{oxide} = \frac{M_r}{V_m^{oxide}}$$

Equation 3.32

However, use of Equation 3.33 must recognise the fact that post-oxidation sample dimensions, x_2 will not be the same as pre-oxidation dimensions, x_1, i.e. sample surface area will change, so the mass gain data must first be used to find the equivalent sample volume change. Figure 3.27a shows how Equation 3.33 (derivation in Appendix 3) was derived, reflecting the fact that the volume of oxide formed, V_{gain}, will be cubic volume using the new sample dimensions, V_2, minus the existing volume of the sample before oxidation, V_1 (assuming an equal oxidation rate on all sample surfaces). This approach also depends on assuming a homogeneous oxide, i.e. a fully dense oxide layer or a constant porosity within the oxide.

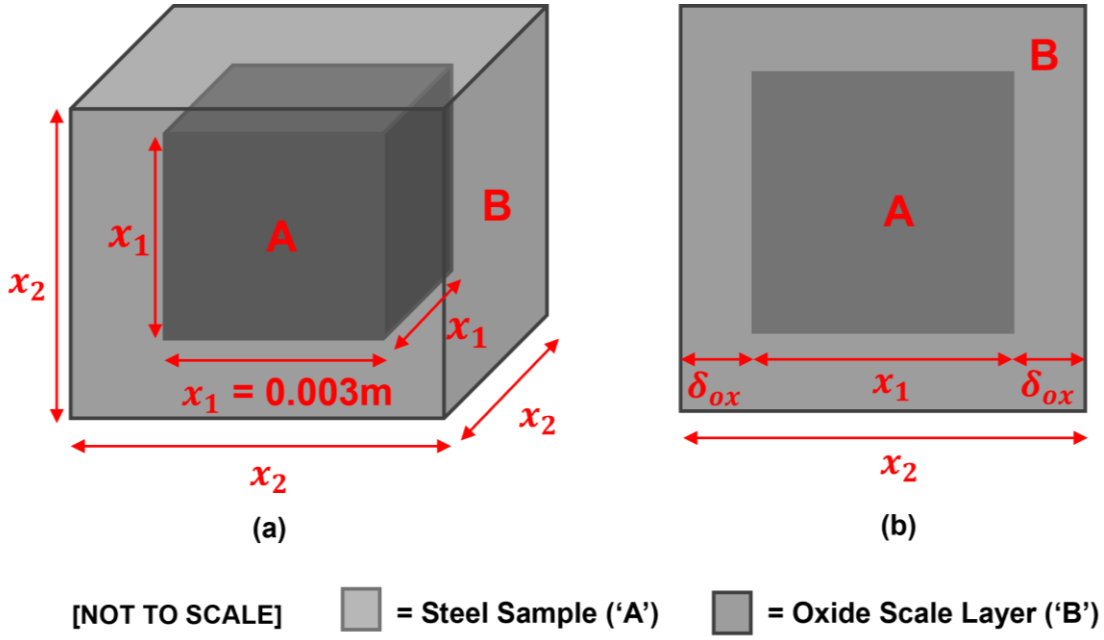


Figure 3.27: Schematic showing assumed pre-, x_1, and post-oxidation, x_2, dimensions of post-oxidation samples in (a) isometric and (b) end views ¤. These dimensions are used to calculate the oxide thickness gain, δ_{ox} ¤.

$$x_2 = \sqrt[3]{V_{\text{gain}} + x_1^3}$$

Equation 3.33

Figure 3.27b shows how oxide thickness, δ_{ox}, can therefore be calculated from Equation 3.34.

$$\delta_{ox} = \frac{x_2 - x_1}{2}$$

Equation 3.34

Initial validation checks were performed by running the total mass gain for the two steel samples through the above algorithm coded in MATLAB R2024b. This gave a value of 41.4µm and 36.3µm oxide thickness for E24 and E41 respectively.

However, an alternative approach was to handle the raw mass gain data from the STA experiments and convert the model's oxide thickness output to a mass gain (see Equation 3.35). This was arguably a more accurate approach as, unlike the STA samples, within the model definition there was the existing parameter which justified the assumption of equal oxide growth across the surface, and only a single surface area, A, to consider, unlike the cubic STA samples. Equation 3.35 was used to convert the model oxide thickness predictions to a total mass gain value, Δm, for the isothermal test simulated. Extension of the 1D model to 3D was achieved by extending backwards to 3mm to match the STA samples' depth, x_1 (see Figure 3.29).

$$\Delta m = \rho A x_1$$

Equation 3.35

Figure 3.28 shows the comparison between the STA and model sample geometry, used to derive Equation 3.35.

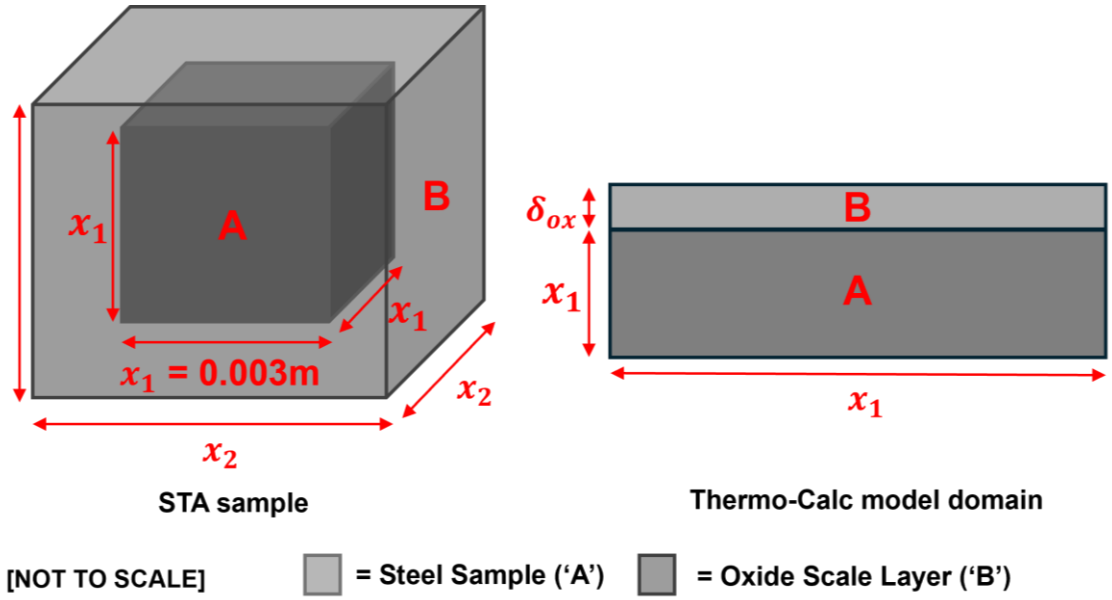


Figure 3.28: Comparison of 1D geometry domain in Thermo-Calc© model (*right*) and the cubic simultaneous thermal analysis (STA) samples (*left*) ¤.

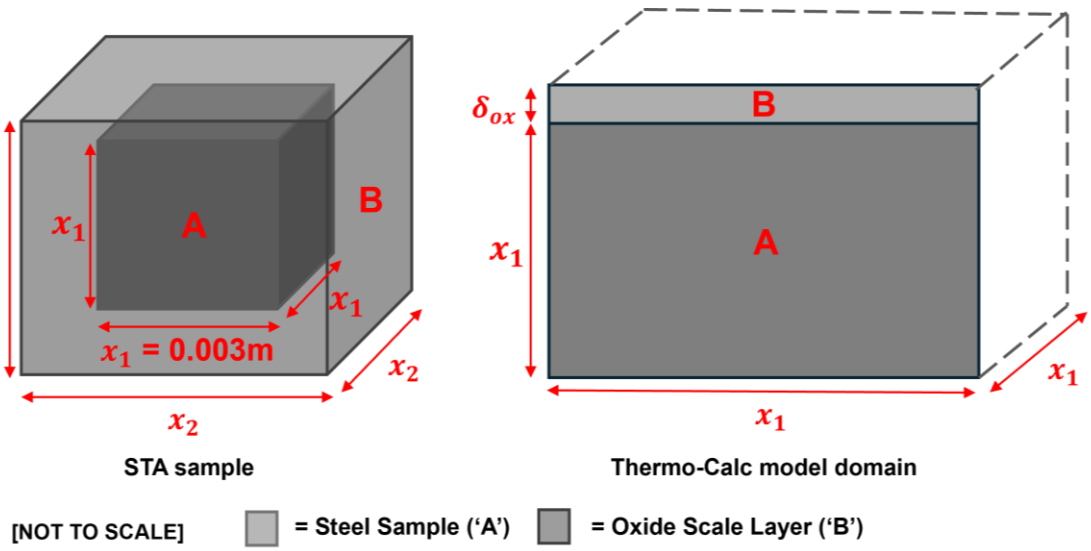


Figure 3.29: Diagram showing hypothetical extension of computational domain into the third dimension (*right*) for validation comparison with the real 3D simultaneous thermal analysis (STA) sample (*left*) ¤.

In light of the geometry-related deviation of the oxidation kinetic profiles observed on planar vs. cylindrical geometries in the work of Imbrie and Lagoudas [93] (see Section 1.7.1), the previously described experiment was repeated with identical parameters but with a 72hr

soak period at the same temperature of 1000°C. This provided kinetic data for an extended soak of planar geometry.

Non-isothermal Considerations

For the sake of comparison, attempts were made to modify the Thermo-Calc© model to reflect the unavoidable heat ramp of the STA experiment (a sample can only be added to a crucible at the start of the thermal cycle, i.e. not once temperature has stabilised to the isothermal soak value). However, this caused the model to fail to converge to a stable solution due to the steep thermal gradients. The model complexity was also exacerbated by the introduction of a non-isothermal period due to the temperature dependence of so many of the parameters in both the thermodynamic and kinetic databases, thus introducing many more calculations to achieve a solution. For example, diffusion coefficient, which contributes significantly to the model and databases, has a proportional relationship with temperature [239] and will therefore need to be recalculated for each temperature node within the transient region of the model. Changes to diffusion coefficient will also affect oxide kinetics [222] and therefore oxide gain.

Instead, a baseline mass gain obtained after the application of the heating ramp was obtained by repeating the initial 5 minute soak experiment described above. The mass gain after the non-isothermal period was obtained and then subtracted from the mass gains obtained for the isothermal period. This technique was applied for all future STA validation experiments.

As part of the geometric validation, an initial attempt to run the model to simulate 24hrs worth of oxidation (a shorter extended period, and large maximum timestep of 100s, was used for these initial explorations to shorten the convergence time as only broad conclusions were needed). This initial attempt failed due to the model anticipating the disappearance of the austenite region. Thus, the initial hypothesis was that the entire austenite layer thickness was consumed before the end of the simulation period. Further investigations gradually decreasing the simulation time revealed that the austenite layer was fully consumed after 4.84 hrs. To support this, investigation of the console output revealed that at the final time step (4.77 hrs) before the model failed due to consumption of the austenite region, the SSI position was 7.7μm, i.e. only 0.3% of the initial 3mm thickness. In contrast, when compared with *exi3a* example file previously discussed [326] (although the file uses different pre-processing conditions – see Section 3.1.1) the SSI position had only reduced to 98.8% of the initial 4.99mm thickness (from 4.99mm to 4.93mm, a reduction of only 1.2%).

The initial hypothesis was that the diffusivity of iron in wüstite was too high and rapid diffusion of the cations out of the substrate meant the substrate was consumed too quickly. This would also explain the overestimate of oxide gain (mass and thickness) compared to the STA data. Investigation revealed that an incorrect units conversion, due to the older nature of the data sources, resulted in the mobility pre-exponential factor being three orders of magnitude too big. Correction of this issue, and a sense check comparison to existing spinel phase data, solved both the issue of the overestimate, reducing the predicted total oxide thickness to 123.8μm and allowing a 72hr simulation to be run as a result of the more realistic substrate consumption rate.

The initial 72hr simulation was run with an initial maximum allowable timestep of 1000s for the sake of brevity to assess the effect of the decrease in diffusivity. This initial run only took 236s and had 253 datapoints. The initial predicted oxide thickness after 72 hours was 3.42mm. With the aim of improving on existing accuracy, the maximum allowable timestep was decreased to 100s (although the initial timestep was still only 0.4% of the total simulation time). However, the total oxide thickness changed by only 0.6% (increase to 3.44mm) but with a considerable increase in simulation time of >20mins.

Figure 3.30 shows the comparison between the mass gain in the isothermal region (1000±1°C) of STA testing (planar geometry heated at 1000°C for 5 minutes), for both grades, compared to iron oxidised in the Thermo-Calc© model (converted from oxide thickness to mass gain using wüstite density). It should be noted that the data in Figure 3.30 only represents a few hundred seconds worth of data from an STA dataset with a total length of almost seven hours, as this is reflective of the short isothermal heating region modelled by the Thermo-Calc© model under validation and is representative of the normalisation conditions used in conveyance tube manufacturing (see Section 1.2). This highlights one of the limitations in performing industrially representative experimental investigations of oxidation kinetics due to hardware operating procedure. For example, the STA hardware used does not allow samples to be inserted 'at temperature' and they must be in the heating crucible for the entire thermal cycle, therefore isothermal oxidation kinetics cannot be studied in isolation using STA. Each plot is annotated with its respective parabolic rate constant (obtained by a first order *polyfit* function in MATLAB R2024b).

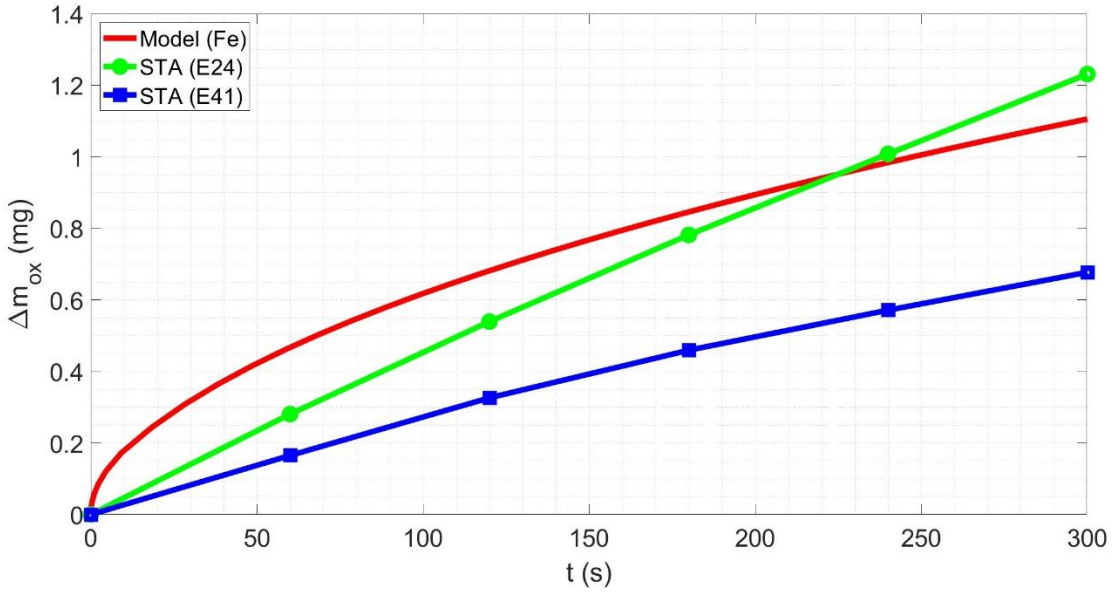


Figure 3.30: Comparative plot of mass gain, Δm_{ox}, following heating to 1000°C for a time, t, of 300s for Thermo-Calc© Fe model (*red*) vs. STA testing for E24 (*green*) and E41 (*blue*) tube grades, annotated with parabolic rate constant, k_p ¤.

Although the model's predicted total mass gain lay within the range observed for the STA samples, suggesting a sufficiently accurate pre-processing methodology, its oxidation rate was higher overall. Both experimental datasets also had barely noticeable correlation to a parabolic profile (which is inherent in the model due to its theoretical foundations – see Section 1.7.1). The discrepancy between the computational and experimental results was assumed to be multi-dimensional. Firstly, whilst the experimental data can be obtained directly from the equipment as continuous mass gain, the model data must be converted from a continuous thickness gain form, owing to the moving phase boundary methodology used to make computational predictions. In doing so, whilst the experimental samples are 3x3x3mm cubes, i.e. with six surfaces sharing the same, only a single surface, i.e. 1D geometry, can be modelled, hence that single surface of equivalent area theoretically has access to six times as much material as each individual surface in the experimental samples. Hence, the mass gain associated with the model must nominally be divided by six to allow for an equivalent comparison. Furthermore, a key assumption of the model and its post-processing calculations, particularly those concerning density, was that of a perfectly compact scale layer, i.e. no porosity. However, porosity is a key property affecting diffusion mechanisms at the microstructural level. In this manufacturing case, porosity was most likely to arise due to thermal deformation mismatch between the steel and scale [332], mechanical strength differences between phase layers (in the real case where multiple oxide phases form) [77], and growth stresses due to oxidation-induced volumetric changes [104].

This is discussed in greater detail in the geometric validation aspect of this work in Chapter 4 but ultimately it is concluded that only a modified diffusion coefficient can account for porosity and its associated effects, rather than in the pre-processing of the model [93]. Furthermore, the diffusion coefficient is further complicated by the stoichiometric nature of the wüstite phase used in the model. In addition to temperature, an increase in the contribution of iron to the molar fraction evolves a linear increase in diffusivity and thus accelerates ion diffusion [97]. Stoichiometry, and related partial pressure effects, was not accounted for in the initial project-specific database. This will increase discrepancy with real-world phenomena.

The STA data alone revealed a 13% difference in total mass gain between the two grades tested. This was attributed to the interactions of the dominant non-carbon alloy elements, manganese and silicon (see Table 3.1), with iron and oxygen to form oxides which affect oxidation kinetics and adhesion. Phenomena associated with alloy element interaction were discussed in Section 1.6.1 [239]. This was beyond the scope of investigation at this stage but is discussed in Chapter 3 as the model chemistry is complexified to reflect tube-specific steel composition. Table 3.5 summarises the comparison of the model thickness output and relevant literature sources [59].

Table 3.5: Comparison of oxide thickness, δ_{ox}, and thickness-based parabolic rate coefficient, k_p, for model and literature results for a sample soaked for 5 mins at 1000°C.

Result	Material	δ (μm)	$k_{p,\delta}$ ($cm^2.s^{-1}$)
Thermo-Calc© simulation	Iron	123.8	4.99×10^{-7}
Paidassi (1957)	Iron	142.2	6.74×10^{-7}
Chen and Peterson (2003)	Low carbon steel	57.5	1.10×10^{-7}

Finally, the model at this stage only comprises a binary Fe-O system which is not reflective of the higher-order system of steel in natural gas combustion with air. Chen and Peterson compiled findings regarding the difference in oxidation response when considering iron vs. steel and their environments [257]. Iron shows an overall higher oxidation rate than steel, with the value showing negligible variation between pure oxygen and air gas environments. In contrast, steel oxidises at a faster rate in pure oxygen than air (~21% oxygen [382]). Hence, at this stage the comparison is between oxidation of iron in pure oxygen in the model and steel in 10% O_2 -90% N_2 composition to reflect the reheat furnace combustion atmosphere. Therefore, to align the model better with validation testing and the reality of

tube manufacturing, carbon and potentially additional influential alloy elements must be added to the model element system and the input oxygen activity must be modified to better reflect the real-life gaseous conditions.

Further Considerations of Heating Profile

As previously discussed, the computational thermochemistry approach does not yet lend itself to efficiency over its empirical counterpart when considering non-isothermal scenarios, and what was formerly a two minute calculation remains unresolved after an hour. Furthermore, attempts to include non-isothermal heating led to convergence failure due to the steep thermal gradients evolved. Hence, this work is limited to consideration of isothermal oxidation, as in other studies [234]. Saputo et al. investigated AISI 1040, a low carbon micro-alloyed steel alloy with a composition similar to that of E41, for its potential to oxidise to a damaging level when used as a diesel engine piston [383]. Automotive combustion chamber materials with higher thermal resistance increase the potential for higher efficiency diesel engines by releasing more design and capability space. Like the tube manufacturing process, thermo-chemical degradation within diesel engine combustion chambers by oxide growth and spalling is complicated by the transient and non-uniform nature of the combustion environment which contains aggressive combustion species, e.g. carbon/nitrogen oxides, water vapor, short lived OH- radicals (see Section 1.6.1), and variable heat flux. As with the tube manufacturing process these phenomena manifest as spatial and temporal variations in temperature and mechanical stress (the latter being more relevant for stretch reduction in the tube manufacturing case).

Although Saputo et al. investigated cyclic heating rather than a single heat-soak-cool cycle form of non-isothermal heating, the approach used to compare isothermal and non-isothermal heating was still valid. Isothermal oxidation kinetic data (for both mass gain and thickness) were collected using TGA and literature, and temperature-dependent parabolic rate coefficients were derived graphically using the Arrhenius equation (see Equation 3.36). However, it should be noted that mass- and thickness-based parabolic rate coefficients are not directly comparable as transitioning between mass and thickness via oxide density and volume values do not account for porosity. Porosity has been shown to increase the diffusion coefficient by multi-directional diffusions over a larger effective diffusion length [260, 361]. Porosity also worsens significantly across a narrow high temperature range (830°C-1150°C), even when the higher temperature sample is heated for less than 10% of the time of the lower temperature sample (1500s vs. 100s) [77, 118] and on external tube

surfaces [85]. As seen in this work, the diffusion coefficient should be calculated directly from the oxide mass or thickness gain-time data respectively.

$$k_p = k_0 e^{\frac{-Q}{RT}} \Leftrightarrow lnk_p = lnk_0 - \frac{Q}{RT}$$

Equation 3.36

Due to the transient nature of heating, the Arrhenius equation (Equation 1.7) becomes iterative in order to predict oxide thickness for non-isothermal conditions based on the isothermally determined parabolic rate coefficients (see Equation 3.37).

$$k_{pi} = k_0 e^{\frac{-Q}{RT_i}}$$

Equation 3.37

Similarly, Equation 1.7 also becomes iterative (see Equation 3.38). There was good agreement between the measured and predicted oxide thickness in Saputo et al.'s work [383].

$$x_i^2 = k_i t_i + x_{i-1}^2$$

Equation 3.38

It should be noted that the mass gain data yielded an activation energy close the literature value for iron diffusion in wüstite, arguably due to inner wüstite layer diffusion being the rate-limiting scale growth step (see Section 1.3.1). Although the scale thickness-derived activation energy was 14% higher than the iron through wüstite diffusion value, this was attributed to the complex oxide morphology and challenges in measuring thickness on the SEM micrograph. This shows how conversion from mass gain may be more accurate. Saputo et al. [383] also gave a detailed discussion of experimental uncertainty due to the '…dynamic and highly complex…' nature of physical phenomena inherent within combustion, experimental measurements and manufacturing variability. They argued that although surface temperature was recognised as a dominant factor in oxide thickness prediction, uncertainty in the calculation of surface heat flux and telemetric errors in temperature measurements were deemed to have a small contribution to predicted-measured oxide thickness discrepancy. Conversely, the contribution of local kinetic variability due to rate constant derivation errors and the transient, non-uniform nature of combustion were deemed significant. The lack of a clear uniform relationship between

oxide thickness and temperature on the piston sample led Saputo et al. to conclude that a single set of rate constants cannot describe oxidation across the entire sample due to local chemical environmental variation causing deviation from ideal kinetic theory. The derived activation energy was only approximately a fifth of values associated with the typical iron oxide phases (wüstite, haematite, magnetite) observed during micrograph inspection. A combination of high pressure, air-fuel mixing fluid dynamics, and laboratory idealisation of air-water vapour content, led to the conclusion that combustion only reflects the ideal oxidation in the initial stages of oxidation due to fresh air contacting the part. Overall, it was concluded that isothermal oxidation kinetics can capture oxide kinetics in transient environments but not variable environments, however information about the severity of oxidation and its potential to accelerate degradation, is still valid, as seen in the piston study. This may become relevant for tubes as at a small enough radius (possible in the Install® Plus range [2]) that the local gaseous environment at the inner surface of the tube is significantly different to the global environment. However, in the interest of computational efficiency, it was questioned whether, in the case of the STA data, it was not reasonable to assume the start of the parabolic region coincided with the start of the isothermal region (see Figure 3.31). Thus, an accurate assessment of the STA parabolic rate constant was not being achieved. It was decided that a technique was required which could automatically differentiate between the linear and parabolic oxidation regimes for any data set.

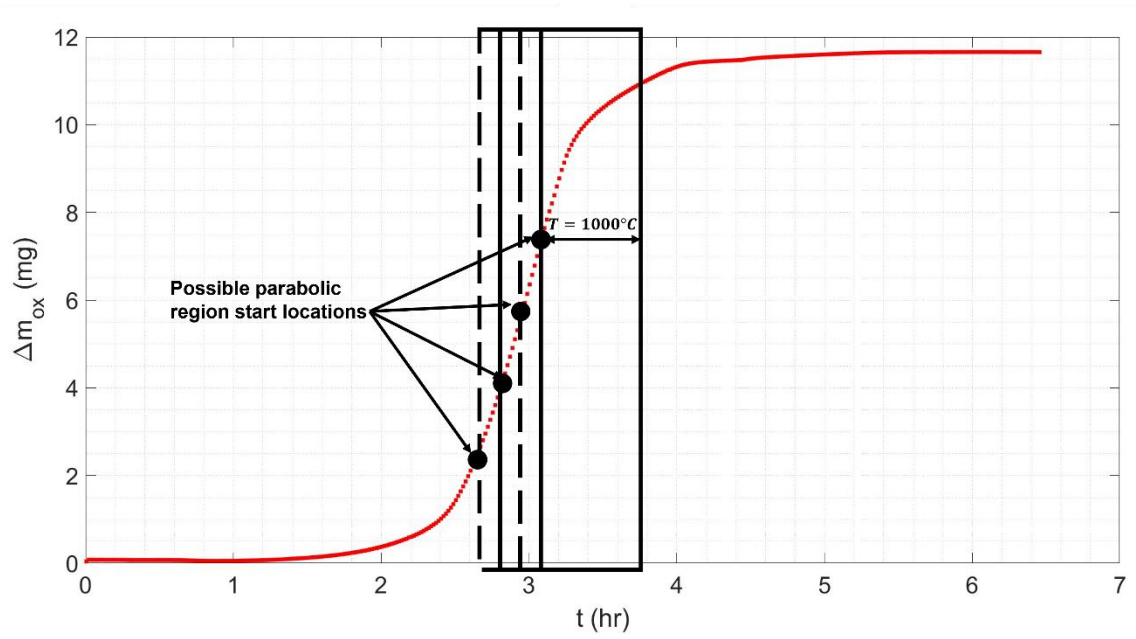


Figure 3.31: Demonstration, on a plot of oxide mass gain, Δm_{ox}, against time, t, of how the isothermal heating region may exclude some of the parabolic heating region and lead to an inaccurate assessment of parabolic rate constant ¤.

Technique 1: Statistical Correlation Assessment

Firstly, the parabolic region was sought using the Pearson correlation coefficient, $\boldsymbol{r}$, for oxide mass gain, $\Delta \boldsymbol{m_{ox}}$, and time, $\boldsymbol{t}$, (see Equation 3.39) based on their respective mean, $\boldsymbol{\sigma}$, and standard deviation, $\boldsymbol{\mu}$ [384]. It was anticipated that there would be a distinct difference between the strong correlation observed in the initial linear region ($\boldsymbol{r} \rightarrow 1$) and the subsequent parabolic region with a poorer correlation ($\boldsymbol{r} \rightarrow 0$).

$$\boldsymbol{r_{\Delta m_{ox},t}} = \frac{\mathbb{E}\left[\left(\Delta \boldsymbol{m_{ox}} - \boldsymbol{\mu_{\Delta m_{ox}}}\right)\left(\boldsymbol{t} - \boldsymbol{\mu_t}\right)\right]}{\boldsymbol{\sigma_{\Delta m_{ox}}\sigma_t}}$$

Equation 3.39

Figure 3.32 and Figure 3.33 show how the correlation coefficient follows a completely different trend which did not correlate to the linear-parabolic transition. For E24, there is an absence of linear correlation which improves steadily before stabilising at a value of 0.5 after almost 3 hours (which coincides in a rapid increase in mass gain). Beyond this rapid increase region (beyond 6 hours), strength of correlation continues to increase steadily to a final value of ~0.9 at the end of testing. An identical trend is followed by E41. This was attributed to the fact that Pearson correlation coefficient measures the "strength" of relationship between two variables rather than numerically quantifying the linear relationship itself i.e. it does not measure linear gradient [384].

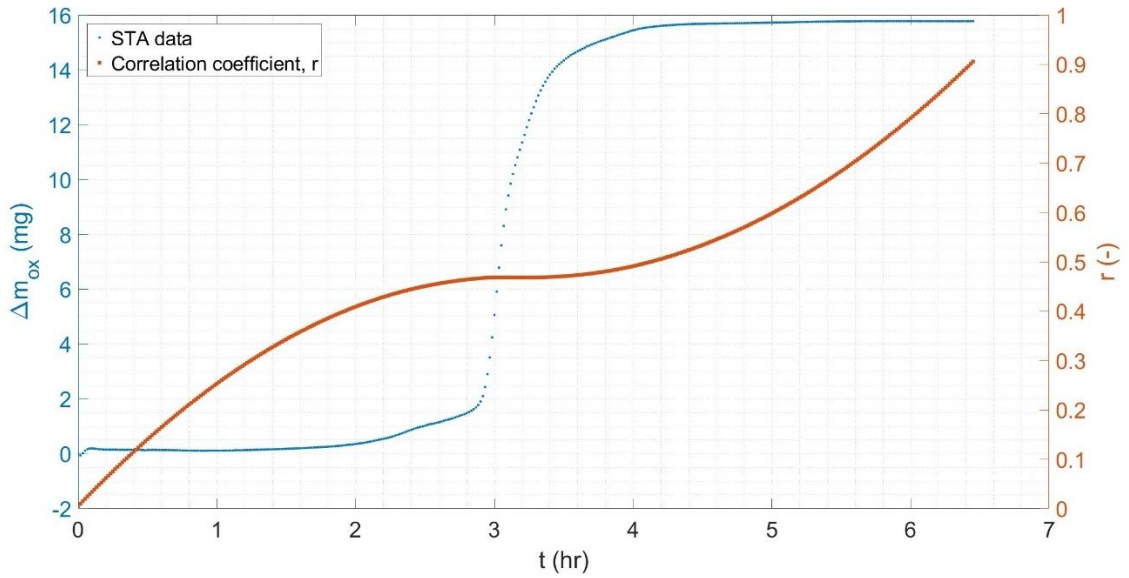


Figure 3.32: Pearson correlation coefficient, $\boldsymbol{r}$, result for E24 simultaneous thermal analysis (STA) data plot of oxide mass gain, $\boldsymbol{\Delta m_{ox}}$, against time, $\boldsymbol{t}$, ¤.

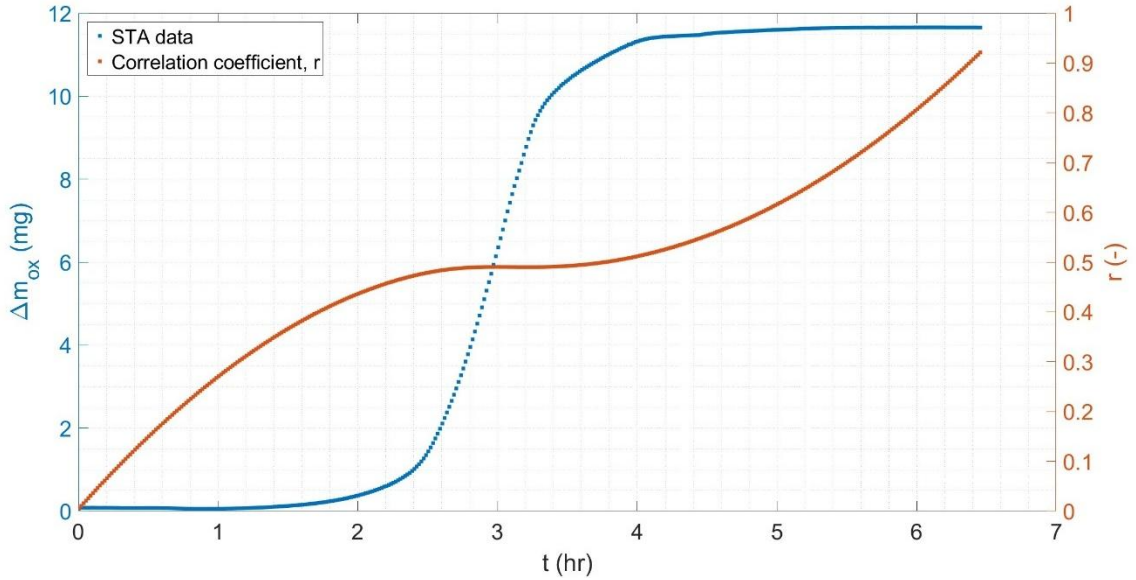


Figure 3.33: Pearson correlation coefficient, r, result for E41 simultaneous thermal analysis (STA) data plot of oxide mass gain, Δm_{ox}, against time, t, ¤.

Although the square of r is associated with an assessment of the 'goodness of fit' of a linear model, it offered no more insight into the linear-parabolic transition for either grade (see Figure 3.34 and Figure 3.35) [384].

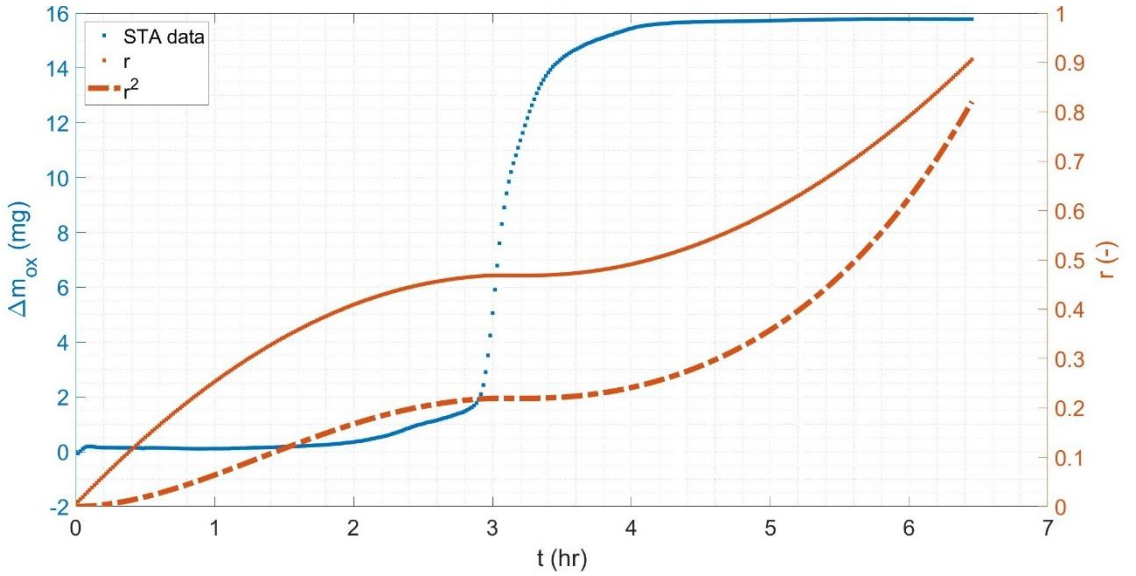


Figure 3.34: Demonstration of lack of insight into linear and parabolic trends provided by both the Pearson correlation coefficient, r, and its square, r^2, for E24 simultaneous thermal analysis (STA) data plot of oxide mass gain, Δm_{ox}, against time, t, ¤.

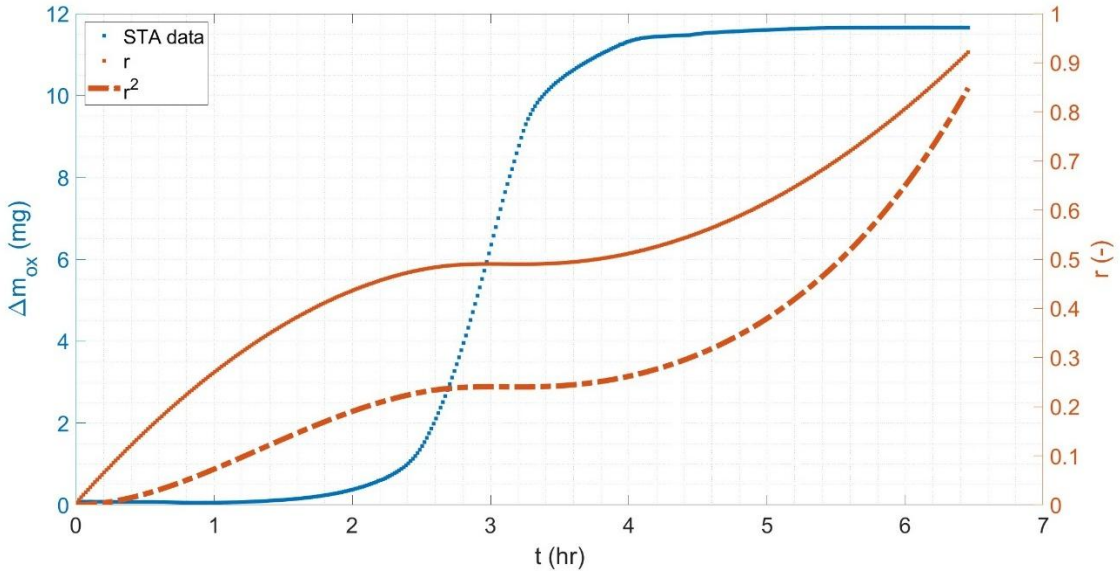


Figure 3.35: Demonstration of lack of insight into linear and parabolic trends provided by both the Pearson correlation coefficient, r, and its square, r^2, for E41 simultaneous thermal analysis (STA) data plot of oxide mass gain, Δm_{ox}, against time, t, ¤.

Technique 2: Local Gradient Assessment

The alternative technique involved evaluation of the 'local' gradient, m_{local}, between each data point (see Equation 3.40).

$$m_{local} = \frac{\Delta m_{ox_{i+1}} - \Delta m_{ox_i}}{t_{i+1} - t_i}$$

Equation 3.40

where Δm_{ox} is oxide mass gain and t is time.

It was hypothesised that local gradient would be consistent up to the end of the linear region before changing dramatically once the parabolic region was reached (see Figure 3.36 for the derivation of this hypothesis). However, Figure 3.36 also shows the small fluctuations which are present in the linear data (for the E41 STA data as an initial example of the principle) which could register as a false parabolic transition once an appropriate condition is applied.

The parabolic region is identified by marking adjacent point as true ('1') and all others as false. The start and end of these consecutive regions is identified using [0 1] and [1 0] strings, with the longest string of 1 (the biggest difference in location of corresponding [0 1] and [1 0] strings) denoting the parabolic region.

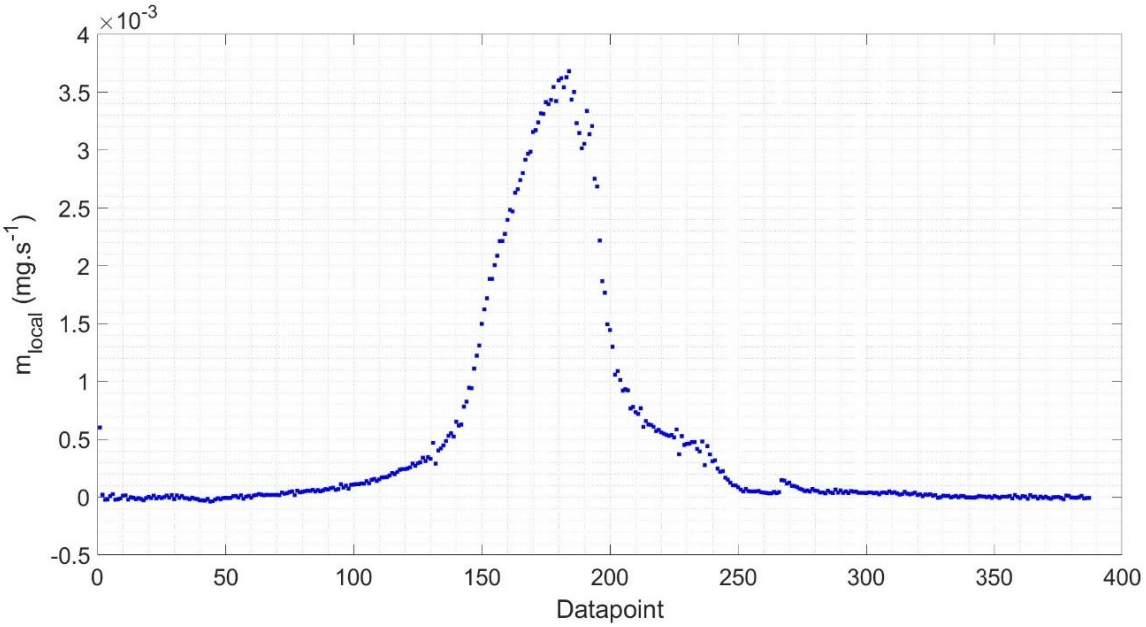


Figure 3.36: Local gradient, m_{local}, plot for each datapoint of E41 simultaneous thermal analysis (STA) data ¤.

Therefore, the mass gain data was filtered using a Moving Point Average technique with a window of 3 datapoints initially (see Equation 3.41) [385].

$$f_i = \frac{1}{window} \sum_{j=0}^{window-1} x[i+j]$$

Equation 3.41

This removed some fluctuations (see Figure 3.37). Figure 3.38 shows a plot of local gradient at each (smoothed) datapoint plotted alongside the STA data itself, which highlights the improvement in correlation between changes in mass gain rate and changes in local gradient.

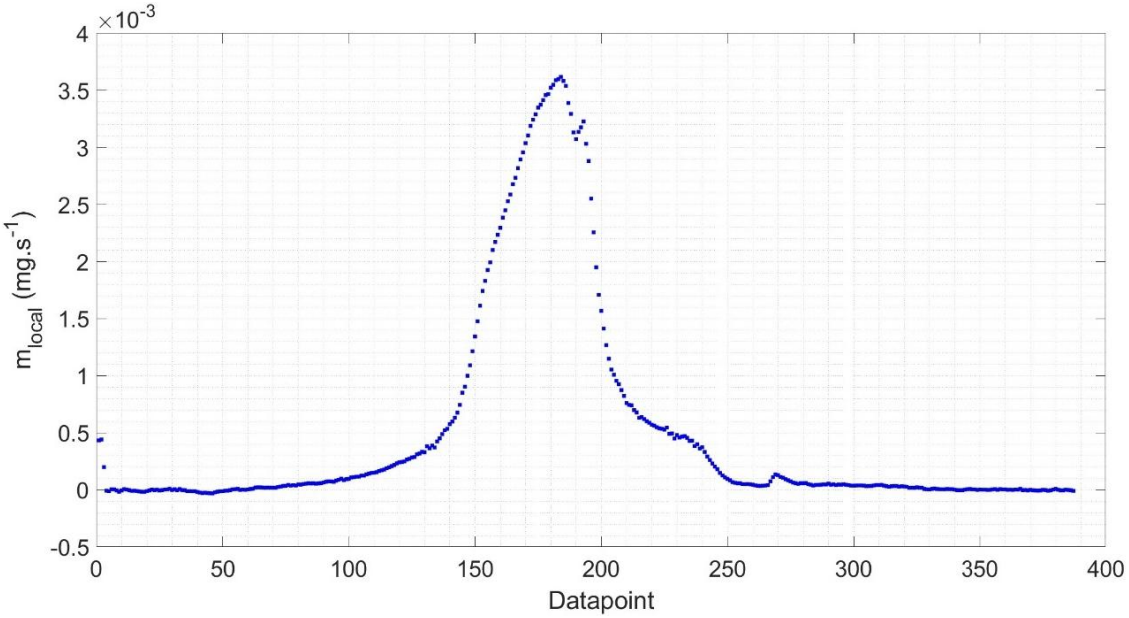


Figure 3.37: Local gradient, m_{local}, plot for each datapoint of smoothed E41 simultaneous thermal analysis (STA) data ¤.

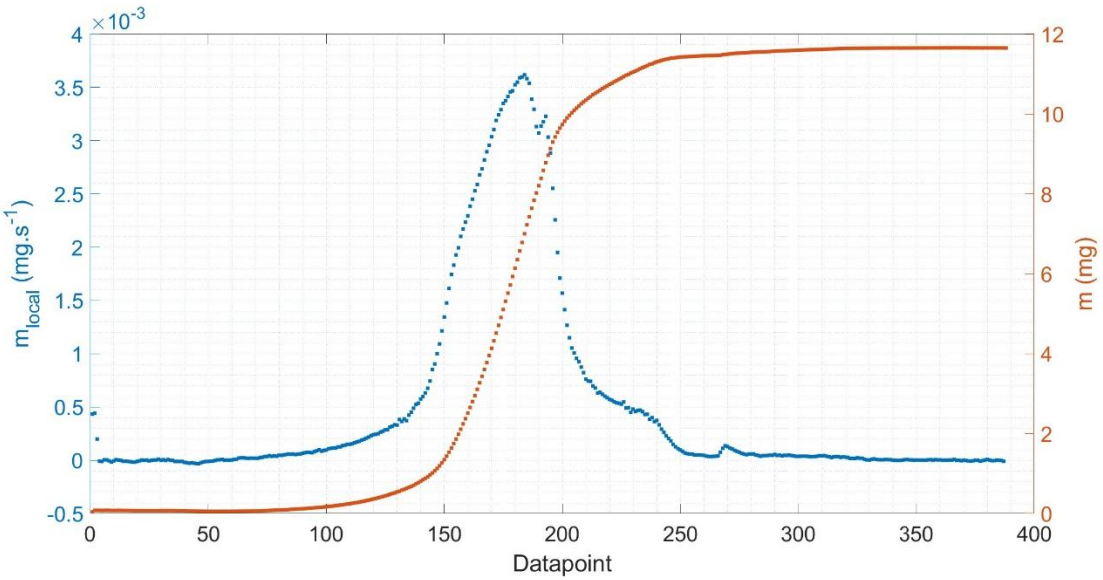


Figure 3.38: Local gradient, m_{local}, plot for each datapoint of smoothed E41 simultaneous thermal analysis (STA) data compared to the original STA oxide mass gain, Δm_{ox}, against time, t, data ¤.

3.4 Conclusions from Chapter 3

Within this chapter, the development of a computational model for external oxidation of the outer conveyance tube surface is described. Thermo-Calc©'s DICTRA diffusion module is used to numerically solve a Stefan moving phase boundary problem. Microsoft Visual Studio (VS) Code and Thermo-Calc©'s TDB Editor extension were used to encrypt user-defined thermodynamic and kinetic databases using literature data. For the simulations, microstructural defect pre-processing was used to improve tube manufacturing representativeness, with a focus on grain boundary diffusion in the type B kinetic regime. Convergence analysis revealed that the optimal time step for accuracy was 1000s. Using this constraint, the model resolved several hundred data points in approximately two minutes. However, there were inaccuracies in the model, with respect to the difference in oxide thickness predictions compared to experimentally derived samples under the same thermomechanical conditions, associated with microstructure, alloy chemistry, stoichiometry, and propagated error during data conversion. Overall, the model is a simplification of the real, complex, industrial scenario, and could be refined but already agrees well the experiments. The model is also a novel use of Thermo-Calc© DICTRA to solve the diffusion equation for the Fe-O system using Gibbs free energy minimisation, CALPHAD, bespoke thermochemical databases, and the moving phase boundary methodology to predict oxidation kinetics and oxide thickness.

For the experiments, a high accuracy Simultaneous Thermal Analysis (STA) approach comprising Thermogravimetric Analysis (TGA) and Differential Scanning Calorimetry (DSC) techniques was used to validate the initially planar geometry model. A new method was used, taking geometry, material properties, and heating profile into account, to convert model oxide thickness predictions to mass gain values comparable with the experimental data. There was good agreement (±10% difference)between model and experimental values of oxide gain but parabolic rate constant agreement was less precise due to the difference in thermal cycle (purely isothermal for the model but largely non-isothermal with a very short isothermal cycle for the experimental). The inability to study isothermal conditions in isolation was a limitation of the experimental hardware used. The model data showed stronger agreement, in terms of parabolic rate constant, with the literature due to the ability to directly compare pure iron samples and the availability of literature data derived from purely isothermal oxidation data.

Chapter 4 Investigation of Effect of Curvature on Oxidation Using Thermo-Calc©

In Chapter 3, a thermochemical model for predicting oxide kinetics was developed in Thermo-Calc® and validated for a planar geometry using Simultaneous Thermal Analysis (STA). For this model to be used for conveyance tube applications, it must be extended to cylindrical geometries and their associated diffusion equation (see Section 1.7). This chapter discusses the potential for the model to be successfully used for cylindrical geometries, and the geometry-related phenomena which must be accounted for in pre- and post-processing of associated data. The region of the research flowchart (Figure 1.33) under discussion in this chapter is shown in Figure 4.1.

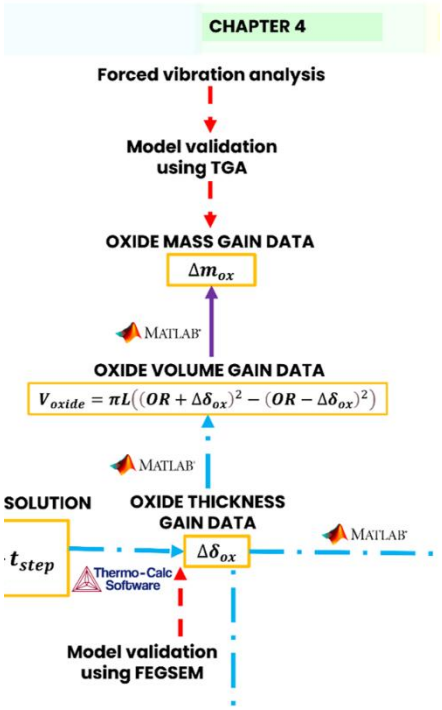


Figure 4.1: Region of the overall research flowchart (see Figure 1.33) which is under discussion in this chapter.

The work in this chapter also contributed to the following peer-reviewed publications:

- M. Kendall, M. Coleman, H. Cockings, E. Sackett, C. Owen, and M. Auinger, "Computational Thermochemistry for Modelling Oxidation During the Conveyance Tube Manufacturing Process," *Metals*, vol. 14, no. 12, December 2024. [Online]. Available: https://doi.org/10.3390/met14121402.

- M. Kendall, M. Auinger, C. L. J. Robinson, C. Owen, and E. Sackett, "In Situ Thermogravimetric Analysis of Curved Surfaces During High-Temperature Oxidation," *Materials,* vol. 18, no. 11, May 2025. [Online]. Available: https://doi.org/10.3390/ma18112463.

4.1 Oxidation for Cylindrical Geometry

To develop the model from Chapter 3 further and improve its representation of the real-life manufacturing scenario, a cylindrical geometry was introduced into the command lines. A geometrical exponent of 1 was selected to generate a hollow cylinder (tube) of infinite length and the inner radius and wall thickness (the two definable parameters in console mode command lines) were set at 35mm and 10mm respectively to reflect the average of the upper and lower bounds of the Tata Install® range options [2]. Control of these two parameters makes the model well-suited to TSUK's tubes, which are manufactured with a controlled outer diameter ($\boldsymbol{OD}$) and a variable wall thickness, $\boldsymbol{r_{wall}}$, (and subsequently inner diameter ($\boldsymbol{ID}$)) according to the corresponding weight category ('heavy' or 'medium'). The initial wüstite thickness was unchanged at 0.1nm and the existing grid definitions were used for the austenite and wüstite regions.

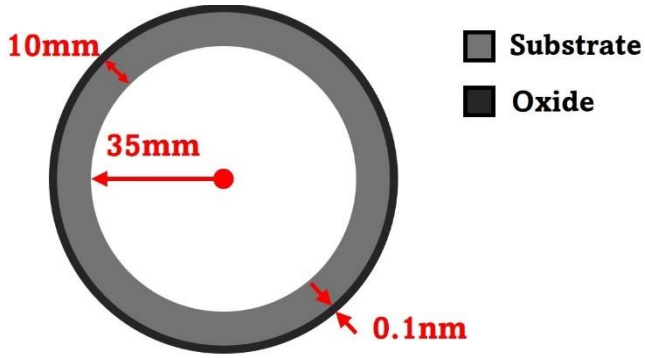


Figure 4.2: Geometry used for initial hollow cylindrical geometry set-up test [NOT TO SCALE] ¤.

Initial results suggested a negligible difference in the oxide scale generated after three minutes when the geometry was changed to a hollow cylindrical form. However, there were subtle differences in values which indicated that changing the geometry from planar to cylindrical contributed a small difference in the order of $\frac{\boldsymbol{D}}{\boldsymbol{r}}\left(\frac{\boldsymbol{\partial c_k}}{\boldsymbol{\partial r}}\right)$, as described by Equation 1.31, and there was no error or omission in the code. To confirm this, a plot of the position of the lower austenite interface was generated to demonstrate the stable but different position of the planar and cylindrical surfaces (see Figure 4.3). The position of the inner surface of the tube is defined as an offset from the origin, therefore the lower austenite interface moves from zero, i.e. at the origin, in the planar case to 35mm in the cylindrical case (as shown in Figure 4.2). Although the model is based on a moving phase boundary methodology, only the outer surface of the cylinder (tube) is oxidised in the simulation and the inner surface is assumed to be inert. Oxidation of the inner tube surface requires

separate consideration due to its different stress state [85], and therefore extent of spalling [84], and the potential of the oxide to provide passive protection from conveyance fluids during service [68]. This is outside the scope of this project.

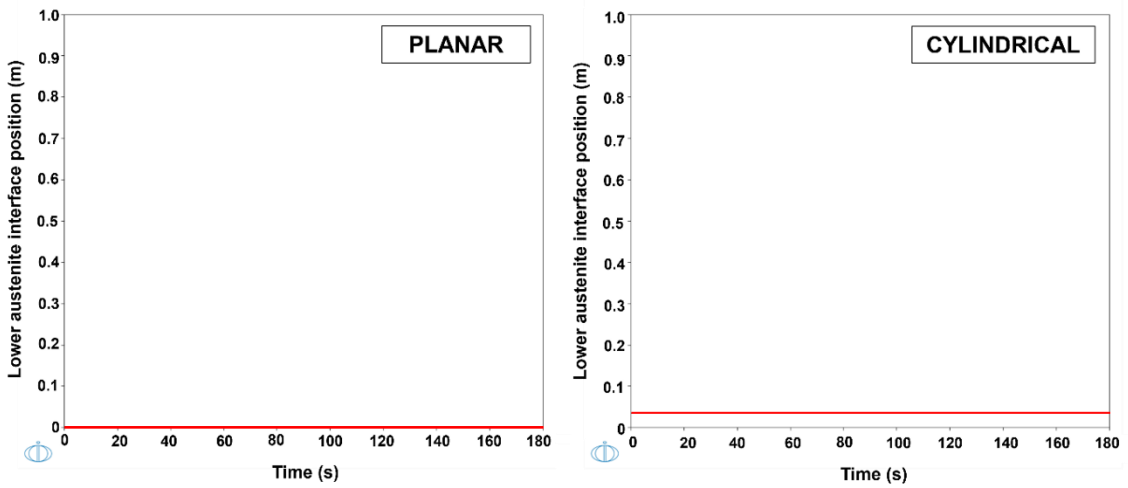


Figure 4.3: Comparison of lower austenite interface position of zero, i.e. the origin, for planar case (*left*) and 35mm for the cylindrical (tube) case (*right*) during a three minute normalisation simulation in Thermo-Calc© ¤.

Figure 4.4 shows the negligible discrepancy between the predicted oxide thickness for the planar and cylindrical geometries respectively, with maximum oxide thicknesses, $\boldsymbol{\delta_{oxide}}$, of 85.934μm and 85.947μm respectively. This gives an initial indication that simply transitioning from a planar to cylindrical geometry, without considering dimensions, has a negligible impact on oxide kinetics.

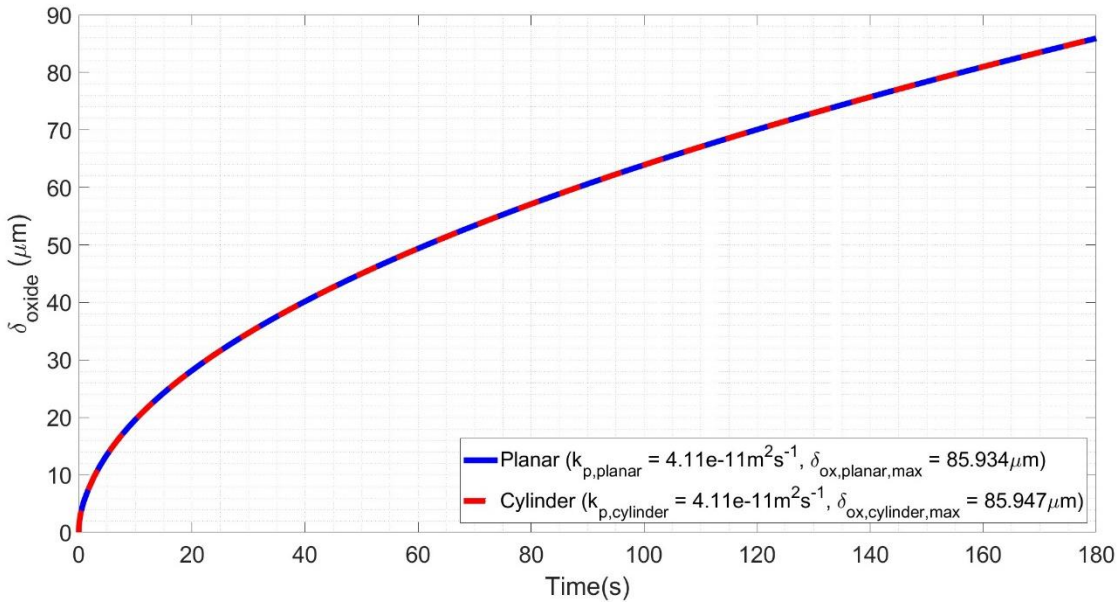


Figure 4.4: Plot of Thermo-Calc© model predicted oxide thickness, $\boldsymbol{\delta_{oxide}}$, against time, $\boldsymbol{t}$, using a flat plate geometry (*blue*) and hollow cylinder geometry (*red*) at 950°C for three minutes ¤.

However, when a graph of the absolute difference between predicted oxide thickness for corresponding data points is plotted (rather than for corresponding timesteps since it cannot be assumed that the resolved models for each geometry had equivalent timesteps) there is a monotonic deviation trend. Figure 4.5 shows this trend and also suggests a strong linear relationship with a correlation coefficient, $\boldsymbol{R^2}$ (see Equation 4.1), of 0.999 between the original data and a least-squares regression fit [317], this is most likely due to the short heat treatment simulated which does not allow for development of a valid trend on the macroscopic scale. Deviation between the two geometries (though small) approaches a maximum value of 12.3nm. This value is a negligible percentage (~0.01%) of the maximum oxide thickness of both geometries). However, the timestep profiles for both geometries were identical, with minimum and maximum timesteps of $1x10^{-7}$s and 1s respectively (see Figure 4.6). It was noted that CPU requirements for both models were similar at 77s and 74s for the planar and cylindrical geometries respectively. Overall, Figure 4.5 shows how the difference between predicted oxide thicknesses for planar and cylindrical geometries, under identical thermomechanical conditions, at corresponding spatial datapoints, increases linearly as the model proceeds through the spatial field. The black line represents the absolute difference between predicted oxide thicknesses for planar and cylindrical geometries, $\left|\boldsymbol{\delta_{oxide,planar} - \delta_{oxide,cylinder}}\right|$, and the red line represents the trend expected if the relationship between $\left|\boldsymbol{\delta_{oxide,planar} - \delta_{oxide,cylinder}}\right|$and the position of the datapoint in the spatial field was perfectly linear.

$$\boldsymbol{R^2 = 1 - \frac{\sum_{i=1}^{n}\left(\delta_{oxide,i} - \widehat{\delta}_{oxide,i}\right)^2}{\sum_{i=1}^{n}\left(\delta_i - \overline{\delta}\right)^2}}$$

Equation 4.1

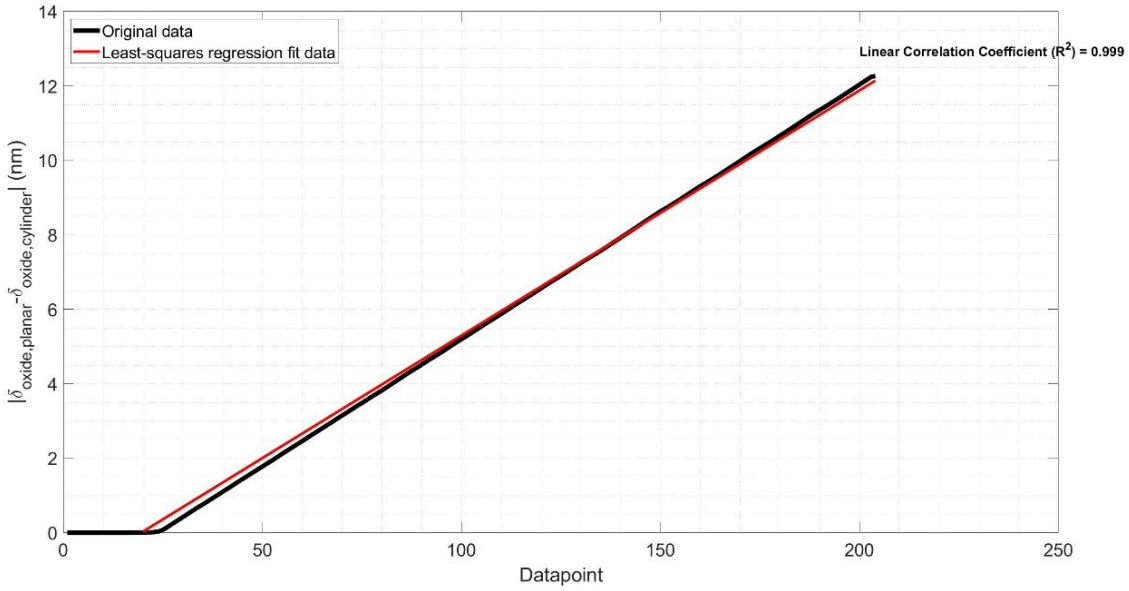


Figure 4.5: Plot of the absolute difference between predicted oxide thicknesses, δ_{oxide}, at corresponding datapoints for planar and cylindrical geometries, $|\delta_{oxide,planar} - \delta_{oxide,cylinder}|$, under identical thermochemical conditions. This figure demonstrates the strength of the positive linear relationship (with a linear correlation coefficient, R^2, of 0.999) between the difference, $|\delta_{oxide,planar} - \delta_{oxide,cylinder}|$, and the number of spatial datapoints solved¤.

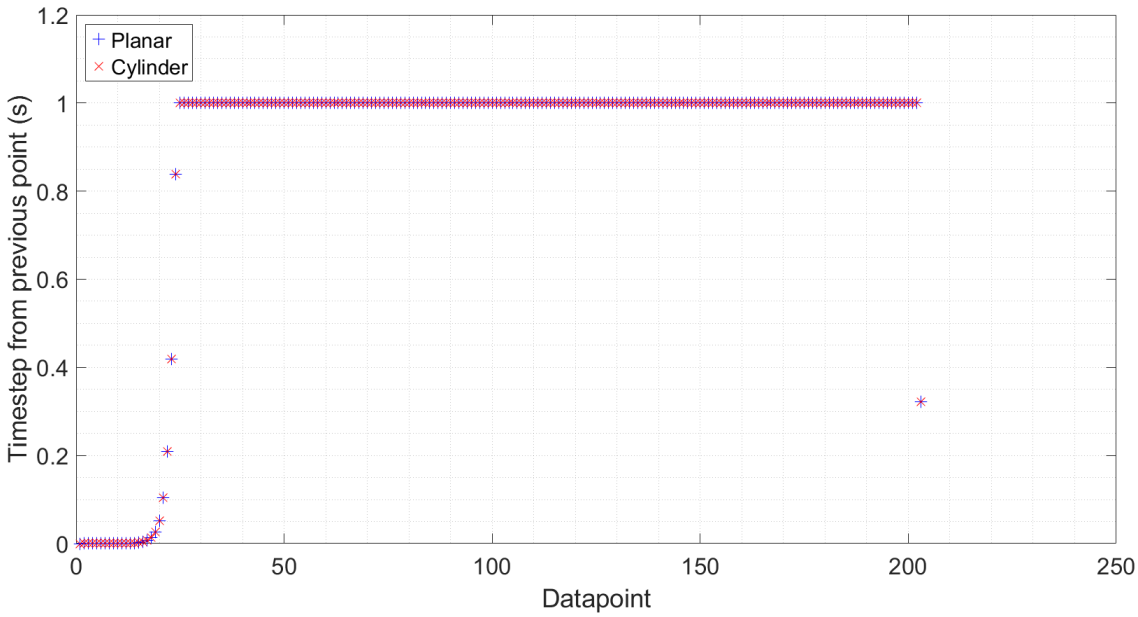


Figure 4.6: Timestep profiles for planar and cylindrical geometries used in 950°C, 3min normalisation simulation ¤.

4.1.1 Parametric Study

The model was applied to geometries in alignment with the three smallest nominal bore (n.b.) tube samples supplied by TSUK Tubes (21.3mm, 26.9mm and 33.7mm outer diameter, OD, with 3.2mm, 3.2mm and 4.0mm wall thickness, r_{wall}, respectively (see Figure 4.7)).

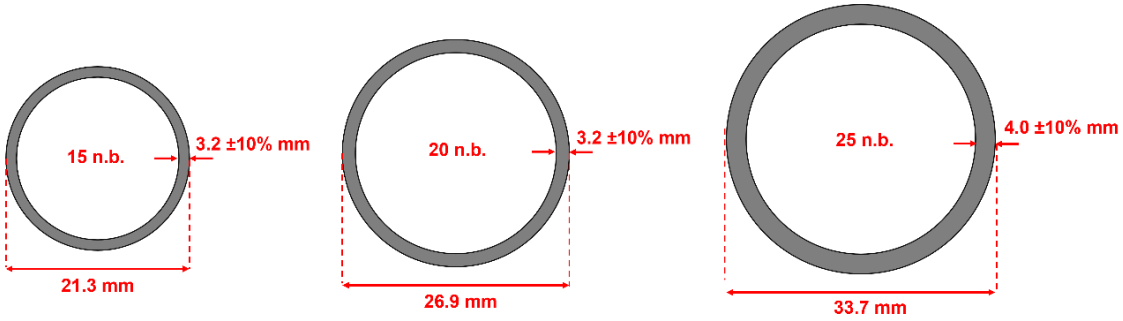


Figure 4.7: Dimensioned cross-sections of the three smallest products (15 n.b., 20 n.b., and 25 n.b.) supplied as part of the Install® Plus range. Dimensions are defined according to a set outer diameter and wall thickness. Wall thicknesses of the sample are 'heavyweight' ¤.

A maximum timestep limit of 1000s was applied to make an initial assessment of the successes and limitations of the cylindrical model compared to planar geometries. This allowed an effective simulation with all three sample dimensions demanding two minutes of CPU for 120 datapoints. The first observation was that the sample (of similar thickness to that used in the planar tests) was consumed faster than the planar sample, this being the only model difference. The steel was consumed within ~33 hours so the parameters were adjusted to simulate a 24 hrs heat treatment initially. Initial results indicated minimal variation between the samples with only millimetre differences in dimensions, yielding ~2.5mm of scale after 24 hours of oxidation. The variables investigated were simulation run time, number of datapoints, thickness gain and its associated parabolic rate coefficient, and mass gain and its associated parabolic rate coefficient. The final dimensional combinations used accounted for the difference between inner diameter (ID) and nominal bore (n.b.), and the use of a 'heavyweight' wall thickness and 10% manufacturing tolerance, as well as further combinations of potential outer diameter and wall thickness values which allowed exploration of the influence of their respective variation in isolation [2]. Table 4.1 details the 18 geometries simulated, again applying 1000°C heat treatment for 24 hours.

Table 4.1: Combinations of outer diameter, OD, and wall thickness, r_{wall}, dimensions. Wall thickness can vary ±10% from the prescribed wall thickness in the medium (^{m}) and heavy (^{h}) weight cases. The dimension combinations of the 15(*), 20(**), and 25(***) nominal bore (n.b.) products, specified in Tata's technical specifications [2], are highlighted.

OD (mm)	r_{wall} (mm)	OD (mm)	r_{wall} (mm)
* = 15 n.b., ** = 20 n.b., *** = 25 n.b., ^{m} = medium weight wall thickness, ^{h} = heavy weight wall thickness			
21.3	2.9	26.9	3.6
21.3*	3.2*^{m}	26.9	4.0^{h}
21.3	3.5	26.9	4.4
21.3	2.6	33.7	2.9
21.3	4.0^{h}	33.7	3.2^{m}
21.3	4.4	33.7	3.5
26.9	2.9	33.7	3.6
26.9**	3.2**^{m}	33.7***	4.0***^{h}
26.9	2.5	33.7	4.4

Figure 4.8 shows how an increase in both outer diameter and wall thickness is accompanied by a decrease in oxide thickness, $\boldsymbol{\delta_{ox}}$, and oxide-based parabolic rate coefficient, $\boldsymbol{k_{p,thickness}}$, and an increase in oxide mass gain, $\Delta \boldsymbol{m_{ox}}$, and mass-based parabolic rate constant, $\boldsymbol{k_{p,mass}}$. It was noted that the material was consumed approximately twice as quickly in the cylindrical case than the planar case (30 hrs vs. 60 hrs). This limited the simulation time to only a 24 hr period (as opposed to the original 72 hrs seen in Entchev et al.'s study using tubes of similar dimensions [85]) and was used in the STA validation procedure).
Figure 4.9, Figure 4.10, and Figure 4.11 show how outer diameter control for 21.3mm, 26.9mm, and 33.7mm is achieved by varying wall thickness for the fixed outer diameters

associated with the 15 n.b., 20 n.b., and 25 n.b., and the converse for wall thickness control using heavyweight wall thicknesses of 3.2mm and 4.0mm (see Figure 4.12 and Figure 4.13).

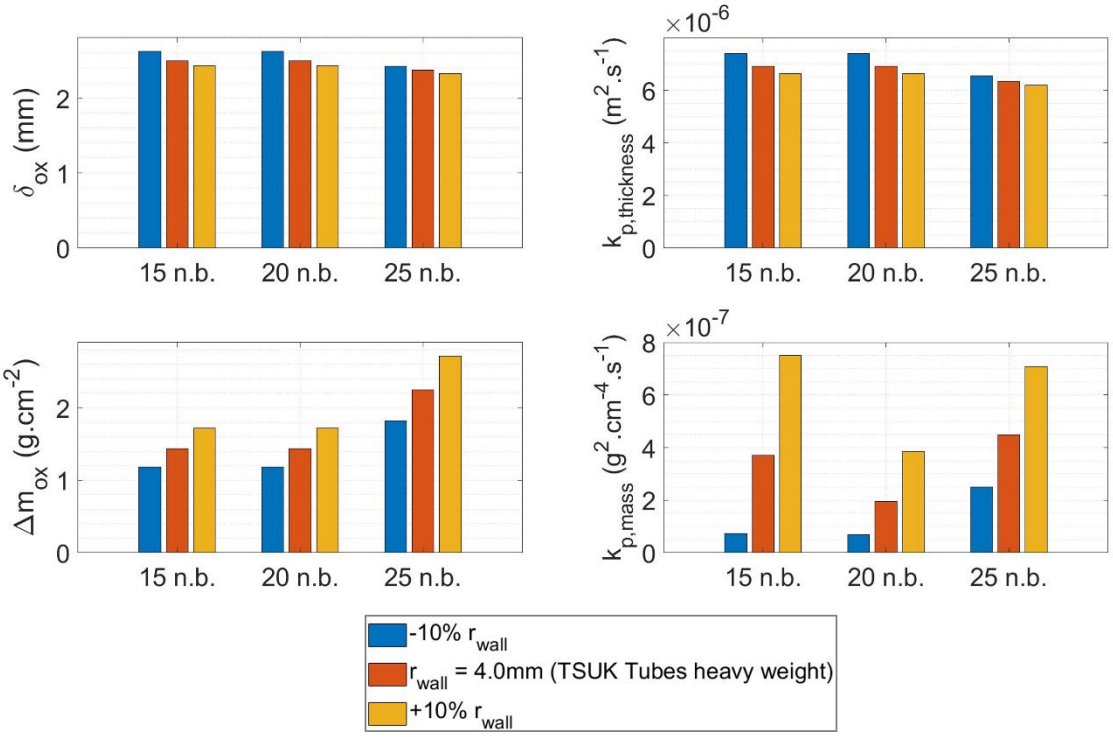


Figure 4.8: Bar charts highlighting the difference in Thermo-Calc© model predictions of thickness gain, δ_{ox}, mass gain per unit surface area, Δm_{ox}, and parabolic (thickness-based, $k_{p,thickness}$, and mass-based, $k_{p,mass}$) rate constant across the three sample geometries provided by TSUK Tubes, including a dimensional manufacturing tolerance of ±10% and using heavy weight wall thickness values ¤.

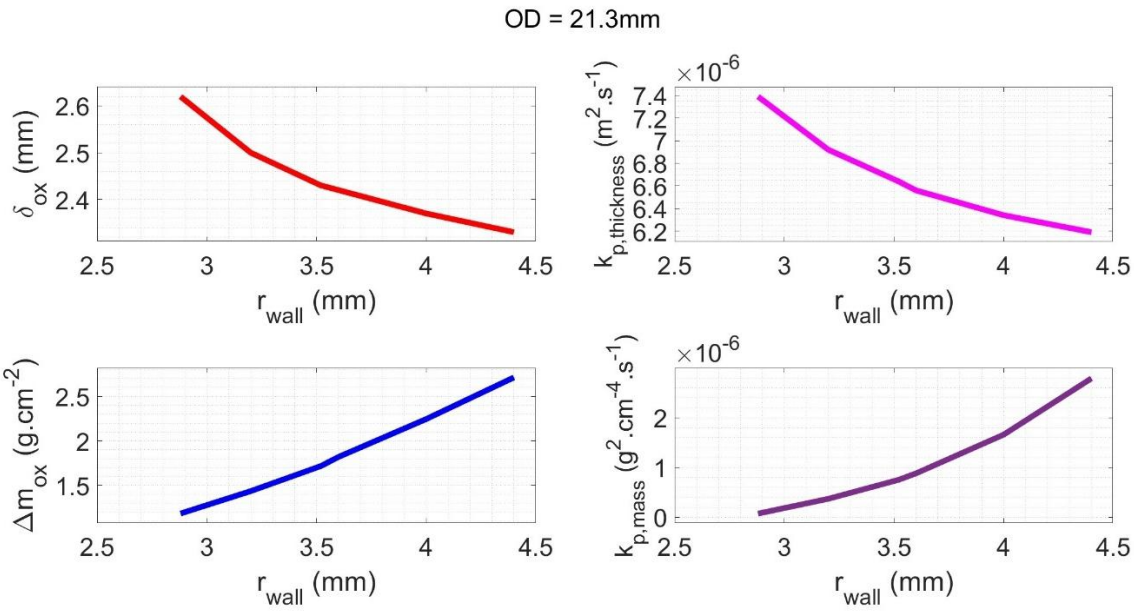


Figure 4.9: Graph showing the effect of wall thickness, r_{wall}, on Thermo-Calc© model predictions of thickness gain, δ_{ox}, mass gain per unit surface area, Δm_{ox}, and parabolic (thickness-based, $k_{p,thickness}$, and mass-based, $k_{p,mass}$) rate constant on a 21.3mm (15 n.b.) outer diameter, OD, tube ¤.

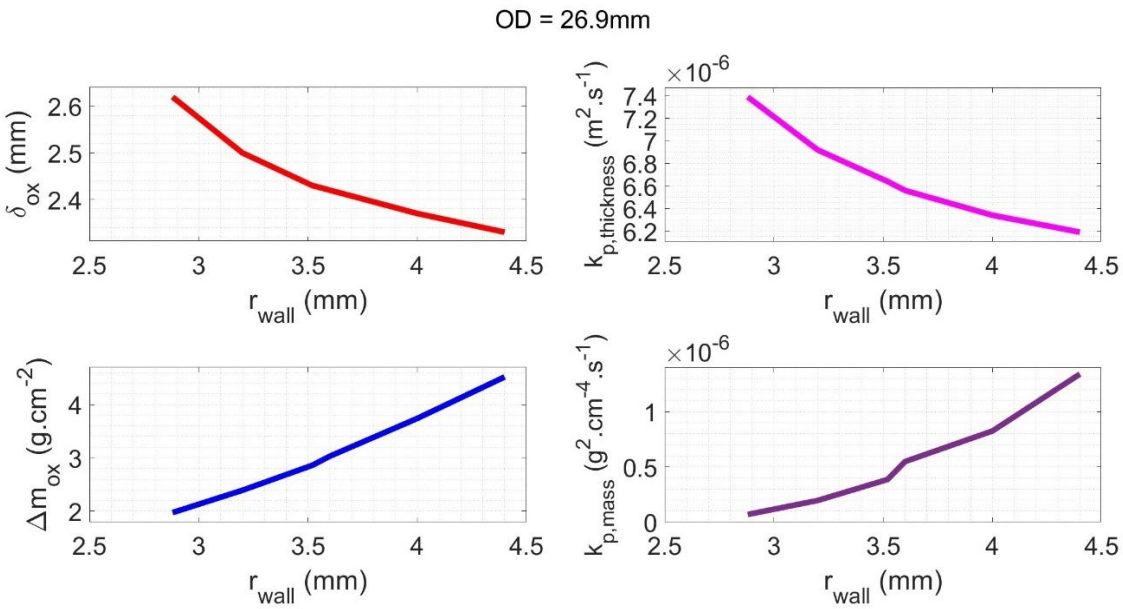


Figure 4.10: Graph showing the effect of wall thickness, r_{wall}, on Thermo-Calc© model predictions of thickness gain, δ_{ox}, mass gain per unit surface area, Δm_{ox}, and parabolic (thickness-based, $k_{p,thickness}$, and mass-based, $k_{p,mass}$) rate constant on a 26.9mm (20 n.b.) outer diameter, *OD*, tube ¤.

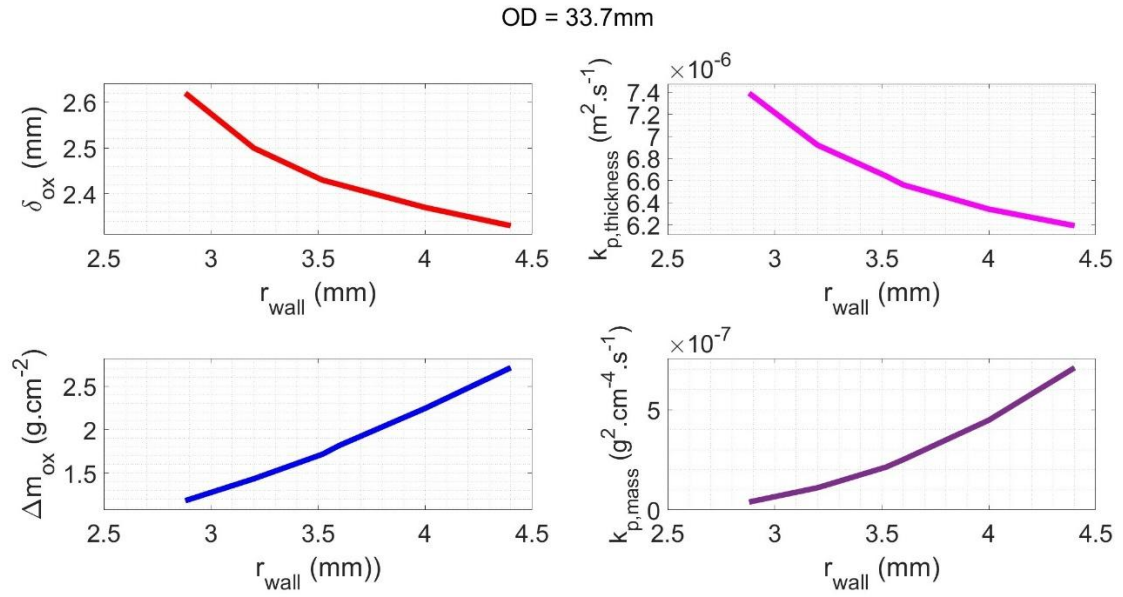


Figure 4.11 Graph showing the effect of wall thickness, r_{wall}, on Thermo-Calc© model predictions of thickness gain, δ_{ox}, mass gain per unit surface area, Δm_{ox}, and parabolic (thickness-based, $k_{p,thickness}$, and mass-based, $k_{p,mass}$) rate constant on a 33.7mm (25 n.b.) outer diameter, *OD*, tube ¤.

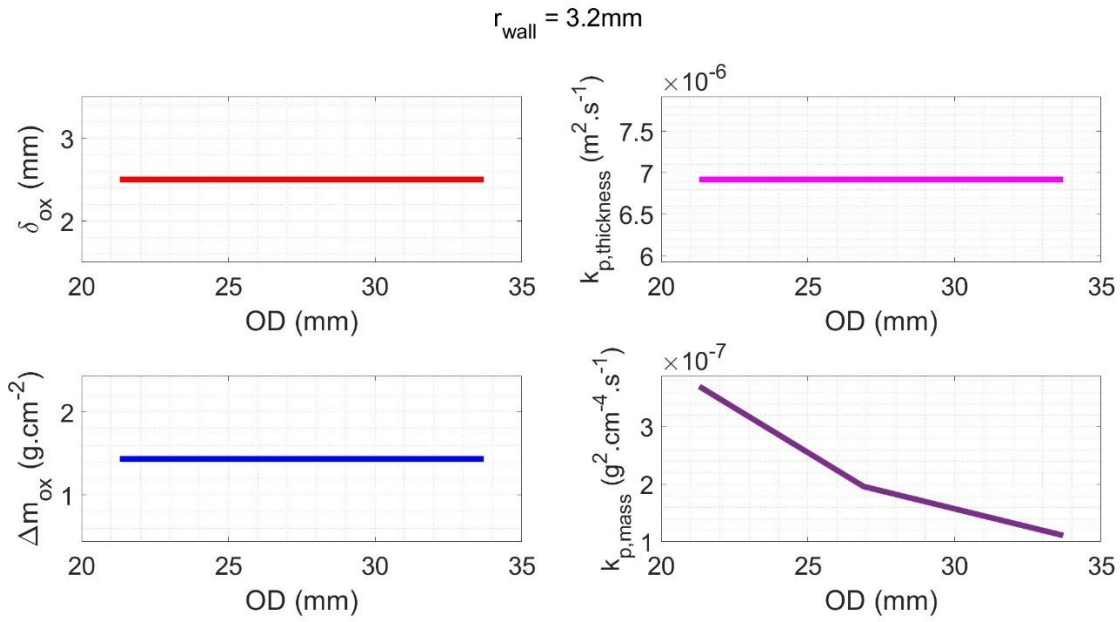


Figure 4.12: Graph showing effect of outer diameter, ***OD***, (in the ±10% manufacturing tolerance range associated with 15 n.b., 20 n.b., and 25 n.b. tubes) on Thermo-Calc© model predictions of thickness gain, δ_{ox}, mass gain per unit surface area, Δm_{ox}, and parabolic (thickness-based, $k_{p,thickness}$, and mass-based, $k_{p,mass}$) rate constant. A medium weight wall thickness, r_{wall}, of 3.2mm was used ¤.

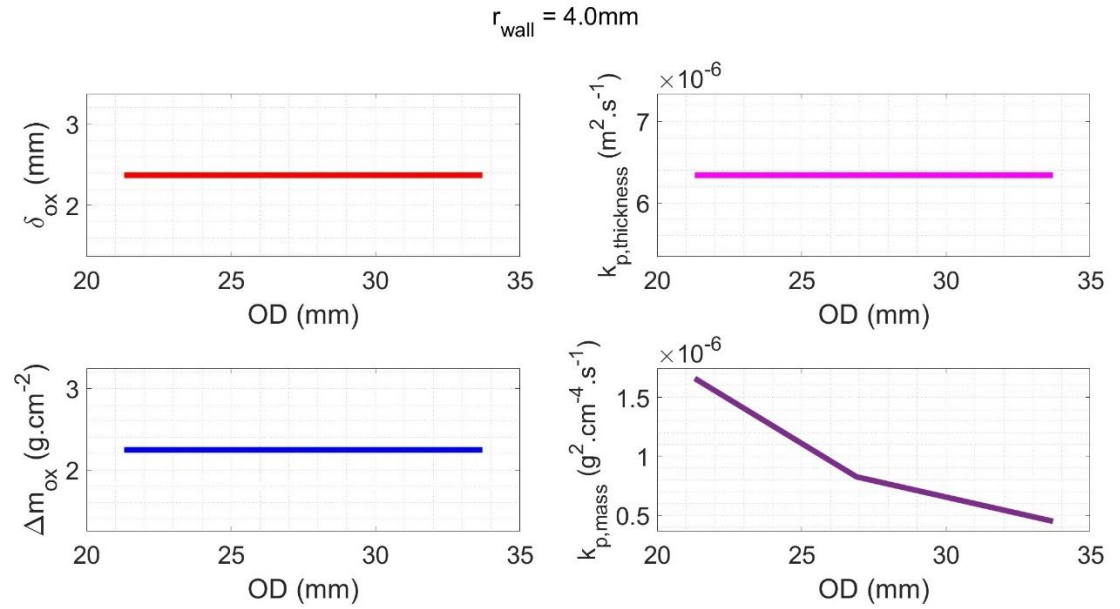


Figure 4.13: Graph showing effect of outer diameter, ***OD***, (in the ±10% manufacturing tolerance range associated with 15 n.b., 20 n.b., and 25 n.b. tubes) on Thermo-Calc© model predictions of thickness gain, δ_{ox}, mass gain per unit surface area, Δm_{ox}, and parabolic (thickness-based, $k_{p,thickness}$, and mass-based, $k_{p,mass}$) rate constant. A heavy weight wall thickness, r_{wall}, of 4.0mm was used ¤.

The three simulations (one per sample) had the same computational demands (120 datapoints resolved in 115±3s) but clear trends were exhibited in oxide thickness gain, mass gain and parabolic rate coefficient (mass- and thickness-based) (see Figure 4.8). For comparison, the planar model with a thickness of 3.15mm resolved in 104s with 120 datapoints. Overall, oxidation rate tended to decrease with respect to thickness gain but

increase with respect to mass gain per unit surface area.

Figure 4.12 and Figure 4.13 show how an increase in wall thickness, whilst controlling outer diameter, leads to a decrease in thickness-based oxidation but an increase in mass-based oxidation. An increase in wall thickness will increase the diffusion path length, increasing the distance for ions to migrate to the reaction interface and hence decreasing the rate of oxidation [386]. An increase in wall thickness also increases the material available for reaction and therefore the overall oxide mass gain possible for a given system. An increase in outer diameter, whilst controlling wall thickness, has no effect on predicted oxide thickness and mass gain, and thickness-based parabolic rate coefficients (see Figure 4.12). However, an increase in outer diameter caused a decrease in mass-based parabolic rate coefficient. This is because the volume of reacting material is unchanged when wall thickness is controlled so the same thickness and mass of oxide is formed, but the surface area to volume ratio decreases, leading to a decrease in rate of reaction [16]. There was a deviation from the trendline in the form of a small jump in mass-based parabolic rate coefficient at a wall thickness of 3.6mm in Figure 4.10. This is because the parabolic rate coefficient is derived using an automatic polynomial fitting function (*polyfit*) in MATLAB R2024b which is sensitive to fluctuations in the data and therefore why the mass gain data are unaffected as they depend on an independent calculation.

Overall, the parametric study of 18 different small bore, heavyweight wall thickness tube geometries revealed that a high accuracy of oxide thickness prediction can be achieved with reasonable CPU demands and realistic sensitivity to manufacturing routine-defined dimensional tolerances. Although wider tubes with the same wall thickness showed no increase in oxidation thickness or rate, increasing their wall thickness led to slower oxidation and thinner scale, which was attributed to an increase in diffusion path length. The transition from a cartesian to cylindrical coordinate diffusion equation was shown to be influential, as the introduction of the previously mentioned term of order $\frac{D}{r}\left(\frac{\partial c_k}{\partial r}\right)$, which is not present in the planar case, will quickly tend to zero as radius increases due to the term's reciprocal nature. Beyond the specifics of this study, the power of modelling for parametric studies was demonstrated. Only a single working day (8 hrs) was required to go from pre- to post-processing of 18 tests, when using a maximum timestep of 1000s, whilst an experimental approach is not only more time-consuming approach (especially as the in-situ TGA furnaces can often only take a single sample at a time and have a restrictive maximum heating and cooling rate), but sample range is limited dimensionally and compositionally by

the company's manufacturing routine, i.e. only the three smallest tubes manufactured by Tata can fit in TGA furnace used for validation. However, the output of the cylindrical geometry model is validated using microstructural imaging via SEM and thermogravimetry in Sections 4.2.1 and 4.2.2 respectively.

4.1.2 Volume Changes with a Moving Phase Boundary

The initial oxide volume calculation approach, used to transfer between oxide thickness and mass gain datasets, did not account for the entire sample mass, i.e. some mass remained unoxidized substrate. Although, in the case of the STA data discussed in Section 3.3.1, the samples were very small (3x3x3mm) and all the steel substrate was oxidised in the test period. The volume of oxide, $\boldsymbol{V_{oxide}}$, on an equivalent flat plate, i.e. an oxide layer formed on the unformed metal sheet used to generate specified tube geometry, was calculated using this approach (see Equation 4.2).

$$\boldsymbol{V_{oxide} = \pi \cdot OD \cdot L \cdot \delta_{ox}}$$

Equation 4.2

To account for this incorrect assumption in the cylindrical parametric study, the remaining volume of unoxidised substrate was subtracted from the volume associated with a cylinder with the final outer diameter (assuming the outer diameter is inherently unchanged due to the inwardly moving nature of the steel-scale interface). Since the steel-scale interface recedes with substrate consumption by oxidation, the final inner diameter is assumed to be the final oxide thickness subtracted from the original unoxidized outer diameter (see Figure 4.14). This calculation is summarised in Equation 4.3 using the outer radius, $\boldsymbol{OR}$. Analysis of the repeated parametric study, discussed above, included this correction but did not affect the overall trends observed for the effect of outer diameter and wall thickness. Figure 4.14 also shows how tube geometry changes, as discussed by Entchev et al. [85], during external surface oxidation.

$$\boldsymbol{V_{oxide} = \pi L\left((OR + \Delta\delta_{ox})^2 - (OR - \Delta\delta_{ox})^2\right) = 4\pi \cdot L \cdot OR \cdot \Delta\delta_{ox}}$$

Equation 4.3

This part of the investigation highlighted the hypothesised dependency of oxidation kinetics on radius when exploring a cylindrical coordinate system for diffusion. An initial avenue for exploring this was to run the model systematically for different dimensions. This yielded the same oxide thickness and parabolic rate profile (when wall thickness was maintained at

3mm) of 2.57mm regardless of tube diameter, but the equivalent volume gain increased linearly as tube diameter increased. However, for radii below 5mm, a drastic change in the kinetic weight gain profile was observed as the scale-gas interface advanced to a distance beyond the initial metal-scale interface position, i.e. the substrate was consumed by the oxidation reaction before the end of the normalisation soak time (see Figure 4.14).

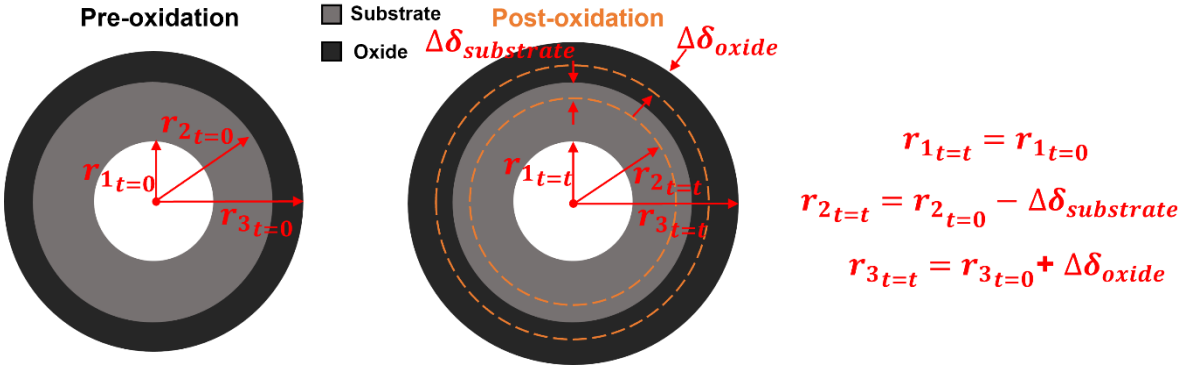


Figure 4.14: Diagram showing changes in cylinder outer radius before (*left*) and after (*right*) surface oxidation (*adapted from source*) [89] ¤.

These changes in radius are accompanied by a change in available reactive surface area and surface area to volume ratio and highlight how an increase in radius, $\boldsymbol{r}$, is accompanied by an increase in surface area, $\boldsymbol{A}$, (see Equation 4.4) and a decrease in surface area to volume ratio, $\boldsymbol{A}$:$\boldsymbol{V}$ (see Equation 4.5). Therefore, the surface area increases during inner surface oxidation (consumption of the substrate widens the cylinder bore, i.e. inner radius) leads to an overall slower rate of reaction and therefore thinner oxide thickness after a given time and as such the converse is true of the outer surface [85]. Therefore, as surface area increases during oxidation at the inner surface of the tube (consumption of the substrate widens the cylinder bore, i.e. inner radius) leads to an overall slower rate of reaction and therefore a thinner oxide thickness domain after a given time (as seen by Entchev et al. [85]) and as such the converse is true of the outer surface.

$$\boldsymbol{A = 2\pi rL}$$

Equation 4.4

$$\boldsymbol{A:V = \frac{2(r + \Delta r)}{\Delta r(2r + \Delta r)}}$$

Equation 4.5

Beyond the differences arising due to the link between geometry stress states and porosity evolution, there is also the deeper consideration of how geometry affects diffusion pathways. The investigation of a cylindrical geometry transitions the diffusion equation

from cartesian to cylindrical coordinates where c_k is the species, k, concentration expressed as a function of time, t, Dependency on the azimuthal, ϕ, and axial, z, coordinates is eliminated by assuming rotational symmetry during oxidation and changes in oxidation behaviour are only observed along the radial coordinate, r (see Equation 1.31).

$$\frac{\partial c_k}{\partial t} = \frac{D}{r}\frac{\partial}{\partial r}\left(r\frac{\partial c_k}{\partial r}\right)$$

Equation 4.6

Hence, the change of concentration over time becomes a function of $\frac{1}{r}$. Accordingly, assuming the concentration only changes due to diffusion in the radial direction, i.e. 1D form, the radius is the discretised dimension in the numerical solution. It should be noted that in this case the concentration in each segment, i, is an average. When setting initial concentration conditions, $c_{i,t=0}$, and calculating average i^{th} segment concentration, every point of the circumference at radius, r, has a different weight dependent on which segment it occupies. The area of the ring with an average concentration corresponding to $c_{i,t=0}$ is defined by Equation 4.7 and integration of the concentration at individual points around the ring results in an instantaneous initial average concentration (see Equation 4.8) [386].

$$A_i = \pi(\Delta r)^2(2i - 1)$$

Equation 4.7

$$c_{i,t=0} = \frac{1}{A_i}\int_{\Delta r(i-1)}^{\Delta r(i)} 2\pi r \cdot c(r)dr$$

Equation 4.8

This partially explains the results observed in the parametric study performed to reflect heavyweight Install® Plus samples described previously.

As with the planar case, the CPU demand is low with 120 datapoints and approximately 115s run time for each test, using a maximum timestep of 1000s. Decreasing the maximum timestep to 100s had no effect on the predicted oxide thickness but increases CPU demand to 899 datapoints and 684s run time. A range of maximum timestep conditions, between 1s and 1000s, were explored and the resulting linear relationship between central processing unit cost, CPU, i.e. computation time, and the number of datapoints, $N_{datapoints}$, is shown in Figure 4.15.

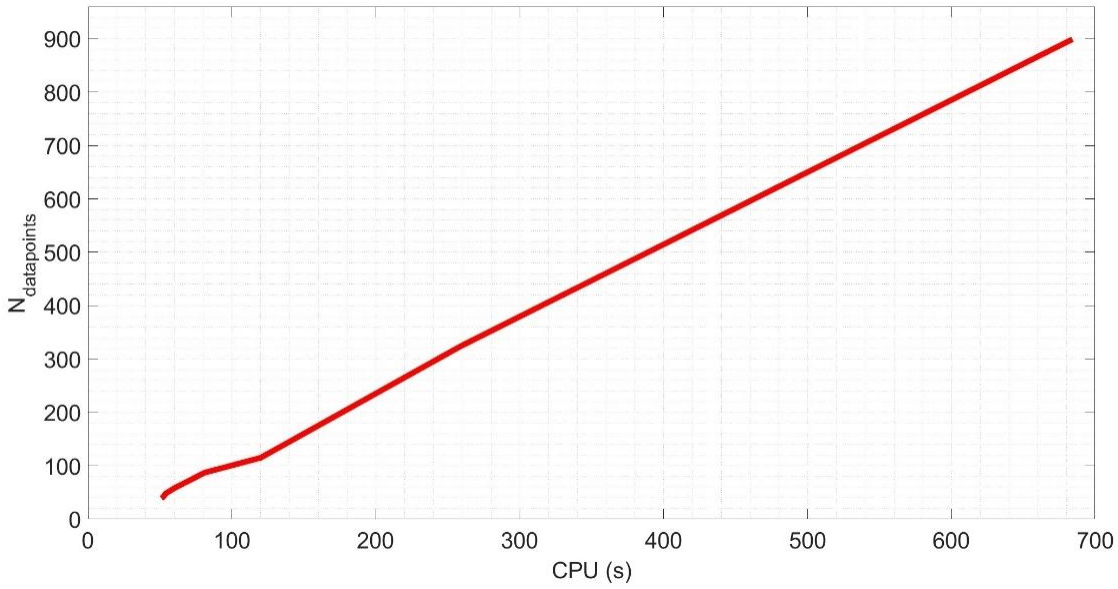


Figure 4.15: Graph showing the linear relationship between computer processing unit (computation time), CPU, and the number of datapoints, $N_{datapoints}$, required for the Thermo-Calc© model of oxidation kinetics for a cylindrical geometry ¤.

Applying the Tata-quoted 10% manufacturing tolerance led to a variation of 1-5% in oxide thickness change, which is a reasonable value given that the variation is not greater than the manufacturing tolerance itself. An increase in wall thickness, whilst controlling outer diameter in the same way as is done during tube stretch reduction and product specification, revealed a decrease in oxide thickness and the corresponding parabolic oxidation rate constants (see Figure 4.9). This is due to the extension of the diffusion pathway so fewer metal cations diffuse to the SSI to react per unit time. It has also been suggested that oxidation kinetics depends on the oxide scale stress state [84], $\boldsymbol{\sigma_{ox}}$, due to the negative correlation between stress magnitude and the mole fraction of intrinsic defects, $\boldsymbol{x_d}$, within the oxide (see Equation 4.9 where $\boldsymbol{\Delta_f g_d}$ is the molar Gibbs energy of formation of intrinsic defects $\boldsymbol{d}$, $\boldsymbol{\Omega}$ is the crystal molar, $\boldsymbol{\Delta v_r}$ is the molar relaxation volume, that is, 1 mol of the local volume variation resulting from the relaxation of the crystal lattice around a defect $\boldsymbol{d}$) [387, 388]. Higher compressive stress is associated with a lower vacancy concentration which can inhibit iron diffusion via iron vacancies [84]. Additionally, Asensio-Jimenez et al. cited the degree of oxide growth stress relaxation by plastic deformation as a source of oxidation kinetics variation across their samples (more influential than minor alloy element depletion which was also discussed) [389]. For example, if a sample is exposed to conditions which promote creep, the compressive and tensile stress evolved in the scale and metal respectively will eventually reach a level that causes substrate creep and therefore growth stress relaxation in the oxide. A thinner sample will reach this critical value sooner, i.e. have

a shorter 'incubation period', and therefore initiate a period of enhanced oxidation associated with stress state changes. The difference in stress state for samples with only a small thickness difference can be significant due to the power law relationship between creep rate, $\frac{d\varepsilon}{dt}$, and the specimen thickness (although this is for flat surfaces). Although the incubation period to observe any difference in oxidation rate due to sample thickness can be far longer than is observed in the tube manufacturing process, compared to a planar surface, curved surfaces will experience additional stresses associated with the forming process [390]. Asensio-Jimenez et al. quoted as much as a 60-fold increase in substrate creep rate by decreasing specimen thickness from 0.5 to 0.3mm. This reinforces the advantages of a computational approach as representative samples in the context of manufacturing components are often limited to their commercial range and can be restricted at a given time to only the specifications required to meet current demand. However, clearly stress cannot be directly accounted for in the thermochemical model developed, but should nevertheless be considered particularly when analysing data in relation to physical validation of the model.

$$x_d(\sigma_{ox}) = e^{\left(\frac{-\Delta_f g_d - \sigma_{ox}(\Omega + \Delta v_r)}{RT}\right)}$$

Equation 4.9

Furthermore, the 2D ($r - \theta$) diffusion pathway associated with the converging and diverging radial path of oxygen and iron ions, and the fact that their concentrations are defined normal to the surface, leads to an overlap of ion pathways, unlike in the planar case [386]. However, the relative effect of these phenomena is dependent on the radial scale, i.e. very large radii may evolve a solution which approaches a flat plate solution as the $\frac{1}{r}$ term tends to 0. This effect is discussed further during the quantitative validation work in the next section.

4.1.3 Radial Dependency Study

Since volume and mass gain were revealed to be dependent on inner radius during oxidation, it was hypothesised that there would be a critical radius value at which the effect of a cylindrical coordinates becomes influential, and the radial coordinate at which the stress state transitions from tensile to compressive in a curved oxide layer. Equally, it was hypothesised that for large oxide curvatures beyond a critical radial value, the stress state would become negligible and reflect that of a flat plate geometry.

An initial investigation was to explore the extremes of tube dimensions in the model (beyond the sizes manufactured by Tata). The inner radial dimensions simulated were 0.5mm, 1mm, 5mm, 10mm, 15mm, 20mm, 25mm, 50mm, 100mm, 200mm, 300mm, 400mm, 500mm, 1000mm. Volume gain, and its dependence on radius was explored first (see Figure 4.16) and showed a strong linear relationship between volume gain and tube radius. To test the previously discussed theory concerning the strong influence of the $\frac{1}{r}$ term in the cylindrical coordinate diffusion equation (see Equation 1.31), the same volume gain data was plotted against the reciprocal of the tube radius and revealed a clear reciprocal relationship. This demonstrated that even with the geometric conversion steps which inner radius is not involved in (see Equation 4.3), the physical diffusion phenomena predicted by the model are not lost, i.e. the reciprocal relation between concentration and tube radius.

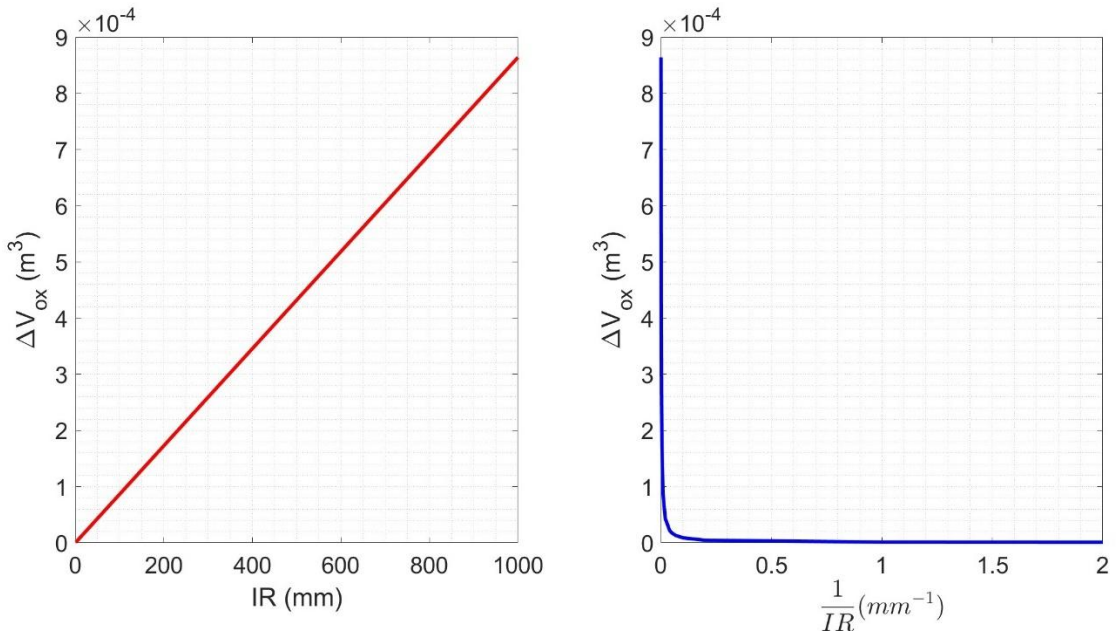


Figure 4.16: Plots of volume gain, ΔV_{ox}, against tube inner radius, IR, (*left*) and its reciprocal (*right*) ¤.

Further investigations were performed by exploring the relationship between mass-based parabolic rate coefficient (normalised against sample surface area) and tube radius (see Figure 4.17). Crucially, the parabolic profile reveals a critical radius where radius no longer has a significant effect on oxidation kinetics. This value appears to be approximately 200mm. This is an industrially relevant conclusion for TSUK Tubes since their Install® tube inner radii range from to 7.5-77.2mm, depending on wall thickness [2]. This radius region shows the sharpest change in oxidation rate. Again, a reciprocal plot was used to show that post-processing calculations were correct and uphold the reciprocal relationship between oxidation parameters and tube radius.

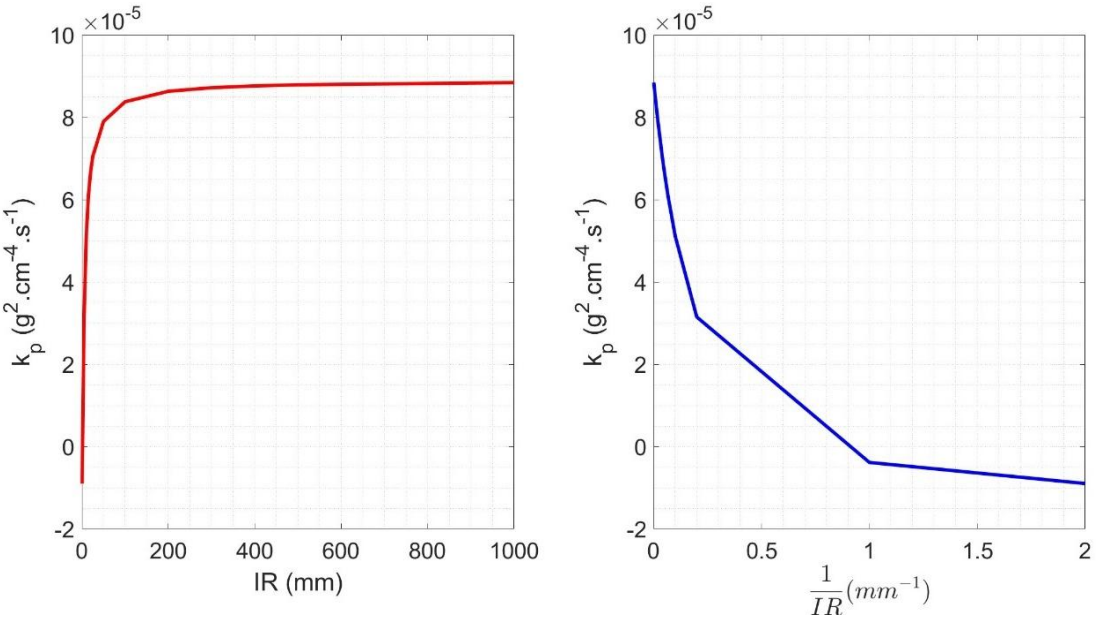


Figure 4.17: Plots of mass-based, surface area normalised parabolic rate coefficient, $k_{p,mass}$, against tube inner radius, ***IR***, (*left*) and its reciprocal (*right*) ¤.

This conclusion was also supported by equivalent plots of thickness gain (see Figure 4.17), again suggesting a critical inner radial value of 200mm. The steepest gradient region is highlighted in Figure 4.18 where model predictions of oxide thickness for the Install® Plus 235 range of heavyweight wall thickness products (assuming a wall thickness of 3mm so that direct comparisons can be made) are demarcated. Crucially, Figure 4.18 highlights how 19% of all radius-related change in oxide thickness gain (and therefore change in oxidation kinetics) occurs across the Install® Plus 235 product size range. A quasi-planar response is observed at radii larger than this range. 98% of all change is reached at the upper bound of the Install® Plus 235 range. A value of 68% change (representing 90% of the total change) for the equivalent range was seen in the parabolic rate constant (mass-based, surface area-normalised) but the inner radius lower bound for this calculation was increased to 5mm, as the smallest value at which the phase boundary did not (physically impossibly) recede beyond the initial inner wall surface position (see Figure 4.19). The three-fold increase in the change contribution in the industrial range for oxidation rate compared to oxide thickness, reflects the non-linear relationship between cylindrical radius and surface area. Furthermore, using the model to generate a separate dataset for the specific Install® Plus dimensions also demonstrated the model's repeatability, as well as time-saving abilities once established due to the flexibility associated with robust pre-processing definitions. Overall, beyond the industrially relevant observation the oxidation kinetic response is more volatile

for cylindrical geometries, this computational approach has been demonstrated to be more resource-efficient.

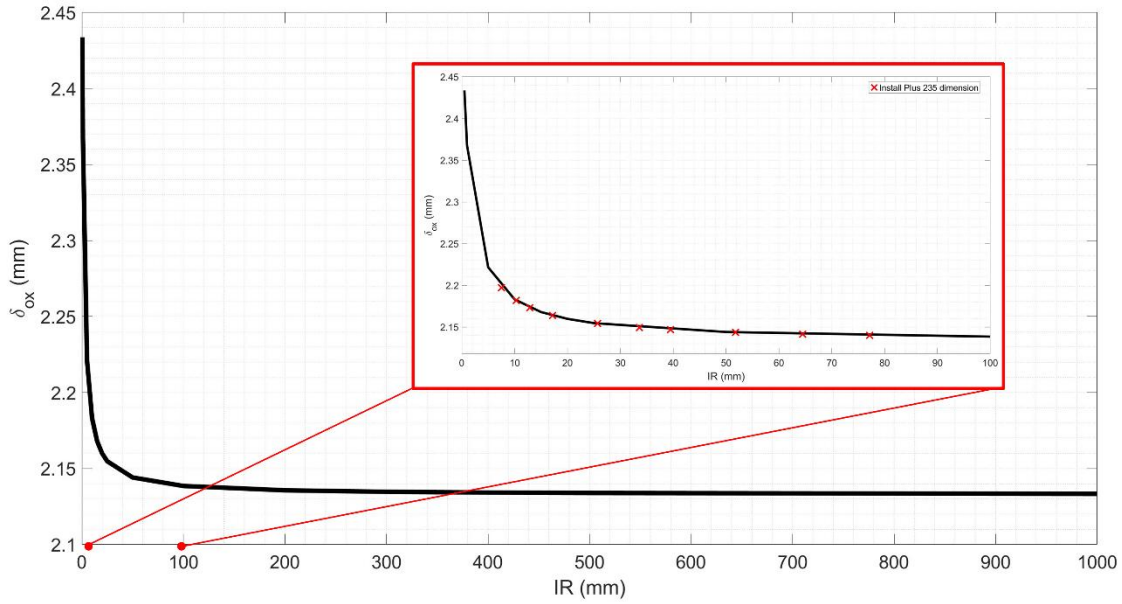


Figure 4.18: Plot of model-predicted oxide thickness gain, δ_{ox}, for inner radii, IR, in the range 0.5-1000mm, with an enlarged view of the dimension range associated with Tata's Install® Plus 235 products (heavyweight wall thickness) ¤.

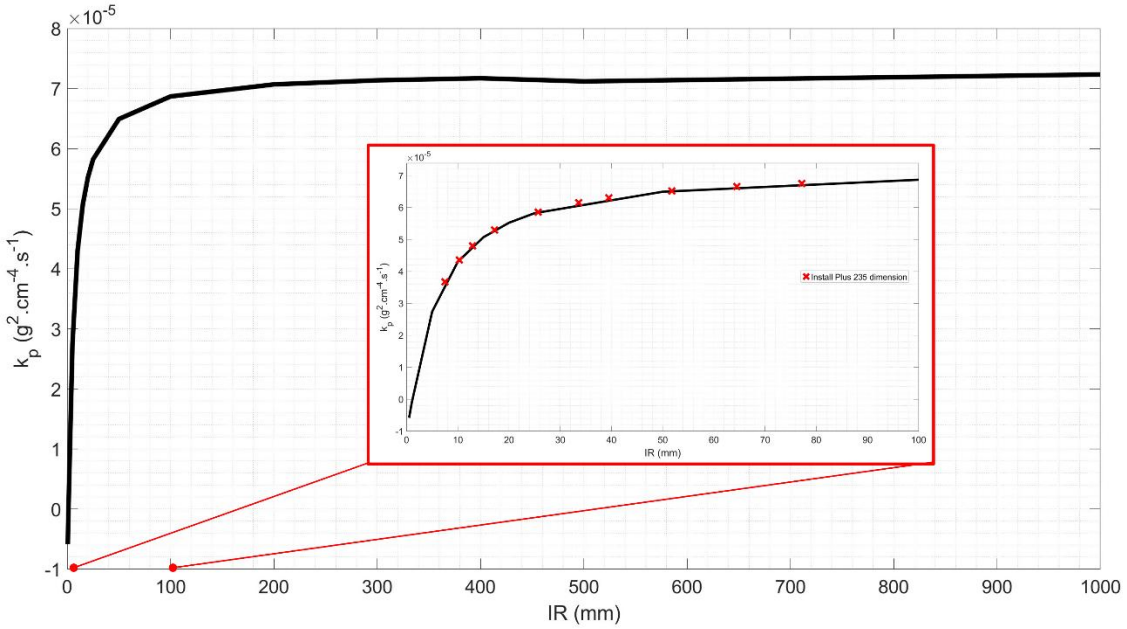


Figure 4.19: Plot of predicted mass-based, surface area-normalised parabolic rate coefficient, $k_{p,mass}$, for inner radii, IR, in the range 0.5-1000mm, with an enlarged view of the dimension range associated with Tata's Install® Plus 235 products (heavyweight wall thickness) ¤.

Krzyzanowski and Beynon suggested that there was a critical temperature where oxide failure transitions from the cohesion-dominated Mode I to the adhesion-dominated Mode II (see Section 1.4) [77]. However, Samal and Mitra's study of the effect of grain boundary on

high temperature metal oxidation highlighted the suggestion that this transition is also controlled by a critical oxide thickness [238]. It was hypothesised that this transition is determined as the energy stored in the oxide layer, which increase in proportion to its thickness, exceeds the fracture strength. For a sufficiently slow oxidation, i.e. low diffusion rates, the oxide layer remains thinner than the critical thickness and hence is less susceptible to cracking. Thus, transition to Mode II failure is ultimately a trade-off between the dominance of critical thickness (which pushes into Mode I) and critical temperature (which pushes into Mode II).

4.1.4 Grain Boundary Effects

Grain boundary effects on diffusion were discussed in Section 3.2.3 and incorporated into the model via calculation of an effective diffusion coefficient based on the grain boundary volume fraction. Given the identification of grain size as a critical parameter during diffusion-based phenomena such as oxidation, the radial dependency study was re-run accounting for grain boundary diffusion. Although this revealed the anticipated increase in oxidation rate, also associated with planar samples, it also confirmed a similar value of an approximately 200mm critical radius at which point changes to the cylindrical geometry do not significantly affect oxidation kinetics anymore (see Figure 4.20 and Figure 4.21). It should be noted that grain boundary diffusion assumes a planar oxidation front, as discussed in Section 3.2.3, which raises questions about whether there is also a critical radius at which the validity of the solution offered by grain boundary analysis breaks down as the geometry is not close enough to a flat plate solution. However, grain boundary diffusion can be described by the same planar and cylindrical diffusion equations [235, 364] defined for bulk diffusion (see Section 1.3). Therefore, the effect of the radial term would also be the same and lead to a critical radius of 200mm.

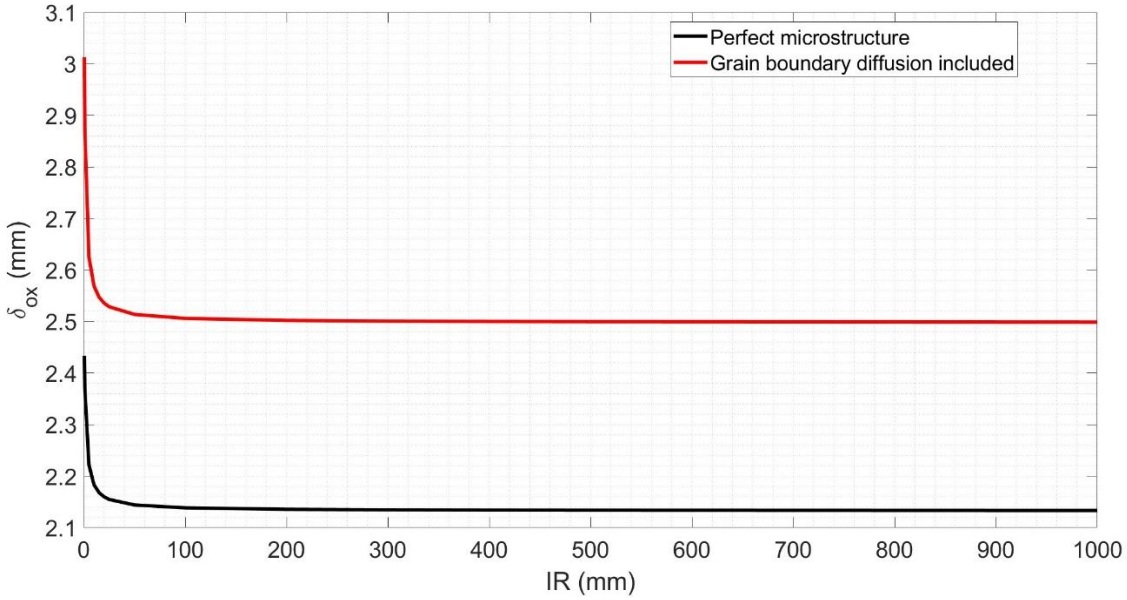


Figure 4.20: Plots demonstrating the effect of inner radius, ***IR***, changes on oxide thickness, δ_{ox}, predictions by the model with a hollow cylindrical geometry ¤.

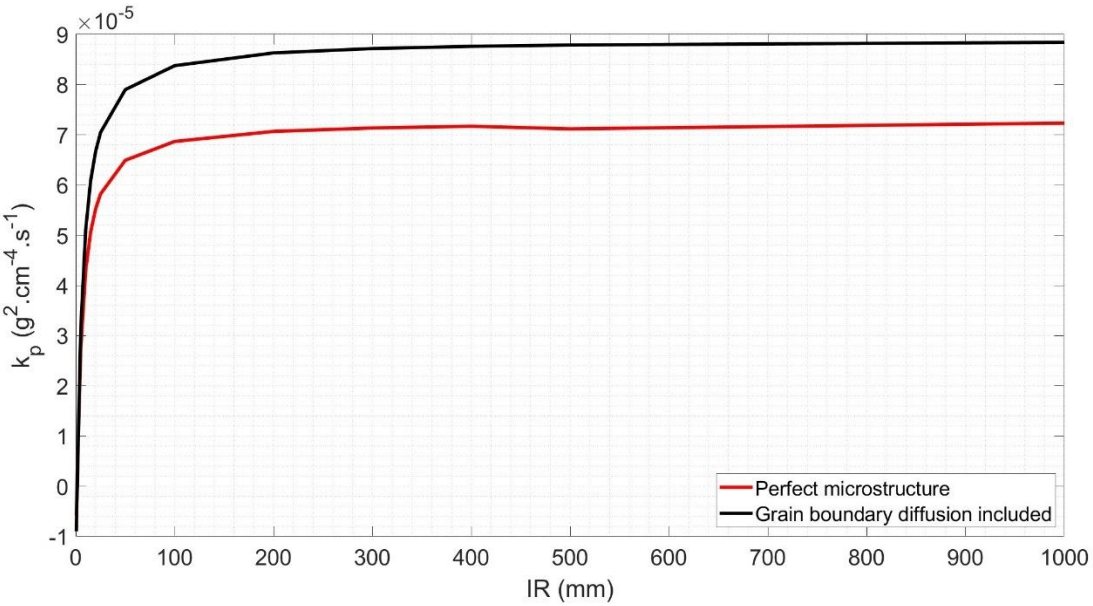


Figure 4.21: Plots demonstrating the effect of inner radius, ***IR***, changes on mass-based, surface area-normalised parabolic rate coefficient, $k_{p,mass}$, predictions by the model with a hollow cylindrical geometry ¤.

4.2 Validation

4.2.1 Microstructural Imaging

Samples for validation were produced from as-welded material provided by Tata Steel UK Ltd (see Figure 4.22). Post-normalised samples (heated by induction) were also supplied for microstructural and oxidation comparison. 25mm lengths were machined from parent samples and a hole drilled for the nichrome suspension wire (see Figure 4.23). The same atmospheric composition, i.e. heating in air, was used for laboratory samples in comparison with industrial samples.

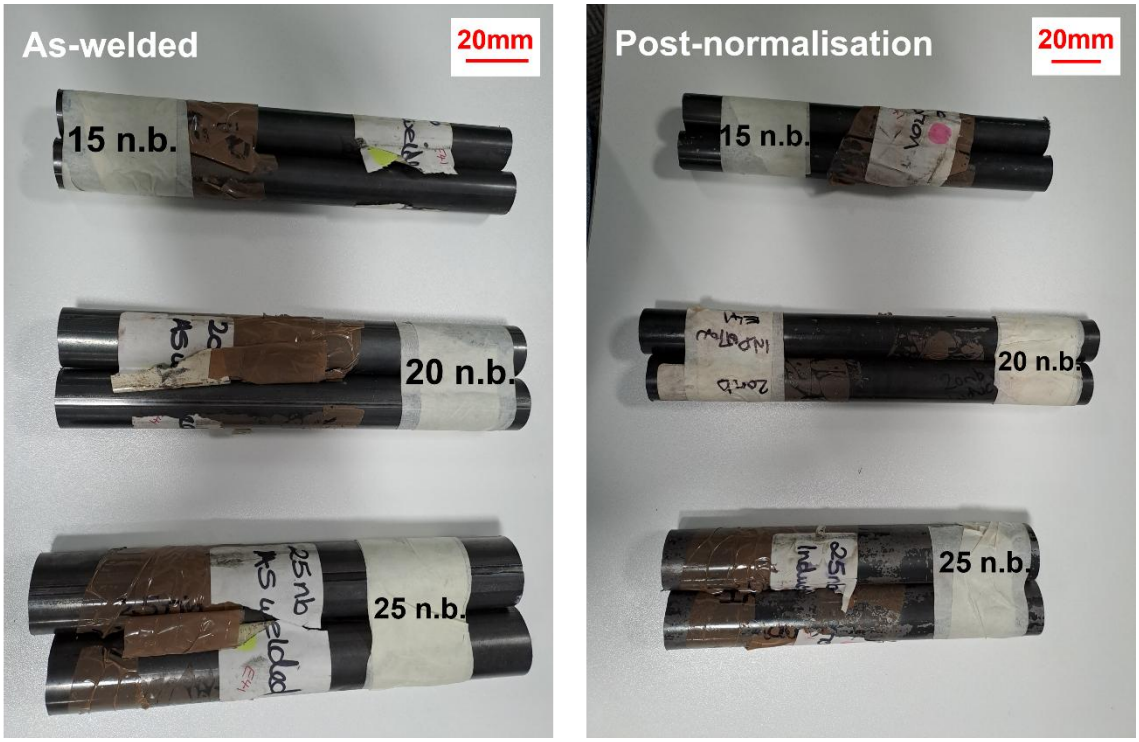


Figure 4.22: As-received samples of Install® Plus tubes in the as-welded (*left*) and post-normalisation (*right*) condition ¤.

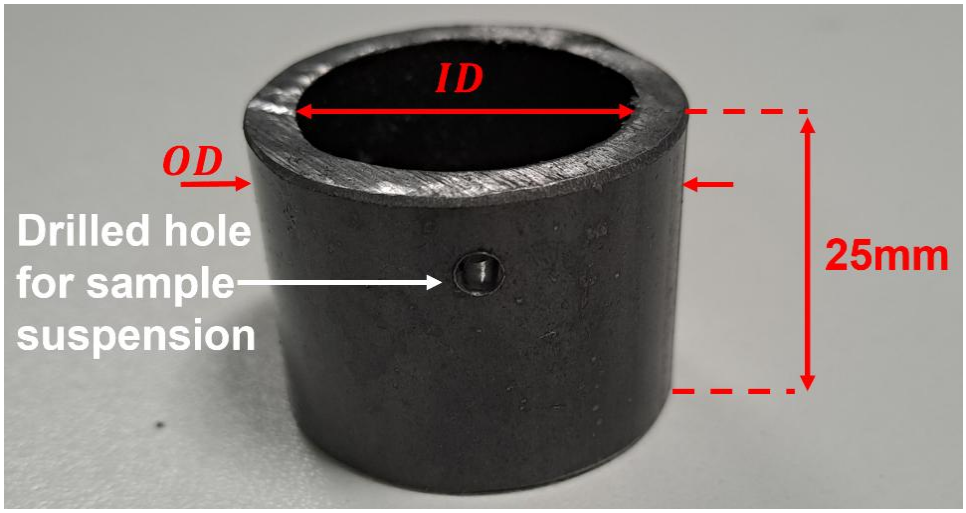


Figure 4.23: Machined sample ready for use in the thermogravimetric furnace, labelled with inner, ***ID***, and outer diameter, ***OD***, dimension definitions ¤.

A thin layer of scale forms pre-normalisation due to the high temperatures of the welding process. This was not removed to obtain representative oxide kinetics for tube manufacturing as descaling in the tube manufacturing process only occurs after heat treatment (see Section 1.2). As a result, samples were mounted first in cold-setting resin to 'lock in' the oxide layer which is brittle and prone to spalling [64]. Once set, the coated samples were prepared as described in Section 2.1.1.

Pre-normalisation Analysis

The 15 n.b. pre-normalised samples' microstructures were analysed in the bulk and heat affected zone (HAZ) using optical light microscopy (see Figure 4.24).

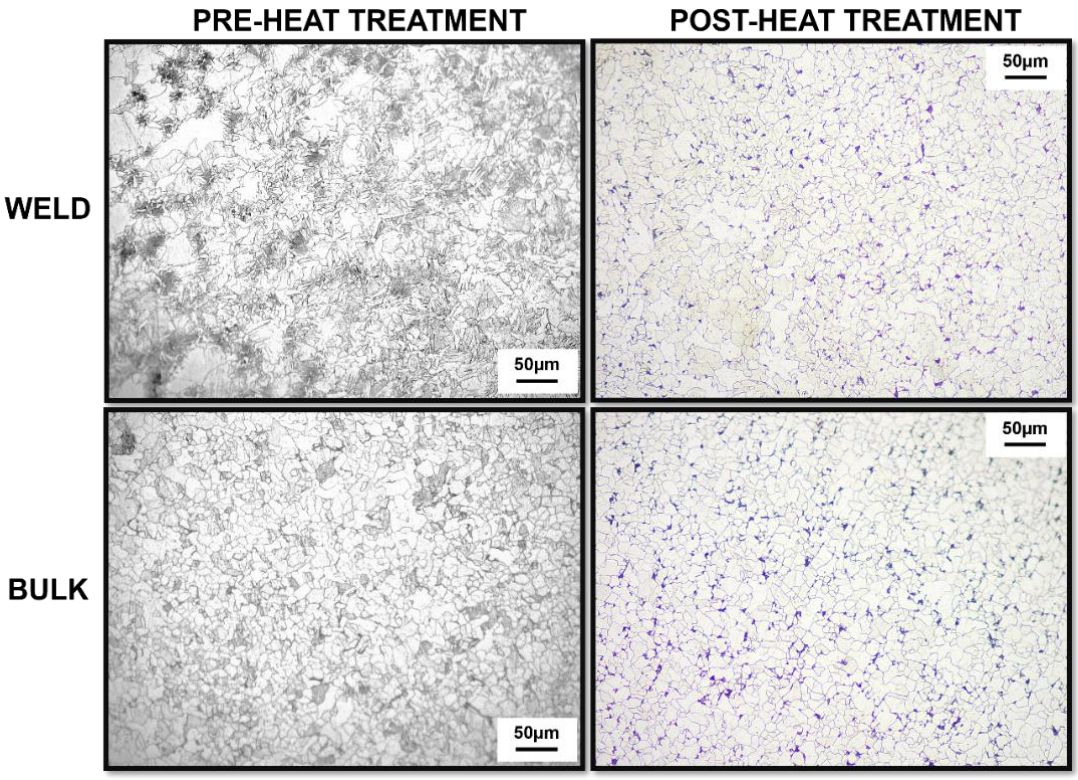


Figure 4.24: Optical light microscopy images of the microstructure of 15 nominal bore (n.b.) tube samples in the bulk (*top*) and HAZ (*bottom*) at the pre- (*left*) and post-normalisation (*right*) stages ¤.

The expected pearlitic microstructure [59] (see Section 1.2.4) was observed in the bulk pre- (*bottom left*) and post-normalisation (*bottom right*), and after normalisation the HAZ also exhibited this microstructure (*top right*). However, pre-normalisation HAZ microstructure (*top left*) displayed more columnar grains than expected. This appeared to be a martensitic microstructure [57] due to rapid post-weld cooling [101] and recrystallised retained austenite [47] (see Figure 1.6). Pre-normalisation thickness was obtained using FEGSEM. Initially, imaging revealed that much of the oxide had still been stripped out despite the cold-mounting resin used. The remaining oxide was shown to be well-adhered to the Bakelite, and thermal contraction of the Bakelite during cooling in the mounting machine was suggested to have accelerated delamination of the oxide from the steel, making it easier to strip during grinding and polishing. This was supported by evidence of a through-thickness crack in the remnant oxide, indicating a higher adhesive strength at the oxide-Bakelite interface than the oxide's own cohesive strength (see Figure 4.26) [77]. However, the effect of thermal shrinkage was mainly widespread on the inner tube surface where

Bakelite within the tube bore contracted and pulled the oxide away from the substrate. Consequently, it was difficult to find extensive regions of oxide to analyse. In contrast, contraction of the Bakelite encasing the outer surface of the tube will have caused the Bakelite to tighten around the outer surface oxide and cause its compression. The oxide was therefore mainly intact on the outer tube surface, however it was noted that the unexpectedly low levels of porosity observed may have been enhanced by this compression-induced compaction of the oxide by the contracting Bakelite. This assumption was supported by the evidence of microcracks in Figure 4.26.

The main purpose of imaging the oxide was to measure the typical oxide thickness around the outer circumference of a conveyance tube (a 15 n.b. sample in this case with an inner radius of 7.5mm and a wall thickness of 3.2mm) as shown in Figure 4.25. The mean oxide thickness was 15±1μm (based on mean oxide thickness measured at 3 different locations equidistant around the sample circumference – see Figure 10.2 in Appendix 5).

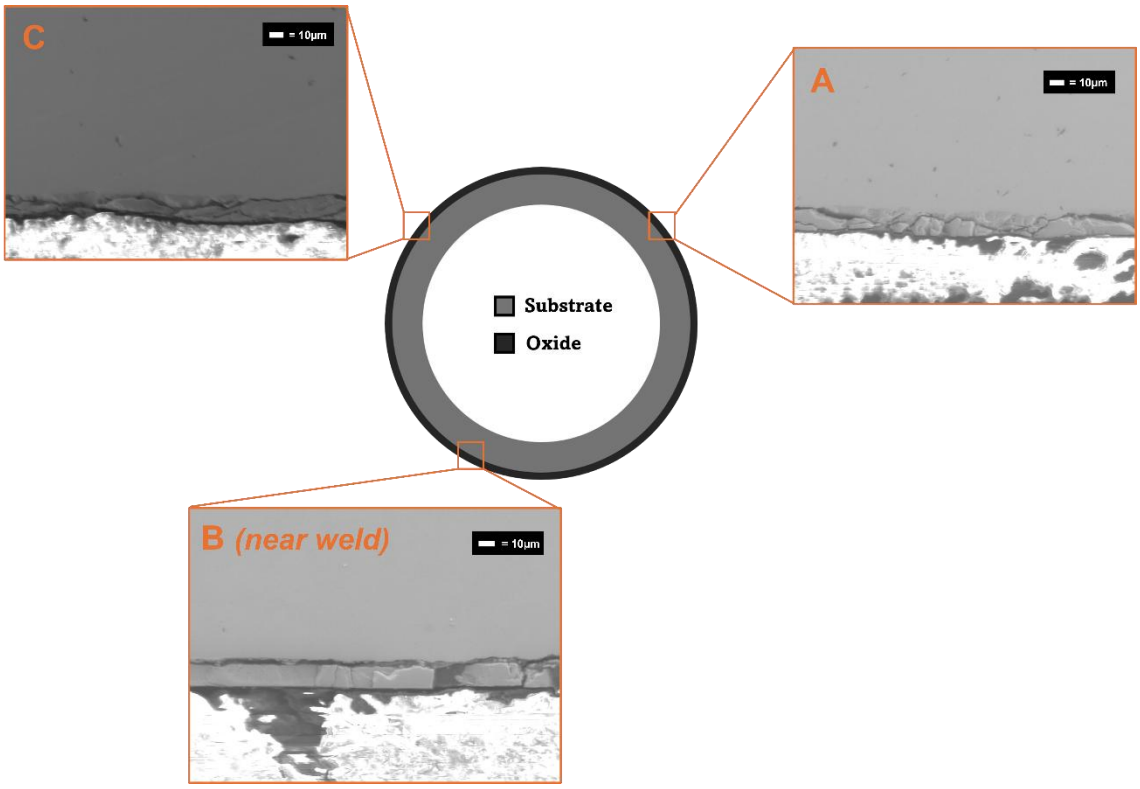


Figure 4.25: Schematic of three approximately equidistant locations used to take mean measurements of oxide thickness, δ_{ox}, for a 15 nominal bore (n.b.) tube having undergone normalisation at 1000°C for three mins ¤.

For repeatability's sake, three equidistantly located FEGSEM images were also taken at the outer edge of a second 15 n.b. sample (see Figure 10.3 in Appendix 6 and Figure 10.4 in Appendix 7) where the average oxide thickness, $\overline{\delta}_{ox}$, was 17±0.3μm and 16±0.7μm (see Table 4.2). Therefore, the average oxide thickness on the industrial sample, $\overline{\delta}_{ox,ind}$, was 16±0.7μm.

For sample 3, the cold-setting resin discussed in Section 2.1 was used to 'seal' the oxide in an attempt to improve scale intactness. However, Figure 10.4 highlights how the layer of resin deposited is often thicker than the oxide scale itself and thus the charging effect of the non-conductive resin depletes the FEGSEM image quality, especially when using the backscatter electron detector (BED), although the effect is mitigated for by the conductive Bakelite layer (see Section 2.1.1).

Table 4.2: Mean oxide thickness, δ_{ox}, measured on the outer edge of three 15 nominal bore (n.b.) conveyance tube samples normalised in industry (Tata Steel UK Ltd). The average oxide thickness in industry, $\delta_{ox,ind}$, is therefore 15.8±0.7μm.

	$\bar{\delta}_{ox}$ (μm)	$\bar{\delta}_{ox,ind}$ (μm)		
Sample 1	15	16	±	0.7
Sample 2	17			
Sample 3	16			

However, it must also be noted that for this pre-normalisation scale, which has not seen temperatures above 900°C at this stage of the tube manufacturing process, mode I failure ('strong interface, weak oxide') via through-thickness cracking and rectangular spalled areas is expected. This conclusion can only be confidently drawn for the outer edge, which is of greatest interest in this work, where beam bending case puts the outer edge in tension (see Figure 4.26) [118, 391]. Furthermore, separation of the oxide-metal interface could also be evidence of the large difference in CTE observed between the oxide and metal, which leads to different thermal expansion rates during mounting heating and cooling cycles [193, 241].

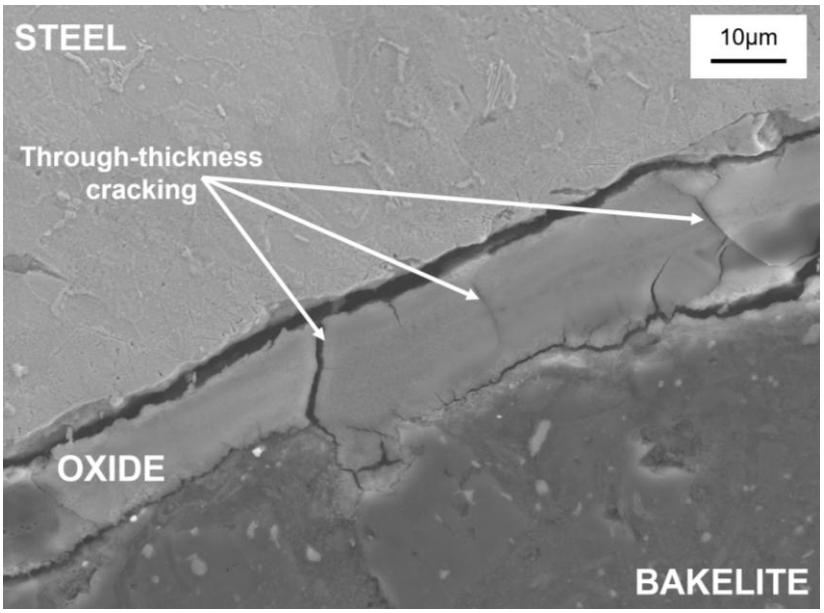


Figure 4.26: Secondary electron emission imaging of outer edge of 15 nominal bore (n.b.) tube pre-normalisation and post-weld ¤.

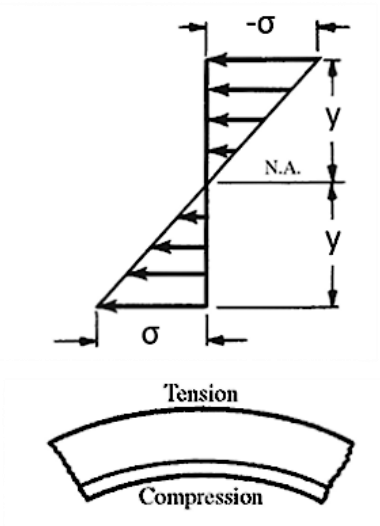


Figure 4.27: Stress diagram for beam in pure bending [82] (*adapted from source*).

Without using cold-set resin, the sample had a higher retention of oxide at the metal surface. A 15 n.b. post-normalisation sample was mounted in this way and analysed. In agreement with expectations, the normalised sample, having seen temperatures in the range >900°C, exhibited Mode II failure in the form of unfractured oxide raft slipping [118] (see Figure 4.28). Transition to this failure mode is accompanied by interface weakening and oxide ductility at the interfaces [77]. Further 15 n.b. post-normalised industrial samples, also with oxide thickness gain of <20μm, also showed evidence of raft slip as the dominant oxide failure mode (see Figure 4.28 and Figure 4.29). In Figure 4.29, the raft also appears to be aligned with cracking of the steel substrate, suggesting that raft formation is a partially geometry-driven phenomenon due to the difference in stress state compared to a planar sample [84, 85, 106]. It should be noted that in the case of duplex phase oxides, raft slipping is also possible along the oxide-oxide interface, e.g. wüstite-magnetite interface (see Figure 4.29). The low level of porosity in the scale was also noted, as is typical of the layer of oxide closest to the metal-scale interface. As Entchev et al. discussed, thicker scale exhibits higher levels of large, non-uniformly distributed pores [85]. Thus, porosity is minimised when normalisation time is minimised such as in the tube manufacture case [93].

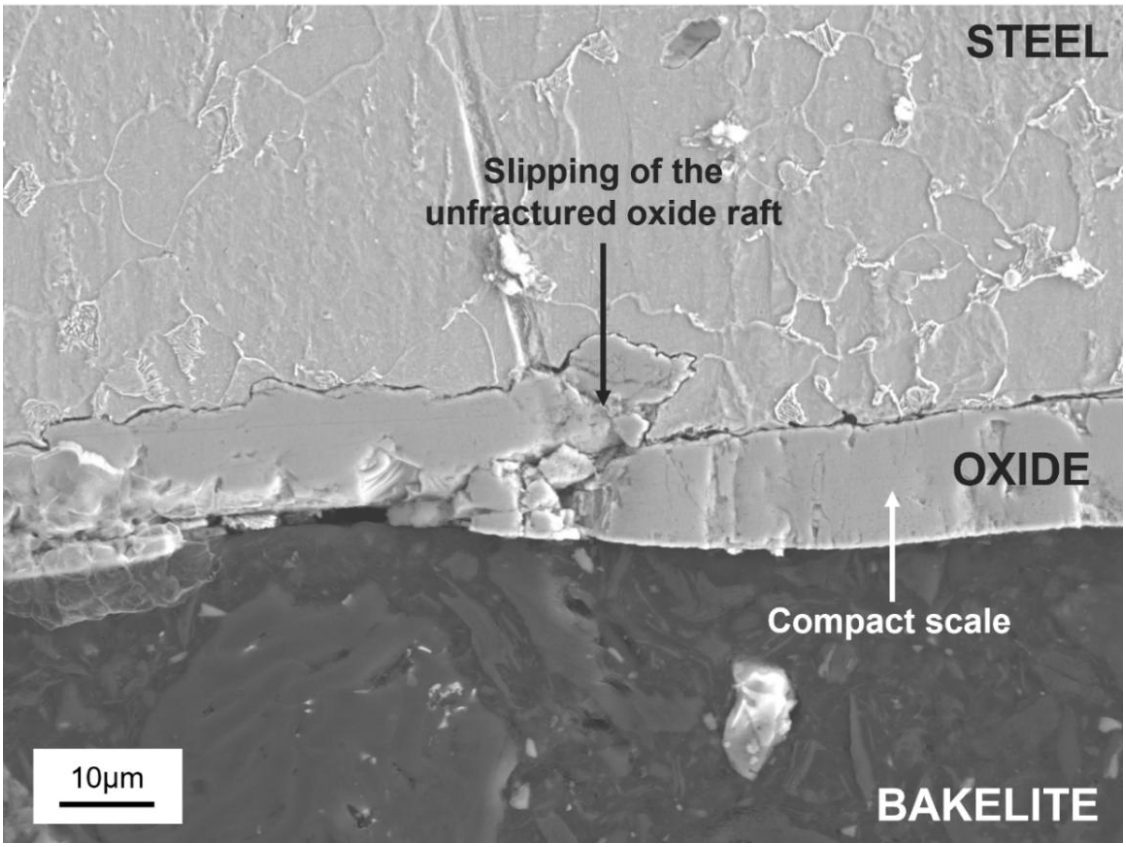


Figure 4.28: Secondary electron emission imaging for outer edge of 15 nominal bore (n.b.) tube sample post-normalisation ¤.

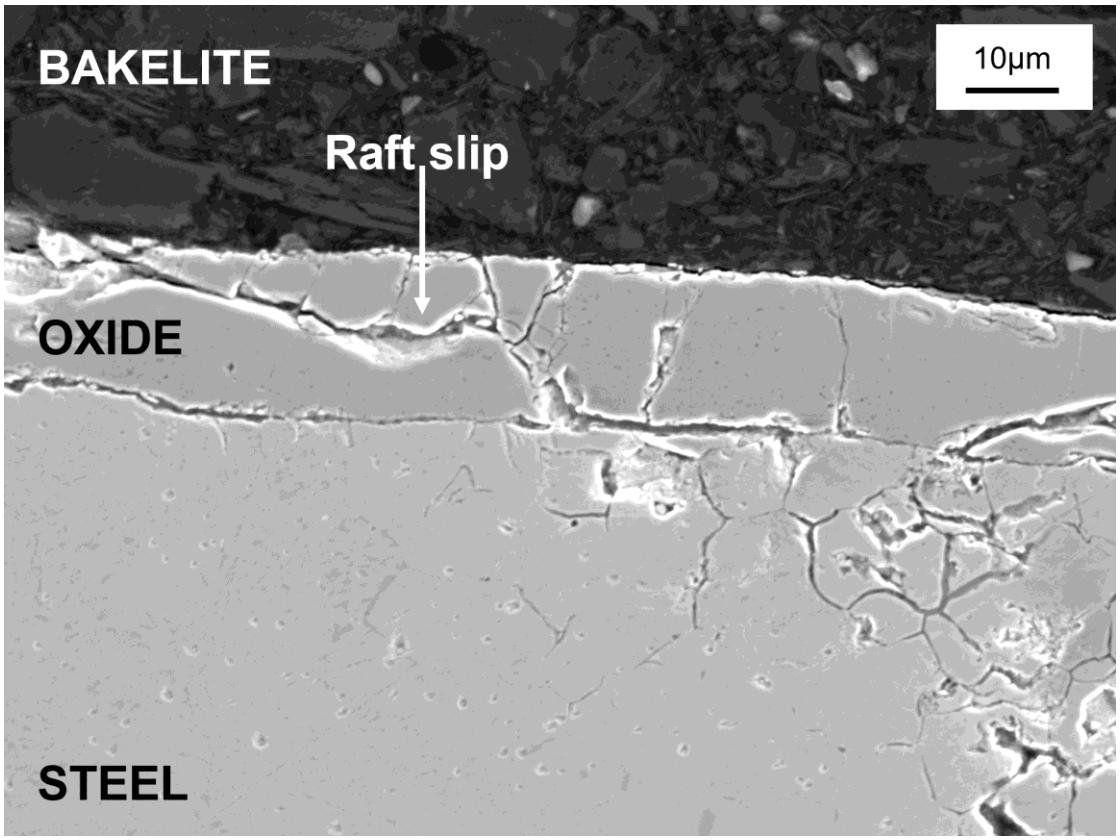


Figure 4.29: Evidence of oxide raft slip in a 15 nominal bore (n.b.) sample normalised at 1000°C for 3 mins ¤.

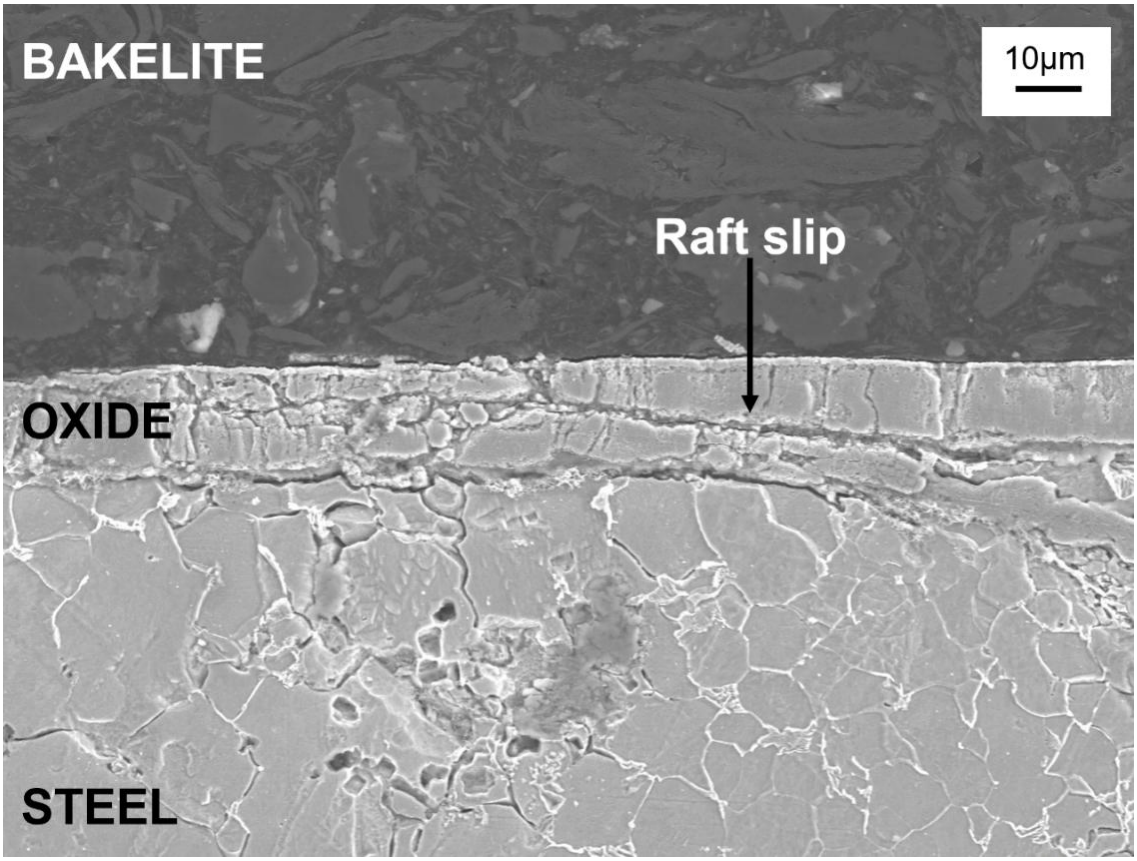


Figure 4.30: Evidence of oxide raft slip in a 15 nominal bore (n.b.) sample normalised at 1000°C for 3 mins ¤.

In compressive regions, i.e. the inner edge of the tube, failure is shown to be a complex multi-stage process, comprising interfacial crack growth, buckling, crack deflection towards the oxide surface, and spalling, which proceeds as strain increases [186]. Although this is less important in this project context, imaging of the inner edge did reveal spalling of the oxide (see Figure 4.31). Schütze summarised much of this failure information in an Advanced Oxide Scale Failure Diagram (AOSFD) [186]. The failure mode transition temperature discussed by Krzyzanowski and Beynon [94] is significant for tube manufacturing as both steel exhibit transition temperatures in the normalisation range, which could lead to mixed failure mode and thus complicate scale management, alongside stress states, and explain why scale is hard to control and its delamination (Mode I vs. Mode II) is unpredictable. This could be especially true if heat transfer is not uniform due to the low thermal conductivity and high specific heat capacity of the scale compared to the steel substrate [15, 73]. However, Figure 4.32 also highlights that, under the same conditions, transition temperature still varies by approximately 130°C and this is attributed to chemical compositions differences.

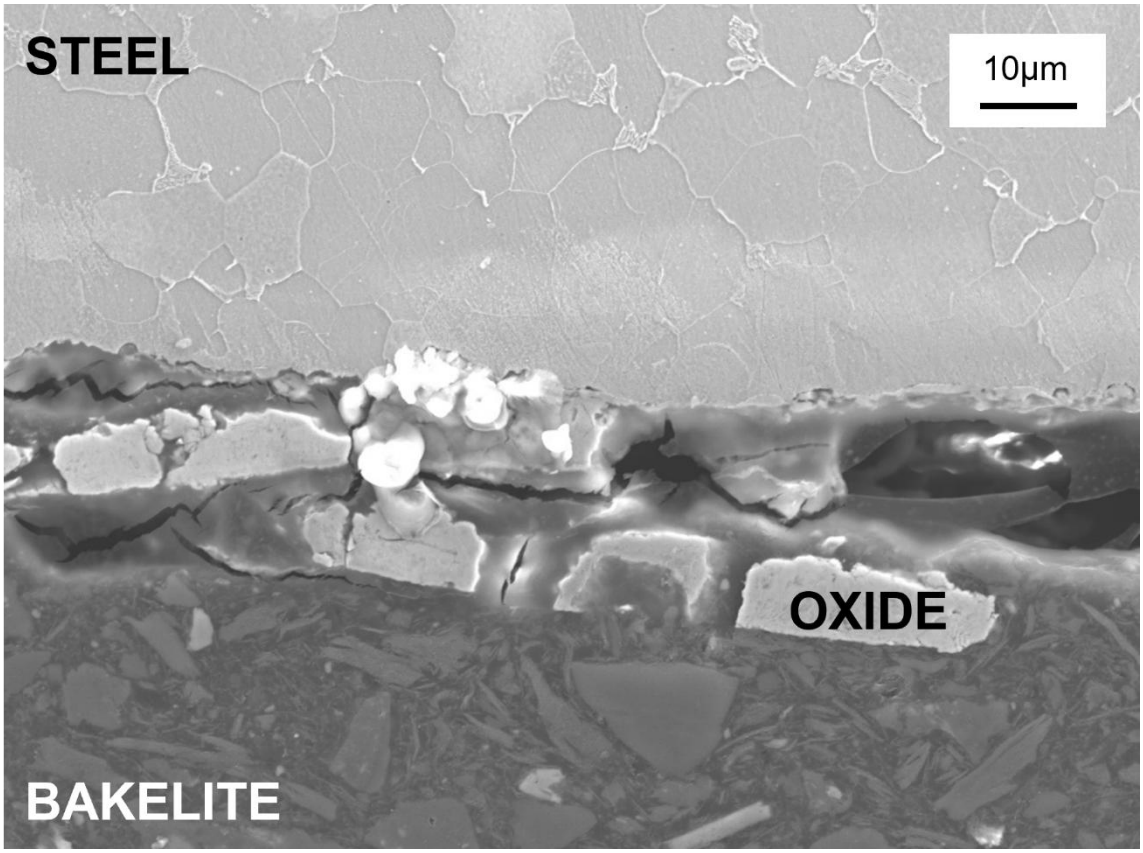


Figure 4.31: Secondary electron emission image of spalled oxide at the inner edge of a 15 nominal bore (n.b.) tube sample post-normalisation ¤.

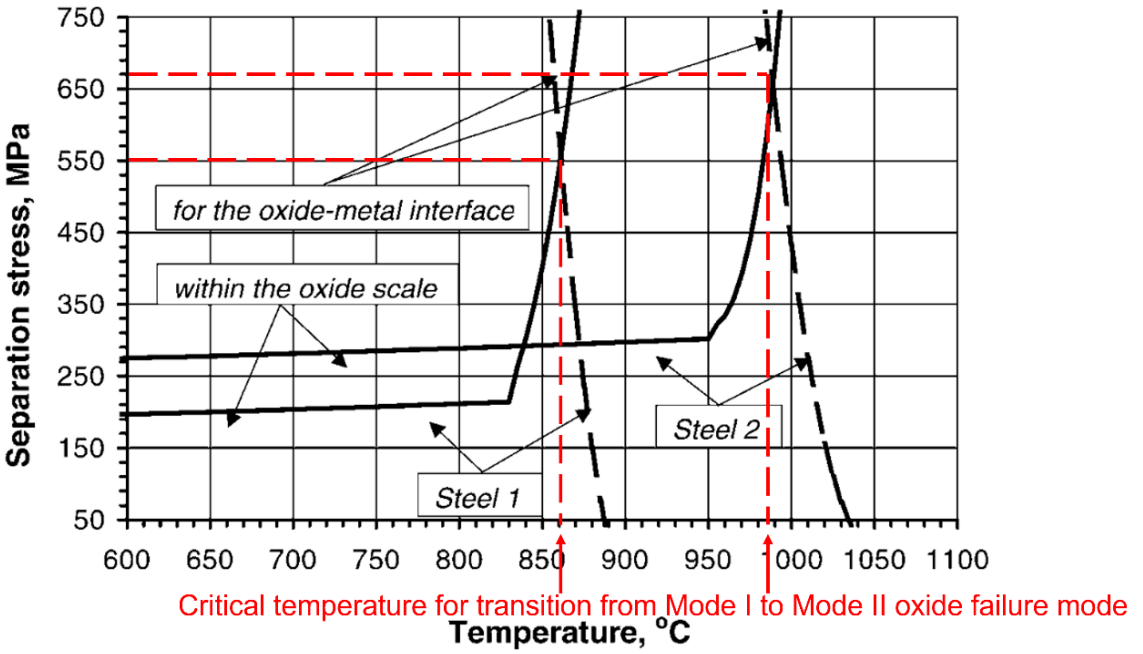


Figure 4.32: Annotated separation stress-temperature plot highlighting the transition from Mode I to II failure at a given temperature influenced by steel chemistry [77] (*adapted from source*).

4.2.2 Thermogravimetry

Equipment Modification

The basic principles of thermogravimetry and specific experimental set-up used were discussed in Section 2.1.3.1. The sample mass was 45.0528g (although this level of precision was far greater than that of the Carbolite Gero Ltd mass balance at 0.05g). A 15 min period was left between switching the balance on and starting any mass measurement operations, to ensure accurate weighing results. This testing faced several technical challenges, the first being the 'overload' of the mass balance during sample loading with a sample weighing only 0.3% of the maximum 15kg load possible for the mass balance model used. Therefore, a more sensitive mass balance would be an improvement for future work. This invalid overload was attributed to incremental movement of the furnace tube due to persistent laboratory environmental vibration and thermal currents during previous temperature data-only collections (where the issue would not be detected). The movement resulted in the furnace tube no longer being isolated from the mass balance and caused it to overload. The furnace tube was repositioned, and the correct position was recorded by marking the adjustable (for calibration purposes) mass balance feet with a pen for future reference (see Figure 4.33).

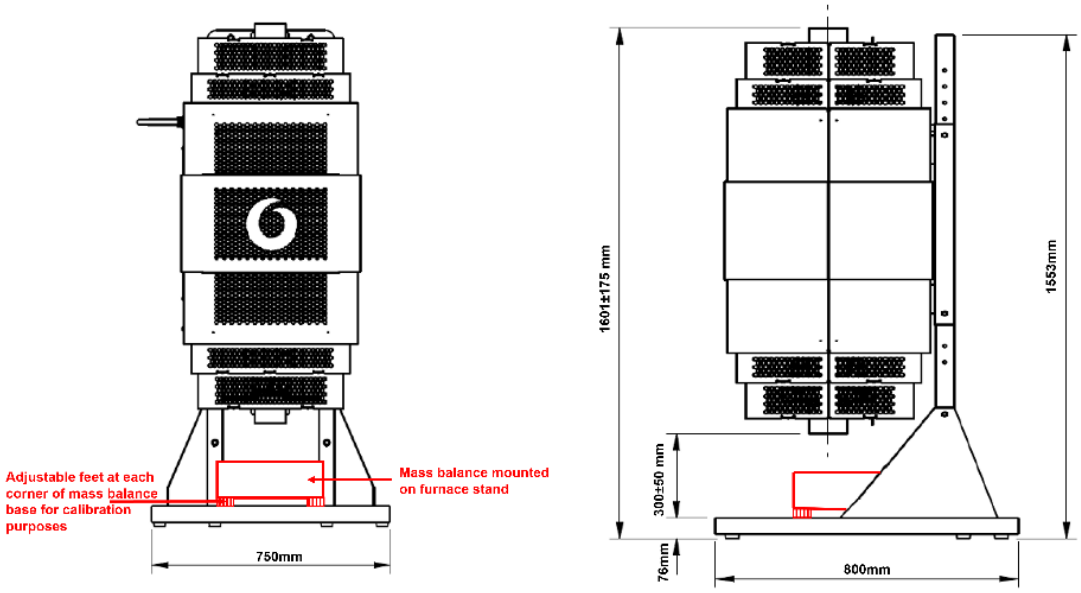


Figure 4.33: Technical drawing (taken from model TF1 16/100/450 furnace manual) showing the incorporation of a mass balance into vertically mounted Carbolite Gero Ltd High Temperature TGA Tube furnace (model TF1 16/100/450) (*adapted from source*).

A second test, with the repositioned mass balance feet, was run using a 20 n.b. sample, with its mass again being checked on the high-precision Fisher Scientific mass balance and revealed to be 45.7490g (see Figure 4.34).

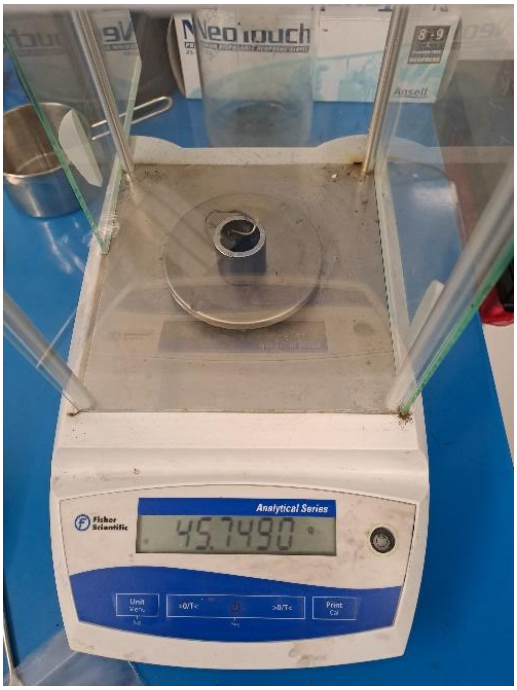


Figure 4.34: 20 nominal bore (n.b.) sample and nichrome wire during pre-testing mass assessment ¤.

The pre-test mass balance reading with the sample installed and the thermocouple connected lacked stability due to the downwards movement of the thermocouple wire under its own weight (see Figure 4.36). Therefore, the first trial was run without the thermocouple connected and during post-processing, the furnace temperature data was instead taken from the Eurotherm nanodac data acquisition unit, which is based on heating element temperature measurements by an in-built thermocouple [272]. Overall, there was a variation in the difference between simultaneous furnace and thermocouple temperature data, $\left|\boldsymbol{T_{thermocouple}} - \boldsymbol{T_{furnace}}\right|$, of 25±29°C with the most significant variation during heating and cooling at lower temperatures ($200 < \boldsymbol{T} < 500$°C). However, Figure 4.35 shows that in the isothermal normalisation soak region of interest, 1000±50°C, there was much less erratic variation in the difference between the two temperature datasets at 26±8°C. Use of the furnace temperature data was therefore acceptable as the variation compared to the thermocouple lay well within the potential normalisation temperature range during manufacturing [9] and within a range which kept external oxidation stable in the expected kinetic regime (see Section 1.3.1) [59].

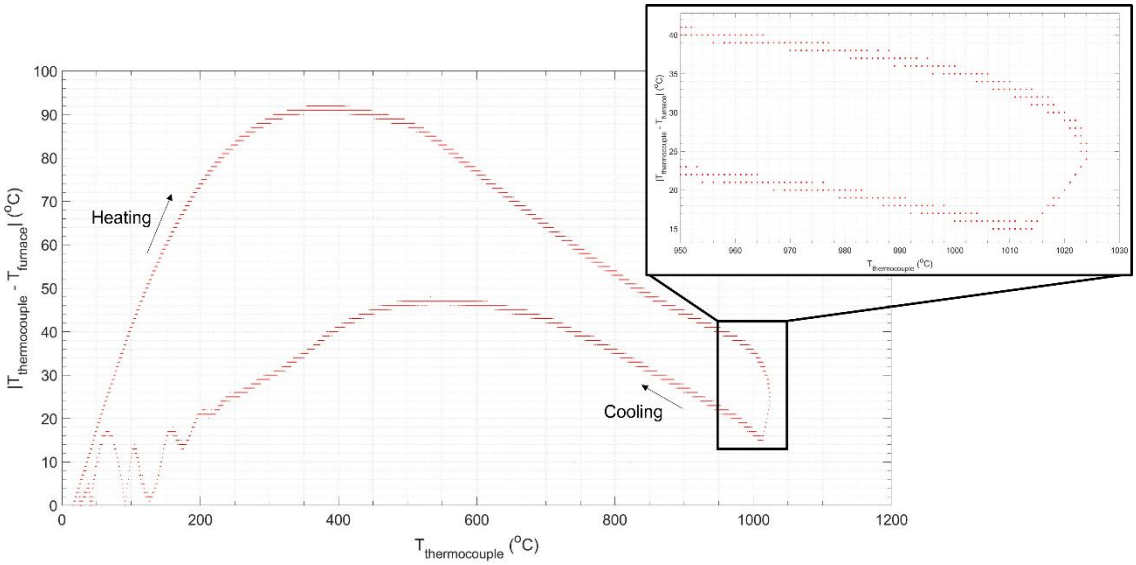


Figure 4.35: Absolute difference between the thermocouple and furnace temperature data, $|T_{thermocouple} - T_{furnace}|$, with the isothermal soak region enlarged ¤.

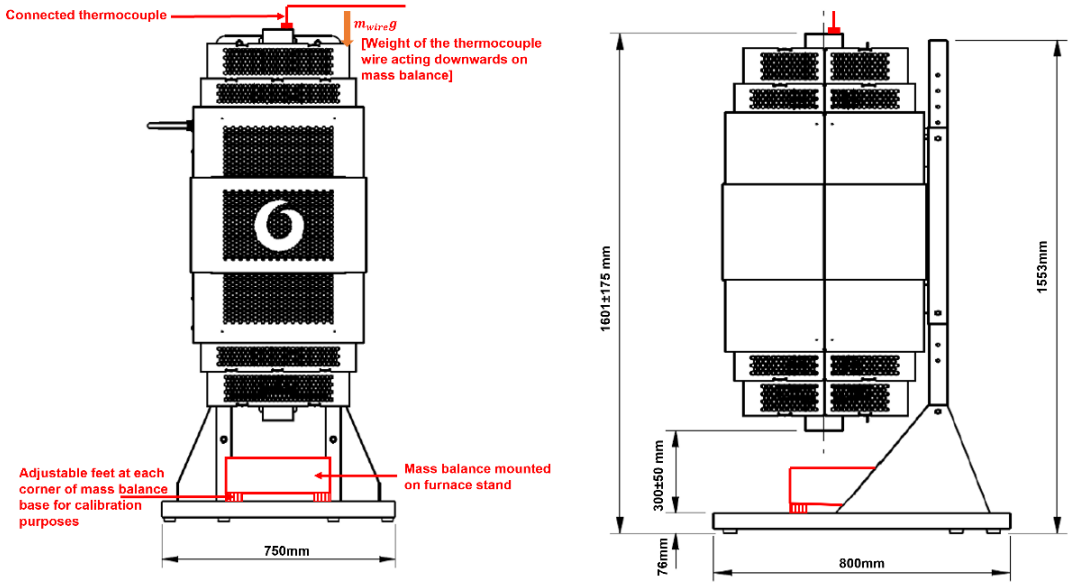


Figure 4.36: Technical drawing (taken from model TF1 16/100/450 furnace manual) showing the incorporation of a mass balance and thermocouple into vertically mounted Carbolite Gero Ltd High Temperature TGA Tube furnace (model TF1 16/100/450) (adapted from source [272]).

Testing for Validation

A successful TGA run was performed on the 15 n.b. sample. The thermal cycle comprised a 5°C.min^{-1} ramp to 1000°C, followed by a 15 min dwell, and finally a 5°C.min^{-1} cooling ramp (see Figure 4.37). Unexpectedly, the sample exhibited a 19% mass loss during the heating and cooling periods of the thermal cycle, and a significant signal-to-noise ratio (***SNR***) and coefficient of variance (***CV***) of 94.0 and 1.1% respectively (based on the mean, $\boldsymbol{\mu}$, and standard deviation, $\boldsymbol{\sigma}$, values), during the isothermal soak period (red region in Figure 4.37)

compared to the less noisy region post-cooling (blue region in Figure 4.37) which had an $\boldsymbol{SNR}$ and $\boldsymbol{CV}$ of 402.4 and 0.2% respectively (see Equation 4.10) [392]. A higher $\boldsymbol{SNR}$ and lower $\boldsymbol{CV}$ typically indicate better quality data. The latter (post-cooling) region acts as a data quality baseline, i.e. noise is minimised to only a statistical level [392], hence the four-fold reduction in $\boldsymbol{SNR}$ in the isothermal region is reflective of the reduction in data quality associated with flow-induced vibration (FIV). Disregarding the subsequent mass losses and gains over the thermal cycle, the net mass change was -0.3g (see Figure 4.37).

$$\boldsymbol{SNR = \frac{\mu}{\sigma}; CV = \frac{100}{SNR}}$$

Equation 4.10

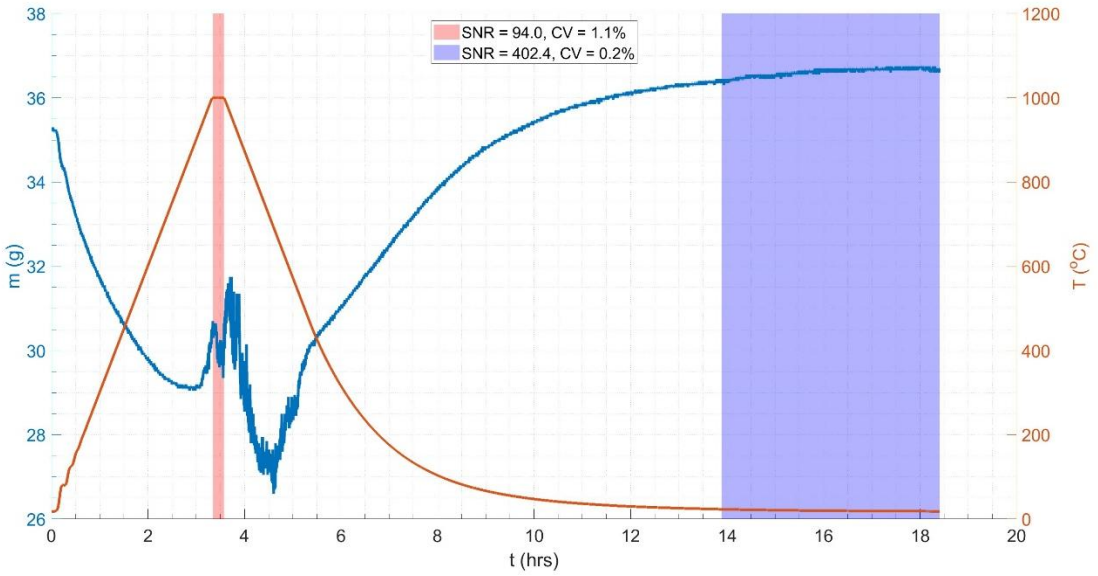


Figure 4.37: Plot of sample mass, $\boldsymbol{m}$, (left) and temperature, $\boldsymbol{T}$, (right) against time, $\boldsymbol{t}$, for a tube normalisation heat treatment replica thermal cycle on a 15 nominal bore (n.b.) tube sample ¤.

Thermally induced gas flow dynamics were proposed to be the greatest proponent of both noise and mass loss in the sample during heating and cooling periods. The large temperature change in the thermal cycle used demands analysis via conservation of momentum (see Equation 4.11) so that the ratio of flow velocity and temperature is constant (see Equation 4.12) [393-395]. It is suggested that a compressible analysis, underpinned by non-constant fluid density, $\boldsymbol{\rho}$, i.e. $\frac{\boldsymbol{d\rho}}{\boldsymbol{dt}} \neq 0$, would be required to describe the air flow experiencing a large temperature increase and cross-sectional area reduction in moving from the 750mm diameter furnace chamber to the 75mm diameter furnace work tube followed by the 14.9mm diameter tube sample, which is currently difficult to suspend with a fully vertically aligned bore. There is no pressure change as the work tube and tube sample are open-ended

and the flow is subsonic. Density, $\boldsymbol{\rho}$, varies spatiotemporally whilst pressure, $\boldsymbol{P}$, varies only spatially. For a temperature change, $\boldsymbol{T_2 - T_1}$, from ambient ($\boldsymbol{T_1}$ = 25°C) to normalisation ($\boldsymbol{T_2}$ = 1000°C), there will be a flow velocity, $\boldsymbol{v}$, increase of a factor of 4.3, i.e. $\frac{\boldsymbol{v_2}}{\boldsymbol{v_1}} = 4.3$ (see Equation 4.12). Newton's Second Law [396] indicates that the acceleration of the furnace gas will enact an instantaneous force on the sample and initiate damped free vibration [397].

$$\frac{\boldsymbol{\partial \rho}}{\boldsymbol{\partial t}} + \frac{\boldsymbol{\partial}}{\boldsymbol{\partial x_i}}(\boldsymbol{\rho u_i}) = \boldsymbol{0}$$
$$\frac{\boldsymbol{\partial}}{\boldsymbol{\partial t}}(\boldsymbol{\rho u_i}) + \frac{\boldsymbol{\partial}}{\boldsymbol{\partial x_j}}(\boldsymbol{\rho u_i u_j}) + \frac{\boldsymbol{\partial P}}{\boldsymbol{\partial x_i}} - \boldsymbol{\rho g_i} = \boldsymbol{0}$$

Equation 4.11

$$\frac{\boldsymbol{V_1}}{\boldsymbol{V_2}} = \frac{\boldsymbol{T_1}}{\boldsymbol{T_2}}$$

Equation 4.12

During the isothermal period, the fluid around the sample flows at a steady speed well below that needed to reach its critical Reynolds number ($\boldsymbol{Re} \ll 200{,}000$) [398], i.e. laminar flow state, and the walls of the sample act as blunt bodies which retard the flow. The flow becomes detached from the sample in its wake region. Flow detachment from the sample promotes the formation of a von Karman vortex street: a series of counter-rotating vortices are shed periodically from the sample into its wake (see Figure 4.38) [399]. Turbulent thermal currents also explain the larger variation in difference between thermocouple and furnace sample during heating and cooling periods. The probe thermocouple is directly next to the sample but the furnace temperature is based on in-built thermocouple measurements of heating element temperature in the far-field around the furnace work tube circumference, i.e. outside of the thermal flow field [272].

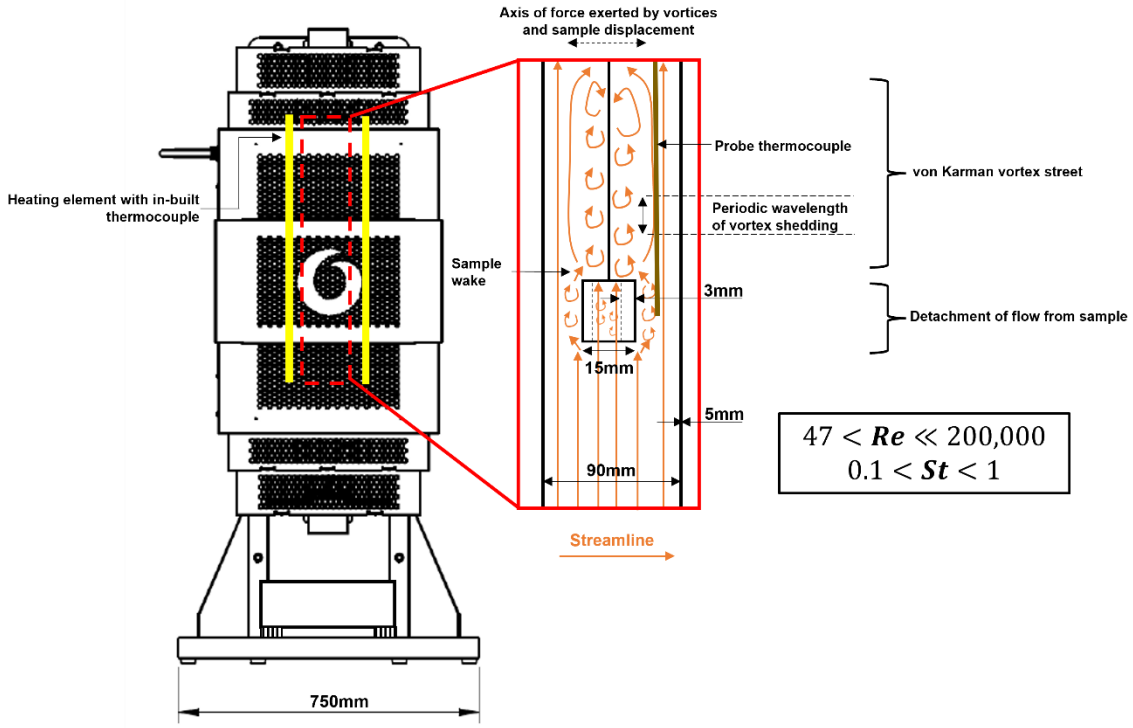


Figure 4.38: Schematic of the streamline profile induced during vortex induced vibration (VIV), within the furnace work tube, associated with laminar ($\boldsymbol{Re} \ll 200{,}000$), viscous ($0.1 < \boldsymbol{St} < 1$) thermally-induced gas flow around the sample blunt body.

The von Karman vortex street exerts a resultant sinusoidal lift force on the sample, perpendicular to the gas flow direction, which can excite the sample into damped oscillator motion if the vortex shedding frequency is close to the sample resonant frequency [398]. This is known as vortex induced vibration (VIV) [400], of which there are specific examples of around long blunt bodies [401, 402]. VIV is most often described by higher Strouhal number, $\boldsymbol{St}$, values ($\boldsymbol{0.1 < St < 1}$), where there are high levels of viscous compared to local acceleration [403].

The overall consequence of these vibration phenomena will be damped free vibration due to thermal buoyancy of the sample in heating and cooling periods, and a pendulum effect from the forced vibration due to VIV in the isothermal period, if the gas excitation frequency is equal to the tube resonant frequency [404]. Mass balance fluctuations will therefore be due to force balance changes. Although decreasing the gas flow rate could reduce the impact of vibration, the ambient environment means there is limited opportunity to control intake flow velocity but an alternative solution would be to use a chain instead of a single wire to reduce the effective pendulum length.

Without the ability to control the gas flow, the alternative is to run a dummy test on a similar geometry high-temperature refractory sample, i.e. a sample which will not gain mass due to oxidation. The instantaneous oxide mass gain, $\Delta \boldsymbol{m}_{\boldsymbol{ox},\boldsymbol{t}_i}$, at time, $\boldsymbol{t}_i$, is therefore

obtained by subtracting any each instantaneous mass measurement in the dummy test, $\boldsymbol{m_{alumina,t_i}}$, arguably due to the gas flow effects discussed, from the original steel tube test, $\boldsymbol{m_{steel,t_i}}$ (see Equation 4.13).

$$\Delta \boldsymbol{m_{ox,t_i}} = \boldsymbol{m_{steel,t_i}} - \boldsymbol{m_{alumina,t_i}}$$

Equation 4.13

The discrete Fourier transform (DFT) (see Equation 4.14) can be used to express periodic time-series, data, $\boldsymbol{x(t)}$, as a frequency spectrum, $\boldsymbol{X(k)}$, where $\boldsymbol{k}$ is the product of time, $\boldsymbol{t}$, and frequency, $\boldsymbol{\omega}$ [405]. Given that periodic functions of time can be expressed as the sum of a number, $\boldsymbol{N_{sine}}$, of discrete sine function components with their own amplitude, $\boldsymbol{A_{n=1\ldots N_{sine}}}$, frequency, and phase angle, $\boldsymbol{\phi_i}$, (see Equation 4.15), the forcing frequency, and any associated harmonics, can be identified from equivalent frequency domain data [397].

$$\boldsymbol{X(k)} = \sum_{\boldsymbol{n=0}}^{\boldsymbol{N_{sine}-1}} \boldsymbol{x(t)e^{-i\frac{2\pi kn}{N_{sine}}}} \Leftrightarrow \boldsymbol{x(t)} = \frac{\boldsymbol{1}}{\boldsymbol{N_{sine}}} \sum_{\boldsymbol{k=0}}^{\boldsymbol{N_{sine}-1}} \boldsymbol{X(k)e^{j\frac{2\pi}{N_{sine}}nk}}$$

Equation 4.14

$$\boldsymbol{x(t) = A_0 + A_1 \sin(\omega t + \phi_1) + A_2 \sin(2\omega t + \phi_2) + A_3 \sin(3\omega t + \phi_3) + \cdots},$$

Equation 4.15

The fast Fourier transform (FFT) in-built algorithm in MATLAB R2024b was used to evaluate the frequency domain data using the noisy isothermal region from the original TGA time series data where the proposed forced vibration is present. The results are shown in Figure 4.39 and clearly show 1.21mHz as the pendulum resonance frequency, assuming the peak observed at the lowest frequency is the first harmonic.

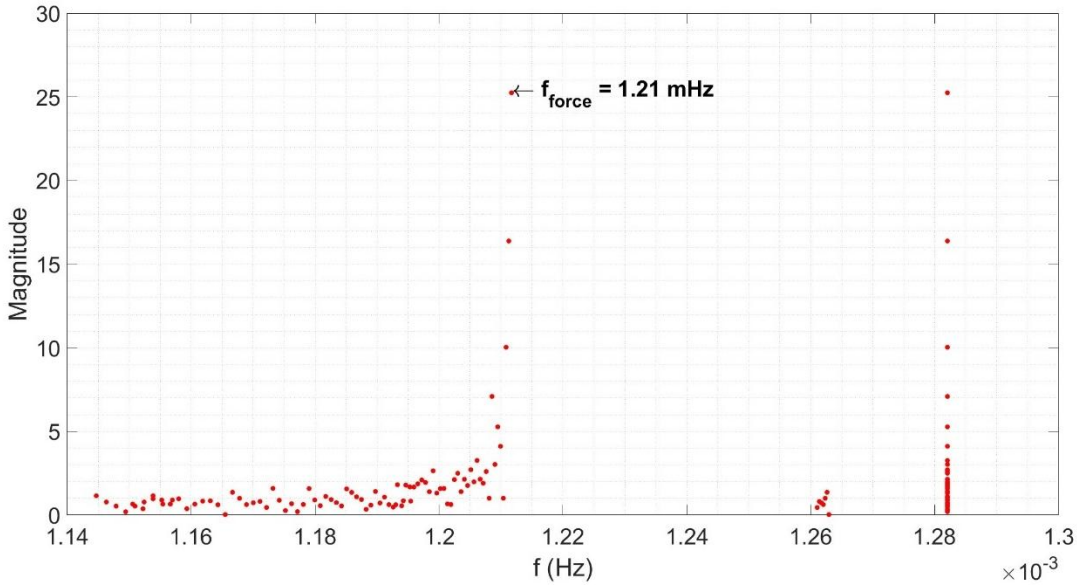


Figure 4.39: Frequency spectrum, $\boldsymbol{f}$, for the isothermal period of a 1000°C normalisation heat treatment cycle on a 15 nominal bore (n.b.) steel conveyance tube ¤.

A dummy sample was run using an alumina ($\boldsymbol{Al_2O_3}$) furnace tube with outer diameter 38mm, 3mm wall thickness, and 25mm length. Its initial mass, 33.4823g, was measured using a 4 decimal place (d.p.) Fisher Scientific mass balance. The thermal cycle used was identical to that used for the steel tube sample (see Figure 4.41). No net mass gain due to oxidation of the sample was anticipated during this cycle except for the oxidation of the nichrome suspension wire, a minimum length of which was used to minimise any pendulum effect (see Figure 4.40). All mass gain was expected to be due to the thermofluid dynamics phenomena described above. The total mass of the sample and wire was 34.4524g. It should be noted that, in order to comprehensively explore the effect of the tube geometry on gas flow dynamics, and due to the brittle nature of the ceramic tube material, the nichrome suspension wire was attached through the bore and around the entire tube thickness, but not secured to allow it to be removed post-treatment, instead of drilling a suspension hole as in the steel sample case. Figure 4.40 also highlights how uneven oxidation can arise due to the effect of the gas flow on the extent of oxidation at each part of the sample geometry, as discussed in Section 1.6.4 [212].

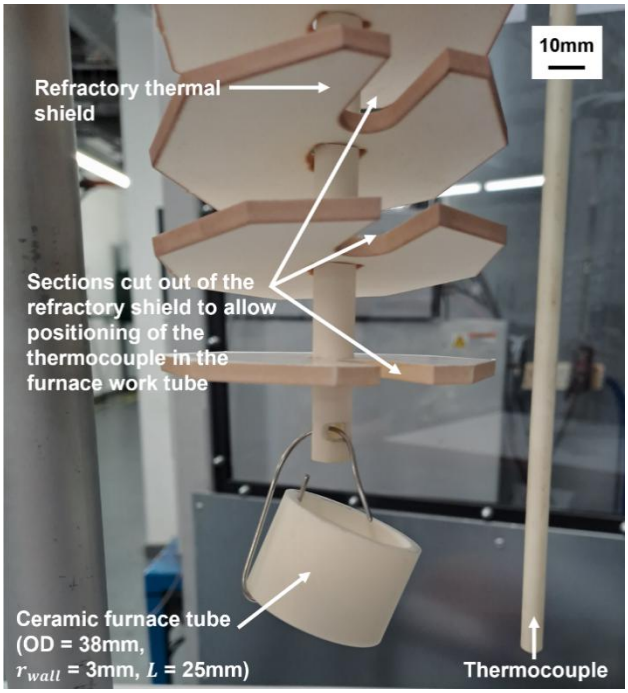


Figure 4.40: Ceramic furnace tube dummy sample (38mm outer diameter, ***OD***, 3mm wall thickness, ***r_{wall}***, and 25mm length, ***L***) suspended from the refractory shield using nichrome wire. Cut-out sections in the refractory shield allow the thermocouple to be positioned within the shield radius once the assembly is in the furnace work tube ¤.

Figure 4.41 shows the results of the dummy test. A net mass change of -0.3g was observed post-test once minor oxidation of the nichrome wire had been accounted for. Again, there is a large (six-fold) reduction in ***SNR*** during the isothermal test region (red in Figure 4.41) compared to the stable region (blue in Figure 4.41) which matches that observed in the steel sample, indicating that data quality is affected by VIV.

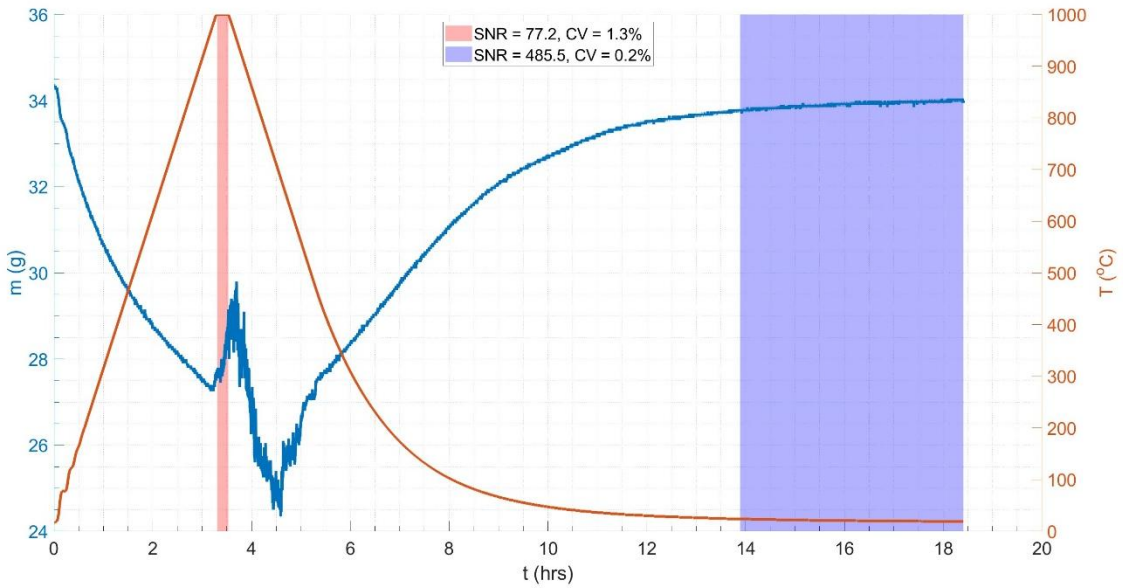


Figure 4.41: Mass and temperature profiles for a representative normalisation cycle using a refractory (Al_2O_3) 'dummy' sample. Annotated to include evaluation of signal-to-noise ratio (SNR) and coefficient of variance (CV) in the isothermal (left) and non-isothermal (right) data regions. The higher SNR and lower CV in the non-isothermal data region indicates higher quality data with less noise ¤.

Figure 4.42 shows an unanticipated issue with cyclic loading and creep of the nichrome wire due to the free movement of the sample on the wire during pendulum motion under forced vibration. This caused the nichrome wire to open and put the sample to the risk of falling from the sample hook during test, or during transfer after testing. When testing the 15 n.b. sample, the original technique of attaching the wire via a drilled through-thickness hole in the wall was used, although this meant accepting a greater axial tilt in the sample during testing (see Figure 4.43). The 15 n.b. sample used had an initial mass of 34.1996g. Matching the dummy and real sample masses is more important than matching the geometry when considering the case of thermally induced damped free vibration as mass, $\boldsymbol{m}$, is a key variable (alongside system stiffness, $\boldsymbol{k}$) in determining the damping ratio, $\boldsymbol{\zeta}$, and natural frequency, $\boldsymbol{\omega_0}$, (see Equation 4.16 and Equation 4.17) of the governing damped harmonic oscillator motion equation for sample displacement, $\boldsymbol{x_{sample}}$, as a function of time, $\boldsymbol{t}$ (see Equation 4.18) [397]. The forcing function, $\boldsymbol{F}$, a constant energy source associated with VIV, although also influenced by mass via natural frequency, is more influenced by the energy source of the continuous convective gas flow and its interaction with sample geometry.

$$\boldsymbol{\zeta = \frac{c}{2\sqrt{mk}}}$$

Equation 4.16

$$\boldsymbol{\omega_0 = \sqrt{\frac{k}{m}}}$$

Equation 4.17

$$\boldsymbol{\frac{d^2x_{sample}}{dt^2} + 2\zeta\omega_0\frac{dx_{sample}}{dt} + \omega_0^2 x_{sample} = F}$$

Equation 4.18

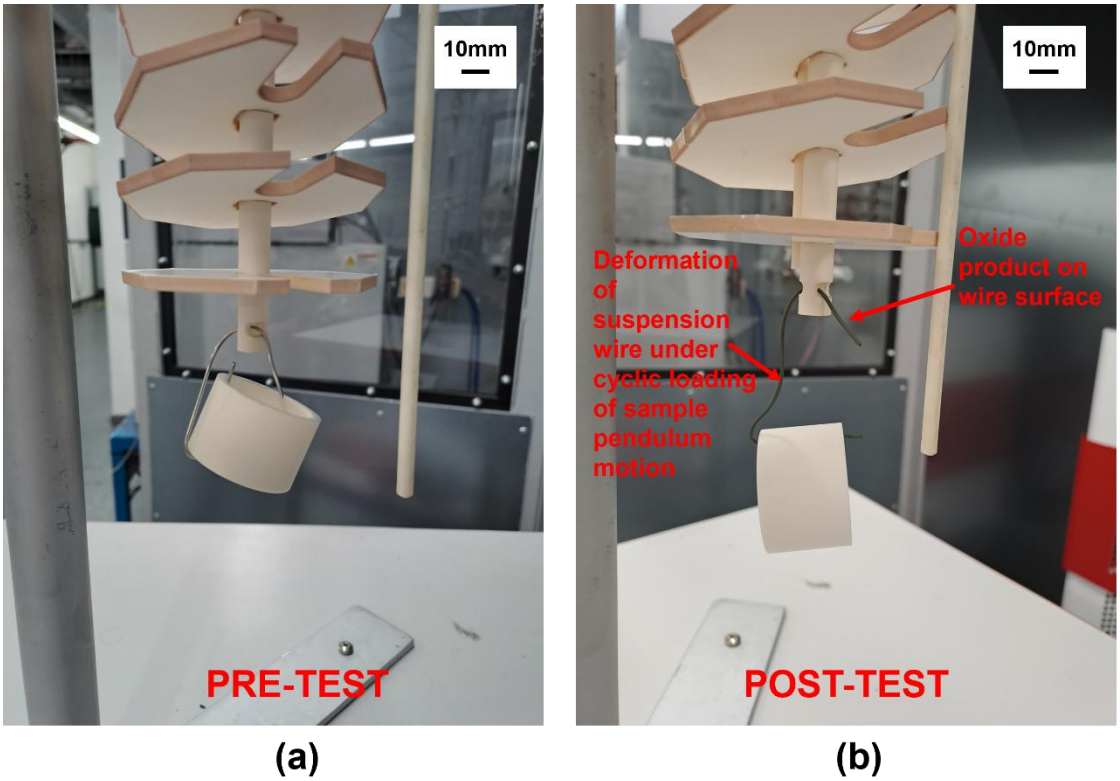


Figure 4.42: Comparison of ceramic sample (a) before and (b) after normalisation treatment. The nichrome suspension wire shows evidence of oxidation and deformation under the cyclic loading of the sample pendulum motion ¤.

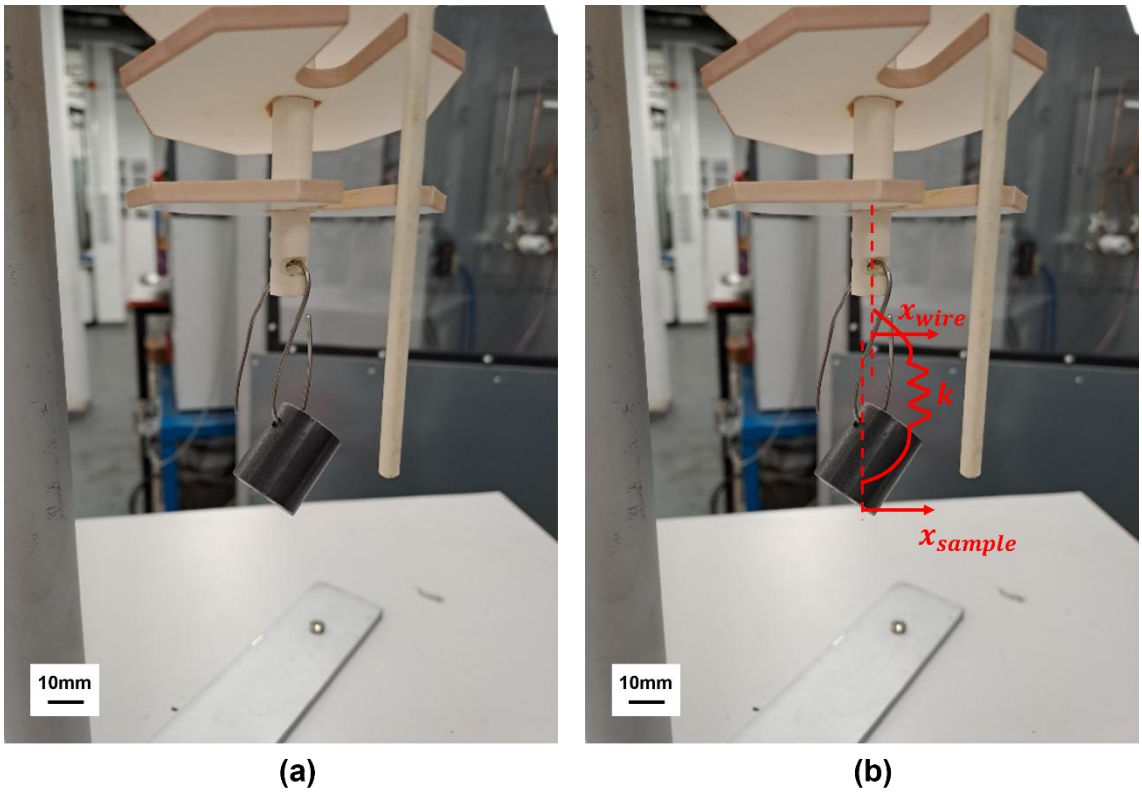


Figure 4.43: (a) Pre-test setup of 15 n.b. sample with annotations (b) indicating the potential for double pendulum motion due to difference resonant frequencies of the sample leading to different displacements, x_{sample}, and wire, x_{wire} ¤.

Figure 4.37 shows the mass and temperature profiles of the 15 n.b. sample subjected to the same thermal cycle as the ceramic dummy. The mass of the sample post-test, measured again using the Fisher Scientific mass balance, was 35.8579g, indicating an oxide mass gain of 1.6583g.

Figure 4.44 shows the results of the FFT applied to the ceramic sample results, resulting in a 2 d.p. agreement between the forcing frequency for the steel and ceramic samples, indicating the consistency of the vibration effect. However, only a single resonant frequency was observed for the ceramic sample, whilst the steel sample had evidence of a secondary harmonic which was potentially due to the vibration of the steel-scale interface [406]. There is also a possibility that the second resonant frequency of ~1.28mHz (see Figure 4.39) arises from double pendulum motion associated with the difference in resonant frequency of the suspension wire, $\boldsymbol{\omega_{wire}}$, and the steel sample, $\boldsymbol{\omega_{sample}}$, which is free to oscillate (see Figure 4.43) [407]. The ceramic sample cannot oscillate as it is fixed rigidly by the positioning of the suspension wire (see Figure 4.42).

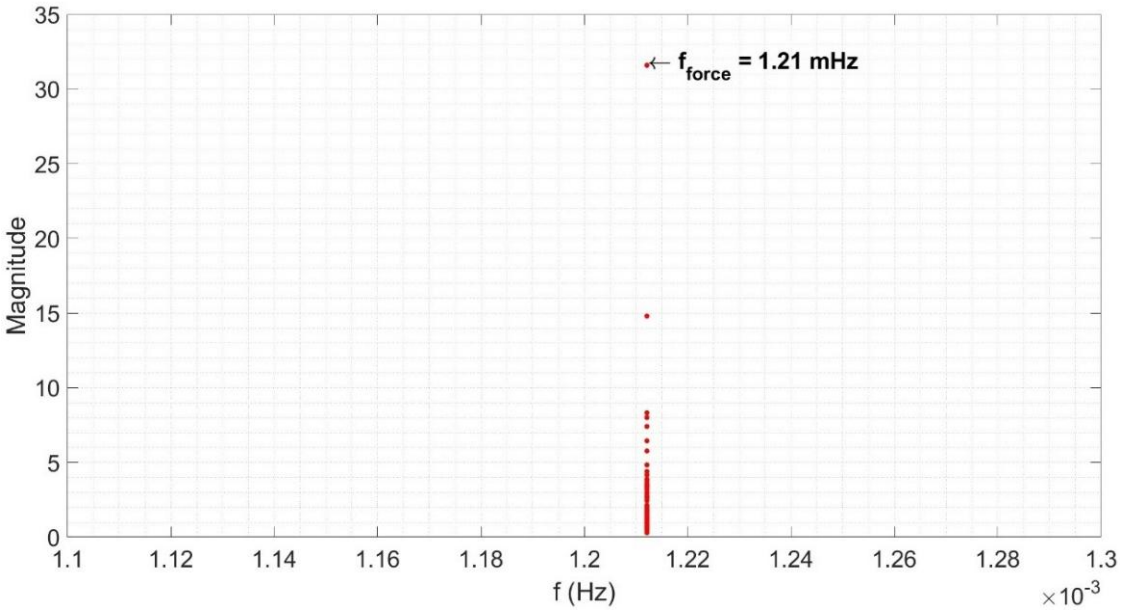


Figure 4.44: Frequency spectrum, $\boldsymbol{f}$, for the isothermal period of during a 1000°C normalisation heat treatment cycle on an alumina tube ¤.

The profiles for the dummy and real tests were overlaid (see Figure 4.45). The difference in mass, given the similar profiles, was taken to be the oxide mass gain, once the initial difference in mass between the two samples was subtracted. A plot of oxide mass gain against time is shown in Figure 4.46. There are discretised data where mass change, at the sampling rate of 0.2Hz, is less than balance resolution so a moving average filter with a window of 9 datapoints was applied which represents a time window of 45s at the given

sampling rate. There is clear evidence of free damped oscillator motion, described in Section 4.2.2, in the first hour of mass measurement during the heating period and at the onset of the isothermal soak and initial cooling period, although in the latter cases the damped oscillator motion appears forced, before mass settles at a stable value (see Figure 4.46 and Figure 4.47) [408, 409].

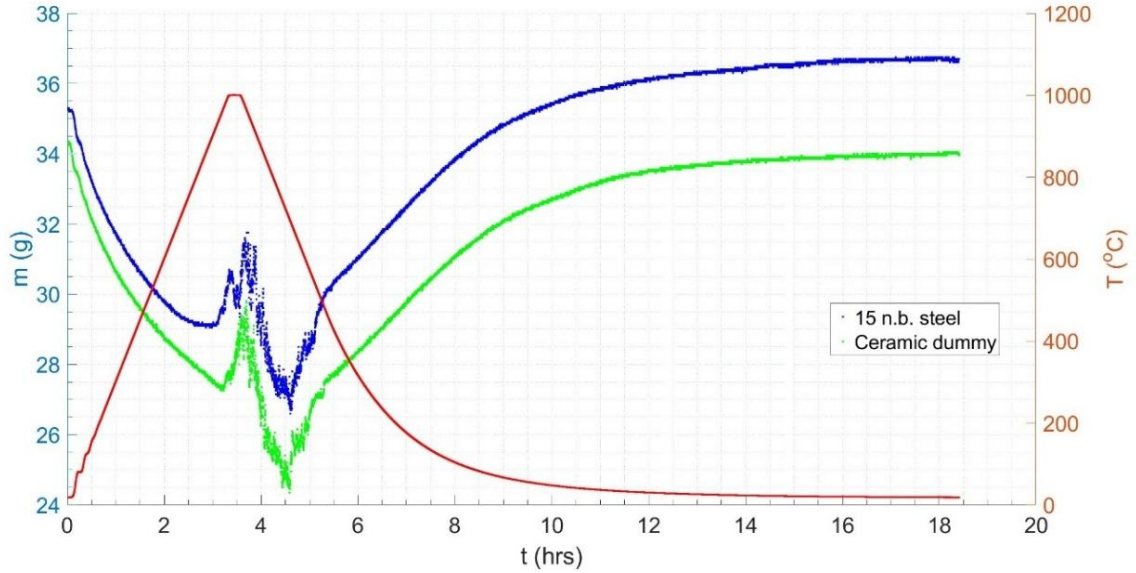


Figure 4.45: Combined sample mass, ***m***, -temperature, ***T***, plots for the steel (15 nominal bore) (*blue*) and ceramic (*green*) samples following a representative normalisation thermal cycle ¤.

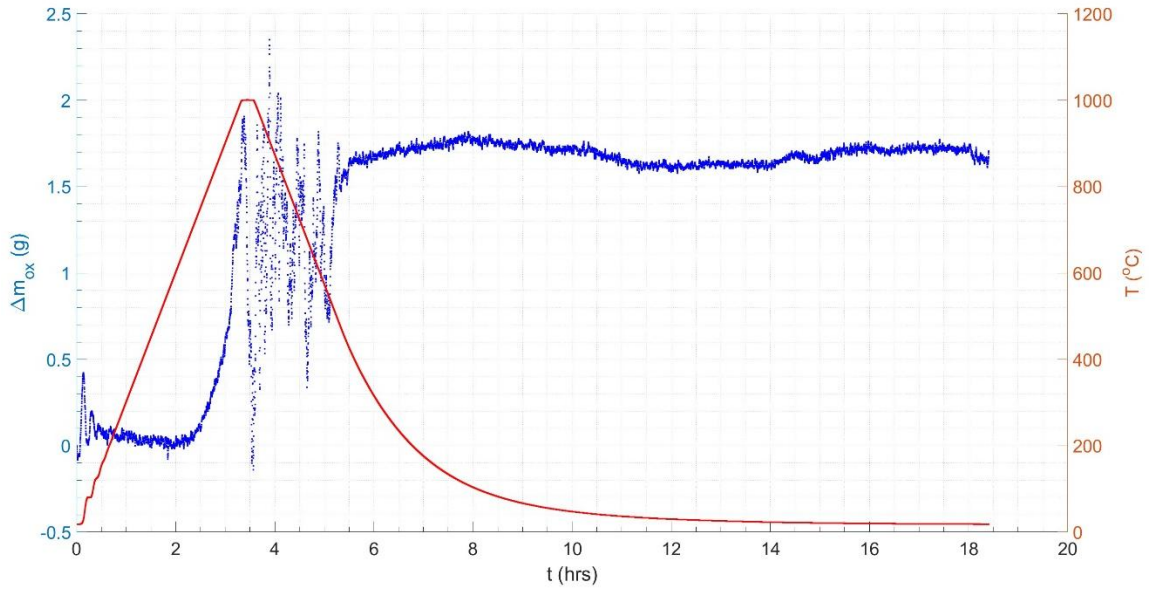


Figure 4.46: Combined sample mass, ***m***, -temperature, ***T***, plot for oxide mass gain on 15 nominal bore (n.b.) sample ¤.

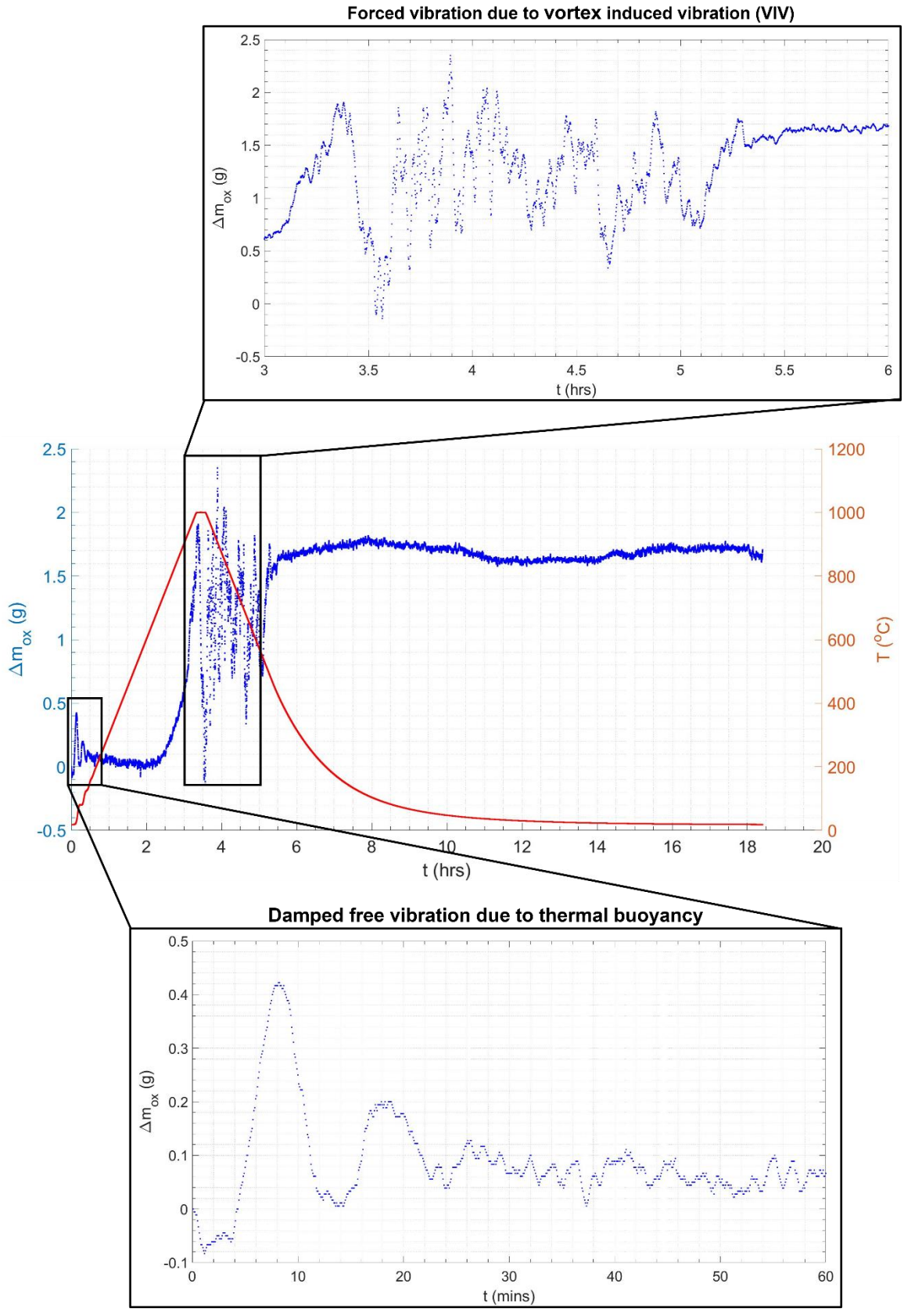


Figure 4.47: Sample mass, ***m***, -temperature, ***T***, plot for oxide mass gain on 15 nominal bore (n.b.) sample with enlarged regions exhibiting damped free vibration during heating and cooling due to heating and cooling, and forced vibration during the isothermal period due to vortex induced vibration (VIV).

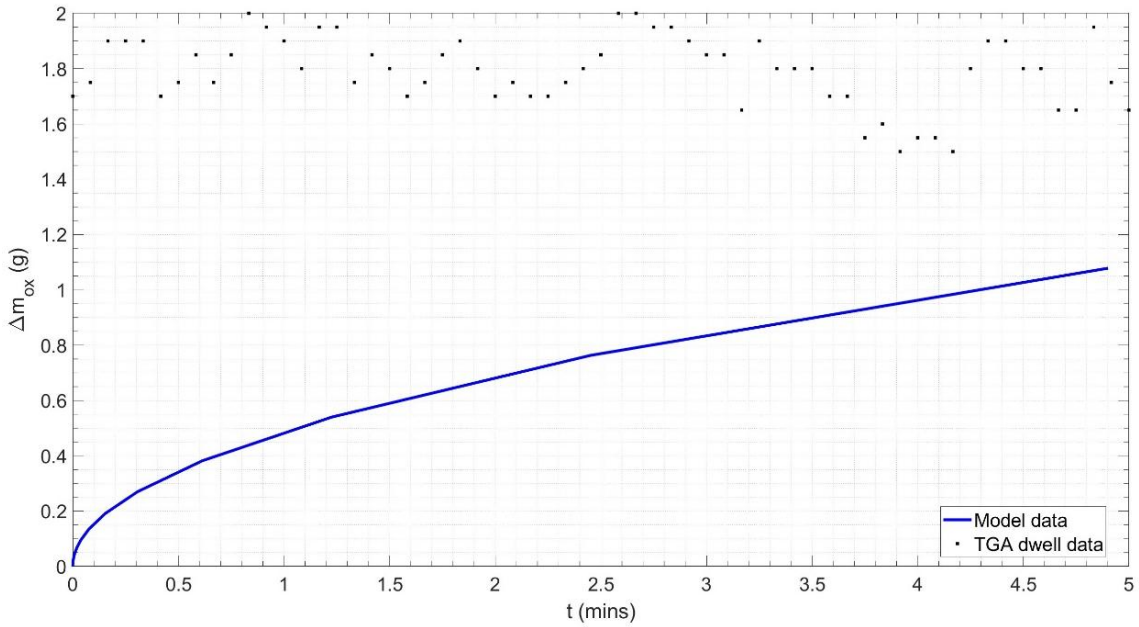


Figure 4.48: Oxide mass gain, Δm_{ox}, observed during model simulation and thermogravimetric dwell data for a 15 nominal bore (n.b.) tube during a normalisation heat treatment cycle at 1000°C for a time, t, of 5 mins ¤.

However, once the challenges associated with sample vibration have been mitigated during the experiment and/or post-processing, overall, there is very good agreement between the model and experimental datasets. For the same sample geometry, 21.3mm outer diameter and 3.2mm wall thickness, and isothermal conditions, 1000°C for 5 mins, the oxide mass gain predicted by the model was 1.52g, whilst the sample in the experiment gained 1.60g of oxide, a difference of only 5%. The mass-based parabolic rate coefficient, k_p, for the model and experiment was 1.6752×10^{-5} $g^2.cm^{-4}.s^{-1}$ and 2.0435×10^{-6} $g^2.cm^{-4}.s^{-1}$, with the experiment exhibiting oxidation at only 12% of the rate of the model. However, the difference will be partially due to the idealised parabolic equation used to define the model, and in greater part due to the severe fluctuation in mass gain observed during the isothermal period of TGA testing. Figure 4.49 shows how k_p maintains a stable value of 1.4133×10^{-5} $g^2.cm^{-4}.s^{-1}$ as oxidation proceeds during normalisation, after a short initial period of rapid decrease due to the parabolic nature of the oxide growth. However, k_p fluctuates across a range of 3.6596×10^{-6} $g^2.cm^{-4}.s^{-1}$ during the isothermal period of the TGA ('Experimental') test. The mean of the instantaneous k_p value reflects this at 5.2234×10^{-5} $g^2.cm^{-4}.s^{-1}$ and 1.5209×10^{-6} $g^2.cm^{-4}.s^{-1}$ for the experiment and model respectively. The difference in scaling between the experimental and model parabolic rate coefficient values serves as further evidence of the issue of double pendulum motion and forced vibration in the thermogravimetric furnace set-up. Hence, the discrepancy is therefore a product of the experimental challenges previously discussed rather than issues with the model.

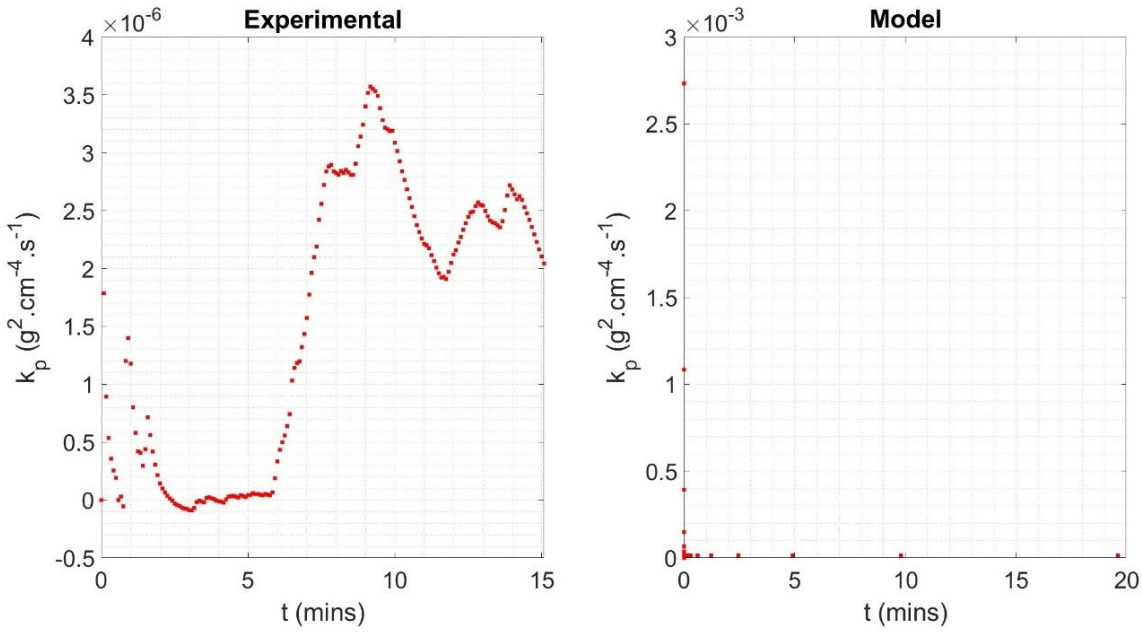


Figure 4.49: Instantaneous mass-based parabolic rate coefficient, Δm_{ox}, plotted against time, t, for the isothermal period of thermogravimetric ('Experimental') testing (*left*) and model (*right*) data, which lasts approximately 15 minutes ¤.

The resonant frequency associated with VIV, f_{force} =1.12mHz, was used to improve the agreement between the experimental and computational oxide mass gain by its pointwise subtraction from the frequency-series experimental oxide mass gain dataset. The resulting resonance-suppressed data was returned to its time-series form via an inverse Fourier transform (see Equation 4.14) and processed in the same way as the original data. Figure 4.50 shows the improved agreement between computational and experimental data, with an improving agreement with time. This is supported by the evidence of a stable instantaneous value of mass-based parabolic rate coefficient of 2.5×10^{-6} $g^2.cm^{-4}.s^{-1}$ after normalisation (t = 5mins) in Figure 4.51. Figure 4.51 also highlights how the parabolic rate coefficient numerical scales become better aligned, with the exception of approximately 10 points around one minute into experimental testing due to random sample movement, once the double pendulum and forced vibration motion have been mitigated using a Fast Fourier transform to remove resonant frequencies. However, the persistent difference in the test time (15 mins for the experimental data, 20 mins for the model data) is due to the difficulty in pinpointing the end of the isothermal heating period in the thermogravimetric data, due to the forced vibration and resultant noise discussed.

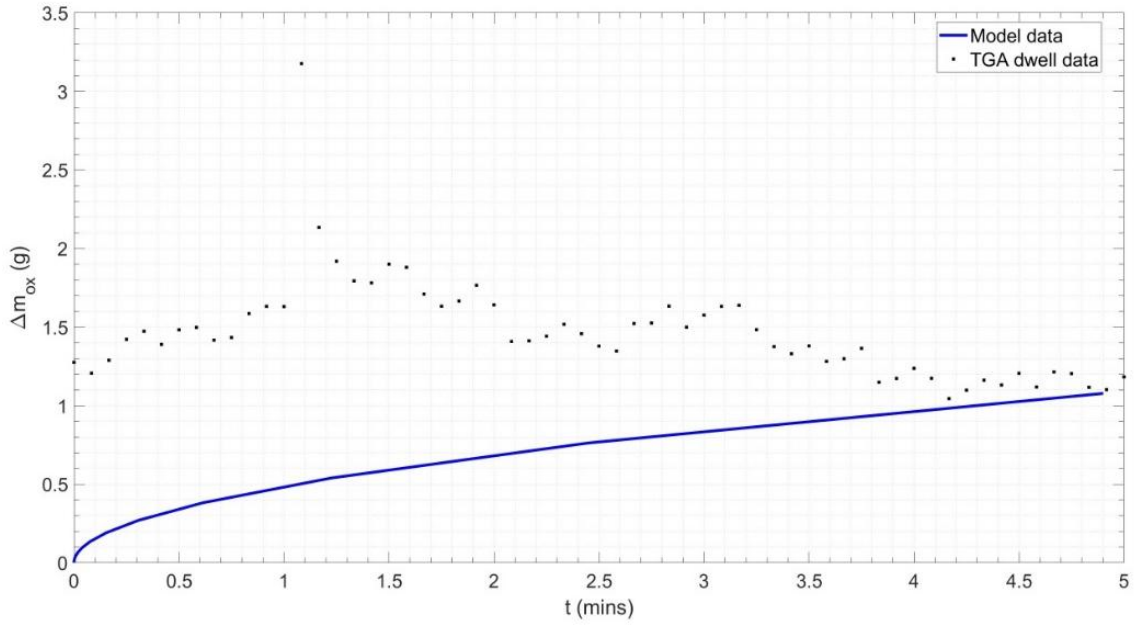


Figure 4.50: Oxide mass gain, Δm_{ox}, observed during model simulation and thermogravimetric (TGA) dwell data for a 15 nominal bore (n.b.) tube during a normalisation heat treatment cycle at 1000°C for a time, t, of 5 mins. The TGA dwell data has gone through Fourier transform operations to suppress resonance caused by vortex induced vibration ¤.

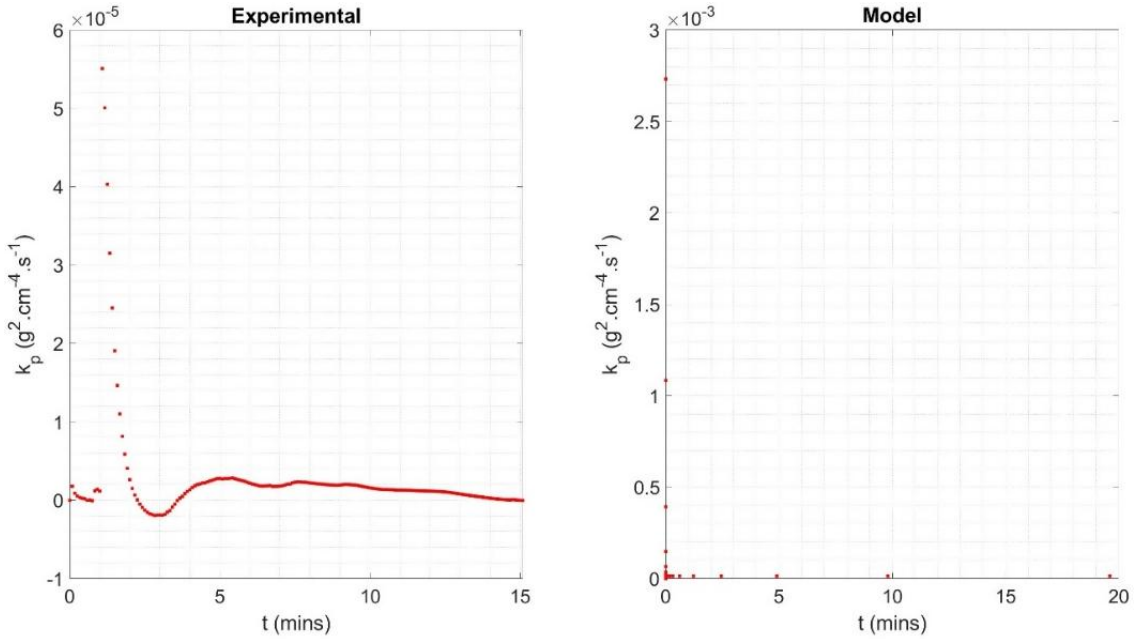


Figure 4.51: Instantaneous mass-based parabolic rate coefficient, $k_{p,mass}$, plotted against time, t, for the isothermal period of thermogravimetric ('Experimental') testing (*left*) and model (*right*) data, which lasts approximately 15 minutes. The experimental data has gone through Fourier transform operations to suppress resonance caused by vortex induced vibration ¤.

As there is most discrepancy between the computational and experimental data in the first two minutes of isothermal heating, this indicates some residual instability from the thermally induced free vibration observed in the heating period. This project is most concerned with the isothermal period associated with normalisation and therefore addresses mitigation strategies for VIV. However, separate considerations for the specific physical

features of thermal buoyancy-induced free vibration could be addressed in further work. Additionally, oxide mass gain data from computational and experimental simulation of longer industrial heat treatments, e.g. hot mill reheating as discussed in Section 1.6.1, could be an opportunity to investigate whether the improved agreement is sustained as oxidation proceeds further at a constant soak temperature.

Comparison with Industrial Samples

Figure 4.53 and Figure 4.54 highlight the thicker, porous, multiphase oxide present on the experimentally grown sample compared to both the industrial and model samples. The mean oxide thickness was measured at 382.6±63.5µm using the same methodology of the average of three measurements at three different locations (A, B, and C) (see Figure 4.52), as for the samples in Section 4.2.1 (see Appendix 8).

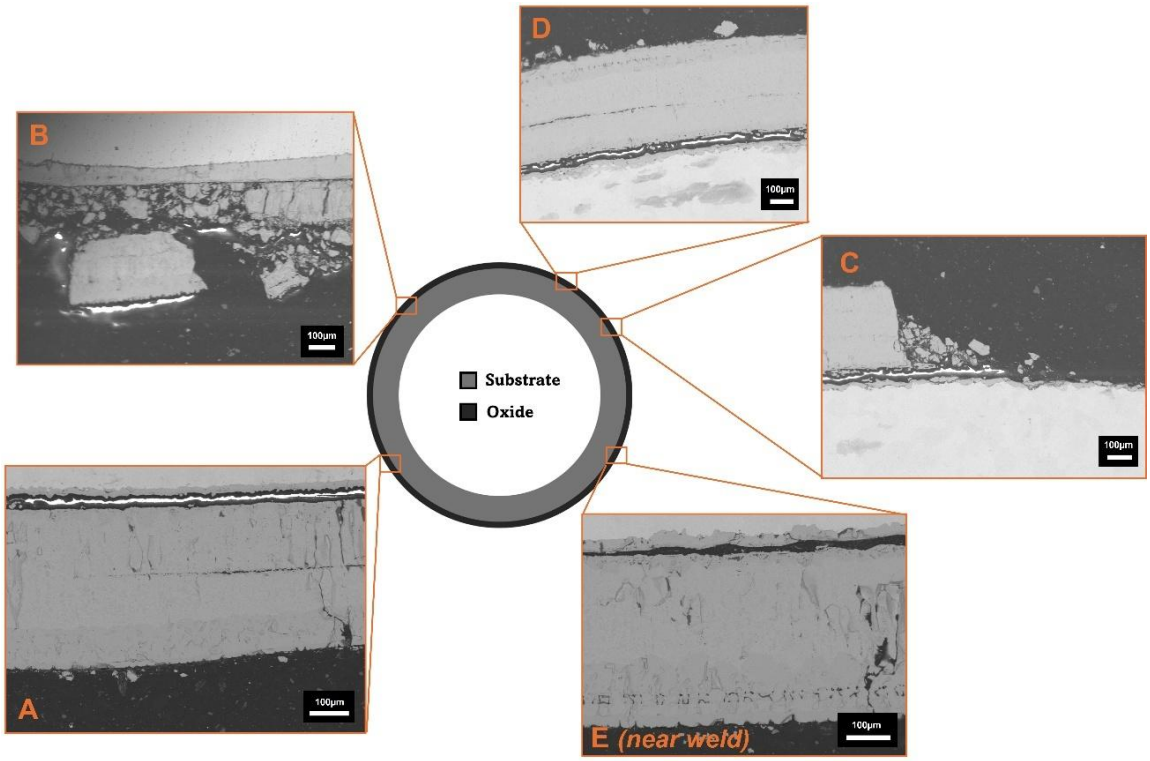


Figure 4.52: Schematic of three locations used to take mean measurements of oxide thickness for a 15 nominal bore (n.b.) tube having undergone normalisation at 1000°C for 15 mins in a thermogravimetric furnace ¤.

In the isothermal soak time of 15 mins, 224µm of oxide is formed according to the model, which falls short of the lower limit, 397µm, of the mean oxide thickness measured using optical microscopy on a Zeiss Primotech. Although the model underpredicts the oxide thickness gain, it neglects the total time which the sample spent at a temperature where parabolic oxidation starts (2hrs 15 mins at 700°C [34]). For the same conditions the model predicts an oxide thickness of 671µm but the model is isothermal and therefore predicts this

thickness for a sample soaked at 1000°C and is an overestimate. Thus, the same problem arises in attempting to use the model to predict the scale thickness formed at a lower temperature, to use as an offset value, since temperature is continually increasing so a soak time will always be an overestimate and measuring the oxide gain at the intervals created by the sampling rate (0.2Hz) would be inefficient in terms of the total length of the treatment (~11 hrs including heating, soaking, and cooling). Furthermore, below the austenisation temperature, the model command lines and databases would need to be revised to reflect the formation of ferrite [10] and different oxide phase morphologies [22]. Although Chen et al. noted that the exothermic nature of oxidation creates the potential for an overtemperature effect [34], which the model does not account for, this is most often in the case of small samples and limited equipment capability to conduct heat away from the sample. The furnace work tube has an internal diameter of 90mm therefore for a 15 n.b. sample with an OD of 21.3mm, there should be sufficient clearance of over 30mm either side of the sample to allow heat to be lost by thermal conduction. The oxide thickness gain observed in the sample lies almost equidistant between the under- and overprediction scenarios tested for the model. The mean of the values predicted is 447µm (compared to 401±4µm measured on the TGA sample).

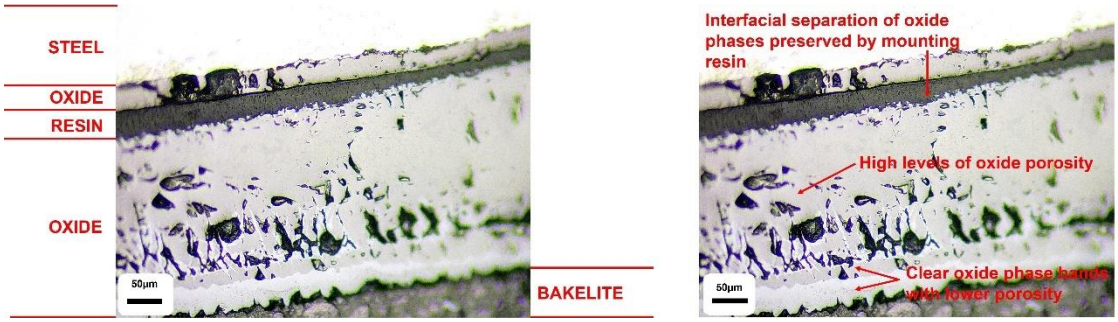


Figure 4.53: Optical microscopy inspection of oxide formed on outer edge of 15 nominal bore (n.b.) conveyance tube sample oxidised in a thermogravimetric furnace at 1000°C for 15 mins. The left image highlights the phase regions whilst the right image highlights particular features related to oxide morphology and spalling risk ¤.

Although without continuous data the experimental and industrial samples are not comparable due to the difference in soak time, the model demonstrates its advantage in flexibility and continuous data prediction and suggests a mass gain of ~7.5g for the same thermal cycle as experienced by the experimental sample (which gained 2.0g based on pre- and post-test weight measurement). Model overprediction is likely multi-factorial owing to the absence of an adequate technique to include porosity in the model, except via diffusion coefficient modification (see Section 3.2.3), as well the effect of stress in both the oxide and substrate, which is discussed in more detail in this and subsequent chapters. Furthermore,

where the mass balance is not integrated into the TGA apparatus, there is always significant risk of material loss during sample transfer, especially given the brittle nature of the oxide evolved on conveyance tube steel grades [106, 188, 410, 411].

Arguably, the most significant factor is the surface condition of the sample pre-oxidation. Laboratory-based oxidation studies tend to prepare samples to a minimal level of surface roughness, using either 1200 or 2400 grit size grinding paper [5, 134, 143, 172]. However, as was discussed in Section 1.4, increased surface roughness can contribute to thicker scale, particularly in reference to its effect on external gas flow dynamics [177] and the stress state of the substrate and oxide where surface asperities promote imperfect adhesion and greater opportunity for oxygen penetration to unoxidised surfaces [64, 123].

Humidity can have a similar effect on oxide kinetics and adhesion (see Section 1.6.1) via exposure of unoxidised surfaces [66, 388]. It has been shown that the adherence of scale to steel is improved and parabolic oxidation rate is increased significantly even when moving from dry to ambient air (1-2% water vapour) [59]. Scale in dry air was far more likely to separate from the substrate since water vapour can increase scale plasticity and creep [66, 128].

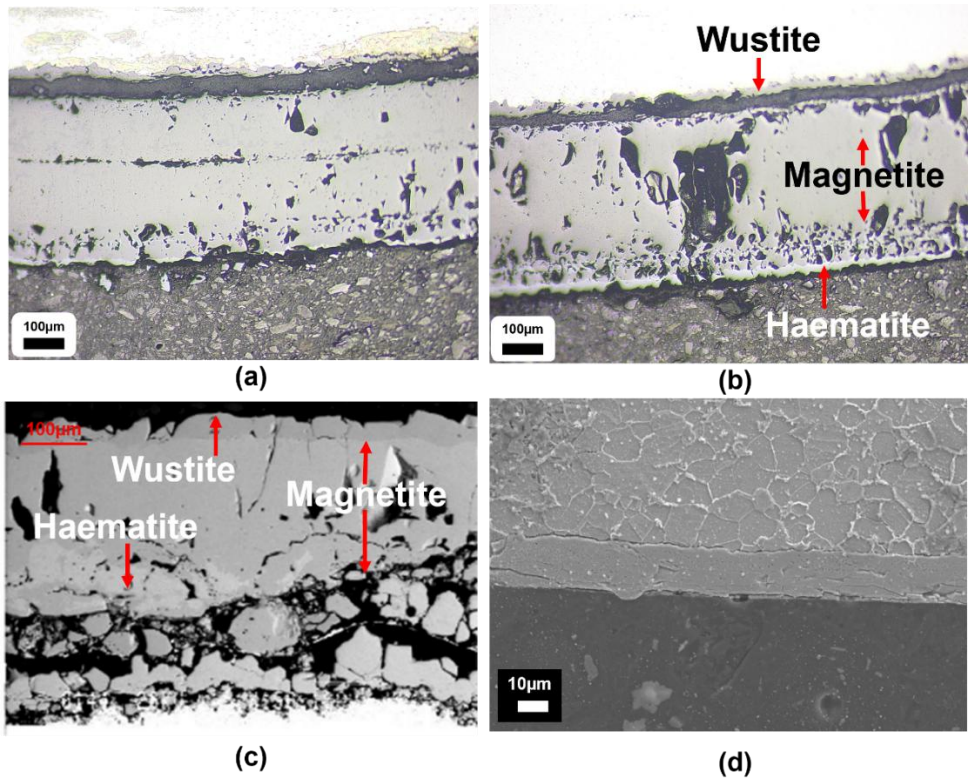


Figure 4.54: Light microscopy images of the outer edge of a 15 n.b. sample heated for 3 hrs in the TGA furnace, revealing (a) a thick, porous oxide of 401.0±4.3µm with ¤ (b) clear phases (wüstite, magnetite, haematite) in the ratio observed ¤ in (c) literature example with thickness 124±32µm [60]. Equivalent industrial samples viewed via FEGSEM reveal a (d) much thinner, compact, homogeneous oxide of 15.8±0.7µm ¤. In this case, the wüstite,

magnetite, and haematite phases (present at $\boldsymbol{T} > 833K$) are denoted as 3, 1, and 2, respectively to match Wilkstrom et al. [60].

Although the thicker nature of the oxide grown in the TGA experiments, compared to industrial samples, made it easier to measure oxide thickness using optical light microscopy, FEGSEM was also used to more accurately measure oxide thickness (see Figure 10.6 in Appendix 9), as well as assess any microstructural damage to the oxide. The average oxide thickness measured was 401±4μm, based on measurements taken at locations A and D, which displayed intact, adhered oxide. This value lies within the uncertainty bounds of the less accurate optical light microscopy average oxide thickness measurement of 383±64μm. Locations B, C, and E were excluded from average oxide thickness calculations due to the extensive damage to the oxide found at that location and its surrounding area, with approximately 75% in a spalled state. The use of the backscatter electron detector (BED) within FEGSEM allows oxide phases to be detected based on atomic weight differences. The heavier iron element, with its larger nucleus, will induce greater electron scatter, emitting more backscattered electrons and generating a brighter image [275]. For example, magnetite, Fe_3O_4, has a higher Fe:O ratio, i.e. a greater contribution of the heavier Fe atoms, and will appear brighter than haematite, Fe_2O_3, both of which are typically adjacent phases in the multi-phase scales observed on low carbon steel during conveyance tube manufacturing [9, 15, 70, 71, 74]. The different oxide phases observed showed varying porosity levels and interfacial boundaries (see Figure 4.55). Porosity differences in the scale, considering only kinetics as discussed in Section 1.3.1, are evidence of the difference in dominant ion transport mechanism (discussed in Section 1.3). The difference in diffusion rate of cations vs. anions, in wüstite and magnetite, can lead to a higher concentration of defects at the wüstite-magnetite phase interface, as shown in Figure 4.55. The outer layers of magnetite and haematite formed on low carbon steel can exhibit large pores associated with outward cation diffusion [75, 77]. Crucially, the oxide phases closest to the oxide-air boundary displayed evidence of delamination and the lowest interfacial strength and cohesion, whereas the innermost phase, 81±9μm. remained adhered to the steel, suggesting high metal-oxide interfacial strength and adhesion. The latter state was similar to that seen in an as-received industrial sample which had a compact, homogeneous oxide of 16±0.7μm.

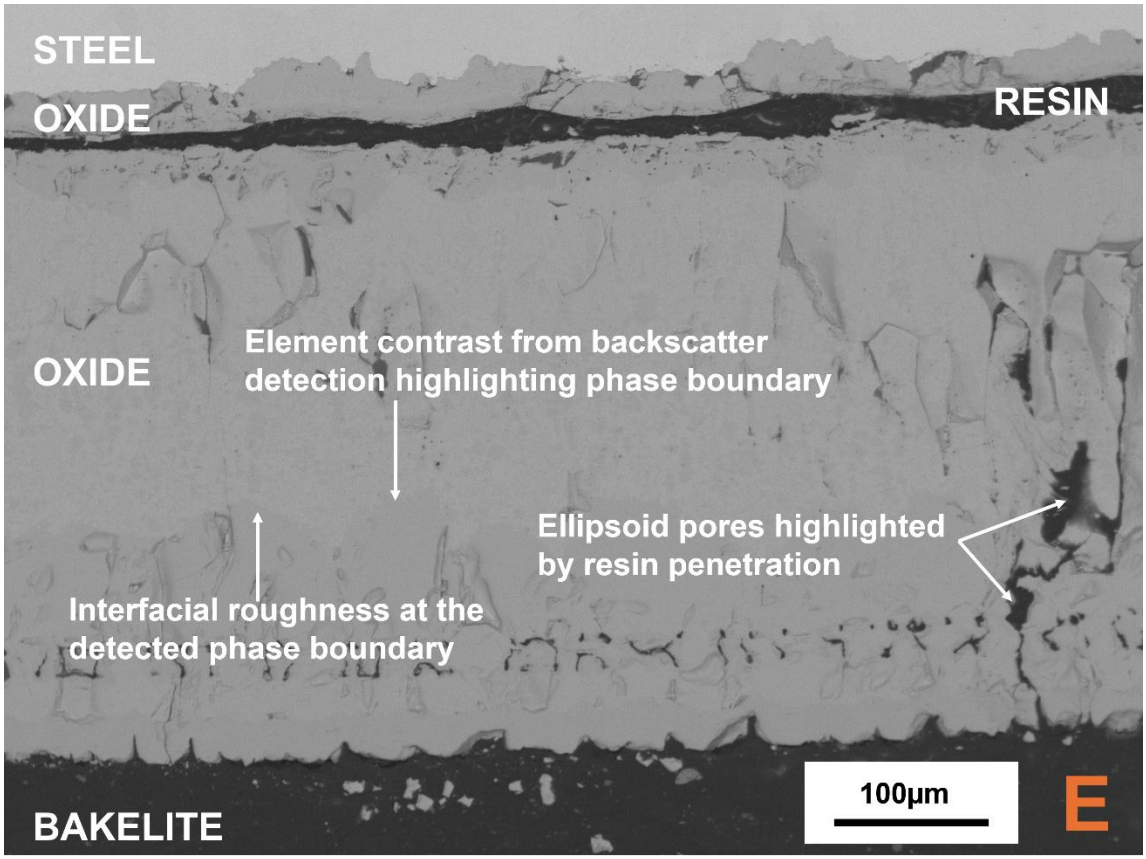


Figure 4.55: Annotated field emission gun electron micrograph, obtained via the backscatter electron detector (BED), from location E showing evidence of porosity, phase boundaries in the oxide, and interfacial roughness at some phase boundaries ¤.

Notably, the damage at location B (see Figure 4.56) highlights how the higher porosity, thicker, outer oxide layers delaminated along an oxide phase boundary, indicating lower interfacial strength and cohesion, whilst the most compact, thinner, innermost layers remains adhered to the steel, suggesting high metal-oxide interfacial strength and adhesion. It is argued that in industry this phenomenon could be attributed to the descaling process performed at the end of the tube manufacturing routine, i.e. there is no opportunity for secondary scale formation, explaining the much thinner, more compact scale observed on industrial samples. Metallographic preparation appears to replicate this effect as it is analogous to the combination of thermal (hot mounting-induced), depositional compressive (oxidation), and impact (abrasive particles and lubricant) stress applied during descaling [66]. Hydraulic descaling is associated with a significant reduction in substrate grain size [53]. Smaller grains are associated with a greater number of grain boundaries and at higher temperatures, grain boundary diffusion, $\boldsymbol{D_{gb}}$, is favoured as a high diffusivity pathway (as discussed in Section 3.2.3). However, although grain boundary diffusion was incorporated into the Thermo-Calc© model, via a modified diffusion coefficient, in Section 3.2.3, the thicker oxide formed during the associated accelerated diffusion will eventually be inhibited

by the passive external layer of oxide formed which acts as a barrier to inward oxygen diffusion [78]. As previously discussed, changes to oxygen diffusion will affect phase morphology so scale growth accelerated by a greater degree of grain boundary diffusion will be more likely to be dominated by wüstite, where limited exposure to air is quickly achieved by the passive layer described [24]. Furthermore, the prevalence of wüstite post-descaling supports the choice of initial conditions of the thin wüstite layer within the Thermo-Calc© model as any pre-normalisation scale formed which is not removed by pre-normalisation mechanical damage during interaction with tooling, rather than descaling operations which do not take place pre-normalisation, can be assumed to be wüstite based for the same reasons.

However, the persistent evidence of scale present on the industrial samples, which has been exposed to a far greater level of mechanical damage, highlights the scale of the issue. It is clear that the inconsistent surface condition on conveyance tubes, discussed in Section 1.2, associated with the degree of oxide spalling arises from an oversimplification of the scale to a single body which can also be mechanically removed as a single body. In reality, the multi-phase nature of the scale is more accurately represented as multiple bodies whose adhesive and cohesive properties vary in the same way as their intrinsic mechanical properties [22]. Several authors have alluded to the importance of the interaction of phase transformations and descaling processes but were limited to planar samples, with the exception of Jiang et al. [23], and focused on other aspects of oxidation such as mechanical response [118], heat transfer behaviour [15, 23], and microstructural characterisation [260].

However, since the model is limited to a single moving phase, and the biggest challenge arguably arises from the adhered inner layer which is resistant to hydraulic descaling, further uses of the model with respect to stress analysis will be limited to a compact layer of homogeneous oxide. It is still valid to assume that this homogeneous phase will be wüstite as this is typically found closest to the metal-oxide reaction interface as it has the lowest oxygen content of the three phases typically detected in oxide formed on low carbon steel (see Section 1.3.1). The oxide will therefore be assumed to have already been exposed to descaling-related stresses, as described by Basabe and Szpunar [66], during stress analysis, rather than add further complexification. Furthermore, as discussed in Section 1.6.1.2, silicon (Si) strongly influences carbon steel oxidation behaviour as an element liable to segregate towards the scale-metal interface at the temperatures of interest to form diffusion-inhibiting fayalite (Fe_2SiO_4) [60, 77, 133, 134]. Although steel-scale adhesion is lower on Si

steels than on pure iron, the silica and/or fayalite (Fe_2SiO_4) to substrate adhesion is stronger and introduces descaling challenges [169]. Wilkstrom et al. [60] described how, at high reheat temperatures, the low thermal gradient evolved between the slab and atmosphere means a fast exothermic fayalite reaction initiates and the development of significant latent heat and poor heat transfer conditions melts the fayalite and Fe-O systems, causing enhanced diffusion which generates further heat. The application of this observation was highlighted in Wassilkowska et al.'s work as the potential to improve corrosion resistance by easily mechanically removing the top oxide layer to expose the silicon-rich layer [173]. Whilst this well-adhered layer is advantageous in experimental contexts and when attempting to preserve the protective passivating oxide on the inner surface of tubes (which is beyond the scope of this work), it also promotes the incomplete descaling and outlines a key issue for the external tube surface during conveyance tube manufacturing. Krzyzanowski et al. cited quantification of interfacial separation stress as a key area for further work, where silicon content is clearly important [77]. Furthermore, this evidence of the non-negligible effect of thermomechanical operations during conveyance tube manufacturing, such as hydraulic descaling, supports the hypothesis made in Section 1.6.1 about Grant's work where negligible silicon was detected in oxide scale formed on industrial and laboratory samples of E41 [9] where it was suggested that an incomplete insight into oxide kinetics and morphology would occur without incorporation of representative industrial thermomechanical conditions.

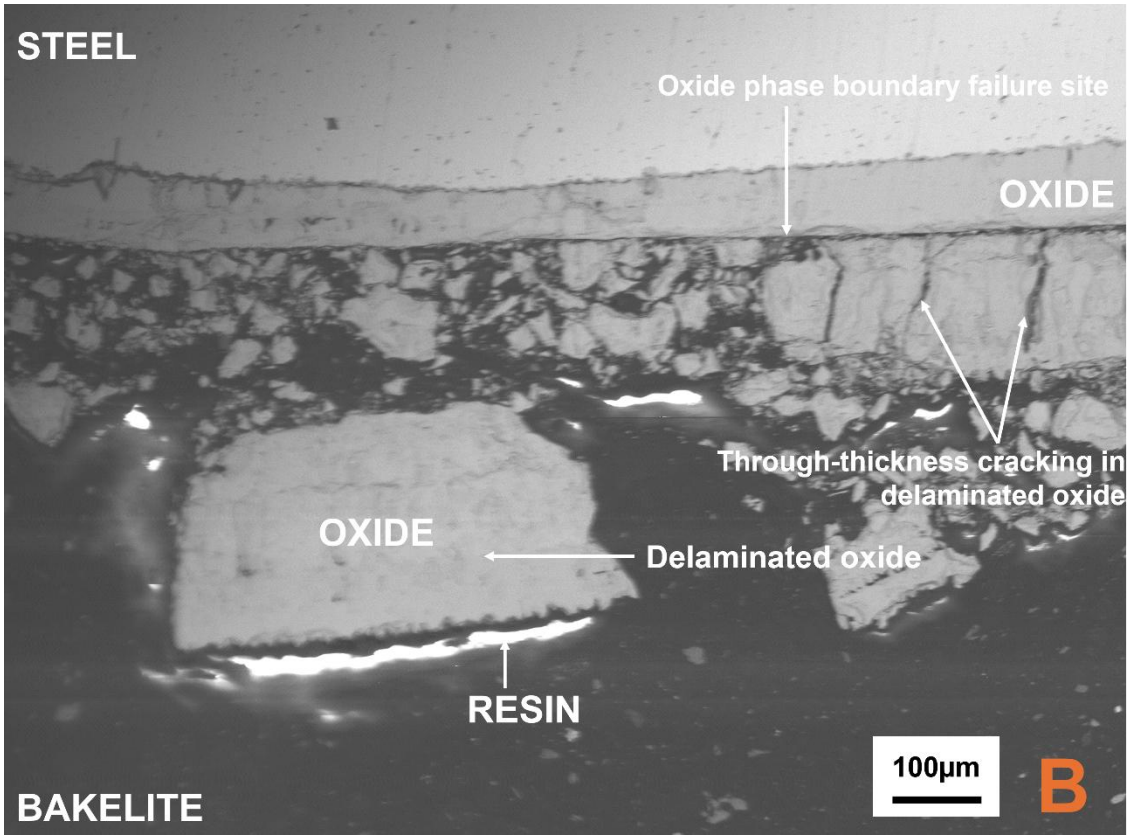


Figure 4.56: Annotated field emission gun electron micrograph, obtained via the backscatter electron detector (BED), from location B showing evidence of through-thickness cracking and interfacial failure ¤.

In the case of interfacial oxide phase failure, the use of cold-setting resin to seal the oxide in its post-TGA test state prior to metallographic preparation is advantageous in distinguishing between thermomechanical and sample preparation-related damage. For example, in Figure 4.55 and Figure 4.56 the resin has preserved the interfacial separation of the thinner inner and thicker outer oxide phases. The gap present can then be locked in place by the hot mount resin. This is further reinforced by Figure 4.57 where there was a gap in coverage of the oxide by the cold-setting resin. The abrupt end in the thick oxide layer followed by a very thin layer highlights the importance of selecting the appropriate mounting technique, as well as supporting conclusions about the effect of descaling on oxide thickness and microstructural topography in laboratory vs. industrial settings.

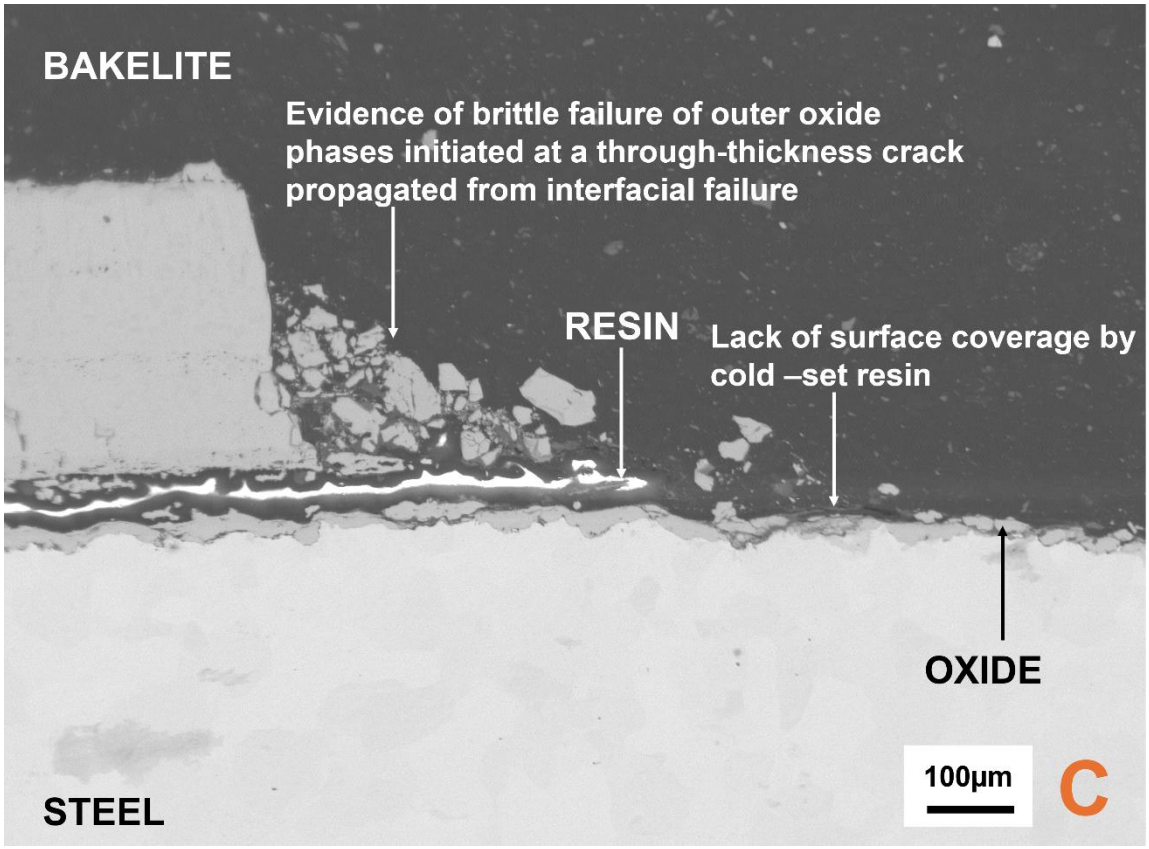


Figure 4.57: Annotated field emission gun electron micrograph, obtained via the backscatter electron detector (BED), from location C showing evidence of interfacial failure-initiated through-thickness cracking in the absence of sufficient cold-set resin coverage. The thinner compact layer of homogeneous oxide remains intact and adhered ¤.

The use of the BED again highlights how the spalled scale is an oxide phase duplex and emphasises why the scale observed on industrial samples, in contrast with traditional scale growth kinetics (see Section 1.3.1), presents as homogeneous. Furthermore, the literature highlights how the outermost oxide phase has the highest tensile strength value [22], but the dominance of interfacial failure highlights how the adhesion and cohesion of the oxide (and steel) is more important for oxide damage during tube manufacture than intrinsic mechanical properties. Furthermore, there appears to be much higher levels of interfacial roughness for the two outermost oxide which are ultimately spalled. This has also been shown to negatively affect both kinetic and adhesion behaviour [22, 64, 65]. However, it should be noted that, as discussed in Section 1.4, failure mode is temperature-dependent and mechanical properties may be more important for oxides formed at lower temperatures [77]. The challenge of porosity has already been discussed in this work, in particular how pores become larger and non-uniformly distributed as the oxide grows on a curved geometry and the outermost oxide moves further from the metal-oxide reaction interface, thus making the model, which cannot account for porosity in a meaningful way (see Section 3.2.3), less

accurate [85]. The pores in Figure 4.55 are highlighted by infiltration with the cold-set resin and agree with the trend proposed by Entchev et al. [85]. Furthermore, much of the microstructural and microtextural properties of the laboratory-grown scale, e.g. ridges, roughness, through-thickness, interfacial cracking, and severe spalling, are typical of laboratory scale formed in air, i.e. heating atmosphere has been shown to be important [24, 69, 118]. Wang et al. highlighted that electrochemically grown oxides, i.e. oxides with limited exposure to air, are far more likely to be compact, homogeneous, uniform, and intact [24]. Hence, the oxide of the same description found in industrial samples can only have grown with limited access to air caused by existing layers of oxide above its outer surface. This further supports the idea that descaling causes delamination as opposed to any spalling during the oxidation reaction itself, since then the outer layers of oxide on the industrial sample would begin to show characteristics of air-based oxidation. Multiple authors have highlighted that poor scale adhesion is ultimately a combination of kinetic and mechanical phenomena (see Section 1.3.1 and Section 1.4) and the kinetic phenomena which propagate circular pore formation are deformed to ellipsoids (observed in Figure 4.55) under compressive thermal and growth stress [24, 120]. However, it could be argued that the excellent mass gain agreement between the model and TGA sample is skewed by the presence of significant porosity in the majority of oxide thickness formed on the TGA sample. For example, estimations of porosity in wüstite vary between 10-44% [81, 128, 412, 413] therefore in the worst case scenario the volume of oxide, and subsequently calculated density, could be almost half that expected (see Equation 3.32). Therefore, mass change is reduced compared to if it were fully compact.

4.3 Conclusions from Chapter 4

The model for oxidation kinetics on a planar geometry has been extended to a cylindrical geometry and applied to tube dimensions consistent with the smallest conveyance tubes manufactured by TSUK Tubes. A parametric study demonstrated the influence of wall thickness and tube radius (surface curvature) on oxidation rate via changes to diffusion path length but also how the 2D nature of the model (due to the assumed rotational symmetry) means that, in isolation, it cannot capture the effect of outer diameter changes on surface area. Conversion of the model's oxide thickness data to mass gain data via calculation of volume change captures the effect of changes to outer diameter on the surface area to volume ratio and subsequently oxidation kinetics. The model oxide thickness data can be converted to mass gain data via a volume gain calculation. The mass gain data can be used to evaluate the change in tube outer diameter and therefore to extract the kinetics of the oxidation process. However, this effect has been shown to be limited to tubes with inner radii of less than 200mm. Beyond this critical value, the scale of diffusion is small enough to render the effect of the radial coordinate in the diffusion negligible, and the solution approaches that of a planar geometry. Hence, although the cylindrical geometry model is valid, a simpler planar geometry will accurately capture oxidation of tubes with an inner radius of more than 200mm. Hence, the oxidation kinetics model offers a novel route for insight into the effect of geometry on diffusion phenomena at the micro-scale and therefore oxidation kinetics at the macro-scale, with a transferrable application to industrial scenarios such as conveyance tube manufacturing.

Thermogravimetric analyses of the oxide formed on conveyance tubes under normalisation conditions revealed good agreement (±5%) between the model and experimental results, which was supported by microstructural imaging. However, this aspect of the work also further highlighted the challenges associated with experimental investigations of oxide on cylindrical geometries, e.g. damage during sample mounting and metallographic preparation and flow-induced vibration during heating. The latter effect was quantified using a refractory dummy sample. The computational approach, though a simplification of complex real conditions, offers an alternative approach without these issues and has scope to be refined to better reflect specific complexities, e.g. transient heating, in future work. This point was reinforced by a key finding that the 25-fold difference in average oxide thickness observed on laboratory formed compared to industrial oxides is defined by the presence of interfacial failure at oxide phase boundaries, induced by metallographic preparation or

hydraulic descaling processes respectively. The model currently considers a homogeneous oxide phase and cannot predict relative thicknesses of phases within multiplex scales. Each interface would have to be modelled using separate moving phase boundary domains to provide more accurate predictions. Porosity was also shown to be influential when comparing model and experimental oxide gain outputs, depending on the variable measured, i.e. mass vs. thickness gain, and a more effective method than modified diffusion coefficient is needed to reflect this influence. However, where consideration is only given to the challenges associated with the ~20μm adhered, intact, compact, homogeneous scale observed in industrial samples, the thickness predicted by the model is valid for a descaled surface. Therefore, the model describes the industrial conditions of conveyance tube manufacturing to a sufficiently accurate extent. However, the key advantage of the model, its ability to provide continuous data efficiently, still stands as conclusions about the oxide microstructural and microtextural properties only apply for the oxide formed after-the-fact in experimental scenarios. However, the model has also been shown to aid understanding of microstructural development during heat treatment.

Chapter 5 Mechanical Modelling of Oxide Scale Stability

A key challenge identified in Chapter 4 for oxide scale is the inconsistent and unpredictable spalling of the external surface oxide [24, 29, 102]. This issue is amplified for conveyance tubes, and other non-planar geometry components, due to their enhanced stress state [82, 85, 414]. Analytical models for oxidation- and heat treatment-related stress partially depend on oxide thickness, which is usually measured experimentally during post-processing [9]. Consequently, only the final residual stress state can be evaluated and the dynamic nature of the stress state associated with a continuously growing oxide is lost, with the exception of continuous thermogravimetric data [72], which is not without its challenges as discussed in the previous chapter. Furthermore, experimental techniques with high-temperature capabilities are often limited in their temperature and/or sample dimensional range [415]. The model developed in the Chapter 3 and Chapter 4 offers continuous oxide thickness predictions which can contribute to evaluation not only of the oxide stress state after normalisation, but also at dwell temperature [178]. During this chapter, approaches for mechanical analysis of an external oxide are explored to assess the stress state of the scale, in preparation for application with a failure diagram, as well the potential contribution of oxide thickness data. Stress analysis is supported by novel uses of experimental and computational techniques for determining oxide material properties, including nanoindentation and molecular dynamics simulations, and residual stress state is validated on real conveyance tube samples using X-ray diffraction. The region of the research flowchart (Figure 1.33) under discussion in this chapter is shown in Figure 5.1.

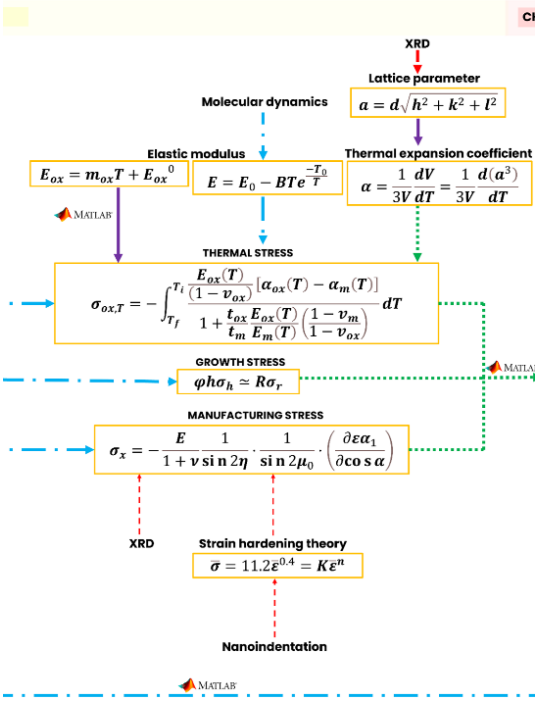


Figure 5.1: Region of the overall research flowchart (see Figure 1.33) which is under discussion in this chapter.

5.1 Application to Analytical Models

5.1.1 Thermal Stress in the Oxide

A key observation by Huntz and Schütze highlights that determination of residual stress at room temperature does not provide much information about the stress state of the system at oxidation temperature [416]. Furthermore, they highlighted the need to distinguish between evolved growth, $\boldsymbol{\sigma_{ox,g}}$, and thermal, $\boldsymbol{\sigma_{ox,T}}$, stresses, which are often dealt with separately (see Section 1.4). This is important as they argue that experimental data reveals that stresses generated by oxidation are dominated by thermal stress (see Equation 5.1) and the majority of spalling occurs during cooling, as well as stress relaxation via microcracking (fast cooling) or creep (slow cooling), although this is not accounted for in Equation 5.1 (where $\boldsymbol{E, \upsilon, \alpha}$, and $\boldsymbol{\delta}$ are the elastic modulus, Poisson ratio, coefficient of thermal expansion, and thickness respectively). elastic modulus and coefficient of thermal expansion are dependent on temperature, $\boldsymbol{T}$, due to increased atomic vibrations and change of lattice parameters with temperature [417]. Furthermore, Samal and Mitra also highlight that any measured stress associated with adhesion analysis is not equivalent to true adhesion stress due to the residual compressive stress in the oxide associated with the thermal expansion differential between the substrate and scale [238]. Including the thermal stress in the

resultant stress state of the oxide is therefore essential to obtain an accurate value. The specific values of each variable used are shown in Table 5.1.

$$\sigma_{ox,T} = -\int_{T_f}^{T_i} \frac{\frac{E_{ox}(T)}{(1-\nu_{ox})}[\alpha_{ox}(T) - \alpha_m(T)]}{1 + \frac{\delta_{ox}}{\delta_m}\frac{E_{ox}(T)}{E_m(T)}\left(\frac{1-\nu_m}{1-\nu_{ox}}\right)} dT$$

Equation 5.1

Table 5.1: Mechanical properties, (elastic modulus, E, Poisson ratio, ν, coefficient of thermal expansion, α) of the steel substrate and wüstite phase oxide scale evolved at ambient (298K) and tube normalisation (1273K) temperatures, T (assuming isobarothermal conditions).

	Wüstite		E41	
T	298	1273	298	1273
E (GPa)	130	83.6	200	120
ν (-)	0.36 [77]	0.36	0.3 [418]	0.3
α (K^{-1})	17.7 x 10^{-5}	15.0 x 10^{-5}	7.5 x 10^{-6}	21.4 x 10^{-5}

Saeki et al. argue that the elastic modulus for wüstite has a limited dependency on temperature, see Equation 10.2, and high temperature data in the range 973K-1273K (see Appendix 13 for data points) can be described linearly (see Equation 5.6) and extrapolated to lower temperatures if necessary [419]. Saeki et al.'s data were in agreement with measurements and predictions of temperature-dependent elastic modulus made by other authors [420, 421]. However, Picque et al. highlighted that the elastic modulus of the oxide is independent of the steel substrate alloy composition [12].

Temperature-dependent elastic Modulus of Wüstite using Molecular Dynamics

As has already been demonstrated in this project, gaps in critical data can also limit model optimisation and potential function development (see Section 3.2.1). The following section analyses the data output of a novel use of molecular dynamics (MD) [246, 422] to predict elastic modulus of ionic compounds, in an as yet unpublished collaboration with Dr Michael Auinger at the University of Warwick. The author of this thesis wishes to make it clear that the MD simulation was defined and run by Dr Auinger, and the author's contribution was limited to post-processing of the raw computational output data which was used for the mechanical analyses work within this chapter. The theoretical basis of MD is described in Section 2.2.4. The molecular dynamics simulation data used were derived from a supercell geometry of 5x5x5 unit cells (~1000 atoms) for a volume of 2.1x2.1x2.1nm. Interatomic Fe-

O potential data were taken from Byggmastar et al.'s work [243] whose approach centres around the analytical bond order potential (ABOP) formalism. Fe-O elemental interactions, based on existing Fe-Fe and O-O interaction data, although originally derived for covalently bonded materials, are appropriate for metal-oxides [243]. The results of the virtual tensile tests, performed across a temperature range of $200 \leq \boldsymbol{T} \leq 1500$K, are shown in Figure 5.2. The temperature-dependent elastic modulus, $\boldsymbol{E}(\boldsymbol{T})$, of wüstite was calculated from the mean of the stress-strain slope for each point, $\boldsymbol{i}$, observed for each temperature up to the maximum stress value observed, i.e. yield onset. The physically invalid replica stress-strain profiles in the lower temperature tests were not considered (see Figure 5.2).

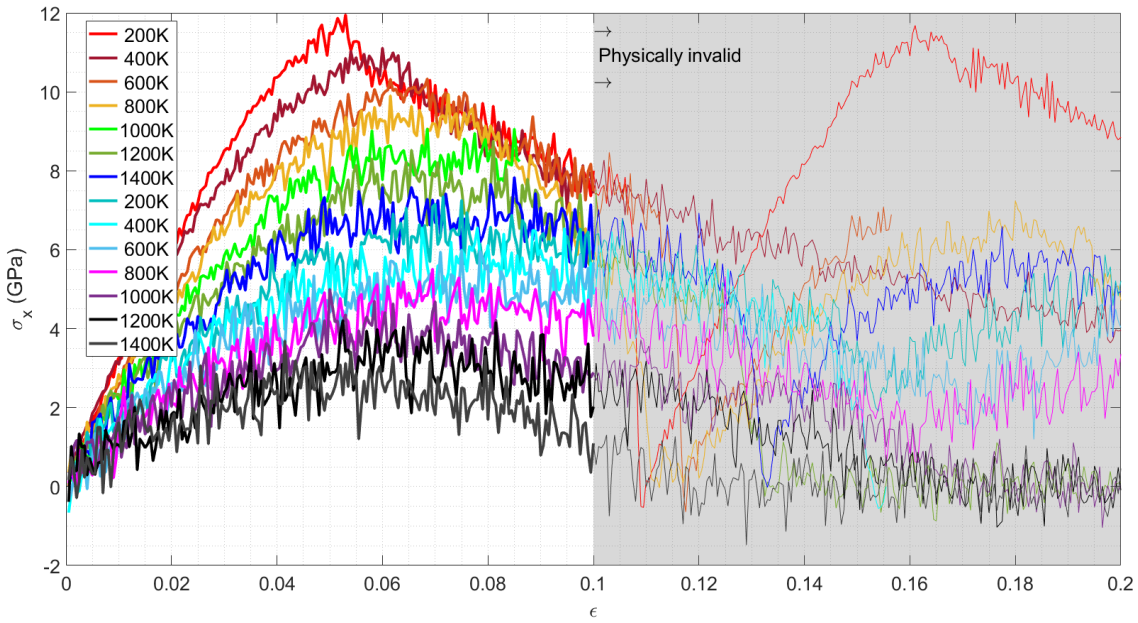


Figure 5.2: Plot of stress, $\boldsymbol{\sigma}$, -strain, $\boldsymbol{\varepsilon}$, data obtained from molecular dynamics (MD) simulation of tensile test of wüstite across a temperature range of $200 \leq \boldsymbol{T} \leq 1500$K. The physically invalid range found at strain greater than 0.1, is excluded from data analyses and denoted by thinner lines and a shaded region ¤.

The results are shown in Figure 5.5and compared to the elastic modulus measured by Saeki et al. in their experimental work using dynamics to determine the elastic modulus of wüstite in the temperature range $973 \leq \boldsymbol{T} \leq 1273$K [419]. It should be noted that the range of interpolation of their data (the shaded region) is far narrower than the temperature range tested in the simulation.

The data had very high noise levels, especially at higher temperatures, attributed to small cell size imposed by computational power efficiency restrictions, and the decision to only run one simulation for each temperature to obtain a useful statistical average. A moving average filter (see Section 3.3.1 for details of this technique), with a window size of 15, was applied to all the tests (see Figure 5.3). With greater computational power resources,

running the same simulation repeatedly and/or using a larger cell could reduce noise and achieve a better statistical average.

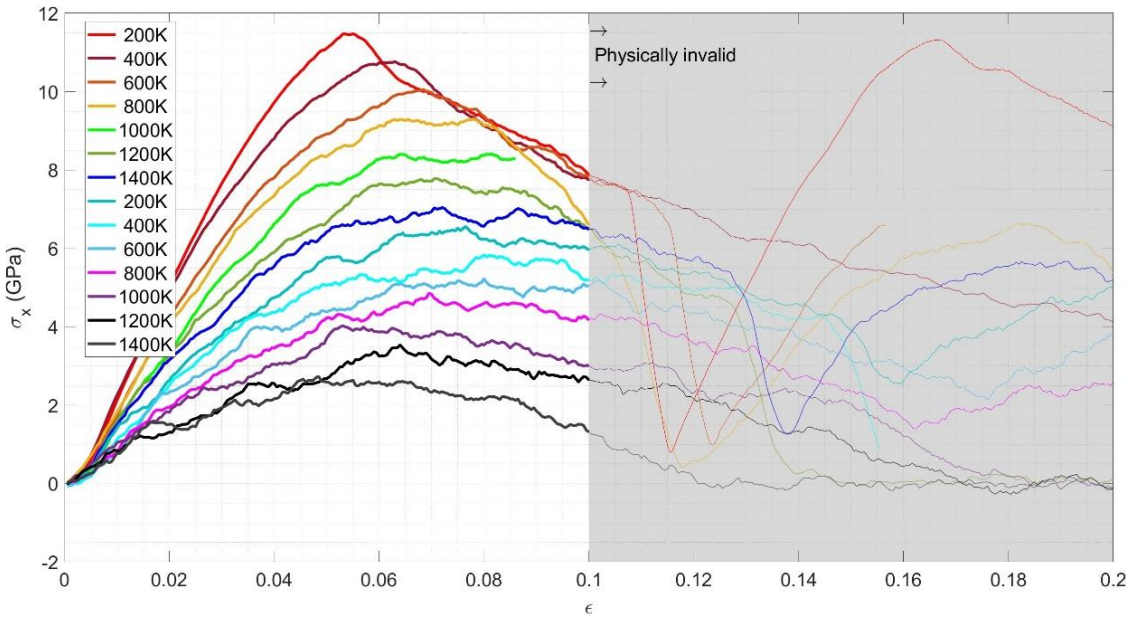


Figure 5.3: Plot of filtered stress, $\boldsymbol{\sigma}$, -strain, $\boldsymbol{\varepsilon}$, data (window size = 15) obtained from molecular dynamics (MD) simulation of tensile test of wüstite across a temperature range of 200 ≤ $\boldsymbol{T}$ ≤1500K ¤.

The window size selected was wide enough to smooth the noise in each dataset, without compromising the overall stress-strain profiles, i.e. linear increase to a maximum stress value at yield followed a decrease in stressed during plastic deformation to failure.

Figure 5.4 and Table 5.2 show how an increase in the moving average filter window size can improve the agreement between the experimental and simulated data up to a window size of 15 (for the relevant temperature range of 600 ≤ $\boldsymbol{T}$ ≤1400K for oxide formation on low carbon steel conveyance tubes), beyond which smoothing eliminates some of the subtleties of the mechanical trends and agreement starts to deteriorate in the high temperature region ($\boldsymbol{T}$ ≥ 1000K). The large standard deviations again emphasise the limitations of a cell size due to computational resource restrictions.

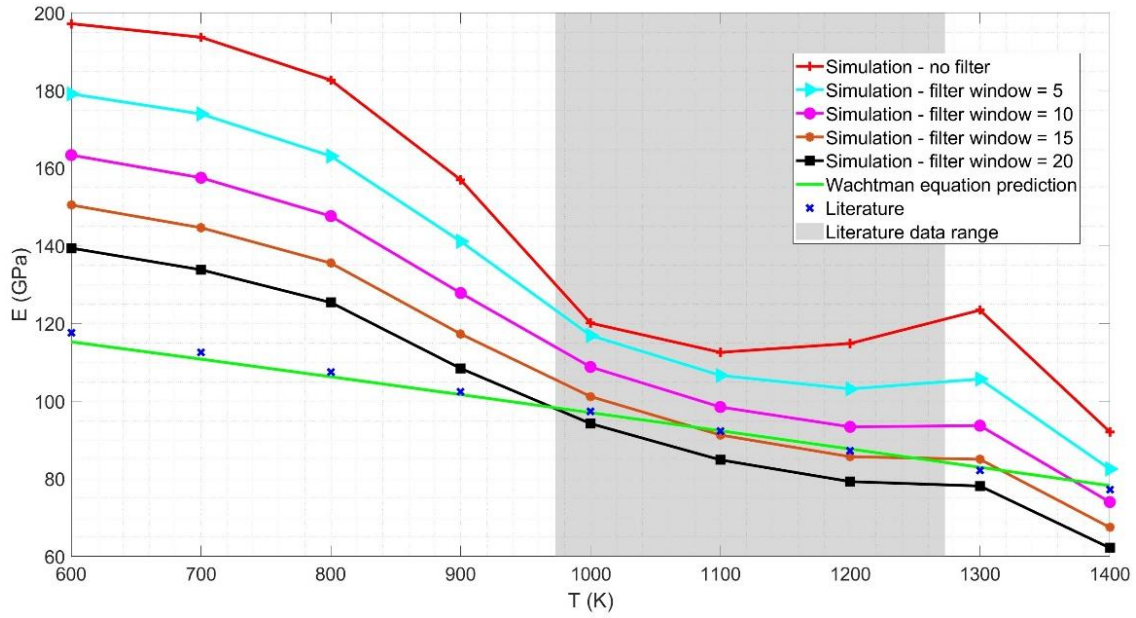


Figure 5.4: Plot of elastic modulus, $\boldsymbol{E}$, as a function of temperature, $\boldsymbol{T}$, based on molecular dynamics (MD) simulation results for 600 ≤ $\boldsymbol{T}$ ≤ 1400K (with no filter, and using a range of filter windows from 5-20) and extrapolated data from the literature [419]. Outside of the literature data range of 973 ≤ $\boldsymbol{T}$ ≤ 1273K (grey shading) the experimental data has been extrapolated using linear regression ¤.

Table 5.2: Mean, $\boldsymbol{\mu}$, and standard deviation, $\boldsymbol{\sigma}$, of difference between simulated and experimental values of elastic modulus, $\overline{\boldsymbol{E_{sim,i}}}$, at temperature, $\boldsymbol{T}$, in different data ranges.

Window	$\boldsymbol{\mu}_{\lvert\overline{E_{sim,i}}-\overline{E_{exp,i}}\rvert} \pm \boldsymbol{\sigma}_{\lvert\overline{E_{sim,i}}-\overline{E_{exp,i}}\rvert}$		
	$200 \leq T \leq 1500$K	$T \leq 1000$K	$T \geq 1000$K
0	31.3 ± 27.2	45.3 ± 27.6	12.6 ± 10.8
5	29.8 ± 26.3	44.3 ± 25.6	10.4 ± 10.0
10	29.0 ± 26.4	43.9 ± 25.0	9.2 ± 10.2
15	28.4 ± 24.9	41.9 ± 24.7	10.5 ± 9.1
20	27.9 ± 23.8	39.8 ± 24.8	12.1 ± 8.9

A key phenomenon evolved by this computational approach is the convergence towards similar stress-strain data at ~0.07 strain during lower temperature tests (200 ≤ $\boldsymbol{T}$ ≤ 500K) before a sudden drop in stress at ~0.0115 strain followed by a replica stress-strain cycle for the remainder of the test. Although conventionally this would indicate material failure, and the separation of atomic planes, the control of the deformation solely along the x-axis accompanied by the model's ability to realign its atoms means tensile testing recommences after the first proposed material failure. In practice, this is physically invalid and should be ignored, i.e. mechanical phenomena are only valid up to a strain of ~0.1 (dependent on the simulation temperature).

Figure 5.5 shows the strong agreement between the simulated and interpolated experimental results (see Appendix 13), with the simulation predicting values slightly below

that of the literature, although this is negligible when considering a regression has been applied to the literature data to assign a linear function. Outside of the experimental data temperature range, there is weakening agreement between the two data sets, and the simulation results do not appear to follow the linear profile assumed for the experimental data extrapolation. At the highest temperatures, the consistent discrepancy of ~±10GPa is attributed to the noise in the simulation data (see Figure 5.2), the effect of which cannot be fully eliminated without affecting the overall mechanical trend.

However, as temperature decreases outside the experimental data range, the difference between the experimental and simulation data increases. At 900K, the simulation prediction of elastic modulus is only 5GPa greater than the extrapolated experimental value, but this difference increases to almost 100GPa by 200K. The discrepancy reaches a level beyond ~±10GPa, i.e. the level associated with noise, at ~500K, where the Debye temperature of wüstite, $\boldsymbol{T_{Debye}}$= 385K [423], is approached. The Debye temperature is typically a low value [424], but it could be argued that it is significant in this case as other authors have reported higher values of Debye temperature, up to 650K [425-427]. Below this temperature, atoms no longer vibrate individually, but are coupled and vibrate collectively as a continuous medium [428]. Below the Debye temperature, not all the vibrational modes of this continuous medium have necessarily been excited and their eventual excitation is also a gradual process. elastic modulus is related to Debye temperature via its square root, $\boldsymbol{E} \propto \sqrt{\boldsymbol{T_{Debye}}}$ [424]. Siethoff proposed that the long wavelength of coupled atom vibration at lower temperatures means next-neighbour atomic position, and therefore interatomic potential, is of negligible influence [424]. As the theoretical foundations of the simulation are interatomic potential, the model is therefore likely to overestimate elastic modulus by accounting for interatomic potential at lower temperatures. Also, the potential used was not assessed and/or fitted for lower temperatures. Ak et al. also commented on the importance of the influence of interatomic interactions in where their study of elastic modulus of a Cu-Ni alloy also revealed overprediction by the model compared to experimental data [429]. Furthermore, the strain rate in MD is high compared to experiments due to the small timestep required and Kedharnath et al. cited this is a limitation of MD which makes it more likely to overpredict elastic modulus [309].

Wachtman et al. proposed a semi-empirical expression for variation of elastic modulus in oxides with absolute temperature, $\boldsymbol{T}$, based on the value of elastic modulus at absolute zero, $\boldsymbol{E_0}$ (see Equation 5.2) [430]. This equation was later analytically derived by Anderson [431]

and physical meaning was given to the temperature-independent constants, $\boldsymbol{B_G}$ and $\boldsymbol{T_0}$, which relate to bulk modulus and Debye temperature respectively [432].

$$\boldsymbol{E = E_0 - B_G T e^{\frac{-T_0}{T}}}$$

Equation 5.2

As a temperature-independent constant, $\boldsymbol{B_G}$, can be calculated by rearranging Equation 5.2 and using the known experimental datapoints presented in Figure 5.5 (non-extrapolated region only, i.e. 973≤ $\boldsymbol{T}$ ≤1273K). The mean value of $\boldsymbol{B_G}$, for these datapoints was 0.048GPa±1%. This value of $\boldsymbol{B_G}$ was then used in Wachtman's equation (Equation 5.2) to predict elastic modulus across the temperature range of the MD simulation. Figure 5.5 also shows the strong agreement of Wachtman's equation with Saeki et al.'s experimental data in both the physically validated and extrapolated regions. Hence, the existing Wachtman's equation approach for calculating temperature-dependent elastic modulus is sufficient for this project. At normalisation temperature, $\boldsymbol{T}$ = 1273K, Wachtman's equation predicts an elastic modulus of 84.2GPa, which is the value used for the mechanical analyses in this chapter. However, MD has been shown to be a successful technique for modelling the temperature-dependence of ionic crystals where other experimental and/or theoretical data may not available.

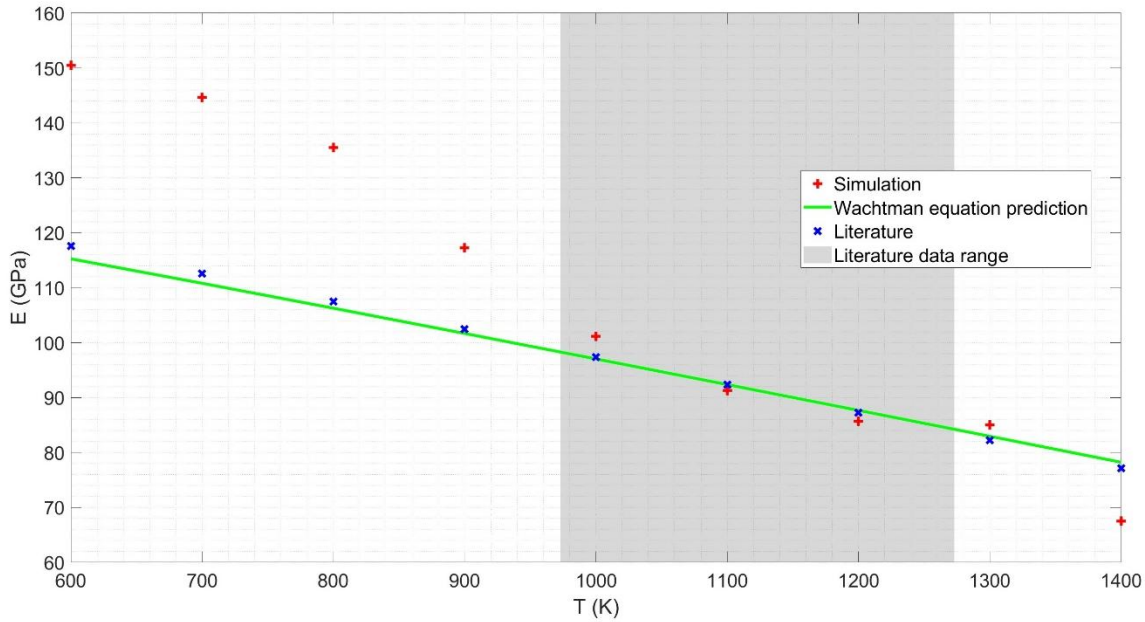


Figure 5.5: Plot of elastic modulus, $\boldsymbol{E}$, as a function of temperature, $\boldsymbol{T}$, based on molecular dynamics (MD) simulation results for 600 ≤ $\boldsymbol{T}$ ≤ 1400K, extrapolated data from the literature [419] and predictions based on Anderson's analytical derivation of Wachtman's equation [431]. Outside of the literature data range of 973 ≤ $\boldsymbol{T}$ ≤ 1273K (*grey shading*) the experimental data has been extrapolated using linear regression ¤.

Derivation of Temperature-Dependent Coefficient of Thermal Expansion

As previously discussed in Section 3.2.1, volumetric thermal expansion coefficient, $\boldsymbol{\beta}$, is directly proportional to linear thermal expansion coefficient, $\boldsymbol{\alpha}$, since $\boldsymbol{\beta = 3\alpha}$ for isotropic materials, and the temperature-dependent lattice parameter, $\boldsymbol{a}$, can be used to determine volume at a given temperature (see Equation 5.3) [433]. The derivation for this expression can be found in Appendix 14. A discontinuous linear function for temperature-dependent lattice parameter of iron was determined based on data collated by Basinski et al. in the temperature range 1173-1673K [338] (see Appendix 13). Temperature-dependent lattice parameter data for wüstite were based on data from Hayakawa et al. [434]. With the metal and oxide both having a linear variation in $\boldsymbol{a}$ with temperature, $\boldsymbol{T}$, (see Equation 5.4) a binomial expansion [435] was applied to Equation 5.4 to obtain an expression for $\boldsymbol{a^3}$, i.e. $\boldsymbol{a^3 = (pT + q)^3}$, for volume (see Equation 5.5) in Equation 5.3. Although empirical functions exist which define $\boldsymbol{\alpha}$ as a polynomial function of temperature with empirical coefficients on each term [328, 329], use of an analytical expression for $\boldsymbol{\alpha}$ provides a more numerically stable solution.

$$\boldsymbol{\alpha = \frac{1}{3V}\frac{dV}{dT} = \frac{1}{3V}\frac{d(a^3)}{dT}}$$

Equation 5.3

$$\boldsymbol{a = pT + q}$$

$$\left[\boldsymbol{p_{oxide}} = 79.5 \times 10^{-6}\text{Å}.K^{-1}; \boldsymbol{q_{oxide}} = 4.25\text{Å}; \boldsymbol{p_{metal}} = 22.2 \times 10^{-6}\text{Å}.K^{-1}; \boldsymbol{q_{metal}} = 2.89\text{Å}\ (273 \leq T < 1173K); \boldsymbol{p_{metal}} = 82.0 \times 10^{-6}\text{Å}.K^{-1}; \boldsymbol{q_{metal}} = 2.77\text{Å}\ (1173 \leq T \leq 1673K);\right]$$

Equation 5.4

$$\boldsymbol{V = a^3 = p^3T^3 + 3q^2pT^2 + 3pq^3T + q^3}$$

Equation 5.5

Furthermore, although quoted thermal expansion coefficient values are evaluated for linear scenarios, the scale of expansion is assumed small enough compared to the overall tube curvature to be linear at-scale. The coefficient of linear thermal expansion, $\boldsymbol{\alpha}$, at the normalisation temperature, was derived for both the metal substrate (Fe fcc) and oxide using the same literature as was used to collate molar volume data for the thermodynamic database in Section 3.2.1 [240, 328, 329, 436].

The elastic modulus showed significant temperature dependence with a 40% and 37% decrease across a 1000K range for the steel and wüstite respectively (see Figure 5.7).

However, the linear coefficient of thermal expansion showed limited variation with temperature in the oxide case at 15% across 1000K range (see Figure 5.8), although it should be noted that the precise lattice parameter will depend on the iron vacancy concentration in the lattice [243]. However, there was a step-increase (although the overall trend was still a small linear gradient once the new regime was established) which coincided with the phase transformation associated with normalisation, i.e. austenising temperature dictated the step-change location. The CTE in metal in the high temperature region was over double its low temperature equivalent and 1.4 times its oxide equivalent. The metal therefore expands and/or contracts at a faster rate than the oxide, leaving the oxide in a compressive state (see Figure 5.6).

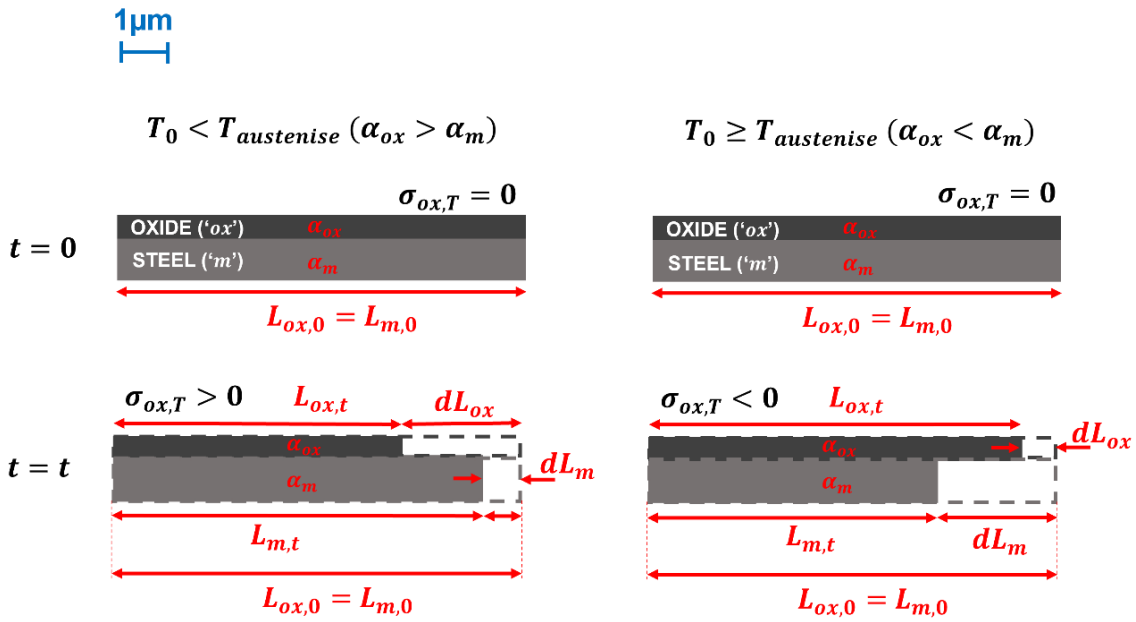


Figure 5.6: Schematic demonstrating the evolution of tensile and compressive stress, $\boldsymbol{\sigma}$, over time, $\boldsymbol{t}$, in the oxide depending on the temperature, $\boldsymbol{T}$, at which cooling begins and therefore the relative values of coefficient of linear thermal expansion, $\boldsymbol{\alpha}$, which influence the rate of thermal contraction of the steel ('*m*') and oxide ('*ox*'). A 1D viewpoint is used as the arc length of the tube considered, L_{tube}, is small compared to the radius of curvature of the tube ¤.

Hence, on cooling the CTE difference becomes much larger and the metal CTE drops to only 0.42 of the oxide equivalent (for a given temperature) (see Figure 5.9) and the oxide experiences a now tensile and higher magnitude stress as $|\boldsymbol{\alpha_{ox}(T)} - \boldsymbol{\alpha_m(T)}|$ increases.

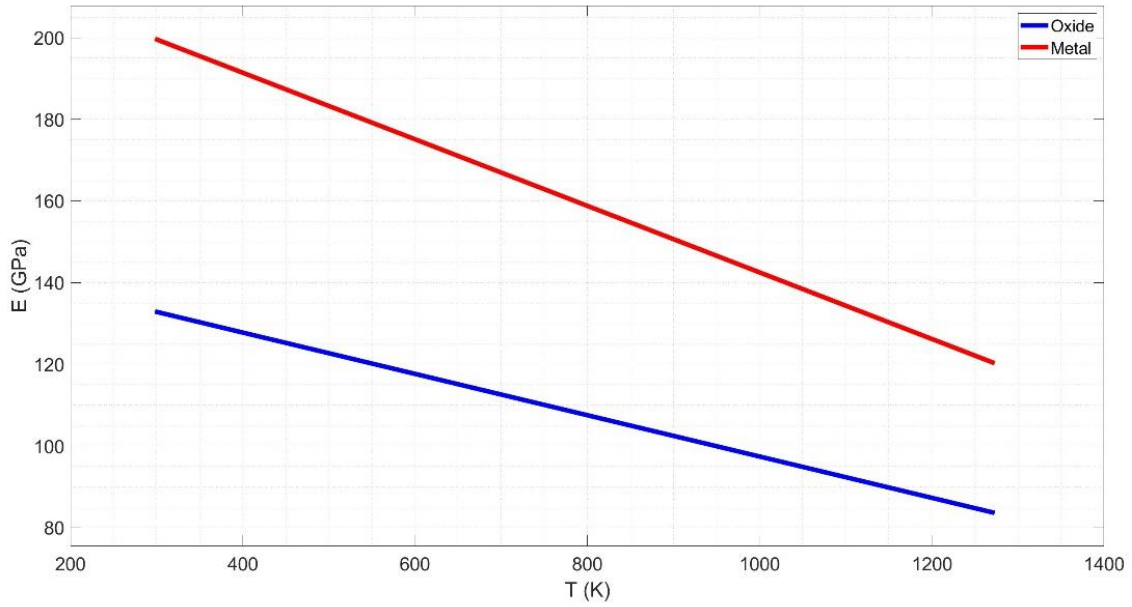


Figure 5.7: Plot of elastic modulus, ***E***, as a function of temperature, ***T***, for the oxide scale (*blue*) and steel substrate (*red*) ¤.

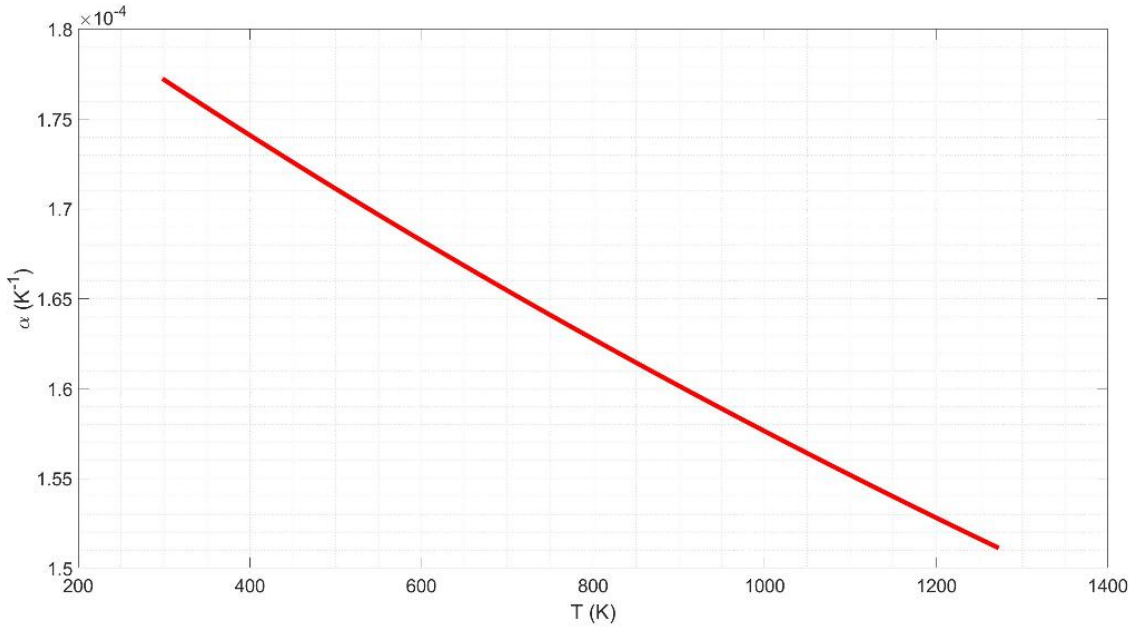


Figure 5.8: Plot of linear thermal expansion coefficient, ***α***, as a function of temperature, ***T***, for wüstite ¤.

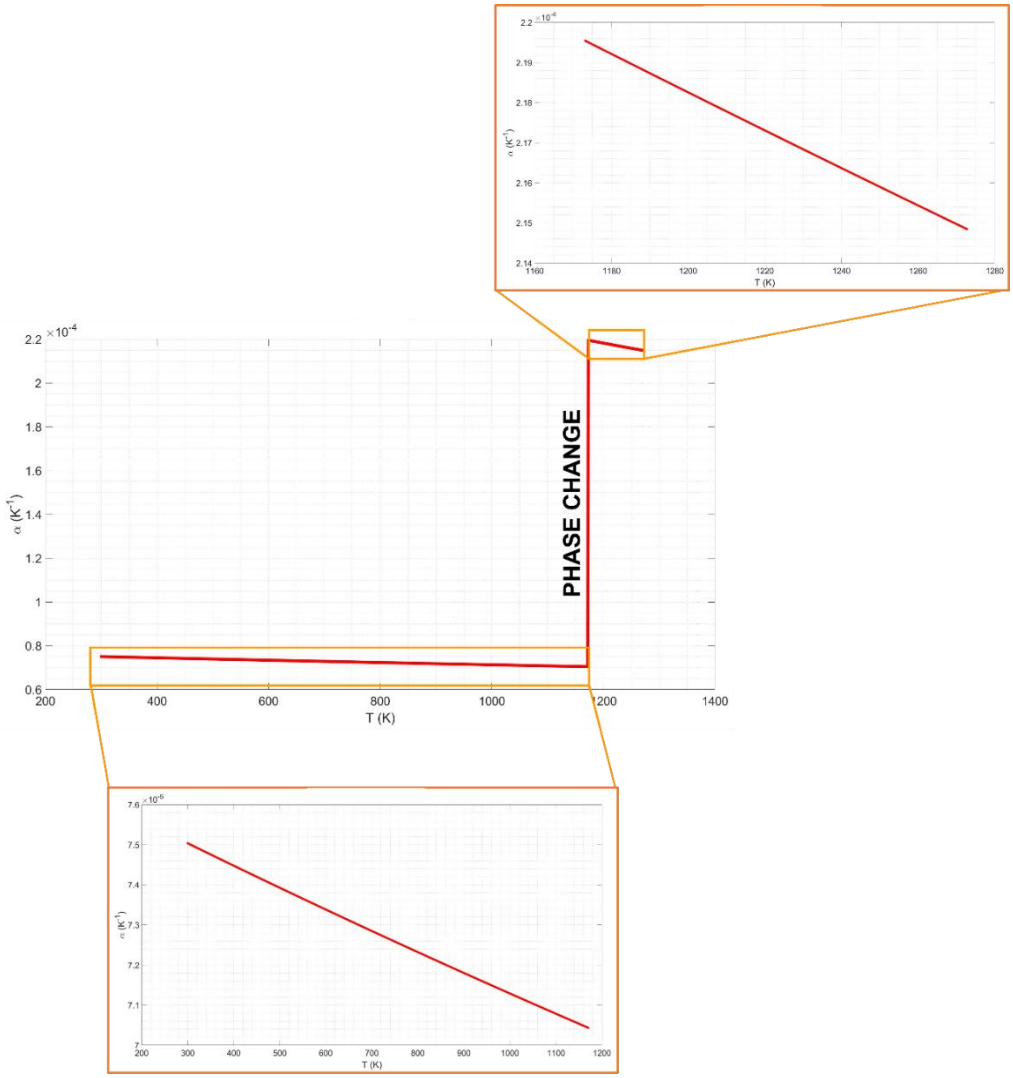


Figure 5.9: Plot of linear thermal expansion coefficient, $\boldsymbol{\alpha}$, as a discontinuous function of temperature, $\boldsymbol{T}$, due to a phase change, for the steel substrate (*left*), with enlarged views (*right*) of each temperature region demonstrating the linear function in that region ¤.

The new method for describing the interfacial positions was used as an instantaneous value of metal thickness, $\boldsymbol{t_m}$. As with the oxide, the base metal elastic modulus temperature dependence can be expressed using Equation 5.7, derived from linear gradient, $\boldsymbol{m_m}$, and y-axis intercept, $\boldsymbol{E_m}^{\boldsymbol{0}}$, values calculated using Li et al.'s data [437]. Again, their results agreed with results determined by other authors [438].

$$\boldsymbol{E_{ox}} = \boldsymbol{m_{ox}T} + \boldsymbol{E_{ox}}^{\boldsymbol{0}} \left[m = -0.0506 GPa.K^{-1};\ {E_{ox}}^{0} = 148 GPa\right]$$

Equation 5.6

$$\boldsymbol{E_m} = \boldsymbol{m_m T} + \boldsymbol{E_m}^{\boldsymbol{0}} \left[m = -0.0815 GPa.K^{-1};\ {E_m}^{0} = 224 GPa\right]$$

Equation 5.7

Figure 5.11 shows the dependency of $\boldsymbol{\sigma_{ox,T}}$ on the oxide thickness, the details of which are provided by the model, for samples with geometries associated with the 15 n.b. (IR =

7.45mm, r_{wall} = 3.2mm) and 20 n.b. (IR = 10.25mm, r_{wall} = 3.2mm) Install Plus® tubes. As the 15 n.b. and 20 n.b. tubes have the same initial wall thickness, the predicted stress profile is identical, with only slightly higher thickness of oxide predicted for the 20 n.b. (and therefore a higher maximum $\sigma_{ox,T}$). Due to the complex nature of the function defined by Huntz and Schütze (see Equation 5.1), numerical integration is necessary, via the composite Simpson's rule [298] (see Equation 2.31), to obtain an estimate of the stress in the oxide associated with the thermal expansion coefficient mismatch previously described (see Equation 2.31). In this case, the function, $f(T)$, is the integrand in Equation 5.1 which describes the thermal stress in the oxide, $\sigma_{ox,T}$, where the independent variable is temperature, T, and the numerical interval, h, is defined across the tube manufacturing normalisation temperature bounds of the normalisation temperature, T_{test}, and ambient temperature, $T_{ambient}$, across an appropriate even number of intervals, $2n$, (see Equation 5.8) defined by a code-automated convergence study (see Figure 5.10). For the maximum oxide thickness predicted by the Thermo-Calc© model (2.2mm) on a 15 n.b. tube, the optimal number of intervals was not definitively determined as it exceeded the 100 intervals stipulated.

$$\sigma_{ox,T} = \int_{T_{ambient}}^{T_{test}} f(T)\,dT = \frac{h}{3}(f_0 + 4f_1 + 2f_2 + 4f_3 + 2f_4 + \cdots + 4f_{n-1} + f_n)$$

$$where\ h = \frac{T_{test} - T_{ambient}}{2n}$$

Equation 5.8

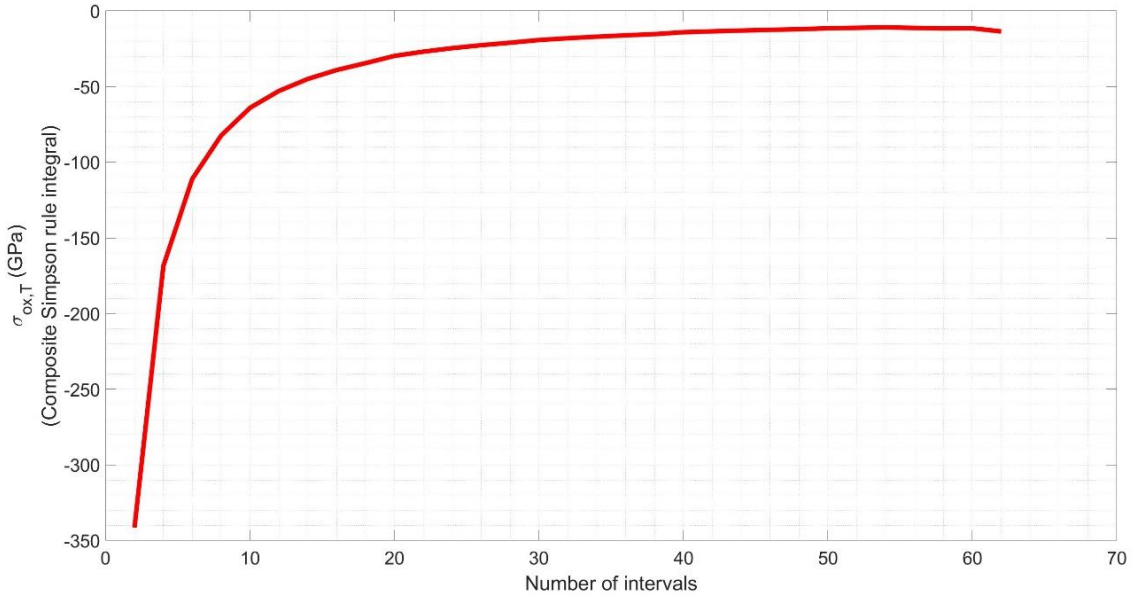


Figure 5.10: Convergence study for composite Simpson rule-based numerical integration, used to derive oxide thermal stress, $\sigma_{ox,T}$, with a convergence condition of a less than 1% change in integral between successive iterations ¤.

The stress for a given oxide thickness is shown in Figure 5.11. It is noted that there is still a short region of instability in the integral which is attributed to the fact that there is a period of numerical instability when oxide thickness is very small (<0.05 mm). The Composite Simpson rule error bound, ξ, was calculated using Equation 2.32) [298]. The original thermal stress integrand was rewritten in terms of its base functions of temperature which comprise expressions for elastic modulus (Equation 5.6 and Equation 5.7) and coefficient of linear thermal expansion (see Equation 5.4). $\sigma_{ox,T}(T)$ can be defined according to Equation 5.9 where, $a = p_{oxide}; b = q_{oxide}; i = p_{metal}; j = q_{metal}; k = m_{ox}; l = m_m; x = T; z = \frac{\delta_{ox}}{\delta_m}\left(\frac{1-\nu_m}{1-\nu_{ox}}\right)$. Given that the function requires a combination of product and quotient rules to differentiate [112], the overall resulting function is given in Appendix 15 (differentiation performed using Wolfram|Alpha [439] due to the complexity of the differential resulting in >30 terms).

$$\sigma(x) = \frac{\left(\frac{3\,a^3x^2 + 6\,a^2b\,x + 3\,a\,b^3}{a^3x^3 + 3\,a^2b\,x^2 + 3\,a\,b^3x} - \frac{3\,i^3x^2 + 6\,i^2j\,x + 3\,i\,j^3}{i^3x^3 + 3\,i^2j\,x^2 + 3\,i\,j^3x}\right) k\,x}{1 + z\frac{k\,x}{l\,x}}$$

Equation 5.9

The maximum absolute error, 30.1Pa, is predicted when the oxide is thinnest (0.1nm as defined during model development in the previous chapter) (see Figure 5.12). However, this is clearly an error of negligible value at <<1% of the magnitude of stress predicted at that value (15.4GPa) and when plotted as error bars is therefore invisible in Figure 5.11

compared to the scale of the thermal stress data. The initial instability can also not be attributed to the temperature-dependent discontinuity due to phase transition observed in the metal substrate linear coefficient of thermal expansion function since the integral has the same temperature bounds and any discontinuity would be carried through all oxide thickness and interval variations. This is one of the disadvantages of handling continuous data since if only the final oxide thickness was experimentally observed, the numerical instability would not be observed. It is therefore notable that oxide thickness influences the stability of thermal stress trend. Furthermore, this instability is problematic for drawing conclusions about the stress state of the oxide since it appears that the maximum compressive stress of -15.4GPa is observed when the scale is thinnest (although these instantaneous stress measurements for given thickness do not account for the stress exerted on adjacent scale by its neighbours). However, since the thermal stress does not appear to stabilise until the oxide is ~0.02mm thick (200,000 times its initial value), the maximum compressive stress could actually be less at -13.2GPa leading to an overengineered solution were this to be applied in the Advanced Oxide Scale Failure Diagram (AOSFD) developed in the following chapter of this work.

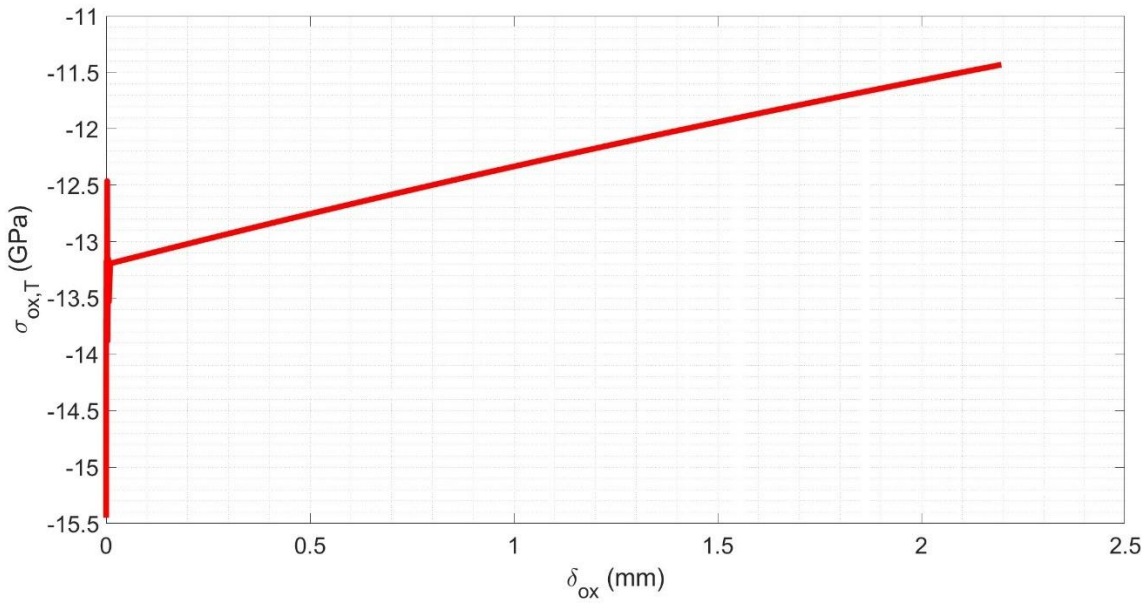


Figure 5.11: Stress developed in the oxide, $\sigma_{ox,T}$, due to thermal expansion coefficient mismatch between the steel substrate and oxide layer during cooling including error bars calculated using the Composite Simpson error condition. The error of negligible value at <<1% of the magnitude of stress predicted at that value (15.4GPa) and when plotted as error bars is therefore in invisible compared to the scale of the thermal stress data. Stress is plotted against the instantaneous oxide thickness, δ_{ox}, computationally predicted based on kinetic and diffusion theory. Expressions for linear coefficient of thermal expansion as a function of temperature were derived from lattice parameter data based on molar volume data. ¤.

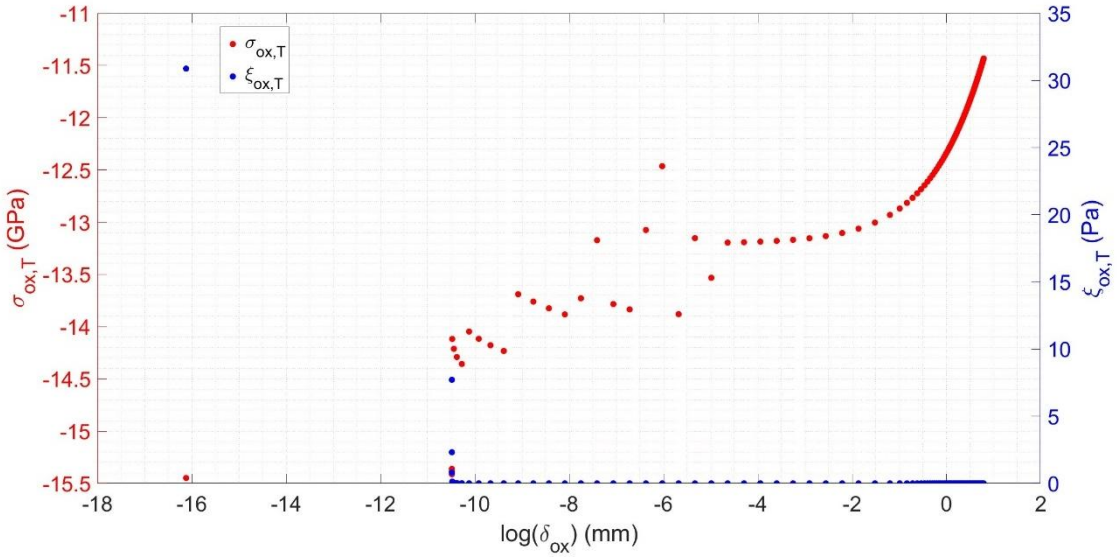


Figure 5.12: Stress developed in the oxide, $\sigma_{ox,T}$, due to thermal expansion coefficient mismatch between the steel substrate and oxide layer plotted (*left*) against instantaneous oxide thickness, δ_{ox}, on a logarithmic scale alongside the error, $\sigma_{ox,T}$, associated with its calculation (*right*) via the composite Simpson rule ¤.

Conventional analysis of thermal stress for an externally constrained component depends on the temperature operation history, ΔT and its temperature-independent mechanical properties isothermal elastic modulus, E, and coefficient of thermal expansion (CTE), α (see Equation 5.10) [440]. However, Figure 5.13 highlights how failure to account for the temperature dependence of elastic modulus and CTE, as well as the difference between in the thermomechanical properties of the adhered steel substrate, i.e. assuming internal constraint and an absence of external constraint, leads to a maximum of a 3.7 to 4.1 fold increase (moving from the inner to the outer edge of the oxide respectively) in the thermally induced stress predicted and therefore its contribution to the overall stress state of the oxide.

$$\sigma_T = E\alpha\Delta T$$

Equation 5.10

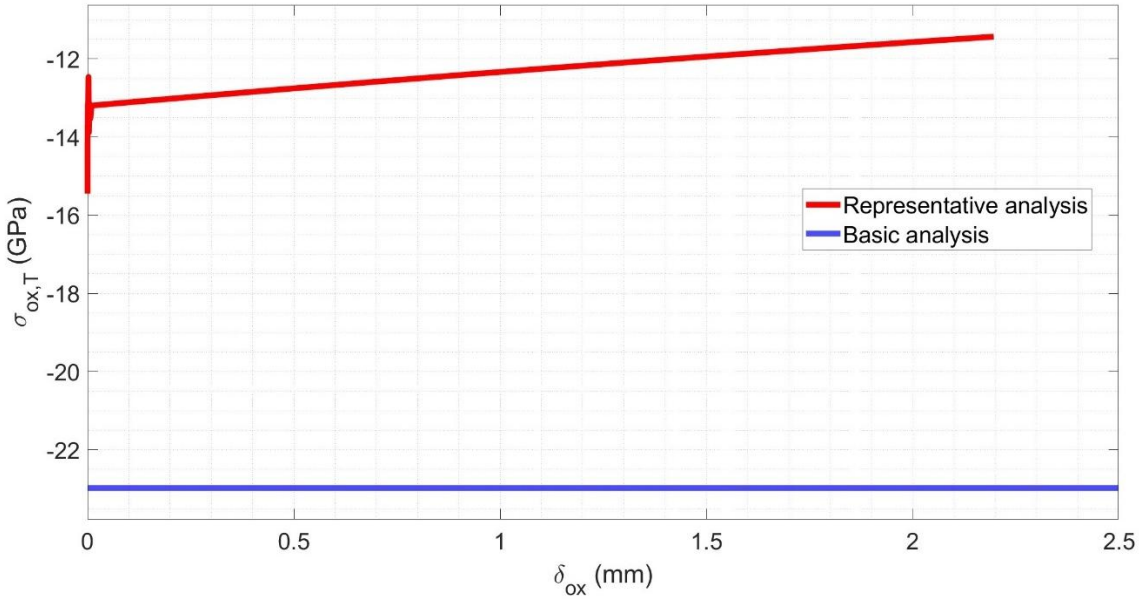


Figure 5.13: Plot of full integral-based ('representative') analysis (*red*) of thermal stress, $\sigma_{ox,T}$, in the oxide, compared to the 'basic' equivalent (*blue*), against oxide thickness, $\sigma_{ox,T}$. The representative analysis accounts for internal constraint by adhesion to metal substrate, temperature-dependency of elastic modulus and linear coefficient of thermal expansion, and the thermal expansion discrepancy between the metal and oxide. The basic analysis assumed that mechanical properties of the metal and oxide are independent of temperature and does not account for the effect of the difference in coefficient of thermal expansion between the oxide and the metal to which it is adhered ¤.

5.1.2 Growth Stress in the Oxide

The continuous data from the model also allows an insight into the instantaneous stress state of the oxide across its entire thickness during growth. Crucially, it highlights that the stress in the oxide decreases linearly from the inner to the outer edge of the oxide. It is worth re-emphasising that this stress is purely based on the difference in thermal expansion, and geometric factors such as curvature of a surface have not yet been considered (planar vs. cylindrical as discussed previously), although as previously shown the oxide thickness prediction data from the model is influenced by the geometry used during system definition. The difference compared to the basic analysis also highlights the need to consider the effect of adhesion to the substrate and the mechanical properties of the steel-scale interface [441]. Although in-situ experiments are possible, Huntz and Schütze also emphasise that several factors can promote data scatter, namely oxidation conditions, oxide thickness, substrate initial surface condition, impurities (type and concentration), and microstructural features [416]. Most importantly, as previously discussed, the growth mechanism will affect oxide kinetics, morphology, and adhesion. They argue that it is now accepted that oxide growth stress is more heavily influenced by the growth mechanism than the Pilling-Bedworth ratio which wrongly predicts compressive stresses in all parts of existing oxide scale. Tensile

strains are anticipated when it is recognised that oxygen diffusion is a non-negligible phenomenon which generates compressive stress at the metal-scale interface [84]. Experimental methods for determining stress state are limited by the equipment's geometric and thermal limitations as ideally the selected method would be capable of through-thickness measurements at high temperatures [416]. Few techniques can satisfy all of these requirements. Furthermore, Clarke highlighted that typically successful methods used to directly measure growth stress or strain, namely cantilever beam deflection and X-ray diffraction (XRD) respectively, encounter significant uncertainties in key mechanics and materials parameters, e.g. linear coefficient of thermal expansion [110]. These include measurement uncertainties, variations across the sample as well as interplay in lattice expansion as a function of temperature and pressure (local stress state), when employed to determine growth stress [110]. Furthermore, if high temperature predictions are based on extrapolation of ambient measurements, in addition to parametric uncertainties, it is near-impossible to account for stress relaxation during cooling in the form of diffusional creep and intra-oxide plastic deformation (regardless of whether the substrate thickness is great enough to prevent its own plastic deformation, and even this technique is limited in the cantilever beam technique by the need to minimise thickness to achieve observable deflection). However, the same author did go on to credit the improvement in experimental resources for oxidation growth stress purposes to the growing need to understand thermal barrier coatings and their failure in relation to fracture mechanics [114]. The global data which can be provided from the Thermo-Calc© computational domain, including the interfacial and bulk states, may offer a more accurate insight into the stress state of the metal and/or oxide during heat treatment and how likely this is to lead to the failure and damage described above. This is explored further in Chapter 6.

Growth stresses themselves comprise contributions from different sources, including geometric induction due to curved surfaces (especially for thick oxides or low radii curvature), intrinsically due to lateral oxide growth, and in some cases epitaxial (crystalline order-matching growth direction) constraints, phase transformations, or scale composition changes. The first two are most likely to contribute to a level that activates stress relief mechanisms in oxides with low cohesion and/or adhesion and large number and/or size of scale or metal-scale interface defects. Magnetite scale with defects has shown evidence of cracking at a compressive stress over 18 times lower than their defect-free equivalent [416]. One potential consideration of oxide growth stress in its continuously expanding state under

growth kinetics is analogous to stretch drawing (see Figure 5.14). The oxide is considered to be "clamped", i.e. no scope for plastic flow due to total adhesion to the steel substrate, with a continuously increasing surface area accommodated by changing blank thickness. Although in this case the continual growth of the oxide layer negates this effect and the overall thinning of the oxide is not observed as new oxide is formed [442]. This can be confirmed by comparing the final oxide thickness accounting for growth (2.2mm) which is greater than the expected thickness of the oxide after stretching if no further oxide layers were added ($\boldsymbol{\delta_{ox_{post-stretch}}}$=1.3mm) (see Equation 5.11). Equation 5.11 forms part of a series of generic sheet deformation expressions (see Appendix 11) which can be modified to the specific nature of the equal biaxial stretching observed in stretch drawing, i.e. plane stress conditions [443].

$$\boldsymbol{\delta_{ox_{post-stretch}} = \delta_{ox_{initial}} e^{\varepsilon_3}}$$

Equation 5.11

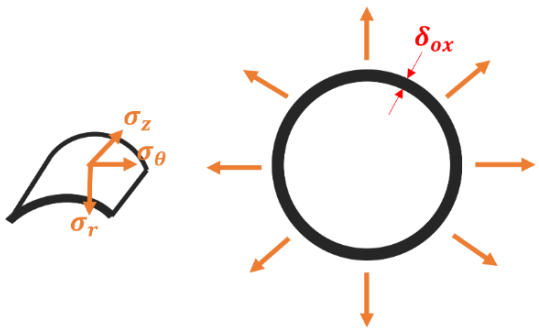


Figure 5.14: 'Stretch drawing' of a cylindrical oxide layer (continuous outwards expansion of a constant thickness oxide under biaxial tension) ¤.

In this case, both the stress ratio, $\boldsymbol{\alpha}$, and strain ratio, $\boldsymbol{\beta}$, are equivalent to 1. The major (azimuthal), $\boldsymbol{\sigma_1}$, and minor (hoop), $\boldsymbol{\sigma_2}$, stresses and strains ($\boldsymbol{\varepsilon_1}$, $\boldsymbol{\varepsilon_2}$) are therefore equal [444]. As with all plane stress scenarios, the thickness (radial), $\boldsymbol{\sigma_3}$, is 0 but the thickness strain, ε_3, is a function of the strain ratio and major strain. Since the major stress is derived via its association with the effective stress, $\bar{\boldsymbol{\sigma}}$, the same plastic power law derived from Hidaka et al.'s tensile test data was used to derive effective stress (effective strain, $\bar{\boldsymbol{\varepsilon}}$, only being dependent on the strain ratio and major strain so directly calculable from oxide deformation predictions).

A Mohr's circle can be derived from these results and used to obtain a maximum value of shear stresses, $\boldsymbol{\tau_2, \tau_3}$, found on 45° to the minor and thickness planes [443, 445] (see Figure

5.15). Figure 5.16 shows how the major (and minor stress given its equal state in biaxial tension) varies monotonically over as the oxide grows with time.

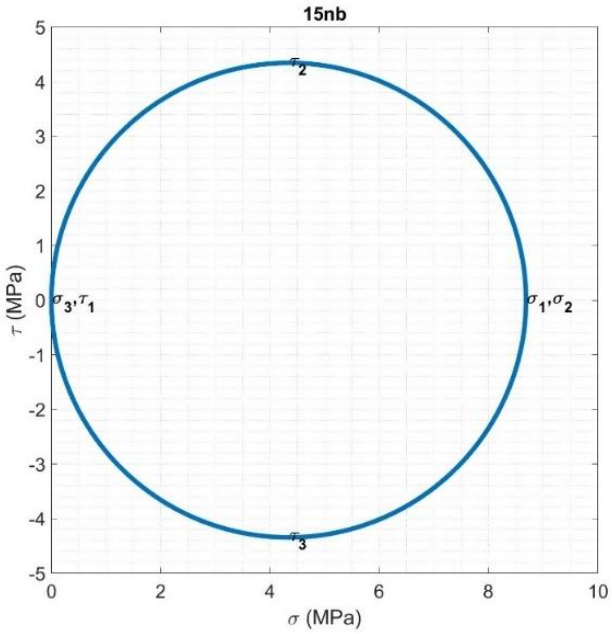


Figure 5.15: Mohr's circle of normal, $\boldsymbol{\sigma}$, and shear, $\boldsymbol{\tau}$, describing the biaxial tension state observed during oxide growth analogously to a stretch drawing procedure ¤.

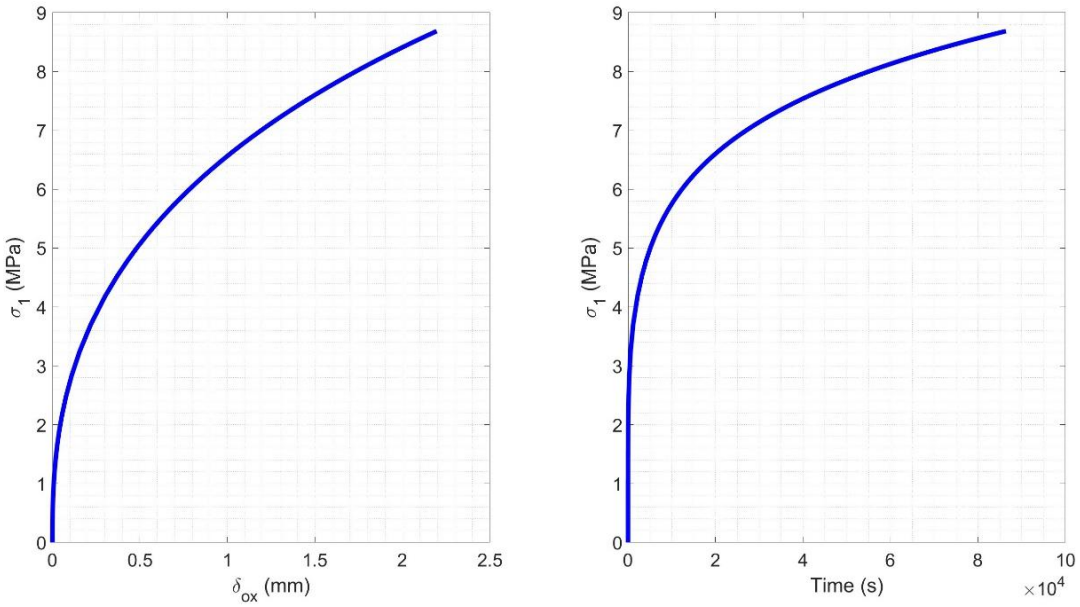


Figure 5.16: Plots of principal stress, $\boldsymbol{\sigma_1}$, against oxide thickness, $\boldsymbol{\delta_{ox}}$, (*left*) and time (*right*) as oxidation proceeds ¤.

Beam bending theory can again be applied to determine the overall tension by integrating the monotonic major stress function by parts over the instantaneous oxide thickness (see Equation 5.12), with a constant, $\boldsymbol{A}$, derived from the stretch drawing analysis above, to demonstrate the competing tensile and compressive regions of the outer and inner scale

respectively as the scale formation proceeds (see Figure 5.17). However, this analysis is only valid if the scale is bent without tension which is clearly not the case when considering stretch drawing and its biaxial tensile state.

$$\sigma_1 = A\varepsilon_1{}^n$$

$$where\ A = \frac{K\left(\sqrt{\frac{4}{3}(1+\beta+\beta^2)}\right)^n}{\sqrt{1-\alpha+\alpha^2}}$$

Equation 5.12

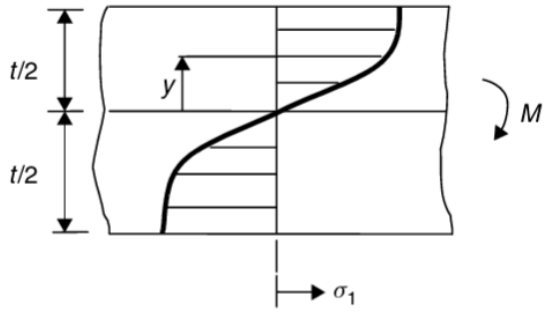


Figure 5.17: Oxide through-thickness stress, σ_1, distribution under strain-hardening pure bending where M is the applied bending moment and y is the distance from the neutral axis ($y = 0.5t$ at the outer edges) [82].

In the absence of a suitable mechanical approach, geometric stresses are most commonly predicted using Manning's analysis of the effect of geometry on oxide scale integrity, which can be used to predict strain in the oxide [106] (see Section 1.4.1). It should be noted that densities for both metal and oxide can easily be obtained from the molar volume, V_m^k, values collated for the model thermodynamic database via molecular weight, M_r, values in the same way that density for wüstite was derived when converting between thickness and mass gain during in-situ oxidation experiments described in Section 4.2 (see Equation 5.13). For the molecular weight of wüstite, the non-stoichiometric contribution of iron ('$1-x$') is taken to be 0.92 [241, 446]. Table 5.3 shows these values collated. The same molecular weight theories were used to obtain volume fraction data from the mole fraction derived from the model.

Table 5.3: Molecular weights, M_r, and densities, ρ, of metal and oxide used to calculate growth strains.

$M_{r_{oxide}}$ (g)	67.38
$M_{r_{metal}}$ (g)	55.85
ρ_{oxide} (g.cm^{-3})	5.91
ρ_{metal} (g.cm^{-3})	8.33

$$M\rho = \frac{M_r}{V_0^k}$$

Equation 5.13

In extending the analysis to curved surfaces (see Figure 5.18), it is assumed that curvature is unidirectional and uniform oxidation of smooth micro-planar interfaces is assumed. Hoop stress, σ_h, is introduced as a result of the need to translate the existing bulk scale. This can be related to the radial stress, σ_r, acting across the interface via Equation 5.14.

$$\varphi h \sigma_h \simeq R\sigma_r$$

Equation 5.14

Huntz and Schütze then translated this information into expressions for oxide hoop, ε_{ox}^h, and radial, ε_{ox}^r, strains (see Equation 5.15 and Equation 5.16) [416].

$$\varepsilon_{ox}^h = -\frac{M}{R\varphi} d$$

Equation 5.15

$$\varepsilon_{ox}^r \approx \frac{d}{R} \varepsilon_{ox}^h$$

Equation 5.16

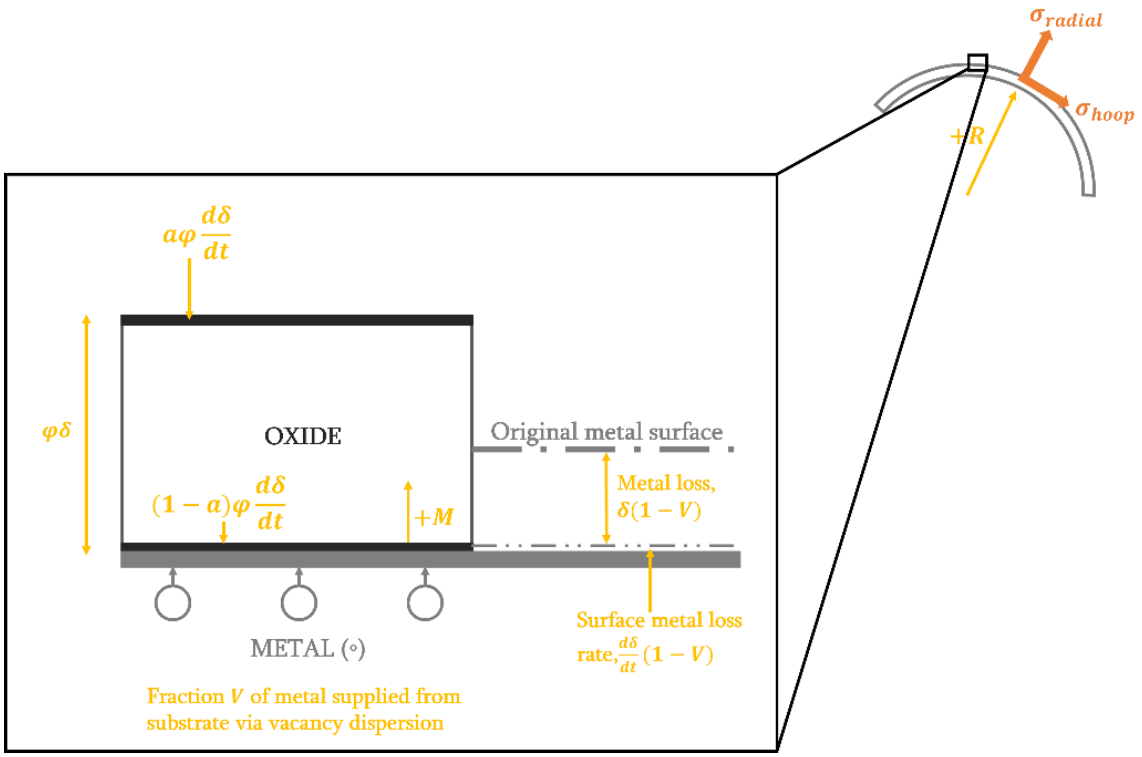


Figure 5.18: Dimensional theory for derivation of expression of geometric effect growth stress in oxide scale ¤.

These strain values were converted to stress, $\boldsymbol{\sigma}$, using Equation 5.17 [114, 447] and a literature value of elastic modulus, $\boldsymbol{E}$, for wüstite measured using acoustic resonance (assuming isotropic properties) [419]. The temperature dependence of elastic modulus was accounted for using the method as in the thermal stress calculations in Section 5.1.1.

$$\boldsymbol{\sigma = \frac{E}{1-\upsilon}\varepsilon}$$

Equation 5.17

Initial attempts were made to assess molar fraction data for tube dimensions reflecting that of the 15 n.b. (IR = 7.45mm) and 20 n.b. (10.25mm) heavyweight wall thickness (3.2mm) Install tubes, since these were available as samples which could be later validated (see Section 5.1.4). Since the theory in Equation 5.15 and Equation 5.16 has shown that oxide thickness forms part of the calculation of dimensional oxidation stress, the kinetic analysis described in Chapter 3 was also performed, revealing an oxide thickness of 2.916mm after ~24 hrs heat treatment.

Figure 5.19 shows the mole fraction contribution of iron (Fe) across the global computational domain for a 15 n.b. sample. The sudden decrease in this value from ~1.0 to ~0.45 (with minor spatial variation) highlights the position of the interface, $\boldsymbol{x_{SSI}}$, between the bulk metal and wüstite regions. This is the kind of valuable additional information that the model can provide as previously the steel-scale interface was assumed to have retreated

to the same extent as that of the scale-gas interface (for oxide volume calculations). However, with this additional mole fraction data the position of the metal-scale interface, 8.7mm in this case, can be accurately determined and supplied to the volume equation (see Equation 5.18). These data also give clear information about the scale-gas interface, $\boldsymbol{x_{SGI}}$. This equation can be modified to include this new information (see Equation 5.18).

$$\boldsymbol{V_{oxide} = \pi L\left(x_{SGI}{}^{2} - x_{SSI}{}^{2}\right)}$$

Equation 5.18

However, applying this technique, though more easily verifiable, revealed only a negligible (0.03%) change in volume and mass predictions, which suggests the assumptions about metal-scale interface dynamics within the former method were accurate. However, the new method was still implemented going forward as it did not rely on such an assumption and instead on physical data. Furthermore, and crucially in the context of the oxidation stress analysis aspect of this work, Figure 5.19 also offers the necessary bulk and interfacial metal contribution volume fraction data necessary for Manning's methodology. An average was taken from both regions to determine molar equivalent values of, $\boldsymbol{V_{bulk}}$ and $\boldsymbol{\alpha_{interfacial}}$ as 1.00 and 0.4618 respectively. These were converted to volume fraction values using the atomic theory previously described in Equation 5.13. Key results from the 20 n.b. sample were a final oxide thickness of 2.18mm, and molar equivalent values of $\boldsymbol{V_{bulk}}$ and $\boldsymbol{\alpha_{interfacial}}$ as 1.00 and 0.4619 respectively when the metal-scale interface was found at 11.5mm (see Figure 5.20).

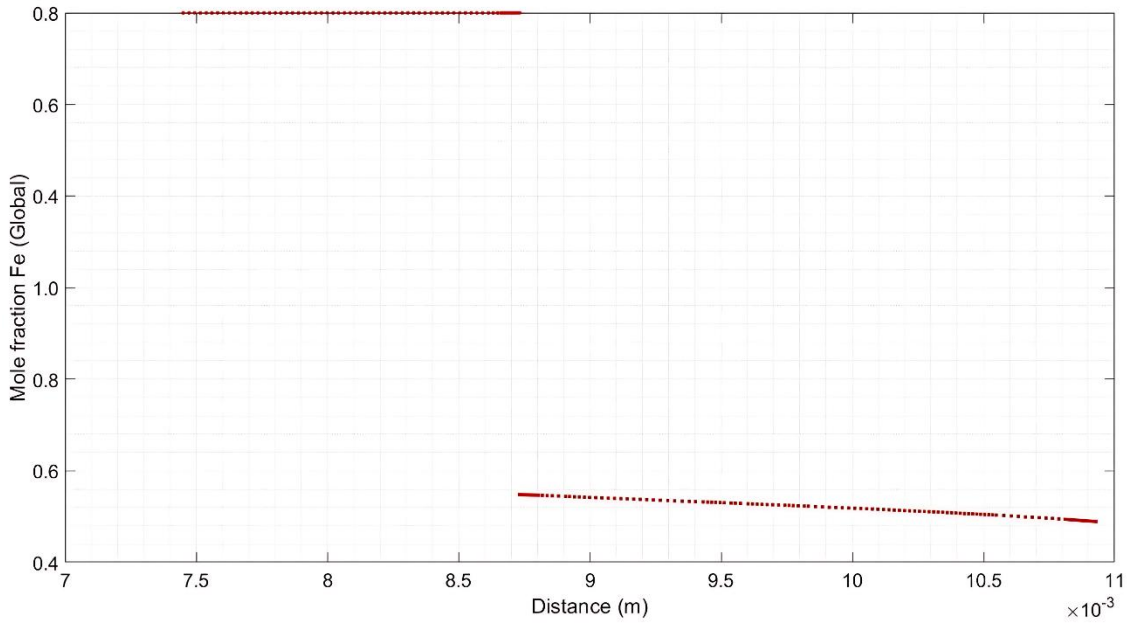


Figure 5.19: Plot of Fe mole fraction across the global computation domain, for a 15 nominal bore (n.b.) tube, revealing details about the instantaneous position of the metal-scale interface during oxidation (based on a moving phase boundary theory) ¤.

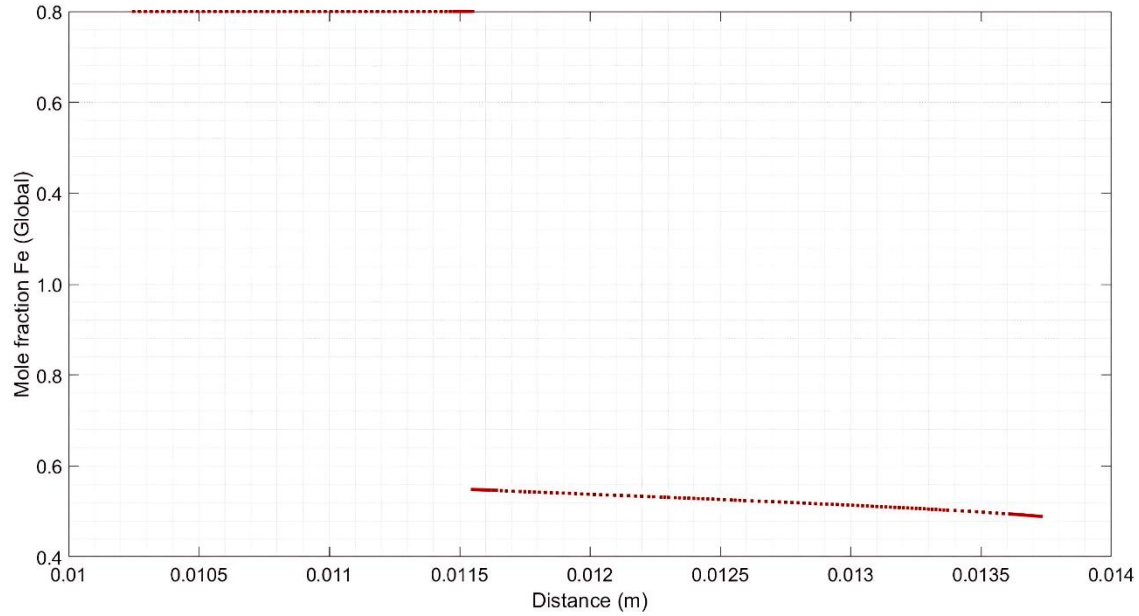


Figure 5.20: Plot of Fe mole fraction across the global computation domain, for a 20 nominal bore (n.b.) tube, revealing details about the instantaneous position of the metal-scale interface during oxidation (based on a moving phase boundary theory) ¤.

Figure 5.19 and Figure 5.20 also provide evidence of the effect of the double geometric mesh discussed in Section 3.1.1 with a clear increase in mesh resolution (higher number of datapoints) near interfacial regions of interest (metal-scale and scale-gas).

The results of the stress prediction of hoop and radial growth stress by application of Equation 5.15 and Equation 5.16 respectively (and Equation 5.17 in both cases) are shown in Figure 5.21 and Figure 5.22 for the 15 n.b. sample as a function of time and oxide thickness

respectively. Although the values of stress arising due to oxidation volumetric changes seem high at several GPa, Clarke et al. remarked that the development of oxide at its own vertical grain boundaries, as discussed above in reference to the work of Rhines and Wolf [108], can induce a large stress if the substrate is constrained by the geometry (see Section 1.4), due to the low compressibility of the oxide compared to the substrate [114]. For example, Clarke et al. cited that for an aluminium oxide layer, of only several microns, formed on an Fe alloy, a 0.5GPa can be evolved [110]. They commented that it is not surprising that external oxide layers, typically protective, experience augmented growth stress and strain compared to other surface films and coatings owing to the combined effect of compressibility differences and thermal expansion coefficient mismatch, as well as high temperature operation exceeding that required for dislocation plasticity. They went on to comment on the significance of how few atoms are required to generate this high level of stress and strain [114]. For example, they cited that only 10^7 atoms are required per micron of grain boundary to generate a 1μm thick new plane of oxide. Crucially, Clarke also highlighted that lateral growth strain is only generated when simultaneous outward cation and inward anion diffusion in an imperfect lattice is present [110, 114], as discussed in Section 1.7.2 and Section 3.2.3. In this case, oxide is formed along grain boundaries perpendicular to the steel-scale interface and the volume change associated with oxidation cannot be accommodated by rigid body interfacial metal-scale displacement in the normal direction. However, as discussed in Section 1.4, wüstite is predominantly the result of outward cation diffusion rate control [81].

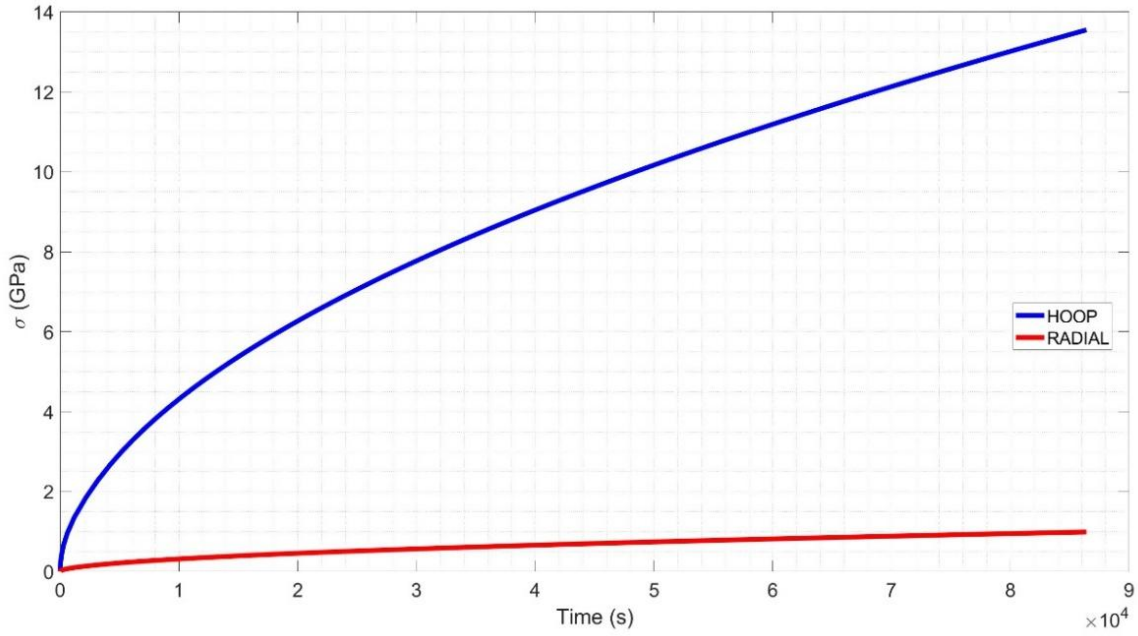


Figure 5.21: Plot of hoop (blue) and radial (red) stress, $\boldsymbol{\sigma}$, as a function of time, $\boldsymbol{t}$ ¤.

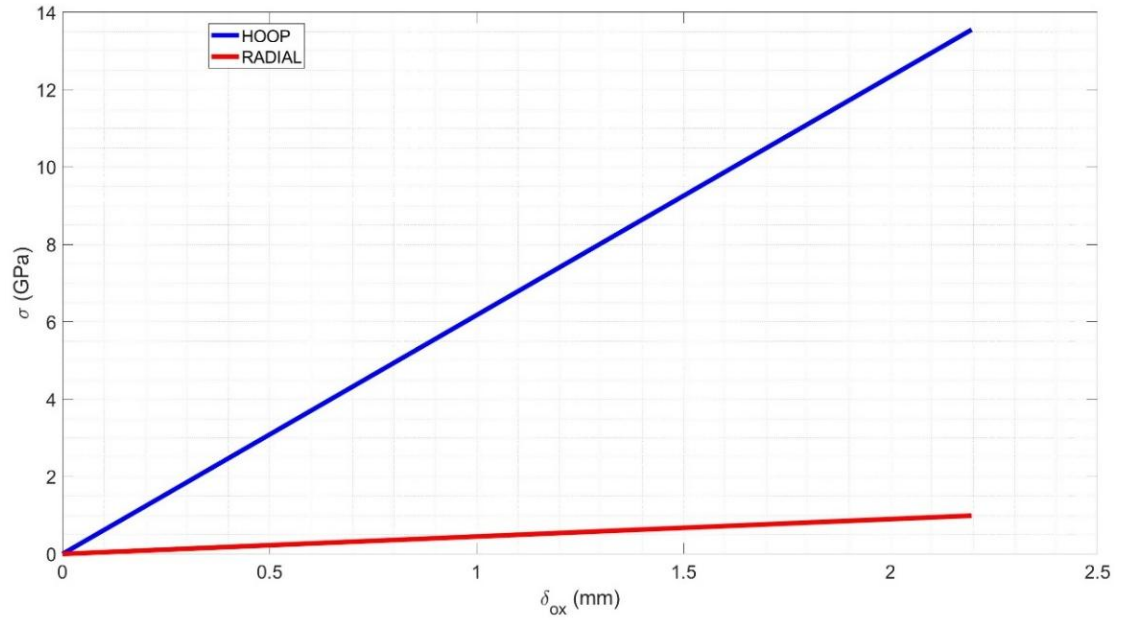


Figure 5.22: Plot of hoop (blue) and radial (red) stress, $\boldsymbol{\sigma}$, as a function of model-predicted oxide thickness, $\boldsymbol{\delta_{ox}}$ ¤.

This work was done on a 24hr normalisation to maximise the data points available, but data from the 3 minute (average normalisation soak period) time stamp was needed for use during validation. Intrinsic growth stresses are more difficult to predict due to their dependence on grain boundary structure and diffusion rates. However, Schütze highlighted that relaxation stress values, $\boldsymbol{\sigma_{relax}}$, can be used as an estimate for the contribution of intrinsic growth stresses to the overall stress field under continuous operating conditions, which favours the preference in the model for isothermal heating conditions.

The relationship between oxide kinetics, adhesion and geometry was also hypothesised to be

bound by the stress profile associated with the formed (and welded) tube. An initial assessment of the bend ratio, $\boldsymbol{\zeta_{bend}}$ (see Equation 5.19) observed in firstly the industrial dimensions manufactured by Tata, and then at the larger scale of inner radial dimensions explored within the radial dependency study discussed previously, revealed that multiple stress states existed across the range considered.

$$\boldsymbol{\zeta_{bend} = \frac{\rho_{bend}}{y} = \frac{IR}{y}}$$

Equation 5.19

where

$\boldsymbol{\rho_{bend}}$ is the radius of curvature of bending, this is equivalent to the inner radius, $\boldsymbol{IR}$, previously described, and $\boldsymbol{y}$ is the distance within the sheet axis from the neutral axis (in the outer surface case this will be half the total sheet thickness, i.e. $\boldsymbol{r_{wall}}$ in the case of conveyance tube forming).

Assuming plane strain conditions as are found in sheet metal bending, a bend ratio of less than four demands a thick-walled analysis where there is through-thickness stress, i.e. $\boldsymbol{\sigma_3 \neq 0}$. Beyond this value of bend ratio, analysis becomes thin-walled and through-thickness stress is negligible. At this scale, strain hardening is a significant effect in both analyses, and a power law can be used to calculate the principal stress, $\boldsymbol{\sigma_1}$, from the principal strain, $\boldsymbol{\varepsilon_1}$. For a bend ratio of 50 or greater, strain hardening effects become negligible and a simpler elastic-plastic thin wall analysis can be used. Table 5.4 outlines the methodology used to calculate principal stress and strain, minor stress and strain values, and the overall effective stress, $\boldsymbol{\bar{\sigma}}$, as shown (see Equation 5.20).

$$\boldsymbol{\bar{\sigma} = \sqrt{\frac{1}{2}\{(\sigma_1 - \sigma_2)^2 + (\sigma_2 - \sigma_3)^2 + (\sigma_3 - \sigma_1)^2\}}}$$

Equation 5.20

Effective stress was used to assess the stress states across the radial range in order to account for the effect of stress reversal and dislocation annihilation which can put the inner tube surface in tension and cause the overall stress profile to deviate from the outer surface tension-inner surface compression state conventionally assumed [101]. For all mechanical analyses discussed, an isotropic material was assumed and unless otherwise stated, mechanical theory was taken from chapters two and six of Marciniak et al.'s metal forming textbook [82, 443].

Table 5.4: Description of the methodologies used to calculate principal strains, $\boldsymbol{\varepsilon}$, and stresses, $\boldsymbol{\sigma}$, for different mechanical conditions.

Methodology	ε_1	ε_2	ε_3	σ_1	σ_2	σ_3
elastic-plastic, thin-walled	$ln\left(\frac{\boldsymbol{\rho}}{\boldsymbol{y}}\right)$	0	$-\boldsymbol{\varepsilon_1}$	$\boldsymbol{E'\varepsilon_1}$	$\frac{\boldsymbol{\sigma_1}}{\boldsymbol{2}}$	$\boldsymbol{0}$
Strain hardening, thick-walled	$ln\left(\frac{\boldsymbol{\rho}}{\boldsymbol{y}}\right)$	0	$-\boldsymbol{\varepsilon_1}$	$\boldsymbol{K{\varepsilon_1}^{n_{work}}}$	$\frac{\boldsymbol{\sigma_1+\sigma_3}}{\boldsymbol{2}}$	$\boldsymbol{\sigma_1-\sigma_f}$ (Tresca criterion)
Strain hardening, thin-walled	$ln\left(\frac{\boldsymbol{\rho}}{\boldsymbol{y}}\right)$	0	$-\boldsymbol{\varepsilon_1}$	$\boldsymbol{K{\varepsilon_1}^{n_{work}}}$	$\frac{\boldsymbol{\sigma_1}}{\boldsymbol{2}}$	0

Table 5.4 also shows how successful calculations require several coefficients and parameters, namely a modified elastic modulus, $\boldsymbol{E'}$, flow stress, $\boldsymbol{\sigma_f}$, and power law hardening coefficient, $\boldsymbol{K}$, which were calculated using Equation 5.21 and Equation 5.22 respectively. For the Rajendran method used to calculate $\boldsymbol{K}$ [448], a strain hardening exponent, $\boldsymbol{n_{work}}$, value of 0.12 was obtained from Xu et al.'s work, when considering the outer surface of a formed tube [101]. Yield strength, $\boldsymbol{\sigma_Y}$, was based on the nomenclature of the E41 steel itself, i.e. P235GH has a yield strength of 235MPa respectively [2].

$$\boldsymbol{E' = \frac{E}{1-\nu^2}}$$

Equation 5.21

$$\boldsymbol{\sigma_f = \frac{\sqrt{3}}{2}\sigma_1}$$

Equation 5.22

5.1.3 Oxide Plastic Power Law via Nanoindentation

To obtain accurate plastic power law coefficients, engineering stress-strain ($\boldsymbol{\sigma-\varepsilon}$) data must be converted to their true equivalents, $\boldsymbol{\sigma_t-\varepsilon_t}$ (see Equation 5.26 and Equation 5.27) [221]. The appropriate plastic power law [444] (see Equation 5.29, where effective stress, $\boldsymbol{\overline{\sigma}}$, is given in MPa) for wüstite was derived from nanoindentation test data using the methodology described in Section 2.1.6. A 15 n.b. tube sample was indented at 3 locations along its length (avoiding the weld region) with a user-defined maximum indenter displacement of 2μm (10% of the typical oxide thickness observed in Section 3.3). The value

for typical oxide thickness was corroborated against an in-situ optical light microscope image taken pre-indentation (see Figure 5.23).

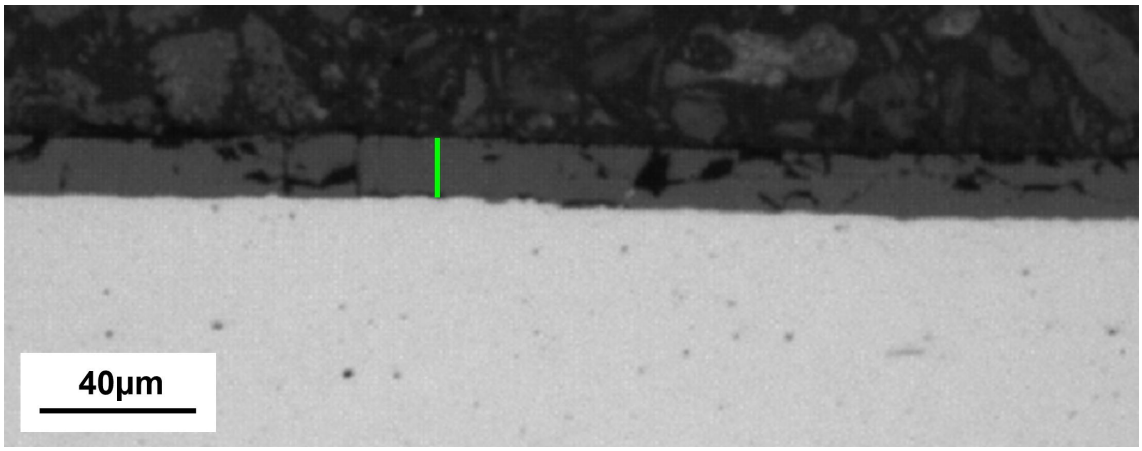


Figure 5.23: Optical light microscope image taken in-situ pre-nanoindentation on a 15 n.b. tube sample to corroborate typical oxide thickness values of ~20µm ¤.

To identify the plastic contact region, Hertzian contact mechanics for a sphere on a flat plate, i.e. a convex surface in contact with a planar surface (see Figure 5.24) (assuming that the conveyance tube radius is far greater than that of the blunted Berkovich indenter [285], i.e. $\boldsymbol{R_{sample}} = \infty$) can be plotted (see Equation 5.28) as a function of the reduced modulus, $\boldsymbol{E_r}$ (see Equation 5.24), and reduced indenter radius of curvature, $\boldsymbol{R_{ind}}^*$ (see Equation 5.23, which is simplified from the overall radius of curvature equation since the a spherical (volumetrically symmetrical) indenter is assumed and the radius is equal in all directions), alongside the original test load-displacement data [449].

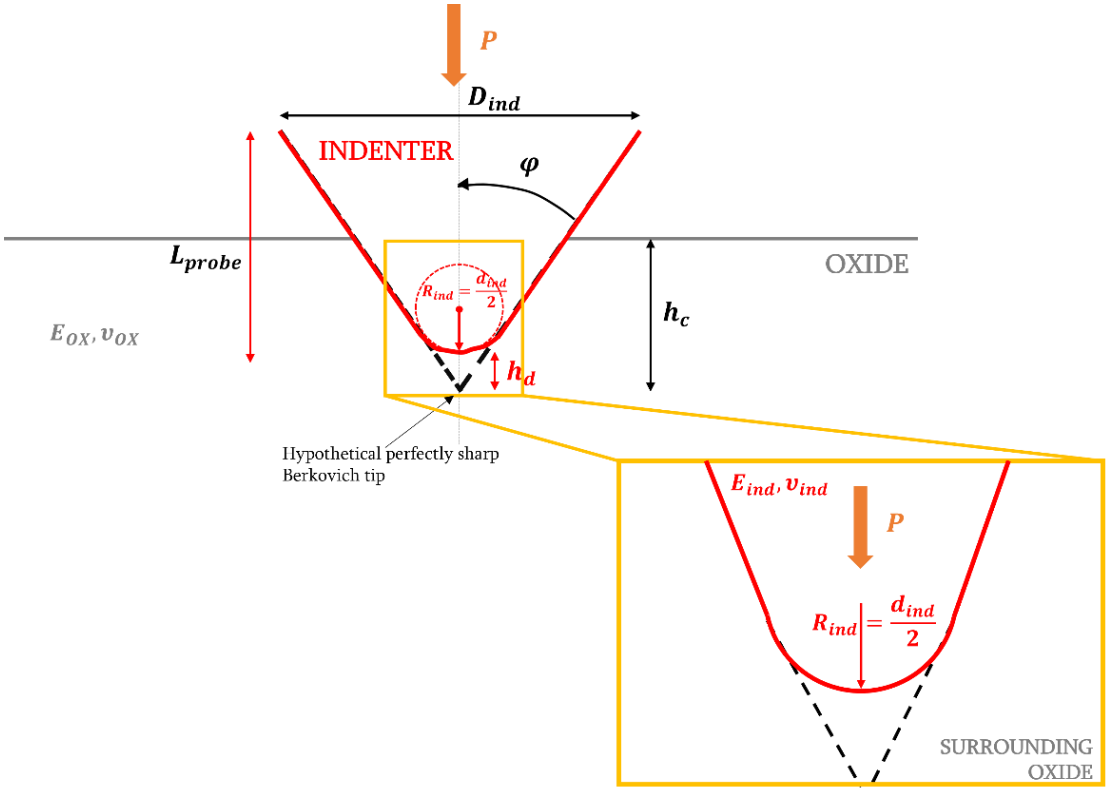


Figure 5.24: Schematic showing the descriptive geometry of a blunted Berkovich indenter and the relevant contact mechanics theory necessary to analyse the force, P, present in a convex-planar surface elastic contact scenario ¤.

This analytical validation approach undoubtedly satisfies three out of the five assumptions in Hertz' theory comprising homogeneous contact materials not experiencing stress above their yield, only normal contact forces, and a small contact area in comparison with the components' overall dimensions [450]. However, the components are not at rest and in equilibrium, and given that minimal metallographic preparation could be applied to avoid stripping the oxide from the tube surface to expose the steel substrate, it is likely unreasonable to assume no roughness effects.

$$R_{ind}^{*} = \frac{R_{ind}}{2}$$

Equation 5.23

$$\frac{1}{E_r} = \frac{1}{2}\left(\frac{1-\upsilon_{ind}^{2}}{E_{ind}} + \frac{1-\upsilon_{ox}^{2}}{E_{ox}}\right)$$

Equation 5.24

For calculation of the reduced modulus, values of Poisson's ratio, υ_{ind}, and elastic modulus, E_{ind}, for diamond were taken from the work of Spear and Dismukes [451] (equivalent values for the oxide, υ_{ox} and E_{ox}, had already been obtained in earlier in Section 5.1.1 of the chapter and were evaluated at 298K). The first point of deviation by the data from the

Hertzian contact theory denotes the onset of yield which is known as the detection of incipient plasticity, i.e. a 'pop-in' event - where either there is displacement without an increase in load, or load increases rapidly at a constant displacement.

Pop-in events are associated with incipient plasticity, particularly for very high stress levels (approaching the theoretical strength) during the loading period [452]. The phenomenon is based on a strain-burst event associated with the creation and nucleation of dislocations in a perfect crystal lattice. Leading up to a pop-in, deformation is purely elastic. As such, the critical load for a pop-in event should correlate with a load value predicted by Hertzian elastic contact mechanics. However, it should be noted that pop-in events have a high energy barrier and occur only with a low density of pre-existing dislocations. Given that the oxide could not be metallographically prepped due to its brittle and inconsistent adhesion material profile, a high density of dislocations is expected which may reduce the probability of pop-in events. Furthermore, Ohmura and Wakeda [452] highlighted that there is still uncertainty in the engineering perspective associated with the differentiation between 'microyielding' behaviour associated with pop-in events and localised phenomena preceding macroyielding, e.g. high stress close to theoretical strength could be described as analogous to the enhanced stress intensity in the stress field closest to a crack tip.

The maximum acceptable radius of the indenter is stipulated by BS EN ISO 14577-2 (200nm for the nano range, 500nm for the micro range) [453]. The probe length, $\boldsymbol{L_{probe}}$, was 367nm. Determining the indenter radius demanded an understanding of the effect of Berkovich indenter blunting [285]. Contact area function was dependent only the contact depth, $\boldsymbol{h_c}$, and using this value as the indenter radius led to a significant overestimate in the contact load (see Figure 5.25). However, when considering the spherical indenter profile which makes contact with the surface, the indenter radius, $\boldsymbol{R_{ind}}$, is greatly reduced and it is no longer valid to assume that the indenter radius and contact depth are equal (as shown in Figure 5.24). However, as Figure 5.24 shows, contact depth is still a relevant value in determining the ratio between the base diameter, $\boldsymbol{D}$, taken at the surface of the sample, and the blunted tip diameter,

$\boldsymbol{d_{tip}}$, based on the typical Berkovich indenter half-induced angle, $\boldsymbol{2\varphi}$, of 70.3° [285]. The geometric details of a spherically blunted cone, most often investigated as part of aerodynamics theory. Using Equation 5.25, the ratio between the probe depth, $\boldsymbol{L_{probe}}$ and $\boldsymbol{D}$, and the NASA technical note report N66-12138 on the 'Aerodynamic Characteristics of

Spherically Blunted Cones at Mach Numbers from 0.5 to 5.0' [454], an approximation for the $\frac{dd_{tip}}{D}$ ratio can be found and the indenter radius ($R_{ind} = \frac{d_{tip}}{2}$) can be determined.

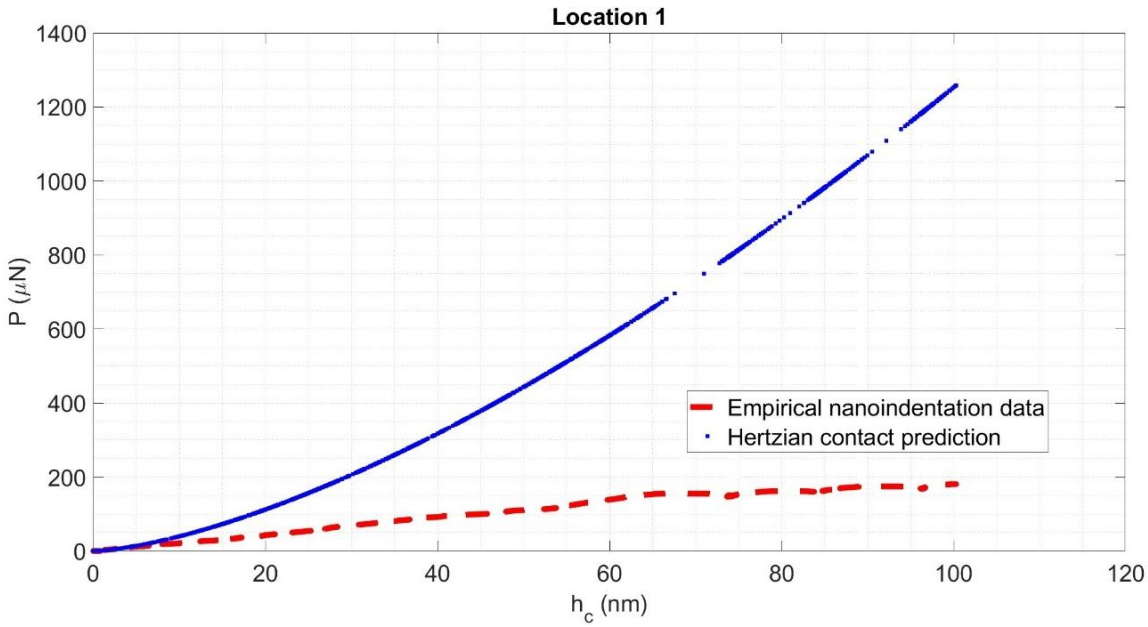


Figure 5.25: Plot of measured load, P, against indenter displacement, h_{ind}, based on measured (*red*) and analytically predicted (*blue*) values (at location 1) ¤.

$$R_{ind,b} = 2h_{ind}sin\varphi$$

Equation 5.25

The values of the half-included angle and $\frac{h_c}{D}$ approximates the tip blunter shape to that of 'C-2' which gives $\frac{d}{D}$ a value of 0.2 and therefore a tip radius of 84.2nm which is both in the range set by BS EN ISO 14577-2 for the nano range and gives a better alignment of measured and predicted Hertzian elastic contact load.

During application of the plastic power law to obtain the strength coefficient, K, and strain hardening index, n, the dataset must also be restricted to only the loading region which can be identified as the point where load reaches a maximum value. The regions of negative displacement, associated with surface roughness which cannot be eliminated via metallographic preparation due to the brittle and inconsistent adhesion profile of the oxide, for each location also had to be eliminated during any analyses. Surface roughness was also the most likely cause of sudden rises and falls in force for higher displacements for the oxide measured at location 3 (see Figure 5.26) [12]. There were also issues with some locations having outliers which made it difficult to achieve a well-fitted linear polynomial. Outliers are common in nanoindentation data due to the scale of measurement and thus the percentage contribution of any uncertainty to an overall measurement. MATLAB R2024b

has an in-built outlier removal function which defaults to removing datapoints not lying within 3 standard deviations of the mean. A better linear fit was achieved by applying this function.

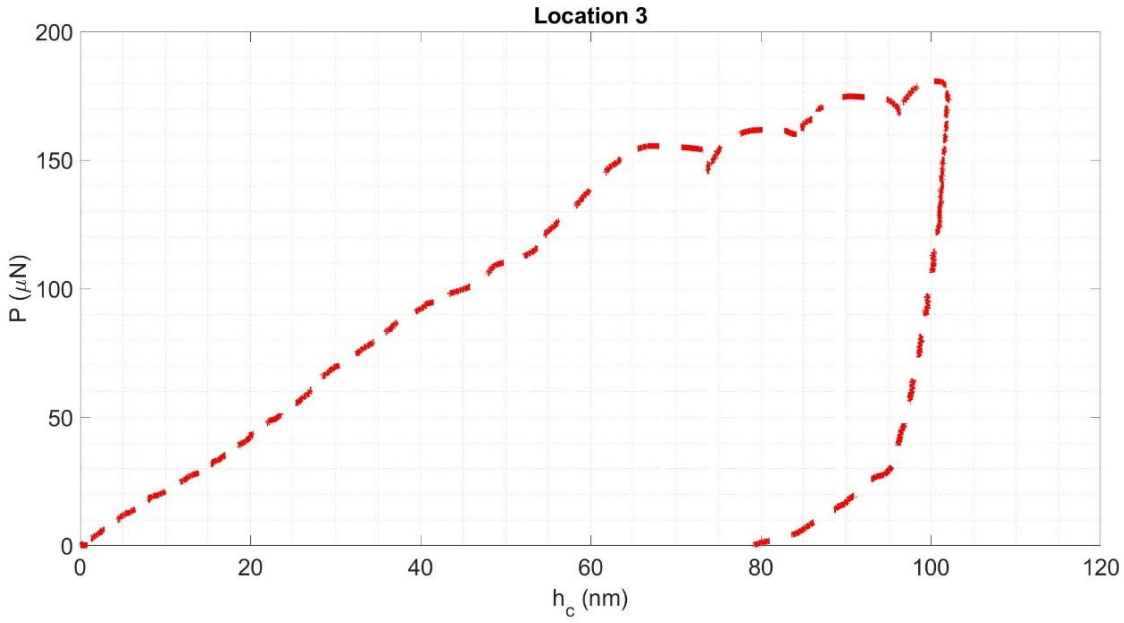


Figure 5.26: Load, ***P***, -displacement, h_c, plot (full loading-unloading cycle) for location 3 showing the presence of surface roughness-related anomalies in force data at higher displacements during loading ¤.

Using this successful procedure it becomes possible to define a cut-off for the elastic period of loading. However, it is worth noting that a minimum displacement value of 40nm was applied, as is standard with nanoindentation techniques [455], as the equipment is not calibrated below this value. Figure 5.25 highlights how for force-displacement profile has established deviation from the Hertzian elastic region beyond this displacement criterion. In metallic materials (including alloys), this deviation from elasticity occurs at a pop-in event [452].

$$\boldsymbol{\varepsilon_t = \ln(1+\varepsilon)}$$

Equation 5.26

$$\boldsymbol{\sigma_t = \sigma(1+\varepsilon)}$$

Equation 5.27

$$\boldsymbol{P = \frac{E_r R_{ind}^{\frac{1}{2}}}{\sqrt{2}} h_c^{\frac{3}{2}}}$$

Equation 5.28

The start of the loading period was defined as when the difference between the measured and Hertzian contact mechanics predicted load exceeded a 5% tolerance value. Due to

fluctuation in the data, the mean value of the measured to predicted load was evaluated for windows of 10 datapoints and the start of plasticity was defined as the point when this criterion was met by the mean value for that window. Plastic power law values were then determined for all three locations and means values for both $\boldsymbol{K}$ and $\boldsymbol{n}$ (see Figure 5.27).

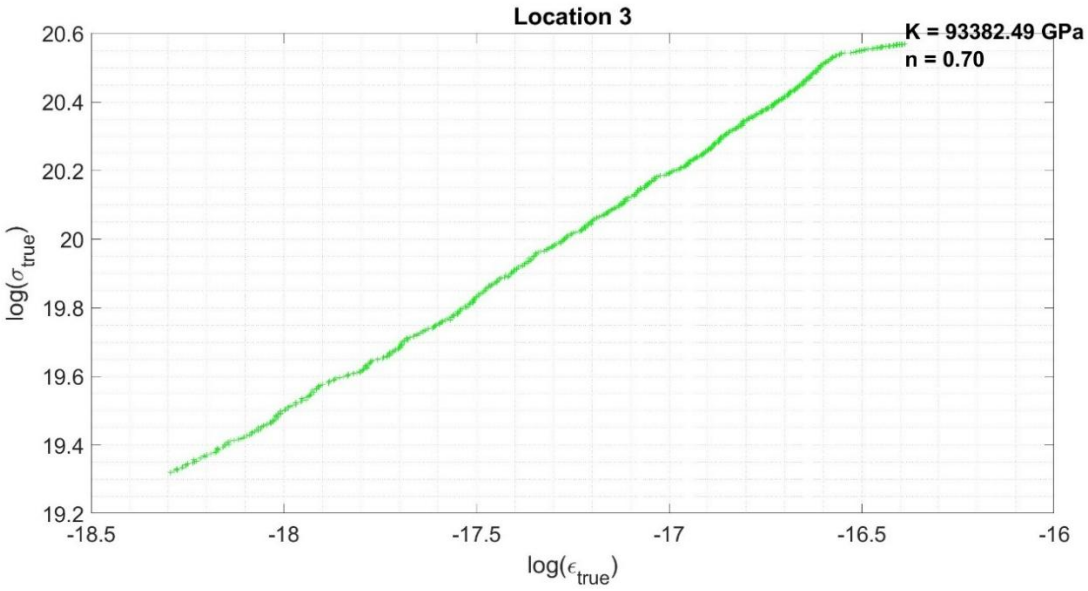


Figure 5.27: Logarithmic plot of true stress, σ_{true}, against true strain, ε_{true}, for location 1 of a 15 nominal bore (n.b.) tube sample ¤.

The plastic power law results for the three locations tested are shown in Table 5.5, and the engineering stress and strain predicted using the resultant laws are shown in Figure 5.28. Figure 5.28 shows that although the power law predictions are mathematically accurate, based on the nanoindentation acquired, they are not physically valid [456]. Furthermore, the nanoindentation equipment was restricted to ambient conditions. Therefore, data measured by Hidaka et al. [457] at $\boldsymbol{T}$ = 1000°C, i.e. a normalisation representative temperature, were used with values of 11.2MPa and 0.4 for the constants $\boldsymbol{K}$ and $\mathbf{n}$ respectively.

$$\bar{\sigma} = 11.2\bar{\varepsilon}^{0.4} = K\bar{\varepsilon}^{n}$$

Equation 5.29

Table 5.5: Plastic power law parameters (strength coefficient, $\boldsymbol{K}$, and strain hardening coefficient, $\boldsymbol{n}$) determined via nanoindentation at three locations along a 25mm length of 15 nominal bore (n.b.) tube sample.

Location	Strength coefficient, K (Pa)	Strain hardening coefficient, n
1	3.78×10^{14}	0.76
2	9.23×10^{13}	0.70
3	3.67×10^{13}	0.70

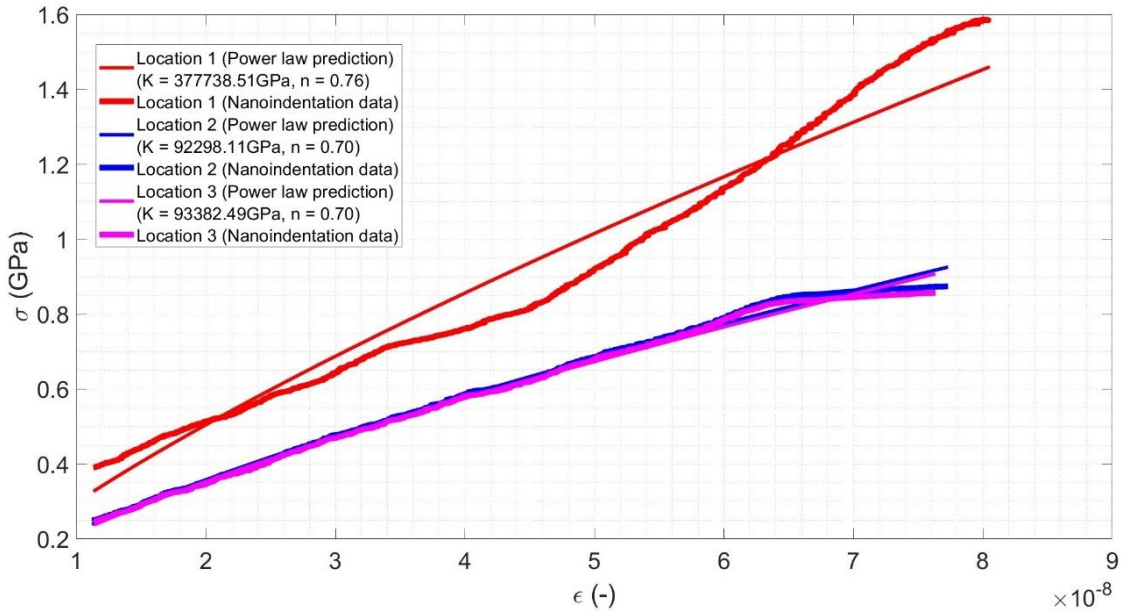


Figure 5.28: Plot of engineering stress, $\boldsymbol{\sigma}$, against engineering strain, $\boldsymbol{\varepsilon}$, for each location using the raw nanoindentation data and their respective power law prediction for three locations along a 25mm length of 15 nominal bore (n.b.) tube sample ¤.

Plots of the Install Plus® range ($3.2mm \leq \boldsymbol{y} \leq 5.4mm$, $7.5mm \leq \boldsymbol{\rho} \leq 77mm$) [2] revealed that both thick- and thin-walled conditions existed (see Figure 5.29). It should be noted that in the 'Industrial Test' case, a range of wall thicknesses were used so a blanket inner radius criterion could not be applied across the entire data set to denote the start and end of different stress model regions.

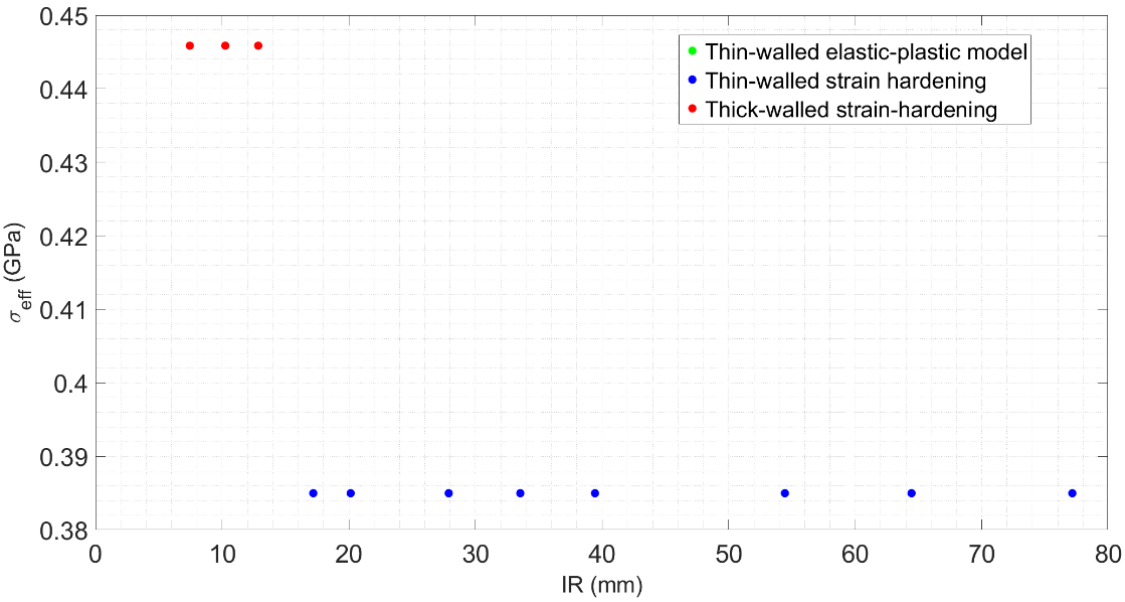


Figure 5.29: Plots of effective stress, $\boldsymbol{\sigma_{eff}}$, at the outer edge of tube wall using dimensions specified for heavyweight range of Install® 235 range. The transition from a thin-walled elastic-plastic to strain hardening model is observed at an inner radius, $\boldsymbol{IR}$, of approximately 15mm ¤.

However, in the radial dependency study, a standard wall thickness of 3mm was applied which allowed a critical radius for each stress model to be identified, also revealing a

correlation between the critical radius for flat plate-approaching oxidation kinetics during the Thermo-Calc© model radial dependency study and the points of stress model transition, thus further complicating oxide behaviour, especially adhesion, across the range of tubes manufactured by Tata (see Figure 5.30).

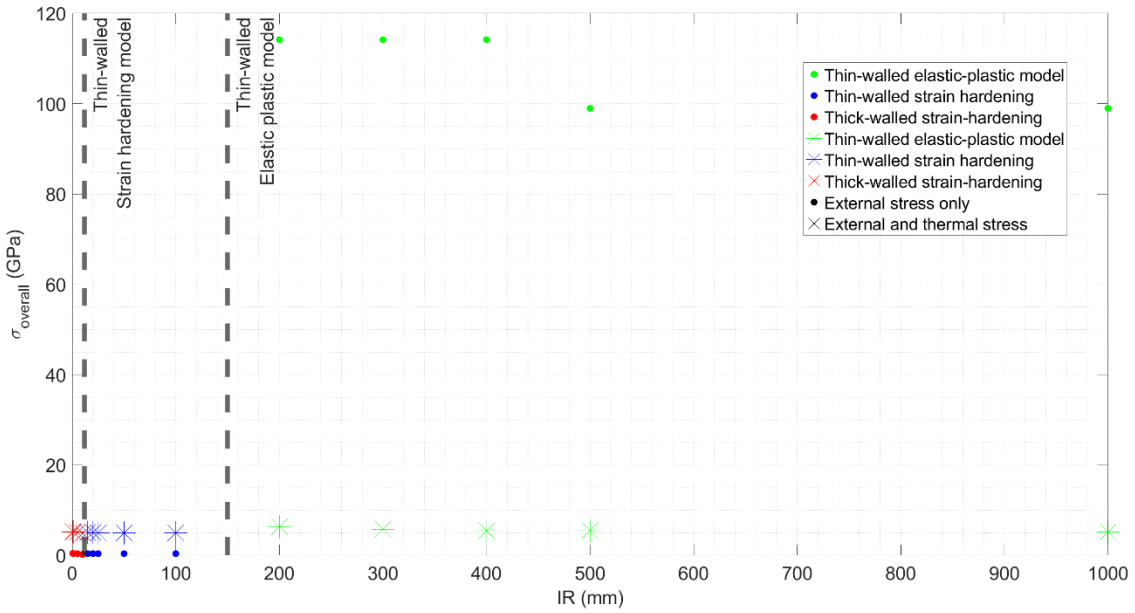


Figure 5.30: Plots of effective stress, σ_{eff}, at outer edge of tube wall using inner radii dimensions in the range 0.5-1000mm. The transition from a thin-walled elastic-plastic to strain hardening model is observed at an inner radius, IR, of approximately 15mm whilst further transition to a thick-walled, strain hardening model is observed at 200mm ¤.

One option for mechanical analysis of the oxide itself is to use the identical forming stress analysis i.e Equation 5.19 to Equation 5.22 to assess the its state purely from its being shaped into alignment with the cylindrical substrate profile. Pure beam bending theory also highlights how the centralised position of the neutral axis creates equal size outer and inner regions of tensile and compressive stress respectively [82].

5.1.4 Manufacturing-Induced Stress Evaluation and Overall Experimental Validation using X-ray Diffraction

Overall, using mechanical analysis of the steel, scale, or both, it is challenging to find an established approach which is representative of conveyance tube outer surface oxidation. X-ray diffraction (XRD)-based measurements of residual stress were used to evaluate the stress associated with pre-normalisation manufacturing operations (forming and welding), in addition to validation of the post-normalisation stress state of the steel and scale.

During this work, the Pulstec μ-X360n apparatus at the University of Bristol was used comprising a chromium Kα ($\lambda = 2.2897$ Å) X-ray tube and 0.5mm collimator. Before

taking any measurement, a stress-free iron reference sample was used to calibrate the X-ray machine. During all measurements, the XRD machine was positioned 39mm from the sample surface and held at an angle, ψ, of 35±5° relative to the measurement surface. Figure 5.25 shows how the samples were marked for measurement, with the 0° location for the angle, ω, set at the weld centre line (WCL).



Tube 1 (T1): As-welded condition, un-sectioned. Measurement taken at 71mm along tube length, 0° at the weld centre line (WCL).



Tube 2 (T2): Normalised via induction, un-sectioned. Measurement taken at 71mm along length, 0° at the weld centre line (WCL).



Tube 3 (T3): As-welded condition, sectioned. Measurement taken at 13mm along length, 0° at the weld centre line (WCL).



Tube 4 (T4): Normalised via induction, sectioned. Measurement taken at 13mm along length, 0° at the weld centre line (WCL).

Figure 5.31: Photographs of the four tube samples used during their mark-up stage (*Image taken by Chris Truman, University of Bristol*).



Figure 5.32: A photograph of the residual hoop stresses measured at 180° for T1 (*Image taken by Chris Truman, University of Bristol*).

Samples were measured under computer control to a depth of 10μm which is well within the thickness of oxide observed on normalised samples in Section 3.3. X-rays are exponentially attenuated by the sample material as soon as they are incident so the X-ray penetration depth is assumed to be where 63% of the reflection intensities originate from [287]. In the $\boldsymbol{cos\alpha}$ method, sample tilt, $\boldsymbol{\psi}$, and azimuthal, $\boldsymbol{\alpha}$, angle affect the penetration depth (for a given material and reflection angle). The measurement diameter on the surface was approximately 1.1mm. Each measurement provided a uniaxial measurement. For each site, two measurements were taken and a mean value calculated for each pair.

The technique uncertainty is dependent on the quality of the D-S ring and thus how the X-ray beam interacts with the sample's crystal structure. The D-S ring and residual stress peak for T1 is shown in Figure 5.33. Peak fitting followed a Lorentzian technique, suitable for symmetric deflections [458]. The D-S ring was divided into 500 points and each point is transformed into stress, to shift the D-S ring from its stress-free position, using Equation 2.16, Equation 2.17 and Equation 2.18. The mean result of all 500 points gives the final value for residual hoop and axial stresses, accompanied by their standard deviation. It is noted that there is some oscillation in the signal intensity around the D-S ring circumference which may be due to a minor preferential orientation in the random polycrystal structure of the oxide (see Figure 5.33) [287].

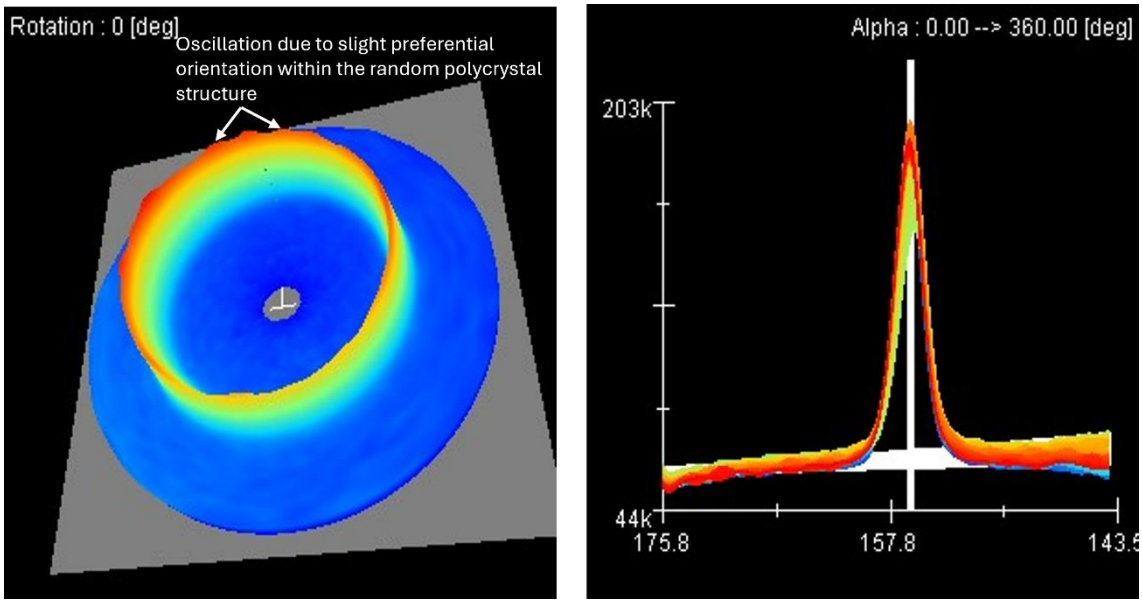


Figure 5.33: The diffraction Debye-Scherrer (D-S) ring (*left*) and peak at a diffraction angle at 156.396° (*right*) for the residual hoop stresses measured at (0°,71mm) on T1. (*Image generated by Chris Truman, University of Bristol*).

XRD was not only used to validate the stress state of the as-welded pipes, but also to obtain the lattice parameter, $\boldsymbol{\alpha}$, for corroboration with values used during temperature-dependent analysis of coefficient of thermal expansion. When a lattice parameter is used to predict a coefficient of thermal expansion which is expected to be more than $23.6 \times 10^{-6} K^{-1}$, as is the case for wüstite and steel (see Section 5.1.1), a maximum lattice parameter measurement accuracy of 0.06% is required [459].

Lattice parameter measurement is an indirect process which uses the sample's cubic structure [$\boldsymbol{hkl}$] and interplanar spacing, $\boldsymbol{d}$, to calculate lattice parameter (see Equation 5.30). It should be noted that since the Bragg equation (see Section 2.1.7) is used to calculate the interplanar spacing, the precision of the lattice parameter is dependent on $\boldsymbol{sin\theta}$ with the highest uncertainty for smallest angles (the Bragg angle in this case being $\boldsymbol{2\theta} = 156.396°$). During the experiments described in this work, the diffracted rays detected were emitted from the (211) atomic lattice plane. However, both the fact that a measurement was able to be taken from a mixed plane of odd and even Miller indices which added up to an even number, and the resulting calculation revealing a lattice parameter of 2.86Å, suggested that the inconsistent nature of the oxide adhesion meant that the ferritic steel substrate had been investigated (see Appendix 7).

$$\boldsymbol{a = d\sqrt{h^2 + k^2 + l^2}}$$

Equation 5.30

The tube, and its adhered oxide (an idealised assumption) is exposed to both mechanical loading and environmental stress during the manufacturing process. Figure 5.34 shows the results of the XRD analysis on the steel substrate. Although axial stress data is presented, hoop stress is the focus of discussion as using 2D model data assumes no axial stress in relation to the oxide.

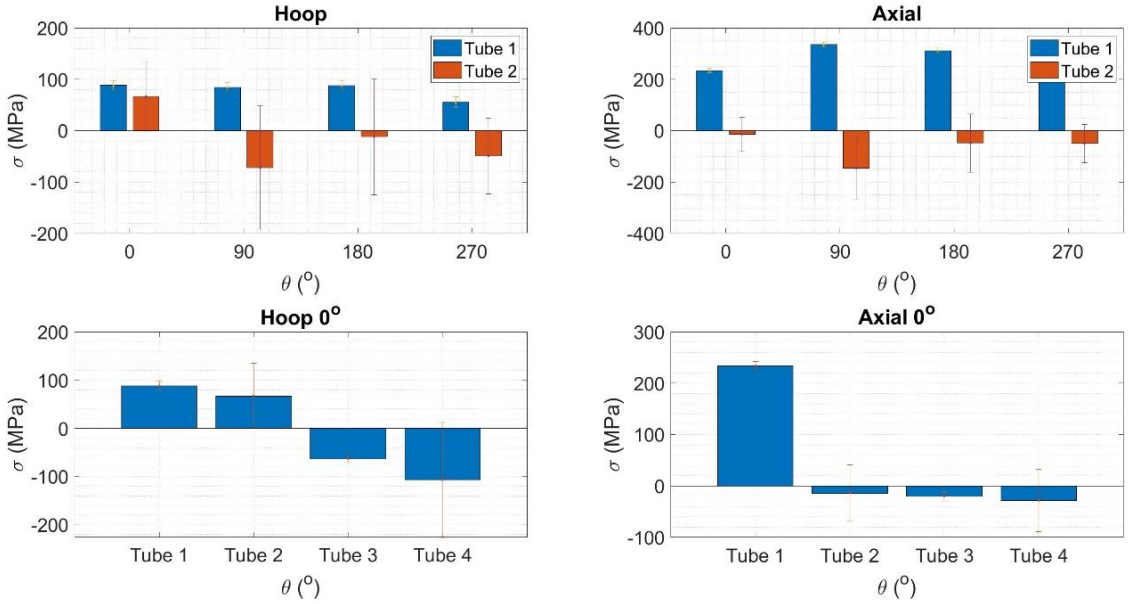


Figure 5.34: Hoop and axial stress, σ, state of full length (Tube 1 and Tube 2) and 25mm 15 nominal bore (n.b.) sectioned (Tube 3 and Tube 4) carbon steel conveyance tube samples before (Tube 1 and Tube 3) and after (Tube 2 and Tube 4) normalisation at weld (θ = 0°) and parent metal locations (θ = 90°, 180°, 270°) ¤.

The layer theory presented in Section 1.4.1 was used to plot the stress state of the oxide in Figure 5.35. The linear relationship between oxide and steel stress state in a multi-layer scenario (see Equation 2.25) means the trends are the same, but the stress observed in the steel is 1.4 times that of the oxide.

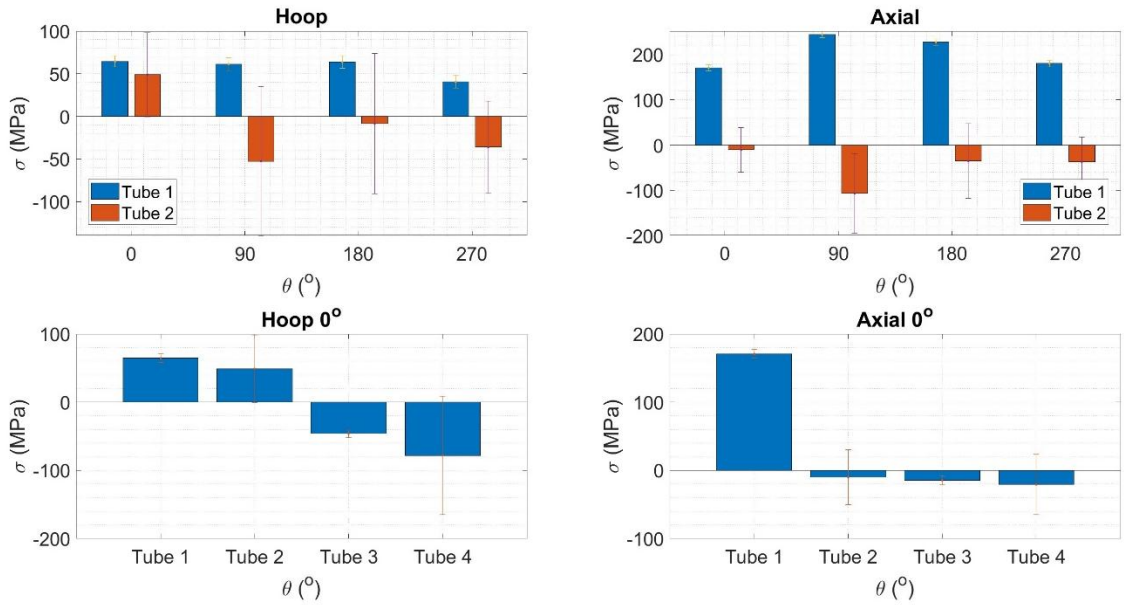


Figure 5.35: Hoop and axial stress, σ, state of full length (Tube 1 and Tube 2) and 25mm 15 n.b. sectioned (Tube 3 and Tube 4) for oxide scale found on carbon steel conveyance tube samples before (Tube 1 and Tube 3) and after (Tube 2 and Tube 4) normalisation at weld (θ = 0°) and parent metal locations (θ = 90°, 180°, 270°) ¤.

Figure 5.34 shows how there is an overall reduction in residual hoop and axial stresses following heat treatment and generally residual stress transitions from a tensile to compressive state for full length (T1 and T2) and sectioned (T3 and T4) tubes at weld (0°) and parent (90°, 180°, and 270°) locations (although for parent locations there is significant variability in residual stress measurements). There is an exception to this trend in that residual stress remains tensile on the full tube length after heat treatment for the weld location (0° on T1). Furthermore, for tubes which have been sectioned, their initial compressive stress state at the weld location is augmented by heat treatment, which suggests that, overall, a compressive stress is introduced by heat treatment which relieves residual stress. The magnitude of stress is always lower after heat treatment, regardless of tensile or compressive state. This is better visualised for both the steel (Figure 5.36) and oxide (Figure 5.37) using compass plots which give a clear indication of the overall reduction, to variable degrees, in stress around the tube circumference after heat treatment.

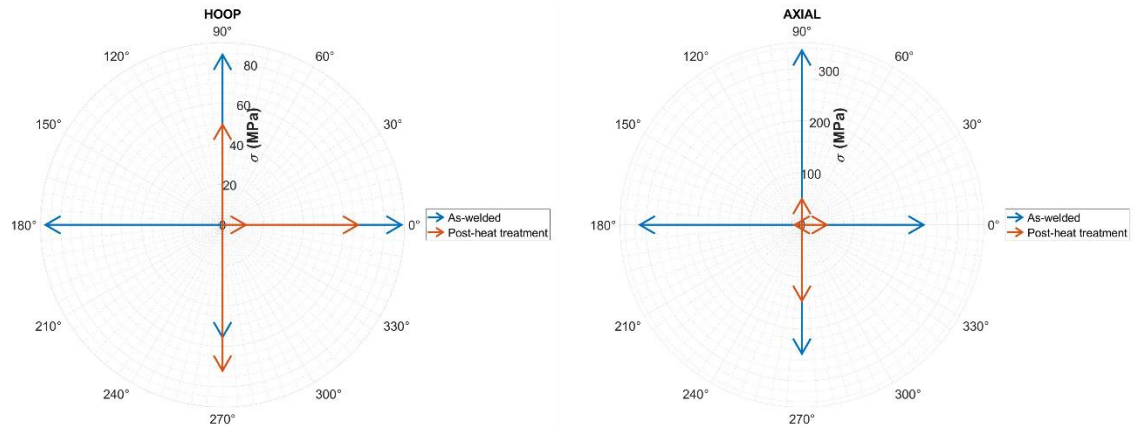


Figure 5.36: Compass plot of hoop (*left*) and axial (*right*) stress states in the steel substrate at various positions around the tube circumference, including the weld seam (0°) ¤.

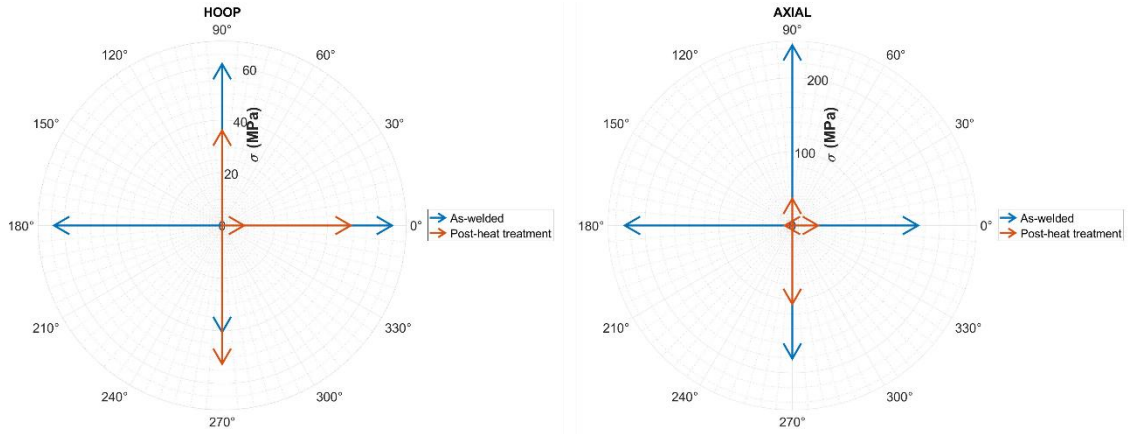


Figure 5.37: Compass plot of hoop (*left*) and axial (*right*) stress, σ, states in the oxide scale at various positions around the tube circumference, including the weld seam (θ = 0°) ¤.

As previously stated, the weld seam was aligned with the 0° position. Particular attention was devoted to this region and hoop and axial measurements taken for all four samples. Goviazin et al. proposed that the elastic residual stress in a tube 'slice' will be equivalent to the von Mises stress necessary to close a slitted ring and counteract the bidirectional (hoop and axial) stress applied during manufacturing [460]. However, this theory is limited to the assumption that a residual stress will arise from the forming operation necessary to form the ring geometry (estimated 100MPa) and makes no reference to the effect of sectioning from a parent tube to generate the rings, i.e. residual stress introduced by the cutting operation itself. It should be noted that the authors made no reference to the surface oxide they observed and its potential effects. Hence, it is anticipated that the residual stress in the sectioned sample in this project will be significantly larger than that predicted for a formed tube alone.

Conventional machining mechanics [461] concludes that the plastic deformation caused by the mechanical and thermal loading associated with cutting operations can manifest as

compressive and tensile, or only tensile residual stress on the workpiece surface layer respectively, which is the only region with the potential for plastic flow. Tensile stress in the machined surface arises due to the 'pull' experienced by the portion of a grain whose near-surface region has been pulled out parallel to the workpiece surface. This remaining portion which maintains connection with the rest of the material attempts contraction when released from the pull by chip breakage, but its maintained contact with the workpiece prevents complete contraction and tension is partially retained [462]. Thus, the tensile stress observed will be within range of the real tensile stress at break. Tata test reports state that the tensile strength of E41 is 383MPa, a value which can lie in the range 320-500MPa according to BS EN 10217-2 [4]. Henriksen highlighted how the hyperbolic stress profile associated with tangentially point loading an elastic, clamped workpiece leads to tensile and shearing stress which decrease in magnitude as the distance from the point load in the direction of cutting increases. Although stresses decrease as the tool (point load) moves away, permanent deformation means some stress is retained. Once the workpiece becomes unclamped, the elastic deformation which follows causes a rearrangement of stress and the residual tensile stress acts as an eccentric axial-compressive load causing axial compression and lateral bending. Henriksen considers residual stress from cutting as a surface tension per unit width acting as an axial load. In carbon steel, the residual tensile stress along the tool path dominates as almost exactly equates to the stress directly induced by cutting. It should also be noted that whilst thermal loading leads to approximately equal stress in all directions, this is not the case for mechanical loading, since grains are pulled out parallel to the workpiece surface, and hence tension is concluded to originate from mechanical distortion [462]. In particular, heterogeneous plastic deformation can result from thermal expansion and phase transformation (as previously discussed) [463]. Thermal stress is most influential at the beginning of cooling when critical phase transformation temperatures have not yet been reached.

In ductile materials such as a carbon steel, these highly concentrated residual stresses are usually tensile and exacerbated by an increase in carbon content and cutting speed, with the maximum stress at the workpiece surface [462]. The normal, $\boldsymbol{N}$, friction, $\boldsymbol{F}$, shear, $\boldsymbol{F_s}$, and normal-to-shear, $\boldsymbol{N_s}$, forces are defined according to the cutting, $\boldsymbol{F_c}$, and thrust forces, $\boldsymbol{F_t}$ and the rake (chip-workpiece interface to horizontal), $\boldsymbol{\alpha}$, and shear (chip-tool interface to normal), $\boldsymbol{\phi}$, angles [461]. As discussed by Shajan et al. [48], during their investigation of the residual stress condition of steel pipes manufactured by TSUK Tubes, the weld region (pre-

heat treatment) can be divided into multiple zones namely the fusion line (FL), coarse-grain HAZ (CG-HAZ), fine-grain HAZ (FG-HAZ), intercritical HAZ (I-HAZ), and bulk metal. There is an increasing presence of bainite as the fusion line is approached due to the higher rate of cooling in the weld as was observed in the microstructural imaging Chapter 4. In particular, it should be noted that Shajan et al.'s study used annealing (furnace-cooled) to heat treat as opposed to the normalisation (air-cooled) used by TSUK Tubes for the samples analysed so cooling will be faster and the presence of bainite will therefore be more influential. Bainite increases hardness and therefore the total force necessary to achieve cutting, imparting greater residual stress. Inconsistent distribution of bainite in the post-heat treatment parent metal could partially explain the low precision in residual stress measurements, as was observed by Shajan et al. [48]. They also concluded that tube manufacturing is heavily influenced by the localised straining of the parent metal due to the presence of hard phases, like bainite, at the weld. The effect of variable hardness phase distribution can also be exacerbated by the presence of discontinuous cooling, as was shown by Brunbauer et al. on seamless tubes [57]. They also showed that phase transformations may have a stepwise nature if cooling is not continuous, e.g. in between 'cooling baskets' a tube's cooling rate may be much faster if there is hydraulic descaling or a reheat period may be observed, and the effect of axial temperature gradient will vary depending on the length of the tube. This explains why lower axial stress magnitude is measured in T3 and T4 as they are comparatively short sections which would have had a negligible axial temperature gradient compared to the overall length of the manufactured parent hollow. Internal cooling can mitigate against radial temperature gradients to an extent, since phase transformation can proceed from both sides if they are simultaneously cooled, but the outer surface will still dominate due to its higher surface area and the resulting phase distribution will still be antisymmetric.

Some stresses can be relaxed if there are subsequent passes of seam welding which causes localised annealing but higher temperature materials have lower plastic limit so more likely to deform and introduce thermal expansion stress [464]. Figure 5.35 also demonstrates how the post-heat treatment stress, although not exclusively compressive, is always lower in magnitude than its pre-treatment counterpart, due to the residual stress relief reduction associated with heat treatment [464]. Shajan et al. attributed stress changes during tube processing to plastic deformation, solidification, and solid-state phase transformations and their associated volume changes [48]. The highest hoop stress (89MPa) is observed at the

weld location (0°) before heat treatment, and is higher than the parent metal residual (76MPa). It should be noted that whilst the parent metal stress value was based on an average of the three remaining locations, i.e. 90°, 180°, 270°, this has an implied assumption of a linear residual hoop stress around the tube wall section [13]. The stress difference was attributed to the addition of phase transformation [48] and oxide growth stress [117, 194] discussed in Section 5.1, to the existed residual stress evolved during forming [37, 64, 444]. This differs from previous works which assumed diffusionless phase transformations and therefore neglected the effect of oxide growth stress [57]. Although phase transformation is particularly important on the tube outer surfaces, where it begins due to thermal conduction from the furnace to the part (Brunbauer et al. measured a steep thermal gradient of a 10-fold temperature increase across the wall thickness of 12.65mm [57]) and forces competition between the heated austenitic and cooled martensitic regions, oxidation is arguably an important phenomenon to consider as volume expansion, also introduced by oxidation, plays a key role in the transition of stress state from tensile to compressive, also reflected in this data. Furthermore, the cooled surface experienced far greater compressive stress which decreased to zero before reaching a maximum of 200MPa tensile stress only 3mm from the outer surface. Shajan et al. also observed a higher stress in the weld metal (370MPa) than the parent (225MPa). Rozenbaum et al. observed a decrease in hoop stress of 30MPa after heat treatment [13], however, experimental results here exhibit a less consistent change. At the weld, there is a decrease of 22MPa after heat treatment, with the metal remaining in the tensile state. The decrease in hoop stress in the parent metal was less consistent at different locations, ranging from 99-156MPa, but significant enough in all cases to make the stress compressive. However, the validity of this conclusion is called into question by the exceptionally large standard deviations, observed due to the low precision for repeat measurements taken at the same location, which are larger than the magnitude of the stress measured and range into the tensile region. This trend in standard deviation is consistent for all stress measurements made on post-heat treatment samples. Although the typical uncertainty in XRD measurements of steel materials is ±30-50MPa, this will have been increased by the inherent roughness of the tube sample oxidised surface [287]. Furthermore, the peak fitting method has a significant impact on repeatability and the data discussed here were fitted using a Lorentzian function [286]. However, the National Physical Laboratory (NPL) suggests the Average Sliding Gravity, Pseudo-Voigt, and Sliding Gravity fit functions offer the best repeatability for materials, including steel [465].

Overall, the pre-normalisation hoop stress state of the tube at non-weld locations appears to be in reasonable agreement with the forming stress predicted in 5.1.4 using the oxide thickness gain data from the model. After normalisation, a forming stress of 100MPa is predicted and the stress measured by XRD at the location furthest from the weld (180°) lies within the 50MPa window of uncertainty.

5.2 Mapping Stress in the Oxide

Based on the mechanical analyses described in the previous two sections, the resultant stress in the oxide from thermal mismatching, growth, and manufacturing operations, can be determined. Using the parabolic rate coefficient derived from the model in Chapter 3, the oxide thickness after normalisation on a 15 n.b. conveyance tube is predicted to be 99.7μm. Table 5.6 outlines the hoop stress, σ_h, evolved in the oxide from each individual source for that oxide thickness. Individual and resultant stress values are used in the following chapter to apply an Advanced Oxide Scale Failure Diagram (AOSFD) to conveyance tube manufacturing scenarios.

Table 5.6: Hoop stress, σ_h, evolved in the oxide due to different stress sources during conveyance tube manufacturing.

Source	σ_h (GPa)
Thermal mismatching	-13.1
Growth	0.1
Manufacturing operations (forming and drawing)	0.1

5.3 Conclusions from Chapter 5

The continuous oxide thickness data, obtained from the cylindrical geometry model in the previous chapter, were used to evaluate stress from different sources during conveyance tube manufacturing. Namely, thermal mismatching, growth, and manufacturing operation-induced stresses. Crucially, the continuous data from the oxidation kinetics model offer a novel insight into the instantaneous mechanical state of a thickening oxide, in contrast to experimental data, obtained from techniques such as X-ray diffraction, which can only provide an insight into the post-formation mechanical state of the oxide.

The model proposed by Huntz and Schütze for thermal stress, which required several temperature-dependent functions for elastic modulus and linear coefficient of thermal expansion, was used to assess thermal mismatch stress. Data sets for temperature-dependent mechanical properties are limited, especially for the coefficient of thermal expansion, but a

function for coefficient of thermal expansion was derived using data for lattice parameter variation with temperature. This highlighted the significant difference in thermal expansion coefficient evolved during cooling, the effect of which is lost when the oxide stress state is only considered for an instantaneous temperature. The growth stress in the oxide was also evaluated using an appropriate analytical model. Further stress analysis included that associated with forming operations, specifically stretch drawing as the oxide 'stretches' outwards from the tube surface during growth. X-ray diffraction was used to provide validation of the overall stress state of the tube before and after normalisation, and measurement of oxide lattice parameter, although the technique was revealed to be limited to the steel substrate. Multi-layer stress transfer theory was therefore used to quantify the stress in the oxide under the same conditions.

The resultant stress state of the oxide following this analysis was -12.9GPa and dominated by thermal mismatching. The stress values derived in this chapter will be applied to an Advanced Oxide Scale Failure Diagram in the following chapter.

Chapter 6 Development of an Advanced Oxide Scale Failure Diagram

In Chapters 3 and 4, a kinetic model for oxidation on curved surfaces was developed using Thermo-Calc© and validated for a range of dimensions, including those of TSUK Tubes' conveyance tube products. In Chapter 5, the oxide thickness prediction data derived from the model were used to mechanically analyse the oxide before, during, and after conveyance tube normalisation and determine its resultant strain. The combination of oxide thickness and resultant strain is used in this chapter to develop an Advanced Oxide Scale Failure Diagram (AOSFD).

The AOSFD provides an instantaneous description of how likely certain oxide failure modes are for a given thickness of oxide, whilst accounting for all the influential parameters in the operation history of conveyance tube manufacturing. EPRI report FP 686 [411] outlines the types of mechanical oxide scale failure which results from exceeding a critical tensile or compressive stress in the scale via either fracture in tension modes (through-scale cracking, combined deflection and delamination) or fracture in compression (interfacial crack growth, buckling, crack deflection, spalling) modes. Oxide scale failure prediction depends on accurate descriptions of the main physical phenomena present in the oxide: stress-directed diffusion, fracture and adhesion, strain, strain rate, and temperature [84]. Generating an Advanced Oxide Scale Failure Diagram (AOSFD) depends on many parameters, and the relative 'impact' on scale failure must be assessed according to levels of influence on the plant operation parameters and their effect on scale properties via the termed 'operation history'. Operational strain, comprising external, thermal, intrinsic, and geometric growth sources, can be compared to the critical strains defined by each failure mode, which ultimately delineate between the regions of scale in its protective and various failure modes [186]. However, it should be noted that the oxide stress analysis previously discussed in Chapter 5 is not applicable to oxide on the inner surface and is less relevant as the crack tip blunting and crack closure phenomena associated with protective healing are beyond the scope of this project. The region of the research flowchart (Figure 1.33) under discussion in this chapter is shown in Figure 6.1.

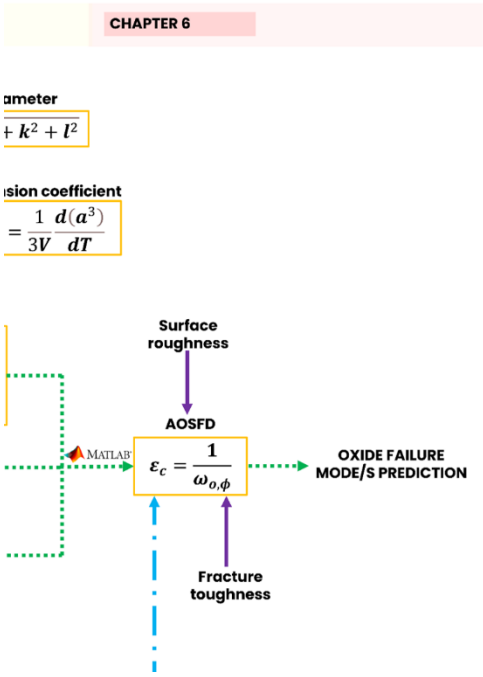


Figure 6.1: Region of the overall research flowchart (see Figure 1.33) which is under discussion in this chapter.

6.1 Oxide Scale Failure Diagram Development

The theoretical basis of an AOSFD was outlined in Section 1.6.2 and highlighted the need to select an appropriate level, (1, 2, 3…$\boldsymbol{n_{AOSFD}}$) of AOSFD to reflect the impact of relevant parameters. A higher level diagram is associated with a greater number of parameters with a high level of impact on scale failure probability and mode [186]. Poisson ratio is unlikely to change during conveyance tube manufacturing so is a low impact parameter favouring a Level 1 or 2 AOSFD. However, oxide scale fracture toughness will have temperature dependency since the tube normalisation temperature is above 600°C [186]. Chemical composition is less problematic if there is no oxide lattice structure or composition change but this is not the case during tube manufacturing where there is a heat treatment with a temperature high enough to cycle the steel between its ferritic (BCC) and austenitic (FCC) states [186]. Therefore, it becomes necessary to apply the full operation parameter ($\boldsymbol{\omega_0}$) concept and a level 3 AOSFD is required. Figure 6.2 shows the AOSFD for the standard 15 n.b. tube investigated in previous chapters with an outer diameter, $\boldsymbol{OD}$, of 21.9mm and wall thickness, $\boldsymbol{r_{wall}}$, of 3.0mm. Table 6.1 outlines the parameters used to develop a level 3 AOSFD for oxidation during conveyance tube manufacturing.

The through-scale cracking equation represents the depth of the defect, $\boldsymbol{c}$, so is analogous to the oxide thickness [128]. Murakami's stress intensity factor handbook was used to determine the necessary geometric values for "a circular ring with a radial crack under

external tension or internal pressure" [466]. To determine defect size, $\boldsymbol{a}$, the value was set at 10% of the instantaneous scale thickness, based on visible cracks during FEGSEM imaging. Since the geometric parameter is determined via an empirical graph relating the ratio $\frac{\boldsymbol{a}}{\boldsymbol{r_i}}$, and radial ratio, $\boldsymbol{\beta} = \frac{\boldsymbol{r_o}}{\boldsymbol{r_i}}$, the worst case scenario value was used, i.e. maximum geometric factor when $\boldsymbol{r_i}$ is minimised and the crack dimension, $\boldsymbol{a_c}$, is maximised (at maximum oxide thickness) where $\boldsymbol{r_o}$ is dependent on the instantaneous oxide thickness. Porosity volume fraction, $\boldsymbol{p}$, was set at 25% in line with a literature value [128]. The porosity volume fraction also contributes to the calculation, using Equation 1.28, of the high impact, temperature-dependent parameter elastic modulus, $\boldsymbol{E_{ox}}$, which was derived, along with Poisson's ratio, $\boldsymbol{v_{ox}}$, in Chapter 5 [77, 437, 438]. An estimate of radius of decohesion, $\boldsymbol{R_{dec,}}$ based on the work of Sabau et al. was applied based on tube geometry application at 2mm, which is less than the 15 nominal bore (n.b.) tube wall thickness, and therefore physically valid [193].

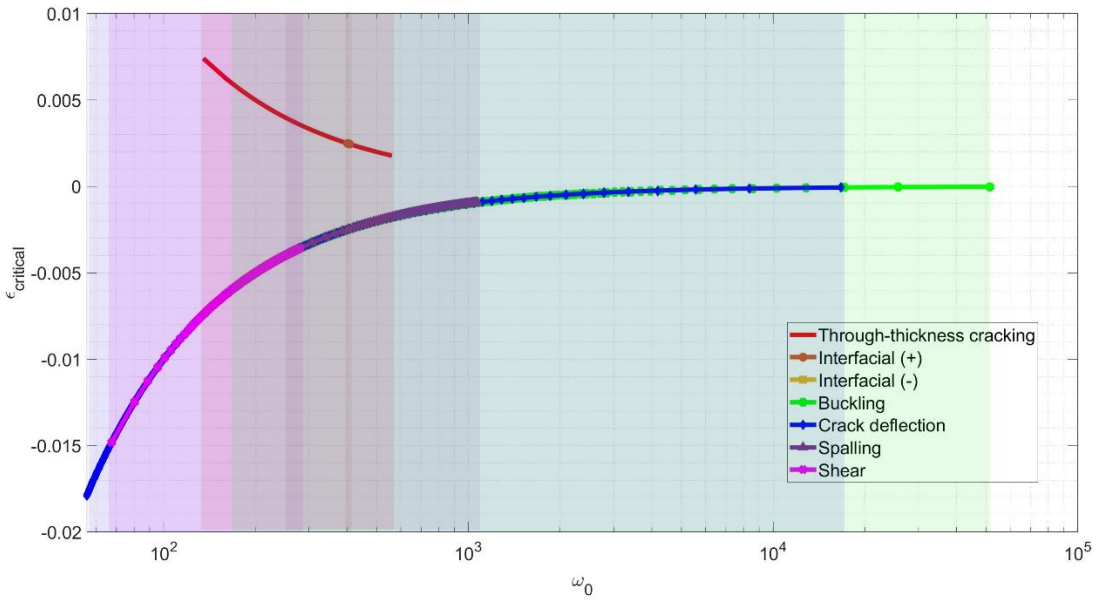


Figure 6.2: Advanced Oxide Scale Failure Diagram (critical failure strain, $\boldsymbol{\varepsilon_{critical}}$, against failure mode-based, $\boldsymbol{\phi}$, operation parameter, $\boldsymbol{\omega_{0,\phi}}$) for a 15 nominal bore (n.b.) conveyance tube after normalisation using the full range of oxide thicknesses predicted, heated for 22 hours at 1000°C, by the Thermo-Calc© model developed in Chapter 3 and Chapter 4 ¤.

Table 6.1: Definition of parameters used to construct an Advanced Oxide Scale Failure Diagram (AOSFD) for wüstite on a curved surface. Fields marked with an asterisk (*) are geometrically dependent and require revision if the tube sample is changed.

Parameter	Value (for wüstite on a curved surface)	Units
K_{Ic}	0.9	$MPa.\sqrt{m}$
f^*	0.95	-
c	$0.1\delta_{ox}$	m
E_{ox}	133	GPa
v_{ox}	0.36	-
δ_{ox}	≤200	μm
$R_{dec}{}^*$	2000	μm
γ_0	3	$\mathrm{J.m^{-2}}$
r	14.3μm	μm
λ	143μm	μm

It is noted that although a curved geometry is present, which will change the contact dimensions of the spalled section of oxide, the dimensions of the spalled section are negligible compared to the overall radius of the tube (<0.2% in the 15 n.b. tube case for mean oxide thickness, $\overline{\boldsymbol{\delta}}_{\boldsymbol{ox}}$, vs. inner radius, $\boldsymbol{IR}$, where the inner radius is 7.5mm). For example, even if the entire section of oxide visible in a x1000 magnification FEGSEM image were delaminated (which has not been observed to be the case in this work), the arc length, $\boldsymbol{L_{frame}}$, 116.8±3.4μm, for the sample shown in Figure 6.3, for a segment of that size would only subtend an angle, $\boldsymbol{\theta_{arc}}$, of 0.90±0.03° (see Figure 6.3). The calculations of the values in Table 6.2 are based on FEGSEM image analysis using Equation 6.1 [38] and Figure 6.3. The mean arc length of spalled oxide, $\boldsymbol{L_{spall}}$, based on measurements at locations A, B, and C, at equidistant distances around the sample shown in Figure 6.3, was 21.8±0.6μm, which is only a fifth of the mean arc length of oxide per microscope frame.

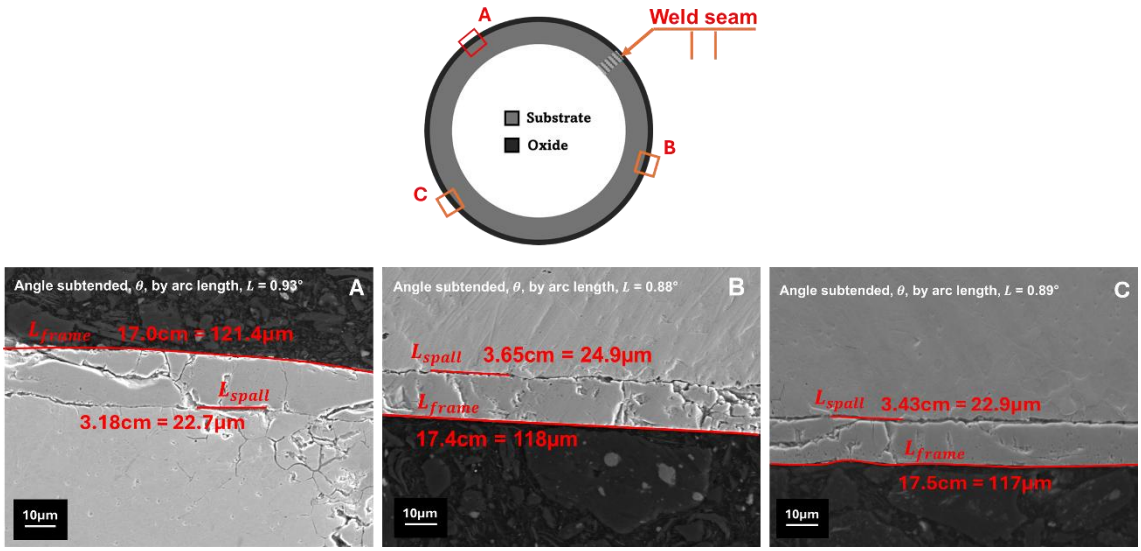


Figure 6.3: Measurement of typical radius of decohesion, R_{dec}, at three different circumferential locations on a 15 nominal bore (n.b.) post-normalised tube ¤.

Table 6.2: Arc length of spalled oxide, L_{spall}, measured on the outer edge of three 15 nominal bore (n.b.) conveyance tube samples normalised in industry (Tata Steel UK Ltd). The radius of decohesion, L_{spall}, is therefore 21.8±0.6µm. The ratio between the mean oxide thickness, δ_{ox}, are also presented to show the overall arc length of the oxide captured in the electron micrograph frame, L_{frame}, and the angle subtended, θ, by the total thickness of oxide captured in each frame.

Location	$\overline{\delta}_{ox}$ (µm)	$\frac{\overline{\delta}_{ox}}{IR}$	L_{frame} (µm)	θ_{arc} (°)	L_{spall} (µm)
A	16.6	0.002	121.4	0.93	22.7
B	14.5	0.002	115.6	0.89	21.6
C	13.5	0.002	113.3	0.87	21.2

$$\theta_{arc} = \frac{360L}{2\pi . IR}$$

Equation 6.1

Interfacial scale separation energy, γ_0, was calculated using first principles of Coulombic potential and crystal face orientation described by Robertson and Manning [188, 420]. Surface topography data were previously collected during previous White Light Interferometry (WLI) studies on tube-grade steels performed by Grant [9]. The full experimental details of WLI can be found in Chapter 2. Grant noted that previous research has shown that high temperature treatments can enhance surface roughness by several hundred percent, as discussed in Section 1.6.1 [64, 193, 467]. Oxide surface roughness length, λ, is typically 10 times the oxide roughness amplitude, r, for oxide formed on low carbon steel samples investigated by Noh et al. [65] and Lee et al. [64].

The Thermo-Calc© oxide kinetic model developed in Chapter 3 and Chapter 4 contributes at several stages of defining the AOSFD. The geometrical parameter, $\boldsymbol{f}^*$, is dependent on (i) the ratio of the defect size, $\boldsymbol{c}$, and SSI position and (ii) $\boldsymbol{\beta}$, the ratio of the SGI and SSI positions [466]. A methodology for calculating these positions was developed in Chapter 4. The scale thickness itself, $\boldsymbol{\delta_{ox}}$, with a normalising value, $\boldsymbol{\delta_{ox0} = 1\mu m}$, was also determined from the Thermo-Calc© model data [186]. Finally, mode I fracture toughness, $\boldsymbol{K_{IC}}$, is a material constant quoted from the literature [84, 188]. The operation parameter, $\boldsymbol{\omega_{0,\phi}}$, which is specific to failure mode, $\boldsymbol{\phi}$, as defined in Section 1.6.2, and encompasses the complete oxide thickness gain, $\boldsymbol{\delta_{ox}}$, dataset when the 15 n.b. tube was heated to 1000°C for 22 hours (the maximum period before the entire tube wall thickness of steel was consumed) [186]. For most failure modes, an increase in the operation parameter (by only increasing oxide thickness) leads to a decrease in the critical failure strain. Buckling and crack deflection are an exception to this trend as the reciprocal nature of the oxide thickness term $\left(\frac{\mathbf{1}}{\boldsymbol{\delta_{ox}}^{\mathbf{2}}}\right)$ in their governing equation means that the greatest value of operation parameter is associated with the thinnest oxide (see Equation 1.21). The mathematical trend in critical failure strain change is dependent on the failure mode and its associated governing equation but for all failure modes the majority of change in critical failure strain occurs at $\boldsymbol{\omega_{0,\phi}} \leq 100$. Figure 6.4 plots the same critical strain values against only oxide thickness gain highlights the same trends. Figure 6.5 highlights how even by constraining the thickness to only the extent grown during normalisation, i.e. maximum 4 minutes of heating at 1000°C, very low critical failure strains are predicted for buckling and/or crack deflection failure. This is again due to the exceptional nature of Equation 1.21 which predicts a higher critical failure strain for thinner scales, in direct contrast to all other failure modes. However, all interpretations of the data (Figure 6.2, Figure 6.4, and Figure 6.5) highlight how the probability of oxide failure increases dramatically during the first 5 mins of normalisation as the critical failure strain in most failure modes decreases rapidly. Conversely, the probability of oxide failure by buckling and/or deflection is highest when the oxide is thinnest.

Figure 6.4 also shows how the datasets for each failure mode vary greatly in range for both critical failure strain and operation parameter. The governing equations for the operation parameter, and subsequently critical failure strain, of each failure mode (see Section 1.6.2) are independent of each other and dependent on different mechanical parameters in addition to oxide thickness. Not only is a mathematical operation applied to oxide thickness

data to obtain the abscissa but also the ordinate value range. Each equation varies in terms of the mathematical operation applied to oxide thickness, e.g. raised to a half power for interfacial cracking (see Equation 1.23) vs. the reciprocal of its square for buckling and crack deflection (see Equation 1.21). Hence, even for the same range of oxide thicknesses assessed, each failure mode analysis will map the operation parameter on to the critical failure strain in a different manner. For assessing only the effect of oxide thickness on critical failure strain, as opposed to the overall state of scale after conveyance tube manufacturing, the critical failure strain is plotted against only its corresponding oxide thickness (see Figure 6.5). Clearly, the most comprehensive study would investigate the relationship between oxide thickness and every other parameter used in each failure mode assessment. However, obtaining data sets for such a wide range of parameters is beyond the scope of this project and less industrially relevant.

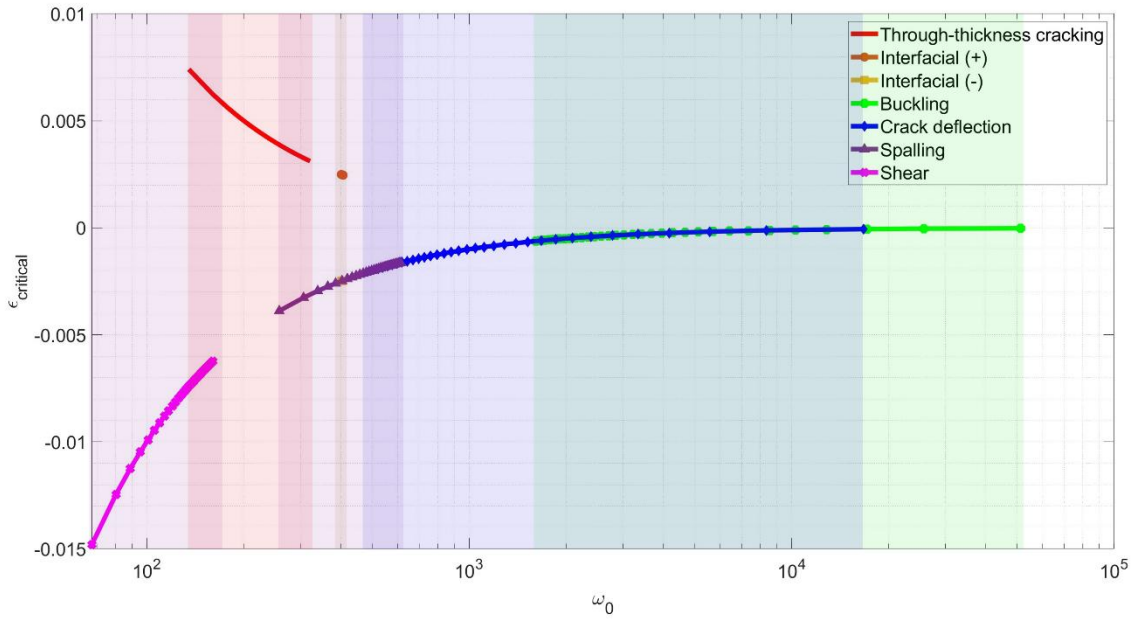


Figure 6.4: Plot of critical failure strain, $\varepsilon_{critical}$, against failure mode-based, ϕ, operation parameter, $\omega_{0,\phi}$) for a 15 nominal bore (n.b.) conveyance tube after normalisation up to the oxide thickness gain associated with normalisation heat treatment (99.7µm after 4 mins) predicted, at 1000°C, by the Thermo-Calc© model developed in Chapter 3 and Chapter 4 ¤.

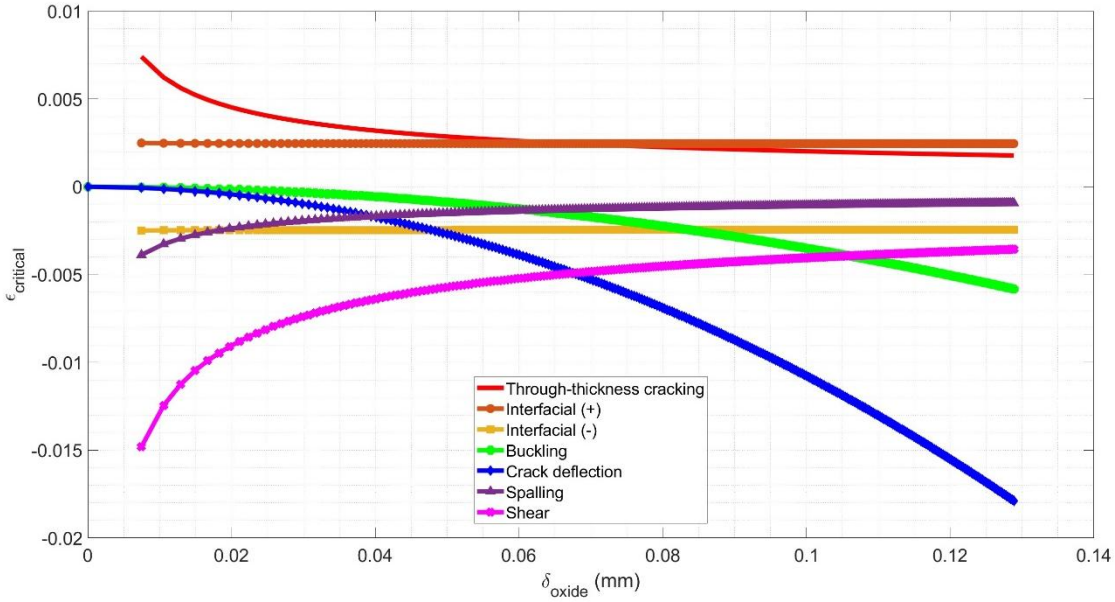


Figure 6.5: Plot of critical failure strain, $\varepsilon_{critical}$, against oxide thickness, δ_{ox}, for a 15 nominal bore (n.b.) conveyance tube after normalisation up to the oxide thickness gain associated with normalisation heat treatment (99.7µm after 4 mins) predicted, at 1000°C, by the Thermo-Calc© model developed in Chapter 3 and Chapter 4 ¤.

Aside from general trends concerning how the likelihood of failure changes as oxidation proceeds, the AOSFD can also offer insight into the effect of changes in oxide stress state, due to manufacturing operation history changes, on the likelihood and mode of failure.

6.2 Application of the Advanced Oxide Scale Failure Diagram

6.2.1 Case Study: Tube Oxidation and the Transition to Induction Heating Technology

The physical principles behind induction heating were covered in Section 1.2, where the environmental and economic advantages of a high power density and carbon-free heating technology were explored. Table 6.3 shows the various stresses evolved via the oxidation- and manufacturing-related sources described and analysed in Chapter 5, which have been converted to strain using Equation 5.17 and the values of 130GPa and 0.36 for the ambient elastic modulus, $\boldsymbol{E}$, and Poisson ratio, $\boldsymbol{\upsilon}$, respectively. For the induction heating case, $\boldsymbol{\sigma_{ind}}$, the thermal component has been replaced with the 100MPa limit reported by Drobenko et al. using current frequency control [161]. Overall, the compressive thermal stress observed is due to the higher coefficient of thermal expansion of the steel substrate, allowing it to contract a greater rate and place any adhered oxide under compression. In contrast, the tensile nature of the oxide growth stress reflects the formation of new oxide underneath the existing surface oxide as the oxidation reaction proceeds. Manufacturing-induced stress was

evaluated using the X-ray diffraction (XRD) data from pre-normalised samples discussed in Chapter 5 since the analytical forming stress assessment presented in the same chapter does not account for the effect of the stretch forming operations within conveyance tube manufacturing. Using linear superposition [468], the resultant strain in the oxide can be calculated to be -0.0948 and 0.0032 for the gas-barrel and induction heating cases respectively. These values are used in the AOSFD.

Table 6.3: Comparison of gas-barrel ('gas') and ('ind') and induction heating methods for normalisation in terms of their effect on stress, $\boldsymbol{\sigma}$, and strain, $\boldsymbol{\varepsilon}$, components evolved from oxidation- (thermal and growth) and manufacturing- (forming and drawing) related sources.

Stress Source		σ_{gas} (GPa)	σ_{ind} (GPa)	ε_{gas} (-)	ε_{ind} (-)
Oxidation-induced	Thermal	-13.11	-0.10	-0.0988	-0.0008
	Growth	0.62	0.62	0.0047	0.0047
Manufacturing-induced	Forming	-0.09	-0.09	-0.0007	-0.0007
	Drawing				

Applying Strain Data to the AOSFD

The computational oxide thickness gain data obtained in Chapter 4 for a 15 n.b. sample, and its derived parabolic rate coefficient, can be used to predict the exact oxide thickness (using Equation 1.7), due to its continuous nature, after the average normalisation soak time, 180s. As a result a 1s resolution is sufficient for this application where heating periods are at least minutes, or often hours, long. Linear interpolation was used, with a window of 3 datapoints, to increase the resolution of the steel-scale interface position where a mathematical description was not possible [297]. This increased resolution data set can also be used to improve the AOSFD. It should be noted that any investigations involving numerical integration of the thermal stress function, discussed in Chapter 5, are limited to the maximum array size of 7.7GB [469]. For example, when using computational oxide thickness gain data from a 24 hr period, the 85680x85680 matrix is too large to solve at 54.7GB in MATLAB R2024b.

The oxide thickness gain predicted by the Thermo-Calc© model after 180s at 1000°C is 99.7μm. Figure 6.6 demonstrates how an AOSFD can be used to predict how this specific oxide thickness is likely to fail after gas-barrel vs. induction heating. Crucially, the transition from gas-barrel to induction heating, and the increased process control associated with the latter technique, leads to a transition in the oxide from a compressive to tensile state, as well as a 30-fold decrease in strain magnitude (see Figure 6.6). As a result,

compressive failure modes like spalling and through-thickness cracking are eliminated and replaced by interfacial cracking. Spalling, through-thickness cracking, and interfacial failure modes were observed in the pre- and post-normalised samples presented in Chapter 4. Although, changes to oxide failure mode can be correctly attributed to temperature, as was seen in the work of Krzyzanowski and Beynon [77], the use of the AOSFD in this way highlights the importance of considering the effect of mechanical phenomena. As previously discussed, the conveyance tube manufacturing process is short and fast with a high feed rate. Hence, high levels of thermomechanical stress are expected and should be considered in parallel when attempting to proactively control scale. The AOSFD offers additional mechanical insight based on the kinetic data and allows for a degree of this parallel consideration.

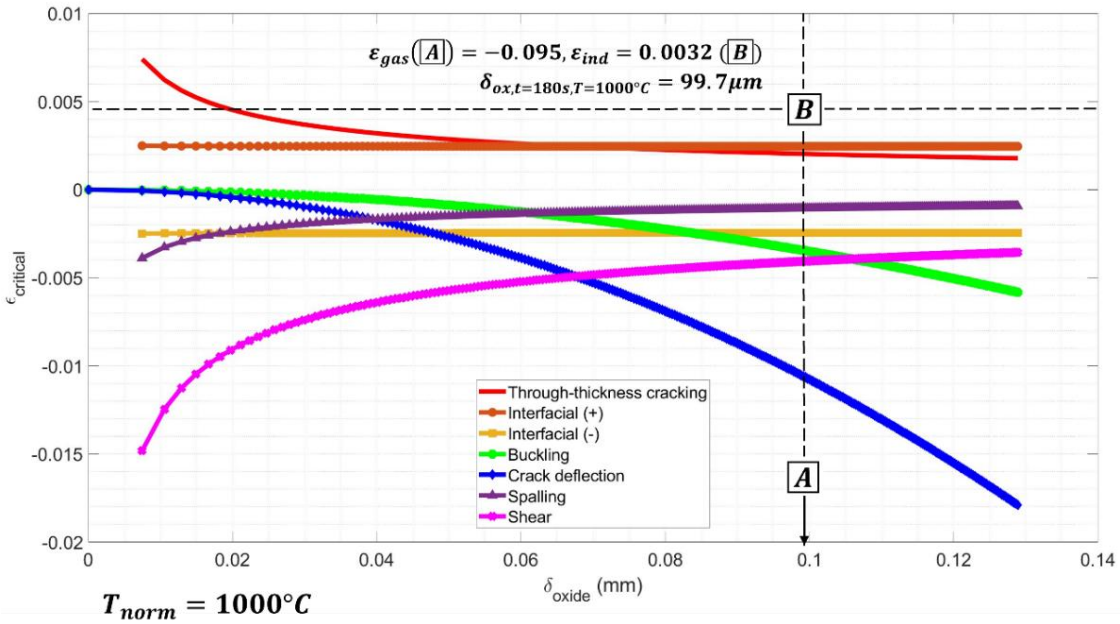


Figure 6.6: Advanced Oxide Scale Failure Diagram (Plot of critical failure strain, $\varepsilon_{critical}$, against oxide thickness, δ_{ox},) for a 15 nominal bore (n.b.) conveyance tube normalised at 1000°C (T_{norm}) for 3 mins, forming 99.7µm of oxide. For identical thermal conditions, 'A' represents the resultant strain for 99.7µm of gas-barrel furnace-grown oxide, while 'B' represents the resultant strain for 99.7µm of induction-grown oxide. For accessibility, each failure mode boundary is denoted by both colour and symbols indicating their start and end datapoint ¤.

As previously discussed, the critical strains calculated for each failure mode account for the entire operation parameter history during the formation of a specific thickness of oxide scale. Table 6.4 presents the critical strains for each failure mode for a ~100µm scale when strain is at the level associated with gas-barrel vs. induction heating. This serves to further highlight how certain failure modes, namely shear, buckling, and crack deflection, are eliminated by transitioning to fully induction-based heating technology.

Table 6.4: Comparison of strain, $\boldsymbol{\varepsilon}$, evolved in a ~100μm oxide scale formed using normalisation with gas-barrel ('gas') vs. induction ('ind') heating, to critical strain ('crit') for each potential failure mode.

Failure Mode	ε_{crit} (-)	$\varepsilon_{gas} \geq \varepsilon_{crit}$? ($\varepsilon_{gas}$ = -0.0948)	$\varepsilon_{ind} \geq \varepsilon_{crit}$? ($\varepsilon_{ind}$ = 0.0032)
Buckling	-0.0035	✓	x
Crack deflection	-0.0107	✓	x
Interfacial cracking *(Tensile or compressive)*	-0.0025	✓	N/A
	0.0025	N/A	✓
Shear	-0.0041	✓	x
Spalling	-0.0011	✓	✓
Through-thickness cracking	0.0020	✓	✓

6.2.2 The Effect of Normalisation Temperature Control During Induction Heating

As previously demonstrated, the implementation of fully induction-based heating technology offers greater manufacturing control and the opportunity to proactively manage scale kinetics and adhesion via increased heating speed and electromagnetic operation parameter adjustment respectively. Consequently, the success of induction heating as a technique depends on strategic selection of the combination of coil structure, current levels, and heating times, especially in the case of curved geometries where these parameters will be dependent on cross-sectional profile consistency and curvature radius [160]. Good heating efficiency is essential to maximise heat dispersion and prevent temperature overshoot in certain regions of the tube [159]. In the initial stages of implementation of induction technology, temperature control must be investigated to mitigate against the risk of workpiece overheating. The low carbon region (≤0.2wt%) [165] of the Fe-C phase diagram, derived using Thermo-Calc©, can be used to identify the melting point of the steel at 1475°C for 0.12wt% C (see Figure 1.2) with the latter value selected based on the cast analysis results discussed in Chapter 3. This temperature is still within the upper temperature limits of the data used to develop the thermodynamic and kinetic databases also described in Chapter 3. The model was therefore employed for a normalisation temperature, $\boldsymbol{T_{norm}}$, range of 1000-1400°C, in 100°C intervals, to evaluate the potential effect of normalisation temperature overshoot by induction heating on oxide kinetics and adhesion. From inspection of Figure 1.2 the austenitic region encompasses the entire temperature range investigated, and the validity of the model is not undermined. However, the increased

rate of oxidation associated with higher temperatures (see Section 1.3) is a significant enough change, combined with a comparatively low wall thickness of 3mm, that the total normalisation temperature soak time was decreased to ensure the substrate material was not used up before the end of the soak period leading to simulation failure. However, in all cases the simulation could still be run for long enough to obtain sufficient data points to accurately assess parabolic rate coefficient, k_p, based on gradient and maintain a constant time step size. Table 6.5 shows the maximum soak time, $t_{norm,max}$, possible for at each temperature (1000-1400°C), T_{norm}, and the associated number of datapoints, $N_{datapoint}$, before the steel substrate was completely consumed at t_{fail}.

Table 6.5: Time, t_{fail}, and number of datapoints, $N_{datapoint}$, at which the Thermo-Calc© oxide kinetic model failed for each temperature, T_{norm}, due to complete consumption of the steel substrate. The maximum soak time for each temperature before complete consumption of the substrate, $t_{soak,max}$, is also shown.

T_{norm} (°C)	t_{fail} (hrs)	$N_{datapoint}$ (-)	$t_{soak,max}$ (hrs)
1000	-	121	24
1100	-	121	24
1200	15.1	88	15
1300	8.5	63	8
1400	5.2	52	5

The data for a typical five minute normalisation soak time, $t_{norm,min}$, were used for all analyses below. Figure 6.7 shows that, for a constant tube geometry, an increase in normalisation temperature, T_{norm}, will cause a linear increase in oxide thickness (see Equation 1.7). The same is true for the mass-, $k_{p,mass}$, and thickness-, $k_{p,thickness}$, based parabolic rate coefficients, which follow the Arrhenius-type exponential increase described by Equation 1.8 (see Figure 6.8 and Figure 6.9). This supports the physical validity of the Thermo-Calc© model, as it is originally numerically derived from a diffusion-based PDE (see Equation 1.30) but still agrees with typical analytical temperature trends for oxide kinetics.

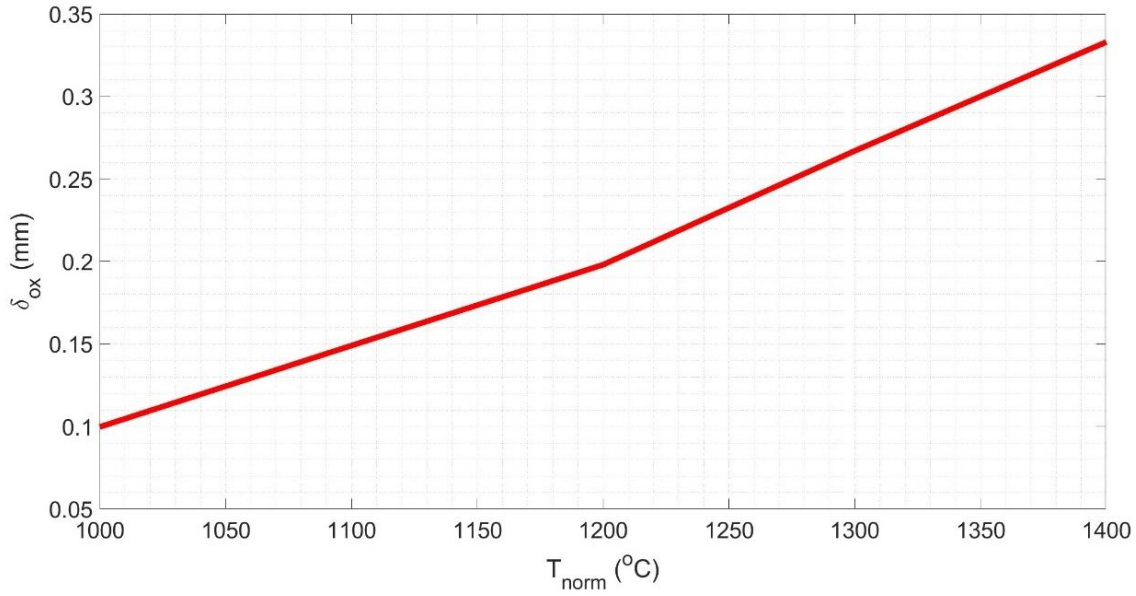


Figure 6.7: Plot of oxide thickness, δ_{ox}, against normalisation temperature, T_{norm}, for a 15 nominal bore (n.b.) conveyance tube normalised at 1000°C for 3 mins ¤.

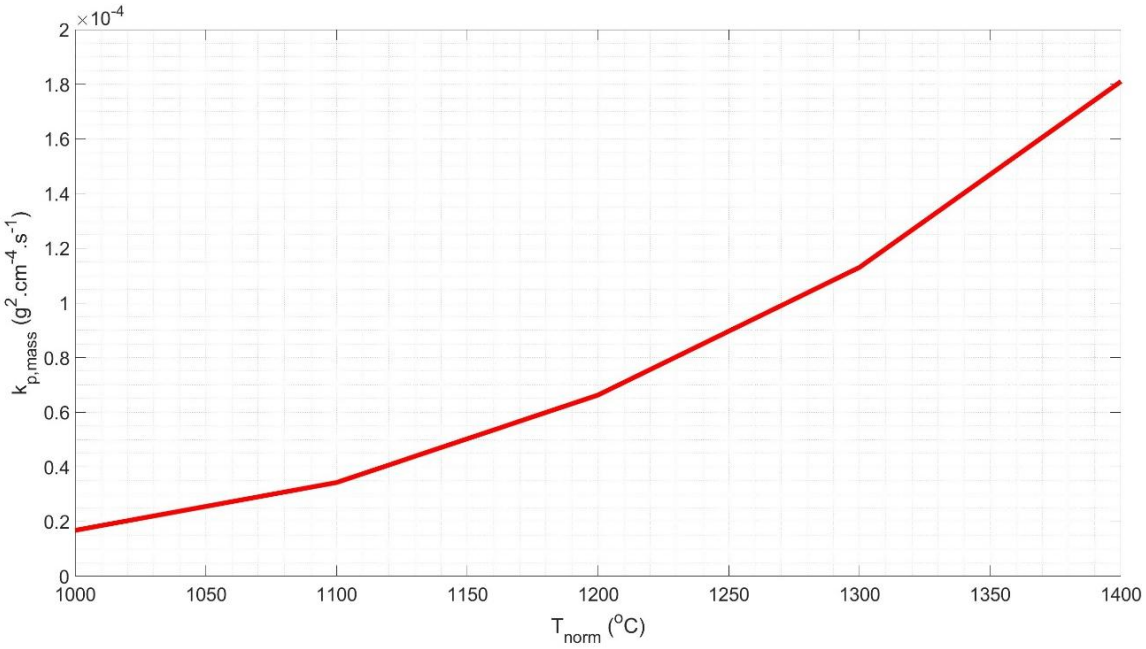


Figure 6.8: Plot of mass-based parabolic rate coefficient, $k_{p,mass}$, against normalisation temperature, T_{norm}, for a 15 nominal bore (n.b.) conveyance tube normalised at 1000°C for 3 mins ¤.

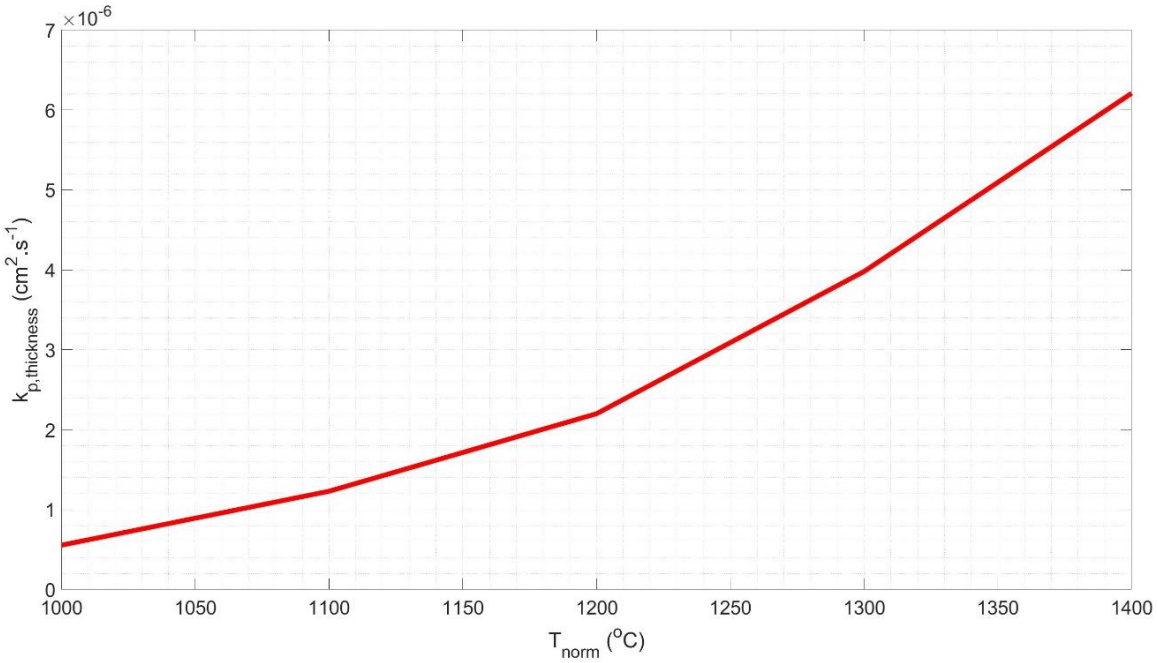


Figure 6.9: Plot of thickness-based parabolic rate coefficient, $k_{p,thickness}$, against normalisation temperature, T_{norm}, for a 15 nominal bore (n.b.) conveyance tube normalised at 1000°C for 3 mins ¤.

In the case of gas-barrel heating, there is an overall linear decrease in compressive thermal strain magnitude associated with an increase in temperature (and therefore oxide thickness) (see Figure 6.10). At 1400°C, there is an exception to this trend as strain increases. This temperatures lies on the upper bound of validity of expressions for expressions of elastic modulus [437] and linear coefficient of thermal expansion [338]. Anderson concluded that Wachtman's equation (see Equation 5.2) for the temperature dependence of elastic modulus is only valid when the variation of Poisson ratio with temperature is negligible [431]. Vigilante et al. measured the variation in Poisson ratio of steel over a temperature range of 25-400°C and observed a less than 0.1 change in Poisson ratio [470]. However, extrapolation of the linear trend observed would lead to a physically invalid value of Poisson ratio at temperatures >1000°C and indicates that there is a different relationship for temperature and Poisson ratio in this temperature range. However, assuming a general decrease with increasing temperature, based on Vigilante et al.'s work [470], a decrease in Poisson ratio would cause an overall decrease in lateral strain magnitude [468]. Furthermore, a decrease in Poisson ratio would have the inverse effect on thermal stress and increase its magnitude (see Equation 5.1). Additionally, the rate of increase in the linear coefficient of thermal expansion shows an anomalous acceleration at temperatures close to its melting point. Drebushchak attributed this to the increase in mean interatomic distance at higher temperatures, compared to changes at lower temperatures even with same energy change

[433]. Hence, the difference between the linear coefficient of thermal expansion between the metal and oxide is expected to increase, and overall increase the magnitude of stress in the oxide due to thermal expansion mismatching.

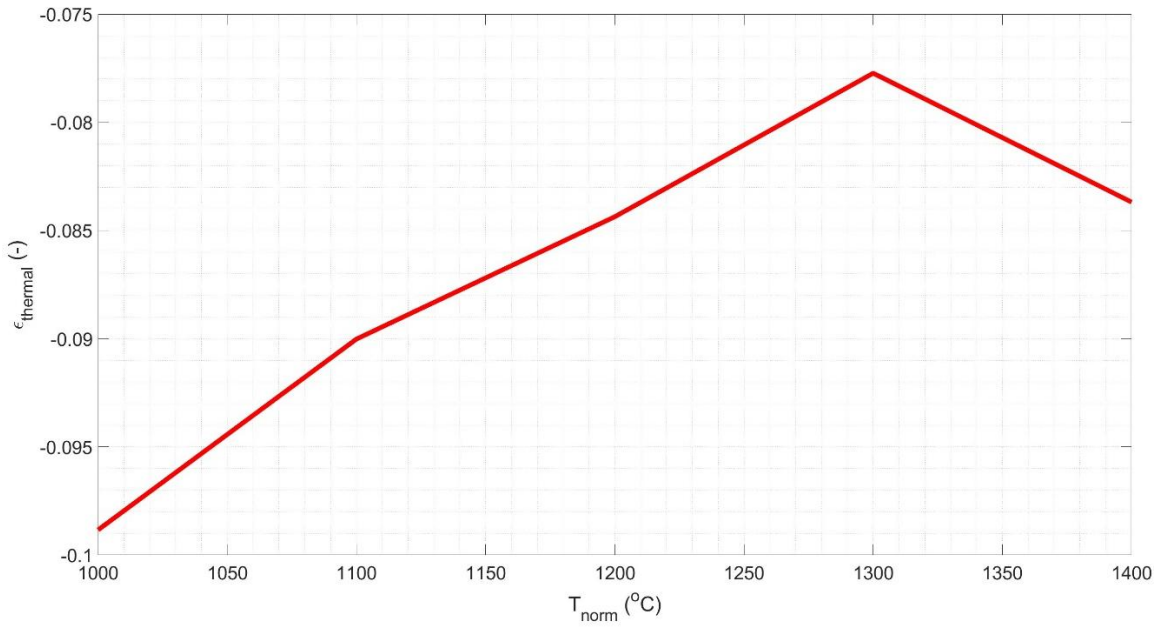


Figure 6.10: Plot of thermal strain, $\varepsilon_{thermal}$, against normalisation temperature, T_{norm}, for a 15 nominal bore (n.b.) conveyance tube normalised at 1000°C for 3 mins ¤.

Similarly, growth strain increases linearly with temperature and oxide thickness but does not display an anomaly at 1400°C (see Figure 6.11). Growth stress is calculated based on ambient temperature values of elastic modulus and does not depend on Poisson ratio or the linear coefficient of thermal expansion. Therefore, the observation in Figure 6.11 supports the hypothesis that the anomalous increase in thermal stress at high temperatures is due to the limits of the validity of expressions for temperature-dependent mechanical properties at high temperatures. Interestingly, a three times thicker scale, obtained by increasing normalisation temperature by 400°C, leads to a two-fold increase in growth strain. This is greater than the change elicited in thermal strain by the same temperature and oxide thickness increase, at a factor of only 1.2.

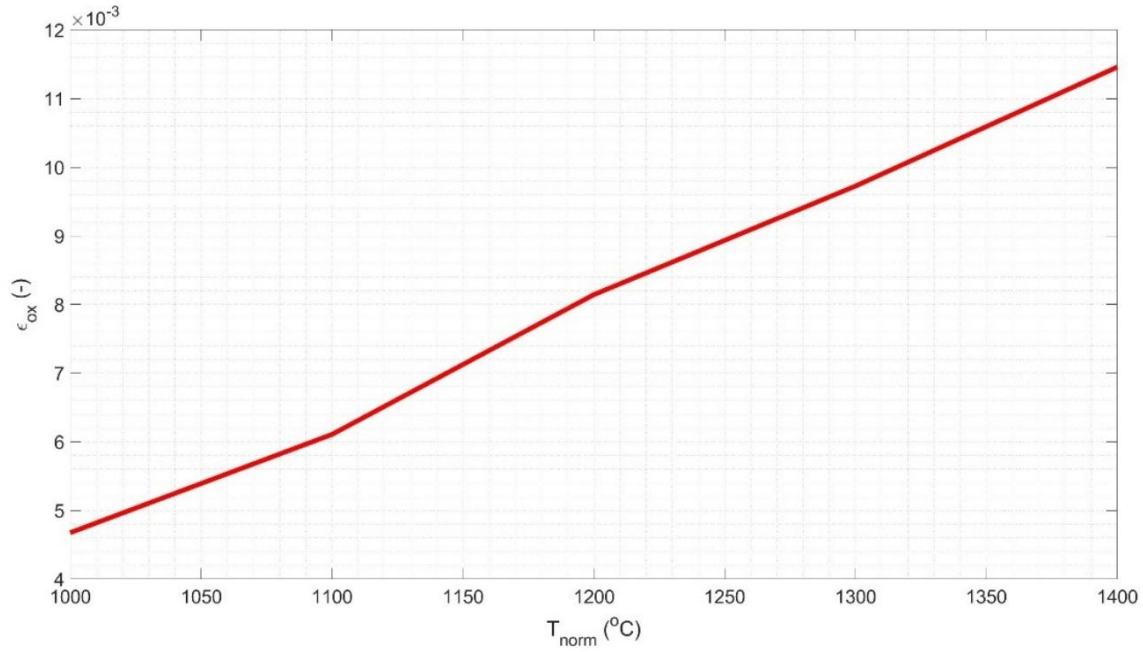


Figure 6.11: Plot of growth strain, ε_{ox}, against normalisation temperature, T_{norm}, for a 15 nominal bore (n.b.) conveyance tube normalised at 1000°C for 3 mins ¤.

Figure 6.12 highlights how an increase in normalisation temperature leads to an increase in the contribution of tensile strain to the overall state of the oxide, regardless of whether it was formed under gas-barrel or induction heating technology. However, the thermal stress can be maintained at a constant value by appropriate current frequency control, thus reducing its compressive contribution and making the overall stress state tensile. Where the gas-barrel grown oxide is in an overall compressive state, the effect of the increase in temperature within the two heating techniques has opposing effects. The introduction of additional tensile growth stress, and oxide thickness which increases the critical failure strain for each mode, serves to decrease the strain magnitude in the gas-barrel grown oxide, to the extent that the AOSFD shows that beyond 1300°C the strain is low enough to eliminate failure by crack deflection. In contrast, although the absence of any increase in thermal stress, via operational control, limits the overall strain magnitude increase, the introduction of additional tensile growth strain increases the overall strain magnitude and makes the critical failure strain for interfacial cracking much more likely to be exceeded. In light of the innermost oxide phase descaling challenges discussed in Chapter 4, this phenomenon could be advantageous in ensuring that oxide is more likely to be fully descaled as the stress applied during descaling will be more likely to result in a critical failure strain being exceeded. However, there is still a balance to be struck between effect of temperature increase on oxide behaviour, mechanical properties, component-tooling interaction and component softening, as discussed in Section 1.2. Figure 6.13 to Figure 6.17

highlight the power of the AOSFD developed in its ability to encapsulate all the information in a single graph.

Overall, the conclusions of the AOSFD are in agreement with those discussed in Chapter 4 and Chapter 5 based on Krzyzanowski and Beynon's findings about increased temperature being associated with a higher probability of Mode II failure, i.e. interfacial cracking and raft slip, where it is easier to achieve consistent delamination. However, the AOSFD is supported by evidence in addition to experimental observation, and comprises information from manufacturing operation history, physics-based modelling, and analytical fracture mechanics.

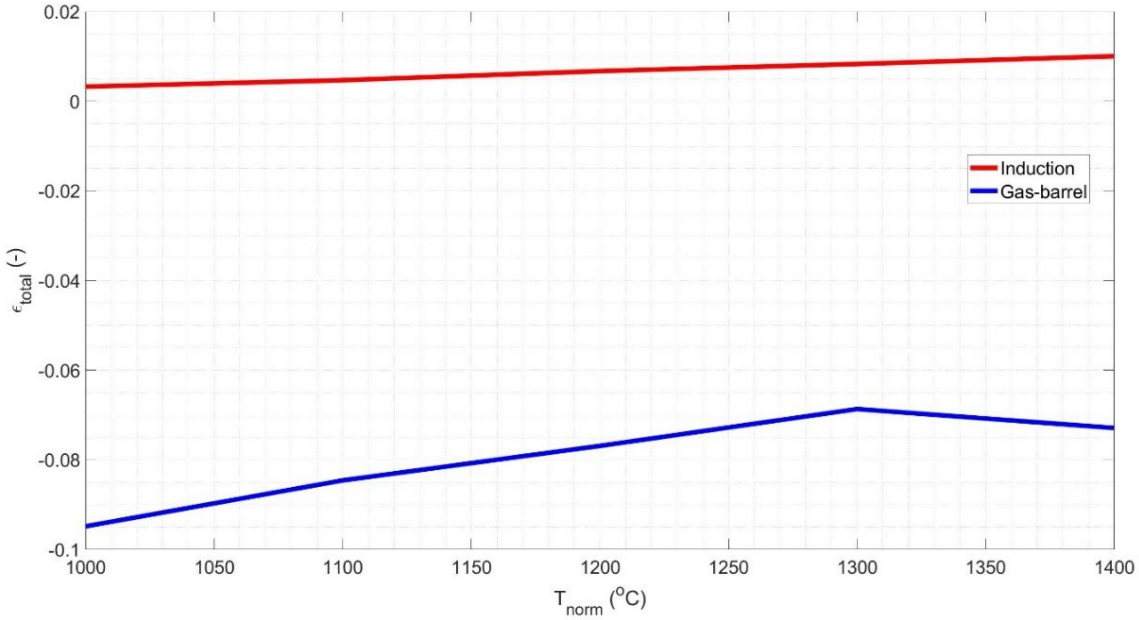


Figure 6.12: Plot of resultant strain, ε_{total}, against normalisation temperature, T_{norm}, for a 15 nominal bore (n.b.) conveyance tube normalised at 1000°C for 3 mins under induction (*red*) and gas-barrel (*blue*) heating ¤.

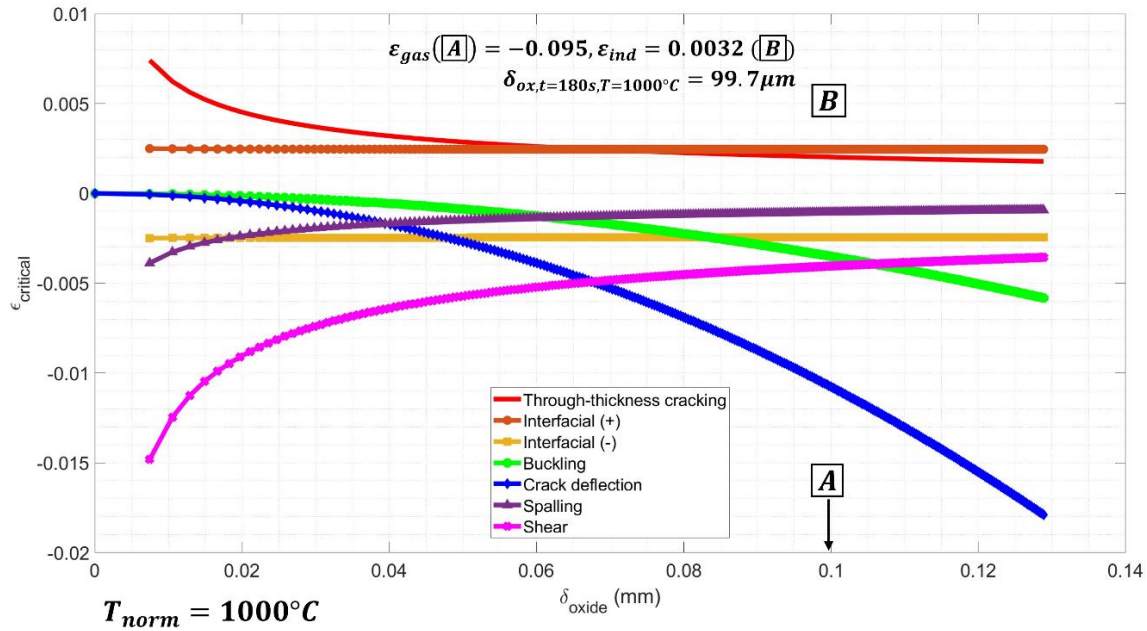


Figure 6.13: Advanced Oxide Scale Failure Diagram (Plot of critical failure strain, $\varepsilon_{critical}$, against oxide thickness, δ_{ox},) for a 15 nominal bore (n.b.) conveyance tube normalised at 1000°C (T_{norm}) for 3 mins, forming 99.7µm of oxide. For identical thermal conditions, 'A' represents the results strain for 99.7µm of gas-barrel furnace-grown oxide, while 'B' represents the resultant strain for 99.7µm of induction-grown oxide. For accessibility, each failure mode boundary is denoted by both colour and symbols indicating their start and end datapoint ¤.

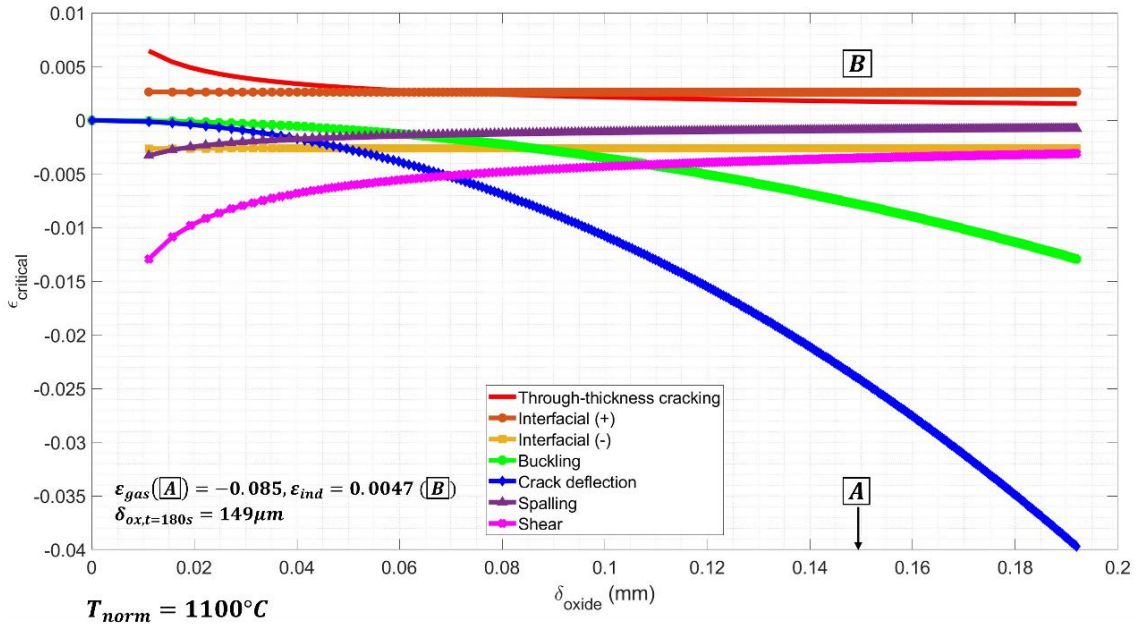


Figure 6.14: Advanced Oxide Scale Failure Diagram (Plot of critical failure strain, $\varepsilon_{critical}$, against oxide thickness, δ_{ox},) for a 15 nominal bore (n.b.) conveyance tube normalised at 1100°C (T_{norm}) for 3 mins, forming 149µm of oxide. For identical thermal conditions, 'A' represents the results strain for 149µm of gas-barrel furnace-grown oxide, while 'B' represents the resultant strain for 149µm of induction-grown oxide ¤.

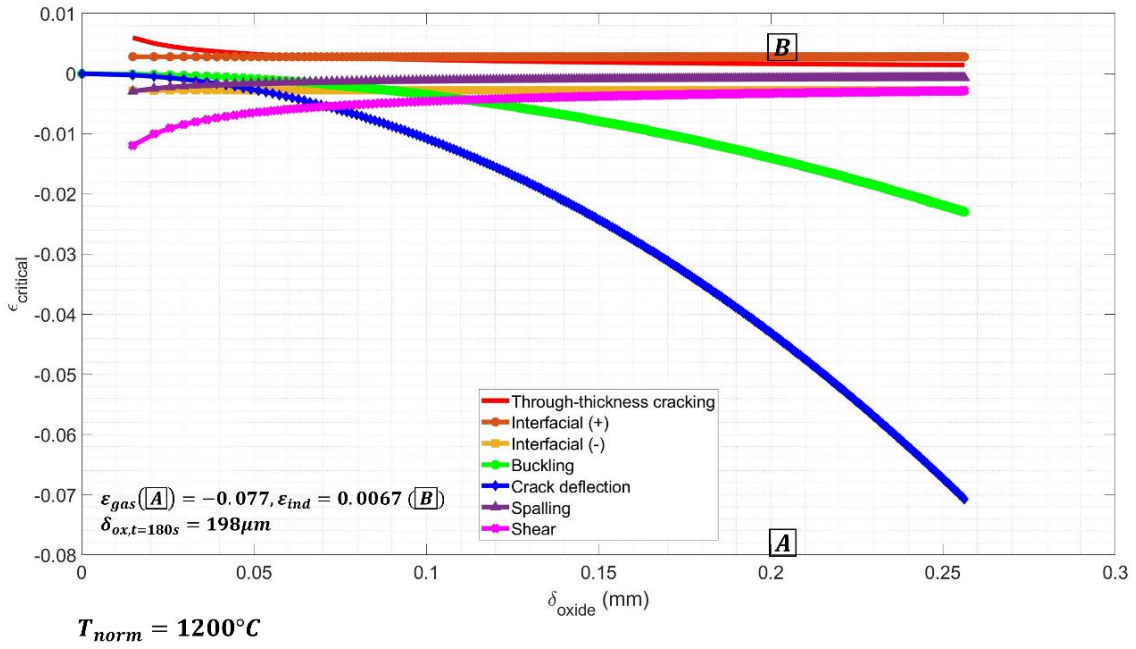


Figure 6.15: Advanced Oxide Scale Failure Diagram (Plot of critical failure strain, $\varepsilon_{critical}$, against oxide thickness, δ_{ox},) for a 15 nominal bore (n.b.) conveyance tube normalised at 1200°C (T_{norm}) for 3 mins, forming 198µm of oxide. For identical thermal conditions, 'A' represents the results strain for 198µm of gas-barrel furnace-grown oxide, while 'B' represents the resultant strain for 198µm of induction-grown oxide ¤.

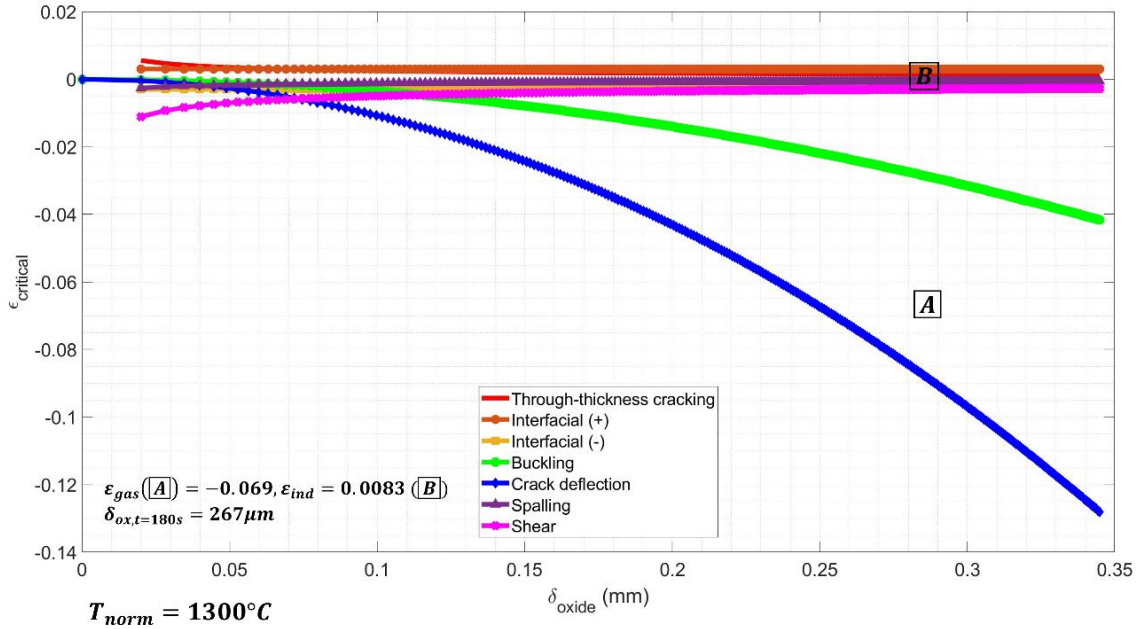


Figure 6.16: Advanced Oxide Scale Failure Diagram (Plot of critical failure strain, $\varepsilon_{critical}$, against oxide thickness, δ_{ox},) for a 15 nominal bore (n.b.) conveyance tube normalised at 1300°C (T_{norm}) for 3 mins, forming 267µm of oxide. For identical thermal conditions, 'A' represents the results strain for 267µm of gas-barrel furnace-grown oxide, while 'B' represents the resultant strain for 267µm of induction-grown oxide ¤.

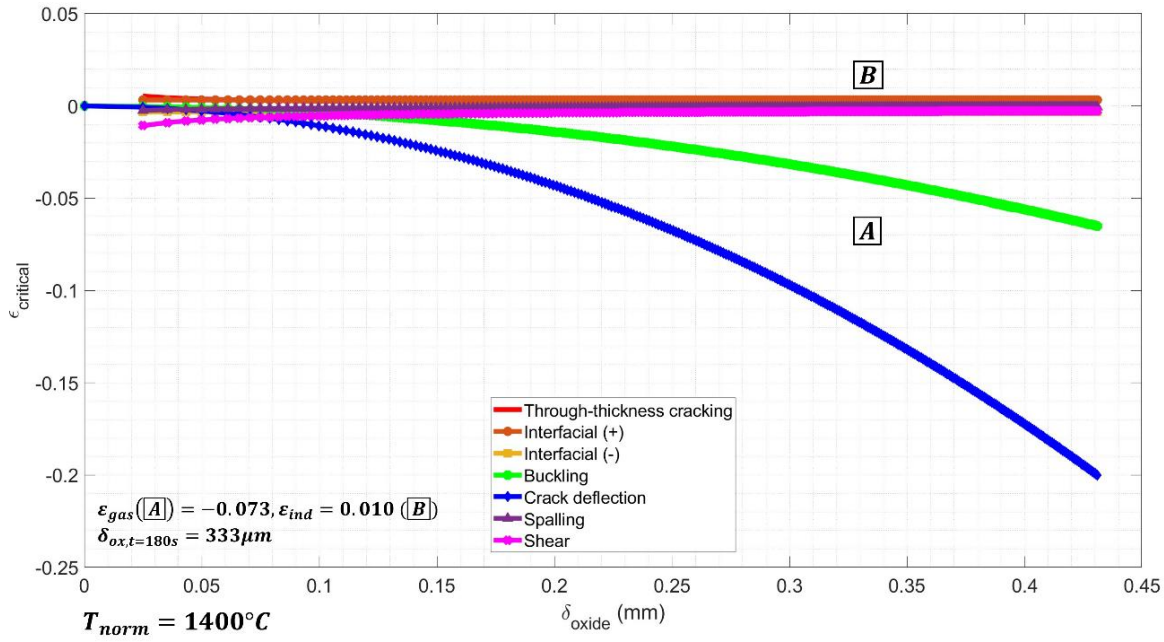


Figure 6.17: Advanced Oxide Scale Failure Diagram (Plot of critical failure strain, $\varepsilon_{critical}$, against oxide thickness, δ_{ox},) for a 15 nominal bore (n.b.) conveyance tube normalised at 1400°C (T_{norm}) for 3 mins, forming 333µm of oxide. For identical thermal conditions, 'A' represents the results strain for 333µm of gas-barrel furnace-grown oxide, while 'B' represents the resultant strain for 333µm of induction-grown oxide ¤.

It should be noted that the effect of gas impurities, such as water and other oxidation-enhancing or -inhibiting species, on parabolic rate coefficient cannot be quantified within the model or AOSFD at this stage. However, as both heating techniques occur in air, the degree to which these species vary should not be as significant as in the case of fossil fuel-based heating [28]. This aspect of work is better suited to experimental work where controlled atmosphere furnaces can be used.

6.3 Conclusions From Chapter 6

Analysis of the stress state of the oxide following the tube manufacturing process to allow development of an Advanced Oxide Scale Failure Diagram (AOSFD) specifically for oxide growing on a curved surface was explored in this chapter. This development could allow manufacturing parameters to be varied in an informed manner to minimise inconsistency in oxide adhesion (within the bounds of mechanical property limitations in effect during thermomechanical processing). Although analytical models for the relationship between oxide stress and thickness (amongst other parameters), have been proposed by several authors, accounting for the effect of the heat treatment, alongside the geometry and intrinsic growth stresses, must be addressed to allow accurate predictions.

To demonstrate the translatable application of the AOSFD for Tata, a comparison was drawn between the oxide state after induction vs. gas-barrel heating, in light of the improved operational control provided by induction heating. This illustrated that current frequency control during induction heating can decrease strain magnitude and lead to a tensile resultant strain which eliminates the compressive failure modes observed during gas-barrel heating. To conclude the work in this chapter, the original Thermo-Calc© oxide kinetic model was run at higher than typical normalisation temperatures (1000-1400°C), within the limits of validity of the temperature-dependence of relevant mechanical properties, to investigate the effect of increased temperature reported by Tata during temperature control investigations for the initial implementation of fully induction-based normalisation at their tube manufacturing site in Corby. Overall, it was demonstrated that temperature overshoot eliminated compressive failure modes such as buckling but increased the likelihood of interfacial failure.

This conclusion agrees with purely temperature-based studies of oxide failure mode. However, the work in this project accounts for mechanical phenomena of the oxide, derived from conveyance tube manufacturing, in parallel with kinetic phenomena by combining diffusion- and fracture-mechanics based analyses into a single diagram. Therefore, this work represents a novel, holistic, and industrially transferrable approach for the assessment of the relationship between manufacturing process changes and oxide failure, and is made possible by the continuous oxide kinetics data derived using the model developed in earlier chapters.

Chapter 7 Conclusions

Physics-based computational modelling of the oxidation process has the potential to offer a faster, more accurate, and more representative insight into oxidation kinetics and adhesion response to conveyance tube manufacturing parameters, where analytical and experimental approaches are limited by oversimplification and/or practical equipment restrictions. The technical challenges associated with conveyance tube manufacturing which have not been addressed in existing literature were identified as the thermochemical properties of wüstite, the effect of curved geometry on oxide kinetics, and the adaption of experimental validation techniques to investigation of curved surface samples of oxidation. This project aimed to explore the potential for the use of appropriately validated computational modelling to investigate the effect of conveyance tube manufacturing parameters on oxide scale kinetic and mechanical behaviour. The main conclusions are described below in the context of the objectives defined in Section 1.1.

1. *To use computational thermodynamics to predict oxide thickness gain and model external oxide scale kinetic and mechanical response under conveyance tube manufacturing conditions.*

The development of a computational model for external oxidation of the outer conveyance tube surface was described in Chapter 3. Thermo-Calc©'s DICTRA diffusion module, Microsoft Visual Studio (VS) Code and Thermo-Calc©'s TDB Editor extension were used to numerically solve a Stefan moving phase boundary problem. Overall, the model is a simplification of the real, complex, industrial scenario, and could be refined but already agrees well the experiments. The analytical model proposed by Huntz and Schütze for thermal stress, which required several temperature-dependent functions for elastic modulus and linear coefficient of thermal expansion, was used in Chapter 5 to assess thermal mismatch stress. A function for coefficient of thermal expansion of the oxide was derived using data for lattice parameter variation with temperature. This highlighted the significant difference in thermal expansion coefficient evolved during cooling, the effect of which is lost when the oxide stress state is only considered for an instantaneous temperature. The growth stress in the oxide was also evaluated using an appropriate analytical model. Further stress analysis included that associated with forming operations. The resultant compressive stress in the oxide following this analysis was 12.9GPa and dominated by thermal stress.

2. *To validate the oxide scale computational model output data and the data derived on its basis using quantitative experimental techniques assessing kinetic and mechanical response.*

Thermogravimetric analyses of the oxide formed on conveyance tubes under normalisation conditions revealed good agreement (±5%) between the model and experimental results, which was supported by microstructural imaging, in Chapter 4. However, this aspect of the work also further highlighted the challenges associated with experimental investigations of oxide on cylindrical geometries, e.g. damage during sample mounting and metallographic preparation, and flow-induced vibration during heating. Sample mounting challenges were mitigated against by applying a thin layer of polyester resin for cold mounting to all surfaces of the oxidised tube to seal the oxide in position before using standard metallographic preparation techniques. Vibration during heating was successfully quantified and removed from oxide mass gain data by applying an identical thermal cycle to an alumina dummy sample. X-ray diffraction was used to provide validation of the overall stress state of the steel tube before and after normalisation, and adhered layer stress transfer theory was used to calculate the stress state of the oxide.

3. *To investigate the effect of curved surfaces, and specifically tube geometry, on oxide scale behaviour.*

In Chapter 4, the effect of wall thickness on oxidation rate via changes to diffusion path length, was shown to be limited to tubes with inner radii of less than 200mm. Beyond this critical value, the scale of diffusion is small enough to render the effect of the radial coordinate in the diffusion negligible, and the solution approaches that of a planar geometry. However, conveyance tubes can be manufactured in sizes below this critical value and therefore demand a fully cylindrical defining equation when investigated using the computational model developed in Chapter 3. Furthermore, this conclusion only applies to oxidation kinetics and not its mechanical response and effect on curved surfaces.

4. *To use kinetic and mechanical response data to develop and implement an Advanced Oxide Scale Failure Diagram to identify the critical strain failure mechanism/s associated with different conveyance tube manufacturing parameters and operation history.*

Computational techniques were shown to be better equipped to provide continuous oxide thickness gain data as conclusions about the oxide microstructural and microtextural properties identified in Chapter 4, e.g. porosity, only apply for the oxide formed after-the-fact in experimental scenarios. The kinetic and mechanical data obtained in Chapter 3,

Chapter 4, and Chapter 5 were used to develop an Advanced Oxide Scale Failure Diagram (AOSFD), using fracture mechanics theory, outlining the relationship between critical strain and oxide thickness and providing a 'map' of how and at what strain level a given thickness of oxide formed at a given temperature will fail. To demonstrate the translatable application of the AOSFD for Tata, a comparison was drawn between the oxide state after induction vs. gas-barrel heating, considering the improved operational control provided by induction heating. This illustrated that current frequency control during induction heating can decrease strain magnitude and lead to a tensile resultant strain which eliminates the compressive failure modes observed during gas-barrel heating. The original Thermo-Calc© oxide kinetic model was run at higher than typical normalisation temperatures (1000-1400°C) to investigate the effect of increased temperature reported by Tata during temperature control investigations. Overall, it was demonstrated that higher temperatures (>1000°C) eliminated compressive failure modes such as buckling but increased the likelihood of interfacial failure. This conclusion agreed with purely temperature-based studies of oxide failure mode, but the work in this project accounts for mechanical phenomena of the oxide, derived from conveyance tube manufacturing (at any length scale), in parallel with kinetic phenomena by combining diffusion- and fracture mechanics-based analyses into a single diagram.

The successful completion of the above objectives demonstrates the viability of computational techniques to predict oxide kinetic and adhesion behaviour on conveyance tubes during manufacturing. The resulting novel AOSFD is simple and quick to use and therefore offers a practical tool for making informed decisions during conveyance tube manufacturing using continuous data derived via a novel application of computational thermochemistry to high temperature oxidation of curved surfaces.

Chapter 8 Research Impact

Reed at al define research impact as the "…demonstrable and/or perceptible benefits to individuals, groups, organisations and society (including human and non-human entities in the present and future) that are causally linked (necessarily or sufficiently) to research." [471]. Sufficient causation is preferable at best as it implies that a piece of research work is sufficient to generate impact whereas necessary causation defines the work as a significant contributing factor to a wider body of research work which generated impact [471]. Significance (impact magnitude) and reach (impact extent) are core criteria within the UK's Research Excellence Framework (REF) and contributing factors to Medr's assessment of research quality and culture in Wales [472, 473]. Impact evaluation, which assesses the significance and reach of both positive and negative effects of research, spans different time horizons, social (individual to society) and spatial (local to international) scales, and domains (social, economic, environmental etc) as well as intermediary domains associated with awareness and attitudinal, behavioural and decision-making, and policy change [471]. Bamford et al. identified the dyadic dimensions associated with university-industry (U-I) collaboration as knowledge transfer and dissemination, innovation diffusion, product and service commercialisation, workforce development, strategy deployment, and technology advancement [474]. Impact in an engineering research context is most often based on counterfactual (evidence of the absence of impact in the absence of research) and additive (evidence of a dynamic relationship between research and impact parameters) causation using summative experimental and statistical methods as a sufficient cause of impact as well as some systems analysis methods which provide only a necessary cause of impact [471]. As summarised by Yun et al.: "Experimental data should validate simulation results, while simulations should provide insights to guide experimental work. Collaborative efforts between industry and academia are crucial to translating fundamental research into practical applications, bridging the gap between theoretical advancements and real-world implementation." [246].

8.1 Qualitative Impact Analysis

8.1.1 Materials and Waste Management

Bamford et al. define impact in a U-I collaboration as being tangibly associated with increased capability, leading to "…sustainable performance improvement…" [474]. The work in this project encourages improved oxide kinetic and adhesion control by adjustment

of manufacturing parameters. It was highlighted in Chapter 1 that 600 tonnes of steel are lost to oxidation for every one of the storage warehouses filled at the TSUK Tubes site in Corby. Therefore, not only does a reduction in material loss contribute to business operations impact including improved product quality, faster process speed, extended plant and product life, and decreased process cost, but also has a further reaching impact on the success of manufacturing operations adversely affected by oxidation, including conveyance tube manufacturing, in meeting uni- [153] and multi-lateral [155] goals concerning industrial waste. For example, metals are a priority material targeted by the Welsh Assembly Government's zero waste strategy and eliminating material waste by recycling ferrous materials can reduce an ecological footprint by 36%-52% per tonne depending on the type of recycling used [153]. Conventionally, the delaminated oxide was collected in a crucible [9] and returned to the start of the steelmaking process for reduction in the blast furnace to recover the steel content [9]. However, the closure of the Tata's blast furnaces [475] in light of decarbonisation goals [148, 156, 476], will be followed by an electric arc furnace replacement, a technology which depends on steel scrap and slag rather than iron ore (oxide) [477]. Furthermore, whilst oxide scale is a suitable raw material for blast furnace-based steelmaking, the role of scale as an oxidiser during EAF-based steelmaking is made redundant by the introduction of oxygen lancing technology which achieves large electrical energy savings [478]. Disposal of scale into landfill also carries risk of heavy metal leaching into soil and groundwater [478]. Therefore, the waste associated with oxidation will no longer be readily recyclable and oxidation kinetic and adhesion control will aid in reducing steel waste in the absence of the conventional recycling process.

8.1.2 Manufacturing Technology and Plant Life

Oxide adhesion control could reduce, or potentially eliminate, the need for additional resources to process spalled oxide and repair associated damage to plant tooling. De Oliveira Junior et al. showed how the entrainment of iron oxide particles could increase counter-body wear rate (assuming the conveyance rolls used are harder than the conveyance tubes themselves) by 65% and 15% when considering haematite and magnetite respectively [479]. Vergne et al. later addressed wüstite, as the dominant oxide phase formed on low carbon steel work rolls, but highlighted that cubic oxides exhibit greater ductility and a lower contribution to abrasion, which is prominent when oxide particles become entrained in the tube-roll contact and enable third-body abrasion [480, 481]. Hence, a reduction in oxide brought about by a change in parameters informed by the work in this project, since thicker

oxides have a greater negative impact on roll wear rate by dispersing more spalled oxide particles into the environment to become entrained in the tube-roll contact, will contribute to plant life extension. Extended plant life and longevity of resources is also important beyond company level, for the same reasons as reducing material loss.

Dubar et al.'s recent study highlights the need to consider the effect of oxide at the workpiece-tool interface during manufacturing operations [482] in terms of its effect on forming conditions, contact pressure (they observed a potential reduction of 40%), material flow, and thermal conditions. All of these parameters were also considered over the course of this project in terms of their interaction with the steel and scale. Furthermore, Dubar et al. [482] highlighted how oxide scale could improve contact pressure distribution owing to the wear-changes in geometry. For example, convex surfaces see a greater increase in oxide thickness, compared to flat and concave surfaces, near the end of tool life but also showed a 23% drop in contact pressure, compared to 30% and 10% for flat and concave surfaces respectively. This is reflective of the conclusions of this project, that geometry is a critical parameter affecting oxide kinetics and mechanics and directly impact manufacturing operations such as conveyance tube production.

8.1.3 Industry 4.0 and Digital Steelmaking

Additionally, the oxide kinetics and adhesion control outcomes in this project are founded on computational analyses and this project is therefore a good example of impact across multiple domains (economic, environmental and societal), time horizons (manufacturing process length and long-term waste management goals) and spatial (national and international ferrous metal waste reduction) scales. Furthermore, the computational aspects of this project contribute to the need, cited by Jung et al., to account for accurate thermodynamics and kinetics of chemical reactions (including oxidation) within related Industry 4.0 techniques, i.e. digitalisation for steelmaking [148], namely digital twinning and the Smart Factory, which can simulate manufacturing scenarios to predict potential outcomes at an accelerated rate without affecting physical production [483]. Jung et al. argue that CALPHAD-based techniques, such as those used in this project, and their associated thermodynamic databases, will be increasingly required to meet future materials design and processing demands [483]. For example, in 2024, steel producer Georgsmarienhütte GmbH (GMH) successfully used Thermo-Calc© to develop an automated physical model of secondary steelmaking metallurgy, including tapping from the electric arc and ladle furnaces, vacuum degassing, and final treatment process, to deepen

insight into parameters including temperature, composition, and inclusion composition [484]. Their model can aid the 'Green Steel' process by informing decisions which optimise steel quality and cleanliness and minimise energy consumption and emissions, as well as enable other process technology improvements such as extended ladle life.

8.1.4 Technology and Infrastructure Design for Decarbonisation

Changes to traditional manufacturing technology will be prevalent across many sectors, including steel, as standard practices evolve to accommodate the need for global decarbonisation [148, 156, 476]. This project tackles oxidation during the conveyance tube manufacturing process using a proactive approach based on new applications of computational thermochemistry (via Thermo-Calc©) and Advanced Oxide Scale Failure Diagrams (AOSFDs) to oxidation of curved surfaces in a manufacturing context. Both outputs create an opportunity for enhanced practice and systems based on informed decision making, provided there is full and consistent access to appropriate data, made possible by this U-I collaboration with TSUK Tubes [474]. A key example of the impact of this project in terms of informed decision-making is the development of the AOSFD in Section 6.1 and its ability to aid Tata's insight of their transition from predominantly gas-barrel- to fully induction-based heating technology. This transition is motivated by decarbonisation goals. The AOSFD, developed based on oxide kinetic and mechanical analyses data derived in earlier chapters, highlighted the potential to reduce oxide multi-mode failure probability by exploiting the higher levels of operational control available in induction heating and optimising the current frequency used during the conveyance manufacturing process.

Induction heating technology has been identified as a suitable technology for decarbonised steelmaking during high temperature operations, such as normalisation, within manufacturing however the manufactured parts will also contribute to new decarbonisation-friendly technologies. A key example for a conveyance tube context is the introduction of hydrogen into energy infrastructure [476]. Current research in this area includes the need to assess existing steel infrastructure for its suitability for hydrogen conveyance [20, 485, 486]. Understanding oxide kinetics and adhesion is considered an integral element of protecting conveyance infrastructure steels from hydrogen permeation and embrittlement [487, 488] as hydrogen diffusion through an iron oxide is approximately eight times slower than steel [489, 490]. The work in this project can contribute to this technology shift by offering an insight into oxidation kinetics and adhesion specifically for

curved surfaces, and at the accelerated rate required via the use of computational resources as discussed.

8.1.5 Product Perception

Finally, the inconsistent spalling obtained on the conveyance tube outer surface during descaling was outlined at the beginning of this project as a source of customer product rejection. Stylidis et al. argue that the greatest commercial advantage is reached by capitalising on the customer quality perception [491]. Although the spalled oxide does not affect the mechanical strength of the tube products, it creates a perception of reduced product quality and safety in service, as it is proposed that perception of incident severity carries more weight than perception of incident probability [492, 493]. Furthermore, Cai et al. cite perceived risk concerning safety, reputation, aesthetics, and performance as key considerations during customer purchase [494], all of which are shown to be negatively impacted by oxide scale and its inconsistent spalling profile. Therefore, using the work in this project to improve oxide adhesion by understanding its failure modes and probabilities under conveyance tube manufacturing conditions will help improve customer quality perception.

8.2 Quantitative Impact Analysis

Table 8.1 shows how each impact spoke discussed here can be quantified for comparison. Quantitative analysis of different aspects of impact within this project based on impact time horizon, social scale, spatial scale, and domain/s. A score was assigned to each level of each category, from 1-3. In the case of domain, a score of 1 was given to each domain, with the exception of intermediary domains which received a score of 0.5. The maximum scores were used to determine relative impact reach, $\boldsymbol{R}$, and the number of impact domains were used to determine relative significance, $\boldsymbol{S}$.

Table 8.1: Quantitative analysis of different aspects of impact within this project based on impact time horizon, social scale, spatial scale, and domain/s. A score was assigned to each level of each category, from 1-3. In the case of domain, a score of 1 was given to each domain, with the exception of intermediary domains which received a score of 0.5. The maximum scores were used to determine relative impact reach, ***R***, and the number of impact domains were used to determine relative significance, ***S***.

Impact Description	Time Horizon	Social Scale	Spatial Scale	Domain (* indicates an intermediary domain)	Relative Reach, *R*	Relative Significance, *S*
	1 = Immediate (s/m/hr); 2 = Short-term (d/wk); 3 = Long-term (m/yr)	1 = Individual; 2 = Demographic group; 3 = Society	1 = Local; 2 = Regional/National; 3 = International	S = Societal; E = Environmental; C = Economic/Commercial; P = Policy change*; B = Behavioural and Decision-Making*; A = Attitudinal and Awareness*;	*R = Maximum Time Horizon x Maximum Social Scale x Maximum Spatial Scale*	*S = Total number of domains impacted (half score for intermediary domain)*
Materials and Waste Management	1, 2, 3	2, 3	1, 2, 3	S, E, C, B	**27**	**3.5**
Manufacturing Technology and Plant Life	3	2	1, 2, 3	E, C	**18**	**2**
Industry 4.0 and Digital Steelmaking	2, 3	2, 3	1, 2, 3	S, E, C, B, P	**27**	**4**
Technology and Infrastructure Design for Decarbonisation	3	2, 3	1, 2, 3	S, E, C, B, A, P	**27**	**4.5**
Product Perception	3	2	3	C, A	**18**	**1.5**

Chapter 9 Future Work

Computational thermochemistry has been the core of this project, and is undoubtedly interdisciplinary in its nature, comprising knowledge and skills for experimentation, theory, engineering, and computation. As such, the potential for future work is vast dependent on which aspect should be deemed most necessary and resource-efficient to be pursued further.

9.1 Multi-Phase Oxide Boundary Modelling

Throughout this project, the oxide scale generated on the external conveyance tube surface has been modelled as 100% homogeneous wüstite based on the widely accepted ratio of wüstite, magnetite, and haematite as 95:4:1 in the literature [15, 70, 71, 74], and experimental evidence of industrial samples, from previous work by Grant [9] and work within this project, which revealed that the inner layer of oxide was dominated by wüstite. The TGA work in Chapter 4 also revealed additional phases only when inspecting laboratory samples which are, crucially, not subjected to industrial descaling. Therefore, when considering the oxide kinetic model in isolation for simulating oxidation on conveyance tubes, a homogeneous wüstite scale is a valid assumption. However, in future work to expand the applicability of the model to other manufacturing scenarios affected by oxidation, and to more closely align the validation the model via TGA (where in-situ descaling replication is not possible), it is anticipated that multiple oxide phases will need to be modelled.

Given the complexity of model development, particularly with respect to thermodynamic and kinetic database collation and encryption, this work could begin by modelling the individual moving phase boundaries under normalisation conditions, i.e. wüstite-magnetite, magnetite-haematite, and superposing individual results to find the overall thickness gain of each phase. In the same manner, a more detailed analysis of the effect of porosity, especially if individual oxide phases are modelled, would improve the representativeness of the oxide kinetic and adhesion models. Porosity was discussed in previous chapters and significant differences between the industrial and laboratory samples, again attributed to the absence of descaling replication in the latter case.

9.2 Silicon and Its Interaction with Oxidation

This project has focused on modelling the base metal, iron, as the dominant reductant. Although it is recognised that steel is a multi-element alloy, as discussed in Section 1.6.1,

minor alloy element depletion is likely a secondary effect in steels [389]. However, Asensio-Jimenez et al. also reported on the effect of minor element reservoir depletion for samples of variable thickness, alongside the effect of creep, on oxide kinetics and adhesion. They highlighted how extremely low levels of reaction elements in ferritic steels, e.g. lanthanum, can have an amplified effect on oxidation kinetics for thinner samples since a greater percentage of the total lanthanum reservoir is used up [389]. Furthermore, they used this hypothesis to explain why higher temperature oxidation is more affected by sample thickness since the faster reaction rates associated with higher temperatures [495] will accelerate minor alloy reservoir depletion. Clarke also remarked, in their work on growth stress effects due to oxidation, that inward and outward flux of ions is affected by the concentration of alloy elements due to the latter's ability to promote or impede diffusion [110].

Initial compositional analysis discussed in Section 3.1.1 revealed silicon as one of the greatest contributing alloy elements, and the alloy with the biggest difference in contribution across the two grades used in tube manufacturing at TSUK Tubes (P195GH and P235GH [4]). Furthermore, SEM characterisation during initial sample characterisation revealed an unidentified layer at the steel-scale interface, which was suspected to be fayalite. However, the distinct layer was only observed on the sample obtained under the same idealised, atmospheric furnace conditions used by Grant to investigate planar samples of P195GH and P235GH [9]. Neither the industrial samples supplied from TSUK Tubes nor the laboratory tube samples normalised in air displayed a similar fayalite layer, which could be attributed to a lack of representative thermomechanical conditions during Grant's in-situ oxidation testing. Nevertheless, existing literature has already shown how silicon and its tendency to segregate and form an iron-silicon-oxide intermetallic system can affect scale kinetics, morphology and adhesion, especially given the low thermal gradient between fayalite and low carbon steel [60, 77, 133, 134]. Even studies specifically looking at silicon in the context of oxidation on curved surfaces [173] neglect to consider how dimensions such as wall thickness and internal radius affect diffusion, concentration gradients, and growth stress. The model, and subsequent analyses presented in this project, could be developed to include silicon and assess its effect on kinetics and adhesion. Further comparisons could be drawn between the two steel grades used by TSUK Tubes to support this work. As with the case of multi-phase scale, introducing silicon, and the potential to develop fayalite, would

introduce additional reaction interfaces and moving phase boundaries, and therefore additional complications.

9.3 Artificial Intelligence and Data-driven Technology Implications

Steel design using artificial intelligence (AI) and data-driven technology is a fast-growing area of research. Geng et al. suggest that a paradigm shift is required in conventional steel materials research as trial-and-error methods lead to protracted and expensive research cycles [496]. They argue that so-called 'forward design', using a Machine Learning (ML)-derived prediction model achieve target materials performance quantities based on input material parameters as input. Rao et al. also highlighted that alloy design, even when only considering the most used elements, spans an unmanageable space of more than 10^{50} alloy variants [497], which Geng et al. reflect in their acknowledgement of a 'vast' candidate material feature space as a barrier to global algorithm optimisation [496]. However, the sheer quantity of possible material design makes conventional alloy design techniques, such as CALPHAD and Density Functional Theory (DFT), entirely unfeasible [497]. Furthermore, CALPHAD can only provide equilibrium phase diagrams, and combinatorial experiments, e.g. combining CALPHAD with DFT's computationally expensive, predictive abilities, is labour-intensive and only able to cover a restricted area of the alloy variant space. Kwon et al. gave an example of the potential of ML to contribute to accelerated alloy development. They used an experimental dataset, augmented by a CALPHAD-based simulation of microstructural features, to train an ML model and explore the high-dimension space of chemical and processing parameters possible to design an enhanced creep resistant stainless steel [206]. Pei et al. also highlighted that AI-driven prediction of oxidation behaviour offers improved accuracy during the development of multi-component superalloys which deviate from conventional oxidation kinetic trends [498]. They cite oxide doping effects, alloy composition change, and oxidation environment variation as key drivers of deviation from typical parabolic oxidation behaviour, and therefore more complex material systems may depend on ML to derive valid oxide kinetic relationships. However, it was also noted by Rao et al. that the limited amount of composition-property data means ML approaches can be overly dependent on simulation data [497]. They suggest active learning (adaptive design) as an alternative approach with the potential to reduce the computational costs of alloy design and functional material discovery. Active learning uses previous model training to guide the next set of experiments.

A key thread in this project has been the scarcity of data available for the thermodynamic and kinetic properties of wüstite. The Director of Database Development and Innovation Research at Thermo-Calc© highlighted that machine learning (ML) and the CALPHAD methodology share a '…fundamental philosophy…' in their core elements of collecting existing data (both experimental and analytical), assessing its quality, selecting a relevant model (for a particular phase in the case of Thermo-Calc©), optimising and training the model, and finally parameter tuning and validation [499]. Consequently, they also have several challenges in common, including critical data-related (scarcity, heterogeneity, quality), interpretability, explainability, and model generalisation (intra- or extrapolation) challenges. For example, the wüstite thermodynamic and kinetic databases developed within this project were based on several sources of data of varying format with the potential for extrapolation beyond the conditions of the original data source system once applied to industrial conditions such as conveyance tube manufacturing, e.g. temperature range, equilibrium state assumption validity, composition limits. The critical gaps created within the database leave the results open to uncertainty. Furthermore, as has been shown in this project, it is often unfeasible for mechanistic models to encompass all the complexities found in tube manufacturing such as grain boundary diffusion and interfacial interactions and conditions.

ML is not without its own limitations, especially regarding its interpretability and explainability due its black-box nature, which makes physics-based techniques like CALPHAD more reliable, trustworthy (from a researcher trust perspective), and likely to offer industrially valuable insight based on alignment with materials physics and chemistry [500]. As the computational prediction of oxide thickness during tube manufacturing is the foundation of all subsequent analysis of oxide behaviour, particularly in response to geometry, improving the data quality which underpins these predictions would have far-reaching positive implications. ML-generated data could offer a computationally efficient (in terms of both cost and time) route to a completer and more robust dataset for wüstite.

Another challenge of this project has been the heterogeneous nature of the data, especially those used to produce the thermodynamic and kinetic databases. As data quality is one of the three fundamental factors guiding ML advancement [497], although larger datasets (>1000 datapoints) arguably provide more valid training, a small dataset can be effective and accurate provided its data have high enough quality. Although, it should be noted that a

small dataset can cause an ML model to lose fundamental knowledge competency. This is particularly true if data have been generated synthetically by software.

9.4 Quantifying Thermofluid Phenomena during Thermogravimetric Analysis

Finally, this project has highlighted the need to deepen understanding of oxidation phenomena specifically for curved surfaces. This was highlighted during the work in Section 4.2.2 using TGA which revealed thermal buoyancy, vibration, and pendulum effects. It was beyond the scope and themes of this project to conduct a full analysis of the thermofluid dynamics evolved during tube sample heating which led to these phenomena. It is suggested that a compressible analysis, underpinned by non-constant fluid density, $\boldsymbol{\rho}$, i.e. $\frac{\boldsymbol{d\rho}}{\boldsymbol{dt}} \neq 0$, would be required to describe the air flow experiencing a large temperature increase and cross-sectional area reduction in moving from the 750mm diameter furnace chamber to the 75mm diameter furnace work tube followed by the 14.9mm diameter tube sample, which is currently difficult to suspend with a fully vertically aligned bore. There is no pressure change as the work tube and tube sample are open-ended and the flow is subsonic. However, the anticipated boundary layer effects, air flow velocity and Reynolds number need to be quantified to comprehensively understand the contribution of the fluid dynamics effects described in Chapter 3 on output tube sample mass gain data.

Furthermore, the oxide kinetics model developed in Chapter 3 is limited to isothermal normalisation but it is recognised that a more accurate representation of the industrial situation, and TGA laboratory set-up used for model validation, would tackle the issues of convergence attributed to steep thermal gradients to obtain a more versatile transient kinetic model.

Chapter 10 Appendices

Appendix 1: Analysis of dependency of diffusivity on changes to activation energy associated with transition from bulk to grain boundary equivalent values.

$$Q_{gb} = 0.5Q_b$$
$$D_k = D_0 e^{-\frac{Q_k}{RT}}$$

Let (1) = Bulk, (2) = Grain boundary

$$D_1 = D_{0_1} e^{-\frac{Q_1}{RT}}$$

$$D_2 = D_{O_2} e^{-\frac{Q_2}{RT}}$$

$$Q_2 = 0.5Q_1, D_{O_2} \approx D_{O_1}$$

$$\therefore D_2 = D_{O_2} e^{-\frac{0.5Q_1}{RT}}$$

Let $-\frac{Q_1}{RT} = x$

$$D_2 = D_{01} e^{0.5x}; D_1 = D_{01} e^{x}$$
$$\frac{D_2}{D_1} = \frac{e^{0.5x}}{e^{x}} = \frac{(e^{x})^{0.5}}{e^{x}} \quad \therefore \; D_2 = \sqrt{D_i}$$

Appendix 2: Derivation of TGA mass gain data to layer thickness conversion

To obtain oxide mass per unit surface area (kg.m^{-2}):

$$m_{SA} = \frac{\Delta m}{A_{sample}}$$

If m_A is true for a 1m^2 sample area, i.e. $A = 1$:

$$m_A = \rho V = \rho A \delta = \rho \delta$$
$$\therefore \delta = \frac{m_A}{\rho} = \frac{\Delta m}{\rho A_{sample}}$$

Appendix 3: Derivation of oxidation mass to volume gain using STA data (planar, i.e. cuboid geometry)

$$\Delta V = \frac{\Delta m}{\rho}$$
$$V_{\text{gain}} = {x_2}^3 - {x_1}^3$$
$$x_2 = \sqrt[3]{V_{\text{gain}} + x_1^3}$$

Appendix 4: Mean line intercepts for various tube samples used for grain boundary diffusion investigation.

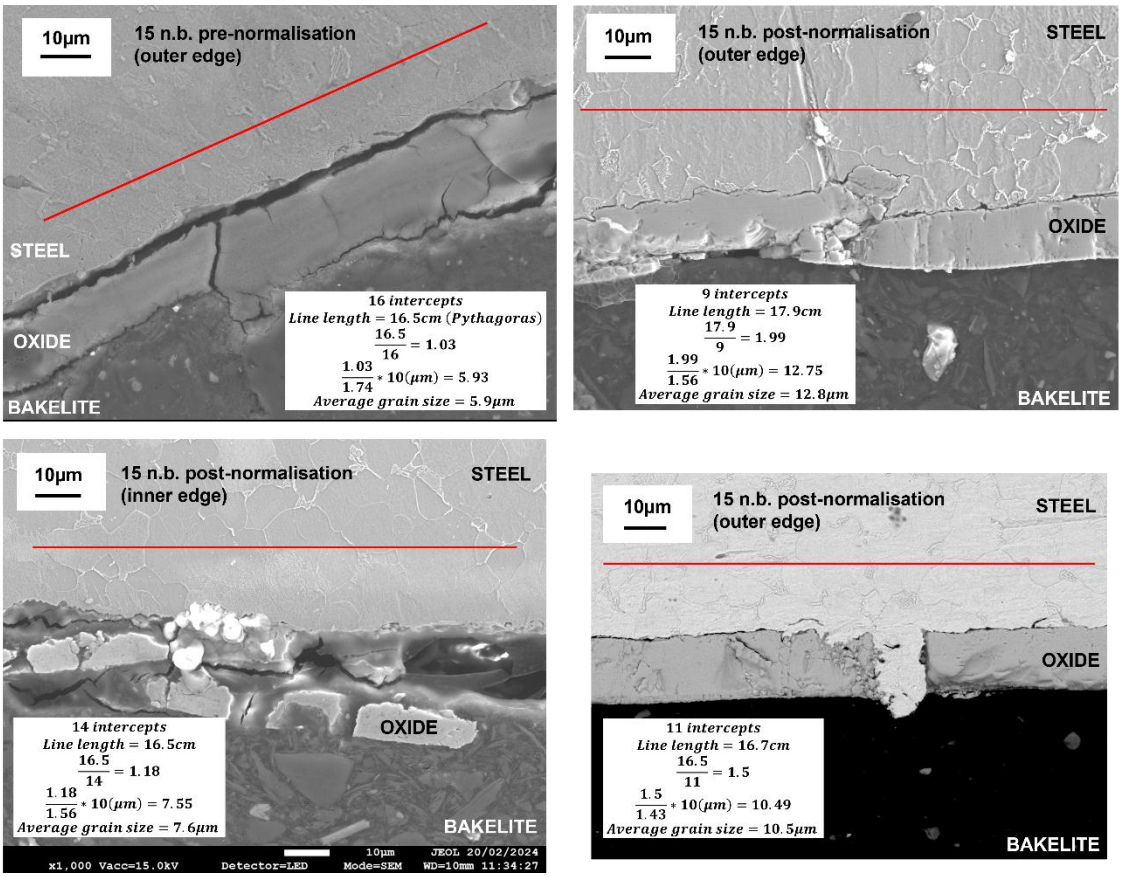


Figure 10.1: Calculations of average grain size using mean line intercept technique for 15 nominal bore (n.b.) samples (a) pre-normalisation at the outer edge, (b) post-normalisation at the outer edge, (c) post-normalisation at the inner edge, and (d) post-normalisation at the outer edge ¤.

Appendix 5: Methodological details of oxide thickness measurement at three different locations around the outer edge of a 15 nominal bore (n.b.) conveyance tube normalised in industry.

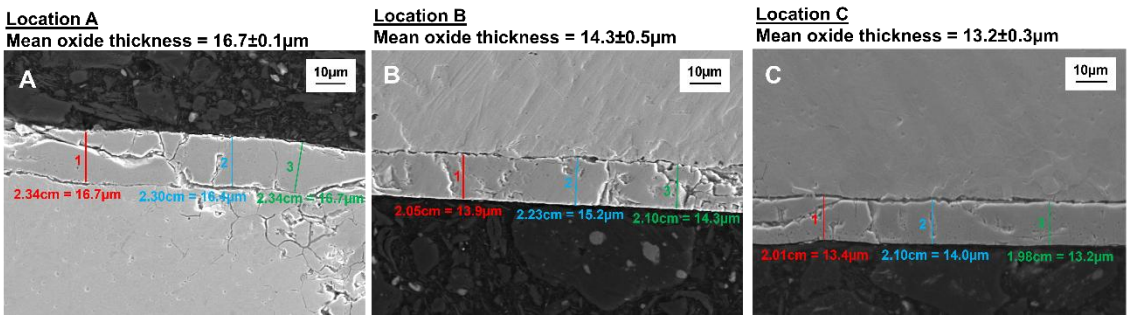


Figure 10.2: Average oxide thickness (14.9±1.3μm) measured for a 15 nominal bore (n.b.) conveyance tube ¤.

Table 10.1: Oxide thickness measurements for a 15 nominal bore (n.b.) conveyance tube. Three measurements were taken at three points at each location ('A', 'B', and 'C'). A mean oxide thickness, $\bar{\delta}_{ox}$, and its standard deviation are calculated.

Location	Image Length (cm)	Actual Length (μm)	$\bar{\delta}_{ox}$ (μm)
A1	2.34	17	17 ± 0.1
A2	2.30	16	
A3	2.34	17	
B1	2.05	14	15 ± 0.5
B2	2.23	15	
B3	2.10	14	
C1	2.01	13	14 ± 0.3
C2	2.10	14	
C3	1.98	13	

Appendix 6: Methodological details of oxide thickness measurement at three different locations around the outer edge of a 15 nominal bore (n.b.) conveyance tube normalised in industry.

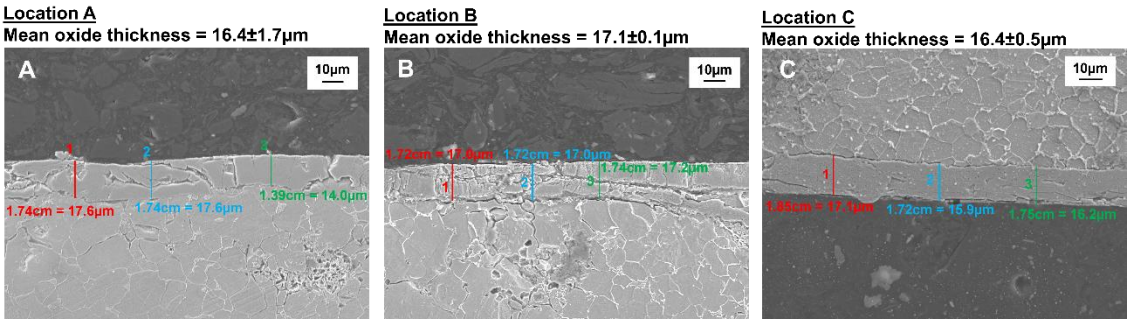


Figure 10.3: Mean oxide thickness (16.6±0.3μm) measured for a 15 nominal bore (n.b.) conveyance tube ¤.

Table 10.2: Oxide thickness measurements for a 15 nominal bore (n.b.) conveyance tube. Three measurements were taken at three points at each location ('A', 'B', and 'C'). A mean oxide thickness, $\bar{\delta}_{ox}$, and its standard deviation are calculated.

Location	Image Length (cm)	Actual Length (μm)	$\bar{\delta}_{ox}$ (μm)
A1	1.74	18	16 ± 2
A2	1.74	18	
A3	1.39	14	
B1	1.72	17	17 ± 0.1
B2	1.72	17	
B3	1.74	17	
C1	1.85	17	16 ± 0.5
C2	1.72	16	
C3	1.75	16	

Appendix 7: Methodological details of oxide thickness measurement at three different locations around the outer edge of a 15 nominal bore (n.b.) conveyance tube heated for 15 mins at 1000°C in a thermogravimetric (TGA) furnace.

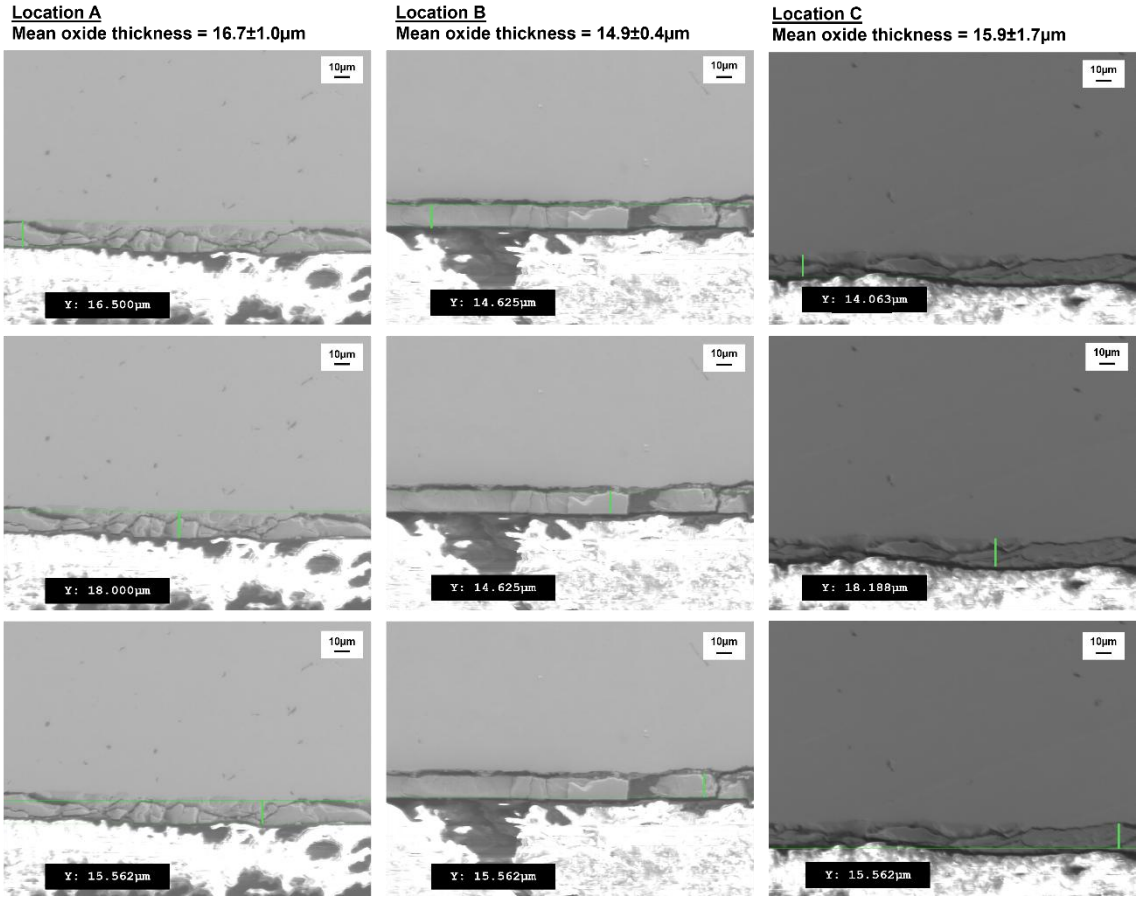


Figure 10.4: Average oxide thickness (15.8±0.7µm) measured for a 15 nominal bore (n.b.) conveyance tube ¤.

Table 10.3: Oxide thickness measurements for a 15 nominal bore (n.b.) conveyance tube. Three measurements were taken at three points at each location ('A', 'B', and 'C'). A mean oxide thickness, $\bar{\delta}_{ox}$, and its standard deviation are calculated.

Location	Actual Length (µm)	$\bar{\delta}_{ox}$ (µm)		
A1	16.500	16.7	±	1.0
A2	18.000			
A3	15.562			
B1	14.625	14.9	±	0.4
B2	14.625			
B3	15.562			
C1	14.063	15.9	±	1.7
C2	18.188			
C3	15.562			

Appendix 8: Methodological details of oxide thickness measurement at three different locations around the outer edge of a 15 nominal bore (n.b.) conveyance tube heated for 15 mins at 1000°C in a thermogravimetric (TGA) furnace.

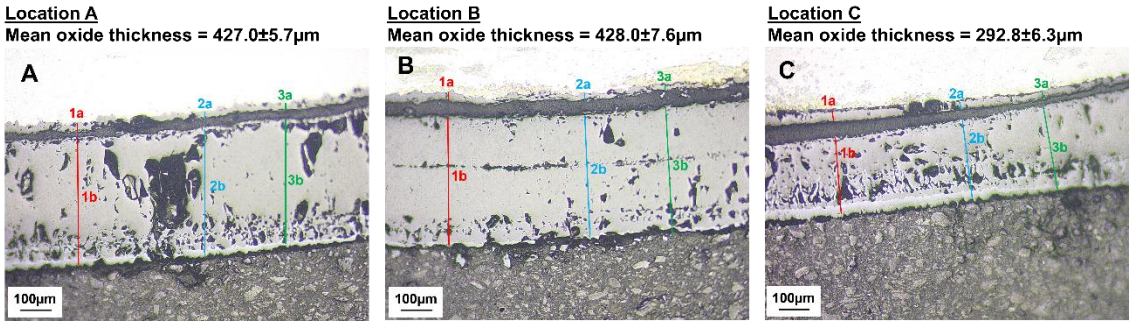


Figure 10.5: Average oxide thickness (382.6±63.5µm) measured for a 15 nominal bore (n.b.) conveyance tube ¤.

Table 10.4: Oxide thickness measurements for a 15 nominal bore (n.b.) conveyance tube. Three measurements, taken at three points at each location ('A', 'B', and 'C') and comprising two interfacially separated parts ('a' and 'b'). A mean oxide thickness, δ_{ox}, and its standard deviation are calculated.

Location	Image Length (cm)	Actual Length (µm)	$\overline{\delta}_{ox}$ (µm)
A1a	0.40	27	427 ± 6
A1b	5.95	405	
A1	6.35	432	
A2a	0.37	25	
A2b	5.95	405	
A2	6.32	430	
A3a	0.34	23	
A3b	5.82	396	
A3	6.16	419	
B1a	0.40	28	428 ± 8
B1b	5.95	410	
B1	6.35	438	
B2a	0.37	26	
B2b	5.71	394	
B2	6.08	419	
B3a	0.29	20	
B3b	5.90	407	
B3	6.19	427	
C1a	0.49	34	293 ± 6
C1b	3.61	252	
C1	4.10	287	
C2a	0.44	31	
C2b	3.71	259	
C2	4.15	290	
C3a	0.44	31	
C3b	3.87	271	
C3	4.31	301	

Appendix 9: Methodological details of oxide thickness measurement at three different locations around the outer edge of a 15 nominal bore (n.b.) conveyance tube heated for 15 mins at 1000°C in a thermogravimetric (TGA) furnace.

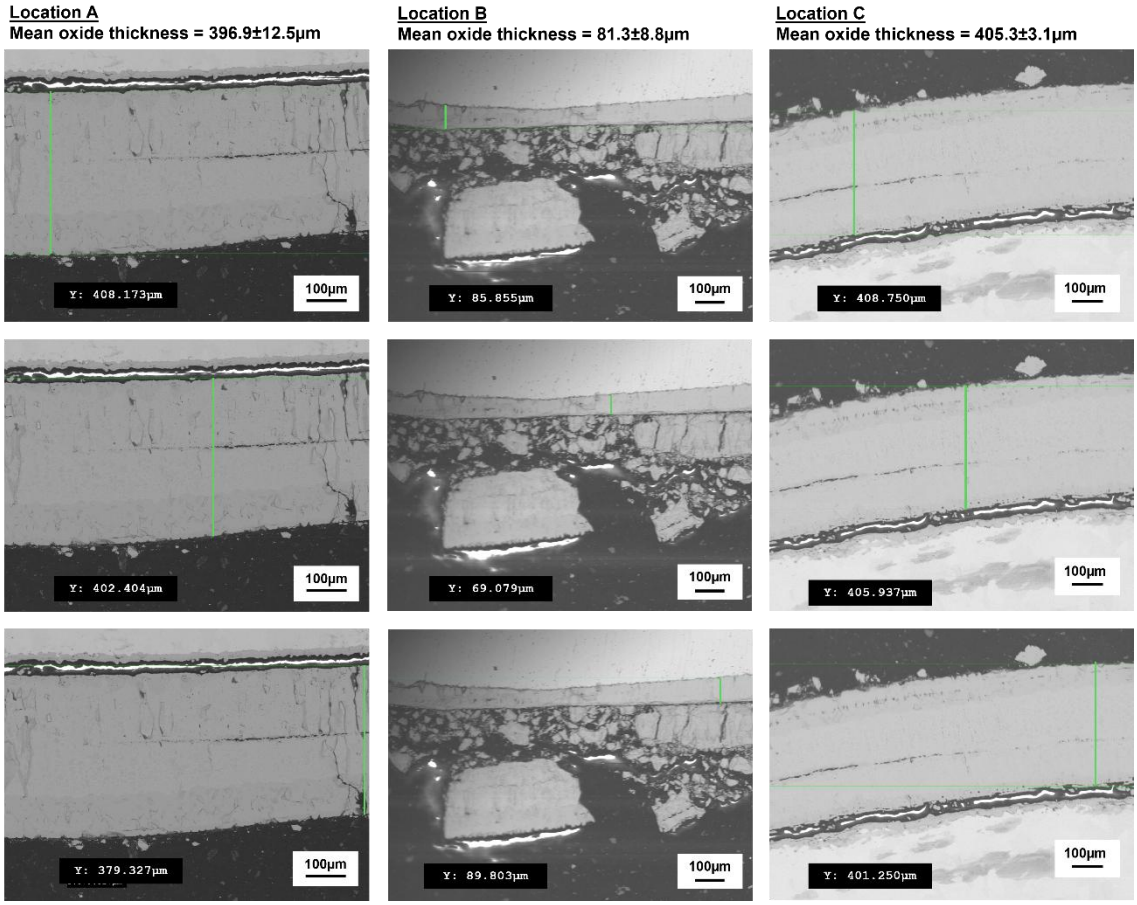


Figure 10.6: Average oxide thickness (401.0±4.3µm) measured for a 15 nominal bore (n.b.) conveyance tube. Location B was not included in calculations of average oxide thickness and standard deviation as it represents the phenomenon of oxide phase interfacial failure ¤.

Table 10.5: Oxide thickness measurements for a 15 nominal bore (n.b.) conveyance tube. Three measurements, taken at three points at each location ('A', 'B', and 'C'). A mean oxide thickness, δ_{ox}, and its standard deviation are calculated.

Location	Actual Length (µm)	$\overline{\delta}_{ox}$ (µm)		
A1	402.404	396.6	±	12.5
A2	408.173			
A3	379.327			
B1	85.855	81.3	±	8.8
B2	69.079			
B3	89.093			
C1	401.250	405.3	±	3.1
C2	405.937			
C3	408.750			

Appendix 10: Derivation of hypothesis that linear to parabolic transition is denoted by sudden variation in local gradient.

For linear model,

$$f(x) = ax + b$$

$$f'(x) = a \ \therefore constant\ local\ gradient$$

For parabolic model,

$$f(x) = ax^2 + bx + c$$

$$f'(x) = 2ax + b \ \therefore local\ gradient\ increases\ with\ x$$

Appendix 11: Sheet deformation process equations

$$Principal\ stresses = \ \sigma_1, \sigma_2, \sigma_3; Principal\ strains = \ \varepsilon_1, \varepsilon_2, \varepsilon_3; Maximum\ shear\ stresses = \ \tau_1, \tau_2, \tau_3$$

$$\varepsilon_1 = \frac{d_{1_1}}{d_{1_0}};\ \varepsilon_2 = \frac{d_{2_1}}{d_{2_0}};\ \varepsilon_3 = \frac{d_{3_1}}{d_{3_0}}$$

$$\beta = \frac{\varepsilon_2}{\varepsilon_1};\ \alpha = \frac{2\beta + 1}{2 + \beta} = \frac{\sigma_2}{\sigma_1}$$

$$\varepsilon_3 = -(1 + \beta)\varepsilon_1$$

$$\bar{\varepsilon} = \sqrt{\frac{4}{3}(1 + \beta + \beta^2)\varepsilon_1} = \sqrt{\frac{2}{3}(\varepsilon_1^2 + \varepsilon_2^2 + \varepsilon_3^2)}$$

$$\sigma_1 = \frac{\alpha}{\sqrt{1 - \alpha + \alpha^2}}$$

$$\tau_1 = \frac{\sigma_1 - \sigma_2}{2}$$

$$\tau_2 = \frac{\sigma_2 - \sigma_3}{2}$$

$$\tau_3 = \frac{\sigma_3 - \sigma_1}{2}$$

Appendix 12: Detailed theoretical and mathematical basis for Density Functional Theory (DFT).

An example of an

$\boldsymbol{N_{body}}$-body problem is a regular crystal, wherein the electrons are not only affected by lattice-located nuclei (protons) but also other orbiting electrons in terms of their charge and spin. The main goal of the DFT approach is to obtain "…a one-electron Schrodinger equation (which predicts particle behaviour in a quantum system, its 'wave function') with a local effective potential for the study of the ground state electronic density of the many-electron systems." [245].

The Hohenberg-Kohn theorem states that "…there is a one-to-one correspondence between

the ground-state density of an

$\boldsymbol{N_{body}}$-electron system and the external potential acting on it…", i.e. system density determines all the ground-state properties of a system. As a result, the ground-state electron density is of interest, as the functional within the ground state energy functional, and the total electronic energy of a system, $\boldsymbol{E_{tot}}$, can be determined if the electron density functional, $\boldsymbol{n}(\underline{\mathbf{r}})$, (a function of time and space) is known, i.e. $\boldsymbol{E_{tot}}[\boldsymbol{n}(\underline{\mathbf{r}})]$. Crucially, the electron density if only a function of three spatial coordinates, $\boldsymbol{x, y, z}$, whereas the electronic wavefunction used in other calculations is a function of all the coordinates of $\boldsymbol{N_{body}}$ individual atoms in the system, i.e. $\boldsymbol{3N_{body}}$. Mathematical description begins with the many-electron Hamiltonian, $\widehat{\boldsymbol{H}}$, which comprises an internal (electron kinetic energy and electron-electron Coulomb interactions) and external (ion-electron potential, ion-ion potential, and exchange-correlation energies, the latter being associated with parallel spin and Coulombic repulsions) components $\boldsymbol{H_{int}}$ and $\boldsymbol{V_{ext}}$ respectively. The number of degrees of freedom of the system is minimised using the Born-Oppenheimer approximation (the assumption that electrons respond instantaneously to ion motion due to their large respective difference in mass, i.e. there is interdependence between electronic energies and nuclear dynamics [501]). The key element is careful selection of the electron density mathematical description. The Hohenberg-Kohn theorem can be most simply described as $\boldsymbol{n}(\underline{\mathbf{r}}) \rightarrow \boldsymbol{v}(\underline{\mathbf{r}}) \rightarrow \widehat{\boldsymbol{H}}$, where $\boldsymbol{v}$ is a functional of the ground state density, $\boldsymbol{n}$, and $\underline{\mathbf{r}}$ represents space-spin coordinates ($\underline{\mathbf{r}}_i \in \mathbb{R}^3$). Thus, the total electronic energy functional combines the universal density functional, $\boldsymbol{F}[\boldsymbol{n}]$, and specific external potential, $\boldsymbol{v_{ne}}(\underline{\mathbf{r}})$, of the system (see Equation 10.1) and can be minimised over

$\boldsymbol{N_{body}}$-electron densities to obtain the exact ground-state energy, $\boldsymbol{E_0}$ (see Equation 10.2).

$$\boldsymbol{E}[\boldsymbol{n}] = \boldsymbol{F}[\boldsymbol{n}] + \int \boldsymbol{v}_{\mathrm{ne}}(\underline{\mathbf{r}})\boldsymbol{n}(\underline{\mathbf{r}})\mathbf{d}\mathbf{r}$$

Equation 10.1

$$\boldsymbol{E_0} = \boldsymbol{\min_{n}}\{\boldsymbol{F}[\boldsymbol{n}] + \int \boldsymbol{v}_{\mathrm{ne}}(\underline{\mathbf{r}})\boldsymbol{n}(\underline{\mathbf{r}})\mathbf{d}\underline{\mathbf{r}}\}$$

Equation 10.2

Appendix 13: Known data points for temperature-dependent mechanical properties of wüstite (FeO) and iron (Fe).

$FeO\ elastic\ modulus -$

$temperature\ dependence\ [T(K), E(GPa)] known\ data\ points\ from\ Saeki\ et\ al$ [419]

$$\boldsymbol{[973, 98.6]; [1273, 83.4]}$$

FeO lattice parameter –

temperature dependence $[T(K), a(\text{Å})]$*known data points from Hayakawa et al* [434]

$$[\mathbf{1192, 4.3408}]; [\mathbf{1450, 4.3613}]$$

$$(7.685 \times 10^{-6}\, T(°C) + 4.2702)$$

Data for comparison with literature values of ambient FeO lattice parameter

Source	$\boldsymbol{a}$ (Å)
Sundman [244]	4.306
Shen et al. [502]	4.332
Hamada et al. [503]	4.308
Schrettle et al. [423]	4.298

Fe elastic modulus –

temperature dependence $[T(K), E(GPa)]$*known data points from Li et al* [437]

$$[\mathbf{300, 220}]; [\mathbf{975, 165}]$$

Fe lattice parameter –

temperature dependence $[T(K), a(\text{Å})]$ *known data points from Basinski et al* [338]

$$[\mathbf{273, 2.860}]; [\mathbf{1173, 2.898}]\ (273 \leq \boldsymbol{T} \leq 1173K)$$

$$[\mathbf{1173, 2.869}]; [\mathbf{1673, 2.910}]\ (1173 < \boldsymbol{T} \leq 1673K)$$

Appendix 14: Derivation of relationship between volumetric, $\boldsymbol{\beta}$, and linear, $\boldsymbol{\alpha}$, thermal expansion coefficients based on thermal expansion theory [433].

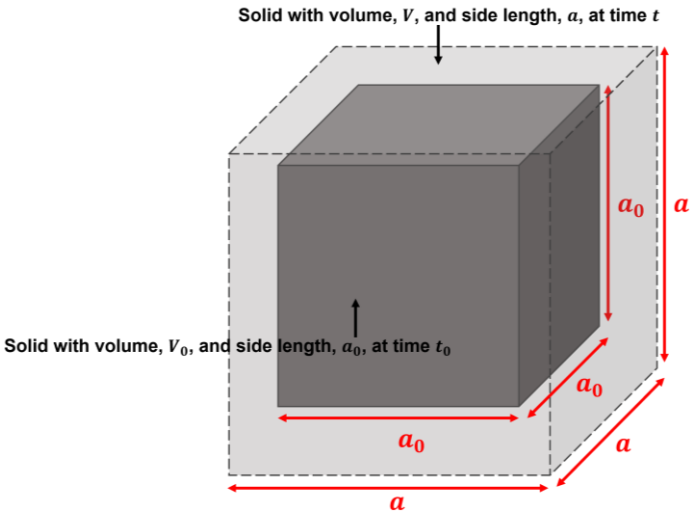


Figure 10.7: Schematic of dimension changes during expansion of a solid ¤.

$$dL = L_0 \alpha dT;\ dV = V_0 \beta dT$$

$$\therefore \alpha = \frac{1}{L_0}\frac{dL}{dT};\ \beta = \frac{1}{V_0}\frac{dV}{dT}$$

$$V = L^3\ (for\ isotropic\ materials)$$

$$\therefore \beta = \frac{1}{L_0^3}\frac{dV}{dT}$$

$$\frac{\beta}{\alpha} = \frac{dV}{dT}\frac{1}{L_0^3}\cdot\frac{L_0 dT}{dL} = \frac{1}{L_0^2}\frac{dV}{dL}$$

$$\frac{dV}{dL} = 3L^2$$

$$\frac{\beta}{\alpha} = 3L_0^2.\frac{1}{L_0^2}$$

$$\therefore \frac{\beta}{\alpha} = 3$$

Appendix 15: Fourth derivative of function used to determine error bound for stability of Composite Simpson's rule parameters.

$$\boldsymbol{a = p_{oxide}; b = q_{oxide}; i = p_{metal}; j = q_{metal}; k = m_{ox}; l = m_m; x = T;} = \frac{\boldsymbol{\delta_{ox}}}{\boldsymbol{\delta_m}}\left(\frac{\boldsymbol{1 - v_m}}{\boldsymbol{1 - v_{ox}}}\right)$$

$$\frac{\partial^4}{\partial x^4}\left(\frac{\left(\frac{3a^3x^2+6a^2bx+3ab^3}{a^3x^3+3a^2bx^2+3ab^3x}-\frac{3i^3x^2+6i^2jx+3ij^3}{i^3x^3+3i^2jx^2+3ij^3x}\right)kx}{1+\frac{z(kx)}{lx}}\right)$$

$$=\frac{1}{\frac{kz}{l}+1}kx\left(36\left(\frac{2(3x^2a^3+6bxa^2+3b^3a)^2}{(3axb^3+3a^2x^2b+a^3x^3)^3}\right.\right.$$

$$\left.-\frac{6xa^3+6ba^2}{(3axb^3+3a^2x^2b+a^3x^3)^2}\right)a^3+(3x^2a^3+6bxa^2$$

$$+3b^3a)\left(\frac{24(3x^2a^3+6bxa^2+3b^3a)^4}{(3axb^3+3a^2x^2b+a^3x^3)^5}\right.$$

$$-\frac{36(6xa^3+6ba^2)(3x^2a^3+6bxa^2+3b^3a)^2}{(3axb^3+3a^2x^2b+a^3x^3)^4}$$

$$\left.+\frac{48a^3(3x^2a^3+6bxa^2+3b^3a)}{(3axb^3+3a^2x^2b+a^3x^3)^3}+\frac{6(6xa^3+6ba^2)^2}{(3axb^3+3a^2x^2b+a^3x^3)^3}\right)+4(6xa^3$$

$$+6ba^2)\left(-\frac{6a^3}{(3axb^3+3a^2x^2b+a^3x^3)^2}\right.$$

$$+\frac{6(6xa^3+6ba^2)(3x^2a^3+6bxa^2+3b^3a)}{(3axb^3+3a^2x^2b+a^3x^3)^3}-\frac{6(3x^2a^3+6bxa^2+3b^3a)^3}{(3axb^3+3a^2x^2b+a^3x^3)^4)}$$

$$-(3x^2i^3+6jxi^2+3j^3i)\left(\frac{24(3x^2i^3+6jxi^2+3j^3i)^4}{(3ixj^3+3i^2x^2j+i^3x^3)^5}\right.$$

$$-\frac{36(6xi^3+6ji^2)(3x^2i^3+6jxi^2+3j^3i)^2}{(3ixj^3+3i^2x^2j+i^3x^3)^4}$$

$$\left.+\frac{48i^3(3x^2i^3+6jxi^2+3j^3i)}{(3ixj^3+3i^2x^2j+i^3x^3)^3}+\frac{6(6xi^3+6ji^2)^2}{(3ixj^3+3i^2x^2j+i^3x^3)^3}\right)$$

$$+4(-6xi^3-6ji^2)\left(-\frac{6i^3}{(3ixj^3+3i^2x^2j+i^3x^3)^2}\right.$$

$$+\frac{6(6xi^3+6ji^2)(3x^2i^3+6jxi^2+3j^3i)}{(3ixj^3+3i^2x^2j+i^3x^3)^3}-\frac{6(3x^2i^3+6jxi^2+3j^3i)^3}{(3ixj^3+3i^2x^2j+i^3x^3)^4}$$

$$\left.-36i^3\left(\frac{2(3x^2i^3+6jxi^2+3j^3i)^2}{(3ixj^3+3i^2x^2j+i^3x^3)^3}-\frac{6xi^3+6ji^2}{(3ixj^3+3i^2x^2j+i^3x^3)^2}\right)\right)$$

$$+\frac{1}{\frac{kz}{l}+1}4k\left(-\frac{18(3x^2a^3+6bxa^2+3b^3a)a^3}{(3axb^3+3a^2x^2b+a^3x^3)^2}+(3x^2a^3+6bxa^2\right.$$

$$+3b^3a)\left(-\frac{6a^3}{(3axb^3+3a^2x^2b+a^3x^3)^2}\right.$$

$$\left.+\frac{6(6xa^3+6ba^2)(3x^2a^3+6bxa^2+3b^3a)}{(3axb^3+3a^2x^2b+a^3x^3)^3}-\frac{6(3x^2a^3+6bxa^2+3b^3a)^3}{(3axb^3+3a^2x^2b+a^3x^3)^4}\right)$$

$$+3(6xa^3+6ba^2)\left(\frac{2(3x^2a^3+6bxa^2+3b^3a)^2}{(3axb^3+3a^2x^2b+a^3x^3)^3}\right.$$

$$-\frac{6xa^3+6ba^2}{(3axb^3+3a^2x^2b+a^3x^3)^2}\Bigg)$$
$$-\left(-\frac{6i^3}{(3ixj^3+3i^2x^2j+i^3x^3)^2}+\frac{6(6xi^3+6ji^2)(3x^2i^3+6jxi^2+3j^3i)}{(3ixj^3+3i^2x^2j+i^3x^3)^3}\right.$$
$$\left.-\frac{6(3x^2i^3+6jxi^2+3j^3i)^3}{(3ixj^3+3i^2x^2j+i^3x^3)^4}\right)$$
$$+3(-6xi^3-6ji^2)\left(\frac{2(3x^2i^3+6jxi^2+3j^3i)^2}{(3ixj^3+3i^2x^2j+i^3x^3)^3}-\frac{6xi^3+6ji^2}{(3ixj^3+3i^2x^2j+i^3x^3)^2}\right)$$
$$+\frac{18i^3(3x^2i^3+6jxi^2+3j^3i)}{(3ixj^3+3i^2x^2j+i^3x^3)^2)}$$

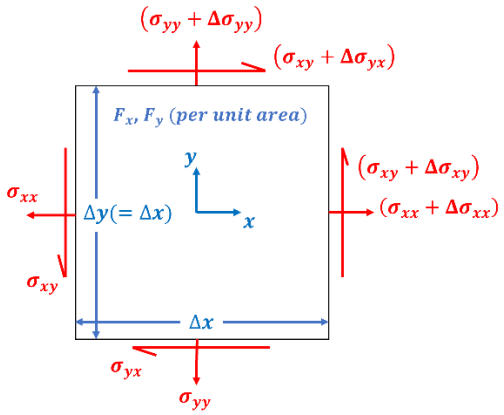
Appendix 16: Calculation of lattice parameter using X-ray diffraction (XRD) data.

$$d=\frac{\lambda}{2sin\theta}=\frac{2.2897\times10^{-12}}{2\sin\frac{156.396}{2}}=1.17\text{Å}$$

$$a=d\sqrt{h^2+k^2+l^2}=1.17\times10^{-12}\sqrt{2^2+1^2+1^2}=2.86\text{Å}$$

$Basinski\ et\ al\ \ a=2.89$Å [338]

Appendix 17: A small area 2D element in equilibrium.



Chapter 11 References

[1] Office for National Statistics. "CPA 08:EU:IM:CP:BOP:SA: 24.5. Cast iron & steel tubes & pipes (UK trade in goods by classification of product by activity time series (MQ10))." https://www.ons.gov.uk/businessindustryandtrade/internationaltrade/timeseries/p3ka/mq10 (accessed June. 12, 2025).

[2] Tata Steel, "Install® Plus 235 & Inline™ 265: Hot-Part-2 PED & high temperature carbon steel tubes for building & industrial services," 2021. [Online]. Available: https://www.tatasteeleurope.com/construction/products/tube/conveyance

[3] British Fluid Power Association, "The diferences between and how to specify 'tube' and 'pipe'," ed. Chipping Norton, UK, 2019.

[4] *Welded steel tubes for pressure purposes - Technical delivery conditions (Part 2: Electric welded non-alloy and alloy steel tubes with specified elevated temperature properties)*, BS EN 10217-2, 2019. [Online]. Available: https://bsol.bsigroup.com/Bibliographic/BibliographicInfoData/000000000030438140

[5] G. D. West, S. Birosca, and R. L. Higginson, "Phase determination and microstructure of oxide scales formed on steel at high temperature," *Journal of Microscopy,* vol. 217, no. 2, pp. 122-129, January. 31, 2005. [Online]. Available: https://doi.org/10.1111/j.1365-2818.2005.01409.x.

[6] S. K. Mandal, "Formation of Microstructures in Steel: Structure–Property Relationship," *Steel Metallurgy: Properties, Specifications and Applications.* India: McGraw-Hill, 2015. [Online]. Available: https://ifind.swansea.ac.uk/permalink/44WHELF_SWA/1jlslid/alma9983828299024117

[7] H. T. Abuluwefa, "Scale formation in a walking-beam steel reheat furnace," M.Eng. thesis, Mining and Metallurgical Engineering, McGill University, Montreal, Quebec, Canada, 1992. [Online]. Available: https://escholarship.mcgill.ca/concern/theses/mg74qn11x

[8] Tata Steel UK Limited. "New hi-tech tubes warehouse at Tata Steel's Corby steelworks." https://www.tatasteeluk.com/corporate/news/New-hi-tech-tubes-warehouse-at-tata-steels-corby-steelworks (accessed June. 11, 2025).

[9] J. Grant, "The Development of Novel Coating Solutions for the Improvement of Pre/Post Heat Treatment Performance Properties of Carbon Steel Conveyance Tubes," Eng.D. thesis, Department of Materials Science and Engineering, Swansea University, Swansea, Wales, UK, 2024. [Online]. Available: http://dx.doi.org/10.23889/SUthesis.66151

[10] D. Llewellyn and R. C. Hudd, "Low-carbon strip steels," *Steels: Metallurgy and Applications,* 3rd ed. Oxford, England: Woburn, 1998, pp. 1-136. [Online]. Available: https://ifind.swansea.ac.uk/permalink/44WHELF_SWA/1sssfk8/alma995312823402417

[11] W. Melfo, H. Bolt, D. Staalman, C. Benito Castro, D. Crowther, and B. Jana, "Experimental Study on Primary Scale Formation and Descalability on Steels Containing Ni and Ni+Si," *ISIJ International,* vol. 53, no. 5, pp. 866-873, 2013. [Online]. Available: https://www.jstage.jst.go.jp/article/isijinternational/53/5/53_866/_pdf/-char/en.

[12] B. Picque, P.-O. Bouchard, P. Montmitonnet, and M. Picard, "Mechanical behaviour of iron oxide scale: Experimental and numerical study," *Wear,* vol. 260, no. 3, pp.

231-242, February 2006. [Online]. Available: https://doi.org/10.1016/j.wear.2005.03.037.

[13] M. A. Rozenbaum, A. V. Serebryakov, I. Bazhukov, and G. V. Shimov, "Study of Residual Stresses and Surface Hardening in Tubes for Nuclear Steam Generators," *Solid State Phenomena,* vol. 265, pp. 53-59, 2017. [Online]. Available: http://dx.doi.org/10.4028/www.scientific.net/SSP.265.53.

[14] M. Krzyzanowski, J. H. Beynon, and D. C. J. Farrugia, "Introduction," in *Oxide Scale Behaviour in High Temperature Metal Processing*. Weinheim, Germany: Wiley-VCH Verlag GmbH & Co. KGaA, 2010, pp. 1-6.

[15] M. Torres and R. Colas, "A model for heat conduction through the oxide layer of steel during hot rolling," *Journal of Materials Processing Technology,* vol. 105, no. 3, pp. 258-263, September, 29 2000, doi: https://doi.org/10.1016/S0924-0136(00)00569-0.

[16] M. Landfahrer, C. Schluckner, R. Prieler, H. Gerhardter, T. Zmek, J. Klarner, and C. Hochenauer, "Numerical and experimental investigation of scale formation on steel tubes in a real-size reheating furnace," *International Journal of Heat and Mass Transfer,* vol. 129, pp. 460-467, February 2019. [Online]. Available: https://doi.org/10.1016/j.ijheatmasstransfer.2018.09.110.

[17] J. Purbolaksono, J. Ahmad, A. Khinani, A. A. Ali, and A. Z. Rashid, "Failure case studies of SA213-T22 steel tubes of boiler through computer simulations," *Journal of Loss Prevention in the Process Industries,* vol. 23, no. 1, pp. 98-105, January 2010. [Online]. Available: https://doi.org/10.1016/j.jlp.2009.06.005.

[18] J. Zhao, L. Ma, M. E. Zayed, A. H. Elsheikh, W. Li, Q. Yan, and J. Wang, "Industrial reheating furnaces: A review of energy efficiency assessments, waste heat recovery potentials, heating process characteristics and perspectives for steel industry," *Process Safety and Environmental Protection,* vol. 147, pp. 1209-1228, March 2021. [Online]. Available: https://doi.org/10.1016/j.psep.2021.01.045.

[19] (2008). *Climate Change Act*. [Online] Available: https://www.legislation.gov.uk/ukpga/2008/27/contents

[20] M. Auinger, M. Buchler, H. Schoneich, C. Gierl-Mayer, and H. Danninger, "Hydrogen accumulation and diffusion in cylindrical-shaped pipeline steels with coating defects," *International Journal of Hydrogen Energy,* vol. 48, no. 88, pp. 34454-34462, October 2023. [Online]. Available: https://doi.org/10.1016/j.ijhydene.2023.05.181.

[21] O. Bouledroua, D. Zelmati, Z. Hafsi, and M. B. Djukic, "Hydrogen embrittlement effects on remaining life and fatigue crack growth rate in API 5L X52 steel pipelines under cyclic pressure loading," *Engineering Failure Analysis,* vol. 166, December 2024. [Online]. Available: https://doi.org/10.1016/j.engfailanal.2024.108917.

[22] O. A. Zambrano, J. J. Coronado, and S. A. Rodriguez, "Mechanical properties and phases determination of low carbon steel oxide scales formed at 1200 °C in air," *Surface and Coatings Technology,* vol. 282, pp. 155-162, November 2015. [Online]. Available: https://doi.org/10.1016/j.surfcoat.2015.10.028.

[23] Z. Y. Jiang, J. Tang, W. Sun, A. K. Tieu, and D. Wei, "Analysis of tribological feature of the oxide scale in hot strip rolling," *Tribology International,* vol. 43, pp. 1339-1345, January 2010. [Online]. Available: https://doi.org/10.1016/j.triboint.2009.12.070.

[24] P. Wang, K. Du, H. Yin, and D. Wang, "Enhancing oxide scale growth and adhesion via electrochemically regulating ion diffusion," *Journal of Materials Science & Technology,* vol. 158, pp. 133-144, September 2023. [Online]. Available: https://doi.org/10.1016/j.jmst.2023.02.032.

[25] (1915). *Scientific Paper 249, The emissivity of metals and oxides. IV. Iron oxide*. [Online] Available: https://archive.org/details/emiss1283891915249249unse/page/n1/mode/2up

[26] D. F. J. Staalman, B. Martin, R. Speets, and P. Pronk, "Improving the Through-Furnace Accuracy of Slab Temperature Prediction and Optimizing Pacing in Reheating Furnaces of a Hot Strip Mill," ed, 2015.

[27] B. Yu, Y. Liu, L. Wei, X. Zhang, Y. Du, Y. Wang, and S. Ye, "A Mechanism of Anti-Oxidation Coating Design Based on Inhibition Effect of Interface Layer on Ions Diffusion within Oxide Scale," *Coatings,* vol. 11, no. 4, April 2021. [Online]. Available: https://doi.org/10.3390/coatings11040454.

[28] C. Schluckner, C. Gaber, M. Demuth, S. Forstinger, R. Prieler, and C. Hochenauer, "CFD-model to predict the local and time-dependent scale formation of steels in air- and oxygen enriched combustion atmospheres," *Applied Thermal Engineering,* vol. 143, pp. 822-835, October 2018. [Online]. Available: https://doi.org/10.1016/j.applthermaleng.2018.08.010.

[29] R. Pillai, A. Chyrkin, and W. J. Quadakkers, "Modeling in High Temperature Corrosion: A Review and Outlook," *Oxidation of Metals,* vol. 96, pp. 385-436, May. 21, 2021. [Online]. Available: https://link.springer.com/article/10.1007%2Fs11085-021-10033-y.

[30] *Non-alloy steel tubes suitable for welding and threading - Technical delivery conditions*, BS EN 10255, 2004. [Online]. Available: https://bsol.bsigroup.com/Bibliographic/BibliographicInfoData/000000000030165691

[31] A. Merchichi, G.-E. Mailloux-Keroack, L. Coudert, C. Bazin, and J.-F. Boulanger, "Graphite processing from beneficiation to final product: a review focused on purification of natural and recycled materials," *Separation and Purification Technology,* vol. 380, 2, February 2026. [Online]. Available: https://doi.org/10.1016/j.seppur.2025.135068.

[32] R. E. Smallman and A. H. W. Ngan, "Phase equilibria and structure," *Physical Metallurgy and Advanced Materials.* Amsterdam, The Netherlands: Butterworth Heinemann, 2007, pp. 37-94. [Online]. Available: https://ifind.swansea.ac.uk/permalink/44WHELF_SWA/1jlslid/alma9982818866024117

[33] J. Andersson, T. Helander, L. Hoglund, P. Shi, and B. Sundman, "Thermo-Calc & DICTRA, computational tools for materials science," *Calphad,* vol. 26, no. 2, pp. 273-312, June 2002. [Online]. Available: https://doi.org/10.1016/S0364-5916(02)00037-8.

[34] Schuler GmbH, "Solid Forming (Forging)," *Metal Forming Handbook.* Berlin, Germany: Springer, 1998, pp. 433-477. [Online]. Available: https://ebookcentral.proquest.com/lib/swansea-ebooks/detail.action?pq-origsite=primo&docID=3092167

[35] S. Reskovic and F. Vodopivec, "An investigation of the stretch reducing of welded tubes," *Materials and Technologies,* vol. 42, no. 6, pp. 257-262, November 2008. [Online]. Available: https://www.researchgate.net/publication/287847548_An_investigation_of_the_stretch_reducing_of_welded_tubes.

[36] S. Zinn, S. L. Semiatin, Electric Power Research Institute, Batelle Memorial Institute, and Columbus Laboratories, "Theory of Induction Heating," *Elements of Induction Heating Design, Control, and Applications.* Materials Park, OH, USA and Polo Alto, CA, USA: ASM International and Electric Power Research Institute, 1988, pp. 9-26. [Online]. Available:

https://ifind.swansea.ac.uk/permalink/44WHELF_SWA/1jlslid/alma9982825937024117

[37] J. Woolman and R. A. Mottram, "Cold-Forming Steels," *vol. 1*, *The Mechanical and Physical Properties of the British Standard EN Steels (BS 970-1955).* New York, NY, USA: The Macmillan Company, 1964, pp. 11-37. [Online]. Available: https://ifind.swansea.ac.uk/permalink/44WHELF_SWA/1jlslid/alma9986115278024117

[38] J. I. Asperheim, P. Das, B. Grande, D. Homberg, and P. T., "Numerical simulation of high-frequency induction welding in longitudinal welded tubes," *Journal of Mathematics in Industry,* vol. 14, no. 10, July 2024. [Online]. Available: https://doi.org/10.1186/s13362-024-00147-8.

[39] J. R. Davis, "Basic Understanding of Weld Corrosion," *Corrosion of Weldments.* Materials Park, OH, USA: ASM International, 2006, pp. 1-13. [Online]. Available: https://ifind.swansea.ac.uk/permalink/44WHELF_SWA/1jlslid/alma9982826309024117

[40] V. P. K. Rao, "Welding," *Manufacturing Science and Technology,* 2nd ed. New Delhi, India: New Age International Limited, 2009, pp. 91-129. [Online]. Available: https://ifind.swansea.ac.uk/permalink/44WHELF_SWA/1jlslid/alma9982887097024117

[41] S. Zinn, S. L. Semiatin, Electric Power Research Institute, Batelle Memorial Institute, and Columbus Laboratories, "Process Design for Specific Applications," *Elements of Induction Heating Design, Control, and Applications.* Materials Park, OH, USA and Polo Alto, CA, USA: ASM International and Electric Power Research Institute, 1988, pp. 85-142. [Online]. Available: https://ifind.swansea.ac.uk/permalink/44WHELF_SWA/1jlslid/alma9982825937024117

[42] R. E. Smallman and A. H. W. Ngan, "Mechanical Properties I," *Physical Metallurgy and Advanced Materials.* Amsterdam, The Netherlands: Butterworth Heinemann, 2007, pp. 289-324. [Online]. Available: https://ifind.swansea.ac.uk/permalink/44WHELF_SWA/1jlslid/alma9982818866024117

[43] C. Kang, C. Shi, Z. Liu, Z. Liu, X. Jiang, S. Chen, and C. Ma, "Research on the optimization of welding parameters in high-frequency induction welding pipeline," *Journal of Manufacturing Processes,* vol. 59, pp. 772-790, November 2020. [Online]. Available: https://doi.org/10.1016/j.jmapro.2020.10.021.

[44] L. A. Weiss. "Melting Point of Metals & Alloys." All Metals & Forge Group. https://steelforge.com/literature/metal-melting-ranges/ (accessed August, 16., 2022).

[45] S. I. Group. "High-frequency induction welding (HFIW)." https://shahab-co.com/tutorials/high-frequency-induction-welding-hfiw/ (accessed August, 16., 2022).

[46] R. Singh, "Physical Effect of Heat on Material During Welding," *Applied Welding Engineering Processes, Codes, and Standards.* Waltham: Elsevier, 2011, pp. 171-175. [Online]. Available: https://ifind.swansea.ac.uk/permalink/44WHELF_SWA/1sssfk8/alma999192384202417

[47] S. M. Hasan, M. Ghosh, D. Chakrabati, and S. B. H. Singh, "Development of continuously cooled low-carbon, low-alloy, high strength carbide-free bainitic rail steels " *Materials Science and Engineering A,* vol. 771, 2020. [Online]. Available: https://doi.org/10.1016/j.msea.2019.138590.

[48] N. Shajan, R. Kumar, R. Manik, B. Asati, S. Dhagde, D. Dhangi, S. Kumar, M. M. Mahapartra, and K. S. Arora, "Role of residual stress in the failure of HF-ERW welded tubes," *Engineering Failure Analysis,* vol. 161, July 2024. [Online]. Available: https://doi.org/10.1016/j.engfailanal.2024.108342.

[49] H. K. D. H. Bhadeshia and R. W. K. Honeycombe, "The iron–carbon equilibrium diagram and plain carbon steels," *Steels: Microstructure and Properties.* Amsterdam, The Netherlands: Butterworth-Heinemann, 2006, pp. 39-70. [Online]. Available: https://ifind.swansea.ac.uk/permalink/44WHELF_SWA/1jlslid/alma9982813363024117

[50] D. Llewellyn and R. C. Hudd, "Low-carbon structural steels," *Steels: Metallurgy and Applications,* 3rd ed. Oxford, England: Woburn, 1998, pp. 137-198. [Online]. Available: https://ifind.swansea.ac.uk/permalink/44WHELF_SWA/1sssfk8/alma995312823402417

[51] Clifton Steels. "Anneal, Normalize, and Stress Relieve." https://www.cliftonsteel.com/knowledge-center/anneal-normalize-stress-relieve (accessed January. 18, 2022).

[52] (1967). *Tech. Paper TM 43-0106, Aerospace Metals – General Data and Usage Factors*. [Online] Available: https://www.liberatedmanuals.com/TM-43-0106.pdf

[53] J. Wang, J. Jiang, S. Wan, G. Yi, X. Yu, W. Fan, W. Jing, J. Kou, Q. Cheng, and Y. Shan, "Effect of microstructure and microtexture evolution of oxide layer over J82B steel on mechanical descaling properties," *Materials Today Communications,* vol. 37, December 2023. [Online]. Available: https://doi.org/10.1016/j.mtcomm.2023.107079.

[54] F. Xiao, B. Liao, Y. Shan, and K. Yang, "Isothermal transformation of low-carbon microalloyed steels," *Materials Characterization,* vol. 54, no. 4-5, pp. 417-422, May 2005. [Online]. Available: https://doi.org/10.1016/j.matchar.2005.01.007.

[55] H. K. D. H. Bhadeshia and R. W. K. Honeycombe, "Bainite," *Steels*4th ed. San Diego, CA, USA: Elsevier Science & Technology, 2017, pp. 205-224. [Online]. Available: https://ifind.swansea.ac.uk/permalink/44WHELF_SWA/1sssfk8/alma9985999914024117

[56] L. Holappa, V. Ollilainen, and W. Kasprzak, "The effect of silicon and vanadium alloying on the microstructure of air cooled forged HSLA steels," *Journal of Materials Processing Technology,* vol. 109, no. 1-2, pp. 78-82, February 2001. [Online]. Available: https://doi.org/10.1016/S0924-0136(00)00778-0.

[57] S. Brunbauer, G. Winter, T. Antretter, P. Staron, and W. Ecker, "Residual stress and microstructure evolution in steel tubes for different cooling conditions – Simulation and verification," *Materials Science and Engineering: A,* vol. 747, pp. 73-79, February 2019. [Online]. Available: https://doi.org/10.1016/j.msea.2019.01.037.

[58] M. Gensamer, E. B. Pearsall, W. S. Pellini, and J. R. Low Jr, "The Tensile Properties of Pearlite, Bainite, and Spheroidite," *Metallography, Microstructure, and Analysis,* vol. 1, pp. 171-189, October 2012. [Online]. Available: https://doi.org/10.1007/s13632-012-0027-7.

[59] R. Y. Chen and W. Y. D. Yeun, "Review of the High-Temperature Oxidation of Iron and Carbon Steels in Air or Oxygen," *Oxidation of Metals,* vol. 59, pp. 433-468, June 2003. [Online]. Available: https://link.springer.com/article/10.1023/A:1023685905159.

[60] P. Wilkstrom, W. Blasiak, and S. C. Du, "A study on oxide scale formation of low carbon steel using thermo gravimetric technique," *Ironmaking & Steelmaking,* vol. 35, no. 8, pp. 621-632, 2008. [Online]. Available: https://doi.org/10.1179/174328108X369116.

[61] British Metal Tube and Fittings Association (BMTFA) and Building Engineering Services Association (BESA) Technical Committee - Pipework Working Group. *More demanding - the range of different service applications*.

[62] Radyne Corporation. "Induction Pipe Heating Equipment and Processes." https://www.radyne.com/induction-heating-applications/induction-pipe-heating/ (accessed September, 6., 2022).

[63] Y.-Z. Jiang, H.-P. Tang, H.-H. Tang, S.-B. Deng, and X. Peng, "Explicit FE modelling of tube stretch reduction and analysis of wall thickness variation," *Ironmaking & Steelmaking,* vol. 42, no. 3, pp. 176-184, April 2015. [Online]. Available: https://doi.org/10.1179/1743281214Y.0000000217.

[64] J. H. Lee, W. Noh, D. Kim, and M. Lee, "Spallation analysis of oxide scale on low carbon steel," *Materials Science and Engineering: A,* vol. 676, pp. 385-394, October, 31. 2016. [Online]. Available: https://doi.org/10.1016/j.msea.2016.09.012.

[65] W. Noh, J. Lee, D. Kim, J. Song, and M. Lee, "Effects of the residual stress, interfacial roughness and scale thickness on the spallation of oxide scale grown on hot rolled steel sheet," *Materials Science and Engineering: A,* vol. 739, pp. 301-316, January, 2. 2019. [Online]. Available: https://doi.org/10.1016/j.msea.2018.10.009.

[66] V. Basabe and J. Szpunar, "Phase Composition of Oxide Scales during Reheating in Hot Rolling of Low Carbon Steel," *Steel Research International,* vol. 27, no. 11, pp. 818-824, November 2006. [Online]. Available: https://onlinelibrary.wiley.com/doi/epdf/10.1002/srin.200606467.

[67] H. T. Abuluwefa, R. I. L. Guthrie, and F. Ajersch, "Oxidation of low carbon steel in multicomponent gases: Part I. Reaction mechanisms during isothermal oxidation," *Metallurgical and Materials Transactions A,* vol. 28, pp. 1633–1641, August 1997. [Online]. Available: https://link.springer.com/article/10.1007/s11661-997-0255-7.

[68] L. J. Arachchige, C. Li, and F. Wang, "Recent advances in understanding iron/steel corrosion: Mechanistic insights from molecular simulations," *Current Opinion in Solid State and Materials Science,* vol. 35, March 2025. [Online]. Available: https://doi.org/10.1016/j.cossms.2025.101216.

[69] D. Poirier, E. Grandmaison, M. Matovic, K. R. Barnes, and B. Nelson, "High Temperature Oxidation of Steel in an Oxygen-enriched Low NOX Furnace Environment," *IFRF Combustion Journal,* September 2006. [Online]. Available: https://www.academia.edu/19759388/High_Temperature_Oxidation_of_Steel_in_an_Oxygen_enriched_Low_NOX_Furnace_Environment.

[70] N. Birks and G. H. Meier, "Mechanisms of Oxidation," in *Introduction to High Temperature Oxidation of Metals*. London, UK: Edward Arnold Ltd, 1983, pp. 31-65.

[71] W. Sun, A. K. Tieu, Z. Jiang, H. Zhu, and C. Lu, "Oxide scales growth of low-carbon steel at high temperatures," *Journal of Materials Processing Technology,* vol. 156, pp. 1300-1306, September, 30 2004, doi: https://doi.org/10.1016/j.jmatprotec.2004.04.172.

[72] I. Iordanova, M. Surtchev, K. S. Forcey, and V. Krastev, "High-temperature surface oxidation oflow-carbon rimming steel," *Surface and Interface Analysis,* vol. 30, pp. 158-160, September 2000. [Online]. Available: https://doi.org/10.1002/1096-9918(200008)30:1%3C158::AID-SIA744%3E3.0.CO;2-6.

[73] J. H. Jang, D. E. Lee, M. Y. Kim, and H. G. Kim, "Investigation of the slab heating characteristics in a reheating furnace with the formation and growth of scale on the slab surface," *International Journal of Heat and Mass Transfer,* vol. 53, no. 20, pp. 4326-4332, 2010. [Online]. Available: http://dx.doi.org/10.1016/j.ijheatmasstransfer.2010.05.061.

[74] D. P. Burke and R. L. Higginson, "Characterisation of multicomponent scales by electron back scattered diffraction (EBSD)," *Scripta Materialia,* vol. 42, no. 3, pp. 277-281, 2000. [Online]. Available: https://doi.org/10.1016/S1359-6462(99)00341-3.

[75] M. Krzyzanowski, J. H. Beynon, and D. C. J. Farrugia, "Scale Growth and Formation of Subsurface Layers," in *Oxide Scale Behaviour in High Temperature Metal Processing*. Weinheim, Germany: Wiley-VCH Verlag GmbH & Co. KGaA, 2010, pp. 29-66.

[76] M. Trull and J. H. Beynon, "High temperature tension tests and oxide scale failure," *Materials Science & Technology,* vol. 19, no. 6, pp. 749-755, 2003. [Online]. Available: https://doi.org/10.1179/026708303225003072.

[77] M. Krzyzanowski and J. H. Beynon, "Modelling the boundary conditions for thermomechanical processing - oxide scale behaviour and composition effects," *Modelling and Simulation in Materials Science and Engineering,* vol. 8, no. 6, pp. 927-945, 2000. [Online]. Available: https://doi.org/10.1088/0965-0393/8/6/312.

[78] M. Schütze, "An approach to a global model of the mechanical behaviour of oxide scales," *Materials at High Temperatures,* vol. 12, no. 2-3, pp. 237-247, 1994. [Online]. Available: https://doi.org/10.1080/09603409.1994.11689491.

[79] M. Krzyzanowski, J. H. Beynon, and D. C. J. Farrugia, "Physically Based Finite Element Model of the Oxide Scale: Assumptions, Numerical Techniques, Examples of Prediction," in *Oxide Scale Behaviour in High Temperature Metal Processing*. Weinheim, Germany: Wiley-VCH Verlag GmbH & Co. KGaA, 2010, pp. 179-205.

[80] S. Foorginezhadab, M. Mohseni-Dargahc, F. K., V. Aryaia, A. Razmjouae, R. Abbassia, V. Garaniyaf, A. Beheshtig, and M. Asadniaaf, "Recent Advances in Sensing and Assessment of Corrosion in Sewage Pipelines," *Process Safety and Environmental Protection,* vol. 147, pp. 192-213, March 2021. [Online]. Available: https://doi.org/10.1016/j.psep.2020.09.009.

[81] M. Krzyzanowski, J. H. Beynon, and D. C. J. Farrugia, "A Pivotal Role of Secondary Oxide Scale During Hot Rolling and for Subsequent Product Quality," in *Oxide Scale Behaviour in High Temperature Metal Processing*. Weinheim, Germany: Wiley-VCH Verlag GmbH & Co. KGaA, 2010, pp. 7-27.

[82] Z. Marciniak, J. L. Duncan, and S. J. Hu, "Bending of Sheet," *Mechanics of Sheet Metal Forming,* Oxford, UK: Butterworth-Heinemann, 2002, pp. 82-107. [Online]. Available: https://ifind.swansea.ac.uk/permalink/44WHELF_SWA/1jlslid/alma9982816360024117

[83] L. S. Bayoumi, "Analysis of flow and stresses in a tube stretch-reducing hot rolling schedule," *International Journal of Mechanical Sciences,* vol. 45, no. 3, pp. 553-565, 2003. [Online]. Available: https://doi.org/10.1016/S0020-7403(03)00047-X.

[84] H. E. Evans, "Stress effects in high temperature oxidation of metals," *International Materials Reviews,* vol. 40, no. 1, pp. 1-40, 1995. [Online]. Available: https://doi.org/10.1179/imr.1995.40.1.1.

[85] P. B. Entchev, D. C. Lagoudas, and J. C. Slattery, "Effects of non-planar geometries and volumetric expansion in the modeling of oxidation in titanium," *International Journal of Engineering Science,* vol. 39, no. 6, pp. 695-714, April 2001. [Online]. Available: https://doi.org/10.1016/S0020-7225(00)00053-7.

[86] C. H. Simmons, N. Phelps, and D. E. Maguire, "CAD Organization and Applications," *Manual of Engineering Drawing: Technical Product Specification and Documentation to British and International Standards,* 4th ed. Oxford, UK: Butterworth-Heinemann, 2012, pp. 23-38. [Online]. Available:

https://ifind.swansea.ac.uk/permalink/44WHELF_SWA/1jlslid/alma9981923682024117

[87] C. Lubich and D. Mansour, "Backward difference time discretization of parabolic differential equations on evolving surfaces," *IMA Journal of Numerical Analysis,* vol. 33, pp. 1365-1385, 2013, doi: 10.1093/imanum/drs044.

[88] S. R. K. Iyengar and R. K. Jain, "Boundary Value Problems in Ordinary Differential Equations and Initial and Boundary Value Problems in Partial Differential Equations," *Numerical Methods,* New Delhi, India: New Age International Ltd, 2009, pp. 201-309. [Online]. Available: https://ifind.swansea.ac.uk/permalink/44WHELF_SWA/1jlslid/alma9982886993024117

[89] C. H. Hsueh and A. G. Evans, "Oxidation induced stresses and some effects on the behavior of oxide films," *Journal of Applied Physics,* vol. 54, pp. 6672-6686, November 1983. [Online]. Available: https://doi.org/10.1063/1.331854.

[90] N. Birks and G. H. Meier, "Oxidation of Alloys," in *Introduction to High Temperature Oxidation of Metals*. London, UK: Edward Arnold Ltd, 1983, pp. 91-130.

[91] C. Zeng, A. Neils, J. Lesko, and N. Post, "Machine learning accelerated discovery of corrosion-resistant high-entropy alloys," *Computational Materials Science,* vol. 237, March 2024. [Online]. Available: https://doi.org/10.1016/j.commatsci.2024.112925.

[92] F. Wang, D. Zou, Q. Wang, X. Zhang, L. Tong, X. Liang, Y. Li, and Y. Jiang, "The negative effect of V content on high temperature oxidation resistance of austenitic stainless steels at 850C " *Materials Characterization,* vol. 212, June 2024. [Online]. Available: https://doi.org/10.1016/j.matchar.2024.113967.

[93] P. K. Imbrie and D. C. Lagoudas, "Morphological Evolution of TiO2 Scale Formed on Various 1D and 2D Geometries of Titanium," *Oxidation of Metals,* vol. 55, no. 4, pp. 359-399, April 2001. [Online]. Available: https://link.springer.com/article/10.1023/A:1010368412822.

[94] M. Krzyzanowski and J. H. Beynon, "Modelling the boundary conditions for thermo mechanical processing - oxide scale behaviour and composition effects," *Modelling and Simulation in Materials Science and Engineering,* vol. 8, no. 6, pp. 927-945, 2000. [Online]. Available: https://doi.org/10.1088/0965-0393/8/6/312.

[95] B. Panicaud, J. L. Grosseau-Poussard, and J. F. Dinhut, "On the growth strain origin and stress evolution prediction during oxidation of metals," *Applied Surface Science,* vol. 252, no. 16, pp. 5700-5713, June 2005. [Online]. Available: https://doi.org/10.1016/j.apsusc.2005.07.075.

[96] G. H. Majzoobi and A. Ghomi, "Optimisation of compound pressure cylinders," *Journal of Achievements in Materials and Manufacturing Engineering,* vol. 15, no. 2, pp. 135-145, 2006. [Online]. Available: https://www.semanticscholar.org/paper/Optimization-of-compound-pressure-cylinders-Majzoobi-Ghomi/d6f006e84fc827aa16c5e79864971e9eb6b05a96.

[97] A. Paul, "The Kirkendall Effect in Solid-State Diffusion," Ph. D, Laboratory of Materials and Interface Chemistry, Eindhoven University of Technology, Eindhoven, The Netherlands, 2004. [Online]. Available: https://www.phase-trans.msm.cam.ac.uk/2004/Kirkendall.Aloke.pdf

[98] Y. Kraftmakher, "Equilibrium vacancies and thermophysical properties of metals," *Physics Reports,* vol. 299, no. 2-3, pp. 79-188, June 1998. [Online]. Available: https://doi.org/10.1016/S0370-1573(97)00082-3.

[99] S. Yamaguchi and M. Someno, "The Tracer Diffusivity of Oxygen in Wustite and Cobaltous Oxide," *Materials Transactions,* vol. 23, no. 5, pp. 259-266, 1982. [Online]. Available: https://doi.org/10.2320/matertrans1960.23.259.

[100] L. Bornstein. *Numerical Data and Functional Relationships in Science and Technology: Group III*, vol. 26, 1990.

[101] L. Xu, G. Qiao, X. Lu, Y. Gu, K. Xu, X. Chen, and F. Xiao, "Microstructure evolution and deformation mechanism along the thickness of heavy-wall ferrite-bainite dual-phase offshore pipelines by the progressive forming process," *Journal of Materials Processing Technology,* vol. 326, May 2024. [Online]. Available: https://doi.org/10.1016/j.jmatprotec.2024.118355.

[102] M. Schütze, "The Role of Stresses in High-Temperature Corrosion: The Potential of Quantitative Approaches," *High Temperature Corrosion of Materials,* vol. 100, pp. 365-397, 2023. [Online]. Available: https://doi.org/10.1007/s11085-023-10191-1.

[103] J. Takada, S. Yamamoto, S. Kikuchi, and M. Adachi, "Determination of diffusion coefficient of oxygen in γ-iron from measurements of internal oxidation in Fe-Al alloys," *Metallurgical Transaction A,* vol. 17, pp. 221-229, 1986. [Online]. Available: https://link.springer.com/article/10.1007/BF02643898.

[104] N. B. Pilling and R. E. Bedworth, "The Oxidation of Metals at High Temperature," *Journal of the Institute of Metals,* vol. 29, pp. 529-591, 1923.

[105] H. E. Evans, "The role of oxide grain boundaries in the development of growth stresses during oxidation," *Corrosion Science,* vol. 23, no. 5, pp. 495-506, 1983. [Online]. Available: https://doi.org/10.1016/0010-938X(83)90099-9.

[106] M. I. Manning, "Geometrical effects on oxide scale integrity," *Corrosion Science,* vol. 21, no. 4, pp. 301-316, 1981. [Online]. Available: https://doi.org/10.1016/0010-938X(81)90005-6.

[107] D. J. Srolovitz and T. A. Ramanarayanan, "An elastic analysis of growth stresses during oxidation," *Oxidation of Metals,* vol. 22, no. 4, pp. 133-146, 1984. [Online]. Available: https://doi.org/10.1007/BF00656901.

[108] F. N. Rhines and J. S. Wolf, "The role of oxide microstructure and growth stresses in the high-temperature scaling of nickel," *Metallurgical Transactions,* vol. 1, no. 6, pp. 1701-1710, June 1970. [Online]. Available: https://doi.org/10.1007/BF02642020.

[109] M. V. Speight and J. E. Harris, "The generation of stresses in oxide films growing by cation diffusion," *Acta Metallurgica,* vol. 26, no. 6, pp. 1043-1045, June 1978. [Online]. Available: https://doi.org/10.1016/0001-6160(78)90054-8.

[110] D. R. Clarke, "Stress generation during high-temperature oxidation of metallic alloys," *Current Opinion in Solid State and Materials Science,* vol. 6, no. 3, pp. 237-244, June 2002. [Online]. Available: https://doi.org/10.1016/S1359-0286(02)00074-8.

[111] A. K. Head, "The Interaction of Dislocations and Boundaries," *The London, Edinburgh, and Dublin Philosophical Magazine and Journal of Science* vol. 44, no. 348, pp. 92-94, 1953. [Online]. Available: https://doi.org/10.1080/14786440108520278.

[112] R. C. Wrede and M. R. Spiegel, "Fourier Series," *Advanced Calculus*, R. C. Wrede and M. R. Spiegel, Eds., 3rd ed.: McGraw-Hill, 2010, pp. 349-376. [Online]. Available: https://ifind.swansea.ac.uk/permalink/44WHELF_SWA/144jshv/alma998382835202417

[113] H. E. Evans, D. J. Norfolk, and T. Swan, "Perturbation of Parabolic Kinetics Resulting from the Accumulation of Stress in Protective Oxide Layers," *Journal of The Electrochemical Society,* vol. 125, no. 7, 1978, doi: 10.1149/1.2131644.

[114] D. R. Clarke, "The lateral growth strain accompanying the formation of a thermally grown oxide," *Acta Materialia,* vol. 51, no. 5, pp. 1393-1407, March 2003. [Online]. Available: https://doi.org/10.1016/S1359-6454(02)00532-3.

[115] F. H. Stott and A. Atkinson, "The modelling of growth stresses during high-temperature oxidation," *Materials at High Temperatures,* vol. 12, no. 2-3, pp. 195-207, 1994. [Online]. Available: https://doi.org/10.1080/09603409.1994.11689487.

[116] H. V. Atkinson, "A review of the role of short-circuit diffusion in the oxidation of nickel, chromium, and nickel-chromium alloys," *Oxidation of Metals,* vol. 24, pp. 177-197, October 1985. [Online]. Available: https://doi.org/10.1007/BF00664231.

[117] H. Steiner, J. Konys, and M. Heck, "Growth Stresses in Oxidized Tubes Under Uni- and Multi-Axial Oxidation Strain," *Oxidation of Metals,* vol. 66, pp. 37-67, 2006. [Online]. Available: https://link.springer.com/article/10.1007/s11085-006-9013-2.

[118] M. Krzyzanowski and J. H. Beynon, "The tensile failure of mild steel oxides under hot rolling conditions," *Steel Research International,* vol. 70, pp. 22-27, 1999. [Online]. Available: https://onlinelibrary.wiley.com/doi/pdf/10.1002/srin.199905596.

[119] G. W. Stachowiak and A. W. Batchelor, "Fundamentals of Contact Between Solids," *Engineering Tribology,* 4th ed. Oxford: Butterworth-Heinemann, 2014, pp. 475-524. [Online]. Available: https://ifind.swansea.ac.uk/permalink/44WHELF_SWA/144jshv/alma998192548202417

[120] F. Matsuno, "Blistering and Hydraulic Removal of Scale Films of Rimmed Steel at High Temperature," *Iron and Steel Institute of Japan (ISIJ) International,* vol. 20, pp. 413-421, June 1980. [Online]. Available: https://doi.org/10.2355/isijinternational1966.20.413.

[121] P. A. Schweitzer, "Coatings," *Corrosion Engineering Handbook. Corrosion of linings and coatings : cathodic and inhibitor protection and corrosion monitoring,* 2nd ed. Boca Raton: CRC Press, 2007, pp. 403-486. [Online]. Available: https://ifind.swansea.ac.uk/permalink/44WHELF_SWA/1jlslid/alma998473166202417

[122] M. Krzyanowski and J. H. Beynon, "The tensile failure of mild steel oxides under hot rolling conditions," *Steel Research International,* vol. 70, pp. 22-27, 1999. [Online]. Available: https://onlinelibrary.wiley.com/doi/pdf/10.1002/srin.199905596.

[123] N. N. Kalasin, S. Yenchum, and T. Nilsonthi, "Adhesion behaviour of scales on hot-rolled steel strips produced from continuous casting slabs," *Materials Today: Proceedings,* vol. 5, no. 3, 2, pp. 9359-9367, 2018. [Online]. Available: https://doi.org/10.1016/j.matpr.2017.10.111.

[124] C. Wagner, "Diffusion and High Temperature Oxidation of Metals," in *Atom Movements*, vol. 43A. Cleveland, OH, USA: American Society for Metals, 1951, pp. 153-173.

[125] J. M. Hulley and R. Rolls, "High-Temperature Cohesion and Adhesion of Oxide Scales on Mild Steel," *The Journal of the Iron and Steel Institute,* vol. 208, 1970.

[126] D. Woods, N. Leveson, and E. Hollnagel, "Properties of a Resilient Organisation: An Initial View," *Resilience Engineering: Concepts and Precepts.* Boca Raton: CRC Press, 2017, pp. 275-288. [Online]. Available: https://ifind.swansea.ac.uk/permalink/44WHELF_SWA/1jlslid/alma998281824602417

[127] O. D. A. Flavio, J. A. Carvalho, P. M. Sobrinho, and A. de Castro, "Analysis of oxy-fuel combustion as an alternative to combustion with air in metal reheating furnaces," *Energy,* vol. 78, pp. 290-297, December 2014. [Online]. Available: https://doi.org/10.1016/j.energy.2014.10.010.

[128] J. S. Sheasby, W. E. Boggs, and E. T. Turkdogan, "Scale growth on steels at 1200°C: rationale of rate and morphology," *Metal Science,* vol. 18, no. 3, pp. 127-136, 1984. [Online]. Available: https://doi.org/10.1179/msc.1984.18.3.127.

[129] B. Sudhangshu, "Oxidation- and Corrosion-Resistant Coatings," *High Temperature Coatings.* Boston, MA, USA: Elsevier, 2007, pp. 71-154. [Online]. Available: https://ifind.swansea.ac.uk/permalink/44WHELF_SWA/1jlslid/alma99828140280241 7

[130] National Materials Advisory Board, *High-Temperature Oxidation-Resistant Coatings*, R. I. Jaffee, R. A. Perkins, and G. Marshall Pound, eds., Washington, D. C., USA: National Academy of Sciences, 1970. [Online]. Available: https://nap.nationalacademies.org/read/20603/chapter/1.

[131] M. Torkar, B. Glogovac, F. Kaucic, D. Finzgar, and S. Triglav, "Diminution of scaling by the application of a protective coating," *Journal of Materials Processing Technology,* vol. 58, no. 3, pp. 217-222, 1996. [Online]. Available: https://doi.org/10.1016/0924-0136(95)02126-4.

[132] P. Liu, L. Wei, S. Ye, H. Xu, and Y. Chen, "Protecting stainless steel by glass coating during slab reheating," *Surface and Coatings Technology,* vol. 205, no. 12, pp. 3582-3587, March 2011. [Online]. Available: https://doi.org/10.1016/j.surfcoat.2010.12.036.

[133] R. L. Higginson, B. Roebuck, and E. J. Palmiere, "Texture development in oxide scales on steel substrates," *Scripta Materialia,* vol. 47, no. 5, pp. 337-342, September 2002. [Online]. Available: https://doi.org/10.1016/S1359-6462(02)00154-9.

[134] S. Birosca, D. Dingley, and R. L. Higginson, "Microstructural and microtextural characterization of oxide scale on steel using electron backscatter diffraction," *Journal of Microscopy,* vol. 213, no. 3, pp. 235-240, March 2004. [Online]. Available: https://doi.org/10.1111/j.0022-2720.2004.01320.x.

[135] G. L. Harris, "Basic Physical Properties," *Properties of Silicon Carbide*, G. L. Harris, Ed., London, UK: The Institution of Electrical Engineers, 1995, pp. 3-14. [Online]. Available: https://books.google.co.uk/books?hl=en&lr=&id=Yy_B8GzxNlgC&oi=fnd&pg=PR15&ots=kJrTvH0ubb&sig=fJoKZ53xJBlHAYs9JHrtBPlg0MA&redir_esc=y#v=onepage&q&f=false

[136] G. Y. Fu, L. Q. Wei, X. M. Zhang, Y. B. Cui, C. C. Lv, J. Ding, B. Yu, and S. F. Ye, "A high-silicon anti-oxidation coating for carbon steel at high temperature," *Surface and Coatings Technology,* vol. 310, pp. 166-172, January 2017. [Online]. Available: https://doi.org/10.1016/j.surfcoat.2016.12.084.

[137] B. Yu, G. Y. Fu, Y. B. Cui, X. Zhang, Y. Tiu, Y. Du, G. Zuo, S. Ye, and L. Wei, "Influence of Silicon-Modified Al Powders (SiO2@Al) on Anti-oxidation Performance of Al2O3-SiO2 Ceramic Coating for Carbon Steel at High Temperature," *Coatings,* vol. 9, no. 3, 2019. [Online]. Available: https://doi.org/10.3390/coatings9030167.

[138] K. W. Ragland and K. M. Bryden, "Gas-Fired Furnaces and Boilers," *Combustion Engineering,* 2nd ed. Boca Raton, FL, USA: Taylor and Francis, 2011, pp. 163-182. [Online]. Available: https://ifind.swansea.ac.uk/permalink/44WHELF_SWA/1jlslid/alma99839233610241 7

[139] H. T. Abuluwefa, R. I. L. Guthrie, and F. Ajersch, "Oxidation of low carbon steel in multicomponent gases: Part II. Reaction mechanisms during reheating," *Metallurgical and Materials Transactions A,* vol. 28, pp. 1643–1651, August 1997. [Online]. Available: https://link.springer.com/article/10.1007/s11661-997-0256-6.

[140] N. Saunders and A. P. Miodownik, "Introduction," *CALPHAD (Calculation of Phase Diagrams): A Comprehensive Guide.* Oxford, UK: Pergamon, 1998, pp. 1-6. [Online]. Available: https://ifind.swansea.ac.uk/permalink/44WHELF_SWA/1sssfk8/alma998280459002417

[141] S. S. Bhavikatti, "Introduction," *Finite Element Analysis.* New Delhi, India: New Age International, 2005, pp. 1-8. [Online]. Available: https://ifind.swansea.ac.uk/permalink/44WHELF_SWA/1jlslid/alma9982886992024117

[142] H. K. Malalasekera and V. A. W., "Introduction," *An Introduction to Computational Fluid Dynamics: The Finite Volume Method,* 2nd ed.: Pearson Prentice Hall, 2007, pp. 1-8. [Online]. Available: https://ifind.swansea.ac.uk/permalink/44WHELF_SWA/1jlslid/alma9983785815024117

[143] M. Auinger, A. Vogel, V. G. Praig, H. Danninger, and M. Rohwerder, "Thermogravimetry and insitu mass spectrometry at high temperatures compared to thermochemical modelling – The weight loss during selective decarburisation at 800 °C," *Corrosion Science,* vol. 48, pp. 188-192, January 2014. [Online]. Available: https://doi.org/10.1016/j.corsci.2013.09.015.

[144] K. Sachs and C. W. Tuck, "Scale Growth during Re-heating Cycles," *Materials and Corrosion,* vol. 21, no. 11, pp. 945-954, November 1970. [Online]. Available: https://doi.org/10.1002/maco.19700211110.

[145] P. Mullinger and B. Jenkins, "Fuels for Furnaces," *Industrial and Process Furnaces : Principles, Design and Operation.* Oxford, UK: Butterworth-Heinemann, 2014, pp. 67-87. [Online]. Available: https://ifind.swansea.ac.uk/permalink/44WHELF_SWA/1jlslid/alma9981924142024117

[146] P. Mullinger and B. Jenkins, "Introduction," *Industrial and Process Furnaces : Principles, Design and Operation.* Oxford, UK: Butterworth-Heinemann, 2014, pp. 1-30. [Online]. Available: https://ifind.swansea.ac.uk/permalink/44WHELF_SWA/1jlslid/alma9981924142024117

[147] P. Mullinger and B. Jenkins, "The Combustion Process," *Industrial and Process Furnaces : Principles, Design and Operation.* Oxford, UK: Butterworth-Heinemann, 2014, pp. 31-66. [Online]. Available: https://ifind.swansea.ac.uk/permalink/44WHELF_SWA/1jlslid/alma9981924142024117

[148] D. Stroud, A. J. Schroder, L. Antonazzo, C. Behrend, V. Colla, A. Goti, and M. Weinel, *Industry 4.0 and the Road to Sustainable Steelmaking in Europe: Recasting the Future*: Springer Cham, 2024. [Online]. Available: https://link.springer.com/book/10.1007/978-3-031-35479-3.

[149] C. E. Baukal, "Fundamentals," *Oxygen-enhanced Combustion.* Boca Raton: CRC Press, 2013, pp. 25-42. [Online]. Available: https://ifind.swansea.ac.uk/permalink/44WHELF_SWA/1jlslid/alma9984020135024117

[150] U. Unver and H. M. Unver, "Comparison of Natural Gas Fired and Induction Heating Furnaces," *Progress in Exergy, Energy, and the Environment,* pp. 1009-1016, May 2014. [Online]. Available: https://doi.org/10.1007/978-3-319-04681-5_96.

[151] N. Schmitz, L. Sankowski, F. Kaiser, C. Schwotser, T. Echterhof, and H. Pfeifer, "Towards CO2-neutral process heat generation for continuous reheating furnaces in

steel hot rolling mills – A case study," *Energy,* vol. 224, June 2021. [Online]. Available: https://doi.org/10.1016/j.energy.2021.120155.

[152] C. Davis, L. Zhou, M. Rainforth, E. J. Palmiere, M. Strangwood, and P. Gong. "Theme 5: New Processes for New Products." Sustain: Future Steel Manufacturing Research Hub. https://www.sustainsteel.ac.uk/new-processes (accessed June. 21, 2022).

[153] Welsh Assembly Government (Environment Sustainability and Housing), "Towards Zero Waste," ed, 2010.

[154] (2020). *Circular Economy Package policy statement*. [Online] Available: https://www.gov.uk/government/publications/circular-economy-package-policy-statement/circular-economy-package-policy-statement

[155] United Nations Environment Programme, "Global Waste Management Outlook: Beyond an age of waste - Turning rubbish into a resource," ed. Nairobi, Kenya, 2024.

[156] T. Skoczkowskia, E. Verdolinib, S. Bieleckia, M. Kochańskia, K. Korczaka, and A. Węglarzc, "Technology innovation system analysis of decarbonisation options in the EU steel industry," *Energy,* vol. 212, December 2020. [Online]. Available: https://doi.org/10.1016/j.energy.2020.118688.

[157] L. Zhou, F. Wu, R. Hall, and C. Davis, "Electromagnetic sensors for in-situ dynamic microstructure monitoring of recovery and recrystallisation in interstitial free steels," *Journal of Magnetism and Magnetic Materials,* vol. 551, 2022. [Online]. Available: https://doi.org/10.1016/j.jmmm.2022.169187.

[158] E. Hill. "Tata Steel's Corby works upgrades induction furnaces." Product Engineering Solutions. https://www.pesmedia.com/tata-steels-corby-works-upgrades-induction-furnaces (accessed June. 17, 2025).

[159] A. Zhang, Y. Zuo, M. Zhang, and H. Zhou, "Numerical study on thermal performance and thermal stress of molten salt receiver tube based on induction heating," *Applied Thermal Engineering,* vol. 235, November 2023. [Online]. Available: https://doi.org/10.1016/j.applthermaleng.2023.121353.

[160] Y. Zhao, S. Jiang, L. Wang, K. Chen, Y. Wang, B. Dou, X. Chen, and Z. Wang, "Influence of half open coil structures on overall continuous induction heating of variable cross section pipe before quenching," *Applied Thermal Engineering,* vol. 261, February 2025. [Online]. Available: https://doi.org/10.1016/j.applthermaleng.2024.125075.

[161] B. Drobenko, P. Vankevych, Y. Ryzhov, and M. Yakovlev, "Rational approaches to high temperature induction heating," *International Journal of Engineering Science,* vol. 117, pp. 34-50, August 2017. [Online]. Available: https://doi.org/10.1016/j.ijengsci.2017.05.001.

[162] R. E. Smallman and A. H. W. Ngan, "Physical Properties," *Physical Metallurgy and Advanced Materials.* Amsterdam, The Netherlands: Butterworth Heinemann, 2007, pp. 239-288. [Online]. Available: https://ifind.swansea.ac.uk/permalink/44WHELF_SWA/1jlslid/alma9982818866024117

[163] N. Di Luozzo, M. Fontana, and B. Arcondo, "Modelling of induction heating of carbon steel tubes: Mathematical analysis, numerical simulation and validation," *Journal of Alloys and Compounds,* vol. 536, no. 1, pp. 564-568, 2012. [Online]. Available: https://doi.org/10.1016/j.jallcom.2011.12.084.

[164] E. El-Kashif and T. Koseki, "Effect of Niobium on HAZ Toughness of HSLA Steels," *Alloy Steels: Properties and Use*, E. Valencia Morales, Ed.: InTech Open, 2011, pp. 87-108. [Online]. Available: http://dx.doi.org/10.5772/1347

[165] *Definition and classification of grades of steel*, BS EN 10020, 2000. [Online]. Available: https://bsol.bsigroup.com/Bibliographic/BibliographicInfoData/000000000030015678

[166] R. E. Smallman and A. H. W. Ngan, "Phase Diagrams and Alloy Theory," *Modern Physical Metallurgy,* 8th ed. Oxford, UK: Butterworth-Heinemann, 2014, pp. 43-93. [Online]. Available: https://ifind.swansea.ac.uk/permalink/44WHELF_SWA/144jshv/alma998192493702417

[167] Total Materia. "The Effects of Alloying Elements on Iron-Carbon Alloys." https://www.totalmateria.com/page.aspx?ID=CheckArticle&site=kts&NM=151 (accessed September, 12., 2022).

[168] R. Y. Chen, W. Y. D. Yeun, and S. M. Taniguchi, "The Effects of Steel Composition on the Oxidation Kinetics, Scale Structure and Scale-Steel Interface Adherence of Low and Ultra-Low Carbon Steels," *Materials Science Forum,* vol. 523, pp. 451-460, August 2006. [Online]. Available: https://doi.org/10.4028/www.scientific.net/MSF.522-523.451.

[169] A. A. Mouayd, A. Koltsov, E. Sutter, and B. Tribollet, "Effect of silicon content in steel and oxidation temperature on scale growth and morphology," *Materials Chemistry and Physics,* vol. 143, no. 3, pp. 996-1004, February 2014. [Online]. Available: https://doi.org/10.1016/j.matchemphys.2013.10.037.

[170] T. Adachi and G. H. Meier, "Oxidation of iron-silicon alloys," *Oxidation of Metals,* vol. 27, pp. 347-366, June 1987. [Online]. Available: https://link.springer.com/article/10.1007/BF00659276.

[171] B. Verdes, I. Chira, M. Virgolici, and I. V. Moise, vol. 74, no. 2, January 2012. [Online]. Available: https://www.researchgate.net/publication/265185764_Thermal_stability_of_fayalite_system_formation_at_the_interface_between_steel_and_mould.

[172] E. J. Song, D. W. Suh, and H. K. D. H. Bhadeshia, "Oxidation of silicon containing steel," *Ironmaking & Steelmaking,* vol. 39, no. 8, pp. 599-604, 2012. [Online]. Available: https://doi.org/10.1179/1743281212Y.0000000007.

[173] A. Wassilkowska and D. Wojciech, "Silicon as a component of ferric oxide scale covering ductile iron pipes after annealing," *Engineering Failure Analysis,* vol. 125, July 2021. [Online]. Available: https://doi.org/10.1016/j.engfailanal.2021.105381.

[174] K. B. Yoo, Y. He, H. S. Lee, S. Y. Bae, D. S. Kim, and K. Shin, "Study of the scale formed on super 304H boiler tube steels after long-term steam oxidation at high temperatures," *Materials Characterization,* vol. 146, pp. 71-80, December 2018. [Online]. Available: https://doi.org/10.1016/j.matchar.2018.09.045.

[175] J. L. Huang, K. Y. Zhou, J. Q. Xu, and C. X. Bian, "On the failure of steam-side oxide scales in high temperature components of boilers during unsteady thermal processes," *Journal of Loss Prevention in the Process Industries,* vol. 26, no. 1, January 2013. [Online]. Available: https://doi.org/10.1016/j.jlp.2012.08.004.

[176] L. Sun and W. Yan, "Estimation of Oxidation Kinetics and Oxide Scale Void Position of Ferritic-Martensitic Steels in Supercritical Water," *Advances in Materials Science and Engineering,* vol. 2017, August 2017. [Online]. Available: https://doi.org/10.1155/2017/9154934.

[177] P. J. Ennis and W. J. Quadakkers, "Implications of steam oxidation for the service life of high-strength martensitic steel components in high-temperature plant," *International Journal of Pressure Vessels and Piping,* vol. 84, no. 2, pp. 82-87, 2007. [Online]. Available: https://doi.org/10.1016/j.ijpvp.2006.09.008.

[178] J. Purbolaksono, A. Khinani, A. Z. Rashid, A. A. Ali, and N. F. Nordin, "Prediction of oxide scale growth in superheater and reheater tubes," *Corrosion Science,* vol. 51, no. 5, pp. 1022-1029, May 2009. [Online]. Available: https://doi.org/10.1016/j.corsci.2009.02.025.

[179] T. F. Wall, S. P. Bhattacharya, D. K. Zhang, D. K. Gupta, and X. He, "The properties and thermal effects of ash deposits in coal-fired furnaces," *Progress in Energy and Combustion Science,* vol. 19, no. 6, pp. 487-504, 1993. [Online]. Available: https://doi.org/10.1016/0360-1285(93)90002-V.

[180] R. M. S. Silveira, M. P. Arenas, C. J. Pacheco, A. C. Rocha, C. B. Eckstein, A. C. Bruno, G. R. Pereira, and L. H. Alemeida, "Characterization of the oxide scale formed on external surface of HP reformer tubes," *Journal of Materials Research and Technology,* vol. 7, no. 4, pp. 573-583, December 2018. [Online]. Available: https://doi.org/10.1016/j.jmrt.2018.08.001.

[181] D. R. H. Jones, "Creep failures of overheated boiler, superheater and reformer tubes," *Engineering Failure Analysis,* vol. 11, no. 6, pp. 873-893, December 2004. [Online]. Available: https://doi.org/10.1016/j.engfailanal.2004.03.001.

[182] L. Sun and W. Yan, "Prediction of wall temperature and oxide scale thickness of ferritic–martensitic steel superheater tubes," *Applied Thermal Engineering,* vol. 134, pp. 171-181, April 2018. [Online]. Available: https://doi.org/10.1016/j.applthermaleng.2018.01.127.

[183] Y. A. Cengel and A. J. Ghajar, "Internal Forced Convection," in *Heat and Mass Transfer: Fundamentals and Applications*, 5th ed. India: McGraw Hill Education, 2016, pp. 494-515.

[184] P. P. Benham, R. J. Crawford, and C. G. Armstrong, "Statically Determinate Stress Systems," in *Mechanics of Engineering Materials*, 2nd ed. Harlow, UK: Pearson Education, 1996, pp. 43-65.

[185] M. Trojan and D. Taler, "Thermal simulation of superheaters taking into account the processes occurring on the side of the steam and flue gas," *Fuel,* vol. 150, pp. 75-87, June 2015. [Online]. Available: https://doi.org/10.1016/j.fuel.2015.01.095.

[186] M. Schütze, P. F. Tortorelli, and I. G. Wright, "Development of a Comprehensive Oxide Scale Failure Diagram," *Oxidation of Metals,* vol. 73, pp. 389-418, 2010. [Online]. Available: https://link.springer.com/article/10.1007/s11085-009-9185-7.

[187] Y. Tanigawa, N. Oka, T. Akai, and R. Kawamura, "One-Dimensional Transient Thermal Stress Problem for Nonhomogeneous Hollow Circular Cylinder and Its Optimization of Material Composition for Thermal Stress Relaxation," vol. 40, no. 2, pp. 117-127, 1997. [Online]. Available: https://doi.org/10.1299/jsmea1993.40.2_117.

[188] M. Schütze, "Mechanical Properties of Oxide Scales," *Oxidation of Metals,* vol. 44, pp. 29-61, August 1995. [Online]. Available: https://doi.org/10.1007/BF01046722.

[189] P. Hancock and J. R. Nicholls, "Application of fracture mechanics to failure of surface oxide scales," *Materials Science and Technology,* vol. 4, no. 5, pp. 398-406, 1988. [Online]. Available: https://doi.org/10.1179/mst.1988.4.5.398.

[190] P. Hancock, J. R. Nicholls, and K. Mahmood, "The influence of imposed strain rate on fracture of surface oxides," *Corrosion Science,* vol. 35, no. 5-8, pp. 979-987, 1993. [Online]. Available: https://doi.org/10.1016/0010-938X(93)90316-9.

[191] X. Dong, X. Feng, and K. W. Hwang, "Oxidation stress evolution and relaxation of oxide film/metal substrate system," *Journal of Applied Physics,* vol. 112, 2012. [Online]. Available: https://doi.org/10.1063/1.4736934.

[192] A. Hajjafar, "Controlled over-relaxation method and the general extrapolation method," *Applied Mathematics and Computation,* vol. 174, no. 1, pp. 188-198, March 2006. [Online]. Available: https://doi.org/10.1016/j.amc.2005.03.023.

[193] A. S. Sabau and I. G. Wright, "On the estimation of thermal strains developed during oxide growth," *Journal of Applied Physics,* vol. 106, 2009. [Online]. Available: https://doi.org/10.1063/1.3157199.

[194] H. Steiner, "Stress effects in cylindrical tubes of austenitic and ferritic/martensitic steels with oxide scales: Materials selection for a HPLWR," Institute for Materials Research, 2002. [Online]. Available: https://publikationen.bibliothek.kit.edu/270053297

[195] S. Espevik, R. A. Rapp, P. L. Daniel, and J. P. Hirth, "Oxidation of Ni-Cr-W Ternary Alloys," *Oxidation of Metals,* vol. 14, pp. 85-108, 1980. [Online]. Available: https://link.springer.com/article/10.1007/BF00603987.

[196] R. P. Wei, "Stress Analysis of Cracks," *Fracture Mechanics: Integration of Mechanics, Materials Science, and Chemistry.* Cambridge, UK: Cambridge University Press, 2010, pp. 26-49. [Online]. Available: https://ifind.swansea.ac.uk/permalink/44WHELF_SWA/1jlslid/alma99831969120241 7

[197] E.-S. Oh, "A Perturbation Analysis for the Metal Oxidation of Cylindrical Geometries," *Journal of Chemical Engineering of Japan,* vol. 39, no. 1, pp. 57-67, 2006. [Online]. Available: https://doi.org/10.1252/jcej.39.57.

[198] N. Sadoun, E.-K. Si-Ahmed, P. Colinet, and J. Legrand, "On the boundary immobilization and variable space grid methods for transient heat conduction problems with phase change: Discussion and refinement," *Comptes Rendus Mecanique,* vol. 340, no. 7, pp. 501-511, July 2012. [Online]. Available: https://doi.org/10.1016/j.crme.2012.03.003.

[199] J. R. Bauer and K. Rose, "Variable Grid Method: An Intuitive Approach for Simultaneously Quantifying and Visualizing Spatial Data and Uncertainty," *Transactions in GIS,* vol. 19, no. 3, pp. 377-397, 2015. [Online]. Available: https://doi.org/10.1111/tgis.12158.

[200] D. C. Lagoudas and Z. Ding, "Numerical computation of metal oxidation problems on bounded domains," *International Journal of Engineering Science,* vol. 36, no. 4, pp. 367-381, March 1998. [Online]. Available: https://doi.org/10.1016/S0020-7225(97)00075-X.

[201] J. Cleeman, K. Agrawala, E. Nastarowicz, and R. Malhotra, "Partial-physics-informed multi-fidelity modeling of manufacturing processes " *Journal of Materials Processing Technology,* vol. 320, 2023. [Online]. Available: https://doi.org/10.1016/j.jmatprotec.2023.118125.

[202] P. R. Nelson, M. Coffin, and K. A. F. Copeland, "Multi-Factor Experiments," *Introductory Statistics for Engineering Experimentation.* Boston, MA, USA: Elsevier, 2003, pp. 338-368. [Online]. Available: https://ifind.swansea.ac.uk/permalink/44WHELF_SWA/1jlslid/alma99828159930241 7

[203] B. S. Sergi, E. G. Popkova, A. V. Bogoviz, and T. N. Litvinova, "Part I. Overview of Future Professions in Industry," *Understanding Industry 4.0: AI, The Internet of Things, and the Future of Work.* Bingley, UK: Emerald Publishing Limited, 2019, pp. 19-38. [Online]. Available: https://ifind.swansea.ac.uk/permalink/44WHELF_SWA/1jlslid/alma99852708530241 7

[204] C. Yu, Q. Li, K. Liu, Y. Chen, and H. Wei, "Industrial Design and Development Software System Architecture Based on Model-Based Systems Engineering and Cloud Computing," *Annual Reviews in Control,* vol. 51, pp. 401-423, 2021. [Online]. Available: https://doi.org/10.1016/j.arcontrol.2021.04.011.

[205] U. R. Kattner, "The CALPHAD Method and its Role in Material and Process Development," *Tecnologia em Metalurgia, Materiais e Mineracao,* vol. 13, no. 1, pp. 3-15, 2016. [Online]. Available: https://tecnologiammm.com.br/doi/10.4322/2176-1523.1059.

[206] S. Y. Kwon, Y. Yanamoto, J. Peng, M. P. Brady, T. R. Watkins, J. A. Haynes, and S. Shin, "Physics-coupled data-driven design of high-temperature alloys," *Acta Materialia,* vol. 284, January 2025. [Online]. Available: https://doi.org/10.1016/j.actamat.2024.120622.

[207] N. Saunders and A. P. Miodownik, *CALPHAD (Calculation of Phase Diagrams): A Comprehensive Guide*, Oxford, UK: Pergamon, 1998. [Online]. Available: https://ifind.swansea.ac.uk/permalink/44WHELF_SWA/1sssfk8/alma999280459002417.

[208] M. Hillert, "The compound energy formalism," *Journal of Alloys and Compounds,* vol. 320, no. 2, pp. 161-176, May 2001. [Online]. Available: https://doi.org/10.1016/S0925-8388(00)01481-X.

[209] H. Larsson et al, "Oxidation of iron at 600 8C – experiments and simulations," *Materials and Corrosion,* vol. 68, no. 2, pp. 133-142, 2017. [Online]. Available: 10.1002/maco.201508781.

[210] I. Jung, "Overview of the applications of thermodynamic databases to steelmaking processes," *CALPHAD: Computer Coupling of Phase Diagrams and Thermochemistry,* vol. 34, no. 3, pp. 332-362, September. 2010. [Online]. Available: doi:10.1016/j.calphad.2010.06.003.

[211] D. L. Poerschke, "Developments in Thermodynamic Models of Deposit-Induced Corrosion of High-Temperature Coatings," *The Journal of The Minerals, Metals & Materials Society,* vol. 24, no. 2, pp. 260-273, 2022. [Online]. Available: https://doi.org/10.1007/s11837-021-04989-0.

[212] S. Mori, A. Pidcock, N. Simms, and J. Oakey, "Fireside Corrosion of Heat Exchanger Materials for Advanced Solid Fuel Fired Power Plants," *Oxidation of Metals,* vol. 97, pp. 281-306, 2022. [Online]. Available: https://link.springer.com/article/10.1007/s11085-021-10094-z.

[213] K. Worden, E. J. Cross, R. J. Barthorpe, D. J. Wagg, and P. Gardner, "On Digital Twins, Mirrors, and Virtualizations: Frameworks for Model Verification and Validation," *ASME Journal of Risk and Uncertainty in Engineering Systems, Part B. Mechanical Engineering,* vol. 6, no. 3, 2020. [Online]. Available: https://doi.org/10.1115/1.4046740.

[214] R. K. Singh Raman, B. M. Gleeson, and D. Young, "Laser Raman spectroscopy: A technique for rapid characterisation of oxide scale layers," *Materials Science & Technology,* vol. 14, no. 5, pp. 373-376, May 1998, doi: http://dx.doi.org/10.1179/026708398790301287.

[215] G. Morari Do Nascimento et al, "The Multiple Applications of Raman Spectroscopy," *Raman Spectroscopy*, G. Morari Do Nascimento, Ed., Universidad Federal Do ABC, Brazil: IntechOpen, 2018. [Online]. Available: https://www.intechopen.com/books/6257

[216] C. Wang, H. Wu, P. Zhang, Z. Li, R. Cao, and C. Shang, "Analysis of the Local Plastic Deformation of the Surface Oxide Layer formed on Low-Alloy High-strength Steel," *Transaction of the Indian Institute of Metals,* January 2022. [Online]. Available: http://dx.doi.org/10.1007/s12666-021-02491-4.

[217] T. J. F. Southern, J. E. Campbell, C. Fang, A. Nemcova, A. Bannister, and T. W. Clyne, "Use of hardness, PIP and tensile testing to obtain stress-strain relationships

for metals," *Mechanics of Materials,* vol. 187, December 2023. [Online]. Available: https://doi.org/10.1016/j.mechmat.2023.104846.

[218] D. Roylance, "Constitutive Equations," *Mechanics of Materials*: Oxford University Press, 2002, pp. 136-146. [Online]. Available: https://ifind.swansea.ac.uk/permalink/44WHELF_SWA/1jlslid/alma9988172973024117

[219] T. W. Clyne, J. E. Campbell, M. Burley, and J. Dean, "Profilometry-Based Inverse Finite Element MethodIndentation Plastometry," *Advanced Engineering Materials,* vol. 23, no. 9, September 2021. [Online]. Available: https://doi.org/10.1002/adem.202100437.

[220] M. Warwick, H. Vaka, C. Fang, J. Campbell, J. Dean, and T. W. Clyne, "Use of Profilometry-Based Indentation Plastometry to Study the Effects of Pipe Wall Flattening on Tensile Stress–Strain Curves of Steels," *Steel Research International,* vol. 94, no. 7, July 2023. [Online]. Available: https://doi.org/10.1002/srin.202200920.

[221] A. E. Tekkaya, "Metal Forming," *Springer Handbook of Mechanical Engineering*, K. H. Grote and H. Hefazi, Eds., Cham: Springer, 2021. [Online]. Available: https://doi.org/10.1007/978-3-030-47035-7_11

[222] C. E. Campbell, "Diffusivity and Mobility Data," *vol. 22*, *ASM Handbook.* Materials Park, OH, USA: ASM International, 2009. [Online]. Available: https://tsapps.nist.gov/publication/get_pdf.cfm?pub_id=854444

[223] J. Philibert, "Diffusion and Drift in Alloys and Compounds," *Atom Movements: Diffusion and Mass Transport in Solids.* Les Ulis, France: Editions de Physique, 1991, pp. 1-32. [Online]. Available: https://ifind.swansea.ac.uk/permalink/44WHELF_SWA/1sssfk8/alma998611634202417

[224] J. Philibert, "Diffusion Mechanisms and Correlation Effects," *Atom Movements: Diffusion and Mass Transport in Solids.* Les Ulis, France: Editions de Physique, 1991, pp. 61-96. [Online]. Available: https://ifind.swansea.ac.uk/permalink/44WHELF_SWA/1sssfk8/alma998611634202417

[225] A. Karimi and M. Auinger, "Nitrogen diffusion in vacancy-rich ferrite and austenite, from first principles to applications," *Acta Materialia,* vol. 220, November 2021. [Online]. Available: https://doi.org/10.1016/j.actamat.2021.117292.

[226] P. D. Zarnas, R. Dingreville, and J. Qu, "Mechanics of point defect diffusion near dislocations and grain boundaries: A chemomechanical framework," *Computational Materials Science,* vol. 144, pp. 99-112, 2018. [Online]. Available: https://doi.org/10.1016/j.commatsci.2017.12.006.

[227] M. Auinger, N. Naraparaju, H. J. Christ, and M. Rohwerder, "Modelling High Temperature Oxidation in Iron–Chromium Systems: Combined Kinetic and Thermodynamic Calculation of the Long-Term Behaviour and Experimental Verification," *Oxidation of Metals,* vol. 247, pp. 247-258, 2011. [Online]. Available: https://link.springer.com/article/10.1007/s11085-011-9252-8.

[228] N. Cabrera and N. F. Mott, "Theory of the oxidation of metals," *Reports of Progress in Physics,* vol. 12, pp. 163-184, 1949, doi: 10.1088/0034-4885/12/1/308.

[229] A. Obaied, I. Roslyakova, and M. To Baben, "Including state-of-the-art physical understanding of thermal vacancies in Calphad models," *Scientific Reports,* vol. 12, August 2022. [Online]. Available: https://doi.org/10.1038/s41598-022-16926-5.

[230] P. Franke, "Modeling of Thermal Vacancies in Metals within the Framework of the Compound Energy Formalism," *Journal of Phase Equilibria and Diffusion,* vol. 35, pp. 780-787, 2014. [Online]. Available: https://doi.org/10.1007/s11669-014-0348-0.

[231] C. H. Ahn, J.-M. Triscone, and J. Mannhart, "Electric field effect in correlated oxide systems," *Nature,* vol. 424, pp. 1015-1018, August 2003. [Online]. Available: https://www.nature.com/articles/nature01878.

[232] C. Leighton, T. Birol, and J. Walter, "What controls electrostatic vs electrochemical response in electrolyte-gated materials? A perspective on critical materials factors," *APL Materials,* vol. 10, no. 4, April 2022. [Online]. Available: https://doi.org/10.1063/5.0087396.

[233] M. U. Fayaz, Q. Wang, S. Liang, H. Bai, F. Pan, and C. Song, "Electric Field Induced Ion Migration and Property Tuning in Functional Oxides," *Accounts of Materials Research,* vol. 5, no. 5, pp. 648-660, April 2024. [Online]. Available: https://doi.org/10.1021/accountsmr.4c00067.

[234] S. Hallstrom, M. Halvarsson, L. Hoglund, T. Jonsson, and J. Agren, "High temperature oxidation of chromium: Kinetic modeling and microstructural investigation," *Solid State Ionics,* vol. 240, pp. 41-50, June 2013. [Online]. Available: http://dx.doi.org/10.1016/j.ssi.2013.02.017.

[235] I. Kaur, Y. Mishin, and W. Gust, "Analytical Models of Grain Boundary Diffusion," *Fundamentals of Grain and Interphase Boundary Diffusion,* 3rd ed. New York: USA: Wiley, 1989.

[236] J. Zhou, H. Zhu, Q. Song, Z. Ding, J. Mao, Z. Ren, and G. Chen, "Mobility enhancement in heavily doped semiconductors via electron cloaking," *Nature Communications,* vol. 13, no. 2482, May 2022. [Online]. Available: https://www.nature.com/articles/s41467-022-29958-2.

[237] T. Hidayat, D. Shishin, E. Jak, and S. A. Decterov, "Thermodynamic reevaluation of the Fe–O system," *Calphad,* vol. 48, pp. 131-144, March 2015. [Online]. Available: https://doi.org/10.1016/j.calphad.2014.12.005.

[238] S. Samal and S. K. Mitra, "Influence of Grain Shape, Size, and Grain Boundary Diffusion on High-Temperature Oxidation of Pure Metal Fe, Cu, and Zn," *Metallurgical and Materials Transactions A,* vol. 46, pp. 3324–3332, 2015. [Online]. Available: https://doi.org/10.1007/s11661-015-2987-0.

[239] S. Hallstrom, L. Hoglund, and J. Agren, "Modeling of iron diffusion in the iron oxides magnetite and hematite with variable stoichiometry," *Acta Materialia,* vol. 59, no. 1, pp. 53-60, January 2010. [Online]. Available: https://doi.org/10.1016/j.actamat.2010.08.032.

[240] O. M. Fabrichnaya and B. Sundman, "The assessment of thermodynamic parameters in the Fe□O and Fe□Si□O systems," *Geochimica et Cosmochimica Acta,* vol. 61, no. 21, pp. 4539-4555, November 1997. [Online]. Available: https://doi.org/10.1016/S0016-7037(97)00256-1.

[241] R. M. Hazen and R. Jeanloz, "Wüstite (Fe1-x O): A review of its defect structure and physical properties," *Reviews of Geophysics,* vol. 22, no. 1, pp. 37-46, February 1984. [Online]. Available: https://doi.org/10.1029/RG022i001p00037.

[242] J. Philibert, "Self-Diffusion," *Atom Movements: Diffusion and Mass Transport in Solids.* Les Ulis, France: Editions de Physique, 1991, pp. 97-148. [Online]. Available: https://ifind.swansea.ac.uk/permalink/44WHELF_SWA/1sssfk8/alma998611634202417

[243] J. Byggmastar, M. Nagel, K. Albe, K. O. E. Henriksson, and K. Nordlund, "Analytical interatomic Fe-O potential for simulations of oxygen defects in iron," *Journal of Physics: Condensed Matter,* vol. 31, March 2019, doi: 10.1088/1361-648X/ab0931.

[244] B. Sundman, "An Assessment of the Fe-O system," *Journal of Phase Equilibria,* vol. 12, no. 1, pp. 127-140, 1991. [Online]. Available: https://link.springer.com/article/10.1007/BF02645709.

[245] G. Grosso and G. Pastori Parravicini, "The One-Electron Approximation and Beyond," *Solid State Physics,* 2nd ed. Oxford, UK: Academic Press, 2014, pp. 135-178. [Online]. Available: https://ifind.swansea.ac.uk/permalink/44WHELF_SWA/144jshv/alma998192443702417

[246] Y. Yun, S. Wu, D. Wang, X. Luo, J. Chen, G. Wang, A. Takao, and L. Wan, "Molecular Dynamics Simulations in Semiconductor Material Processing: A Comprehensive Review," *Measurement,* vol. 241, February 2025. [Online]. Available: https://doi.org/10.1016/j.measurement.2024.115708.

[247] F. Morin, "Electrotransport in Oxides," *Solid State Ionics,* vol. 12, pp. 407-418, 1984. [Online]. Available: https://doi.org/10.1016/0167-2738(84)90171-1.

[248] U. Guth, "Kröger-Vinks Notation of Point Defects," *Encyclopedia of Applied Electrochemistry*, G. Kreysa, K. Ota, and R. Savinell, Eds., New York, USA: Springer, 2014, pp. pp. 1159-1160. [Online]. Available: https://doi.org/10.1007/978-1-4419-6996-5

[249] W. Burgmann, "The Defect Structure Models for Wüstite: A Review," *Metal Science,* vol. 9, pp. 169-175, 1975. [Online]. Available: https://doi.org/10.1179/030634575790445107.

[250] C. R. A. Catlow and B. E. F. Fender, "Calculations of defect clustering in Fe1-xO," *Journal of Physics C: Solid State Physics,* vol. 8, no. 20, pp. 3267-3279, 1975, doi: 10.1088/0022-3719/8/20/005.

[251] A. Cheetham, B. E. F. Fender, and R. I. Taylor, "High temperature neutron diffraction study of Fe1-xO," *Materials Science,* vol. 4, pp. 2160-2165, 1971. [Online]. Available: https://doi.org/10.1088/0022-3719%2F4%2F14%2F029.

[252] M. Gheisari, M. Mozaffari, M. Acet, and J. Amighian, "Preparation and investigation of magnetic properties of wüstite nanoparticles," *Journal of Magnetism and Magnetic Materials,* vol. 320, no. 21, pp. 2618-2621, November 2008. [Online]. Available: https://doi.org/10.1016/j.jmmm.2008.05.028.

[253] S. Samal, "High Temperature Oxidation of Metals," *High Temperature Corrosion*, Z. Ahmad, Ed.: InTechOpen, 2016, pp. 101-121. [Online]. Available: http://dx.doi.org/10.5772/63000

[254] F. Koch and J. Cohen, "The defect structure of Fe1–xO," *Acta Crystallographica Section B Structural Crystallography and Crystal Chemistry,* vol. 25, pp. 275-287, 1969. [Online]. Available: https://doi.org/10.1107/S0567740869002111.

[255] F. Morin, "Electrotransport and self-diffusion in wustite," *Scripta Metallurgica,* vol. 10, no. 6, pp. 553-556, June 1976. [Online]. Available: https://doi.org/10.1016/0036-9748(76)90260-X.

[256] N. N. Greenwood and A. T. Howe, "Mössbauer studies of Fe1–xO. Part I. The defect structure of quenched samples," *Journal of The Chemical Society - Dalton Transactions,* pp. 110-116, 1972. [Online]. Available: https://doi.org/10.1039/DT9720000110.

[257] W. K. Chen and N. L. Peterson, "Effect of the deviation from stoichiometry on cation self-diffusion and isotope effect in wüstite, Fe1–xO," *Journal of Physics and Chemistry of Solids,* vol. 36, no. 10, pp. 1097-1103, October 1975. [Online]. Available: https://doi.org/10.1016/0022-3697(75)90052-9.

[258] P. Yousefian, B. Akkopru-Akgun, C. A. Randall, and S. Trolier-McKinstry, "Electrical degradation in dielectric and piezoelectric oxides: Review of defect chemistry and characterization methods," *Progress in Materials Science,* vol. 153, September 2025. [Online]. Available: https://doi.org/10.1016/j.pmatsci.2025.101473.

[259] Struers LLC. "About Grinding and Polishing (Mechanical Preparation)." https://www.struers.com/en/Knowledge/Grinding-and-polishing# (accessed May, 19., 2022).

[260] S. Birosca and R. L. Higginson, "Phase identification of oxide scale on low carbon steel," *Materials at High Temperatures,* vol. 22, no. 4, pp. 179-184, August 2005. [Online]. Available: https://www.proquest.com/scholarly-journals/phase-identification-oxide-scale-on-low-carbon/docview/1243348952/se-2?accountid=14680.

[261] *Surface chemical analysis. Glow discharge optical emission spectrometry (GD-OES). Introduction to use*, BS ISO 14707:2021, 2021. [Online]. Available: https://bsol.bsigroup.com/Bibliographic/BibliographicInfoData/000000000030426343

[262] H. Pauna, M. Aula, T. Willms, T. Echterhof, M. Huttula, and T. Fabritius, "Optical emission spectroscopy as a method to improve process automation of electric arc furnaces and ladle furnaces," presented at the 14th IFAC Workshop on Intelligent Manufacturing Systems IMS 2022, Tel-Aviv, Israel, 28-30 March, 2022.

[263] H. Fritzsche, "Electromagnetic Radiation," in *Encyclopedia Britannica*, ed, 1998.

[264] A. Bengston, "Laser Induced Breakdown Spectroscopy compared with conventional plasma optical emission techniques for the analysis of metals – A review of applications and analytical performance," *Spectrochimica Acta Part B: Atomic Spectroscopy,* vol. 313, pp. 123-132, August 2017. [Online]. Available: https://doi.org/10.1016/j.sab.2017.05.006.

[265] C. Xhoffer and H. Dillen, "The Versatility of GDOES: From Bulk Analysis to Thin Film and Surface Analysis," *BHM Berg- und Hüttenmännische,* vol. 152, no. 1, pp. 18-23, 2007, doi: http://dx.doi.org/10.1007/s00501-006-0266-5.

[266] M. Kutz, "High Temperature Oxidation," *Handbook of Environmental Degradation of Materials,* 2nd ed. Boston, MA, USA, 2012, pp. 127-195. [Online]. Available: https://ifind.swansea.ac.uk/permalink/44WHELF_SWA/144jshv/alma998192448002417

[267] M. Kutz, "Thermal Degradation of Polymer and Polymer Composities," *Handbook of Environmental Degradation of Materials,* 2nd ed. Boston, MA, USA, 2012, pp. 213-242. [Online]. Available: https://ifind.swansea.ac.uk/permalink/44WHELF_SWA/144jshv/alma998192448002417

[268] S. B. Warrington, "Simultaneous Thermal Analysis Techniques," *Principles of Thermal Analysis and Calorimetry.* , P. J. Haines, Ed., Cambridge, UK: Royal Society of Chemistry, 2002, pp. 166-189. [Online]. Available: https://ifind.swansea.ac.uk/permalink/44WHELF_SWA/1jlslid/alma998284251402417

[269] P. G. Laye, "Differential Thermal Analysis and Differential Scanning Calorimetry," *Principles of Thermal Analysis and Calorimetry*, P. J. Haines, Ed., Cambridge, UK: Royal Society of Chemistry, 2002, pp. 55-93. [Online]. Available: https://ifind.swansea.ac.uk/permalink/44WHELF_SWA/1jlslid/alma998284251402417

[270] G. R. Heal, "Thermogravimetry and Derivative Thermogravimetry," *Principles of Thermal Analysis and Calorimetry*, P. J. Haines, Ed., Cambridge, UK: Royal Society of Chemistry, 2002, pp. 10-54. [Online]. Available: https://ifind.swansea.ac.uk/permalink/44WHELF_SWA/1jlslid/alma998284251402417

[271] NETZSCH-Gerätebau GmbH, "Key Technical Data STA 449 F3 Jupiter," ed, 2025.

[272] Carbolite Gero Ltd, "Installation and Operation Instructions: 1600°C Tube Furnace - TF1/3 450mm ø100mm," ed. Hope Valley, UK, 2022.

[273] D. Grandy, "Wave-Particle Duality," *Everyday Quantum Reality.* Bloomington, IN, USA: Indiana University Press, 2010, pp. 21-36. [Online]. Available: https://ifind.swansea.ac.uk/permalink/44WHELF_SWA/1jlslid/alma9982832749024117

[274] P. J. Goodhew, R. Beanland, and J. Humphreys, "Microscopy with light and electrons," *Electron Microscopy and Analysis,* 3rd ed. Boca Raton, FL, USA: CRC Press, 2014, pp. 1-19. [Online]. Available: https://ifind.swansea.ac.uk/permalink/44WHELF_SWA/1sssfk8/alma998280372102417

[275] P. J. Goodhew, R. Beanland, and J. Humphreys, "Electrons and their interaction with the specimen," *Electron Microscopy and Analysis,* 3rd ed. Boca Raton, FL, USA: CRC Press, 2014, pp. 20-39. [Online]. Available: https://ifind.swansea.ac.uk/permalink/44WHELF_SWA/1sssfk8/alma998280372102417

[276] A. J. G. Hey and P. Walters, "Quantum Tunnelling," *The New Quantum Universe,* 2nd ed. Cambridge, UK: Cambridge University Press, 2003, pp. 73-106. [Online]. Available: https://ifind.swansea.ac.uk/permalink/44WHELF_SWA/1jlslid/alma9983924925024117

[277] P. J. Goodhew, R. Beanland, and J. Humphreys, "The scanning electron microscope," *Electron Microscopy and Analysis,* 3rd ed. Boca Raton, FL, USA: CRC Press, 2014, pp. 122-168. [Online]. Available: https://ifind.swansea.ac.uk/permalink/44WHELF_SWA/1sssfk8/alma998280372102417

[278] X. Llovet, A. Moy, P. T. Pinard, and J. H. Fournelle, "Electron probe microanalysis: A review of recent developments and applications in materials science and engineering," *Progress in Materials Science,* vol. 116, February 2021. [Online]. Available: https://doi.org/10.1016/j.pmatsci.2020.100673.

[279] P. J. Goodhew, R. Beanland, and J. Humphreys, "Chemical analysis in the electron microscope," *Electron Microscopy and Analysis,* 3rd ed. Boca Raton, FL, USA: CRC Press, 2014, pp. 169-213. [Online]. Available: https://ifind.swansea.ac.uk/permalink/44WHELF_SWA/1sssfk8/alma998280372102417

[280] J. Nemecek, "First-Principles Quantum Simulations," *Nanoindentation in Materials Science*, J. Nemecek, Ed., Croatia: IntechOpen, 2012, pp. 3-24. [Online]. Available: https://ifind.swansea.ac.uk/permalink/44WHELF_SWA/1jlslid/alma9985890349024117

[281] W. C. Oliver and G. M. Pharr, "An improved technique for determining hardness and elastic modulus using load and displacement sensing indentation experiments," *Journal of Materials Research,* vol. 7, pp. 1564-1583, 1992. [Online]. Available: https://doi.org/10.1557/JMR.1992.1564.

[282] *Metallic materials. Vickers hardness test. Test method.*, BS EN ISO 6507-1, 2023. [Online]. Available: https://bsol.bsigroup.com/Bibliographic/BibliographicInfoData/000000000030445369

[283] C. A. Schuh, "Nanoindentation studies of materials," *Materials Today,* vol. 9, no. 5, pp. 32-40, May 2006. [Online]. Available: https://doi.org/10.1016/S1369-7021(06)71495-X.

[284] K. Herrmann, "Hardness Measurement of Metals - Static Methods," *Hardness Testing: Principles and Applications,* Materials Park, Ohio, USA: ASM International, 2011, pp. 25-66. [Online]. Available: https://ifind.swansea.ac.uk/permalink/44WHELF_SWA/1jlslid/alma9982865652024117

[285] M. Jamal and M. N. Morgan, "Materials characterization part I: contact area of the Berkovich indenter for nanoindentation tests," *The International Journal of Advanced Manufacturing Technology,* vol. 92, pp. 361-370, 2017. [Online]. Available: https://link.springer.com/article/10.1007/s00170-017-0115-6.

[286] M. E. Fitzpatrick, A. T. Fry, P. Holdway, F. A. Kandil, J. Shackleton, and S. L., "Determination of Residual Stresses by X-ray Diffraction (Measurement Good Practice Guide No. 52)," in "A National Measurement Good Practice Guide," National Physical Laboratory, Teddington, Middlesex, UK, September 2005. [Online]. Available: https://eprintspublications.npl.co.uk/2391/1/mgpg52.pdf

[287] A. Sarmast, J. Schubnell, J. PreuBner, M. Hinterstein, and E. Carl, "Residual stress analysis in industrial parts: a comprehensive comparison of XRD methods," *Journal of Materials Science,* vol. 58, pp. 16905-16929, November 2023. [Online]. Available: https://link.springer.com/article/10.1007/s10853-023-09069-z.

[288] C. Suryanarayana and M. G. Norton, "Practical Aspects of X-ray Diffraction," *X-ray Diffraction: A Practical Approach.* New York, NY, USA: Springer, 1998, pp. 63-96. [Online]. Available: https://ifind.swansea.ac.uk/permalink/44WHELF_SWA/1sssfk8/alma998525880302417

[289] *Non-destructive testing. Test method for residual stress analysis by X-ray diffraction*, BS EN ISO 15305, 2008. [Online]. Available: https://bsol.bsigroup.com/Bibliographic/BibliographicInfoData/000000000030199156

[290] H. M. Yin and P. A. Prieto-Munoz, "Stress transfer through fully bonded interface of layered materials," *Mechanics of Materials,* vol. 62, pp. 69-79, August 2013. [Online]. Available: https://doi.org/10.1016/j.mechmat.2013.03.007.

[291] A. Mezin, "An analytical solution for stress relaxation in cracked coatings," *Surface and Coatings Technology,* vol. 166, no. 2-3, pp. 160-166, March 2003. [Online]. Available: https://doi.org/10.1016/S0257-8972(02)00787-9.

[292] N. A. Dolgov, "Analytical Methods to Determine the Stress State in the Substrate–Coating System Under Mechanical Loads," *Strength of Materials,* vol. 48, pp. 658-667, 2016, doi: 10.1007/s11223-016-9809-5.

[293] J. A. Middleton, "The Sampling Distribution of the Mean," *Experimental Statistics and Data Analysis for Mechanical and Aerospace Engineers.* Boca Raton, FL, USA: CRC Press, Taylor & Francis Group, 2022, pp. 111-140. [Online]. Available: https://ifind.swansea.ac.uk/permalink/44WHELF_SWA/1jlslid/alma9985791640024117

[294] Y. Zhou, J. Liu, H. Li, Z. Li, S. Li, and T. Lai, "High-precision displacement sensor in advanced manufacturing: Principle and application," *Measurement,* vol. 242, B, p. 115988, 2025. [Online]. Available: https://doi.org/10.1016/j.measurement.2024.115988.

[295] Y. Wang, F. Xie, S. Ma, and L. Dong, "Review of surface profile measurement techniques based on optical interferometry," *Optics and Lasers in Engineering,* vol. 93, pp. 164-170, June 2017. [Online]. Available: https://doi.org/10.1016/j.optlaseng.2017.02.004.

[296] S. R. K. Iyengar and R. K. Jain, "Interpolation and Approximation," *Numerical Methods,* New Delhi, India: New Age International Ltd, 2009, pp. 63-108. [Online].

Available: https://ifind.swansea.ac.uk/permalink/44WHELF_SWA/1jlslid/alma9982886993024117

[297] S. R. K. Iyengar and R. K. Jain, "Solution of Equations and Eigen Value Problems," *Numerical Methods,* New Delhi, India: New Age International Ltd, 2009, pp. 109-179. [Online]. Available: https://ifind.swansea.ac.uk/permalink/44WHELF_SWA/1jlslid/alma9982886993024117

[298] S. R. K. Iyengar and R. K. Jain, "Numerical Differentiation and Integration," *Numerical Methods,* New Delhi, India: New Age International Ltd, 2009, pp. 109-179. [Online]. Available: https://ifind.swansea.ac.uk/permalink/44WHELF_SWA/1jlslid/alma9982886993024117

[299] P. J. Spencer, "A brief history of CALPHAD," *Computer Coupling of Phase Diagrams and Thermochemistry,* vol. 32, pp. 1-8, 2008. [Online]. Available: doi:10.1016/j.calphad.2007.10.001.

[300] S. Gordon and B. J. McBride, "Computer program for calculation of complex chemical equilibrium compositions and applications. Part 1: Analysis," NASA Lewis Research Center, Cleveland, OH, USA, NASA-RP-1311, 1994. [Online]. Available: https://ntrs.nasa.gov/citations/19950013764

[301] Thermo-Calc Software AB. "The Calphad Methodology." https://thermocalc.com/about-us/methodology/the-calphad-methodology/ (accessed May, 8., 2025).

[302] T. Nishizawa, "Thermodynamics of Diffusion," *Thermodynamics of Microstructures.* Materials Park, OH, USA: ASM International, 2008, pp. 167-196. [Online]. Available: https://ifind.swansea.ac.uk/permalink/44WHELF_SWA/1jlslid/alma9982827928024117

[303] C. Xia, S. Xia, Y. Li, and X. Lu, "Evaluating atomic mobility and interdiffusivity based on two-dimensional diffusion simulations and diffusion triple experiments," *Scripta Materialia,* vol. 188, pp. 124-129, November. 2020. [Online]. Available: https://doi.org/10.1016/j.scriptamat.2020.07.026.

[304] F. Teso, J. Endal, and J. L. Vazquez, "On the Two-phase Fractional Stefan Problem," *Advanced Nonlinear Studies,* vol. 20, no. 2, pp. 437-458, March 2020. [Online]. Available: https://doi.org/10.1515/ans-2020-2081.

[305] S. Koga and M. Krstic, "Phase Change Model: Stefan Problem," *Materials Phase Change PDE Control & Estimation*: Birkhäuser Cham, 2020, pp. 1-13. [Online]. Available: https://doi.org/10.1007/978-3-030-58490-0_1

[306] T. Nishizawa, "Thermodynamics of Interfaces," *Thermodynamics of Microstructures.* Materials Park, OH, USA: ASM International, 2008, pp. 123-166. [Online]. Available: https://ifind.swansea.ac.uk/permalink/44WHELF_SWA/1jlslid/alma9982827928024117

[307] H. Larsson, "A model for 1D multiphase moving phase boundary simulations under local equilibrium conditions," *Calphad,* vol. 47, pp. 1-8, December 2014. [Online]. Available: https://doi.org/10.1016/j.calphad.2014.06.001.

[308] J. Andersson and J. Agren, "Models for numerical treatment of multicomponent diffusion in simple phases," *Journal of Applied Physics,* vol. 72, no. 4, pp. 1350-1355, 1992. [Online]. Available: https://doi.org/10.1063/1.351745.

[309] A. Kedharnath, R. Kapoor, and A. Sarkar, "Classical molecular dynamics simulations of the deformation of metals under uniaxial monotonic loading: A review," *Computers & Structures,* vol. 254, October 2021. [Online]. Available: https://doi.org/10.1016/j.compstruc.2021.106614.

[310] J. Fan, "Basics of Atomistic Simulation," *Multiscale Analysis of Deformation and Failure of Materials*2nd ed. Chichester, West Sussex, UK: Wiley, 2011, pp. 37-75. [Online]. Available: https://ifind.swansea.ac.uk/permalink/44WHELF_SWA/1jlslid/alma9982833616024 17

[311] L. J. Lapidus (Michigan State University). "Lennard-Jones Potential." https://physicsatmcl.commons.msu.edu/lennard-jones-potential/ (accessed June. 1, 2025).

[312] J. Fan, "Applications of Atomistic Simulations in Ceramics and Metals," *Multiscale Analysis of Deformation and Failure of Materials*2nd ed. Chichester, West Sussex, UK: Wiley, 2011, pp. 76-121. [Online]. Available: https://ifind.swansea.ac.uk/permalink/44WHELF_SWA/1jlslid/alma9982833616024 17

[313] A. Pedone, M. Bertani, L. Brugnoli, and A. Pallini, "Interatomic potentials for oxide glasses: Past, present, and future," *Journal of Non-Crystalline Solids: X,* vol. 15, September 2022. [Online]. Available: https://doi.org/10.1016/j.nocx.2022.100115.

[314] Tata Steel UK Limited, "TATA INSTALL PLUS - 65 080322 Test Report 120/2036/0697," Corby, UK, September, 3. 2020.

[315] Tata Steel UK Limited, "Tata INSTALL PLUS -150 030322 Test Report 120/2144/0115," Corby, UK, November, 11. 2021.

[316] Z. Weiss, "Propagation of Uncertainty in Multi-matrix Analysis by GD-OES," *Journal of Analytical Atomic Spectroscopy,* vol. 16, no. 11, pp. 1275-1282, 2001. [Online]. Available: https://ifind.swansea.ac.uk/permalink/44WHELF_SWA/1m9hta7/cdi_scopus_primary_33037961.

[317] J. A. Middleton, "Simple Linear Regression," *Experimental Statistics and Data Analysis for Mechanical and Aerospace Engineers.* Boca Raton, FL, USA: CRC Press, Taylor & Francis Group, 2022, pp. 271-314. [Online]. Available: https://ifind.swansea.ac.uk/permalink/44WHELF_SWA/1jlslid/alma9985791640024 17

[318] T. Nelis and R. Payling, "Calibration," *Glow Discharge Optical Emission Spectroscopy: A Practical Guide.* Cambridge, UK: Royal Society of Chemistry, 2003, pp. 45-75. [Online]. Available: https://ifind.swansea.ac.uk/permalink/44WHELF_SWA/1sssfk8/alma9982842433024 17

[319] T. Nelis and R. Payling, "Bulk Analysis," *Glow Discharge Optical Emission Spectroscopy: A Practical Guide.* Cambridge, UK: Royal Society of Chemistry, 2003, pp. 110-122. [Online]. Available: https://ifind.swansea.ac.uk/permalink/44WHELF_SWA/1sssfk8/alma9982842433024 17

[320] D. M. Stefanescu, G. Alonso, P. Larranaga, E. De La Fuente, and R. Suarez, "On the crystallization of graphite from liquid iron–carbon–silicon melts," *Acta Materialia,* vol. 107, pp. 102-126, April 2016. [Online]. Available: https://doi.org/10.1016/j.actamat.2016.01.047.

[321] B. Linder, "The First Law of Thermodynamics," *Elementary Physical Chemistry*, N. J. Hackensack, Ed.: World Scientific, 2011, pp. 11-19. [Online]. Available:

https://ifind.swansea.ac.uk/permalink/44WHELF_SWA/1jlslid/alma9982899570024117

[322] H. Larsson and R. C. Reed, "On the numerical simulation of diffusion-controlled reactions under local equilibrium conditions," *Acta Materialia,* vol. 56, no. 15, pp. 3754-3760, September 2008. [Online]. Available: https://doi.org/10.1016/j.actamat.2008.04.008.

[323] Thermo-Calc Software AB. "TCS Steel and Fe-alloys Database (TCFE14): Technical Information." https://thermocalc.com/products/databases/steel-and-fe-alloys/ (accessed June. 18, 2025).

[324] Thermo-Calc Software AB. "TCS Steels/Fe-Alloys Mobility Database (MOBFE8): Technical Information." https://thermocalc.com/products/databases/steel-and-fe-alloys/ (accessed June. 18, 2025).

[325] Thermo-Calc Software AB, "Database Manager User Guide," *Thermo-Calc Documentation Set.* Solna, Sweden: Thermo-Calc Software AB, 2023, pp. 1743-1840. [Online]. Available: https://thermocalc.com/support/documentation/

[326] Thermo-Calc Software AB, "Diffusion Module (DICTRA) Documentation Set," ed, 2025.

[327] M. Kowalski and P. J. Spencer, "Thermodynamic reevaluation of the C-O, Fe-O and Ni-O systems: Remodelling of the liquid, BCC and FCC phases," *Calphad,* vol. 19, no. 3, pp. 229-243, September 1995. [Online]. Available: https://doi.org/10.1016/0364-5916(95)00024-9.

[328] X. G. Lu, M. Selleby, and B. Sundman, "Assessments of molar volume and thermal expansion for selected bcc, fcc and hcp metallic elements," *Calphad,* vol. 29, no. 1, pp. 68-89, March 2005. [Online]. Available: https://doi.org/10.1016/j.calphad.2005.05.001.

[329] X. G. Lu, M. Selleby, and B. Sundman, "Theoretical modeling of molar volume and thermal expansion," *Acta Materialia,* vol. 53, no. 8, pp. 2259-2272, May 2005. [Online]. Available: https://doi.org/10.1016/j.actamat.2005.01.049.

[330] P. Kofstad, "Electrochemical Transport. Defect Dependent Processes," in *Nonstoichiometry, diffusion, and electrical conductivity in binary oxides*. London, UK: John Wiley & Sons, 1972, pp. 96-116.

[331] M. Enomoto and K. Hayashi, "Modeling the growth of austenite in association with cementite during continuous heating in low-carbon martensite," *Journal of Materials Science,* vol. 53, pp. 6911-6921, January 2018. [Online]. Available: https://link.springer.com/article/10.1007/s10853-018-2020-2.

[332] K. Hellstrom, V. L. Diaconu, and A. Dioszegi, "Density and thermal expansion coefficients of liquid and austenite phase in lamellar cast iron," *China Foundry,* vol. 17, pp. 127-136, April 2020. [Online]. Available: https://link.springer.com/article/10.1007/s41230-020-0004-8#change-history.

[333] Y. S. Zhang, X. Lu, X. Tian, and Z. Qin, "Compositional dependence of the Néel transition, structural stability, magnetic properties and electrical resistivity in Fe–Mn–Al–Cr–Si alloys," *Materials Science and Engineering: A,* vol. 334, no. 2, pp. 19-27, 2002. [Online]. Available: https://doi.org/10.1016/S0921-5093(01)01781-6.

[334] M. Acet, H. Zahres, and E. F. Wasserman, "High-temperature moment-volume instability and anti-Invar of y-Fe," *Physical Review B,* vol. 49, no. 9, pp. 6012-6017, 1994. [Online]. Available: https://doi.org/10.1103/PhysRevB.49.6012.

[335] M. Reis, "Hamiltonian of an Electron Under an Electromagnetic Field," *Fundamentals of Magnetism.* Amsterdam, The Netherlands: Academic Press, 2013, pp. 13-24. [Online]. Available:

https://ifind.swansea.ac.uk/permalink/44WHELF_SWA/1sssfk8/alma998192650402417

[336] Y. A. Cengel and M. A. Boles, "Entropy," in *Thermodynamics: An Engineering Approach*, 6th ed. New York, NY, USA: McGraw-Hill, 2007, pp. 323-412.

[337] Y. A. Cengel and M. A. Boles, "Energy, Energy Transfer, and General Energy Analysis," in *Thermodynamics: An Engineering Approach*, 6th ed. New York, NY, USA: McGraw-Hill, 2007, pp. 51-108.

[338] Z. S. Basinski, W. Hume-Rothery, and A. L. Sutton, "The lattice expansion of iron," *Proceedings of the Royal Society A,* vol. 229, pp. 459-467, 1955. [Online]. Available: https://doi.org/10.1098/rspa.1955.0102.

[339] D. Aquilano, F. Otalora, L. Pastero, and J. M. Garcia-Ruiz, "Three study cases of growth morphology in minerals: Halite, calcite and gypsum," *Progress in Crystal Growth and Characterization of Materials,* vol. 62, no. 2, pp. 227-251, June 2016. [Online]. Available: https://doi.org/10.1016/j.pcrysgrow.2016.04.012.

[340] R. E. Smallman and A. H. W. Ngan, "Appendix 2: Conversion factors, constants and physical data," *Physical Metallurgy and Advanced Materials.* Amsterdam, The Netherlands: Butterworth Heinemann, 2007, pp. 629-630. [Online]. Available: https://ifind.swansea.ac.uk/permalink/44WHELF_SWA/1jlslid/alma9982818866024117

[341] Y. Zeng, T. Mittnacht, W. Werner, Y. Du, D. Schneider, and B. Nestler, "Gibbs energy and phase-field modeling of ferromagnetic ferrite (α)→ paramagnetic austenite (γ) transformation in Fe–C alloys under an external magnetic field," *Acta Materialia,* vol. 225, February 2022. [Online]. Available: https://doi.org/10.1016/j.actamat.2021.117595.

[342] J. Philibert, "Solute Diffusion in Pure Materials. Diffusion in Alloys.," *Atom Movements: Diffusion and Mass Transport in Solids.* Les Ulis, France: Editions de Physique, 1991, pp. 149-202. [Online]. Available: https://ifind.swansea.ac.uk/permalink/44WHELF_SWA/1sssfk8/alma9986116342024217

[343] L. Zhang, Y. Du, I. Steinbach, Q. Chen, and B. Huang, "Diffusivities of an Al–Fe–Ni melt and their effects on the microstructure during solidification," *Acta Materialia,* vol. 58, no. 10, pp. 3664-3675, June 2010. [Online]. Available: https://doi.org/10.1016/j.actamat.2010.03.002.

[344] J. Takada and M. Adachi, "Determination of diffusion coefficient of oxygen in α-iron from internal oxidation measurements in Fe-Si alloys," *Journal of Materials Science,* vol. 21, pp. 2133-2137, 1986. [Online]. Available: https://link.springer.com/article/10.1007/BF00547959.

[345] E. Gamsjager, J. Svoboda, and F. D. Fischer, "Austenite-to-ferrite phase transformation in low-alloyed steels," *Computational Materials Science,* vol. 32, no. 4, pp. 360-369, March 2005. [Online]. Available: https://doi.org/10.1016/j.commatsci.2004.09.031.

[346] P. Kofstad, "Oxides of Group VII and VIII Elements," in *Nonstoichiometry, diffusion, and electrical conductivity in binary oxides*. London, UK: John Wiley & Sons, 1972, pp. 213-264.

[347] C. Ararat-Ibarguen, R. A. Perez, and M. Iribarren, "Measurements of diffusion coefficients in solids by means of LIBS combined with direct sectioning," *Measurement,* vol. 55, pp. 571-580, September 2014. [Online]. Available: https://doi.org/10.1016/j.measurement.2014.06.009.

[348] J. H. Swisher and E. T. Turkdogan, "Solubility, permeability, and diffusivity of oxygen in solid iron," *Transactions of the Metallurgical Society of AIME,* vol. 239,

pp. 426-431, 1967. [Online]. Available: https://www.scribd.com/document/585786393/1967-Swisher-Solubility-Permeability-and-Diffusivity-of-Oxygen-in-Solid-Iron.

[349] S. R. K. Iyengar and R. K. Jain, "Initial Value Problems for Ordinary Differential Equations," *Numerical Methods,* New Delhi, India: New Age International Ltd, 2009, pp. 180-240. [Online]. Available: https://ifind.swansea.ac.uk/permalink/44WHELF_SWA/1jlslid/alma9982886993024117

[350] W. H. Press, S. A. Teukolsky, W. T. Vetterling, and B. P. Flannery, "Preliminaries," in *Numerical Recipes: The Art of Scientific Computing*, 2nd ed. Cambridge UK: Cambridge University Press, 1992, pp. 1-36.

[351] B. Jonsson, "On Ferromagnetic Ordering and Lattice Diffusion - A Simple Model," *Zeitschrift für Metallkunde,* vol. 83, no. 5, pp. 349-355, 1992. [Online]. Available: https://whelf-swansea.alma.exlibrisgroup.com/infra/docDeliveryDownload.

[352] Z. D. Sharp, "Determination of oxygen diffusion rates in magnetite from natural isotopic variations " *Geology,* vol. 19, pp. 653-656, June 1991. [Online]. Available: http://pubs.geoscienceworld.org/gsa/geology/article-pdf/19/6/653/3512977/i0091-7613-19-6-653.pdf.

[353] B. Jonsson, "Mobilities in Fe-Ni Alloys: Assessment of the Mobilities of Fe and Ni in fcc Fe-Ni Alloys," *Scandinavian Journal of Metallurgy,* vol. 23, pp. 201-208, 1994.

[354] J. Philibert, "Atomic Theory of Diffusion," *Atom Movements: Diffusion and Mass Transport in Solids.* Les Ulis, France: Editions de Physique, 1991, pp. 33-60. [Online]. Available: https://ifind.swansea.ac.uk/permalink/44WHELF_SWA/1sssfk8/alma9986116342024117

[355] D. Huin, J. B.-. Leblond, I. Darghoum, J. M.-. Bergheau, and F. Bertrand, "Extended Wagner-type models and their application to the prediction of the transition from internal to external oxidation," *Computational Materials Science,* vol. 209, June 2022. [Online]. Available: https://doi.org/10.1016/j.commatsci.2022.111334.

[356] J. Yan and C. W.-. Shu, "Local Discontinuous Galerkin Methods for Partial Differential Equations with Higher Order Derivatives," *Journal of Scientific Computing,* vol. 17, pp. 27-47, December 2002. [Online]. Available: https://link.springer.com/article/10.1023/A:1015132126817.

[357] D. Motreanu, A. Sciammetta, and E. Tornatore, "A Sub-Supersolution Approach for Robin Boundary Value Problems with Full Gradient Dependence," *Mathematics,* vol. 8, no. 5, April 2020. [Online]. Available: https://doi.org/10.3390/math8050658.

[358] Y. A. Cengel and M. A. Boles, "Gas Mixtures," in *Thermodynamics: An Engineering Approach*, 6th ed. New York, NY, USA: McGraw-Hill, 2007, pp. 701-736.

[359] Y. A. Cengel and M. A. Boles, "Chemical Reactions," in *Thermodynamics: An Engineering Approach*, 6th ed. New York, NY, USA: McGraw-Hill, 2007, pp. 773-816.

[360] I. Kaur and W. Gust, "Grain and interphase boundary diffusion," in *Numerical Data and Functional Relationships in Science and Technology: Group III (Landolt-Bornstein)*, vol. 26, H. Mehrer Ed. Berlin: Springer, 1990, pp. 630-708.

[361] P. De, J. Halder, C. C. Gowda, S. Kansal, S. Priya, S. Anshu, A. Chowdhury, D. Mandal, S. Biswas, B. K. Dubey, and A. Chandra, "Role of porosity and diffusion coefficient in porous electrode used in supercapacitors – Correlating theoretical and experimental studies," *Electrochemical Science Advances,* vol. 3, no. 1, February 2023. [Online]. Available: https://doi.org/10.1002/elsa.202100159.

[362] G. Pastore, D. Pizzocri, C. Rabiti, T. Barani, P. Van Uffelen, and L. Luzzi, "An effective numerical algorithm for intra-granular fission gas release during non-equilibrium trapping and resolution," *Journal of Nuclear Materials,* vol. 509, pp. 687-699, October 2018. [Online]. Available: https://doi.org/10.1016/j.jnucmat.2018.07.030.

[363] X. Yu and J. Zhou, "Grain Boundary in Oxide Scale During High-Temperature Metal Processing. ," *Study of Grain Boundary Character*, T. A. Tański and W. Borek, Eds., London, UK.: IntechOpen, 2017. [Online]. Available: https://www.intechopen.com/chapters/52955

[364] Y. Mishin and C. Herzig, "Grain boundary diffusion: recent progress and future research," *Materials Science and Engineering: A,* vol. 260, no. 2, pp. 55-71, February 1999. [Online]. Available: https://doi.org/10.1016/S0921-5093(98)00978-2.

[365] J. C. Fisher, "Calculation of Diffusion Penetration Curves for Surface and Grain Boundary Diffusion " *Journal of Applied Physics,* vol. 22, no. 1, pp. 74-77, January 1951. [Online]. Available: https://doi.org/10.1063/1.1699825.

[366] L. G. Harrison, "Influence of dislocations on diffusion kinetics in solids with particular reference to the alkali halides," *Transactions of the Faraday Society,* vol. 57, pp. 1191-1199, 1961, doi: 10.1039/TF9615701191.

[367] E. N. Borodin and A. E. Mayer, "Influence of structure of grain boundaries and size distribution of grains on the yield strength at quasistatic and dynamical loading," *Materials Research Express,* vol. 4, no. 8, 2017, doi: 10.1088/2053-1591/aa8514.

[368] Y. Zhang, W. Zhang, L. Zeng, J. Liang, J. Xiao, and A. Zhao, "Segregation behavior and precipitated phases of super-austenitic stainless steel influenced by electromagnetic stirring " *Materials Today Communications,* vol. 31, June 2022. [Online]. Available: https://doi.org/10.1016/j.mtcomm.2022.103675.

[369] Y. Sasaki, M. Iguch, and M. Hino, "The Evaluation of Grain Boundary Difussion Coefficient of Iron Ions in Wustite," presented at the Experimental Analysis of Nano and Engineering Materials and Structures, Dordrecht 2007. [Online]. Available: https://doi.org/10.1007/978-1-4020-6239-1_414.

[370] J. H. Bott, H. Yin, S. Sridhar, and M. Auinger, "Theoretical and experimental analysis of selective oxide and nitride formation in Fe–Al alloys," *Corrosion Science,* vol. 91, pp. 37-45, February 2015. [Online]. Available: https://doi.org/10.1016/j.corsci.2014.10.024.

[371] R. P. Oleksak, M. Kapoor, D. E. Perea, G. R. Holcomb, and O. N. Dogan, "The role of metal vacancies during high-temperature oxidation of alloys," *npj Materials Degradation,* vol. 2, no. 25, 2018. [Online]. Available: https://doi.org/10.1038/s41529-018-0046-1.

[372] C. Wagner, "Beitrag zur Theorie des Anlaufvorgangs," *Zeitschrift für Physikalische Chemie,* vol. 21B, no. 1, pp. 25-41, 1933. [Online]. Available: https://doi.org/10.1515/zpch-1933-2105.

[373] J. Gavarri and C. Carel, "The complex nonstoichiometry of wüstite Fe1-zO: Review and comments," *Progress in Solid State Chemistry,* vol. 53, pp. 27-49, March 2019. [Online]. Available: https://doi.org/10.1016/j.progsolidstchem.2018.10.001.

[374] X. Yu, A. Gulec, Q. Sherman, K. L. Cwalina, J. R. Scully, J. H. Perepezko, P. W. Voorhees, and L. D. Marks, "Nonequilibrium Solute Capture in Passivating Oxide Films," *Physical Review Letters,* vol. 121, no. 14, October 2018. [Online]. Available: https://link.aps.org/doi/10.1103/PhysRevLett.121.145701.

[375] M. Jackson, *Periodic table Advanced : Atomic, Physical, Chemical Properties & Natural Isotopes*: BarCharts, Inc., 2015. [Online]. Available:

https://ifind.swansea.ac.uk/permalink/44WHELF_SWA/1jlslid/alma9983604962024117.

[376] S. Mandl, J. W. Gerlach, and D. Manova, "Nitrogen isotope marker experiments in austenitic stainless steel for identification of trapping/detrapping processes at different temperatures," *Surface and Coatings Technology,* vol. 472, November 2023. [Online]. Available: https://doi.org/10.1016/j.surfcoat.2023.129952.

[377] H. Evans, D. A. Hilton, R. Holm, and S. J. Webstert, "The influence of a titanium nitride dispersion on the oxidation behavior of 20%Cr-25%Ni stainless steel," *Oxidation of Metals,* vol. 12, pp. 473-485, December 1978. [Online]. Available: https://api.semanticscholar.org/CorpusID:135705778.

[378] M. Walbruhl, J. Agren, A. Blomqvist, and H. Larsson, "ICME guided modeling of surface gradient formation in cemented carbides," *International Journal of Refractory Metals and Hard Materials,* vol. 72, pp. 33-38, April 2018. [Online]. Available: https://doi.org/10.1016/j.ijrmhm.2017.12.010.

[379] M. Romedenne, F. Rouillard, D. Hamon, B. Malard, and D. Monceau, "Carburization of austenitic and ferritic stainless steels in liquid sodium: Comparison between experimental observations and simulations," *Corrosion Science,* vol. 159, October 2019. [Online]. Available: https://doi.org/10.1016/j.corsci.2019.108147.

[380] F. M. White, "Pressure Distribution in a Fluid," in *Fluid Mechanics*, M. Lange Ed., 7th ed. New York, NY, USA: McGraw-Hill, 2009, pp. 65-138.

[381] E. R. Jette and F. Foote, "An X-Ray Study of the Wüstite (FeO) Solid Solutions," *The Journal of Chemical Physics,* vol. 1, no. 1, pp. 29-36, January 1933. [Online]. Available: https://doi.org/10.1063/1.1749215.

[382] S. J. Simon, "Introduction," *Protecting Clean Air: Preventing Pollution,* New York, NY, USA: Momentum Press Engineering, 2018. [Online]. Available: https://ifind.swansea.ac.uk/permalink/44WHELF_SWA/1jlslid/alma9984616315024117

[383] J. Saputo, F. Caliari, E. Gingrich, M. Tess, and S. Sampath, "Oxidation of Ferrous Alloys and Coatings Under Isothermal, Impulse Heating, and Diesel Engine Operation: Part I—4140 Steel," *Oxidation of Metals,* vol. 98, pp. 341-361, 2022. [Online]. Available: https://doi.org/10.1007/s11085-022-10126-2.

[384] J. A. Middleton, "The General Linear Model: Regression with Multiple Predictors," *Experimental Statistics and Data Analysis for Mechanical and Aerospace Engineers.* Boca Raton, FL, USA: CRC Press, Taylor & Francis Group, 2022, pp. 317-370. [Online]. Available: https://ifind.swansea.ac.uk/permalink/44WHELF_SWA/1jlslid/alma9985791640024117

[385] S. W. Smith, "Moving Average Filters," *Digital Signal Processing : A Practical Guide for Engineers and Scientists,* 1st ed. Boston, MA, USA: Newnes, 2003, pp. 277-284. [Online]. Available: https://ifind.swansea.ac.uk/permalink/44WHELF_SWA/1jlslid/alma9985261449024117

[386] A. Degasperi and M. Calder, "Relating PDEs in Cylindrical Coordinates and CTMCs with Levels of Concentration," *Electronic Notes in Theoretical Computer Science,* vol. 268, pp. 49-59, December 2010. [Online]. Available: https://doi.org/10.1016/j.entcs.2010.12.005.

[387] D. Simon, B. Gorr, and H. J. Christ, "Effect of Atmosphere and Sample Thickness on Kinetics, Microstructure, and Compressive Stresses of Chromia Scale Grown on Ni–25Cr," *Oxidation of Metals,* vol. 87, pp. 417-429, 2017. [Online]. Available: https://doi.org/10.1007/s11085-016-9702-4.

[388] W. J. Quadakkers, J. Zurek, and M. Hansel, "Effect of water vapor on high-temperature oxidation of FeCr alloys," *The Journal of The Minerals, Metals & Materials Society,* vol. 61, pp. 44-50, July 2009. [Online]. Available: https://link.springer.com/article/10.1007/s11837-009-0102-y.

[389] C. Asensio-Jimenez, L. Niewolak, H. Hattendorf, B. Kuhn, P. Huczkowski, L. Singheiser, and W. J. Quadakkers, "Effect of Specimen Thickness on the Oxidation Rate of High Chromium Ferritic Steels: The Significance of Intrinsic Alloy Creep Strength," *Oxidation of Metals,* vol. 79, pp. 15-28, December 2012. [Online]. Available: https://doi.org/10.1007/s11085-012-9323-5.

[390] K. E. Nygren, Z. Yu, F. Rouillard, and A. Couet, "Effect of sample thickness on the oxidation and carburization kinetics of 9Cr-1Mo steel in high and atmospheric pressure CO2 at 550 °C," *Corrosion Science,* vol. 163, February 2020. [Online]. Available: https://doi.org/10.1016/j.corsci.2019.108292.

[391] W. A. Nash and M. C. Potter, "Stresses in Beams," *Strength of Materials.* 5th ed. New York, NY, USA: McGraw-Hill, 2011. [Online]. Available: https://ifind.swansea.ac.uk/permalink/44WHELF_SWA/1jlslid/alma998382841502417

[392] S. W. Smith, "Statistics, Probability and Noise," *Digital Signal Processing : A Practical Guide for Engineers and Scientists,* 1st ed. Boston, MA, USA: Newnes, 2003, pp. 11-34. [Online]. Available: https://ifind.swansea.ac.uk/permalink/44WHELF_SWA/1jlslid/alma998526144902417

[393] B. K. Shivamoggi, "Isentropic Fluid Flows," *Introduction to Theoretical and Mathematical Fluid Dynamics,* Hoboken, New Jersey, USA: John Wiley & Sons, 2021, pp. 309-316. [Online]. Available: https://ifind.swansea.ac.uk/permalink/44WHELF_SWA/1jlslid/alma998888258302417

[394] R. G. Rehm and H. R. Baum, "The Equations of Motion for Thermally Driven, Buoyant Flows " *Journal of Research of the Notional Bureau of Standards,* vol. 83, no. 3, pp. 297-308, January 1978. [Online]. Available: https://doi.org/10.6028/jres.083.019.

[395] H. Zou, L. Wu, W. Li, F. Han, and Z. Deng, "Thermally-induced vibration analysis of tensegrity modules during space deployment using dynamic stiffness method," *International Journal of Solids and Structures,* vol. 282, 2023. [Online]. Available: https://doi.org/10.1016/j.ijsolstr.2023.112454.

[396] I. Newton, *The Principia: The Authoritative Translation : Mathematical Principles of Natural Philosophy*, Berkeley, CA: University of California Press, 2016. [Online]. Available: https://ifind.swansea.ac.uk/permalink/44WHELF_SWA/1jlslid/alma998539195602417.

[397] K. R. Mobley, "Theory: Introduction to Vibration Analysis," *Vibration Fundamentals,* Boston, MA, USA: Butterworth-Heinemann, 1999, pp. 1-64. [Online]. Available: https://ifind.swansea.ac.uk/permalink/44WHELF_SWA/1sssfk8/alma998281599202417

[398] Y. Demchenko, I. Oleg, and V. Vedeneev, "Experimental investigation of rotational vortex-induced vibrations of a circular cylinder attached to an elastic beam," *Journal of Fluids and Structures,* vol. 133, March 2025. [Online]. Available: https://doi.org/10.1016/j.jfluidstructs.2025.104266.

[399] R. N. Govardhan and O. N. Ramesh, "A stroll down Kármán street," *Resonance,* vol. 10, pp. 25-37, August 2005. [Online]. Available: https://link.springer.com/article/10.1007/BF02866744.

[400] B. K. Shivamoggi, "Vortex Flows," *Introduction to Theoretical and Mathematical Fluid Dynamics,* Hoboken, New Jersey, USA: John Wiley & Sons, 2021, pp. 143-172. [Online]. Available: https://ifind.swansea.ac.uk/permalink/44WHELF_SWA/1jlslid/alma99888258302417

[401] B. Murari, S. Zhao, Y. Zhang, and J. Yang, "Vortex-induced vibration of a functionally graded metamaterial plate attached to a cylinder in laminar flow," *Thin-Walled Structures,* vol. 199, June 2024. [Online]. Available: https://doi.org/10.1016/j.tws.2024.111790.

[402] L. Zhao, T. Han, C. Hu, S. Luo, Q. Zhou, and W. Cui, "Pressure and flow patterns during multiple-order vertical vortex-induced vibrations of a 6:1 rectangular cylinder," *Journal of Fluids and Structures,* vol. 135, June 2025. [Online]. Available: https://doi.org/10.1016/j.jfluidstructs.2025.104314.

[403] H. Jiang and L. Cheng, "Strouhal–Reynolds number relationship for flow past a circular cylinder," *Journal of Fluid Mechanics,* vol. 832, pp. 170-188, December 2017. [Online]. Available: http://dx.doi.org/10.1017/jfm.2017.685.

[404] Y. Zhang, L. Sun, and C. He, "Flow induced vibration investigation of a main steam pipe suffering from high temperature steam flow," *Progress in Nuclear Energy,* vol. 143, January 2022. [Online]. Available: https://doi.org/10.1016/j.pnucene.2021.104040.

[405] R. B. Randall and J. Antoni, "Choosing the right signal processing tools for mechanical systems," *Mechanical Systems and Signal Processing,* vol. 224, February 2025. [Online]. Available: https://doi.org/10.1016/j.ymssp.2024.112090.

[406] P. Biglarbeigi, A. Morelli, G. Bhattacharya, J. Ward, D. Finlay, N. Bhalla, and A. F. Payam, "Incongruous Harmonics of Vibrating Solid-Solid Interface," *Small,* 2024. [Online]. Available: https://doi.org/10.1002/smll.202409410.

[407] A. Albu-Schaffer and C. Della Santina, "A review on nonlinear modes in conservative mechanical systems," *Annual Reviews in Control,* vol. 50, pp. 49-71, 2020. [Online]. Available: https://doi.org/10.1016/j.arcontrol.2020.10.002.

[408] A. G. Piersol, T. L. Paez, and C. M. Harris, "Basic Vibration Theory," *Harris' Shock and Vibration Handbook,* 6th ed. New York, NY, USA: McGraw-Hill, 2010. [Online]. Available: https://ifind.swansea.ac.uk/permalink/44WHELF_SWA/144jshv/alma998382892802417

[409] F. Terzioglu and J. A. Rongong, "Selection of granular damper parameters to achieve optimum vibration attenuation on vibrating structures," *Mechanical Systems and Signal Processing,* vol. 229, April 2025. [Online]. Available: https://doi.org/10.1016/j.ymssp.2025.112512.

[410] H. E. Evans and R. C. Lobb, "Conditions for the Initiation of Oxide-Scale Cracking and Spallation," *Corrosion Science,* vol. 24, no. 3, pp. 209-222, 1984. [Online]. Available: https://doi.org/10.1016/0010-938X(84)90051-9.

[411] J. Armitt, R. Holmes, M. I. Manning, D. Meadowcroft, and E. Metcalfe, "Spalling of steam-grown oxide from superheater and reheater tube steels. Technical planning study 76-655. Final report," Central Electricity Research Laboratories, Leatherhead, Surrey, UK, February 1978. [Online]. Available: https://www.osti.gov/servlets/purl/5047517/

[412] B. Weiss, J. Sturn, S. Vogslam, S. Strobl, H. Mali, F. Winter, and J. Schenk, "Structural and morphological changes during reduction of hematite to magnetite and wustite in hydrogen rich reduction gases under fluidised bed conditions," *Ironmaking & Steelmaking,* vol. 38, no. 1, pp. 65-73, January 2011. [Online]. Available: https://doi.org/10.1179/030192310X12700328926065.

[413] K. He, Z. Zheng, and Z. Chen, "A numerical investigation on the hydrogen reduction of wüstite using a 2D mesoscale method," *International Journal of Hydrogen Energy,* vol. 47, no. 12, pp. 8118-8129, February 2022. [Online]. Available: https://doi.org/10.1016/j.ijhydene.2021.12.154.

[414] P. P. Benham, R. J. Crawford, and C. G. Armstrong, "Bending: Stress," in *Mechanics of Engineering Materials*, 2nd ed. Harlow, UK: Pearson Education, 1996, pp. 125-174.

[415] H. Tammpere, P. McKeown, J. Miller, C. Fang, E. Curtis, M. Gaiser-Porter, M. Burley, J. Campbell, M. Artiles, Y. Tang, S. Utada, R. Reed, and T. W. Clyne, "Profilometry-Based Indentation Plastometry at High Temperature," *Advanced Engineering Materials,* vol. 26, no. 21, July 2024. [Online]. Available: https://doi.org/10.1002/adem.202301073.

[416] A. M. Huntz and M. Schütze, "Stresses generated during oxidation sequences and high temperature fracture," *Materials at High Temperatures,* vol. 12, no. 2-3, pp. 151-161, 1994. [Online]. Available: https://doi.org/10.1080/09603409.1994.11689481.

[417] M. Woodcox, J. Young, and M. Smeu, "Ab initio investigation of the temperature-dependent elastic properties of Bi, Te and Cu," *Journal of Physics: Condensed Matter,* vol. 32, no. 48, 2020. [Online]. Available: 10.1088/1361-648X/ababdf.

[418] P. P. Benham, R. J. Crawford, and C. G. Armstrong, "Appendix C: Table of Mechanical Properties of Engineering Materials," in *Mechanics of Engineering Materials*, 2nd ed. Harlow, UK: Pearson Education, 1996.

[419] I. Saeki, T. Ohno, O. Sakai, T. Niya, and T. Sato, "In situ measurement of Young's modulus of FeO scale formed on pure iron at 973–1273 K by acoustic resonance method," *Corrosion Science,* vol. 53, no. 1, pp. 458-463, January 2011. [Online]. Available: https://doi.org/10.1016/j.corsci.2010.09.057.

[420] J. Robertson and M. I. Manning, "Limits to adherence of oxide scales," *Materials Science and Technology,* vol. 6, no. 1, pp. 81-92, 1990, doi: 10.1179/mst.1990.6.1.81.

[421] Y. Sumino, M. Kumazawa, and T. Nishizawa, "The Elastic Constants of Single Crystal Fe1-xO, MnO and CoO, and the Elasticity of Stoichiometric Magnesiowustite," *Journal of Physics of the Earth,* vol. 28, pp. 475-495, 1980. [Online]. Available: https://www.jstage.jst.go.jp/article/jpe1952/28/5/28_5_475/_pdf.

[422] L. Feng, R. Liu, K. Ma, Y. Zhao, X. Fu, X. Zhang, Y. Ling, and J. Li, "Tensile properties and molecular dynamics simulation of FeCrMnAlxCu high-entropy alloys," *Vacuum,* vol. 238, August 2025. [Online]. Available: https://doi.org/10.1016/j.vacuum.2025.114219.

[423] F. Schrettle, C. Kant, P. Lunkenheimer, F. Mayr, J. Deisenhofer, and A. Loidl, "Wüstite: electric, thermodynamic and optical properties of FeO," *The European Physical Journal B,* vol. 85, no. 164, May 2012. [Online]. Available: https://link.springer.com/article/10.1140/epjb/e2012-30201-5.

[424] H. Siethoff, "Debye temperature, self-diffusion and elastic constants of intermetallic compounds," *Intermetallics,* vol. 5, no. 8, pp. 625-632, 1997. [Online]. Available: https://doi.org/10.1016/S0966-9795(97)00037-X.

[425] D. Sherman, "Stability of possible Fe-FeS and Fe-FeO alloy phases at high pressure and the composition of the Earth's core," *Earth and Planetary Science Letters,* vol.

132, no. 1-4, pp. 87-98, May 1995. [Online]. Available: https://doi.org/10.1016/0012-821X(95)00057-J.

[426] R. J. Radwanski and Z. Ropka, "First-principles consistent description of monoxides FeO, CoO and NiO," *Physica B: Condensed Matter,* vol. 403, no. 5-9, pp. 1453-1455, April 2008. [Online]. Available: https://doi.org/10.1016/j.physb.2007.10.159.

[427] R. A. Fischer, A. J. Campbell, G. A. Shofner, O. T. Lord, P. Dera, and V. Prakapenka, "Equation of state and phase diagram of FeO," *Earth and Planetary Science Letters,* vol. 304, no. 3-4, pp. 496-502, April 2011. [Online]. Available: https://doi.org/10.1016/j.epsl.2011.02.025.

[428] S. Eliezer, A. K. Ghatak, and H. Hora, "Gruneisen Equation of State," *Fundamentals of Equations of State,* River Edge, NJ, USA: World Scientific, 2002, pp. 153-164. [Online]. Available: https://ifind.swansea.ac.uk/permalink/44WHELF_SWA/1jlslid/alma9982898874024117

[429] I. Ak, H. Adin, A. Arafat, and M. Okumus, "Mechanical properties of Cu-Ni alloys: Comparison of experimental and MD simulation approaches," *Physica B: Condensed Matter,* vol. 700, March 2025. [Online]. Available: https://doi.org/10.1016/j.physb.2025.416928.

[430] J. B. Wachtman, W. E. Tefft, D. G. Lam, and C. S. Apstein, "Exponential Temperature Dependence of Young's Modulus for Several Oxides," *Physical Review,* vol. 122, no. 6, June 1961. [Online]. Available: https://doi.org/10.1103/PhysRev.122.1754.

[431] O. L. Anderson, "Derivation of Wachtman's Equation for the Temperature Dependence of Elastic Moduli of Oxide Compounds," *Physical Review,* vol. 144, no. 2, pp. 553-557, April 1966. [Online]. Available: https://doi.org/10.1103/PhysRev.144.553.

[432] E. J. Boyd, L. Li, R. Blue, and D. Uttamchandani, "Measurement of the temperature coefficient of Young's modulus of single crystal silicon and 3C silicon carbide below 273 K using micro-cantilevers," *Sensors and Actuators A: Physical,* vol. 198, pp. 75-80, August 2013. [Online]. Available: https://doi.org/10.1016/j.sna.2013.04.032.

[433] V. A. Drebushchak, "Thermal expansion of solids: review on theories," *Journal of Thermal Analysis and Calorimetry,* vol. 142, pp. 1097-1113, 2020. [Online]. Available: https://link.springer.com/article/10.1007/s10973-020-09370-y#Sec18.

[434] M. Hayakawa, J. B. Cohen, and T. B. Reed, "Measurement of the Lattice Parameter of Wustite at High Temperatures," *Journal of the American Ceramic Society,* vol. 55, no. 3, pp. 160-164, March 1972. [Online]. Available: https://doi.org/10.1111/j.1151-2916.1972.tb11243.x.

[435] J. Redden, "Chapter 9: Sequences, Series, and the Binomial Theorem," *Advanced Algebra*: Open Textbook Library, 2012, pp. 1977-2089. [Online]. Available: https://open.umn.edu/opentextbooks/textbooks/1248

[436] Y. M. Kozlovskii and S. V. Stankus, "The linear thermal expansion coefficient of iron in the temperature range of 130–1180 K," *Journal of Physics: Conference Series,* vol. 1382, 2019, doi: 10.1088/1742-6596/1382/1/012181.

[437] W. Li, H. Kou, X. Zhang, J. Ma, Y. Li, P. Geng, X. Wu, L. Chen, and D. Fang, "Temperature-dependent elastic modulus model for metallic bulk materials," *Mechanics of Materials,* vol. 139, December 2019. [Online]. Available: https://doi.org/10.1016/j.mechmat.2019.103194.

[438] W. Koster, "Die Temperaturabhängigkeit des blastizitätsmoduls reiner Metalle," *International Journal of Materials Research,* vol. 39, no. 1, pp. 1-9, 2021. [Online]. Available: https://doi.org/10.1515/ijmr-1948-390101.

[439] Wolfram Research Inc, *Wolfram|Alpha*, Champaign, IL, USA: Wolfram Research Inc, 2025. [Online]. Available: https://www.wolframalpha.com/.

[440] W. C. Young, R. G. Budynas, and A. M. Sadegh, "Dynamic and Temperature Stresses," *Roark's Formulas for Stress and Strain,* 8th ed.: McGraw-Hill, 2012. [Online]. Available: https://www.accessengineeringlibrary.com/content/book/9780071742474/chapter/chapter2

[441] J. L. Ruan, Y. Pei, and D. Fang, "On the elastic and creep stress analysis modeling in the oxide scale/metal substrate system due to oxidation growth strain," *Corrosion Science,* vol. 66, pp. 315-323, January 2013. [Online]. Available: https://doi.org/10.1016/j.corsci.2012.09.035.

[442] Schuler GmbH, "Sheet Metal Forming and Blanking," *Metal Forming Handbook.* Berlin, Germany: Springer, 1998, pp. 123-404. [Online]. Available: https://ebookcentral.proquest.com/lib/swansea-ebooks/detail.action?pq-origsite=primo&docID=3092167

[443] Z. Marciniak, J. L. Duncan, and S. J. Hu, "Sheet deformation processes," *Mechanics of Sheet Metal Forming,* Oxford, UK: Butterworth-Heinemann, 2002, pp. 14-29. [Online]. Available: https://ifind.swansea.ac.uk/permalink/44WHELF_SWA/1jlslid/alma9982816360024117

[444] Z. Marciniak, J. L. Duncan, and S. J. Hu, "Deformation of Sheet in Plane Stress," *Mechanics of Sheet Metal Forming,* Oxford, UK: Butterworth-Heinemann, 2002, pp. 30-44. [Online]. Available: https://ifind.swansea.ac.uk/permalink/44WHELF_SWA/1jlslid/alma9982816360024117

[445] W. A. Nash and M. C. Potter, "Combined Stresses," *Strength of Materials.* 5th ed. New York, NY, USA: McGraw-Hill, 2011. [Online]. Available: https://ifind.swansea.ac.uk/permalink/44WHELF_SWA/1jlslid/alma9983828415024117

[446] M. Jackson, *Periodic Table Basic: A QuickStudy Laminated Reference Guide*. BarCharts, 2018.

[447] W. C. Young, R. G. Budynas, and A. M. Sadegh, "Stress and Strain: Important Relationships," *Roark's Formulas for Stress and Strain,* 8th ed.: McGraw-Hill, 2012. [Online]. Available: https://www.accessengineeringlibrary.com/content/book/9780071742474/chapter/chapter2

[448] J. Li, Y. Qiu, H. Wang, and Z. Wang, "Estimation of the Strength Coefficient and Strain Hardening Exponent from Monotonic Tensile Properties of Steels.," *International Journal of Steel Structures,* vol. 19, pp. 1951-1968, July 2019. [Online]. Available: https://doi.org/10.1007/s13296-019-00256-w.

[449] K. L. Johnson, "Normal Contact of Elastic Solids – Hertz Theory," *Contact Mechanics*: Cambridge University Press, 1985. [Online]. Available: https://ifind.swansea.ac.uk/permalink/44WHELF_SWA/1jlslid/alma99739593402417

[450] G. W. Stachowiak and A. W. Batchelor, "Elastohydrodynamic Lubrication," *Engineering Tribology,* 4th ed. Oxford: Butterworth-Heinemann, 2014, pp. 293-370. [Online]. Available: https://ifind.swansea.ac.uk/permalink/44WHELF_SWA/144jshv/alma99819254820241 7

[451] W. van Enckevort, "Physical, Chemical, and Microstructural Characterization and Properties of Diamond," *Synthetic Diamond: Emerging CVD Science and*

Technology, K. E. Spear and J. P. Dismukes, Eds., New York, NY, USA: Wiley, 1994. [Online]. Available: https://www.wiley.com/en-us/Synthetic+Diamond%3A+Emerging+CVD+Science+and+Technology-p-9780471535898#tableofcontents-section

[452] T. Ohmura and M. Wakeda, "Pop-In Phenomenon as a Fundamental Plasticity Probed by Nanoindentation Technique," *Materials,* vol. 14, no. 8, 2021. [Online]. Available: https://doi.org/10.3390/ma14081879.

[453] *Metallic materials. Instrumented indentation test for hardness and materials parameters. Verification and calibration of testing machines*, BS EN 14577-2, 2015. [Online]. Available: https://bsol.bsigroup.com/Bibliographic/BibliographicInfoData/000000000030248594

[454] R. V. Owens, "Aerodynamic Characteristics of Spherically Blunted Cones at Mach Numbers from 0.5 to 5.0," National Aeronautics and Space Administration, George C. Marshall Space Flight Center, Huntsville, AL, USA, December 1965. [Online]. Available: https://ntrs.nasa.gov/api/citations/19660002849/downloads/19660002849.pdf

[455] J. Nemecek, "Uncertainties and Errors in Nanoindentation," *Nanoindentation in Materials Science*, J. Nemecek, Ed., Croatia: IntechOpen, 2012, pp. 53-86. [Online]. Available: https://ifind.swansea.ac.uk/permalink/44WHELF_SWA/1jlslid/alma99858903490241 7

[456] Z. Marciniak, J. L. Duncan, and S. J. Hu, "Material Properties," *Mechanics of Sheet Metal Forming,* Oxford, UK: Butterworth-Heinemann, 2002, pp. 1-13. [Online]. Available: https://ifind.swansea.ac.uk/permalink/44WHELF_SWA/1jlslid/alma99828163600241 7

[457] Y. Hidaka, T. Anraku, and N. Otsuka, "Deformation of Iron Oxides upon Tensile Tests at 600–1250°C," *Oxidation of Metals,* vol. 59, pp. 97-113, 2003. [Online]. Available: https://doi.org/10.1023/A:1023070016230.

[458] P. Scherrer, "Bestimmung der Größe und der inneren Struktur von Kolloidteilchen mittels Röntgenstrahlen," ed. Gottingen, Physikalisches Institut, 1918.

[459] C. Suryanarayana and M. G. Norton, "Precise Lattice Parameter Measurements," *X-ray Diffraction: A Practical Approach.* New York, NY, USA: Springer, 1998, pp. 153-166. [Online]. Available: https://ifind.swansea.ac.uk/permalink/44WHELF_SWA/1sssfk8/alma9985258803024 17

[460] G. G. Goviazin, D. Rittel, and A. Shirizly, "Achieving high strength with low residual stress in WAAM SS316L using flow-forming and heat treatment," *Materials Science and Engineering: A,* vol. 873, May 2023. [Online]. Available: https://doi.org/10.1016/j.msea.2023.145043.

[461] Z. Huda, "Forces and Power in Machining," *Machining Processes and Machines: Fundamentals, Analysis, and Calculations,* Boca Raton, USA: CRC Press, 2021, pp. 27-44. [Online]. Available: https://ifind.swansea.ac.uk/permalink/44WHELF_SWA/1jlslid/alma99885239490241 7

[462] E. K. Henriksen, "Residual Stresses in Machined Surfaces," *Transactions of the American Society of Mechanical Engineers,* vol. 73, no. 1, pp. 69-76, January 1951. [Online]. Available: https://doi.org/10.1115/1.4016145.

[463] M. Soori and B. Arezoo, "A Review in Machining-Induced Residual Stress," *Journal of New Technology and Materials,* vol. 12, no. 1, pp. 64-83, 2022. [Online]. Available: https://hal.science/hal-03679993v1.

[464] M. Kovac, "A method for residual stress measurement in welded seams," *Journal of Materials Processing Technology,* vol. 52, no. 2-4, pp. 503-514, June 1995. [Online]. Available: https://doi.org/10.1016/0924-0136(94)01733-H.

[465] T. Fry, "Evaluation of the Repeatability of Residual Stress Measurements Using X-Ray Diffraction," National Physical Laboratory, Teddington, UK, MATC(MN)19, May 2022. [Online]. Available: https://eprintspublications.npl.co.uk/2380/1/MATC_MN19.pdf

[466] Y. Murakami, "Cracks in a Circular Plate or in a Cylinder," *vol. 3*, *Stress Intensity Factors Handbook,* Oxford: Pergamon, 1987, pp. 305-346. [Online]. Available: https://ifind.swansea.ac.uk/permalink/44WHELF_SWA/1jlslid/alma99337234340241 7

[467] H. Bidmus, J. Chau, and K. Dechant, "Absolute Roughness of Pipes from Different Manufacturing and Treatment Methods and Impact on Pipeline Design," presented at the PSIG Annual Meeting, London, UK, 2019. [Online]. Available: https://onepetro.org/PSIGAM/proceedings-abstract/PSIG19/All-PSIG19/PSIG-1926/2124.

[468] P. P. Benham, R. J. Crawford, and C. G. Armstrong, "Stress-Strain Relations," in *Mechanics of Engineering Materials*, 2nd ed. Harlow, UK: Pearson Education, 1996, pp. 64-81.

[469] The MathsWorks Inc. "Workspace and Variable Preferences (MATLAB Help Center Documentation)." https://uk.mathworks.com/help/matlab/matlab_env/set-workspace-and-variable-preferences.html (accessed March. 17, 2025).

[470] U. S. Department of Commerce. (1996). *ARCCB-TR-96023, Elevated Temperature Properties of Steels*. [Online] Available: https://ntrl.ntis.gov/NTRL/dashboard/searchResults/titleDetail/ADA317919.xhtml

[471] M. S. Reed, M. Ferre, J. Martin-Ortega, R. Blanche, R. Lawford-Rolfe, M. Dallimer, and J. Holden, "Evaluating impact from research: A methodological framework," *Research Policy,* vol. 50, no. 4, 2021. [Online]. Available: https://doi.org/10.1016/j.respol.2020.104147.

[472] Research England. "Research Excellence Framework 2029: Guidance." https://2029.ref.ac.uk/guidance/ (accessed April, 9., 2025).

[473] Medr (Y Comisiwn Addysg Drydyddol ac Ymchwil). "Medr/2024/08: Wales Research Environment and Culture (WREC) Fund 2024/25." https://www.medr.cymru/en/News/medr-2024-08-wales-research-environment-and-culture-wrec-fund-2024-25/ (accessed April, 9., 2025).

[474] D. Bamford, I. Rein, P. Forrester, B. Dehe, J. Bamford, and M. Papalexi, "An empirical investigation into UK university–industry collaboration: the development of an impact framework," *Journal of Technology Transfer,* vol. 49, no. 4, pp. 1411-1443, August 2024, doi: 10.1007/s10961-023-10043-9.

[475] Tata Steel UK Limited. "Advances being made through Electric Arc Furnaces." https://www.tatasteeluk.com/corporate/news/advances-being-made-through-electric-arc-furnaces (accessed June. 12, 2025).

[476] M. Munday and K. Turner, "Steel Manufacturing in Wales: Ensuring a Sustainable and Prosperous Future," University of Strathclyde Institutional Academic Repository, 2020. Accessed: September, 2. [Online]. Available: https://pureportal.strath.ac.uk/en/publications/steel-manufacturing-in-wales-ensuring-a-sustainable-and-prosperou

[477] W. Xia, Y. Zhou, G. Bao, Z. Hou, S. Chu, P. Ren, Z. Liao, and H. Wang, "Recent research progress on recycling metallurgical waste slag and strengthening directional recovery of impurity elements by applied electric field," *Chemical Engineering Journal,* vol. 499, November 2024. [Online]. Available: https://doi.org/10.1016/j.cej.2024.156562.

[478] R. Farahat, M. Eissa, G. Megahed, and A. Baraka, "Reduction of mill scale generated by steel processing," *Steel Grips,* vol. 8, , pp. 88-92, January 2010. [Online]. Available: https://www.researchgate.net/publication/288874180_Reduction_of_mill_scale_generated_by_steel_processing.

[479] M. M. De Oliveira Junior, H. L. Costa, W. M. Silva Junior, and J. D. B. De Mello, "Effect of iron oxide debris on the reciprocating sliding wear of tool steels," *Wear,* vol. 426-427, pp. 1065-1075, April 2019. [Online]. Available: https://doi.org/10.1016/j.wear.2018.12.047.

[480] P. Lepesant, C. Boher, Y. Berthier, and F. Rezai-Aria, "A phenomenological model of the third body particles circulation in a high temperature contact," *Wear,* vol. 298-299, pp. 66-79, February 2013. [Online]. Available: https://doi.org/10.1016/j.wear.2012.08.019.

[481] C. Vergne, C. Boher, R. Gras, and C. Levaillant, "Influence of oxides on friction in hot rolling: Experimental investigations and tribological modelling," *Wear,* vol. 260, no. 9-10, pp. 957-975, May 2005. [Online]. Available: https://doi.org/10.1016/j.wear.2005.06.005.

[482] M. Dubar, N. Boualem, P. Moreau, J. G. La Barbera-Sosa, T. Sadat, R. Dubois, L. Dubar, and P. Bristiel, "Multi-scale approach to high-temperature impact of oxides and worn geometries on tribological behaviour at the part-tool interface," *Wear,* vol. 570, June 2025. [Online]. Available: https://doi.org/10.1016/j.wear.2025.205958.

[483] I. Jung and M. A. van Ende, "Computational Thermodynamic Calculations: FactSage from CALPHAD Thermodynamic Database to Virtual Process Simulation," *Metallurgical and Materials Transactions B,* vol. 51, pp. 1851-1874, October 2020. [Online]. Available: https://link.springer.com/article/10.1007/s11663-020-01908-7.

[484] Thermo-Calc Software AB. "GMH Teams up with Thermo-Calc Software to Develop a Physical Model of Secondary Steelmaking Metallurgy." Thermo-Calc Software AB,. https://tinyurl.com/2kfkf24e (accessed April. 16, 2025).

[485] A. Raj, I. A. Larsson, A. L.-. Ljung, T. Forslund, R. Andersson, J. Sundstrom, and T. Staffan Lundstrom, "Evaluating hydrogen gas transport in pipelines: Current state of numerical and experimental methodologies," *International Journal of Hydrogen Energy,* vol. 67, pp. 136-149, May 2024. [Online]. Available: https://doi.org/10.1016/j.ijhydene.2024.04.140.

[486] H. Nykyforchyn, L. Unigovskyi, O. Zvirko, O. Tsyrulnyk, and H. Krechkovska, "Pipeline durability and integrity issues at hydrogen transport via natural gas distribution network," *Procedia Structural Integrity,* vol. 33, pp. 646-651, 2021. [Online]. Available: https://doi.org/10.1016/j.prostr.2021.10.071.

[487] J. Liu, Y. Guo, X. Xing, X. Zhang, Y. Yang, and G. Cui, "A comprehensive review on hydrogen permeation barrier in the hydrogen transportation pipeline: Mechanism, application, preparation, and recent advances," *International Journal of Hydrogen Energy,* vol. 101, pp. 504-528, February 2025. [Online]. Available: https://doi.org/10.1016/j.ijhydene.2024.12.379.

[488] C. Tsiklios, M. Hermesmann, and T. E. Muller, "Hydrogen transport in large-scale transmission pipeline networks: Thermodynamic and environmental assessment of

repurposed and new pipeline configurations," *Applied Energy,* vol. 327, December 2022. [Online]. Available: https://doi.org/10.1016/j.apenergy.2022.120097.

[489] T. Rubben, T. Depover, K. Verbeken, R. I. Revilla, V. Barnier, A. Dreano, F. Christien, and I. De Graeve, "Scanning Kelvin probe force microscopy study of the effect of thermal oxide layers on the hydrogen release - Experiments and finite element method modelling," *International Journal of Hydrogen Energy,* vol. 48, no. 87, pp. 34067-34076, October 2023. [Online]. Available: https://doi.org/10.1016/j.ijhydene.2023.05.142.

[490] L. Vecchi, D. Pecko, N. Van den Steen, M. Haile Mamme, B. Ozdirik, D. Van Laethem, Y. Van Ingelgem, J. Deconinck, and H. Terryn, "A modelling approach on the impact of an oxide layer on the hydrogen permeation through iron membranes in the Devanathan-Stachurski cell," *Electrochimica Acta,* vol. 286, pp. 139-147, October 2018. [Online]. Available: https://doi.org/10.1016/j.electacta.2018.08.022.

[491] K. Stylidis, C. Wickman, and R. Soderberg, "Defining Perceived Quality in the Automotive Industry: An Engineering Approach," *Procedia CIRP,* vol. 36, pp. 165-170, 2015. [Online]. Available: https://doi.org/10.1016/j.procir.2015.01.076.

[492] M. F. Hussin and B. Wang, "Industrial safety perception among post-graduate engineering students," *Knowledge-Based Systems,* vol. 23, no. 8, pp. 769-771, December 2010. [Online]. Available: https://doi.org/10.1016/j.knosys.2010.04.013.

[493] R. Amaya-Gomez, V. Dumar, M. Sanchez-Silva, M. A. Torres-Cuello, A. Avila, and F. Munoz, "An analysis of engineering students' risk perception to support process safety learning process," *Education for Chemical Engineers,* vol. 42, pp. 7-19, January 2023. [Online]. Available: https://doi.org/10.1016/j.ece.2022.10.003.

[494] M. Cai, E. N. Seligsohn, Z. Zhang, and Y. Wang, "Risk Perception and Product Safety in User-Centered Design," presented at the ASME 2019 International Design Engineering Technical Conferences and Computers and Information in Engineering Conference, Anaheim, CA, USA, August, 18-21., 2019. [Online]. Available: https://doi.org/10.1115/DETC2019-98371.

[495] R. J. Willson, "Calorimetry," *Principles of Thermal Analysis and Calorimetry*, P. J. Haines, Ed., Cambridge, UK: Royal Society of Chemistry, 2002, pp. 129-165. [Online]. Available: https://ifind.swansea.ac.uk/permalink/44WHELF_SWA/1jlslid/alma9982842514024117

[496] X. Geng, F. Wang, H. H.-. Wu, S. Wang, G. Wu, J. Gao, H. Zhao, C. Zhang, and X. Mao, "Data-driven and artificial intelligence accelerated steel material research and intelligent manufacturing technology," *Materials Genome Engineering Advances,* vol. 1, no. 1, September 2023. [Online]. Available: https://doi.org/10.1002/mgea.10.

[497] Z. Rao, P. Y.-. Tung, R. Xie, Y. Wei, H. Zhang, A. Ferrari, T. P. C. Klaver, F. Körmann, P. T. Sukumar, A. Kwiatkowski da Silva, Y. Chen, Z. Li, D. Ponge, J. Neugebauer, O. Gutfleisch, S. Bauer, and D. Raabe, "Machine learning–enabled high-entropy alloy discovery," *Science,* vol. 378, no. 6615, pp. 78-85, October 2022. [Online]. Available: https://www.science.org/doi/epdf/10.1126/science.abo4940.

[498] C. Pei, Q. Ma, J. Zhang, L. Yu, H. Li, Q. Gao, and J. Xiong, "A novel model to predict oxidation behavior of superalloys based on machine learning," *Journal of Materials Science & Technology,* vol. 235, pp. 232-243, November 2025. [Online]. Available: https://doi.org/10.1016/j.jmst.2025.01.071.

[499] Q. Chen, "CALPHAD by Machine Learning and for Machine Learning," ed. Thermo-Calc AB: Thermo-Calc AB, 2024.

[500] N. Beech, J. Edy, D. Farrugia, and M. Auinger, "Augmenting the Thermodynamic Oxidation Data of Dual Phase Steels using Synthetic Data," in *7th Postgraduate*

Research Symposium on Ferrous Metallurgy, London, UK, 2024. [Online]. Available: https://www.mpiuk.com/postgraduate-research-symposium-2024.htm. [Online]. Available: https://www.mpiuk.com/postgraduate-research-symposium-2024.htm

[501] G. Grosso and G. Pastori Parravicini, "Interacting Electronic-Nuclear Systems and the Adiabatic Principle," *Solid State Physics,* 2nd ed. Oxford, UK: Academic Press, 2014, pp. 333-390. [Online]. Available: https://ifind.swansea.ac.uk/permalink/44WHELF_SWA/144jshv/alma998192443702417

[502] P. Shen, W. A. Bassett, and L. G.-. Liu, "Experimental determination of the effects of pressure and temperature on the stoichiometry and phase relations of wüstite," *Geochimica et Cosmochimica Acta,* vol. 47, no. 4, pp. 773-778, April 1983. [Online]. Available: https://doi.org/10.1016/0016-7037(83)90110-2.

[503] M. Hamada, S. Ganschow, D. Klimm, G. Serghiou, H. J.-. Reichmann, and M. Bickermann, "Wüstite (Fe1–xO) – Thermodynamics and crystal growth," *Zeitschrift für Naturforschung B,* vol. 77, no. 6, pp. 463-468, 2022. [Online]. Available: https://doi.org/10.1515/znb-2022-0071.